Geology, hydrothermal alteration, geochemistry, mineral geochemistry, and alteration textures of the lithocap at Bantug, Negros-Philippines

By

Carlos Andres Jimenez Torres (B. Sc. Eng. Geol., Hons)

Submitted in partial fulfilment of the requirements for the degree of

Doctor of Philosophy

February, 2017

UNIVERSITY OF TASMANIA

Declaration

This thesis contains no material which has been accepted for a degree or diploma by the University or by any other institution, except by way of background information and duly acknowledged in the thesis, and to the best of the candidate's knowledge and belief no material previously published or written by another person except where due acknowledgement is made in the text of the thesis.

Carlos Jiménez

Date: November 23rd, 2017

Confidentiality

This thesis is not to be made available for loan or copy for eighteen months following the date this statement was signed. Following that time, the thesis may be made available for loan and limited copying in accordance with the Copyright Act 1968.

Carlos Jiménez

Date: November 23rd, 2017

Abstract

Negros island is located in a complex tectonic setting in the central Philippines. The lithocap at Bantug is one of several laterally extensive lithocaps in central Negros. Volcanic rocks from the Pleistocene to Holocene Canlaon Volcanic Complex have been altered to advanced argillic and silicic mineral assemblages, and intruded by diorite porphyries and hydrothermal breccias from the Pleistocene Bantug Intrusive Complex (BIC). The lithocap at Bantug extends over 6 km, and has an approximate thickness of 600 m, transitioning downwards into hornfels that has developed in the Pliocene-Pleistocene Caliling Formation. REE and other geochemical anomalies were detected during this study but no significant concentrations of precious and base metals have been found to date.

The Bantug lithocap formed in plagioclase-phyric andesites, aphyric andesites, and volcaniclastic andesitic breccias of the Quaternary Canlaon Volcanic Complex. The lithocap is genetically linked to magmatic-hydrothermal activity caused by the BIC. At least four intrusions and two hydrothermal breccias comprise the BIC. The intrusive complex consists of an early diorite porphyry (U-Pb zircon ages: 1.37 ± 0.10 Ma; 1.35 ± 0.30 Ma), and at least three phases of dikes (U-Pb zircon ages: 1.25 ± 0.31 Ma; 1.06 ± 0.29 Ma). The dikes are dioritic in composition, have plagioclase-phyric textures, and some contain miarolitic cavities filled with epidote and quartz. The diorite porphyry is intensely phyllic-altered and the diorite porphyry dikes have undergone moderate propylitic and argillic alteration.

Drilling in the lithocap intercepted hydrothermal breccias. The breccia bodies have drill hole intercepts of 5 to 325 m. The hydrothermal breccias display advanced-argillic altered clasts, and quartz-pyrite cemented breccias contain juvenile clasts.

Silicic, kaolinite-dominated argillic, montmorillonite-dominated argillic, advanced-argillic, and phyllic hydrothermal alteration assemblages characterise the Bantug lithocap. Surface SWIR analyses over a 2.5 km northeast transect revealed a marked transition from alunite to pyrophyllite and muscovite-bearing samples. Drill hole results transitioned from argillic and advanced argillic alteration associated with hydrothermal breccias in the southwest, to phyllic alteration associated with the diorite porphyry to the northeastern part of the studied area. Index of crystallinity values are higher to the northeast, implying a higher temperature fluid source in this area.

Mass balance calculations for the plagioclase-phyric andesites of the Canlaon Volcanic Complex revealed significant losses of most elements in silicic-altered samples in the northeast.

The same area saw significant gains of SiO_2 and TiO_2. Alteration index and advanced argillic alteration index values increase markedly to the northeast both in surface and drill hole samples.

Magmatism and fragmentation processes produced extensive geochemical anomalism at Bantug. Although base and precious metals results were below ore-grade, trace element concentrations revealed anomalous areas. Rare high copper and gold values from Bantug lithocap are associated with advanced argillic-altered aphyric andesite (i.e., 2,517 ppm Cu) and plagioclase-phyric andesite samples (i.e., 0.56 ppm Au). Systematic analyses of surface and drill hole geochemistry results revealed HFSE, REE, transition metals, and base metals anomalism in the northeastern part of the study area. This coincides with the presence of high temperature minerals (i.e., pyrophyllite, zunyite, and muscovite) and high alteration index values (i.e., 93.6 to 96.3).

LA-ICP-MS analyses of alunite, pyrite, magnetite, chlorite and epidote revealed many similarities between the Bantug lithocap, propylitic-altered rocks from Batu Hijau, and the Mankayan lithocap. The variations in alunite compositions from Bantug (i.e., Na, La, Sr, Pb, Sr/Pb, 100 La/Pb, Pb, La, and Pb/Sr) vary systematically with respect to the location of diorite porphyry intrusions intercepted by drill holes. The trace element composition of alunite samples from Bantug compares favourably with that of alunite samples from Mankayan. Trace element variations represent vectors towards potential mineralised centres. The trace element composition of pyrite, chlorite and magnetite samples from Bantug is comparable with that of samples from Batu Hijau, and indicates a potential heat source located at distances from the sample locations greater than 1.5 km, possibly at depth. Similar results were acquired from comparing trace element results for epidote from Bantug with results from Baguio.

Patchy-wormy (gusano) textures are known to occur at the base of several lithocaps around the world, and were observed in surface and drill hole samples from Bantug. Patchy textures are characterised by amoeboid-like, sub-rounded to rounded clusters of clay minerals, sulfates, and sulfides, in a fine-grained granular quartz groundmass. Wormy texture is characterised by contorted quartz veins, which commonly occur with patchy texture. Patchy features from Bantug are composed of pyrophyllite, alunite, diaspore, muscovite, APS minerals, zunyite, rutile, pyrite, and quartz. These are interpreted to be the product of dissolution of primary volcanic features due to repetitive exposure to fluxes of acid, halogen-bearing hydrothermal fluids.

Sedimentation of the Pliocene-Pleistocene Caliling Formation took place under shallow marine conditions (i.e., 5.33 to at least 1.93 Ma), based on the presence of several limestone horizons along the eastern coast of Negros. The Pleistocene to Holocene Canlaon Volcanic Complex rocks are interpreted to have been deposited above sea level. Magmatism and emplacement of the Pleistocene Bantug Intrusive Complex began around 1.65 Ma. Extensive hydrothermal alteration is genetically linked to emplacement of the BIC. Large areas of silicic and advanced argillic-altered volcanic rocks of the CVC indicate that hydrothermal alteration took place above sea level and that sea water did not dilute hydrothermal acid fluids generated by the BIC. The hydrothermal system at Bantug formed large volumes of silicic-altered volcanic rocks, surrounded by argillic-altered volcanic rocks, which transition to depth to phyllic-altered diorite porphyritic intrusions. Incipient stockwork formed in the phyllic-altered diorite porphyry intercepted by exploration drill holes; however, base and precious metals results in the lithocap and intrusions were below ore grade (i.e., mean values: 147.7 ppm Cu; 9.994 ppm Mo; 0.01499 ppm Au; 0.07056 ppm Ag). The apparent absence of mineralisation at Bantug could indicate that: i) the mineralised centre has not been intersected by drill holes, ii) ore-forming physicochemical conditions were inefficient, or iii) the causative intrusion was metal-depleted. Pathfinder element concentrations in vuggy-quartz intercepted by drill holes, hydrothermal breccias, magmatic-hydrothermal breccias, and patchy-wormy textures development at Bantug provide encouragement for continuing exploration in the lithocap for concealed porphyry and epithermal mineral deposits. Parts of the Bantug lithocap remain unexplored and untested by drill holes. Zunyite, high AI values, muscovite, pyrophyllite, and whole rock geochemistry highlight the northeastern area as a priority target for future exploration. Organic-matter rich horizons within the Pliocene-Pleistocene Caliling Formation may also represent traps for hydrothermal fluids and future exploration should consider the potential occurrence of a skarn deposit in the limestone horizons.

Kindness by Naomi Shihab Nye

Before you know what kindness really is
you must lose things,
feel the future dissolve in a moment
like salt in a weakened broth.
What you held in your hand,
what you counted and carefully saved,
all this must go so you know
how desolate the landscape can be
between the regions of kindness.

Acknowledgements

I would like to begin by acknowledging the University of Tasmania for granting me scholarships that allowed me to develop this research project. I would also like to acknowledge the contributions made by every member of my supervisory panel, as well as their thorough editorial reviews. This manuscript benefited from reviews and edits by Professor David Cooke and Dr Michael Baker. I would like to thank all the staff of the AMIRA project P1060 "Enhanced geochemical targeting of magmatic-hydrothermal systems" for their scientific contributions to my project and the current level of understanding of all things porphyry-lithocap.

I am sincerely thankful to all the staff from Freeport-McMoRan in the Philippines for their help while developing this research project. I would like to thank Ramon Taningco and Dr David First for approval to access the study site and information. Also, thanks to Nicodemo Lobino, Ingemar Arellano, Leonardo Subang, and Djohanne Celiz for their outstanding logistical support while at Bantug and overseas.

Thanks to Al Cuison and Michelle Chapple-Smith for preparing high-quality polished slabs, thin sections, and laser mounts at the lapidary of the University of Tasmania.

I would like to express my most sincere gratitude to the remarkable staff at the Central Science Laboratory of the University of Tasmania: Dr Sandrin Feig, Dr Karsten Goemann, and Dr Thomas Rodemann. It is absolutely necessary to highlight your professionalism and excellent work. Many thanks for your patience and assistance with the FE-SEM, EPMA, and the Raman laser.

Special thanks to Dr Sarah Gilbert, Dr Jay Thompson, and Professor Leonid Danyushevsky for their assistance with the LA-ICP-MS work performed during this project. Your kindness and friendliness made the long hours at the laser more amenable.

Thanks to Professor Sebastien Meffre and Dr Jay Thompson for LA-ICP-MS analyses of zircons. Thanks to Dr Nathan Fox for his contributions with the XRD analyses and interpretations at the University of Tasmania. I sincerely appreciate the urgency with which you treated my requests.

Thanks to Mrs Deborah Macklin, Dr Anita Parbhakar-Fox, Dr Nathan Fox, Dr Jacqueline Halpin, Dr Garry Davidson, Professor Dima Kamenetsky, Dr Julie Hunt, Dr Chun Kit Lai, Dr Jeff Steadman, Dr Rebecca Carey, Dr Karin Orth, and Professor Kim Zaw for their friendly

attitude while I was at CODES. Those smiles and "g'day" greetings in the winter's mornings really did make a difference for some us (i.e., busy and stressed international students). I thank you for that.

I would like to thank Professor Zhaoshan Chang for providing a welcoming and inclusive environment to work at while I visited EGRU at James Cook University, Queensland. Also, I am deeply grateful for all of his encouraging words, objective and constructive observations, and Joy's hospitality. Dr Chang is one of the most welcoming and kind individuals that any human being can come across in their lifetime.

I am very grateful for Dr Lejun Zhang's contribution to my project and to me as a person. Dr Zhang is one of the most outstanding scientists I have ever met; a relentlessly dedicated geologist with an insatiable curiosity, notorious for his attention to the detail. Dr Zhang collected the significantly large SWIR dataset from Bantug, a remarkable task achieved in record time. As a nomad, as a geologist, and a human being I feel a great deal of respect and admiration towards Dr Zhang. Thank you very much for being my unofficial supervisor. Thank you for your generosity and hospitality, for your friendship, and for introducing me to the unparalleled wonders of Chinese cuisine.

I am very grateful and consider myself very fortunate to have had an exceptional postgraduate supervisor and mentor. He is by far the best PhD supervisor any student in the world can have: Professor Noel White. I first met Professor White in 2007 while attending an SEG course in Lima, Peru. Professor White's remarkable presentation skills were simply inspiring. Professor White encouraged me to start the very first SEG student chapter in Colombia and he was a terrific honorary supervisor during my honours thesis (i.e., Sedimentary-hosted copper prospects in the Perija Range, Colombia). Professor White also played a major role as a mentor during the early stages of my career while working on exploration for high-sulfidation and porphyry deposits in Colombia and Panama. I was also fortunate enough to have extensive exposure to Professor White's knowledge while working in the AMIRA project P1060. Professor White is an outstanding geologist and all students around him get to be better at their jobs because of watching him do his. Professor White is characterised for treating others around him with respect regardless of their ethnicity, cultural background, or native language. Noel, you are one of the most respectful, decent, generous, inspiring, and kind human beings I have been able to meet. I got to be a better person just from having known you and learning from your example. I owe you and I thank you for your relentless and restless support.

I would like to acknowledge the innumerable friendly gestures of my peers Cesar Calderon, Jose Piquer, Margy Hawke. Thank you for offering me your friendship.

I have been very lucky and privileged to have had the relentless support and unconditional love of Stephanie Mrozek and my brave parents: Rosita and Melqui. Thank you for your patience and love. You were bright lighthouses when things were dark and foggy.

Table of Contents

List of Figures

Chapter 1: Introduction

Chapter 2: Regional geology

Chapter 3: Geology, geochronology, and geochemistry of the Bantug prospect

Chapter 4: Alteration and mineralisation in the lithocap at Bantug

Chapter 5: Mineral geochemistry

Chapter 6: Patchy-wormy textures at Bantug

Chapter 7: Summary and exploration implications

List of Tables

Chapter 6: Patchy-wormy textures at Bantug

List of Appendices

CHAPTER 1:

INTRODUCTION

1.1. Preamble

Lithocaps are large volumes of hydrothermally altered rocks that may contain magmatic-hydrothermal ore deposits such as porphyry, high or low-sulfidation epithermal deposits, and skarn deposits. The Philippine archipelago contains a large number of porphyry and epithermal (i.e., high and low-sulfidation) deposits, as well as skarn deposits. Porphyry, high and low-sulfidation deposit models have been developed based partly on observations from the Philippines. The current level of understanding of these magmatic-hydrothermal systems is a result of the detailed work by many authors in the Philippines (i.e., Sillitoe and Gappe, 1984; Mitchel and Leach, 1990; Cooke and Bloom, 1990; Hedenquist et al., 1998; Rae, 2002; Braxton, 2007; Rohrlach, 2002; Waters et al., 2011; Chang et al., 2011).

Despite the advanced-stage exploration status of some areas in the Philippine archipelago there are other areas that remain unexplored or underexplored. The lithocap at Bantug is one of those underexplored areas. The Bantug area is located on the eastern part of Negros (Fig. 1.1). Negros has been explored since the 1960s, with most exploration efforts focused on the western side of the island where porphyry-style mineralisation crops out (i.e., the southwest Negros porphyry district). Several large areas of hydrothermal alteration occurring in the eastern side of Negros have also been explored since the 1960s; however, at present no orebodies have been found. These hydrothermally altered areas are mostly lithocaps, large areas of advanced-argillic, argillic, and silicic alteration with no evident concentrations of precious and base metals.

The lithocap at Bantug has been explored by Freeport-McMoRan since 2008. Freeport-McMoRan has been an active partner in collaborative research with CODES at the University of Tasmania. As part of Freeport's exploration effort at Bantug in 2008, the lithocap was included as a study site in the AMIRA project P765A "Geochemical and Geological Halos in Green Rocks and Lithocaps"; this project was completed in 2010. The P765A project was followed in 2011 by the AMIRA project P1060: "Enhanced Geochemical Targeting in Magmatic-hydrothermal Systems", which also included the lithocap at Bantug as a study site. This dissertation elaborates on the research outcomes from Bantug during the AMIRA P1060 project.

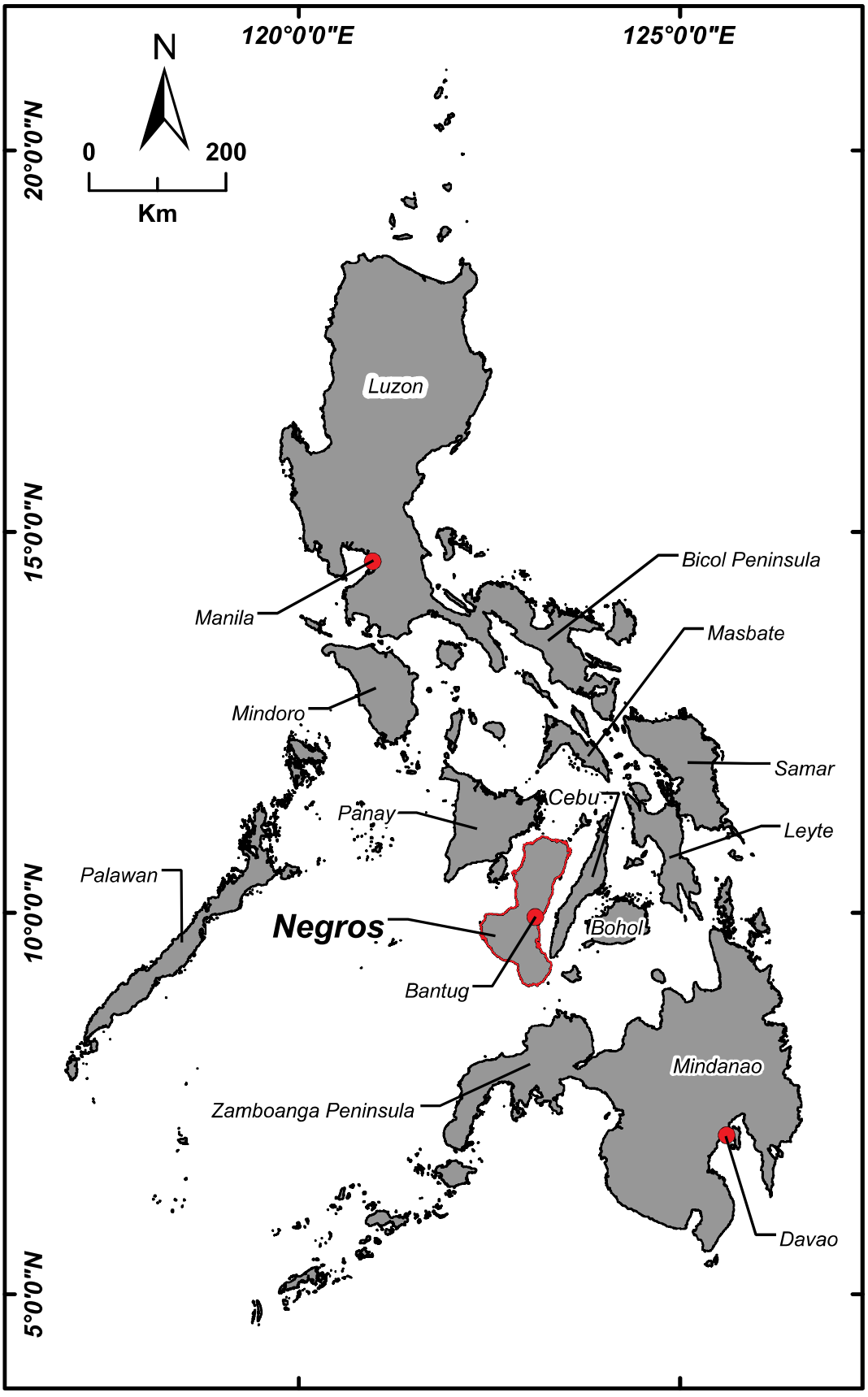

Figure 1.1. The Philippines and Negros island location. Red circles are major cities. The red circle in Negros indicates the position of the Bantug area (this study).

1.2. Lithocaps and their associated porphyry and epithermal deposits

1.2.1. Lithocaps

Lithocaps are large areas (0.32 to 117.9 km^2; Fig. 1.3; Table 1.1), of advanced argillic, silicic, and propylitic altered rocks. Lithocaps can reach up to 2 km in thickness, and they generally exhibit horizontal to sub-horizontal tabular geometry (Fig. 1.5; Sillitoe 2010; Chang et al., 2011; Hedenquist and Taran, 2013). Lithocaps are spatially (Fig. 1.4; Sillitoe, 1999; Hedenquist et al., 2000; Chang et al., 2011), temporally (Hedenquist et al., 1998; Muntean and Einaudi, 2001), and genetically (Fig. 1.5; Hedenquist et al., 1998; Muntean and Einaudi, 2001, Rae et al., 2003; Hedenquist and Taran, 2013) related to underlying intrusions that may be or not genetically associated with porphyry style mineralisation.

Lithocaps can host or be associated with:

- High-sulfidation (Hedenquist et al., 2000) or quartz-alunite (Simmons et al., 2005) Au-Cu epithermal deposits (e.g., Yanacocha district; Teal and Benavides, 2010)
- Low-sulfidation (Cooke and Simmons, 2000) or quartz-adularia (Simmons et al., 2005) Au-Ag epithermal deposits (e.g., Acupan, Baguio Gold, and Nugget Hill, Baguio district; Waters et al., 2011)
- Skarn deposits (e.g., Thanksgiving Au-Zn skarn, Baguio district; Waters et al., 2011)
- Porphyry deposits (e.g., Far-Southeast porphyry Cu-Au, Mankayan district; Hedenquist et al., 1998; Chang et al., 2011)

1.2.2. High-sulfidation epithermal deposits

High-sulfidation (HS) epithermal Au-Cu deposits have been described in great detail by several authors (Stoffregen and Alpers, 1987; White, 1991; Hedenquist et al., 2000; Simmons et al., 2005.).

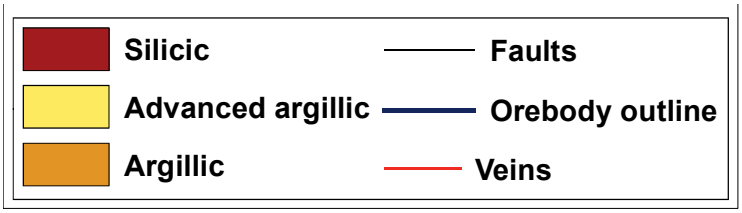

Figure 1.2. Selected lithocaps, high sulfidation, and porphyry deposits around the circum-Pacific. Legend for Figure 1.3.

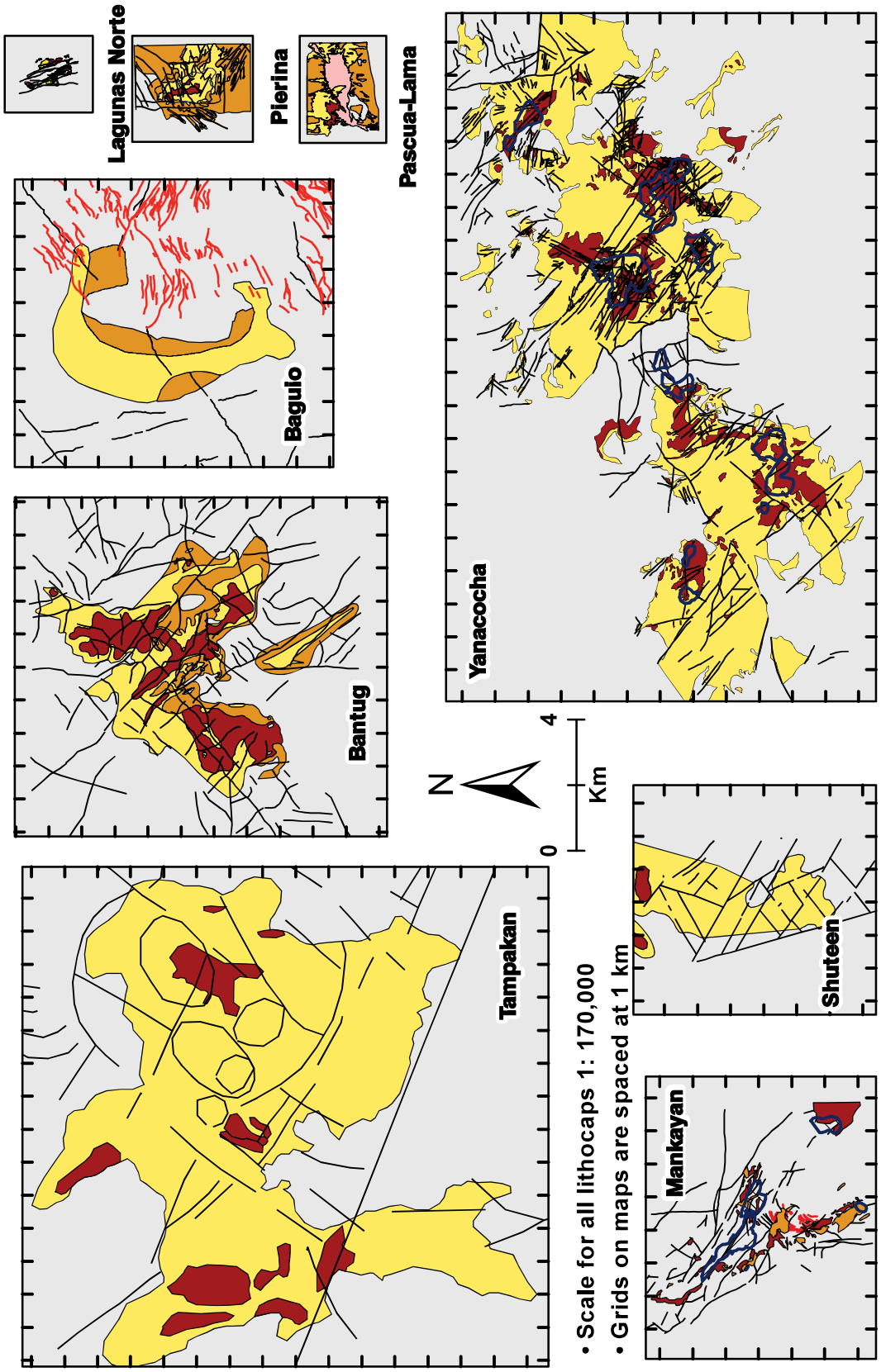

Figure 1.3. Selected lithocaps, high sulfidation, and porphyry deposits around the circum-Pacific. Hydrothermal alteration maps for nine selected lithocaps around the circum-Pacific. All maps are in the same scale (1:170,000) and grids are spaced at 1 km for comparison; references and resources are presented in Table 1.1.

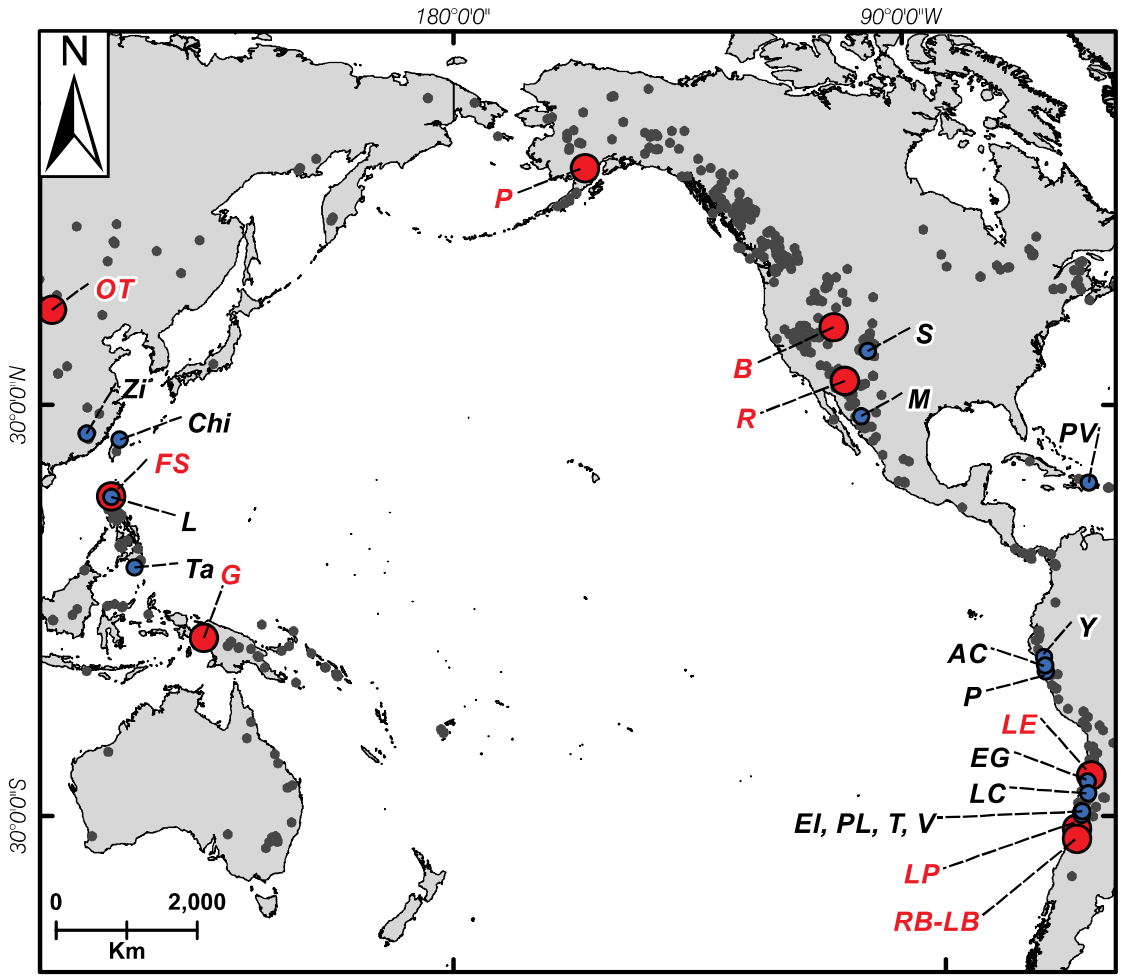

Legend

- Porphyry deposits
- High-sulfidation deposit
- Porphyry occurence

Porphyry deposits

B: Bingham
FS: Far Southeast
G: Grasberg
LE: La Escondida
LP: Los Pelambres
OT: Oyu Tolgoi
P: Pebble
R: Resolution
RB-LB: Rio Blanco-Los Bronces

High-sulfidation deposits

AC: Alto Chicama
Chi: Chinkuashi
EG: El Guanaco
El: El Indio
L: Lepanto
LC: La Coipa
M: Mulatos
P: Pierina
PL: Pascua Lama
PV: Pueblo Viejo
S: Summitville
T: Tambo
Ta: Tampakan
V: Veladero
Y: Yanacocha
Zi: Zijishan

Figure 1.4. Selected lithocaps, high sulfidation, and porphyry deposits around the circum-Pacific. Porphyry occurrences are in black circles, selected porphyry and high-sulfidation deposits are in red and blue circles, respectively. Porphyry deposits locations are from Singer et al. (2008).

HS epithermal deposits are major sources of gold, copper, and silver. Some of the best examples of this deposit type include the Pascua-Lama deposit in Argentina (17.8 Moz. Au; Chouinard et al., 2005), Pueblo Viejo in the Dominican Republic (23.7 Moz. Au; Arribas et al., 2011), and the Yanacocha district in Peru (~70 Moz.; Figs. 1.2 and 1.3; Teal and Benavides, 2010;).

HS epithermal deposits are characterised by the presence of high-sulfidation state ore minerals (i.e., enargite and luzonite), hosted in highly porous and permeable silicic altered rocks known as 'vuggy silica' (Steven and Ratte, 1960). In such rocks SiO_2 is the major (~95 wt %) component.

Table 1.1. Summary of resource figures from selected circum-Pacific lithocaps

Lithocap	Country	Lat.	Long.	Area (Km^2)	Au (Moz)	Cu (Mt)	Reference
Yanacocha	Peru	7.221°	78.445°	84.92	70		Teal and Benavides (2010)
Tampakan	Philippines	6.491°	125.082°	117.49	17.6	15	Rohrlach (2002)
Bantug	Philippines	10.003°	123.053°	29.21	0		This volume
Baguio	Philippines	16.338°	120.642°	15.15	12	1.2	Waters et al. (2011)
Shuteen	Mongolia	44.004°	107.668°	11.66	0		Batkhishig et al. (2010)
Mankayan	Philippines	16.886°	120.784°	2.94	>19.8	4.6	Chang et al. (2011)
Pierina	Peru	9.459°	77.588°	8.56	7.2		Rainbow et al. (2005)
P.-L.[1]	C.-A.[2].	29.323°	70.023°	3.68	17.6		Chouinard et al. (2005)
L.N.[3]	Perú	7.948°	78.243°	0.32	13.1		Cerpa et al. (2013)

[1]P.-L.: Pascua-Lama; [2]C.A.: Chile-Argentina; [3]L.N.: Lagunas Norte.

HS epithermal Au-Cu deposits are characterised by vertical and sub-horizontal bodies of 'vuggy silica' enveloped by zones of advanced argillic alteration mineral assemblages (i.e., alunite, kaolinite, montmorillonite, illite, dickite, pyrophyllite, APS minerals, zunyite, and diaspore). The advanced argillic alteration zone grades outwards to zones of propylitic alteration (e.g., chlorite, epidote).

It is generally accepted that HS epithermal deposits form in a two-stage process involving: alteration, and mineralization (White, 1991; Hedenquist et al., 1994; Hedenquist et al., 2000). Based on isotopic data and textural observations in 'vuggy quartz', it has been suggested that magmatic gas condenses in ground water at shallow levels, reacts with the host rocks to create porosity, and later metal-bearing fluids permeate the altered-porous rocks to precipitate metals (Stoffregen and Alpers, 1987; Hedenquist et al., 1994; Saunders, 1994).

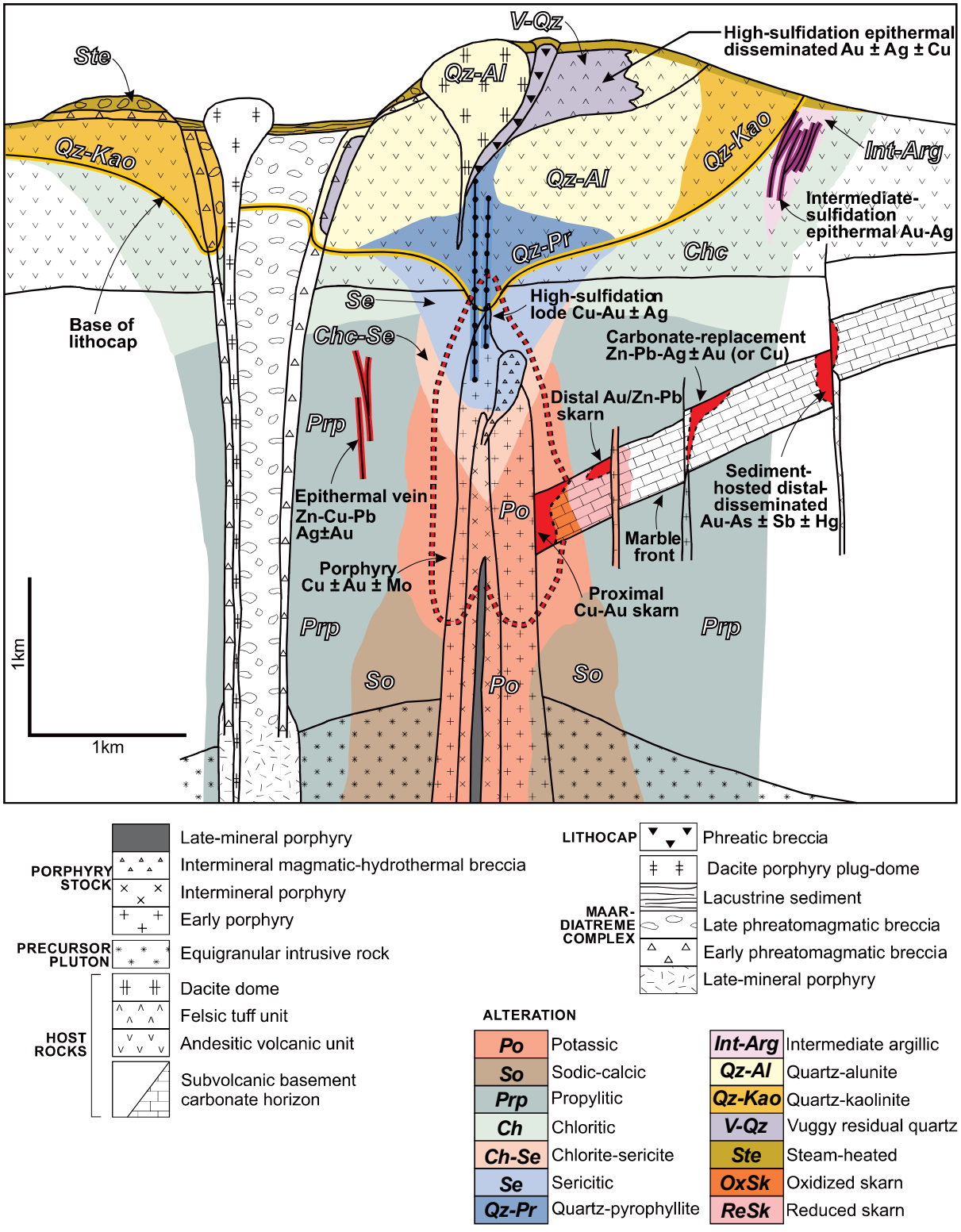

Figure 1.5. Schematic illustration of alteration zoning and overprinting relationships in a porphyry system. Modified from Sillitoe (2010).

Such metal-bearing fluids are considered to form at 200-350°C, and at depths of ~200-600 m based on fluid inclusion homogenization temperatures (Deen et al., 1994; Hedenquist et al., 1994; Hedenquist et al., 1998; Kouzmanov et al., 2010) and isotope fractionation (Rye et al., 1991; Hedenquist et al., 1998; Bethke et al., 2005; Deyell et al., 2005).

1.2.3. Porphyry deposits

Porphyry deposits have been the subject of detailed research, in almost every field of geology, for several decades (Titley and Beane 1981; Seedorff et al., 2005; Sillitoe, 2010). Porphyry deposits are the world's largest sources of Cu and Mo, and can be major sources of other metals such as Au, Ag, W, and Sn. The large volume (up to 8 km^3), diversity of commodities, and considerably long operational lives, make porphyry deposits one of the premium targets for mining companies and explorers around the world. Some of the best examples of porphyry deposits in the circum-Pacific region include the Grasberg deposit in Indonesia (~380 Mt Cu; Leys et al., 2012), Chuquicamata in northern Chile (>130 Mt Cu; Rivera et al., 2012), Oyu Tolgoi in Mongolia (41.7 Mt Cu; Crane and Kavalieris, 2012), and the Bingham Canyon deposit in the U.S.A. (17.4 Mt Cu; Porter et al., 2012).

Porphyry deposits have a spatial, temporal, and genetic association with geodynamic processes at convergent plate margins where hydrous melts are generated in the sub-arc mantle (Richards, 2003). Porphyry deposits form due to magmatic-hydrothermal processes in which the deep-seated hydrous melts transport metals and volatiles to magmatic chambers at depths of approximately 1-6 km, where crystal fractionation and volatile exolution result in stockwork formation or porphyry-style mineralisation (Richards, 2003; Seedorff et al., 2005; Sillitoe, 2010).

Hydrothermal alteration in porphyry deposits defines a three-dimensional zoning pattern in and around the central, mineralized, intrusive complex (Fig. 1.5; Sillitoe, 2010). Porphyry style mineralisation is associated with the development of stockwork veining, and is spatially and genetically related to K-silicate hydrothermal alteration at the core of the intrusive complex. Stockworks are characterised by high density quartz veining with minor amounts of chalcopyrite ± bornite ± magnetite. Porphyry orebodies comprise large volumes of stockwork, high grade breccias (i.e., Rio Blanco – Los Bronces; Toro et al., 2012), and skarns (Kucing Liar, Ertsberg-Grasberg district; Leys et al., 2012). Some porphyry deposits can be enriched by supergene processes that form high grade chalcocite-rich blankets above primary sulfides

(e.g., Oyu-Tolgoi, Perelló et al., 2001; Escondida, Padilla-Garza et al., 2001; Hervé et al., 2012).

Early K-silicate alteration forms at the core of porphyry deposits. This is followed by a halo of propylitic alteration which extends laterally for several kilometres away from the deposit (Fig. 1.5). Later, clay-rich mineral assemblages (i.e., phyllic, intermediate argillic, argillic, and advanced argillic) flare upwards through faults and overprint earlier potassic and propylitic alteration. Roughly coeval, near paleo-surface (<1 km) lateral flow of acidic fluids along permeable horizons may produce lithocaps (Sillitoe, 2010).

The K-silicate alteration footprint in most porphyry deposits coincides with the orebody outline (i.e., Resolution; Henke et al., 2012). Hence, K-silicate alteration represents a direct vector for mineralised intrusive centres. The propylitic alteration footprint in porphyry deposits can extend beyond 3 km from the K-silicate alteration and the porphyry orebody (i.e., Batu Hijau; Garwin, 2000). Detailed mapping of mineral assemblages in the propylitic altered rocks can provide a useful vector toward the potassic altered core of a porphyry deposit (Sillitoe, 2010).

The spatial and genetic relation between lithocaps, HS epithermal deposits, and porphyry Cu-(Mo-Au) deposits has been recognized and well documented at continental, district, and deposit scale. However, accurate targeting and effective vectoring of deposits within the lithocap and the propylitic alteration environments remains a challenge. Chang et al. (2011), Cooke et al. (2014), and Wilkinson et al. (2015) used LA-ICP-MS mineral chemistry data from alunite, epidote, and chlorite respectively, to evaluate their vectoring potential for porphyry deposits. These studies succeeded at defining efficient vectors toward mineralized centres within large areas of hydrothermally altered rocks (i.e., lithocaps, and propylitic alteration) using mineral chemistry.

1.3. Previous work and exploration history

Systematic exploration for base and precious metals in Negros Island started during the 1970s when Maricalum Mining, the Construction and Development Corporation of the Philippines (CDCP) and Lepanto Mining explored the south-western area of the island for copper. Intense exploration programs in south-west Negros resulted in the discovery of Sipalay (807 Mt at 0.47 % Cu, 0.01 % Mo, 1.5 ppm Ag and 0.05 ppm Au; Singer et al., 2008, and references therein), Basay (262 Mt at 0.44 % Cu, 0.008 % Mo, 1.5 ppm Ag and 0.29 ppm Au; Sillitoe and Gappe, 1984; BMG, 1986) and Hinobaan (440 Mt at 0.41 % Cu, 0.34 ppm Ag and 0.14 ppm Au;

Sillitoe and Gappe, 1984) porphyry Cu-Mo±Au deposits. The Sipalay and Basay porphyry Cu-Mo deposits were mined by Maricalum and CDCP, respectively (Border, 2005; Subang et al., 2009).

Brownfields exploration around the Basay mine led to the discovery of the Bulawan breccia-hosted intermediate-sulfidation epithermal Au-Ag deposit (17.5 Mt at 2.25 g/t Au; Philex Mining Corp., 2011), which was acquired by Philex Mining Corporation in 1990 and completed production in 1996. During the 1990s, Selenga Mining (i.e., 1991) and International Pursuit (i.e., 1995-1997) continued resource definition drilling at the Hinobaan porphyry Cu-Au deposit. However, the project has not passed the pre-feasibility stage to date (Border, 2005; Subang et al., 2009). Maglambayan et al. (1998) reported sphalerite, galena, chalcopyrite, tetrahedrite-tennantite with minor amounts of electrum associated with carbonates. This mineralogy reflects and intermediate-sulfidation state of the mineralizing fluid.

Large areas of intense silicic alteration in volcanic rocks of middle Miocene-Pliocene age have been identified in eastern and northern Negros (Sillitoe and Gappe, 1984). Artisanal mining for quartz, sulphur and gypsum has been performed intermittently in eastern and northern Negros since the 1960s. During the 1960s Benguet Corporation explored the areas of Pamplona, Ayungon and Bantug for sulphur. In 1982–1983, Benguet revisited the Ayungon area, exploring for gold (Sillitoe and Gappe, 1984; Subang et al., 2009).

From 1985 to 1987 the Mines and Geosciences Bureau (MGB) and the United Nations Development Programme (UNDP) conducted a training program for local geologists on exploration for precious and base metals in epithermal mineral deposits in the Philippines. The program included geochemical surveys, and geologic and hydrothermal alteration mapping. In Negros Island the program focused on the Amlan, Palinpinon, Pamplona and Ayungon areas. The outcome of the MGB–UNDP project was identification and location of several areas of intense quartz-clay alteration coincident with geochemical anomalies (Mitchell and Leach, 1991).

From 1989 to 1991, Philex Mining Corporation reviewed the MGB-UNDP results on Negros and explored the Ayungon area for gold, but was unable to define a significant mineralized zone. During the same period, the Philippine National Oil Corporation (PNOC) conducted mineral exploration programs in their geothermal fields at Palinpinon. PNOC and Kenmare Resources created a joint venture in 1990 to explore for copper and gold in the geothermal

fields in south eastern Negros. The joint venture program ended in 1995 after a drilling program at Siaton yielded negative results (Domasig, 1999; Subang et al., 2009).

In 1996, using geologists from the MGB-UNDP program, Western Mining Corporation (WMC) started an exploration program in central-eastern Negros. The program aimed to evaluate the potential of the large, intensely altered quartz-clay areas at Ayungon and Bantug. WMC used a high sulfidation Cu-Au epithermal conceptual exploration model for the areas and interpreted the hydrothermally altered outcrops as advanced argillic (AA) altered areas. WMC carried out soil geochemistry surveys and identified weak copper anomalies and point gold anomalies. Based on geochemical survey results and geologic-hydrothermal alteration mapping, WMC interpreted the alteration to be related to low sulfidation epithermal mineralisation of small economic potential and in 1998 decided to terminate exploration activities in Negros (Domasig, 1999; Subang et al., 2009).

During May and June of 1999, Normandy Asia Philippines Inc. (Normandy) carried out a regional bulk leach extractable gold (BLEG) geochemical program in the areas of Ayungon and southern Bantug. Based on the results Normandy considered the southern Bantug area not prospective and considered the Ayungon area to have potential to host low sulfidation epithermal deposits. No further exploration activities were carried out by Normandy (Domasig, 1999; Subang et al., 2009).

In 2002 Phelps Dodge evaluated the Bantug area. Covellite was identified in vugs in quartz altered float from the Guincalaban section of the Hilabangan River, which drains the quartz-clay intensely altered south-eastern part of the Bantug area. This was the first time copper minerals were recognized in the area and it was considered an indicator of potential for high sulfidation style mineralisation (Taningco, 2002).

In 2006 Phelps Dodge revisited the Bantug area and carried out an intense exploration program: regional mapping and geochemical surveys (rock, BLEG and stream sediment sampling) were performed. Enargite with secondary covellite was identified in vuggy quartz and quartz-alunite breccia float; chalcopyrite and sphalerite were found disseminated in biotite-magnetite-carbonate altered basaltic andesite outcrops and float in the eastern and western parts of Bantug. Quartz veinlets resembling stockwork were also identified in intensely quartz-clay altered float in the area.

Recognition of enargite, covellite and chalcopyrite supported the hypothesis formulated in 2002 by Phelps Dodge geologists of possible high sulfidation epithermal mineralisation to explain the large areas of intensely quartz-clay altered rocks (Taningco, 2002). Quartz stockwork veins were observed in intensely quartz-clay altered float, and were interpreted to be related to porphyry style mineralisation that had been overprinted ('telescoped') by advanced argillic alteration assemblages, a feature common in some porphyry terranes (Sillitoe, 2010).

After the acquisition of Phelps Dodge by Freeport-McMoRan, intense exploration activities began at Bantug in August 2008. Freeport-McMoRan conducted soil and rock geochemical sampling, followed by mapping along EW lines spaced 400 m apart, and detailed creek mapping and infill stream sediment sampling. At the end of April 2009 a total of 2380 soil, rock and stream sediment samples had been collected and most of the area (~35 km^2) had been mapped in detail (Subang et al., 2009).

In order to contribute to the understanding of the Bantug lithocap and to the exploration programme carried by Freeport-McMoRan, 54 samples were provided to CODES for the AMIRA P765A project. Short wave infra-red spectroscopy (PIMA), whole-rock geochemistry (ACME AA-litho package) and microanalysis (EPMA, SEM and LA-ICP-MS) were used to study the set of samples provided to CODES. Three conceptual targets were generated based on the results obtained (Chang, 2009).

In September 2010 Freeport-McMoRan formed a joint venture partnership with (JOGMEC) to explore the Bantug area. Seven diamond drill holes were drilled and an eighth drill hole was being drilled at the time of field work for this dissertation. IP-resistivity, ground magnetics and soil geochemical surveys were also performed by the joint venture during 2010 and 2011 (Subang, 2011).

1.4. Research aims

This study represents the first detailed description of the geology and hydrothermal alteration in the Bantug area, Negros, Philippines.

This dissertation aims to:

- Analyse and summarise the tectonic and geologic context in which the Bantug area is located

- Describe and characterise the geology of the Bantug area
- Constrain the age of the magmatism at Bantug
- Provide a geochemical characterisation of the intrusive rocks at Bantug
- Propose a model for the geologic setting of the Bantug area
- Describe and characterise the hydrothermal alteration assemblages overprinting the rocks at Bantug
- Find relationships between hydrothermal alteration assemblages and whole-rock geochemistry
- Collect geochemical information from several alteration minerals in order to define vectors towards potential mineralized centres, and assess the fertility of the lithocap at Bantug using mineral chemistry
- Characterise the patchy-wormy textures, also known as gusano-textures, at Bantug
- Provide a genetic model for the formation of the patchy-wormy textures at Bantug
- Combine several layers of information (e.g., geology, alteration, geochemistry, mineral chemistry) to propose a genetic model for the formation of the lithocap at Bantug
- Provide a sound summary of this project's implications for further exploration and research in the Bantug area

CHAPTER 2:

REGIONAL GEOLOGY

2.1. Introduction

This chapter presents information on the tectonic setting and the regional geology of the Philippines. It begins with an account of the complex subduction zones around the Philippine archipelago and the several bathymetric highs that are being subducted. It reviews the ophiolite belts in the Philippine archipelago and their relationships with the subduction zones. This is followed by an account of the volcanic arcs and their associated magmatism. This chapter also presents a summary of the major magmatic-hydrothermal districts throughout the Philippine archipelago. This is followed by an analysis on the seismic activity in the Central Visayas region and the spatial relation with volcanism and porphyry-epithermal occurrences in Negros. The geology of Negros is summarised, as well as an account of the most important porphyry-epithermal occurrences and active and/or extinct geothermal fields.

2.2. Philippine tectonic setting

The Philippines are located at a complex plate boundary in the West Pacific. The archipelago occupies the area of convergence of the Eurasian plate from the west, the Philippine Sea plate from the east, and the Indo-Australian plate from the south (Rangin, 1991).The western boundary of the archipelago comprises the east-dipping subduction zones of the South China Sea plate (the Early Oligocene-Early Miocene Manila Trench), the Sulu Sea plate (the Early to Middle Miocene Negros and Sulu trenches), and the Celebes basin plate (the Eocene Cotabato trench; Fig. 2.1; Hamburger et al., 1983; Ozawa et al., 2004; Hall, 2002; Yumul et al., 2008). Along the eastern boundary of the archipelago, the Philippine Sea Plate (Eocene) is subducting obliquely along the west-dipping East Luzon Trough-Philippine Trench (Fig. 2.2). The Philippine Mobile Belt lies between these two converging plates (Fig. 2.1; Gervasio, 1967; Rangin, 1991).

The Philippine Mobile Belt comprises a series of accreted continental fragments, ophiolites, marginal basins and volcanic arcs; thus, it is the result of a complex history of collision, subduction, magmatism and strike-slip faulting (Gervasio, 1967; Rangin, 1991). It is an actively deforming tectonic collage of oceanic crustal blocks surrounded on most sides by destructive plate margins (Rangin, 1991, Yumul et al., 2008). Terrane accretion, indenter tectonics (Chamberlin and Anderson, 1989), oceanic basin closure and arc formation have all played a part in shaping the mobile belt (Rangin, 1991; Hall, 2002; Yumul et al., 2008).

The archipelago is surrounded by several marginal basins. These include the South China Sea, Sulu Sea, Celebes Sea, Molucca Sea, and the Philippine Sea basins (Fig. 2.1). Details about these basins and their sub-basins, their geology, geochemistry, geophysical signatures and importance in the regional tectonic context are presented in Yumul et al. (2008) and references therein.

There are at least four major oceanic bathymetric highs associated with the Philippines. They are the NW Luzon oceanic bathymetric high, the Scarborough seamount, the Palawan micro-continental block, and the Zamboanga-Sulu Peninsula (Fig. 2.1). The NW-trending Luzon oceanic bathymetric high was first recognized by Bautista et al. (2001) offshore of north-west Luzon. This bathymetric high is believed to have narrowed the northern extension of the Manila Trench (Bautista et al., 2001).

Yumul et al. (2008) consider the Scarborough Seamount chain, offshore of western Luzon, to represents the extinct spreading centre of the South China Sea basin (Fig. 3). Subduction of the Scarborough Seamount chain beneath northern Luzon has been proposed by Ramos et al. (2005) based on tomographic studies. Low-angle subduction, a gap in the volcanic arc, and elevation of the fore-arc are some of the features attributed to the Scarborough Seamount chain subduction (Yang et al., 1996; Ramos et al., 2005; Yumul et al., 2008). Waters et al. (2011) and Hollings et al. (2011) proposed that porphyry and epithermal mineralisation in northern Luzon were triggered by subduction of the Scarborough Seamount chain.

The Palawan micro-continental block played a major role in the geodynamic evolution of the Philippine archipelago. In the central west portion of the archipelago, the Palawan micro-continental block is subducting in a complex area beneath the islands of Mindoro, Tablas, Romblon, Sibuyan and Panay (Fig. 2.1). Here, ophiolite emplacement and micro-block rotation occurred due to the collision of the bathymetric high (the Palawan micro-continental block) with the Philippine Mobile Belt (Fig. 2.1; Rangin, 1991; Ramos et al., 2005; Yumul et al., 2008).

To the west, in the central part of the Philippine archipelago, the Cagayan de Sulu Ridge (southern part of the Palawan micro-continental block; Fig. 2.1) is colliding with the southern part of Panay Island. The Cagayan de Sulu Ridge (CSR) is oriented parallel to the long axis of Palawan Island and the Palawan trough (Fig. 2.1). The CSR is interpreted to be a volcanic arc, active for a short period in the Early Miocene, which collided with the margin of South China at the end of the early Miocene (Rangin and Silver, 1990; Hall, 2002). This volcanic arc is considered to continue to Mindoro and Tablas (Marchadier and Rangin, 1990; Mitchell and Leach, 1991;

Hall, 2002). K-Ar ages from volcanic rocks in this arc suggest it may have been active from 16.0 to 11.6 Ma (Middle Miocene). However, volcanic activity is considered to have ceased during the last few thousand years (Rangin et al 1990; Hall, 2002; Bergman et al, 2001).

The Zamboanga-Sulu Peninsula on the western side of the Mindanao Island, in the southern part of the Philippine archipelago, is considered to be an accreted bathymetric high (Querubin and Yumul, 2001; Sherlock and Barrett, 2004). The Zamboanga-Sulu Peninsula is thought to have collided obliquely with Mindanao Island during the Middle Miocene. Ophiolite emplacement occurred along the left lateral strike-slip Siayan-Sindangan regional fault, which crosses the western flank of Mindanao Island in a NNW direction and may be related to the Negros Trench (Fig. 2.2). The Zamboanga-Sulu Peninsula is associated with moderately shallow seismic activity and small rates of deformation (Barrier et al, 1991; Pubellier et al., 1991; Jimenez et al., 2002; Yumul et al., 2004; Yumul et al., 2008).

Offshore geophysical data and satellite images have revealed two oceanic bathymetric highs on the eastern flank of the Philippine archipelago. To the north, offshore north-eastern Luzon lies the Benham Plateau (Fig. 2.1). To the south of the Philippine archipelago, offshore eastern Mindanao, a small ridge was interpreted by Sandwell and Smith (1997) based on a gravimetric survey (Eastern Mindanao Ridge; Fig. 2.1).

In summary, the key geodynamic elements of the Philippine archipelago include the aseismic Palawan micro-continental block, the seismically active Philippine Mobile Belt and the Philippine Sea Plate. These tectonic elements are interacting in a setting where subduction is occurring on both the eastern and western sides in opposed directions (Rangin, 1991; Barrier et al., 1991; Hall, 2002; Yumul, 2008). Based on paleomagnetic studies, Hall (2002) proposed a northwest-direction drifting model with clockwise rotation for the Philippines since the Eocene.

Figure 2.1. (opposite). Tectonic features around the Philippine archipelago (after Yumul et al., 2008). a. Digital elevation model (DEM) of the Philippines and bathymetry around the archipelago; brown represents high elevations and mountain chains, green represents plains, light blue represents submarine high elevations, and dark blue represents submarine deep plains or trenches. From NOAA (2014). **b.** Schematic map; bathymetric highs are presented in dark grey, subduction zones are represented by thick red-dented lines, main fault zones are represented by thin red lines, and lineaments and structures are represented by black lines.

20°0'0"N
10°0'0"N
126°0'0"E
120°0'0"E
N
0 100 200
Km
a
b
East Luzon Through
Benham Plateau
Legaspi Lineament
PFZ
Philippine Trench
Cotabato Trench
Negros Trench
NW Luzon OBH
Scarborough Seamount
Manila Trench
Sibuyan Sea Fault
Cagayan de Sulu Ridge
Sulu Trench

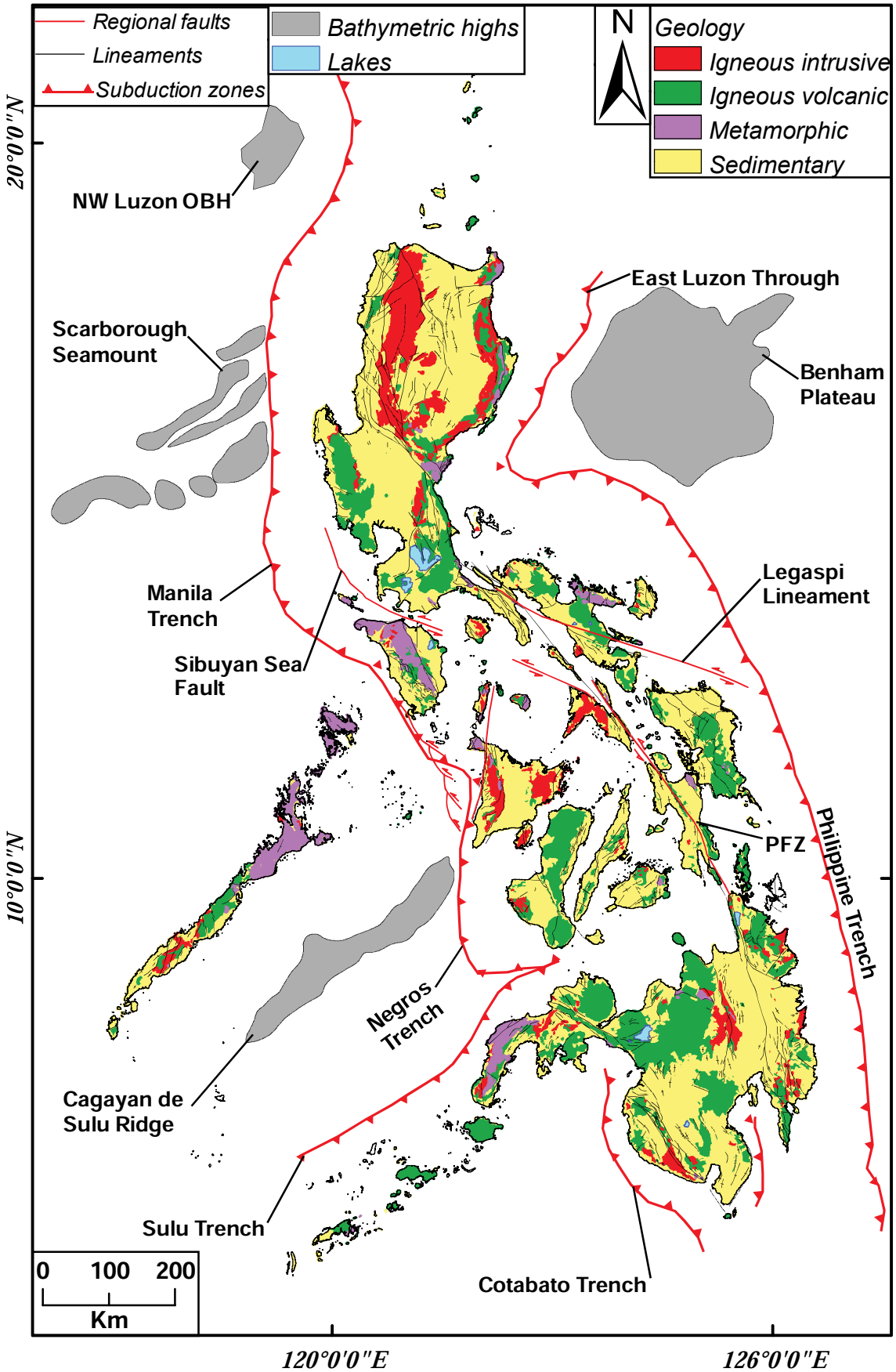

Figure 2.2. Geology and major tectonic features of the Philippine archipelago. Modified after Fernandez (1981), BMG (2004), and Braxton (2007).

2.2.1. Regional structural setting

The Philippine archipelago is dominated by three main crustal structures (Figs. 2.1 and 2.2):

i) A subduction zone in the east defined by the Philippine Trench and East Luzon Trough. The subduction zone is connected by the east-west left-lateral Sibuyan Sea Fault at approximately 15° latitude (Figs. 2.1 and 2.2). This subduction zone is considered to be young based on estimations of recent features such as the length of the subducted slab (i.e., 250 km) and the rate at which plates are moving in the trench (i.e., 6-8 cm/yr.). This subduction zone is associated with well-defined thrust-faulting and intermediate-shallow earthquakes (Cardwell et al., 1980; Barrier et al., 1991; Aurelio et al., 1993; Aurelio, 2000).

ii) A subduction zone in the west defined by the Manila, Negros and Cotabato trenches (Figs. 2.1 and 2.2). This zone is associated with weak and shallow seismic activity which is associated with small deformation rates.

iii) The Philippine Fault Zone, which trends roughly parallel to the active plate boundaries bordering the Philippine archipelago (Figs. 2.1 and 2.2). This major left-lateral strike-slip fault zone accommodates some of the opposing convergence between the Pacific and Eurasia plates (Barrier et al., 1991; Rangin, 1991; Aurelio 2000b).

2.2.2. The Philippine Fault Zone

The Philippine Fault Zone (PFZ) comprises a large group of first order, NW-SE trending, left-lateral strike-slip faults and their associated second and third order faults (Figs. 2.1 and 2.2). It is situated to the west of the Philippine Trench and crosses the entire Philippine archipelago for a length of 1,200 km (Barrier al., 1991; Aurelio, 2000). The PFZ has transpressional and transtensional segments distributed along the length of the archipelago. Based on rotation rate calculations for the Eurasian block, Barrier et al. (1991) proposed slip rate values of 1.9-2.5 cm/yr. along the PFZ in the Visayas and Mindanao. Aurelio (2000) confirmed these values through global positioning satellite (GPS) and geodesic measurements.

The location of the PFZ is defined by young geomorphologic features including fault scarps, sinistral stream offsets, fault-parallel ridges, and narrow, elongate troughs. These have been identified through field investigations, satellite imagery, aerial photographs, and seismic profiles (Barrier et al., 1991; Aurelio, 2000; Yumul et al., 2008).

The northern section of the Philippine Fault is characterized by a significant thrust component (Nakata et al., 1977; Pinet and Stephan, 1988; Malterre, 1989; Barrier et al., 1991). In Luzon, the fault bends from NW-SE in central and southern Luzon to N-S in northern Luzon, where it divides into several segments, of which the westernmost segment appears to be active (Figs. 2.1 and 2.4; Pinet and Stephan, 1988). Karig (1983) considered these segments subvertical, NS-trending shear zones based on internal structural fabrics observed in the field.

The central section is characterized by left-lateral strike-slip motion and intense seismic activity. Over the past 100 years, more than 10 earthquakes have been associated with movement of the PFZ (Fig. 2.1; Rangin, 1991; Yumul et al., 2008). In 1972, the Ragay Gulf earthquake (M = 7.0) in the Bondoc Peninsula was associated with a left lateral displacement of 3.2 m (Morante and Allen, 1973; Barrier et al., 1991). Exposures of the fault plane in Leyte and in Surigao (northern Mindanao) exhibit kinematic indicators characteristic of pure left-lateral strike-slip movement (Barrier et al., 1991). The PFZ outlines a convex trajectory between the Bondoc Peninsula (13° N) and Mindanao (9° N). In this area, the PFZ follows a complex array of structures that splits to satellite structures, forming several branches. A clear example is observed in the volcanic arc in Leyte where the PFZ splits into three main structures (Figs. 2.1 and 2.2; Barrier et al., 1991).

The PFZ is believed to have formed during the Middle Miocene and to be coupled with the Philippine Trench to the south (Aurelio et al., 1993; Quebral et al., 1996). Present-day evidence also shows that the northern and southern ends of the PFZ are characterized by actively propagating fault systems (Pinet and Stephan, 1990; Aurelio, 2000; Yumul et al., 2005). Yumul et al. (2008) reported dissected Holocene sandstones in Mati, Davao Oriental and Southern Mindanao, and they considered these to be evidence of the active status of the PFZ.

Several subordinate faults are intimately linked to the evolution of the PFZ. The left-lateral Legaspi Lineament, acting as a transfer fault, connects the Philippine Fault Zone with the Philippine Trench (Figs. 2.1 and 2.2). The left-lateral Sibuyan Sea Fault, in the central part of the Philippine archipelago (Figs. 2.1 and 2.2), is an offshore extension of the PFZ. The NW-trending Sindangan-Cotabato-Daguma Lineament (SCDL) and the Siayan-Sindangan Suture Zone (SSSZ) form the left-lateral fault zone of western Mindanao (Figs. 2.1 and 2.2; Yumul et al., 2008). The left-lateral fault zone of western Mindanao distributes part of the stress that is not being distributed by the surrounding trenches in Mindanao; it also has served, and continues to serve, as a conduit for hydrothermal fluids. Evidence for this include the ancient and present-

day geothermal fields in the area and the several magmatic-hydrothermal mineral deposits (e.g., Sillitoe and Gappe, 1984; Mitchell and Leach, 1991; Sajona et al., 2002).

In Bondoc and Leyte, late Miocene fold and thrust belts are unconformably overlain by folded Pliocene sedimentary sequences. The Pliocene-Pleistocene folding event is related to movement on the Philippine Fault, whereas the late Miocene event was probably linked to the collision of the Philippine mobile belt with Eurasia (Barrier et al., 1988; Aurelio et al., 1993). Along the central segment of the Philippine Fault, the shaping of the current landscape (e.g., ridges and peninsulas) has been associated with the Philippine Fault. Faulting is considered to have begun between 4 and 2 Ma (Barrier et al., 1988; Rangin, 1991; Aurelio et al., 1993). In Luzon, similar Pliocene-Pleistocene fault activity has been described (Rutland, 1968; Pinet and Stephan, 1988; Malterre, 1989; Barrier et al., 1991), following a late Miocene tectonic event. This suggests that the Philippine Fault began to form during the Pliocene, crosscutting and locally reactivating pre-Pliocene structures. This young age estimate distinguishes it from the middle Miocene transcurrent faults discussed by Karig (1983) and Karig et al. (1986), and relates the Philippine Fault to a different geodynamic context.

2.2.3. Ophiolite belts in the Philippine archipelago

Ophiolitic complexes occur across the entire Philippine archipelago (Fig. 2.2; Nakagawa and Franco, 1996; Peña, 1996; Dimalanta and Yumul, 2006). Metamorphic rocks (e.g., amphibolites, serpentinites and quartz-albite-mica schist) have been mapped at the base of the ophiolitic sequences together with tectonic and sedimentary melanges (Yumul et al., 1997; De Jesus et al., 2000; Tamayo et al., 2004; Faustino et al., 2006; Yumul et al., 2008).

Most of the ophiolitic complexes can be classified in the Tethyan group of Moores (1982), or as Mediterranean in the classification system of Dilek and Furnes (2011). Three classifications have been proposed for the Philippine ophiolites based on:

i) Geographic distribution (Balce et al., 1976)

ii) Age and geochemical data (Tamayo et al., 2004)

iii) Age and lithospheric source (Yumul et al., 2003; Yumul et al., 2007)

Balce et al. (1976) initially grouped the Philippine ophiolites based on their geographic distribution (Fig. 2.3): an eastern belt (Sierra Madre Range and Eastern Bicol-Eastern Mindanao), a western belt (Southern Palawan and Sulu-Zamboanga), and central belt (Zambales-Mindoro, Antique and north-central Mindanao).

Tamayo et al. (2004) grouped the Philippines ophiolites into four belts based on age and geochemistry (Fig. 2.3): 1) the Cretaceous ophiolitic belt, 2) the Eocene ophiolitic belt, 3) the arc collision-related ophiolitic belt of different ages, and 4) the belt of young sequences located to west of the Manila-Negros-Cotabato Trench.

Yumul (2007) grouped the Philippine ophiolites and ophiolitic complexes based on their ages and possible lithospheric sources (Fig. 2.3). Four belts are proposed: 1) the eastern Philippine Late Cretaceous ophiolitic belt, characterised by their metamorphic basement which is considered to have served as the trailing edge of the proto-Philippine Sea plate (e.g., Andal et al., 2005); 2) the Early to Late Cretaceous belt, which is composed of Cordilleran suites with mélanges found along the entire length of the Philippine archipelago, which is considered to be related to the leading edge of the proto-Philippine Sea plate (Encarnacion, 2004; Dimalanta et al., 2006); 3) the Cretaceous-Oligocene ophiolitic belt, considered to have been emplaced along the collision zone between the proto-Philippine Sea plate and the Sundaland-Eurasian margin (Rangin et al., 1989; Jumawan et al., 1998), and 4) the Sundaland-Eurasian margin-derived ophiolitic belt, emplaced in the Palawan and Zamboanga-Sulu regions (Tamayo et al., 2000; Tamayo, 2001; Yumul et al., 2004).

Most of the ophiolitic complexes in the Philippine archipelago are characterised by their supra-subduction zone geochemical signatures (Yumul et al., 1997; Dimalanta et al., 2006). A minor portion of them have mid-oceanic ridge geochemical signature (Yumul et al., 1997; Dimalanta et al., 2006). Most of these ophiolitic complexes are considered to have been generated in fast-spreading volcanic centres, with some having formed in intermediate spreading centres (Yumul, 2003b). The classification systems discussed above imply mechanisms of emplacement for the Philippine ophiolites such as on-ramping, subduction, accretion, and strike-slip faulting (Karig, 1983; Rangin, 1989; Mitchell et al., 1986; Yumul, 2007).

Figure 2.3. (opposite). Ophiolites and ophiolitic rocks found in the Philippine archipelago. After Yumul et al. (2008). **a.** Classification from Balce et al. (1976) based on geographic distribution: 1) Sierra Madre Range, 2) Zambales-Mindoro, 3) Eastern Bicol-Eastern Mindanao, 4) Antique, 5) southern Palawan, 6) Sulu-Zamboanga, and 7) north-central Mindanao. **b.** Classification from Tamayo et al. (2004) based on age and geochemical signatures: 1) Cretaceous sequences, 2) Eocene complexes with subduction signatures, 3) collision-related, 4) young ophiolites. **c.** Classification from Yumul (2007) based on ages and possible lithospheric sources: 1) Late Cretaceous ophiolite complexes with metamorphic basements, 2) Early to Late Cretaceous ophiolites with mélanges, 3) Cretaceous to Oligocene ophiolites along the western collision zone, 4) Sundaland-Eurasian margin-derived ophiolites. See text for details.

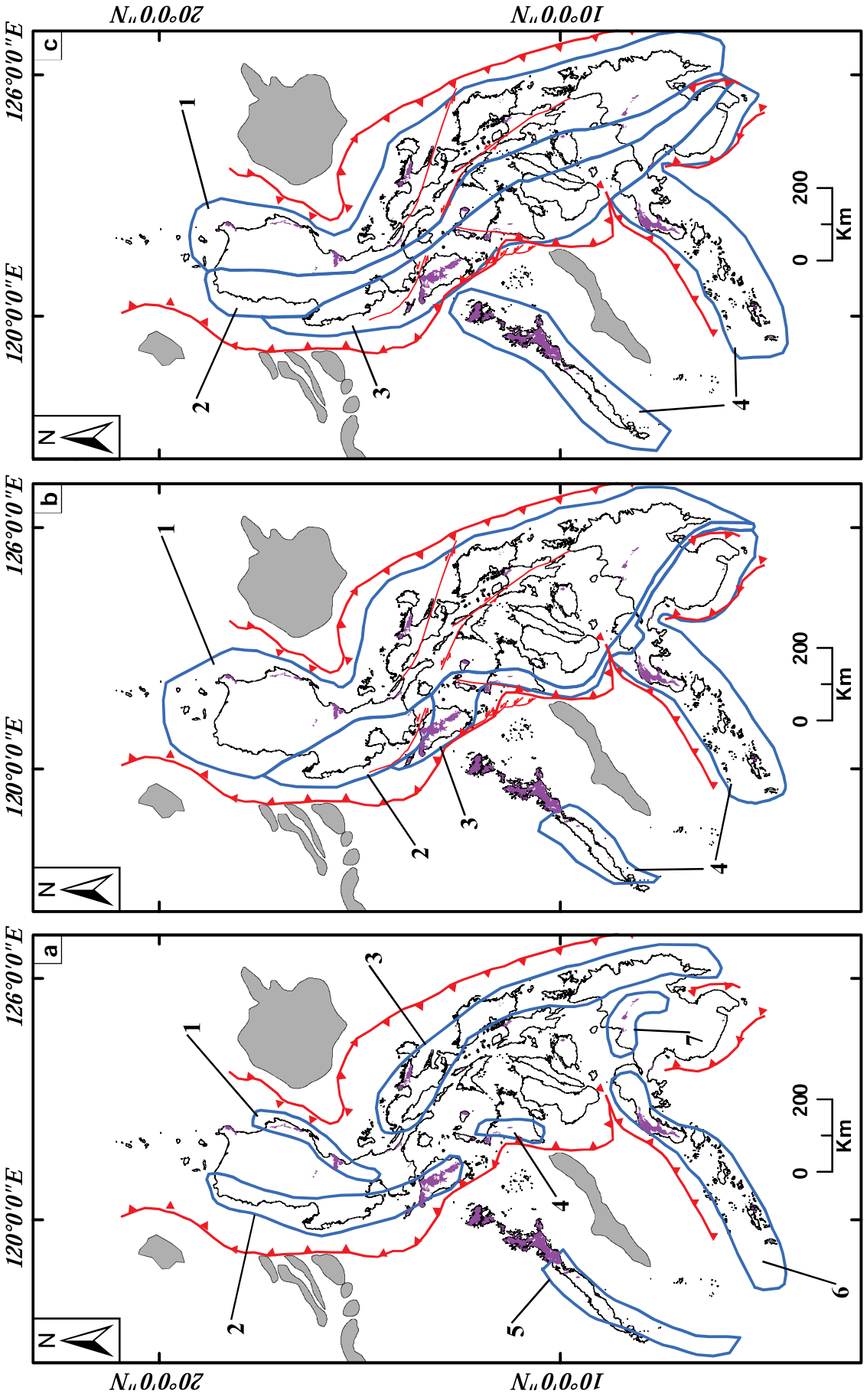
c
b
a
1
2
3
4
5
6
7
N
0
200
Km
126°0'0"E
120°0'0"E
20°0'0"N
10°0'0"N

2.3. Magmatism and volcanism in the Philippine archipelago

The Philippines includes a complex series of volcanic arcs related to subduction zones around the archipelago (Fig. 2.4). These volcanic arcs have been of interest to diverse areas of the geosciences due to their associated mineral deposits, geothermal potential, and related natural hazards.

Yumul et al. (2008), based on the work of Mitchell and Leach (1991), proposed eight magmatic arcs for the Philippine archipelago (Fig. 2.4): *i*) the Luzon arc, Central Cordillera, *ii*) northern Sierra Madre arc, *iii*) southern Sierra Madre-Polillo-Catanduanes arc, *iv*) Negros arc, *v*) east Philippines arc, *vi*) central Mindanao arc, *vii*) Cotabato-Daguma arc, *viii*) Sulu-Zamboanga arc. These are reviewed below.

2.3.1. The Luzon arc (Central Cordillera)

Subduction of the South China Sea along the Manila Trench since the Early Miocene has resulted in the formation of the Luzon arc (Balce et al., 1982; Knittel and Defant, 1988; Teng, 1990; Maury et al., 1998; Yumul et al., 2003a). This arc forms a 1,200 km-long belt of stratovolcanoes and volcanic remnants that extends from eastern Taiwan to Mindoro (Fig. 2.4; Marini et al., 2005; Castillo and Newhall, 2004). Volcanic rocks in the arc vary both in terms of geochemical composition and age. Rocks with tholeiitic through calc-alkaline to shoshonitic composition occur along the arc (Defant et al., 1989; Maury et al., 1998; Polve et al., 2007; Hollings et al., 2011). K-Ar isotopic ages ranging from 32.3-5.6 Ma have been reported for the northern Luzon volcanic arc (Wolfe, 1981; Mitchell and Leach, 1991; Bellon and Yumul, 2000). Adakitic rocks have also been identified among the older (>15 Ma) and younger (<5 Ma) volcanic centres (Bellon and Yumul, 2000; Yumul et al., 2000; Jego et al., 2005; Hollings et al., 2011). K-Ar isotopic ages from the Bataan arc volcanoes range from 7.0-0.2 Ma and K-Ar isotopic ages from the Bataan back-arc volcanoes, including the volcanic rocks at Mindoro, range from 1.7-0.1 Ma (Fig. 2.4; Defant et al., 1989; Yumul et al., 2000). However, older (39-27 Ma) K-Ar isotopic ages have been reported by Mitchell and Leach (1991) for intrusive rocks in the Caraballo Range (e.g., quartz diorites). Waters et al. (2011) presented $^{40}Ar/^{39}Ar$ ages for the Lucbuban gabbro (22.6 ± 0.5 Ma) and the Virac granodiorite (20.23 ± 0.38 and 20.2 ± 0.7 Ma) located in the Central Cordillera Intrusive Complex, which defines the eastern boundary of the Baguio gold-copper district. The variety of ages and geochemical composition reflects the complexity of the tectonic evolution and tectonic setting of the Luzon arc.

2.3.2. Northern Sierra Madre arc

The Northern Sierra Madre arc trends N-S in its northern segment, and trends SW in its southern segment. The Northern Sierra Madre arc joins the NW-SE trending Caraballo Mountains (Fig. 2.4; Sajona et al., 1994). The Northern Sierra Madre arc contains rocks that have island arc geochemical signatures (Wolfe, 1981; Hollings et al., 2011b) for which whole rock K-Ar isotopic ages range from 49-43 Ma (Wolfe, 1981).

The Japan International Cooperative Agency-Metal Mining Agency of Japan (1977) defined a younger arc in the southern portion of the Northern Sierra Madre based on whole rock K-Ar isotopic ages of 33-24 Ma. It comprises volcano-sedimentary rocks, including basaltic flows and dikes. These rocks have island arc tholeiitic to calc-alkaline geochemical signatures.

2.3.3. Southern Sierra Madre-Polillo-Catanduanes

Whole rock K-Ar ages from shoshonites and island arc tholeiites in the Southern Sierra Madre range in age from 36.9 Ma to 1.2 Ma (Fig. 2.4; Japan International Cooperative Agency-Metal Mining Agency of Japan, 1977).

2.3.4. Negros arc

Formation of the Negros volcanic arc is attributed to the subduction of the Sulu Sea along the Negros Trench (Sajona et al., 1993). The medium-K calc-alkaline, basaltic to dacitic volcanism in Negros is characteristic of the Philippine archipelago (Rae et al., 2003, 2004, 2011; Hollings et al., 2011). The adakitic affinities of some of the southern Negros volcanic rocks are comparable to volcanic and intrusive rocks from porphyry-mineralized districts elsewhere in the Philippines (e.g., Sajona and Maury, 1998; Hollings et al., 2011a, b). This suggests that magmatism in this region has been influenced by melting of subducted oceanic basalt and it may have helped to promote porphyry copper-style magmatic-hydrothermal conditions at Palinpinon (Rae et al., 2003, 2004, 2011), comparable to mineralized porphyry deposits elsewhere in the Philippines (e.g., Arribas et al., 1995; Hedenquist et al., 1998; Braxton et al., 2009; Braxton and Mathur, 2011; Chang et al., 2011; Cooke et al., 2011; Deyell and Hedenquist, 2011; Rae et al., 2011; Waters et al., 2011; Wolfe and Cooke, 2011).

Rae et al. (2004, 2011) constrained the age of at least two magmatic events in Negros Island based on $^{40}Ar/^{39}Ar$ dating. The middle Miocene Lower Puhagan Volcanic Formation is the oldest formation intersected by geothermal wells at the Palinpinon geothermal field (Rae et al., 2003, 2004, 2011). It is part of a volcanic sequence that is traceable throughout the Visayas and is related to subduction of the Sulu Sea in a southeast direction beneath the Sulu arc

(Rangin and Silver, 1990). During the late Miocene to early Pliocene, a period of regional subsidence and marine sedimentation produced the Okoy Formation, a thick sequence of calcareous sedimentary rocks. From early Pliocene to recent times, magmatism associated with subduction along the Negros-Sulu Trench produced basaltic-andesites and andesites of the Southern Negros and Cuernos Volcanic Formations (Sajona et al., 2000). The Puhagan andesite dikes and Nasuji diorite pluton intruded the volcano-sedimentary sequences at Palinpinon (Rae, 2002; and references therein). Radiogenic $^{40}Ar/^{39}Ar$ dating results from hornblendes from the Puhagan dikes and the Nasuji pluton yielded ages of 4.2-4.1 Ma and 0.7-0.3 Ma respectively (Rae et al., 2004). This confirms that the intrusions are not coeval and it suggests the possibility of at least two magmatic events (Pliocene and Pleistocene) along the eastern side of Negros Island.

2.3.5. East Philippine arc

The East Philippine Arc extends from Bicol to eastern Mindanao (Fig. 2.4; Andal et al., 2005a; McDermott et al., 2005). Rocks from the Bicol segment of the arc are dominantly medium- to high-K calc-alkaline, high-Al basalts and andesites. Magmatism in this arc is related to the westward subduction of the Philippine Sea plate along the Philippine Trench (Weber and Knittel, 1990; Castillo and Newhall, 2004). In the Leyte segment, the volcanoes define a 250 km-long NW-SE belt from the Biliran to Panaon Islands. Younger volcanism is linked with subduction along the Philippine Trench (Sajona et al., 1994). The Pliocene-Pleistocene lavas are largely calc-alkaline with medium to high-K contents (Ozawa et al., 2004). Mitchell et al. (1986) suggested that the Lower Oligocene-Lower Miocene volcanic rocks in north-eastern Mindanao erupted after an increase in the subduction angle of the oceanic crust along the Philippine Trench. Mitchell and Leach (1991) reported K-Ar results from andesitic rocks in the northern part of eastern Mindanao ranging from late Pliocene to Quaternary.

2.3.6. Central Mindanao arc

The Central Mindanao Volcanic Arc is referred to in previous publications as the Agusan-Lanao flood basalts (Balce et al., 1976). This arc is interpreted to represent a magmatic response to the collision between western and eastern Mindanao at 5 Ma (Fig. 2.4; Pubellier et al., 1991; Castillo et al., 1999). The Pliocene-Pleistocene volcanoes formed in this arc are predominantly of basaltic to basaltic andesite composition, with minor occurrences of more felsic rocks (Sajona et al., 1994).

2.3.7. Cotabato-Daguma arc

Subduction of the Celebes Sea plate along the Cotabato Trench resulted in the formation of the Cotabato arc (Fig. 2.4; Aurelio, 2000b). Pubellier et al. (1991) reported whole rock K-Ar radiogenic ages of approximately 30 Ma for the monzonitic-dioritic-granodioritic core of the Daguma Range. The geochemical signatures of the volcanic rocks in this arc vary from island arc tholeiite to tholeiite-calc-alkaline to exclusively calc-alkaline. The Miocene volcanic rocks in this arc also have adakitic geochemical signatures (Sajona et al., 1994).

2.3.8. Sulu-Zamboanga arc

The Pliocene-Quaternary Sulu-Zamboanga arc extends from the southern side of the eastern portion of the Zamboanga Peninsula to Tawi-Tawi (Figure 2.4). It is associated with subduction of the Sulu Sea plate along the Sulu Trench. Volcanic rocks in the Zamboanga Peninsula yielded whole rock K-Ar ages of 18.9-1.9 Ma (Sajona et al., 1994; Yumul et al., 2004). Most of the volcanic rocks in this arc have an arc-tholeiitic geochemical signature, with a minor group of volcanic rocks showing high-K calc-alkaline geochemical affinities.

2.3.9. Summary

The Philippine archipelago is located in a complex tectonic setting where multiple plates and oceanic bathymetric highs subduct with each other (Fig. 2.1). The Philippine Fault Zone crosses the Philippine archipelago from North to South and redistributes part of the stress generated by the subduction zones. Metamorphic rocks and ophiolites occur along the Philippine archipelago; these are considered to have been accreted onto the main landmasses from the Cretaceous until the Paleocene (Fig. 2.2). Eight volcanic arcs are defined along the Philippine archipelago based on geographic distribution and nearness to subduction zones of active and inactive volcanoes (Fig. 2.4).

Figure 2.4. (opposite). Volcanic arcs in the Philippine archipelago. After Mitchell and Leach (1991). 1-Luzon (Central Cordillera), 2-Northern Sierra Madre, 3-Southern Sierra Madre-Polillo-Catanduanes, 4-Negros, 5-East Philippines, 6-Central Mindanao, 7-Cotabato-Daguma and 8-Sulu-Zamboanga. Volcanoes in the Philippine archipelago, adapted from PHILVOLCS (2014). Active volcanoes are in red circles, potentially active volcanoes in brown circles, and inactive volcanoes in blue circles. Volcanic belts are highlighted in grey polygons. ***NWL-OHB****:* NW Luzon Oceanic Bathymetric High; ***ELT****:* East Luzon Trench; ***SS****:* Scarborough Seamount; ***BP****:* Benham Plateau; ***MT****:* Manila Trench; **SSF***:* Sibuyan Sea Fault; ***LL****:* Legaspi Lineament; ***CSR****:* Cagayan de Sulu Ridge; ***NT****:* Negros Trench; ***PFZ****:* Philippine Fault Zone; ***PT****:* Philippine Trench; ***ST****:* Sulu Trench; ***CT****:* Cotabato Trench.

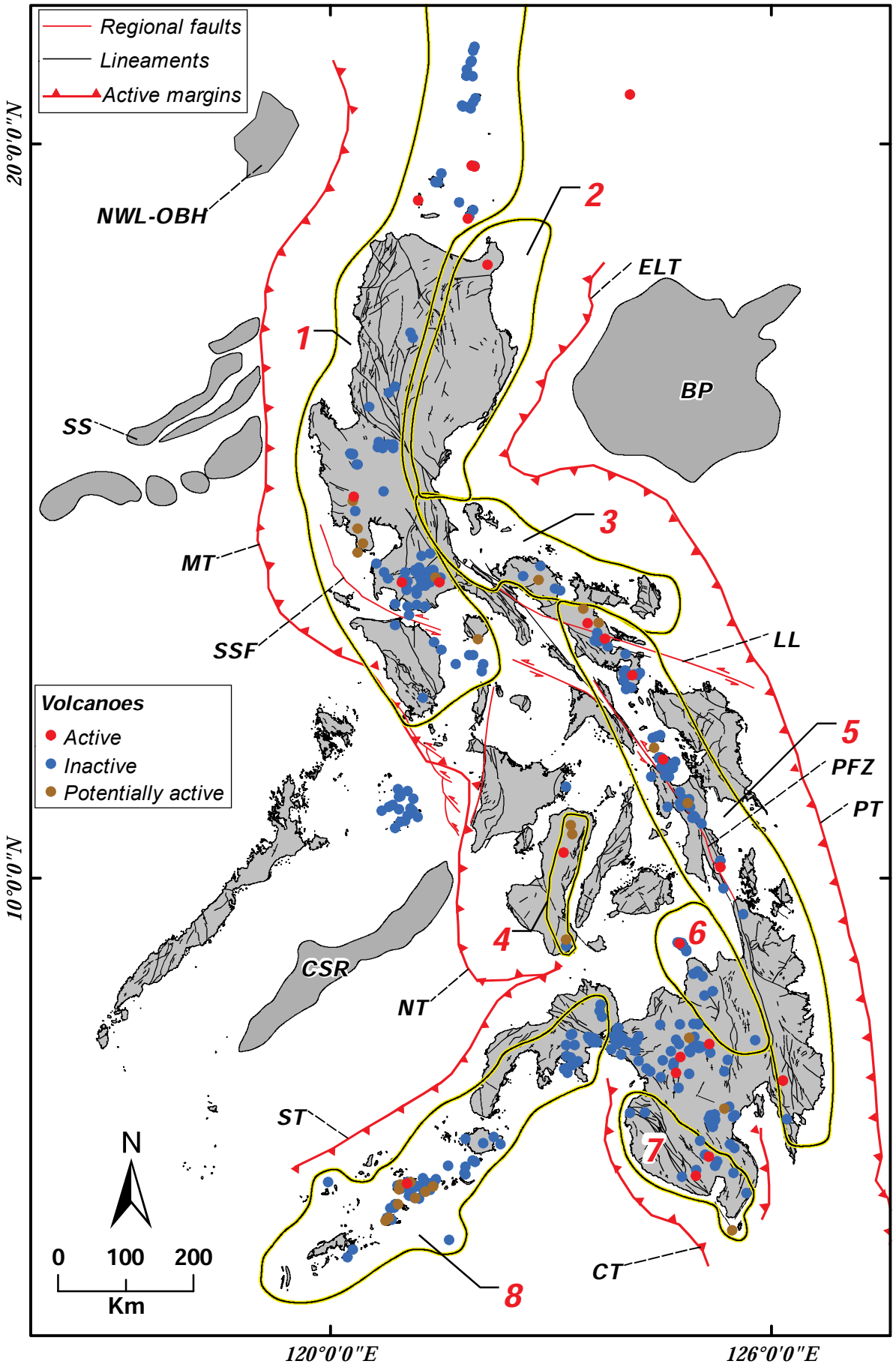
Regional faults
Lineaments
Active margins
Volcanoes
Active
Inactive
Potentially active
NWL-OBH
SS
MT
SSF
ELT
BP
LL
PFZ
PT
CSR
NT
ST
CT
1
2
3
4
5
6
7
8
N
0
100
200
Km
20°0'0"N
10°0'0"N
120°0'0"E
126°0'0"E

2.4. Porphyry, epithermal, and skarn deposits of the Philippines

2.4.1. Introduction

The mineral deposit and metal content endowment of the Philippine archipelago is one of the most attractive in the Southwest Pacific region (Cooke et al., 2005). It is estimated that by 2050 the Philippines will rank as the 20th most stable economy in the world with an estimated GDP of $3.17 trillion (World Bank, 2014).

At least 48 porphyry deposits and 17 epithermal deposits, 15 porphyry prospects and 72 epithermal prospects are known to occur in the archipelago (Sillitoe and Gappe, 1984; Sinclair, 2007). The majority of these have been documented to some extent, and some have been studied in detail. After many years of exploration, nine prolific districts have been outlined in the Philippines (Fig. 2.6; Table 2.1). However, there are still many emerging areas with high potential to host large, high grade porphyry deposits.

This section addresses some major aspects of history and economic importance of porphyry and epithermal deposits in the Philippines. The geographic distribution, age, and relation to magmatic belts is reviewed. The most relevant geologic characteristics of the major mineral districts are summarized and some implications for mineral exploration are also described.

2.4.2. History and economic importance

The Philippines have had a long history of mineral exploration and mining that dates back to at least the 14th century, when Chinese explorers are believed to have mined for gold and silver in the Baguio and Masbate districts (Cooke et al. 2011).

Gold drove the Spanish occupation during the 16th to 19th century (A.C. 1521-1898). During the mid-1800s the Spanish government conducted exploration programs for copper throughout the archipelago which resulted in the opening of the first copper mine in 1842 (San Remigio in Carawisan, Antique), followed by the opening of the Mankayan mines in 1864 (BMG, 1986).

The United States of America regime (A.C.1898-1946) made the exploration of mineral resources one of their priorities. During this period, several alluvial operations were brought to production, as well as the first commercial-scale mine in the country in the Baguio gold district (BMG, 1986).

By the end of the World War II and the Japanese occupation, the Philippines took on the rehabilitation of existing mines and developing new exploration programs. The Philippine Bureau of Mines carried extensive exploration programmes for copper and gold in the early 1950s. A

collaborative program with the International Cooperation Agency (ICA) of the United States of America resulted on the discovery and development of copper mines in the late 1950s (e.g., Atlas, Sipalay, and Santo Tomas), which led to an exploration and production boom in the 1960s and 1970s. Copper production increased significantly during these three decades, reaching its maximum in 1981 with 0.32 Mt (BMG, 1986; Fig. 2.5). In contrast, gold and silver production increased incrementally after World War II from 2 t Au and 1.4 t Ag in 1946 to 31.12 t Au and 45.53 t Ag in 2011 (BMG, 1986; Brooks, 2011; George; 2011; Cooke et al., 2011).

From Brooks (2011) and George (2011) it can be concluded that between 2005 and 2009 the Philippines accounted for approximately 1.5 and 0.1 percent of global gold and silver production, respectively.

During the mid-1970s, right at the peak of the copper mining boom, there were 18 copper producers. This number declined to 5 by the mid-1980s and continued decreasing during the next two decades (Cooke et al., 2011). Closure of the Lepanto enargite mine in 1996 (Chang et al., 2011) started a new period of low copper production with numbers similar to those in the 1950s.

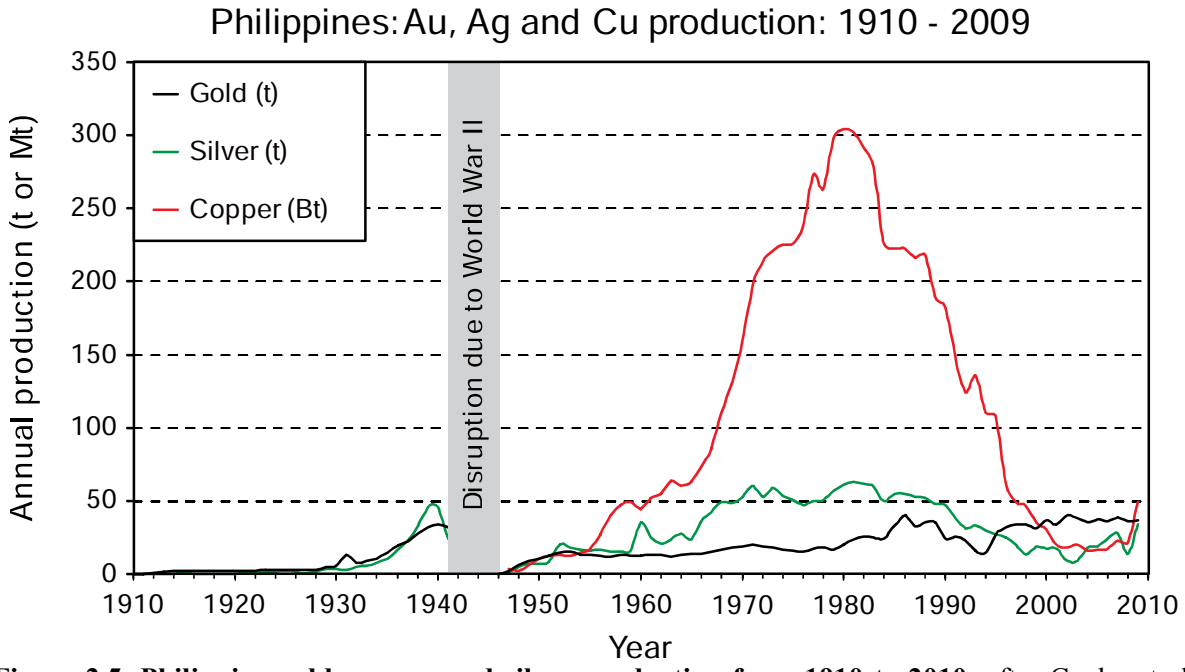

Figure 2.5. Philippine gold, copper and silver production from 1910 to 2010; after Cooke et al. (2011).

Clancy (2005; in Cooke et al., 2011) commented that the marked decline in the Philippine copper mining industry since the 1980s has been related to significant social, political, and environmental challenges for exploration companies. Cooke et al. (2011) noted that due to these challenges the Philippines have been mostly bypassed by recent global mining booms. Evidence to support this is the decline in the contribution of mining and quarrying to the Philippines gross domestic production, from 10 % in 1970 to <5 % in 2003 (Clancy, 2005).

The Philippine's metallogeny, and in particular Philippine porphyry and epithermal deposits, have been addressed in detail by several authors (Bryner, 1969; Sillitoe and Gappe, 1984; Mitchell and Leach, 1991; Arribas et al., 1995; Hedenquist et al., 1998; Braxton et al., 2009; Chang et al., 2011; Cooke et al., 2011, 2011b; Deyell and Hedenquist, 2011; Hollings et al., 2011, 2011b; Rae et al., 2011; Waters et al., 2011; Wolfe and Cooke, 2011). Thus, the remarkable endowment of porphyry and epithermal deposits is well known and it clearly represents encouraging evidence of its unique potential.

2.4.3. Distribution and age

There have been 47 porphyry deposits, 15 porphyry prospects, 4 high-sulfidation deposits, 1 high-sulfidation prospect, 4 intermediate-sulfidation deposits, 9 low-sulfidation deposits, 71 low-sulfidation prospects, and 3 skarn deposits reported and described in the Philippines (Fig. 2.6; Sillitoe and Gappe, 1984; Kirkham and Dunne, 2000; Braxton, 2007; Singer et al., 2008). These magmatic-hydrothermal deposits in the Philippines can be grouped in nine districts. Districts and major deposits are presented in Figures 2.6 and 2.7, as well as in Table 2.1. A complete list of epithermal, skarn and porphyry deposits, as well as location maps and detailed descriptions are presented in Appendix A.

Four districts, containing some of the largest deposits, occur along the Philippine fault zone (e.g., King-King, Surigao, Mankayan, and Baguio). This marked association of porphyry deposits and regional strike-slip faults provide evidence for a major crustal control on magmatism and magmatic-hydrothermal fluids. At the deposit scale, porphyritic intrusions have generally been controlled and emplaced in second order structures at a high angle to the main fault system (Sillitoe and Gappe, 1984; Braxton, 2007). The high angle of such structures suggests localized extension in zones of flexure along the Philippine Fault Zone (Braxton, 2007).

Table 2.1. Major porphyry districts and deposits in the Philippines

	Lat.	Long.	10^6 Ton.	Cu (wt. %)	Au (ppm)	Mo (wt. %)	Ag (ppm)	Age (Ma.)	Reference
Mankayan									
Buaki	16.850	120.780							1
Bulalacao	16.840	120.803							1
Far Southeast	16.858	120.783	650	0.65	1.3		0.93		
Guinaoang	16.792	120.800	500	0.4	0.4				1
Baguio									
Ampucao	16.289	120.654	0.51	0.18	0.95				3
Black Mountain	16.367	120.654	62	0.378	0.33	0.013	4	7	3
Nugget Hill	16.359	120.631		1.17	4.58			1.5	3
Santo Tomas II	16.267	120.617	288	0.375	0.7		1.5	1.48	
Marinduque									
Ino-Capayang	13.500	121.883	50	0.5	0.03		1.3		
Marcopper	13.417	122.000	195	0.57	0.1		1	20.5	
Taipan	13.430	121.979	177	0.52	0.12		0.4		2
Bicol									
Matanlang	14.233	122.733	65	0.35	0.4			20.5	2
Central Cebu									
Biga	10.333	123.733	395	0.43	0.25		1.5	108	1
Carmen	10.500	123.800	390	0.43	0.24		2	102	1
Lutopan	10.333	123.733	533	0.5	0.31		1.4	108	1
Negros Occidental									
Aya Aya	9.433	122.700	40	0.3	0.08		1.5	19.5	2
Basay	9.492	122.679	262	0.44	0.29		1.5	30	2
Hinoba-an	9.750	122.567	440	0.41	0.14		0.34	17.5	1
Sipalay	9.817	122.450	807	0.47	0.05		1.5	30	1
Suguibon	9.567	122.633	26	0.35					1
Surigao Agusan									
Asiga River	9.271	125.629	26	0.36				3.5	2
Bayugo	9.608	125.542	99	0.64	0.65			2.2	4
Boyongan	9.601	125.549	201	0.54	0.78			2.1	4
Madya	9.479	125.591							4
Maraat	9.309	125.663							4
Suyoc	9.661	125.576	5	1	3				4
SE Mindanao									
Amacan	7.336	126.083	116	0.37	0.46		2.5	10	1
Kalamatan	7.592	126.067	26	0.34	0.37				1
King-King	7.196	125.950	400	0.35	0.6		5	10	1
Mapula	7.342	126.018	78	0.4	0.37		3.6	10	1
South Mindanao									2
Salatan	6.559	124.504							
Tampakan	6.465	125.044	2940	0.51	0.19			4.24	5

References: 1: Singer et al. (2008); 2: Sillitoe and Gappe (1984); 3: Waters et al. (2011);4: Braxton (2007); 5: Rohrlach and Loucks (2005)

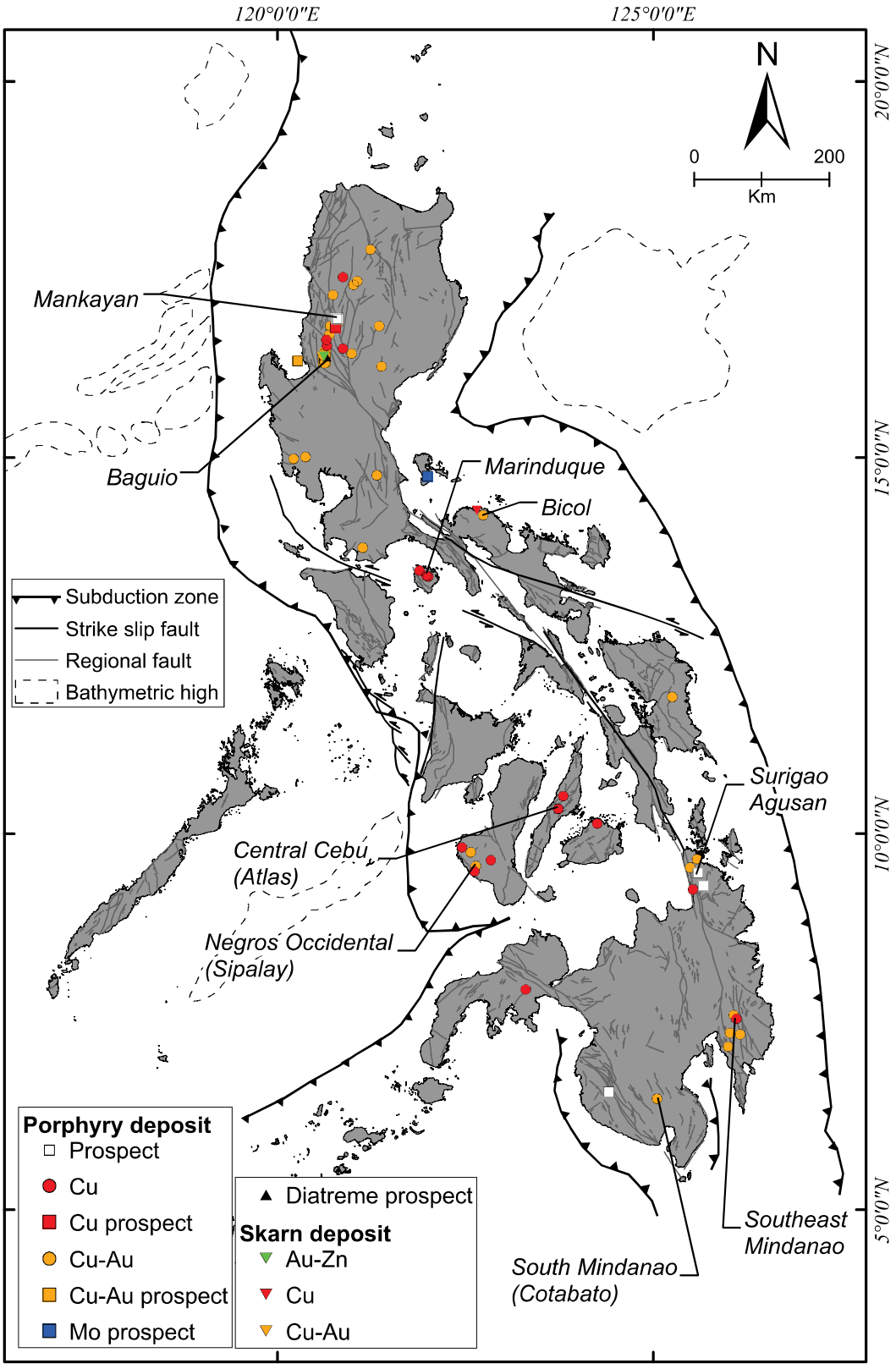

Figure 2.6. Distribution of magmatic-hydrothermal deposits throughout the Philippines. Porphyry and skarn deposits. Dashed lines represent bathymetric highs. Grey lines inside land masses represent faults. References are in Table 2.1. For further details, see Appendix A.

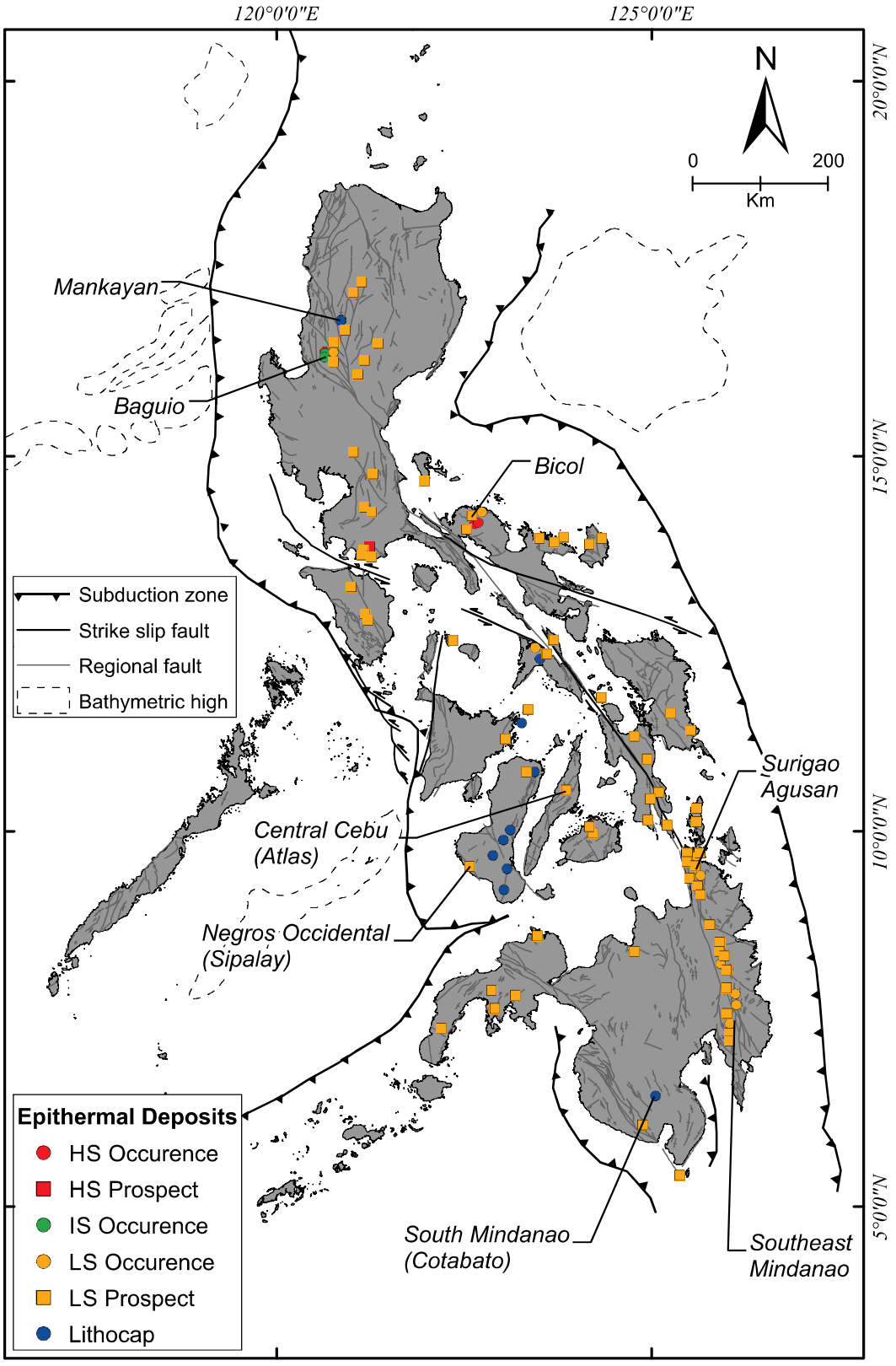

Figure 2.7. Distribution of magmatic-hydrothermal deposits throughout the Philippines. Epithermal deposits. Dashed lines represent bathymetric highs. Grey lines inside land masses represent faults. References are in Table 2.1. For further details, see Appendix A. Abbreviations: HS: high-sulfidation; IS: intermediate-sulfidation; LS: low-sulfidation.

2.4.4. Summary

The Philippine archipelago is located in a complex tectonic setting where several small tectonic blocks are subducting through various opposed subduction zones. Through bathymetry studies, several oceanic topographic features (e.g., Scarborough seamount, Benham seamount, Gaffney ridge, etc.) have been observed to subduct or be in the process of subduction along subduction zones. Such conditions are thought to represent suitable geodynamic triggers for the formation of magmatic-hydrothermal ore deposits (i.e., epithermal, porphyry, and skarn).

The metal endowment of the Philippine magmatic-hydrothermal ore deposits is extraordinary and highly encouraging for explorers. The strong geographic correlation between subduction of oceanic topographic highs, ore deposits, complex subduction zones, trans-crustal geologic structures, suggest an intimate genetic relationship (Cooke et al., 2005).

There are nine known districts that contain the largest porphyry Cu-Au deposits in the Philippines, some of these, amongst the largest porphyry deposits in the world (e.g., Far-South East, and Tampakan). Most of these deposits are of Pliocene age and are related to porphyritic diorite intrusions, and are structurally controlled by second order structures related to the Philippine Fault Zone. Some of these districts (e.g., Mankayan, Baguio, and Tampakan) present clear evidence for the genetic relation between lithocaps, epithermal, skarn, and porphyry deposits (Figs. 2.6 and 2.7).

A number of the Philippine metallogenic districts remain underexplored due to circumstances related to political challenges or lack of infrastructure. These districts provide significant opportunities for new discoveries if such challenges can be surpassed. Understanding of the spatial, geochemical, and chronological relations of these deposits will be critical for the development of effective and efficient geologic and exploration models for porphyry, epithermal, and skarn deposits in similar environments to those encountered in the Philippines.

2.5. Quaternary seismicity in the Visayas

2.5.1. Introduction

The Philippine archipelago is located in one of the most tectonically active areas in the world. The archipelago lies over two opposing subduction zones (i.e., the Philippine Trench and the Manila Trench). Hence, seismic activity is ubiquitous and at least 13,986 earthquakes have been detected between the years 1911 and 2015 (USGS, 2015). This section aims to analyse earthquakes and their spatial distribution in the Visayas region. It begins with a statistical analysis of earthquake depth and magnitude. This is followed by a spatial analysis of earthquake depth and magnitude. This section aims to provide information about the geometry of the subduction zones in the Visayas region and their relationship with active and extinct volcanoes, mineral deposits in Negros, and the Bantug area.

2.5.2. Statistical analyses and spatial distribution of quaternary earthquakes

The Visayas region includes the islands of Panay, Negros, Cebu, Bohol, Leyte, and Samar. 1,866 earthquakes were selected for analyses. The earthquakes were detected between 1973 and 2015 by the USGS (2015) over the Visayas region. Figure 2.8 presents histograms and score diagrams for earthquake depth and earthquake magnitude in the Visayas. The histogram and probability plot for depth (Figs. 2.8a and 2.8b) reveal three clusters of earthquakes; one cluster at 10 km depth with 267 earthquakes, a second cluster at 33 km depth with 761 earthquakes, and a third cluster at 35 km with 116 earthquakes. The histogram and probability plot for earthquake magnitude (Figs. 2.8c and 2.8d) highlights that most earthquakes had magnitude between 4.4 and 4.7 mb. Figure 2.8e presents a magnitude versus depth diagram where the clusters at 10 and 35 km clearly stand out; the deepest earthquakes (i.e., ~600 km) range in magnitude from 4.3 to 6 mb.

Figure 2.9b presents a raster image generated from earthquake-depth data from USGS (2015). The image covers the Visayas region, and it was generated using the Nearest Neighbour interpolation method (Oliver and Webster, 2015). Red colours represent shallow-depth earthquakes (i.e., 9.39-29.02 km) and blue colours represent deeper earthquakes (75.9-307.1 km). The deepest earthquakes are located to the east of the Visayas region, beneath Samar and Leyte island; these define a NW trending belt ~195 km width. The front of the belt is located at ~76 km west from the Philippine trench. The Leyte volcanic belt is located at ~182 km west of the Philippine trench, over the zone of deepest earthquakes (Fig. 2.9b). A zone of shallow earthquakes is located beneath Bohol island and extends under Cebu and central-eastern Negros. This zone of

shallow earthquakes is limited to the west by a zone of deeper earthquakes, the latter extends NS in Negros. The Mount Canlaon and Cuernos de Negros volcanoes (numbers 3 and 4 on Fig. 2.9b), and the Bantug area are located in the boundary between the shallow and deep earthquake zones. A NE trending zone of shallow earthquakes extends from the Manila trench to southwest Negros, this zone contains the southwest Negros porphyry district. Figure 2.10 presents a cross section over the raster image in Figure 2.9 (dashed line A-A'). Figure 2.10a presents earthquake distribution as well as the location of the volcanic line, the Southwest Negros porphyry district, and the Bantug area. The red dashed lines represent interpreted boundaries between the subducting plate and the overlying crust.

From Figures 2.9 and 2.10 it can be inferred that the Philippine Sea plate to the east is subducting along the Philippine trench at approximately 30° to 35°. The top of the subduction zone is defined by a cluster of earthquakes located between 25 and 100 km depth, between longitude 124° and 126°, or over 200 km west from the Philippine trench.

To the west, the Sulu sea plate is subducting along the Negros trench. Earthquakes in the west part of the Visayas are located in discrete clusters at 10 to 75 km depth, between longitude 121.5° and 123°, covering ~100 km to the east from the Negros trench. Earthquakes in the west define a tight cluster which suggest that subduction is taking place currently at a very steep angle and at a short distance.

2.5.3. Summary

The Philippines is located above a complex, tectonically active, subduction zone. At least 13,986 earthquakes have been detected since the years 1911 and 2015. 1,866 earthquakes occurred in this time over the Visayas region. Earthquakes in the region occur at three predominant depths: 10, 33, and 35 km. Most earthquakes range in magnitude between 4.4. and 4.7 mb.

Deepest earthquakes are located to the east of the Visayas region and are associated to the Philippine trench. Shallow earthquakes are located beneath Bohol, Cebu, and central-eastern Negros. The Mount Canlaon and Cuernos de Negros volcanoes, as well as the Bantug area, are located in the boundary between the shallow and deep earthquake zones.

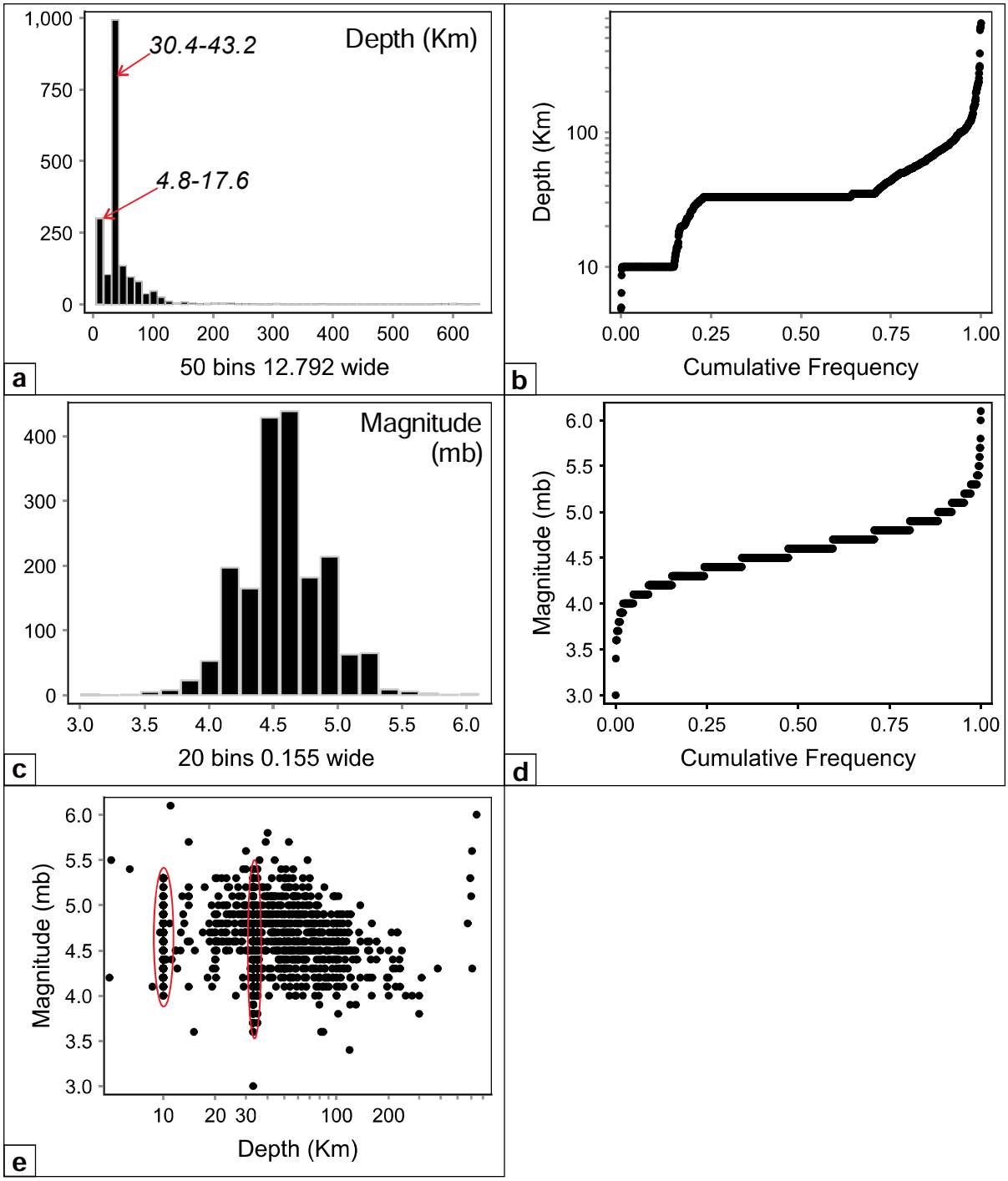

Figure 2.8. Statistical analysis of earthquakes in the Visayas region. a. Histogram for earthquake depth. **b.** Histogram for earthquake magnitude. **c.** Probability diagram for depth. **d.** Probability diagram for magnitude. **e.** Magnitude vs. Depth diagram.

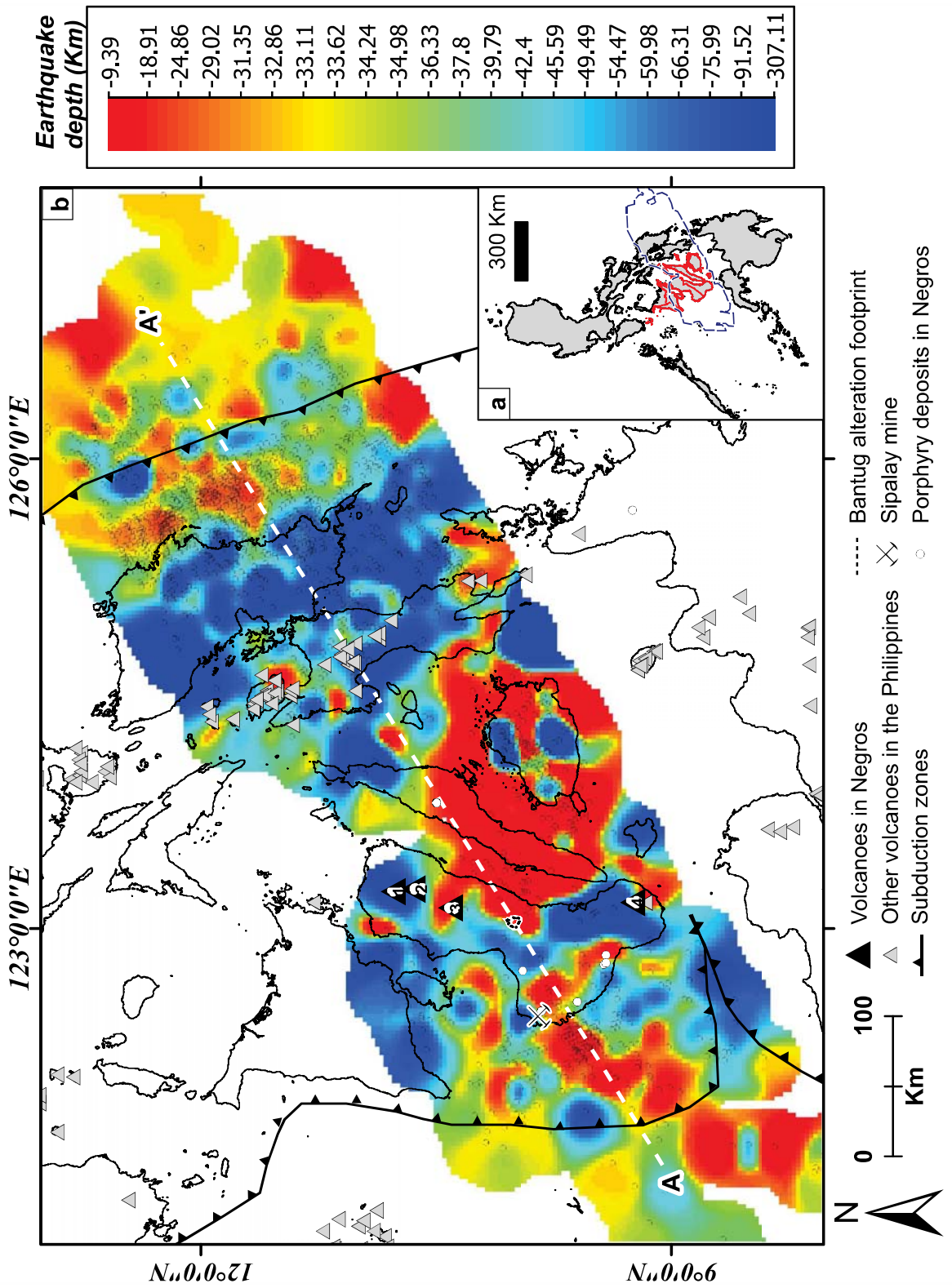

Figure 2.9. Quaternary seismic activity in the Visayas region. a. The Visayas region in the Philippines. **b.** Raster image for earthquake depth in the Visayas region. The raster was created using the Nearest Neighbour method; section A-A' is presented in Figure 2.9. Volcanoes: 1: Mt. Silay; 2: Mandalagan; 3: Mt. Canlaon; 4: Cuernos de Negros.

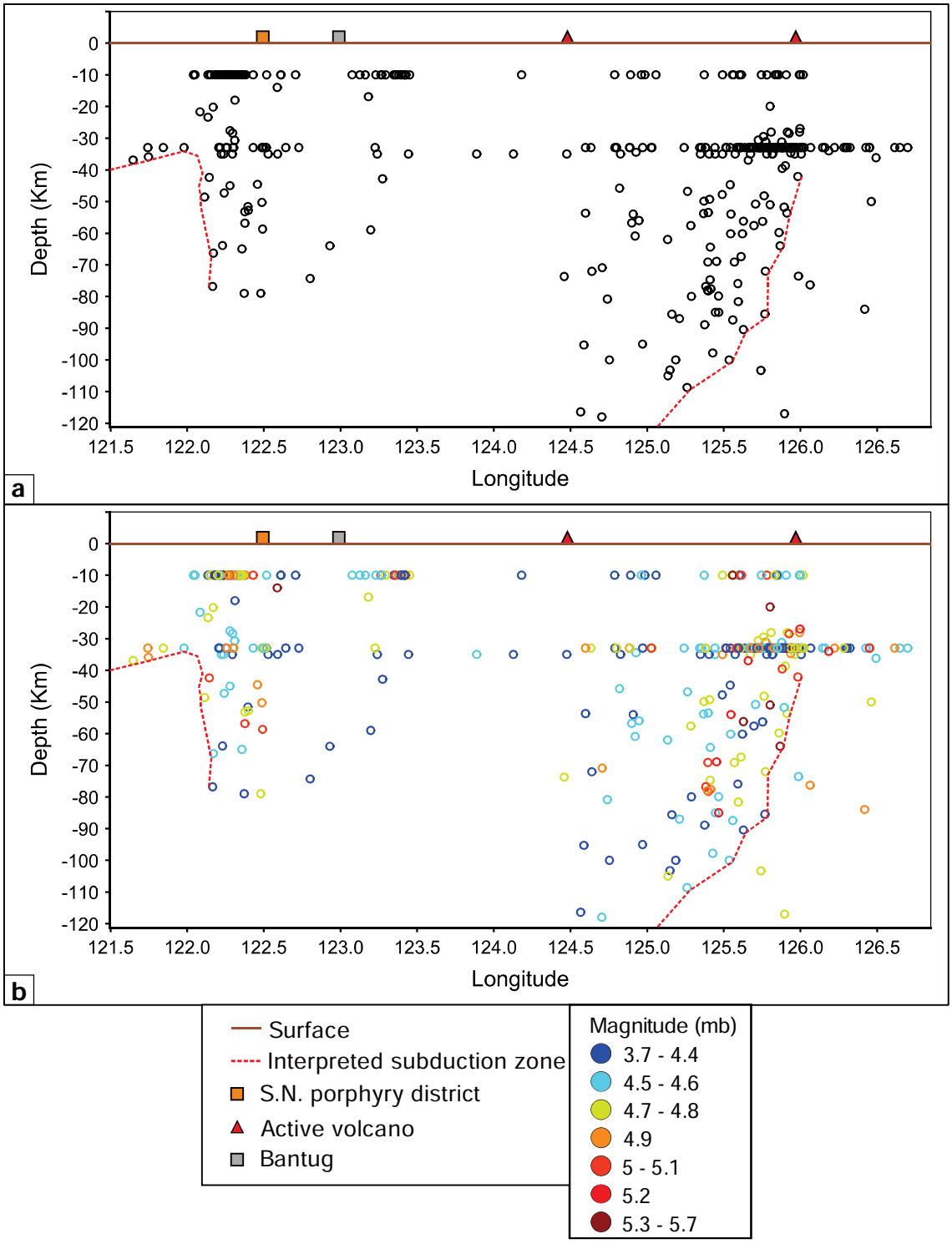

Figure 2.10. Earthquake section. Section A-A' from Figure 2.9. **a.** Earthquake distribution along the section A-A'; yellow square represents the Southwest Negros porphyry district, grey square represents the Bantug area, and red triangles are active volcanoes along the section. **b.** Earthquakes coloured by magnitude; blue colours represent lower magnitude and red colours represent higher magnitude. Abbreviations: S.N.: Southwest Negros.

2.6. Geology of Negros

2.6.1. Introduction

The regional geology of Negros has been documented over the last three decades (Von Biedersee and Pichler, 1995; Solidum, 2002, 2003; Rae, 2002; Rae et al. 2003, 2004, 2011). The Mines and Geosciences Bureau (MGB, 2004) also produced a comprehensive summary of the stratigraphy of the Philippines, including Negros Island. MGB (2004) divides Negros in three tectono-stratigraphic terranes (Fig. 2.11): *(i)* ancient Negros arc, *(ii)* the Visayan sea basin, and *(iii)* the recent Negros arc. The ancient Negros arc is geographically restricted to the western portion of the island, and the Visayan sea basin is geographically restricted to the northern and western margin of Negros. The recent Negros arc comprises the northern, central, and southeastern regions of the island.

2.6.2. Volcano-sedimentary sequences and Oligocene magmatism in Negros

2.6.2.1. Basak Formation

The oldest volcano-sedimentary rocks, the basement of Negros, are the Cretaceous Basak Formation and the Cretaceous Isio Limestone in southwest Negros (i.e., Basak, Cauyan; ***Kv*** in Fig. 2.12b). The Cretaceous Basak Formation consists of basaltic flows and fragmental pyroclastic rocks of basaltic and andesitic composition, interbedded with thin horizons of tuff, conglomerates, sandstones, siltstones, and shales. The base of the formation has not been reported, and so its total thickness is unknown. It crops out in southwest Negros (i.e., Basak, Cauyan; ***Kv*** Fig. 2.12b) and is considered to be of Cretaceous age based on field evidence (MGB, 2004).

2.6.2.2. Pagatban Diorite

The Oligocene Pagatban Diorite intruded the Basak Formation in southwest Negros (i.e., Pagatban River; MGB, 2004). It consists of a cluster of igneous intrusions which extends for ~62 km from the Panay Gulf to Talong Bay (***Oi*** in Fig. 2.12b). This intrusive complex exhibits various textures and compositions, predominantly dioritic to quartz dioritic. Gabbroic, tonalitic and granodioritic facies have also been identified (MGB, 2004). Textures vary from medium-coarse grained to porphyritic. Walther et al (1981) and Burton (1982) reported a radiometric K-Ar age of 30.2 ± 4 Ma from biotite from a porphyritic tonalite at Sipalay. MMAJ-JICA (1988) reported ages ranging from 28 Ma to 25.1 Ma for the diorite; information on the method or the error was not provided.

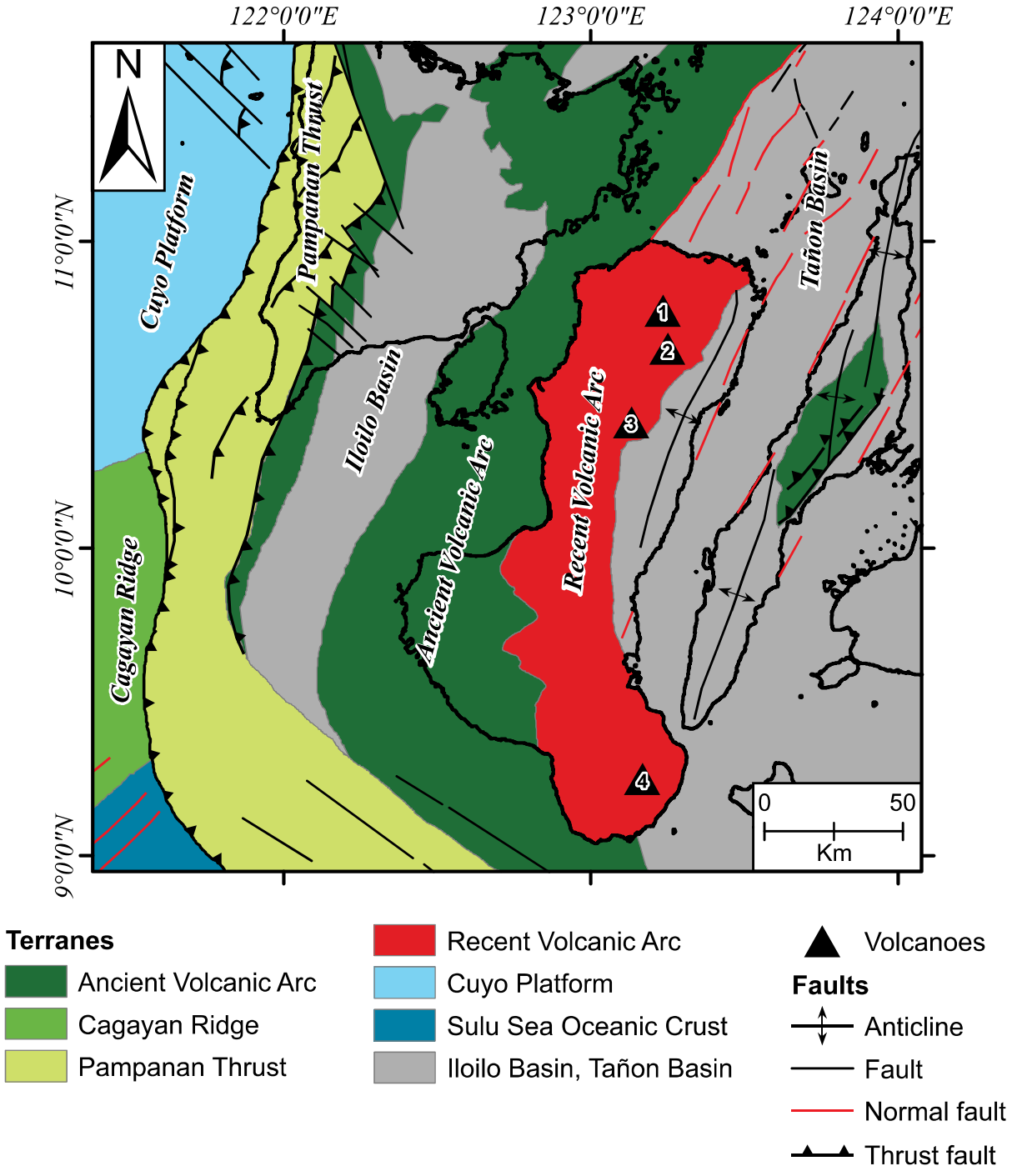

Figure 2.11. Tectono-stratigraphic terranes of Central Visayas. Modified from Ragin et al. (1989). The ancient volcanic arc in Negros is depicted in dark green, the recent Negros arc is depicted in red, and the back-arc Tañon basin is in grey; a remnant of the ancient volcanic arc is located in central Cebu. Black triangles are volcanoes; 1: Mt. Silay; 2: Mt. Mandalagan; 3: Mt. Canlaon; 4: Cuernos de Negros.

2.6.2.3. Isio Limestone

The Cretaceous Basak Formation is unconformably overlain by the Eocene Isio Limestone. This Isio Limestone crops in Negros Occidental (i.e., Basak, Cauayan; ***Esl*** in Fig. 2.12b), and consists entirely of limestone. Balce (1964) describe it as yellow to brown, well bedded, and fossiliferous. David (1982) proposed a late Eocene age for the Isio Limestone based on the presence of foraminifera such as discocyclina and nummulites.

2.6.2.4. Escalante Formation

The Late Oligocene to Early Miocene Escalante Formation crops out in northeast Negros (***OMs*** Fig. 2.12b), and was originally defined by Caguiat (1967). MGB (2004) divided the Escalante Formation into two members, the lower Paitan member and the upper Trankalan limestone; both members are considered to form a total thickness of 1,730 m. The lower Paitan member consists of sandstone, siltstone, mudstone, and marl, and it reaches a thickness of 500 m (MGB, 2004). The upper Trankalan limestone is thickly bedded, partly brecciated, and contains fossils such as orbitoids (MGB, 2004).

2.6.2.5. Malabago Formation

The Early to Middle Miocene Malabago Formation is exposed in northeast Negros (***Ms*** in Fig. 2.12b). It is composed of conglomerate, tuffaceous sandstone, siltstone, tuff, interbedded volcanic breccia, pillow lavas, mudstone, and thin marl-limestone horizons. It lies unconformably over the Escalante Formation and ranges from 500 m to 1,500 m thick (MGB, 2004).

2.6.2.6. Macasilao Formation

The Middle Miocene Macasilao Formation crops out in northeast Negros (***Ms*** in Fig. 2.12b). It conformably overlies the Malabago Formation and is composed of intercalated horizons of sandstone, siltstone, claystone, conglomerate, limestone, and coal seams. Of particular interest is the conglomerate, which has andesitic to basaltic clasts up to 2 m in diameter in a tuffaceous mudstone matrix. Thickness of the Macasilao Formation ranges between 1,400 m and 3,200 m (MGB, 2004). Muller et al. (1989) reported several nanoplankton assemblages (e.g., coccolithus pelagicus, reticulofenestra pseudoumbilica, cyclicargolithus abisectus, cyclococcolithus rotula, discoaster exilis, and rhabdosphaera poculi), pelecypods, gastropods, ostracods, otoliths and fish teeth. These faunas are consistent with a near-shore, inner to middle neritic depositional environment.

2.6.2.7. Talave Formation

The Late Miocene-Early Pliocene Talave Formation crops out in east-central Negros (e.g., Bais city, Razor Back Mountain, ***Nsl*** in Fig. 2.12b), and conformably overlies the Macasilao Formation. MGB (2004) assigned a thickness of 960 m to the Talave Formation. Porth et al. (1989) divided the Talave Formation into a lower calcareous clastic member and an upper massive limestone member. The lower member is made of well bedded, partly marly limestones. It is conformably overlain by coral-head and bivalve bearing massive limestone. The upper member comprises laminated to thin bedded tuffaceous mudstone and conglomerate, and thin bedded grey limestone.

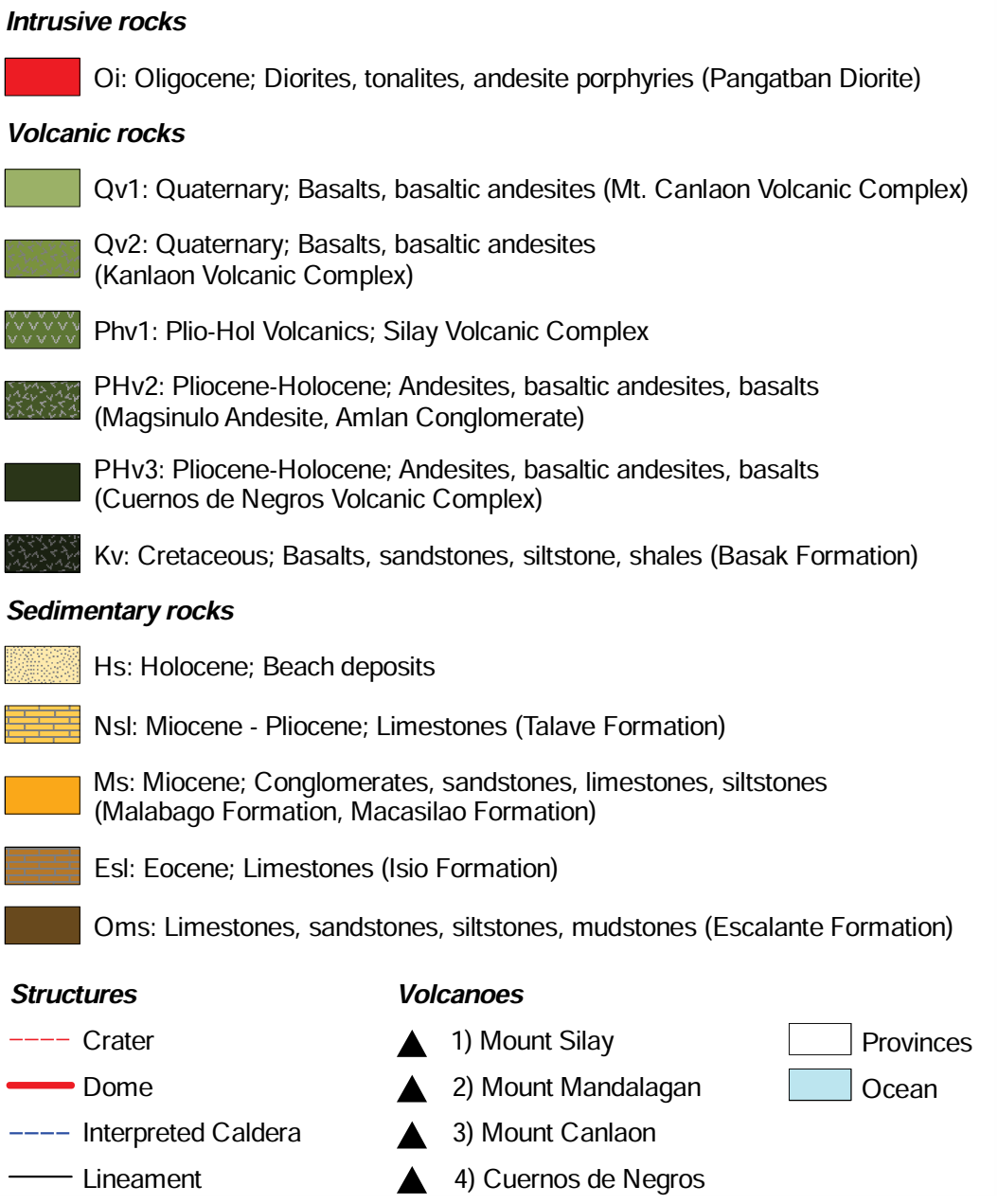

Figure 2.12. Geology of Negros (Opposite page). Legend.

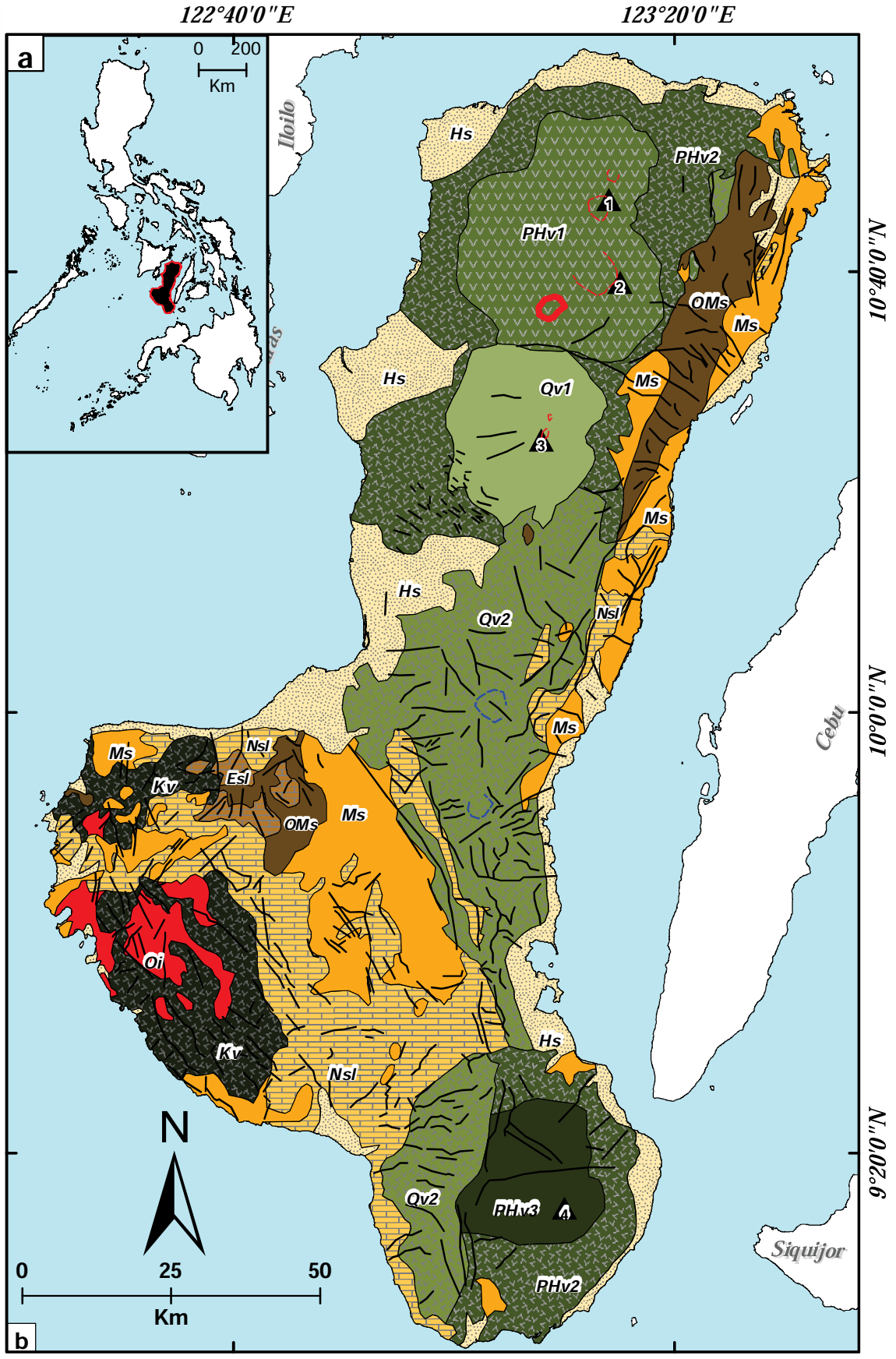

Figure 2.12. Geology of Negros. a. The Philippine archipelago, Negros is highlighted with a red outline. **b.** Geology of Negros, after BMG (2004). Black triangles represent volcanic edifices.

2.6.2.8. Magsinulo Andesite

The Early to Late Pliocene Magsinulo Andesite crops out in southeast Negros (***PHv2*** in Fig. 2.12b). It comprises a series of andesite flow breccias and blocky andesite flows. Ayson (1987) described angular clasts of hornblende-phyric andesite in a yellow vitric matrix with feldspar phenocrysts and ferromagnesian minerals.

2.6.2.9. Amlan Conglomerate

The Late Pliocene Amlan Conglomerate crops out in southeast Negros (part of ***PHv2*** in Fig. 2.12b). It unconformably overlies the Magsinulo Andesite. The Amlan Conglomerate consists of conglomerate horizons, minor sandstones, mudstones, andesitic flows, and pyroclastic rocks (MGB, 2004). The conglomerate clasts are predominantly hornblende-phyric andesites, silicic altered and pyrite altered rocks (MGB, 2004).

2.6.2.10. Caliling Formation

The late Pliocene-Pleistocene Caliling Formation crops out in western (e.g., Sojoton), south-central (e.g., Mabinay), and north-eastern Negros (***Ms*** in Fig. 2.12b; MGB, 2004). This formation unconformably overlies the Miocene formations and reaches a thickness of ~500 m (MGB, 2004). It extends over the northeast coast of Negros over a large area (~380 km^2). The Caliling Formation contains several horizons of limestone, sandstone, siltstone, and shale. It has been divided into a lower limestone member and upper clastic member (MGB, 2004). The upper clastic member, the Mahaba sandstone, comprises a series of coarse sandstones with coral fragments and molluscs and it is considered to represent the back-reef zone of a continental reef (Amiscaray and Quiel, 1987; MGB, 2004).

2.6.2.11. Canlaon Volcanic Complex

The Pleistocene to Holocene Canlaon Volcanic Complex (CVC) extends over the northern, central, and southern part of Negros (***Qv2*** in Fig. 2.12b). It represents the recent Negros volcanic arc, which is associated with the eastward subduction of the Sulu Basin along the Negros Trench. The CVC comprises the volcanic edifices of Mount Silay, Mount Mandalagon, Mount Canlaon, and Cuernos de Negros (1, 2, 3, and 4 respectively in Fig. 2.12). The volcanic edifices are made of basalt, andesite, and dacite flows; as well as large volumes of volcanic breccias and tuffs (von Biedersee and Pichler, 1995; Sajona et al., 2000; Solidum et al., 2002; MGB, 2004; Rae, 2002; Rae et al., 2003, 2004, 2011). Structures such as craters, domes, and calderas have been reported to be associated with the volcanic edifices of the CVC (UNDP, 1987; Rae, 2002). Extensive hydrothermal alteration, geothermal activity, and precious and base metal

anomalies have been genetically and spatially associated to the CVC (UNDP, 1987; Rae, 2002).

2.6.3. Structural interpretation of Negros

Figure 2.13 presents a structural interpretation of Negros based on the digital elevation model (DEM) generated from NOAA (2014). Figure 2.13a presents the DEM for Negros; the recent volcanic arc is distinguishable by the volcanic edifices (Fig. 2.13; 1 to 4). Volcanoes in the north of the island are discrete edifices, whereas Cuernos de Negros is a larger, composite edifice. The Ancient Volcanic Arc does not have obvious volcanic edifices. Figure 2.13b presents a colour coded interpretation of lineaments from the DEM. There are three major structural trends in Negros: NW-SE, N-S, and NE-SW (Fig. 2.13b). Most structures in Negros trend NW-SE (Fig. 2.13b) and are located in the west portion of the island (Fig. 2.13b); a second major trend in this area is NE-SW (Fig. 2.13b). Figure 2.14 presents rose diagrams with structural information from different areas of Negros.

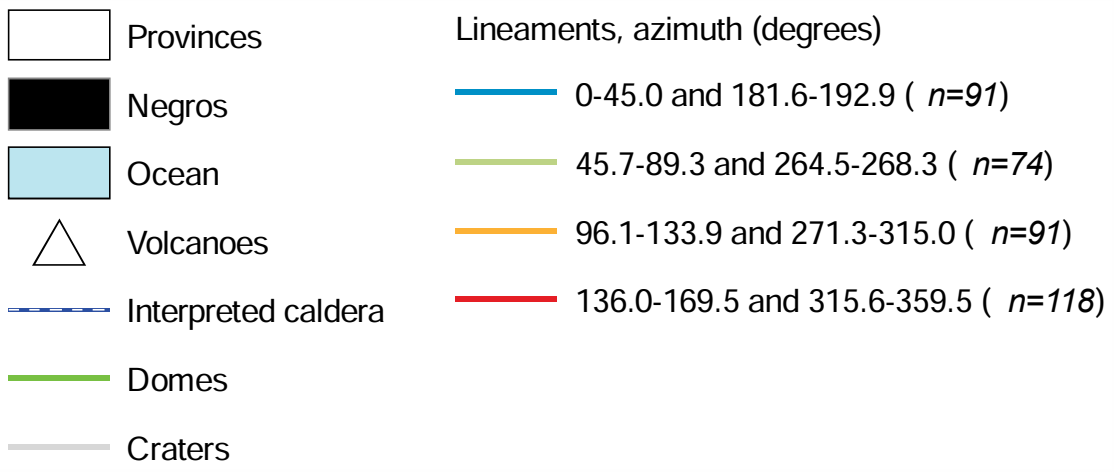

Figure 2.13. Structural interpretation of Negros (Opposite page). Abbreviations: n: number of lineaments.

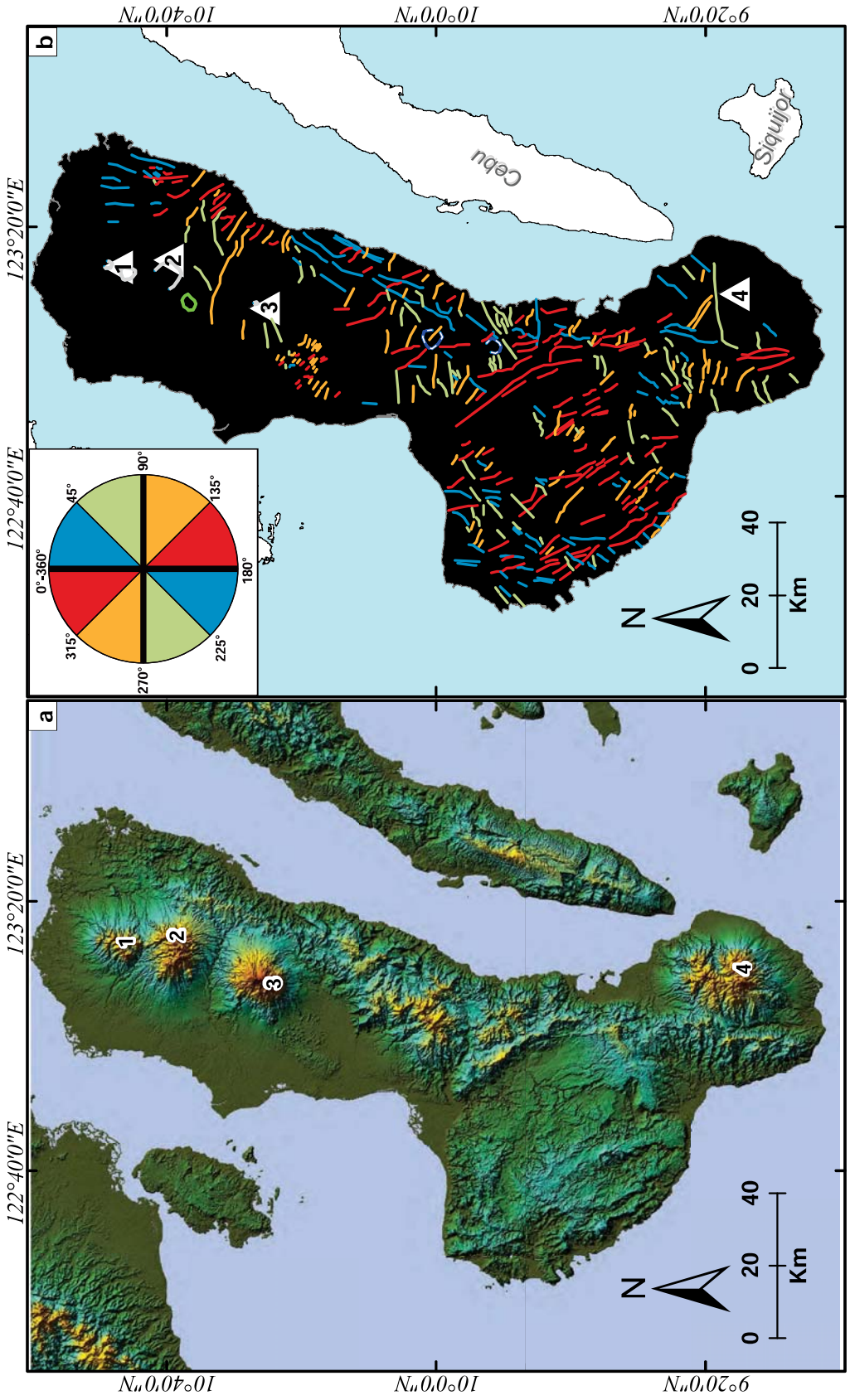

Figure 2.13. Structural interpretation of Negros. a. Digital elevation model (DEM). **b.** Colour coded structures in Negros; inset provides a graphic coloured legend for the structures. Numbers in panels **a.** and **b.** are for volcanoes; 1: Mt. Silay; 2: Mt. Mandalagan; 3: Mt. Canlaon; 4: Cuernos de Negros.

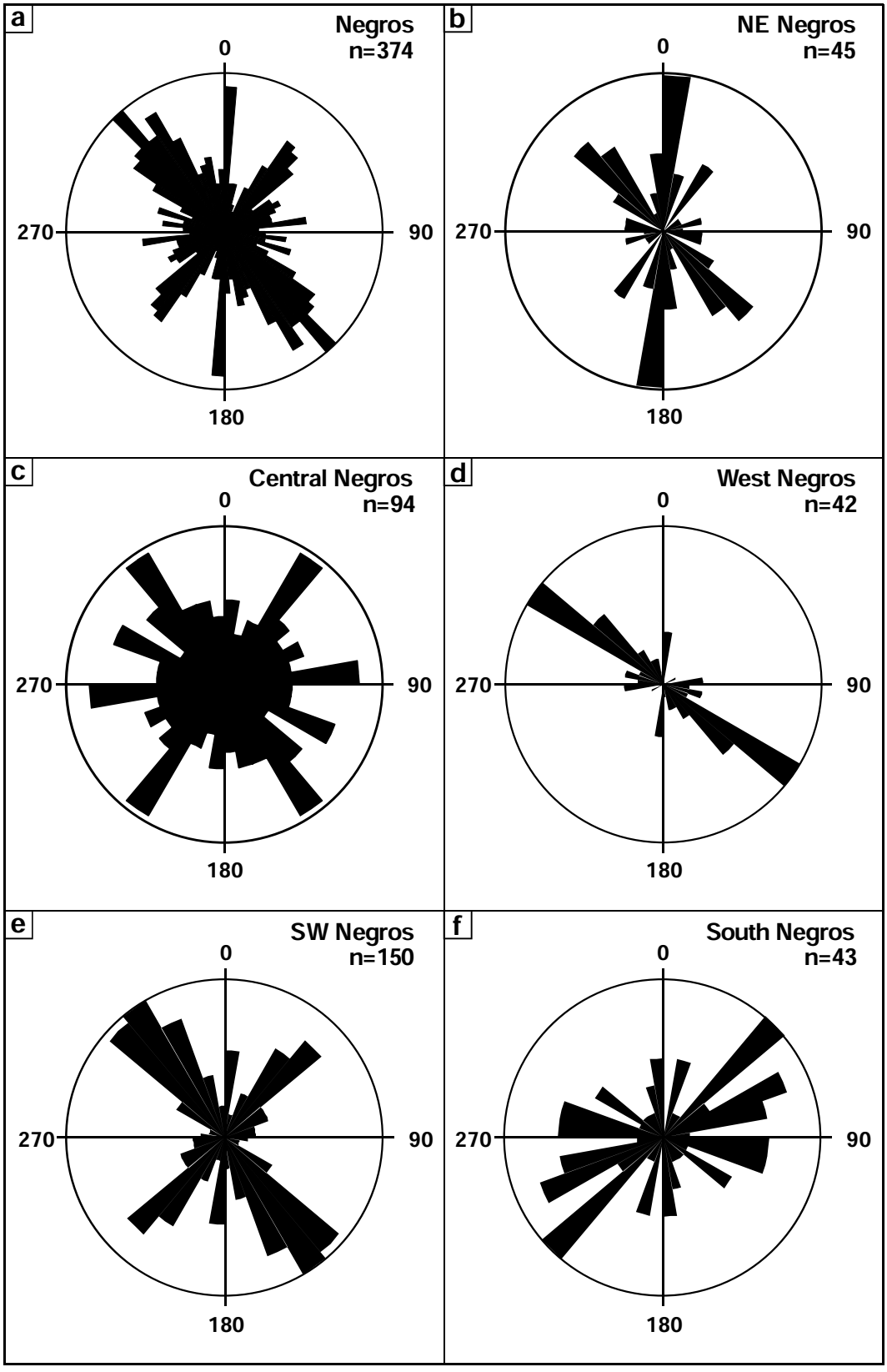

Figure 2.14. Rose diagrams from interpreted lineaments in Negros. a. Rose diagram from all structures in Negros (i.e., n=374). **b.** Rose diagram from 45 structures in northeast Negros. c. Rose diagram from 94 structures in central Negros. **d.** Rose diagram from 42 structures in west Negros. **e.** Rose diagram from 150 structures in southwest Negros. **f.** Rose diagram from south Negros.

2.6.4. Neogene-Quaternary magmatism and volcanism geochemistry

This section provides a summary of the geochemistry of the CVC, and intrusive rocks that have cut the CVC at the Palinpinon geothermal field.

2.6.4.1. Volcanic rocks

The geochemistry of extrusive and intrusive rocks at Negros has been addressed by von Biedersee et al. (1995), Sajona et al. (2000), Rae (2002), and Solidum et al. (2003). Results from previous studies are presented in Appendix B. The distribution of samples from previous studies is presented in Figure 2.15. Results from major and trace element classification from previous studies on these volcanic rocks are presented in Figure 2.16.

Samples from von Biedersee et al. (1995) and Solidum et al. (2003) plot on the line that separates the andesite field from the trachyandesite field on the total alkali-silica plot (Fig. 2.16a). Most samples from Sajona et al. (2000) plot in a similar way, and a few samples plot in the field for basalts. Samples from Rae (2002) vary from basalts to andesites. For the Zr/TiO_2 vs Nb/Y plot and the Zr/Ti vs Nb/Y plot, most samples plot in the andesite field, and some samples plot in the basaltic field (Figs. 2.16b and 2.16c).

Most samples plot in the high-K field, some in the medium-K field, and two samples plot in the low-K field on the K_2O vs. SiO_2 diagram (Fig. 2.16d). Two samples from Sajona et al. (2000) plot in the lower area of the field for shoshonites. The majority of samples plot in the calc-alkaline field of the tectonic classification diagram for mafic igneous rocks (Fig. 2.16e.; Cabanis and Lecolle, 1989). Three samples plot in the late to post-orogenic intracontinental domain field (LPID); two samples are from Solidum et al. (2003) and one sample is from Rae (2002). In Figure 2.16f (i.e., Ti-Zr diagram for basalts; Pearce and Cann, 1973), most samples plot in the calc-alkali basalt field, and some (Sajona et al., 2003) plot in the island arc tholeiites (i.e., IAT) field.

2.6.4.2. Intrusive rocks

Rae (2002) reported 28 analyses from intrusive rocks from the Palinpinon geothermal field (Fig. 2.15). Rae (2002) identified two intrusions at Palinpinon: The Puhagan dikes and the Nasuji pluton. Ar^{40}/Ar^{39} dating of hornblende from the Puhagan dikes and the Nasuji pluton yielded ages of 4.2-4.1 Ma and 0.7-0.3 Ma, respectively. Both units range in composition from gabbro to quartz diorite (Figs. 2.17a and 2.17b). Most samples from the Nasuji pluton plot in the quartz diorite field of the TAS diagram, and most samples from the Puhagan dike plot in the gabbro and monzogabbro fields (Fig. 2.17a and Fig. 2.17b, respectively). The classification diagram of Debon and Le Fort (1983) suggest that there is a group of quartz diorites and another of tonalites in the Nasuji pluton (Fig. 2.17d). Samples from the Puhagan dikes plot in the quartz diorite field (Fig. 2.17d). Intrusive rocks from the Nasuji pluton and the Puhagan dikes exhibit adakite-like composition (Fig. 2.17e and 2.17f; Rae, 2002). Most samples from both units plot in the adakite-like fields of Richards and Kerrich (2007). The relationship between adakite-like intrusions and porphyry Cu-Mo deposits remains controversial. However, Richards (2011) suggested that high Sr/Y ratios in intermediate composition arc magmas should not be uniquely equated with an origin by slab melting, and extending this link to porphyry ore formation is unwarranted. Their compositions are, however, a favourable indicator of the potential for porphyry style mineralisation.

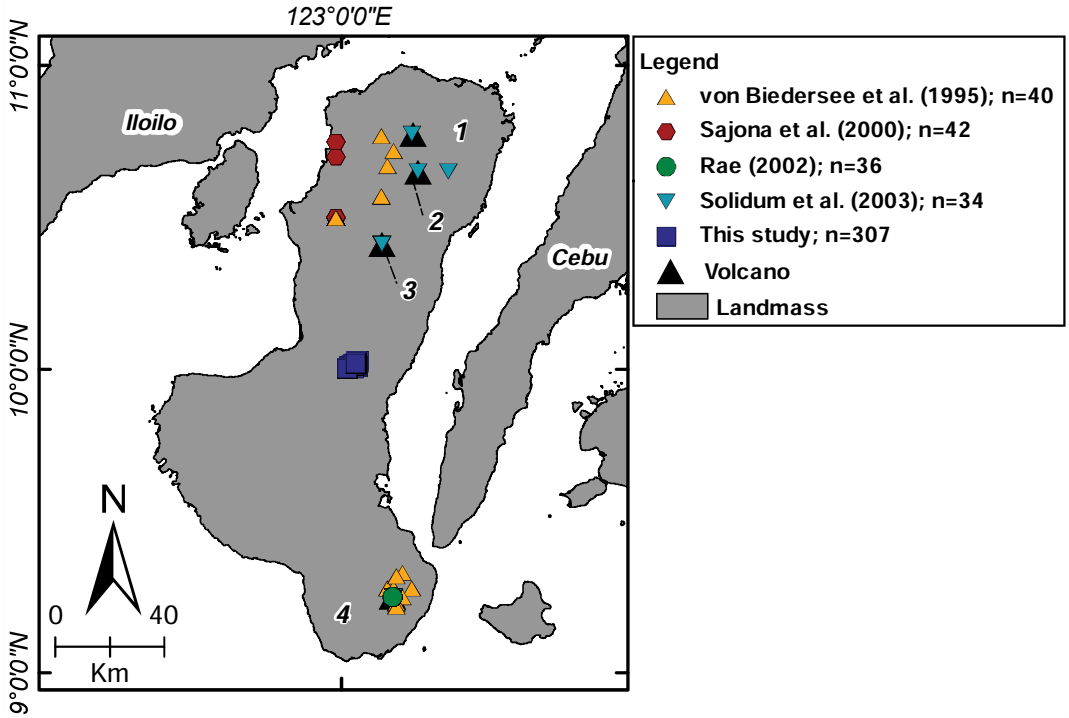

Figure 2.15. Sample distribution of previous geochemical studies in Negros. Black triangles represent volcanoes; 1: Mt. Silay; 2: Mt. Mandalagan; 3: Mt. Canlaon; 4: Cuernos de Negros.

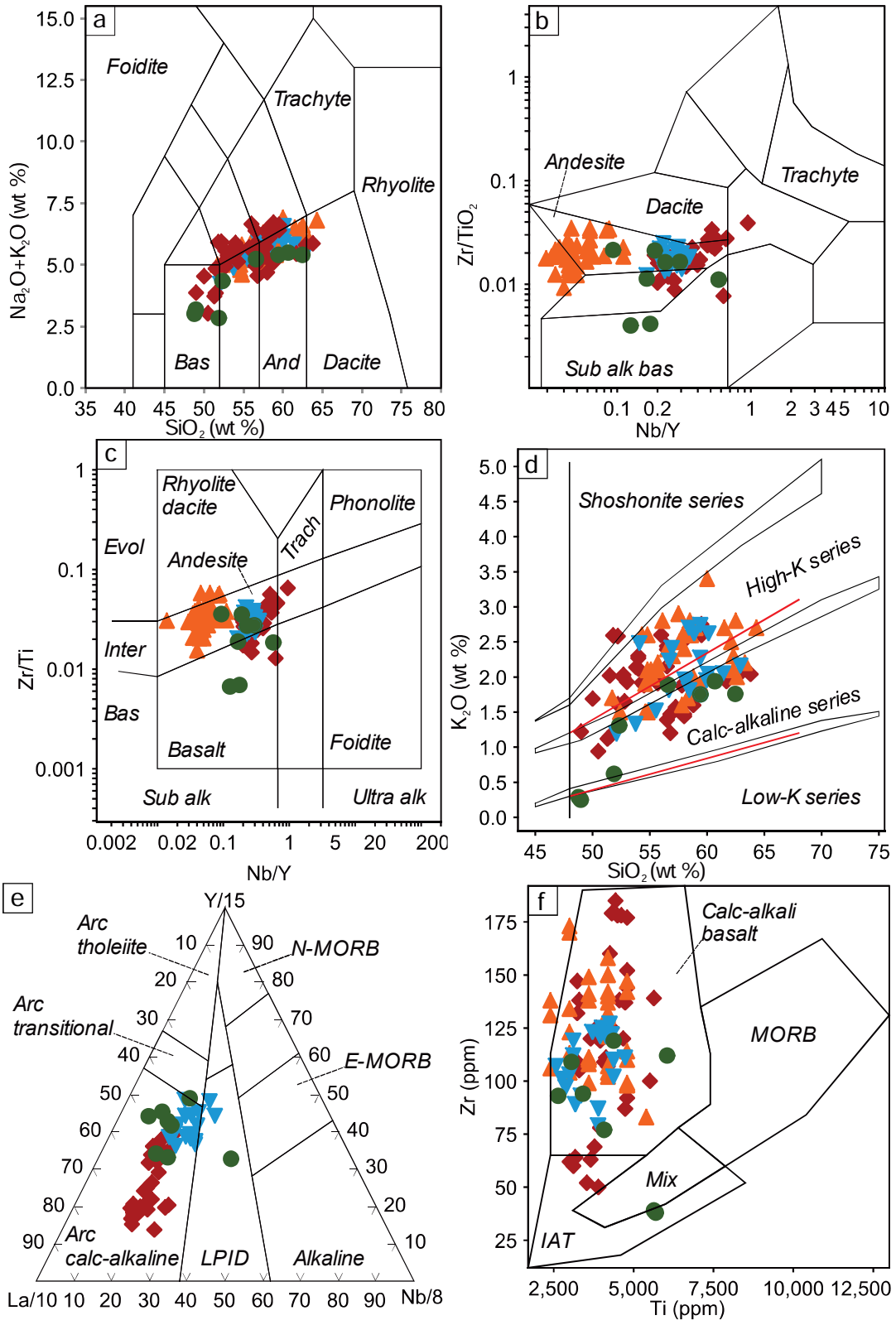

Figure 2.16. Geochemical classification diagrams for volcanic rocks in Negros. a. Total alkali vs. silica diagram for volcanic rocks by Le Maitre (1989). **b.** Trace element classification diagram for volcanic rocks by Winchester and Floyd (1977). **c.** Trace element classification diagram for volcanic rocks by Pearce (1996). **d.** K_2O vs. SiO_2 diagram for subdivision of subalkalic rocks by Le Maitre et al (1989). **e.** Tectonic classification diagram for mafic volcanic rocks by Cabanis and Lecolle (1989). **f.** Ti vs. Zr classification diagram for basaltic rocks by Pearce and Cann (1973). Legend as in Figure 2.13. **Abbreviations:** alk: alkaline; And: andesite; Bas: basalt; IAT: island arc tholeiite; K: potassium; LPID: late to post orogenic intracontinental domains.

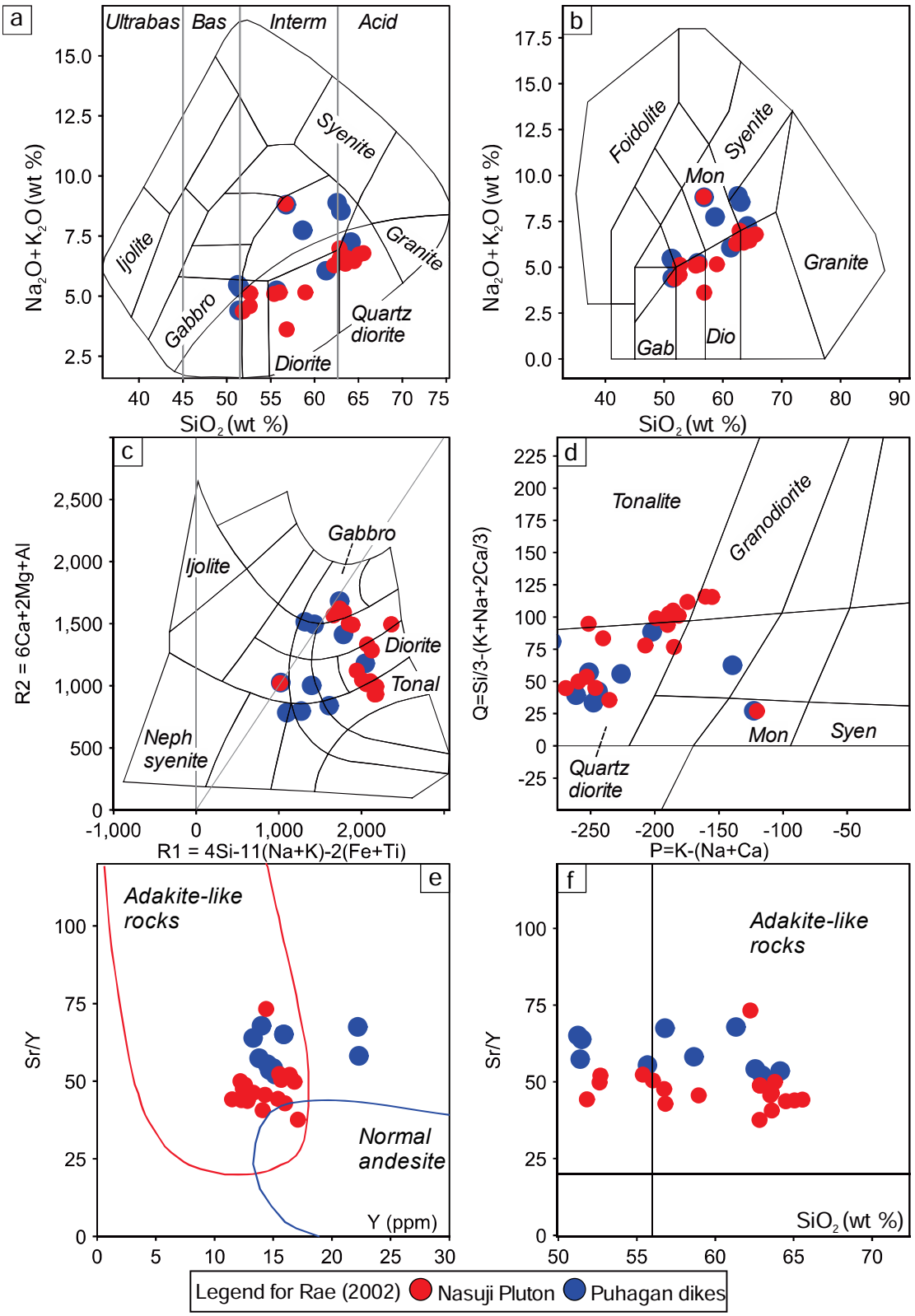

Figure 2.17. Geochemical classification diagrams for intrusive rocks in Negros. a. Total alkali vs. silica diagram for plutonic rocks by Wilson (1989); adapted from Cox et al. (1979). **b.** Total alkali vs. silica diagram for plutonic rocks by Middlemost (1994). **c.** Major cations variation diagram for plutonic rocks by de la Roche et al. (1980). **d.** Classification diagram for plutonic rocks by Debon and Le Fort (1983). **e.** Sr/Y vs. Y discriminant diagram for adakite-like rocks by Richards and Kerrich (2007). **f.** Sr/Y vs. SiO_2 discriminant diagram for adakite-like rocks by Richards et al. (2012). Abbreviations: Bas: basalt; Dio: diorite; Gab: gabbro; Interm: intermediate; Mon: monzonite; Syen: syenite; Tonal: tonalite; Ultrabas: ultrabasic.

2.6.5. Mineralisation, alteration, and geothermal activity in Negros

This section presents a compilation of previous work carried out at the various mineral deposits, mineral occurrences, geothermal fields, and hydrothermally altered areas in Negros.

2.6.5.1. Magmatic-hydrothermal mineral deposits in Negros

There are several porphyry and epithermal occurrences in Negros, as well as active and extinct geothermal fields (Fig. 2.18). The most well-known porphyry deposits are: Sipalay, Basay, and Hinoba-an; these are located in the southwest Negros porphyry epithermal district (Fig. 2.18; Burton, 1983; Singer et al., 2008). In 2008, Freeport-MacMoRan Philippines discovered the Sagay porphyry-high sulfidation Cu-Au prospect in northeast Negros (Fig. 2.18; Celiz, In press).

2.6.5.2. Southwest Negros porphyry-epithermal district

Burton (1983) reported 26 porphyry occurrences in the southwest Negros porphyry district (Table 2.2; Fig. 2.17). Most of the occurrences lie on a NW trending belt of ~50 km length, defined by Burton (1983) as the "central belt" (Fig. 2.19).

The central belt contains the Sipalay deposit, which was the first discovery in the district in 1936. This discovery encouraged exploration in the area by government and industry agencies. Subsequently, several mapping campaigns and studies were carried by the Bureau of Mines (BMG, 1977; Castillo and Escalada, 1979). The geology of the district is characterised by the Cretaceous Basak Formation, overlayed by the Eocene and Oligocene-Miocene Isio and Escalante Formations respectively. Magmatism is considered to have occurred during the Oligocene while emplacement of the Pagatban diorite (Burton, 1983; Santos and Velasquez, 1987). Porphyry-epithermal occurrences in the southwest Negros district are considered to be associated with the Oligocene Pagatban diorite. The Pagatban diorite, technically a batholith, extends NW-SE for ~62 km and NE-SW for ~12 km (Figs. 2.9 and 2.19; BMG, 2008). The Pagatban diorite varies in texture from equigranular to porphyritic, and fine to coarse grained. It also varies compositionally from dioritic to quartz-dioritic (Burton, 1983; BMG, 2008). Gabbroic dikes have also been recognised in the area (Burton, 1983).

A second porphyry belt, located ~10 km to the west of the central belt (Fig. 2.19), host some porphyry-type occurrences, two vein-type prospects (i.e., Sangre and Asia), and the Bulawan breccia deposit (Maglambayan et al., 1998). Burton (1983) reported that an unknown number of test drill-holes had been drilled at Nabulao and Maricalom, and five drill-holes at La Luz; drill-hole locations were not provided. This belt is referred here as "the western belt".

Burton (1983) reported the presence of supergene enrichment in the SW Negros district. Significant quantities of supergene enriched Cu ore were extracted at Basay (Vasquez, 1982), and a 60 m thick supergene enrichment blanket at 1 % vol. Cu was reported at Hinoba-an. Mineralisation was observed to occur near the margins of the batholith and to be associated to late porphyritic intrusions such as: andesite porphyries, diorite porphyries, dacites porphyries.

The Pagatban diorite was dated using the K-Ar method by several authors. Walther et al., (1981) obtained an age of 30.2 ± 4 Ma from biotite; details on the sample location were not provided. Burton (1983) reported two ages, one for the Aya-Aya deposit, and another for the Basay deposit; their ages are: 38.4 ± 2.0 and 34.4 ± 2.0 respectively. Santos and Velasquez (1987) reported three K-Ar ages that range from 28.0 Ma to 25.1 ± 1.4 Ma; details on the analysed minerals and sample locations were not provided. Bobis and Comia (1987) reported K-Ar ages on hydrothermal sericite ranging from 14.4 ± 0.7 Ma. to 13.2 ± 0.6 Ma, details on the analyses and sample locations were not provided.

The southwest Negros district is a significant metallogenic province with large known orebodies. Deposit styles vary from porphyry Cu-Mo with supergene enrichment blankets (i.e., Sipalay) to sphalerite-galena-tetrahedrite-tennantite cemented breccias (i.e., Bulawan). K-Ar dating of intrusive rocks of the Pagatban diorite suggest that magmatism and mineralisation occurred during the Late Eocene to Early Oligocene (i.e., 38.4 ± 2.0 Ma. to 13.2 ± 0.6 Ma). At the time of writing this dissertation, no prospects or deposits are being mined in the district.

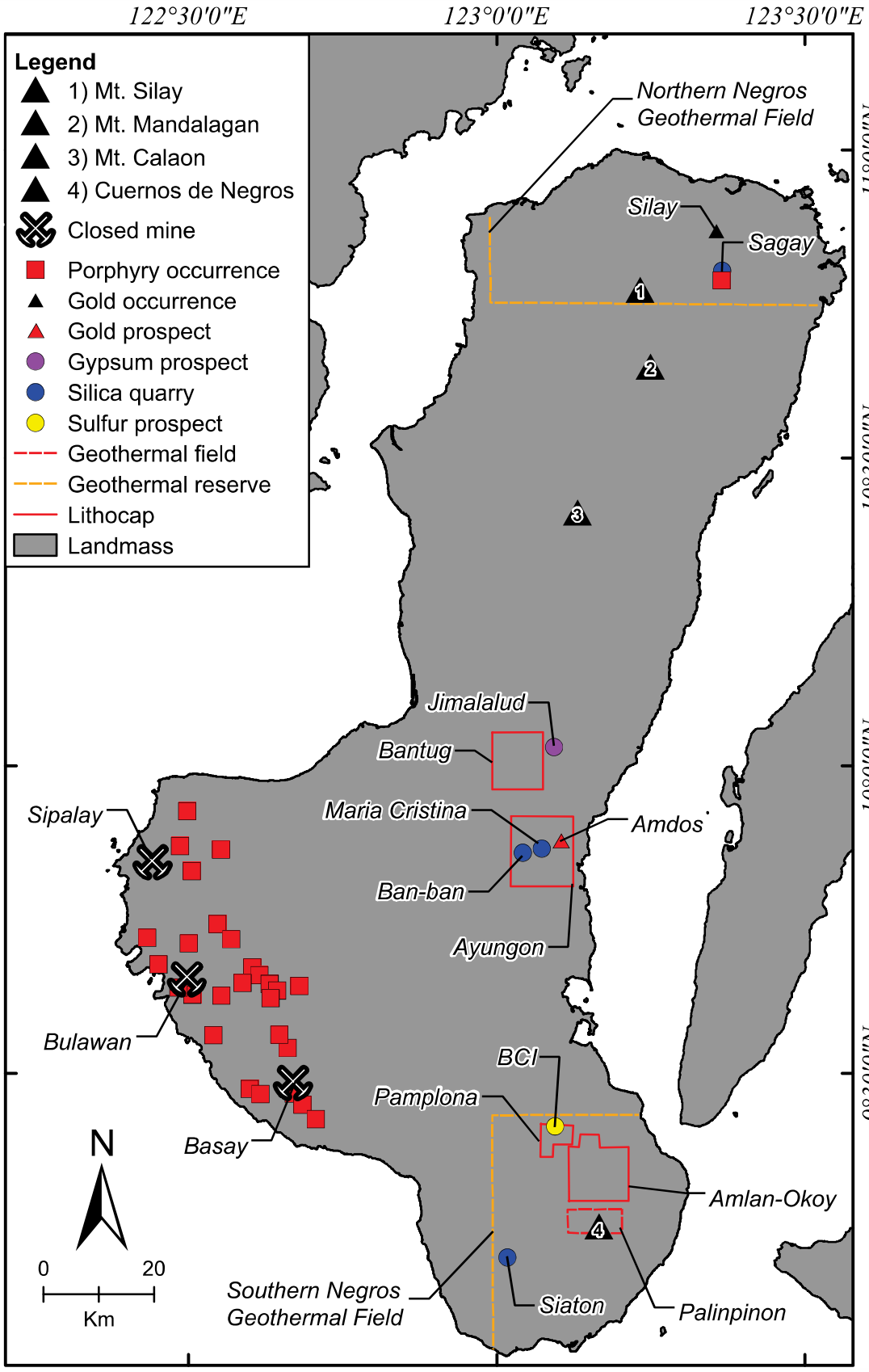

Figure 2.18. Porphyry-epithermal deposits and geothermal areas in Negros. Porphyry and epithermal deposit occurrences are from Burton (1983) and UNDP (1987). Geothermal areas are from UNDP (1987).

Table 2.2. Porphyry, breccia, and epithermal vein deposits in the Southwest Negros Porphyry-Epithermal District

ID	Name	Lat.	Long.	Age (Ma)	Tonnage (Mt)	Cu (wt. %)	Mo (wt. %)	Au (ppm)
1	Sipalay	9.820	122.450	30	807	0.47	0.014	0.05
2	Basay	9.475	122.679	30	262	0.44	0.008	0.29
3	Aya-Aya	9.424	122.705	19.5	40	0.30	0.022	0.08
4	Caltling	9.925	122.496					
5	Metzi	9.869	122.484					
6	Camindanban	9.863	122.551					
7	Umas	9.828	122.504					
8	Maricalum	9.720	122.431					
9	Nagbulao	9.676	122.450					
10	Cayas	9.711	122.498					
11	Luz	9.743	122.545					
12	Hinoba-an	9.717	122.567	17.5	432	0.37	0.000	0.14
13	Soso	9.671	122.602					
14	Ampupuyog	9.658	122.614					
15	Bangol	9.645	122.630					
16	Kabughayan	9.634	122.642					
17	Palayang	9.621	122.632					
18	Manlipo	9.647	122.586					
19	Hola-an	9.625	122.552					
20	Saguibon	9.541	122.659		26	0.35	0.015	0.00
21	La Luz	9.642	122.678					
22	Manlauan	9.474	122.597					
23	Vanguard	9.465	122.616					
24	Nabuangan	9.466	122.670					
25	Ibabao	9.447	122.684					
26	Santa Maria	9.563	122.646					
27	Sangre	9.627	122.504					
28	Asia	9.561	122.538					
29	Bulawan	9.652	122.496					
30	Nagtalay	9.639	122.482					

Deposit locations are from Burton (1983).

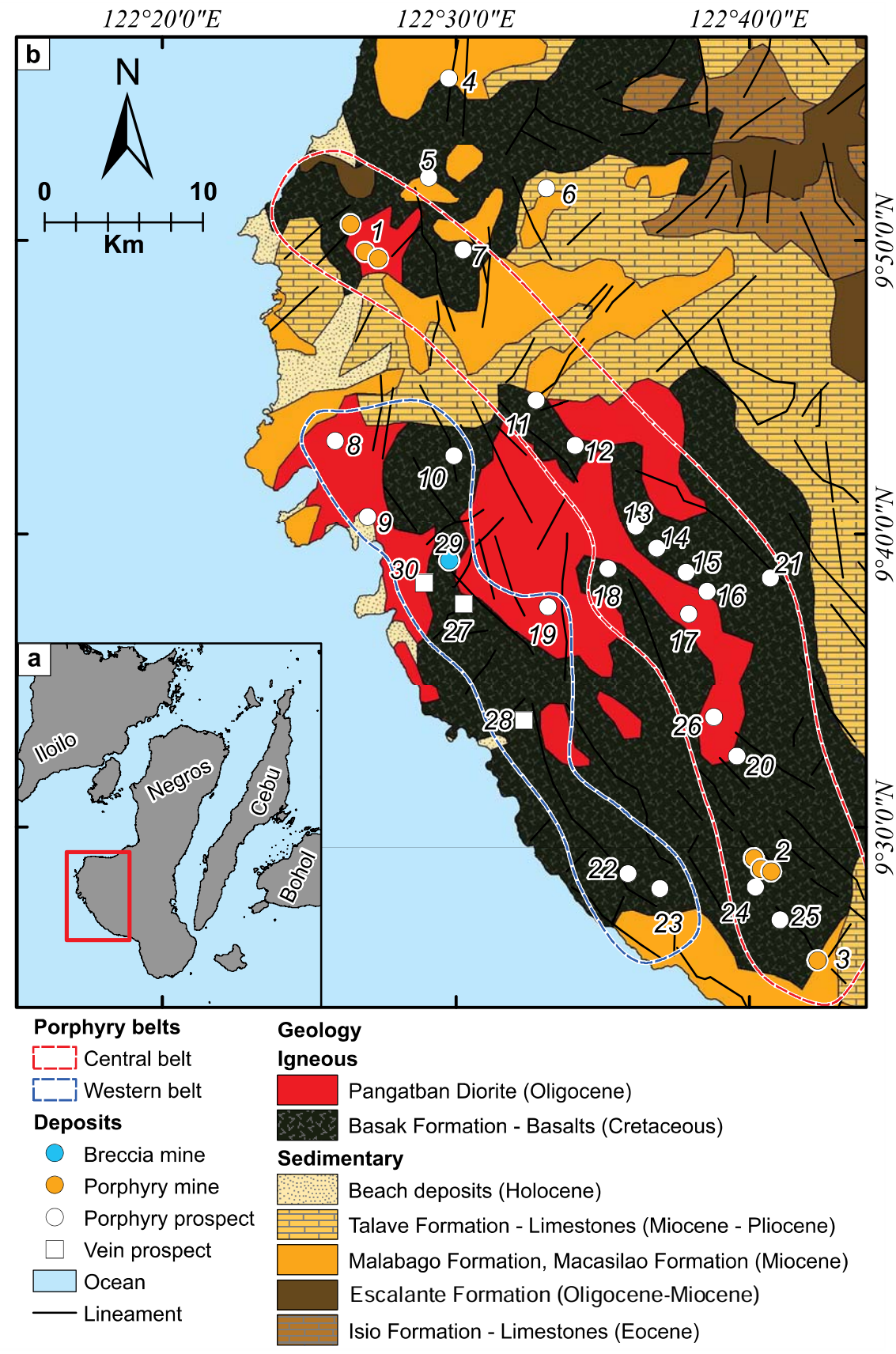

Figure 2.19. The southwestern Negros porphyry-epithermal district. Modified from Burton (1983) and BMG (2004). **a.** The central Visayas region; red square highlights the area of interest. **b.** The southwestern Negros porphyry-epithermal district. The red dashed outline is the "central belt" and the blue dashed outline is the "western belt". Numbers are deposit names in Table 2.2.

2.6.5.3. Geothermal fields and hydrothermally altered areas

The United Nations Development Programme (UNDP) carried out a collaborative exploration project with the Bureau of Mines and Geosciences of the Philippines in 1987. The project aimed to study in detail known hydrothermally-altered and mineralized areas in the Philippine archipelago (UNDP, 1987). Some of the studied areas are located within active geothermal fields (Fig. 2.16). This section focuses on UNDP Technical Report No.2: Geology and hydrothermal alteration of the Amlan-Okoy River, Pamplona, and Ayungon areas, eastern Negros (UNDP, 1987). This section also mentions the highlights of several studies carried at the Palinpinon geothermal field (Rae, 2002; Rae et al., 2003; Rae et al., 2004; Rae et al., 2011).

Figure 2.18 presents the location of some known geothermal fields in Negros, as well as the location of porphyry-style mineralisation occurrences, and the Bantug area. Figure 2.20 presents maps of the geology and hydrothermal alteration in the geothermal fields.

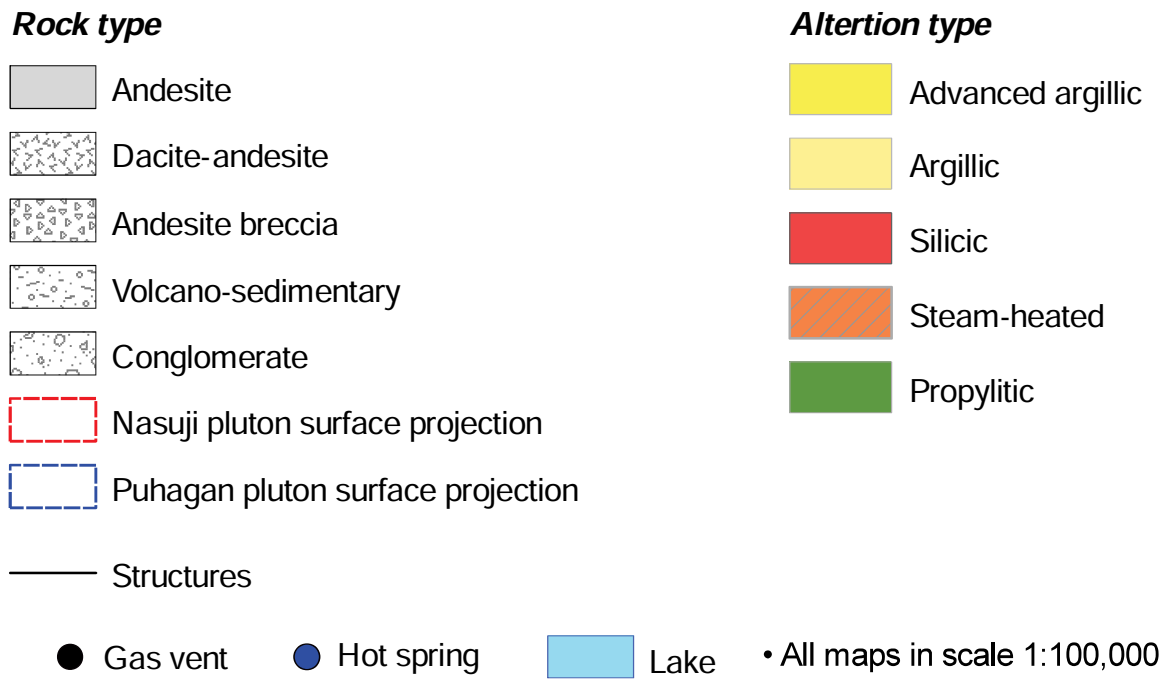

Figure 2.20. Geology and hydrothermal alteration of geothermal fields in Negros (Opposite). Legend.

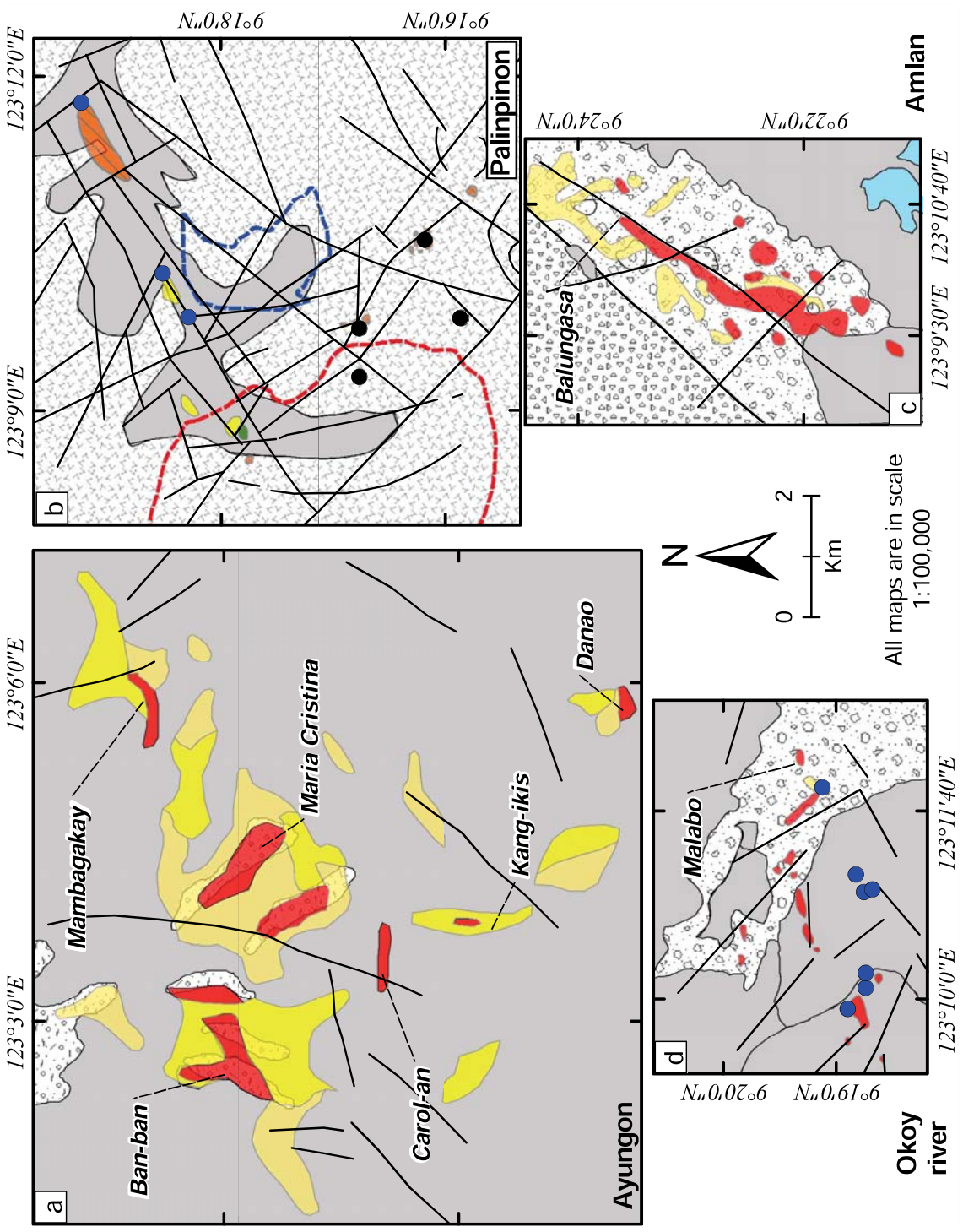

Figure 2.20. Geology and hydrothermal alteration of geothermal fields in Negros. a. The Ayungon area, after UNDP (1987). **b.** The Palinpinon geothermal field; after Rae (2002). **c.** The Amlan area, after UNDP (1987). **d.** The Okoy river area, after UNDP (1987).

2.6.5.3.1. Ayungon

Located in eastern Negros (Fig. 2.18), Ayungon contains the Ban-ban and Maria Cristina silica quarries, and the Amdos gold prospect (UNDP, 1987). The area is entirely covered by the Miocene Paghumayan Formation, which consists of several horizons of volcanic rocks overlayed by sedimentary rocks. The volcanic rocks are mainly hornblende-plagioclase-phyric andesites and andesite breccias. Breccia clasts are angular and range in size from 0.5 to 2.5 m. The overlaying sedimentary rocks are interbedded siltstones, tuffs, and coral bearing limestones (UNDP, 1987). The Miocene Paghumayan Formation is considered to be equivalent to the Solburon and Jayugan andesites in the Amlan-Okoy river area (UNDP, 1987).

Ayungon is an area of ~11 km by ~12 km of hydrothermally altered rocks (Fig. 2.20a). Silicic, argillic, and advanced argillic alteration are widespread in the area (UNDP, 1987). Silicic alteration is best developed in the volcano-sedimentary units as narrow (i.e., < 500 m) elongated bodies trending NW-SE and E-W. XRD analyses by UNDP (1987) revealed the presence of quartz, pyrite, and ilmenite. A hydrothermal breccia with quartz-altered clasts was reported at Ban-ban; vuggy quartz and breccias were reported at Kang-ikis.

Advanced argillic altered zones were recognized around the silicic alteration zones, and were determined to contain pyrophyllite and alunite (i.e., XRD analyses). UNDP (1987) highlighted the presence of advanced argillic alteration at Maria Cristina, Ban-ban, and Kang-ikis. Argillic alteration was reported to be well developed around the silicic altered bodies and to extend for ~2 km. XRD analyses on various samples resulted in smectite, illite, kaolinite, and pyrite.

Precious metal, base metal, As, Sb, Hg, Se, Te, and Tl anomalies were recognised by UNDP (1987) throughout the area. UNDP (1987) analysed 152 rock chip samples; the highest values were: 29 ppb Au, 4 ppm Ag, 260 ppm As, 5.2 ppm Sb, 3,8 pm Hg, and 360 ppm Cu. Areas with the most interesting values are Mambagakay, Ban-ban, Maria Cristina, and Kang-ikis (Fig. 2.20a).

2.6.5.3.2. Palinpinon geothermal field

Located in the northern slopes of the Cuernos de Negros volcano (Fig. 2.18), Palinpinon is the most comprehensively documented geothermal field in Negros.

The geology, hydrothermal alteration, and geothermal potential of Palinpinon has been documented over the last decade by Rae (2002), Rae et al. (2003), Rae et al. (2004), and Rae et al. (2011).

The Palinpinon geothermal field is a high-temperature, liquid-dominated geothermal system in an active volcanic island-arc setting. The stratigraphy of the geothermal system consists of the Miocene Puhagan Volcanic Formation, the Miocene-Pliocene Okoy Formation, the Pliocene to Quaternary Southern Negros and Cuernos Volcanic Formations, the Pliocene Puhagan dikes, and the Pleistocene Nasuji Pluton. $^{40}Ar/^{39}Ar$ dating of hornblende resulted in ages ranging from 4.2-4.1 Ma for the Puhagan dikes, and 0.7-0.3 Ma for the Nasuji Pluton (Rae, 2002). The difference in age confirms that the intrusions are not genetically related; also, that the Puhagan dikes are not the source of heat for the current geothermal system (Rae, 2002).

Hydrothermal alteration in the Nasuji-Sogongon region is associated with the Nasuji pluton and includes: K silicate (i.e., biotite, magnetite), calc-silicate (i.e., garnet, clinopyroxene), hypogene advanced argillic (i.e., andalusite, zunyite), propylitic (i.e., tremolite-actinolite, epidote), distal illite, and steam-heated advanced argillic (i.e., amorphous silica, kaolinite, alunite) assemblages (Rae et al., 2004). Fluid inclusions analyses revealed that biotite alteration and the associated veins formed from magmatic-hydrothermal fluids at temperatures between 267°C and >600°C, salinities of 26-56 wt. % NaCl equiv., and <0.2 wt. % Cu. Hydrothermal biotite ($^{40}Ar/^{39}Ar$ = 0.7-0.6 Ma.) and alunite (K-Ar = 0.9-0.8 Ma) formed contemporaneous with the Nasuji pluton ($^{40}Ar/^{39}Ar$ = 0.7-0.3 Ma), implying a genetic link between intrusion emplacement and hydrothermal alteration (Rae et al., 2003). Calc-silicate, biotite, and propylitic alteration zones developed above the blind intrusion situated at depths >2 km; this intrusion is considered to be the source of the current geothermal system. Parts of the biotite and propylitic alteration zones are in thermal equilibrium with the present-day geothermal system.

Parallels have been drawn between the geologic setting and hydrothermal alteration styles recognized at Palinpinon with those that characterize several types of magmatic-hydrothermal ore deposits (e.g., porphyry, skarn, high and intermediate sulfidation epithermal systems; Fig. 2.20b). However, assays (0.02 wt. % Cu, <0.03 wt. % Pb, <0.01 wt. % Zn, <0.01 wt. % Mo, <8 g/t Ag, and <0.05 g/t Au) show that the alteration zones at Palinpinon are barren. This could be due to insufficient fracture permeability, resulting in a lack of adequate focus for high volume fluid flux. Alternatively, it could relate to an insufficient supply of metals in the magmatic-hydrothermal fluids (Rae et al., 2004).

2.6.5.3.3. Amlan-Okoy river area

Located in the Southern Negros geothermal field, on the north slope of the Cuernos de Negros volcano (Fig. 2.18), the Amlan-Okoy river area contains several silicic altered areas (Fig. 2.20c

and 2.20d). The general geology of the area consists of Miocene-Pliocene andesitic and sedimentary rocks overlayed by Pliocene-Quaternary andesites and tuffs.

UNDP (1987) considered the Miocene Solburon andesite to be the lowermost unit in the stratigraphy. These units are overlaid by the Pliocene Magsinulo andesite breccia, or its equivalent in the Okoy river, the Malaunay andesite breccia. Overlying the Pliocene Magsinulo andesite is the Late Pliocene Amlan river conglomerate, or its equivalent in the Okoy river, the Kaidukan conglomerate. These units are overlaid by the Early Pleistocene Balinsasayao andesite and Early Pleistocene Kang-Ino conglomerate; the latter is considered to be interbedded with the Early Pleistocene Guinsayawan andesite. The Late Pleistocene Guintabon andesite overlays the Guinsayawan andesite, and is overlain by the Quaternary Calo River lavas.

UNDP (1987) reported two K-Ar ages for the Amlan-Okoy river area. Two samples from the Early Pleistocene Balinsasayao andesite yielded ages of 2.24 ± 0.13 Ma and 1.25 ± 0.13 Ma. UNDP (1987) reported the presence of concentric arcuate faults centred on Mt. Guintabon and lakes Balinsasayao and Danao to the southwest. Major north-east trending faults, and minor north-west trending faults were also reported.

Three main hydrothermally altered areas were identified by Tebar et al. (1984) and UNDP (1987); the largest is a north-east trending belt of ~3 km length along the Amlan river (Fig. 2.20c). Silicic altered areas are frequently restricted to conglomerate outcrops, highlighting a selective alteration process related to high permeability. Silicic altered areas were easily identified in the area as prominent elongated ridges oriented to the north-east. XRD analyses by UNDP (1987) on those areas confirmed the presence of quartz, pyrite, and rutile. Extensive, intense propylitic alteration (i.e., epidote-chlorite-calcite identified with XRD), was recognised in the oldest units (i.e., the Miocene Solburon andesite). Argillic and steam-heated alteration were also recognised in the area; outcrops and float were found on river beds, cliffs, and fallen blocks throughout the area. XRD analyses confirmed cristobalite and kaolinite; pyrite-quartz veinlets were observed in the argillic altered rocks in Amlan. XRD analyses in rocks from the Okoy river area confirmed the presence of quartz, illite, illite, chlorite, kaolinite, cristobalite, and alunite.

Hydrothermal breccia float and outcrops were identified in the Amalan-Okoy area (UNDP, 1987). These are characterised by angular to sub-angular clasts, intense silicic-pyrite alteration, and black sulphide cement. Chalcocite, covellite, and minor malachite occur in one of the NE

tributaries of the Amlan river; the area was referred to as the Balungasa copper prospect (UNDP, 1987). The copper minerals were found near to or at the present water table.

UNDP (1987) analysed 183 rock-chip samples in the Amlan river area. Gold was analysed in samples from or around the silicic altered areas. The highest gold values were 780 ppb and 100 ppb; most samples (i.e., 170 samples) had between 10 to 61 ppb Au. Silver values of 34 ppm and 20 ppm were reported from hydrothermal breccias. Antimony, arsenic, bismuth, and tellurium values were also high in the hydrothermal breccias. Lead and zinc values were low, and copper results were higher in hydrothermal breccias and silicic altered rocks (i.e., 520 ppm, and 0.4 wt. %, respectively). UNDP (1987) carried soil and rock sampling in the north bank of the Okoy river area, near Malabo. A quartz veined, argillic altered rock sample with 1.3 ppm Au was reported by UNDP (1987) in the Okoy river area.

2.6.5.3.4. Pamplona

Pamplona is located on the NW slope of the Cuernos de Negros volcano (Fig. 2.18.). The geology of the Pamplona area comprises the Pliocene Magsinulo andesite breccia, the Late Pliocene Amlan river conglomerate, and the Early Pleistocene Balinsasayao andesite.

The Pamplona area contains the BCI sulphur project which is located in a valley in the Cambuslao river drainage at an elevation of 510 m above sea level. This prospect was explored during the 1960s; 140 holes of ~100 m depth were drilled over an area of 800 by 700 m. Drilling confirmed a stratiform body of ~100 m thickness with 60 Mt at 31 wt. % S. XRD analyses by UNDP (1987) confirmed pyrite, marcasite, cristobalite, tridymite, alunite, kaolinite, and native sulphur in the area.

Float in the area were observed to have irregular veinlets, clay patches, and disseminated sulphur, as well as gypsum veinlets. UNDP (1987) considers the stratiform body at the BCI sulphur prospect to be hosted in the Late Pliocene Amlan river conglomerate and to have been formed due to replacement. A combination of hypogene and supergene alteration processes is considered to have formed the hydrothermal alteration assemblages.

2.7. Summary

The Philippine archipelago occupies the area of convergence of the Eurasian plate from the west, the Philippine Sea plate from the east, and the Indo-Australian plate from the south. Subduction occurs in opposed directions on the eastern and western sides of the archipelago. There are three main crustal structures in the Philippine archipelago: a subduction zone in the east defined by the Philippine Trench and the East Luzon Trough, a subduction zone in the west

defined by the Manila, Negros, and Cotabato trenches, and the Philippine Fault Zone which trends roughly parallel to the subduction zones.

Ophiolitic complexes of Cretaceous to Paleogene age occur across the archipelago. Most ophiolites are considered to have formed in fast spreading volcanic centres and to have emplaced due to obduction, accretion, and strike-slip faulting.

The Philippine archipelago contains a complex series of volcanic arcs. Eight magmatic arcs have been outlined in the archipelago; almost every arc holds potential for magmatic-hydrothermal mineral deposits as well as geothermal energy. Different episodes of magmatism and volcanism have been identified on each arc. Most arcs contain intrusive or volcanic rocks which range in age from Eocene to Pleistocene.

The Philippine archipelago has one of the most attractive mineral endowments of the Southwest Pacific region. Porphyry and epithermal deposits occur throughout the archipelago. Nine prolific mineral districts have been identified after several years of exploration. There are still many emerging areas with high potential to host large size-high grade porphyry and epithermal mineral deposits.

Seismic activity has occurred widely in the Philippines; 13,986 earthquakes have been detected by the USGS between the years 1911 and 2015. 1,866 earthquakes, detected between 1973 and 2015, occurred in the Visayas region which includes Negros. Earthquake depth ranges between 4.88 km and 644.5 km; three main earthquake clusters were identified at 10 km, 33 km, and 35 km depth. Earthquake magnitude ranges between 3 mb and 6 mb.

The geology of Negros is divided into three tectono-stratigraphic terranes: ancient Negros arc, the Visayan sea basin, and the recent Negros arc. The geology of Negros comprises Cretaceous volcanic flows and Eocene limestones intruded by Oligocene diorites. These are overlain by volcanic and sedimentary formations of Late Oligocene to Holocene age. The sequence is intruded by Paleocene to Pleistocene diorites at Palinpinon. There are three major structural trends in Negros: NW-SE, N-S, and NE-SW. Most structures in Negros trend NW-SE and are located in the western portion of the island.

Neogene to Quaternary volcanic rocks in Negros are characterised by high potassium content. Most samples are classified as calc-alkaline basalts and andesites based on their geochemical composition. Pliocene to Pleistocene intrusions at Palinpinon are quartz-dioritic to dioritic in composition, and are characterised by adakite-like compositions.

There are several porphyry and epithermal mineral occurrences in Negros. Most deposits occur in the Southwest Negros district which also hosts the large Sipalay porphyry Cu deposit. Mineral deposits are hosted and associated with the Oligocene Pagatban diorite, and occur along a NW-trending belt of ~50 km in length.

There are four known hydrothermally altered areas considered to have been active geothermal fields until very recently. These are: Ayungon, Palinpinon, Amlan-Okoy river, and Pamplona. All the areas contain silicic altered rocks, some contain hot springs, and most contain argillic and advanced-argillic altered rocks. These hydrothermally altered areas remain underexplored, except for Palinpinon, and represent potential areas for future exploration for magmatic-hydrothermal mineral deposits.

CHAPTER 3:

GEOLOGY, GEOCHRONOLOGY, AND GEOCHEMISTRY OF THE BANTUG PROSPECT

3.1. Introduction

This chapter describes and interprets the geologic setting of Bantug. It begins with a summary of previous work in the area, followed by detailed descriptions of the key rock types. Results from graphic logging are presented, as well as interpretative cross sections, petrographic descriptions, and microanalyses. The findings of U-Pb LA-ICP-MS dating of zircons from the intrusive rocks and their volcanic host rocks are also discussed in this chapter, as are results from whole rock geochemical analyses from the key rock types at Bantug. Interpretations of the intrusive history are presented, and the geology of the Bantug area is compared with that of other volcanic centres in Negros.

3.2. Methods

3.2.1. Graphic logging

Three drill holes from Bantug were logged graphically following the method outlined by McPhie et al. (1993), Blackwell (2010), and Blackwell et al (2014). Field logs from drill holes studied during this project are presented in Appendix D.

3.2.2. Sampling

Samples for whole rock geochemistry were collected every ten meters from drill holes BTG-005, BTG-003, and BTG-006. Samples for geochemical and geochronology analyses and interpretation were selected from the least-altered intervals observed in the three drill holes.

3.2.3. Polished slabs

Nineteen polished rock slabs were prepared from drill core samples at the lapidary facilities of CODES-University of Tasmania. Polished rock slabs from the main rock types were used for textural analyses, as well as for stablishing hand sample recognition criteria.

3.2.4. Petrography

Twenty-four polished thin sections from the representative rock types at Bantug were prepared at the lapidary facilities of the CODES-University of Tasmania. Thin sections were studied with a Leica DM 4000 M automated microscope. Sets of three mosaic images (i.e., transmitted

light with crossed polarisers, transmitted light with parallel polarisers, and reflected light with parallel polarisers) using a 5x magnification lens were prepared from each thin section. Mosaic images from the thin sections are provided in Appendix E. Photomicrographs were acquired with the same microscope using 10x and 20x magnification lenses.

3.2.5. Field emission scanning electron microscopy (FE-SEM)

Thin sections and polished laser mounts from the main rock types at Bantug were analysed with a Hitachi SU-70 field emission scanning electron microscope (FE-SEM) at the Central Science Laboratory of the CODES-University of Tasmania. Secondary electrons and back-scattered electron images were acquired at a distance of 14.9 to 15 mm from the sample, using 15.0 kV current during the analyses. Energy dispersive X-ray spectroscopy (EDS) was used to detect the major elements in selected minerals from thin sections and laser sample mounts. The AZtec Software® from Oxford Instruments was used to process the EDS point analyses and to create element maps. The MinIdent-Win 4.0 Software® was used to identify the most probable mineral occurrence in thin sections and mounts according to the EDS results. FE-SEM EDS results from thin sections and laser mounts from the key rock types at Bantug are presented in Appendix F.

3.2.6. Whole rock geochemical analyses

Whole rock analyses were undertaken at ACME Analytical Laboratory, Vancouver, Canada, using method G4A-G4B. A 0.2 g sample split was fused at 1,000°C with 1.5 g of an 80:20 lithium metaborate: tetraborate mix. The cooled bead was digested in 100 mL of 5% HNO_3. Inductively coupled plasma-emission spectroscopy (ICP-ES) analysis determines major element concentrations reported as the common oxides. Loss on ignition (LOI) is reported as % weight loss on a 1 g split ignited at 1,000°C. LECO analysis determined total C and S on a 0.2 g sample split. The same whole rock fusion solution was analysed using ICP-MS (Perkin Elmer Elan 6000) to determine absolute concentrations of trace elements. Method 1F-MS: A 1 g subsample was digested in 6 mL of hot (95°C) modified aqua regia (1:1:1; $HCl:HNO_3:H_2O$) for 1 hour, cooled and made to 20 mL volume with 5% HCl. The solution was analysed by ICP-MS (Perkin Elmer Elan 6000 or 9000). Method G3B: A 30 g sample split was custom mixed with PbO fire assay fluxes and fired for 45 min at 1,050°C. Molten Pb + slag was poured into an iron mould, cooled, and the Pb button was recovered. Heating at 950°C in a MgO cupel rendered a Ag ± Au, Pt, Pd dore bead. The bead was parted in hot HNO_3, digested by adding HCl and aspirated into a Jarrel Ash Atomcomp 875 ICP-ES to determine Au, Pt, and Pd (upper

limits = 10 ppm). Method G7TD: A 0.5-g sample split was digested in 20 mL of 4-acid solution (HNO_3: $HClO_4$: HF: H_2O) at 200°C and heated until dry. Residue was dissolved in 16 mL of 50% HCl at ~95°C for 1 h then made to volume in a 100 mL volumetric flask with 5% HCl. ICP-ES analysis was used to determine total Ni. Whole rock geochemistry results are provided in Appendix G.

3.2.7. U-Pb geochronology

Duplicate samples were collected from the various intrusions and host rocks observed in the three drill holes studied at Bantug. Samples were selected from the least-altered intervals logged, and based on their U and Th contents. The samples were prepared and analysed at CODES, University of Tasmania by Dr Sebastien Meffre and Dr Jay Thompson. Approximately 100 grams of rock were repeatedly sieved and crushed in a Cr-steel ring mill to <400 microns. Non-magnetic heavy minerals were separated using a gold pan and a Fe-B-Nd hand magnet. The zircons were handpicked from the heavy mineral concentrate under the microscope in cross-polarised transmitted light. The selected crystals were placed on double sided sticky tape and epoxy glue was then poured into a 2.5 cm diameter mould on top of the zircons. The mount was dried for 12 hours and polished using clean sandpaper and a clean polishing lap. The samples were then washed in distilled water in an ultrasonic bath.

The analyses in this study were performed on an Agilent 7500cs quadrupole ICP-MS with a 193 nm Coherent Ar-F gas laser and the Resonetics S155 ablation cell at the University of Tasmania in Hobart. The downhole fractionation, instrument drift, and mass bias correction factors for Pb/U ratios on zircons were calculated using two analyses on the primary (91500-standard of Wiedenbeck et al., 1995) and one analysis on each of the secondary standard zircons (Temora standard of Black et al., 2003; JG1 of Jackson et al., 2004) analysed at the beginning of the session and every 15 unknown zircons (approximately every 30 minutes) using the same spot size and conditions as used on the samples. Additional secondary standards (The Mud Tank Zircon of Black and Gulson, 1978; Penglai zircons of Li et al., 2010; and the Plesovice zircon of Slama et al., 2008) were also analysed. The correction factor for the $^{207}Pb/^{206}Pb$ ratio was calculated using large spots of NIST610 analysed every 30 unknowns and corrected using the values recommended by Baker et al. (2004).

Each zircons analysis began with a 30 second blank gas measurement followed by 30 seconds of analysis with the laser switched on. Zircons were sampled on 32 micron spots using the laser at 5 Hz and a density of approximately 2 J/cm^2. A flow of He carrier gas at a rate of 0.35

litres/minute carried particles ablated by the laser out of the chamber to be mixed with Ar gas and carried to the plasma torch. Isotopes measured were Ti^{49}, Fe^{56}, Zr^{90}, Hf^{178}, Hg^{202}, Pb^{204}, Pb^{206}, Pb^{207}, Pb^{208}, Th^{232} and U^{238}. Each element was measured every 0.16 seconds with longer counting times on the Pb isotopes compared to the other elements. The data reduction used was based on the method outlined in detail in Meffre et al. (2008) and Sack et al. (2011), similar to that outlined in Black et al. (2004) and Paton et al. (2010). Element abundances on zircons were calculated using the method outlined by Kosler (2001) using Zr as the internal standard element, assuming stoichiometric proportions and using the NIST610 standard to correct for mass bias and drift. U-Pb LA-ICP-MS age determinations are presented in Appendix H.

3.3. Geology of the Bantug prospect

The lithocap at Bantug is located approximately 15 km to the west of Tayasan village, Negros, on the western flank of a circular topographic feature (Fig. 3.1). This topographic feature is part of the Razorback Mountains of central-eastern Negros (Fig. 3.1). Subang et al. (2009) and Subang (2011) interpreted the circular topographic feature to be a relict caldera. Subang et al. (2009) first reported the presence of intensely silicic-altered rocks, as well as hydrothermal breccias at Bantug. Comprehensive compilations of the work carried out at Bantug by Freeport-McMoRan were produced by Subang et al. (2009) and Subang (2011). Figure 3.2 presents the geology map from the Bantug area, modified from Subang et al. (2009). Aphyric andesite and plagioclase-phyric andesite are the most abundant rocks cropping out at Bantug. Figure 3.2 presents the location and traces of the seven holes drilled by Freeport-McMoRan from 2001 to 2013. Results presented in this study are based on detailed graphic logging and petrographic observations in drill holes BTG-003, BTG-005, and BTG-006. Summary logs are presented in Figure 3.3. Interpretative cross sections from the logs are presented in Figures 3.4, 3.5, 3.6, and an interpretative geology long section is presented in Figure 3.7. Survey details of the drill holes are presented in Table 3.1.

Table 3.1. Drill hole and collar details

Drill hole	Easting[1]	Northing[1]	Elevation (m)	Azimuth	Dip	EOD (m)
BTG-003	504942	1106935	1186.1	270°	57°	722
BTG-005	502144	1105881	1071.3	270°	57°	701.8
BTG-006	505175	1107714	1018.0	270°	57°	704.6

[1] Coordinate system is WGS84, UTM 51 N; EOD: End of drill hole

3.3.1. Structures

Lineaments in the Bantug area have been identified based on prominent topographic features (Fig. 3.2). General trends are presented in a rose diagram in panel b of Figure 3.2. Two main structural trends are interpreted: one set trending NE (N°50-60°E), and the other NW (N40°-50°W). Two minor sets of structures follow similar trends: N40°-50°E and N50°-60°W. The least common structural trends are N-S and E-W.

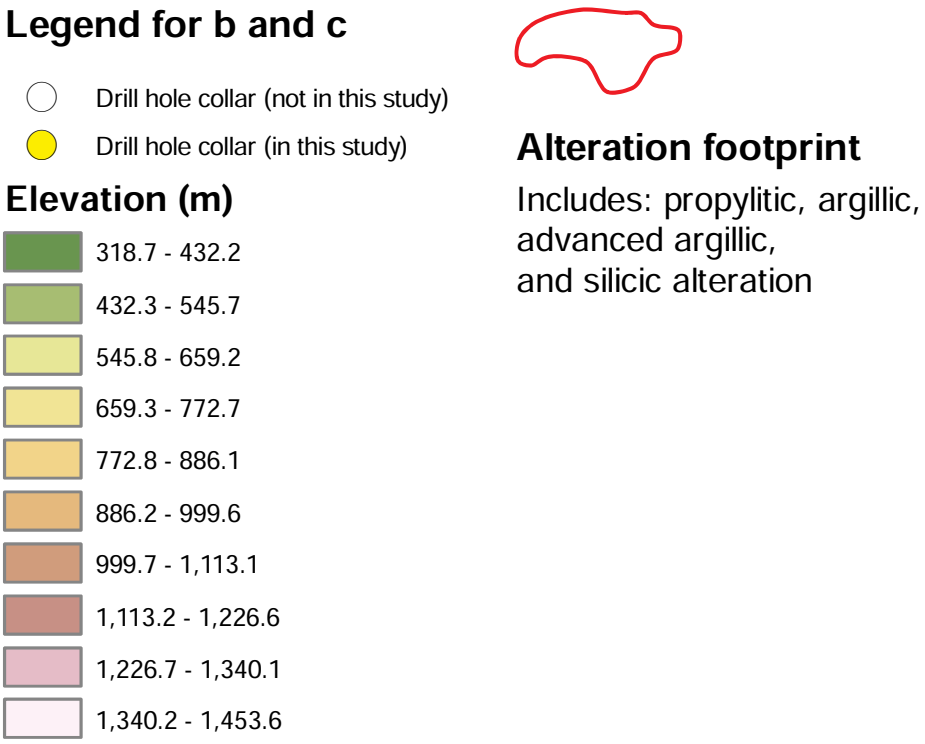

Figure 3.1. Topographic features of central Negros and the Bantug area (Opposite). Legend.

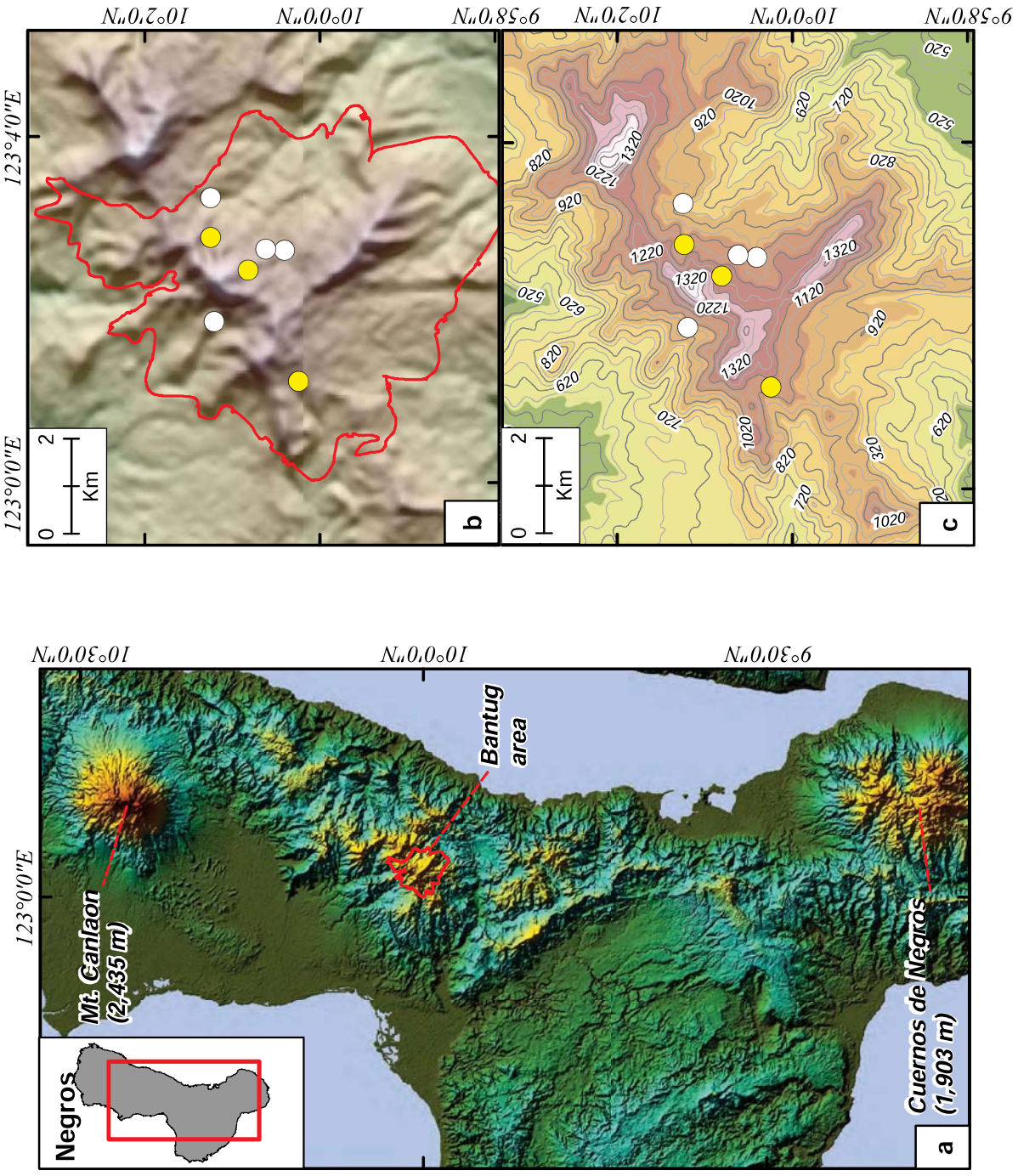

Figure 3.2. Topographic features of central Negros and the Bantug area. a. Digital Elevation Model (DEM) of Negros, dark green colours represent lower (i.e., <100 m) elevation and yellow to dark-brown colours represent higher (i.e., <2,435 m) elevation; the topographic high in the north is Mt. Canlaon Volcano (2,435 m), the red square in the middle highlights the Bantug area. b. Digital elevation model of the Bantug area; the hydrothermal alteration footprint occupies the western flank of the circular topographic feature. **c.** Contours and colour map of the topographic elevation in the lithocap at Bantug.

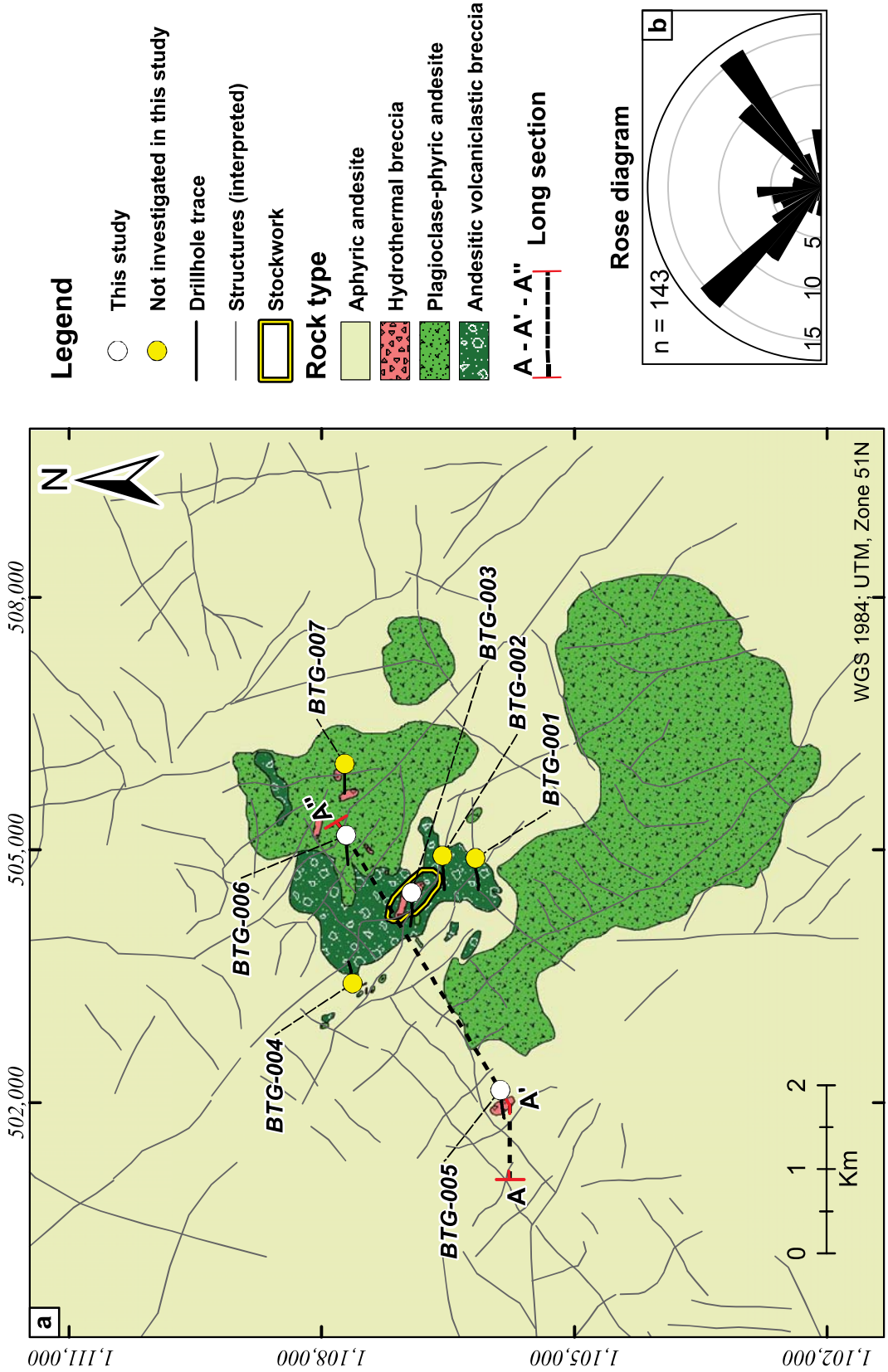

Figure 3.3. Geology of the Bantug prospect. Modified after Subang et al. (2009). **a.** Drill hole collars are presented in white circles (in this study) and black circles (not in this study). Faults and lineaments were interpreted for this study using topographic maps and digital elevation models. Drill holes are projected to surface as drill hole traces. **b.** Rose diagram. Major structural trends are NE and NW.

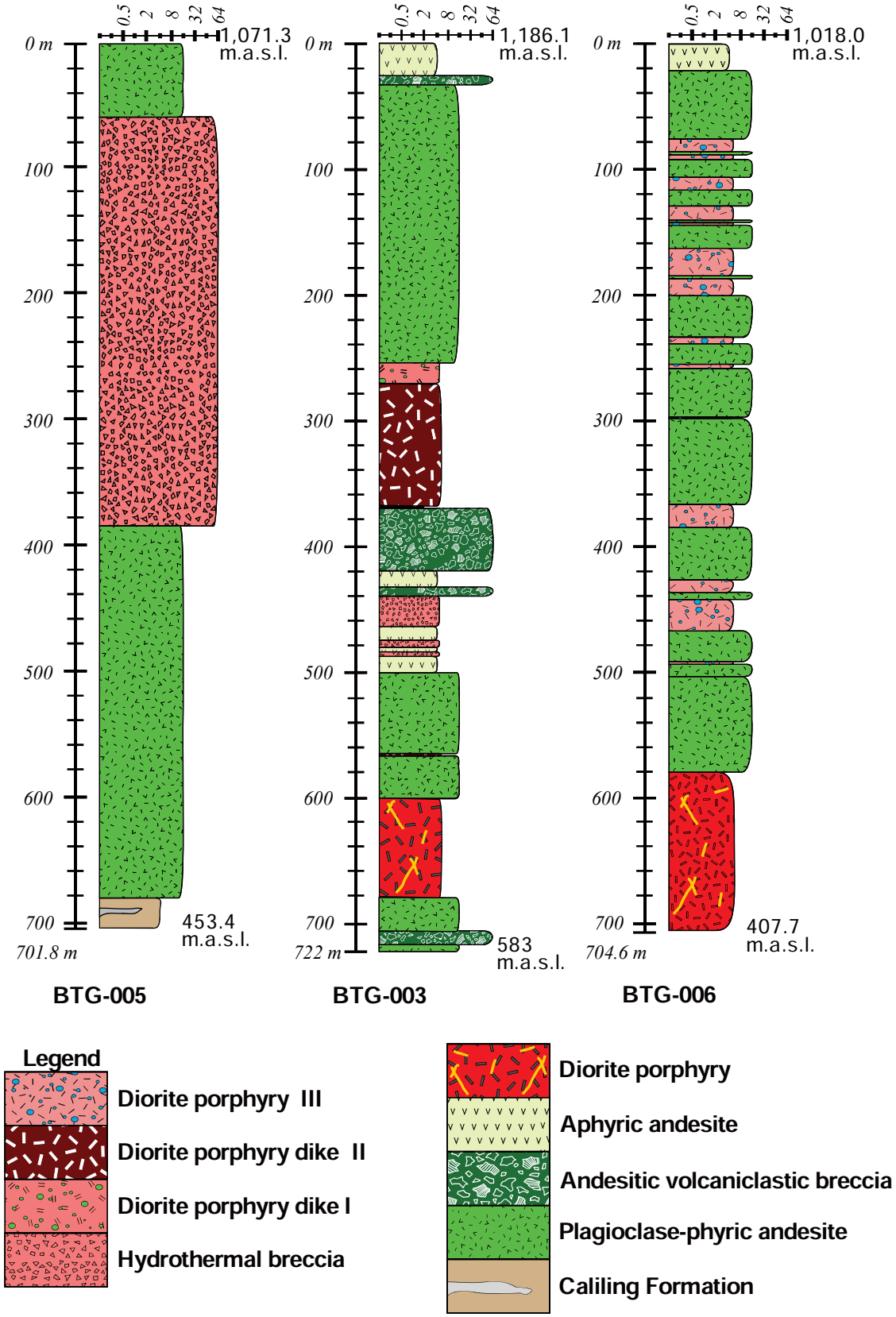

Figure 3.4. Geology strip logs. Drill holes BTG-003, BTG-005, and BTG-006. Abbreviation: m.a.s.l.: meters above sea level. Details of collar location, azimuth, and dip are in Table 3.1.

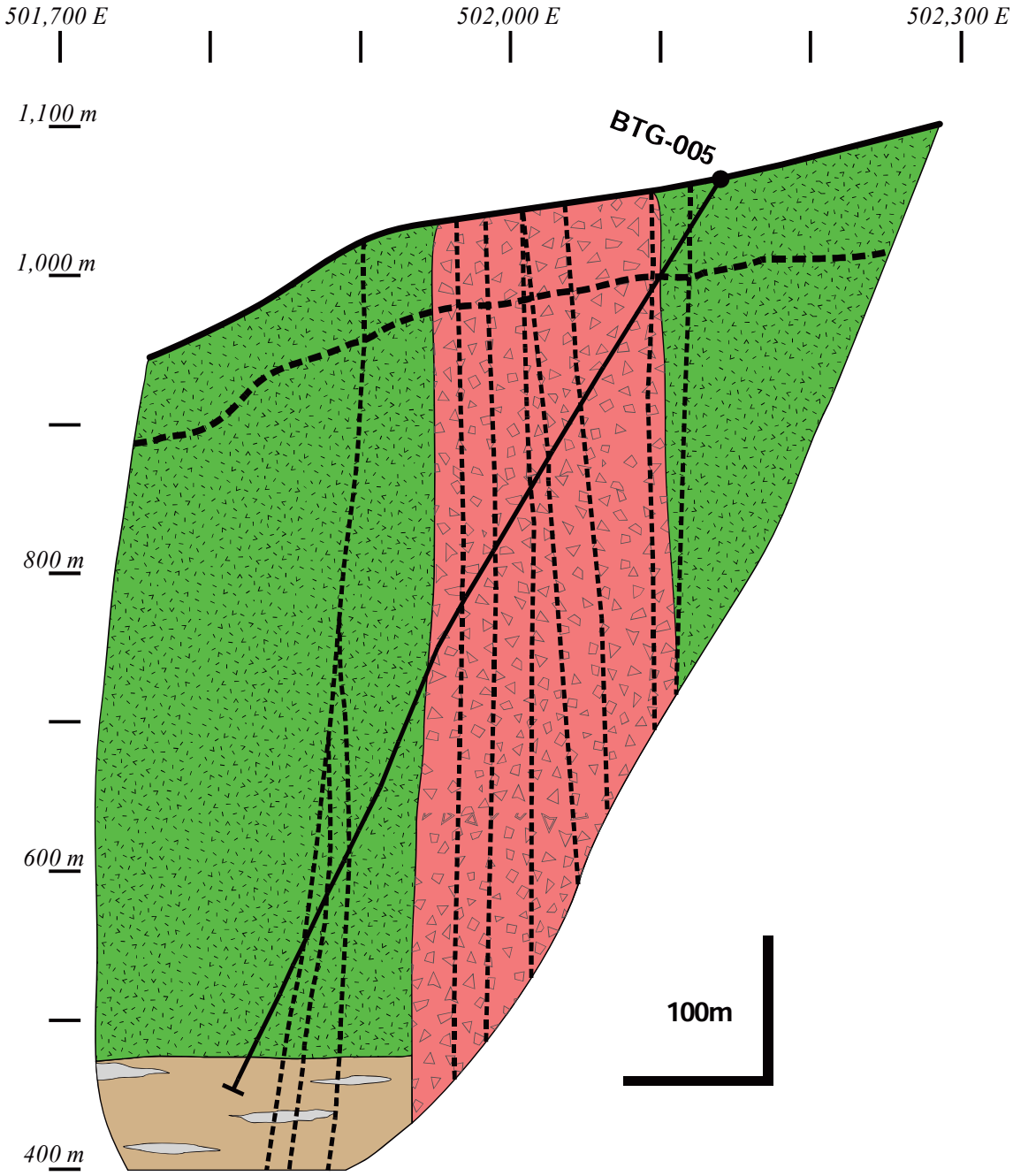

Figure 3.5. Interpretative geology cross section for drill hole BTG-005. Legend as in Figure 3.3.

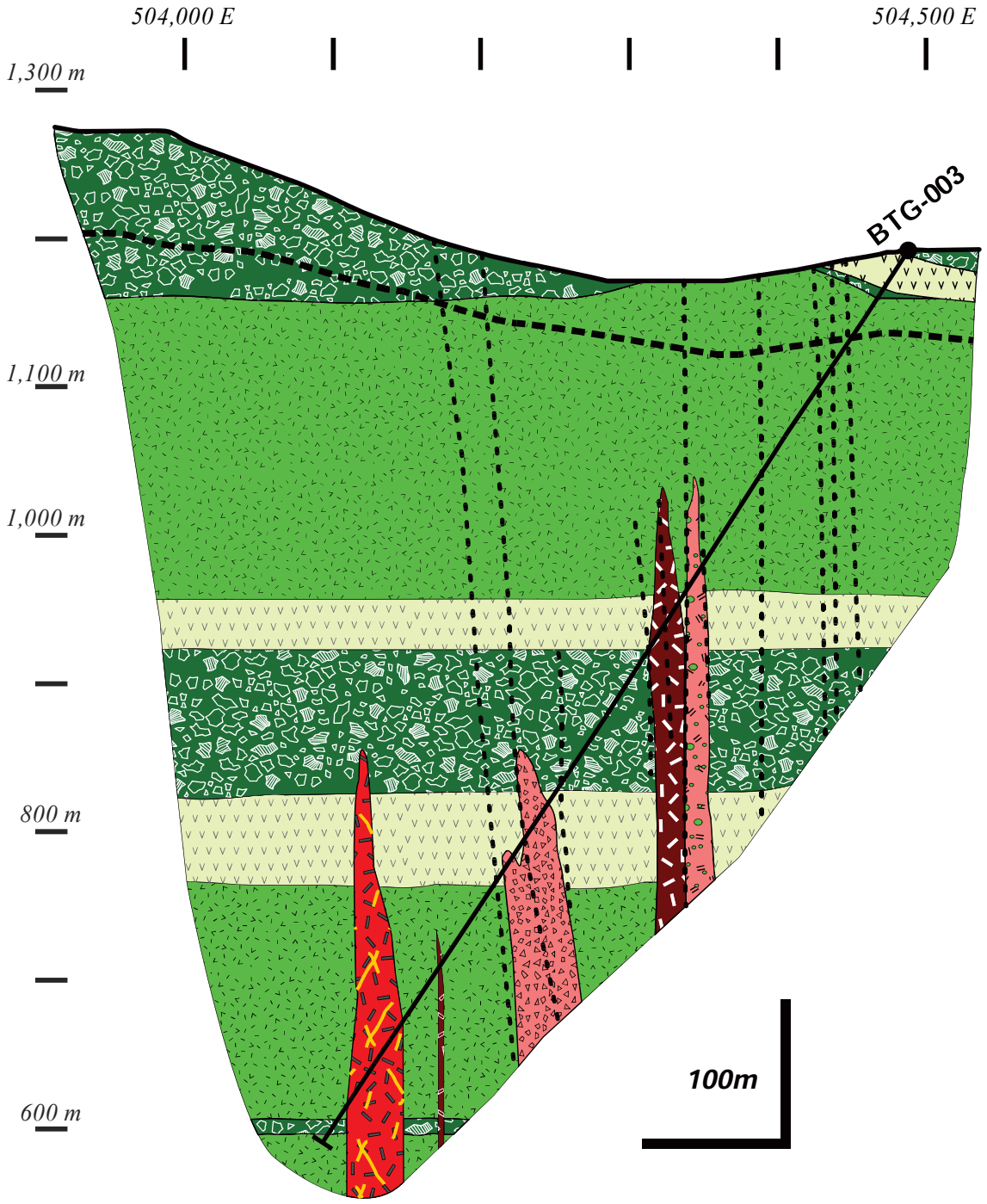

Figure 3.6. Interpretative geology cross sections for drill hole BTG-003. Legend as in Figure 3.3.

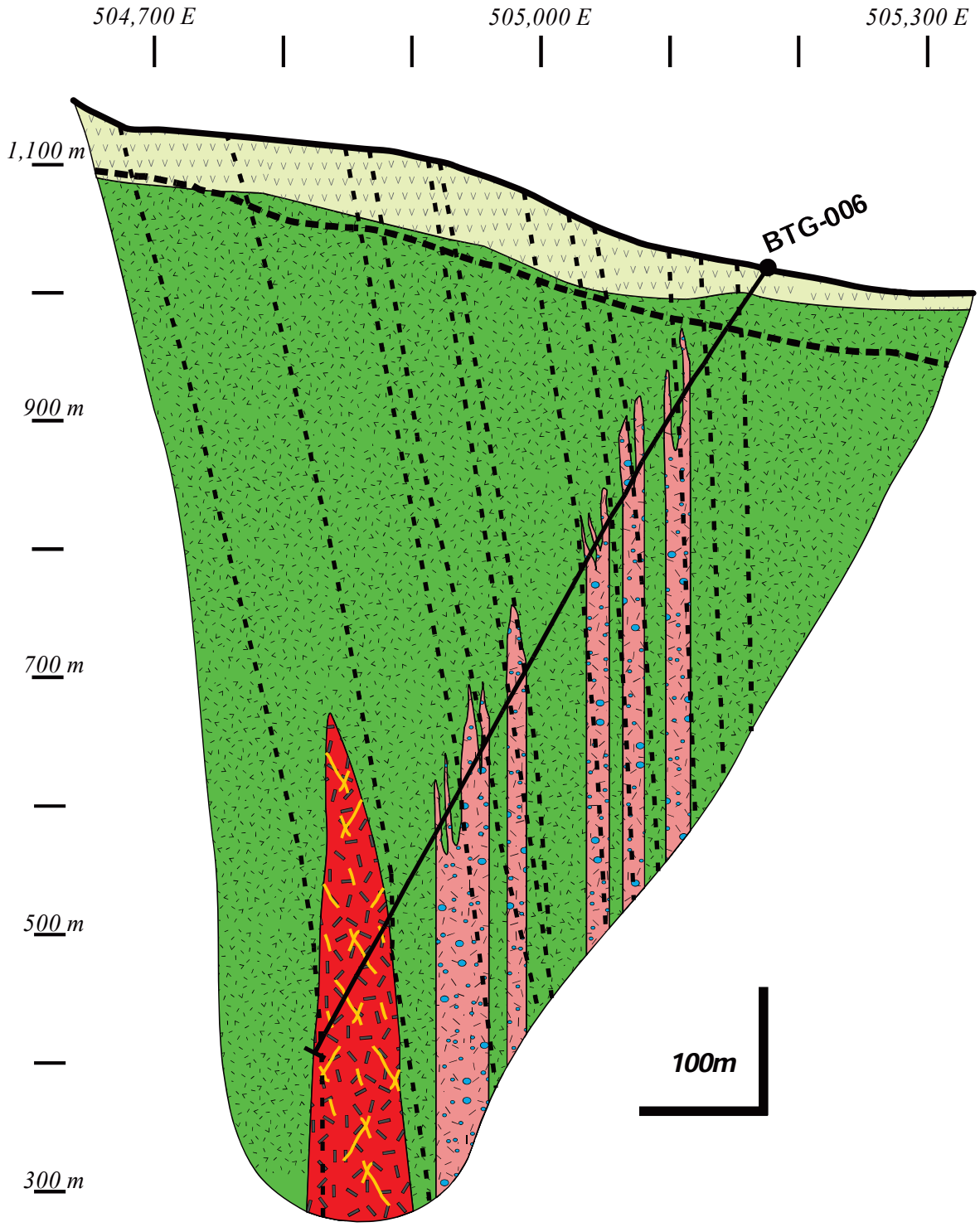

Figure 3.7. Interpretative geology cross sections for drill hole BTG-006. Legend as in Figure 3.3.

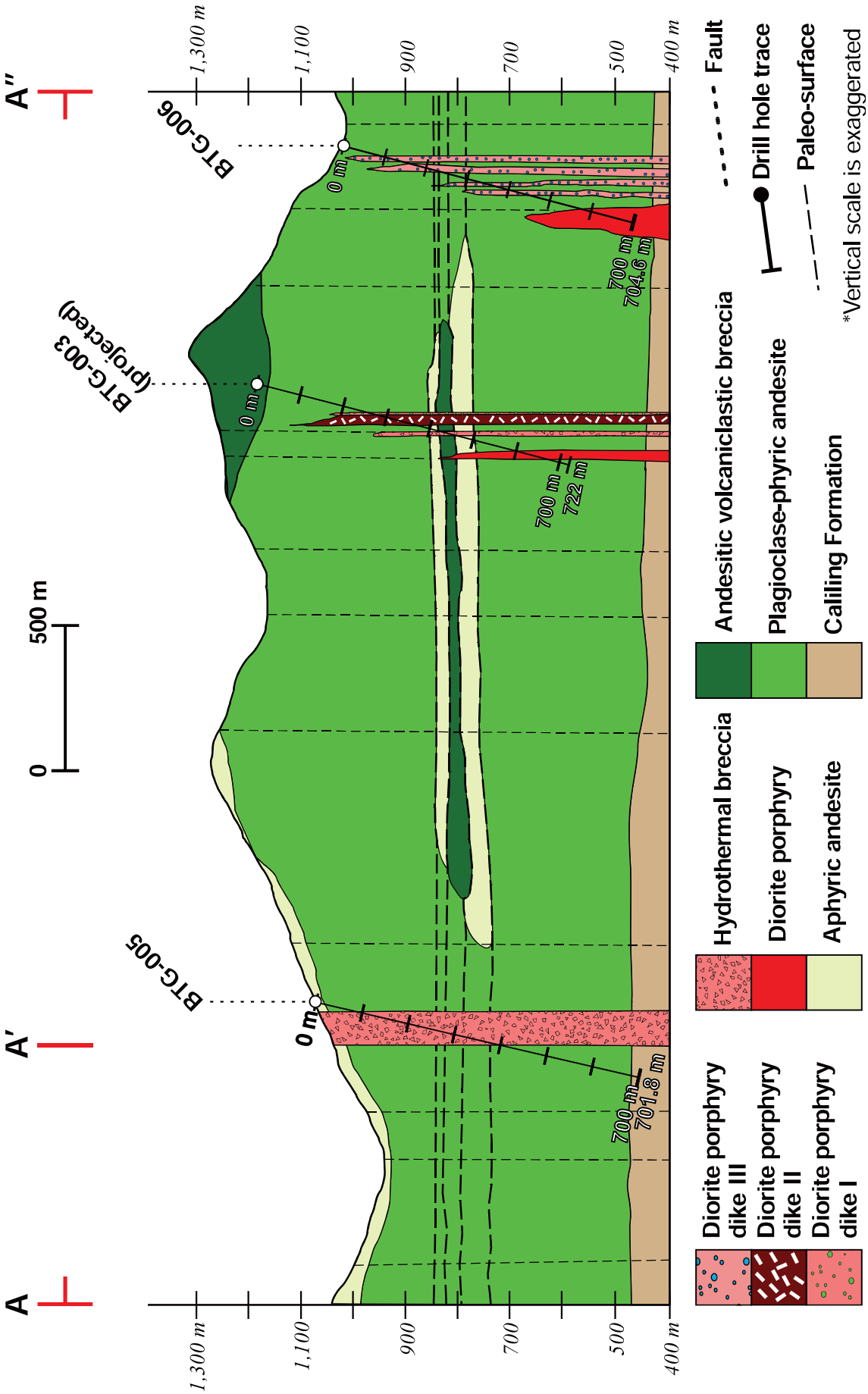

Figure 3.8. Interpretative geology long section from Bantug.

3.3.2. Sedimentary rocks

Late Pliocene-Pleistocene sedimentary rocks comprise the basement of the lithocap at Bantug. Late Pliocene-Pleistocene horizons of quartz-rich carbonate rocks crop along the east coast of central Negros (MGB, 2004; and references therein). These sedimentary rocks underlie the Cenozoic volcanic rocks of the Negros Volcanic Arc including the Canlaon Volcanic Complex (MGB, 2004).

The sedimentary rocks observed at Bantug belong to the Late Pliocene-Pleistocene Caliling Formation of MGB (2004). These rocks were observed in drill hole BTG-005 at 678 m depth to the end of drill hole at 701.8 m (Figs. 3.3 and 3.4). The rocks are characterised by their planar laminations, defined by 0.4 cm to 1 cm parallel clastic bands (Figs. 3.8a, 3.8b, and 3.8c). Poorly sorted, sub-angular to sub-rounded, low sphericity, quartz grains of <50 μm are supported by a fine-grained cement (Fig. 3.8a). The cement consists of chlorite-group minerals (i.e., chamosite; Figs. 3.8d, 3.9c), montmorillonite, and kaolinite. These minerals are considered to be the product of hydrothermal replacement of the diagenetic cement. Other secondary minerals include pyrite, magnetite, chalcopyrite, ilmenite, anatase, illite, muscovite, calcite, allanite, fluorapatite and apatite (Figs. 3.9c, 3.9d, 3.9e, and 3.9f).

Pyrite occurs as ~1 mm anhedral grains in the core of chamosite clusters (Fig 3.9a); it can also occur in veinlets, or as fine (i.e., 200 μm) euhedral disseminations (Fig 3.8c). Hydrothermal magnetite is disseminated in chamosite, and also occurs as acicular crystals <100 μm in length (Fig 3.9b). The latter are likely to pseudomorph after specularite. Chalcopyrite occurs in trace amounts; it is anhedral, and fine grained (i.e., <20 μm; Fig. 3.9c). Chalcopyrite also occurs as inclusions in pyrite and is associated with chamosite and allanite (Fig. 3.9b and 3.9f). Garnet, is fine grained (i.e., <1 mm), red-brown in colour, and occurs in bands and clusters with chamosite and pyrite.

No fossils were observed or recognised in this rock type during this study.

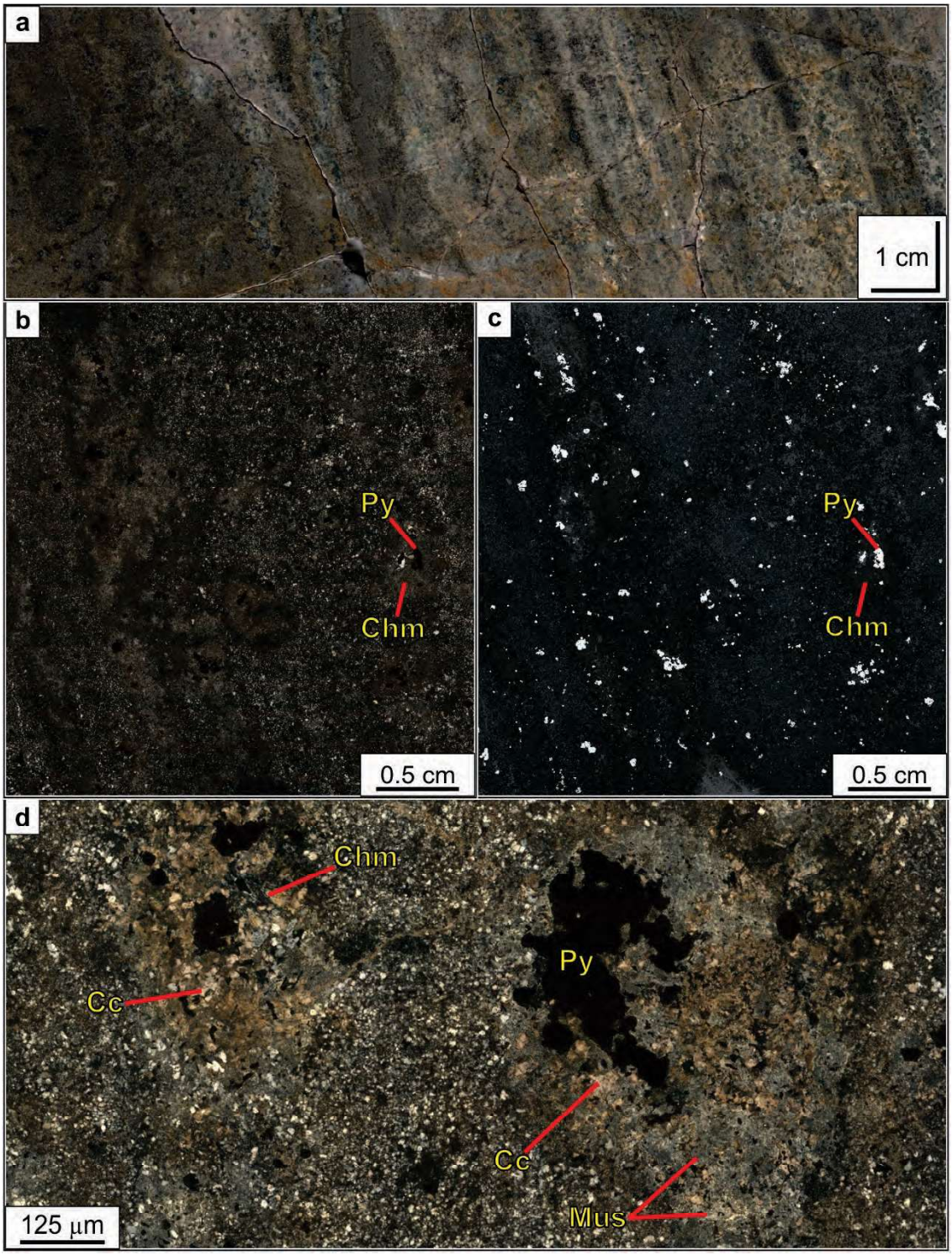

Figure 3.9. Sedimentary rocks. a. Polished slab. Bands of green micas with magnetite contrast against pale bands of micas. Coarser grains of green micas can be observed within the dark-green bands (BTG-005; 695.1 m). **b.** Cross-polarised photomicrograph mosaic. Several sub-round features made of chamosite and calcite nucleated around opaque minerals in a fine-grained quartz groundmass (BTG-005; 691.9 m). **c.** Reflected light photomicrograph mosaic. Pyrite crystals, at the core of the sub-rounded features, and fine grained magnetite disseminated in the quartz-mica groundmass. Same field of view as panel b (BTG-005; 691.9 m.) **d.** Cross-polarised photomicrograph mosaic. Opaque minerals (e.g., pyrite) surrounded by chamosite and calcite in a fine-grained quartz-mica groundmass (BTG-005; 695.1 m). Abbreviations: Alla: allanite; Anh: anhydrite; Apa: apatite; Cc: calcite; Chm: chamosite; Cpy: chalcopyrite; F-Ap: fluorapatite; illi: illite; ilm: ilmenite; Mt: magnetite; Mus: muscovite; Py: pyrite; Qz: quartz.

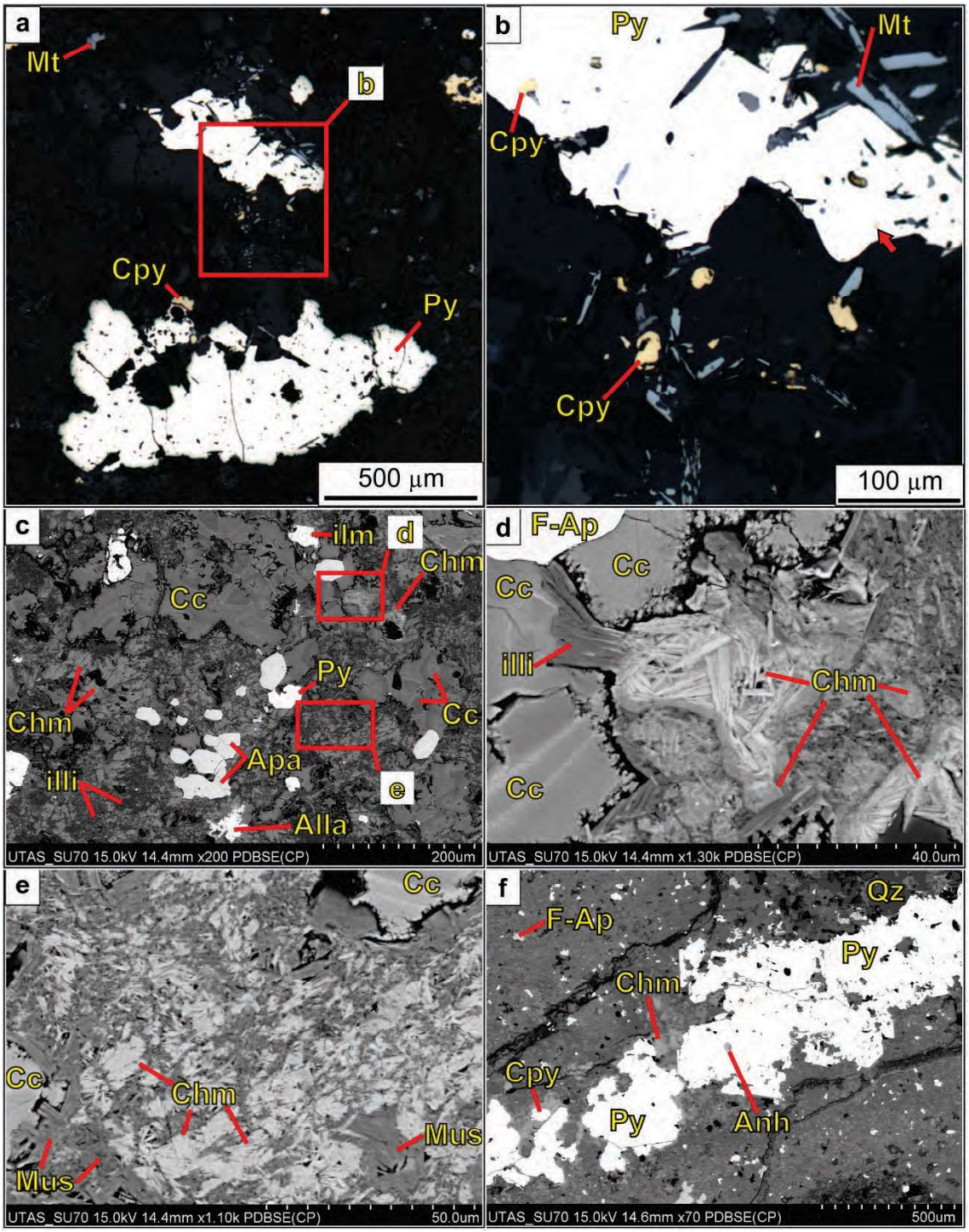

Figure 3.10. Sedimentary rocks. a. Reflected light photomicrograph mosaic. Pyrite grains in a quartz groundmass with fine grained magnetite and chalcopyrite (BTG-005; 691.9 m). **b.** Reflected light photomicrograph mosaic; inset from panel a. Pyrite grain contains chalcopyrite, apatite, and magnetite inclusions (BTG-005; 691.9 m). **c.** Back scattered electrons (BSE) image. Apatite, pyrite, ilmenite, and allanite in chamosite-illite groundmass. Note zoning in calcite crystals (BTG-005; 695.1 m). **d.** BSE image. Inset from panel c. Fluorapatite, calcite, and illite in a chamosite groundmass (BTG-005; 695.1 m). **e.** BSE image. Inset from panel c. Calcite grains in a chamosite-muscovite groundmass (BTG-005; 695.1 m). **f.** BSE image. Pyrite vein with chamosite and anhydrite inclusions and a chamosite halo; fluorapatite and quartz grains are in a chamosite muscovite groundmass (BTG-005; 695.1 m). Abbreviations: Alla: allanite; Anh: anhydrite; Apa: apatite; Cc: calcite; Chm: chamosite; Cpy: chalcopyrite; F-Ap: fluorapatite; illi: illite; ilm: ilmenite; Mt: magnetite; Mus: muscovite; Py: pyrite; Qz: quartz.

3.3.3. Volcanic rocks

The volcanic rocks at Bantug belong to the Quaternary Canlaon Volcanic Complex (CVC) of MGB (2004) which extends over the northern, central, and southern parts of Negros. Solidum (2002), and references therein, described the rocks in the Quaternary Canlaon Volcanic Complex as basalts, basaltic andesites, porphyritic andesites, and porphyritic dacites.

Coherent volcanic rocks were observed at Bantug in each of the three drill holes studied (Figs. 3.3 to 3.7). These volcanic rocks are interpreted to occur as horizons that range from ~1 to 800 m in thickness (Fig. 3.3 to 3.7). The coherent volcanic facies were observed to alternate from plagioclase-phyric to aphyric horizons in drill hole BTG-003 (Fig. 3.3). The thickest intercept of aphyric andesite was logged in BTG-005 (e.g., 300 m).

The plagioclase-phyric volcanic facies have been intensely altered to advanced-argillic assemblages. The presence of plagioclase-shaped vugs (i.e., vuggy quartz texture) was used as a textural guide for protolith recognition (Fig. 3.10a). Former plagioclase phenocrysts were recognized in moderately to weakly altered rocks; however, the phenocrysts had been completely altered to clay minerals (Fig. 3.10b).

Volcaniclastic facies are interbedded with the coherent volcanic rocks (Figs. 3.3. to 3.7). The volcaniclastic rocks were identified while logging drill core, primary texture features are obscured by intense advanced argillic-alteration. Volcaniclastic facies were inferred where patchy-wormy textures occurred (Figs. 3.10c and 3.10d).

Patchy-wormy textures are characterised by rounded to subrounded clusters of clay minerals, sulphates, and sulfides in a fine-grained quartz groundmass (Figs. 3.10c, 3.10d, 3.11a). Clusters of minerals, or patches, are made of alunite, diaspore, pyrophyllite, muscovite, quartz, APS minerals, and pyrite (Figs. 3.11b, 3.11c, 3.11d). Chapter 6 describes in detail patchy-wormy textures at Bantug.

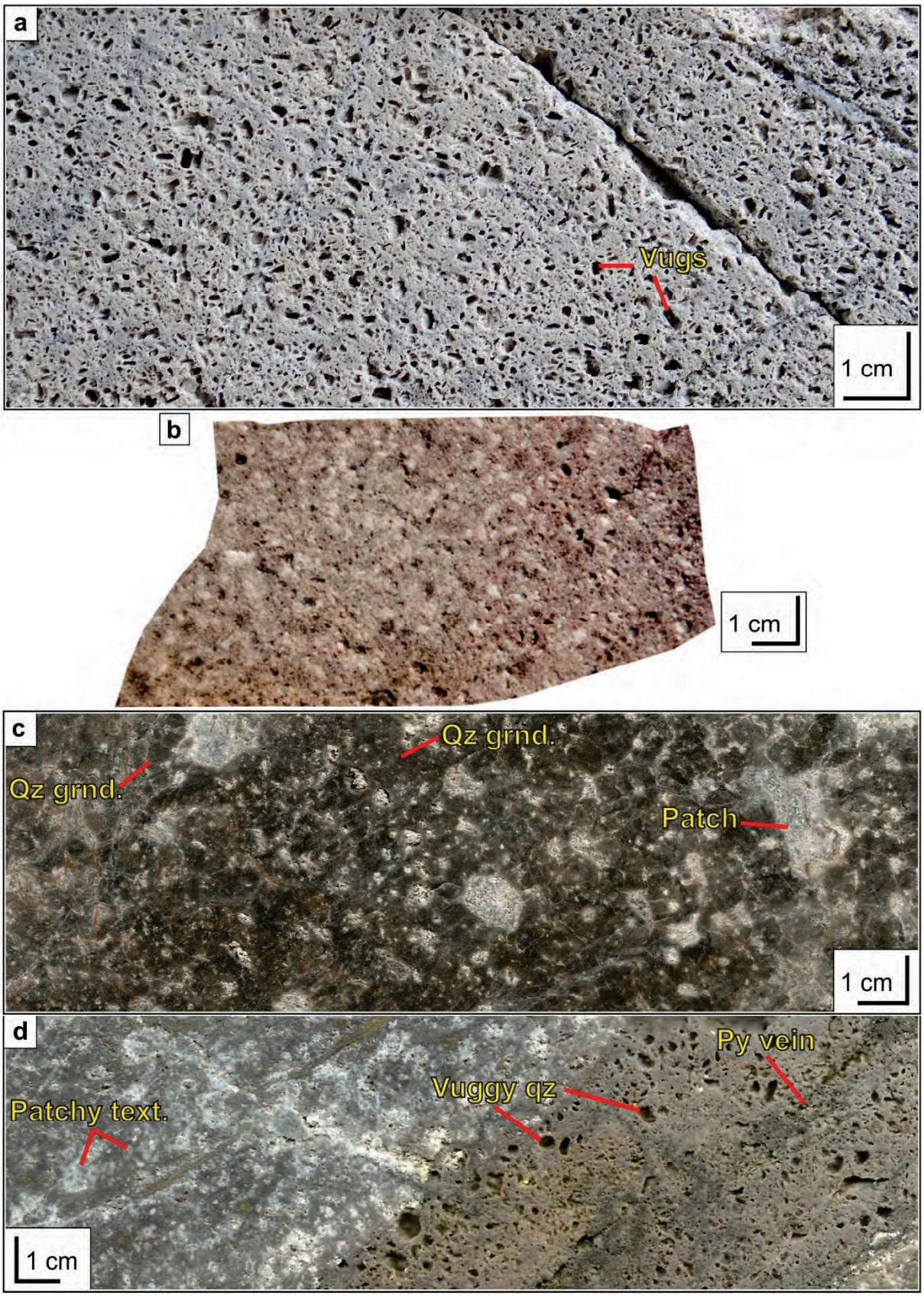

Figure 3.11. Volcanic rocks. a. Hand sample. Vuggy quartz product of silicic alteration on plagioclase-phyric andesite (BTG-003; 241 m). **b.** Hand sample. Vuggy quartz (BTG-003; 220.5 m). **c.** Hand sample. Andesitic volcaniclastic rock, patchy texture result of strong advanced-argillic alteration (BTG-005; 691.9 m). **d.** Hand sample. Vuggy quartz after patchy texture; pyrite vein across the vuggy quartz (BTG-006; 504,8 m). Abbreviations: grnd: groundmass; Py: pyrite; Qz: quartz; text: texture.

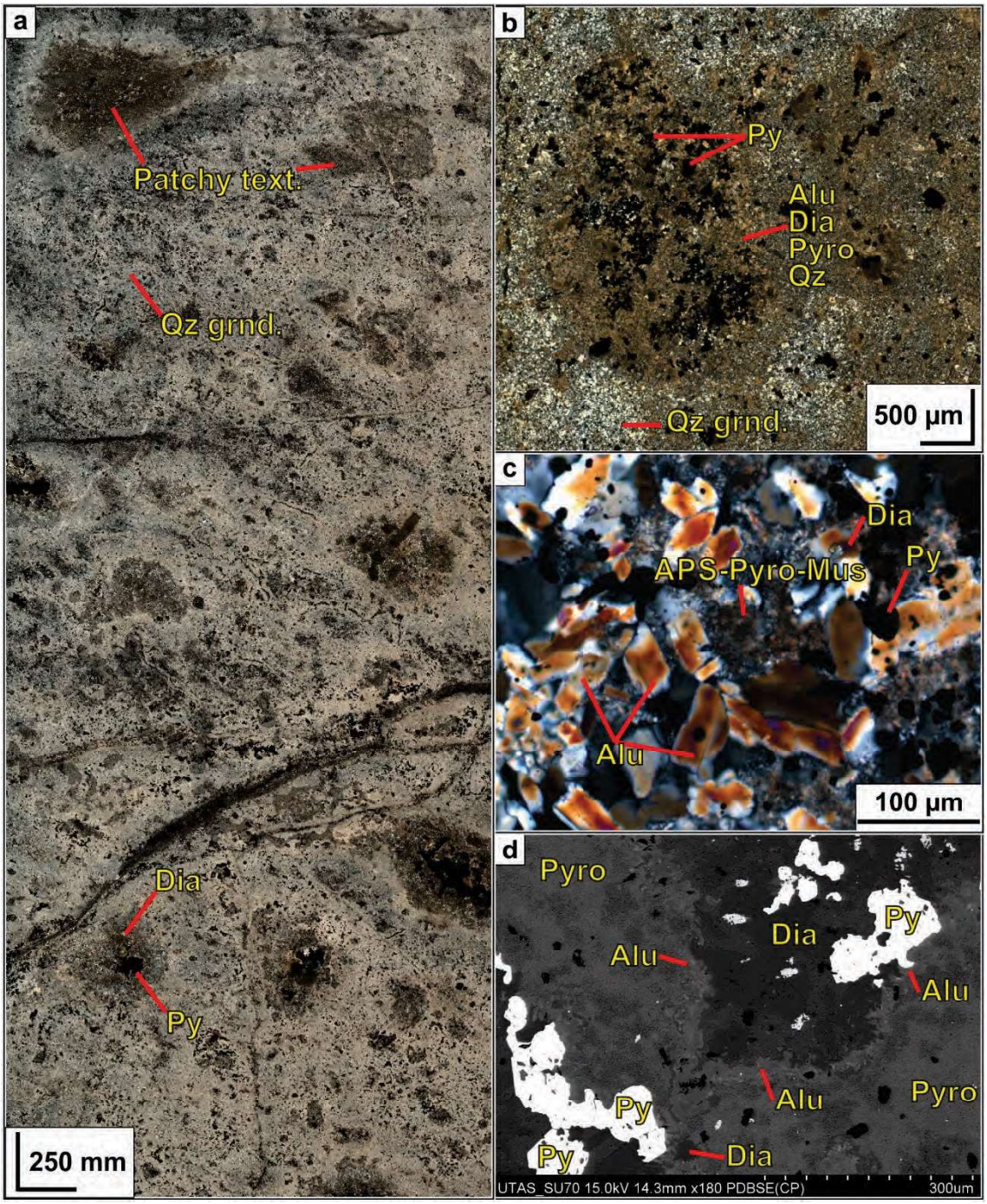

Figure 3.12. Patchy-wormy textured rocks. a. Cross-polarised photomicrograph mosaic. Patchy texture product of strong advanced-argillic alteration on volcaniclastic rock. Bright groundmass consists of fine grained quartz and clay minerals, dark patches consist of alunite, diaspore, pyrophyllite, muscovite and pyrite (BTG-003; 610 m). **b.** Cross-polarised photomicrograph mosaic. Detail of a patchy texture feature (i.e., patch); clay patches are made of pyrophyllite, alunite, diaspore, muscovite, pyrite, quartz and APS minerals (BTG-006; 588.1 m). **c.** Cross-polarised photomicrograph. Detail of a patchy feature; coarse (<100 µm) alunite crystals nucleated around APS-pyrophyllite-muscovite and diaspore crystals. Pyrite crystals are common in patchy features and are disseminated (BTG-006; 259.6 m). **d.** SEM-BSE image. Minerals in a patchy feature: diaspore, APS (i.e., florencite, woodhouseite), muscovite, and pyrite. Woodhouseite nucleates around diaspore and alunite crystals in a pyrophyllite-muscovite groundmass. Alunite crystal contains florencite inclusions. Euhedral pyrite is common and contains quartz inclusions (BTG-006; 540 m). Abbreviations: Alu: alunite; APS: aluminium phosphate-sulphate mineral; Dia: Diaspore; grnd: groundmass; Mus: muscovite; Py: pyrite; Pyro: pyrophyllite; Qz: quartz; Wood: woodhouseite.

3.3.4. Hydrothermal breccias

Two types of hydrothermal breccias have been recognised at Bantug: a natroalunite-pyrite cemented, polymict, hydrothermal breccia; and a quartz-pyrite cemented, polymict, hydrothermal breccia. Clasts in both breccia types display intense silicic and advanced argillic alteration. These breccias have cut both the sedimentary and volcanic rocks at Bantug. The natroalunite-pyrite cemented hydrothermal breccia was observed in drill hole BTG-005 from 137 m to 385.1 m depth. It was also observed in drill hole BTG-003 from 439.3 m to 463.2 m, from 474.4 m to 479.9 m, and from 483.3 m to 487.2 m depth (Figs. 3.3., 3.4, and 3.5). The quartz-pyrite cemented hydrothermal breccia was observed in BTG-005 from 59.6 m to 137 m depth (Figs. 3.3. and 3.4). Chapter 4 describes hydrothermal breccias at Bantug in detail.

3.3.5. Intrusive rocks

Four types of intrusive rocks were recognised at Bantug during this study: i) diorite porphyry (*DP*), ii) plagioclase-pyroxene phyric, crystal crowded diorite porphyry (*DPD I*), iii) pyroxene-plagioclase phyric, miarolitic diorite porphyry (*DPD II*), and iv) plagioclase-pyroxene phyric, miarolitic diorite porphyry (*DPD III*). Their relative timing has been determined based on field and cross-cutting relationships.

3.3.5.1. Diorite porphyry (DP)

This rock type was observed in drill hole BTG-006 from 579.2 m to the end of drill hole (EOD: 704.6 m), and in drill hole BTG-003 from 600 m to 678.4 m (Fig. 3.3 and 3.4). The diorite porphyry is characterised by a porphyritic texture defined by intensely to moderately altered plagioclase phenocrysts (10-15 vol %; 1.5 mm diameter; Figs. 3.12, 3.13a, and 3.13b).

Rock textures vary from porphyritic, defined by plagioclase phenocrysts, to pseudo porphyritic. The latter is defined by clusters of anhedral, fine grained, secondary micas in a groundmass of quartz grains (Figs. 3.12b, 3.13a, and 3.13b). Quartz occurs in the groundmass, as cross cutting veins, and filling in miarolitic cavities (Fig. 3.13). Groundmass quartz grains (7-10 vol %) are anhedral, 250 μm diameter, and rich in pyrite inclusions (Figs. 3.13a and 3.13b).

Quartz in cavities is anhedral (5-7 vol %), 0.5-1.0 mm diameter, and contains pyrite inclusions (Figs. 3.13b, 3.13e, and 3.13f). Pyrite inclusions are rounded to bleb-like and they are located at the edges of quartz crystal facets (Figs. 3.13b, 3.13e, and 3.13f).

Intergrowth of quartz and pyrite in miarolitic cavities suggest that both minerals were precipitated in equilibrium (Figs. 3.13e and 3.13f). Quartz veins are rare, thin (0.5 to 1 mm), wavy, made of grains of distinctive crystalline facets, and contain anhedral pyrite grains of ~50 μm (Figs. 3.7c and 3.13c). Magnetite is rare in the diorite porphyry (<1 vol %). It is typically fine grained (<10 μm), disseminated in the groundmass and occurs as inclusions in groundmass-quartz (Fig. 3.13d). Chalcopyrite and apatite are rare (<1 vol %), fine grained (<50 μm), and occur as inclusions in pyrite in miarolitic cavities (Fig. 3.13f). Apatite also occurs as anhedral crystals of ~50 μm in the groundmass (Fig. 3.14f).

SEM-EDS analyses revealed the groundmass is made of very fine grained muscovite and illite (<3 μm; Figs. 3.14c and 3.14e) supporting coarser phlogopite crystals (~60 μm; Figs. 3.14a, 3.14c to 3.14f; Appendix F). Fine grained phyllosilicates (i.e., muscovite and illite) were observed as intergrowths replacing plagioclase phenocrysts. Figures 3.15b to 3.15e present SEM-EDS spectral results from spot analyses on diorite porphyry samples. Figure 3.15e compares the SEM-EDS results from spot analyses on phlogopite and muscovite grains observed in the diorite porphyry.

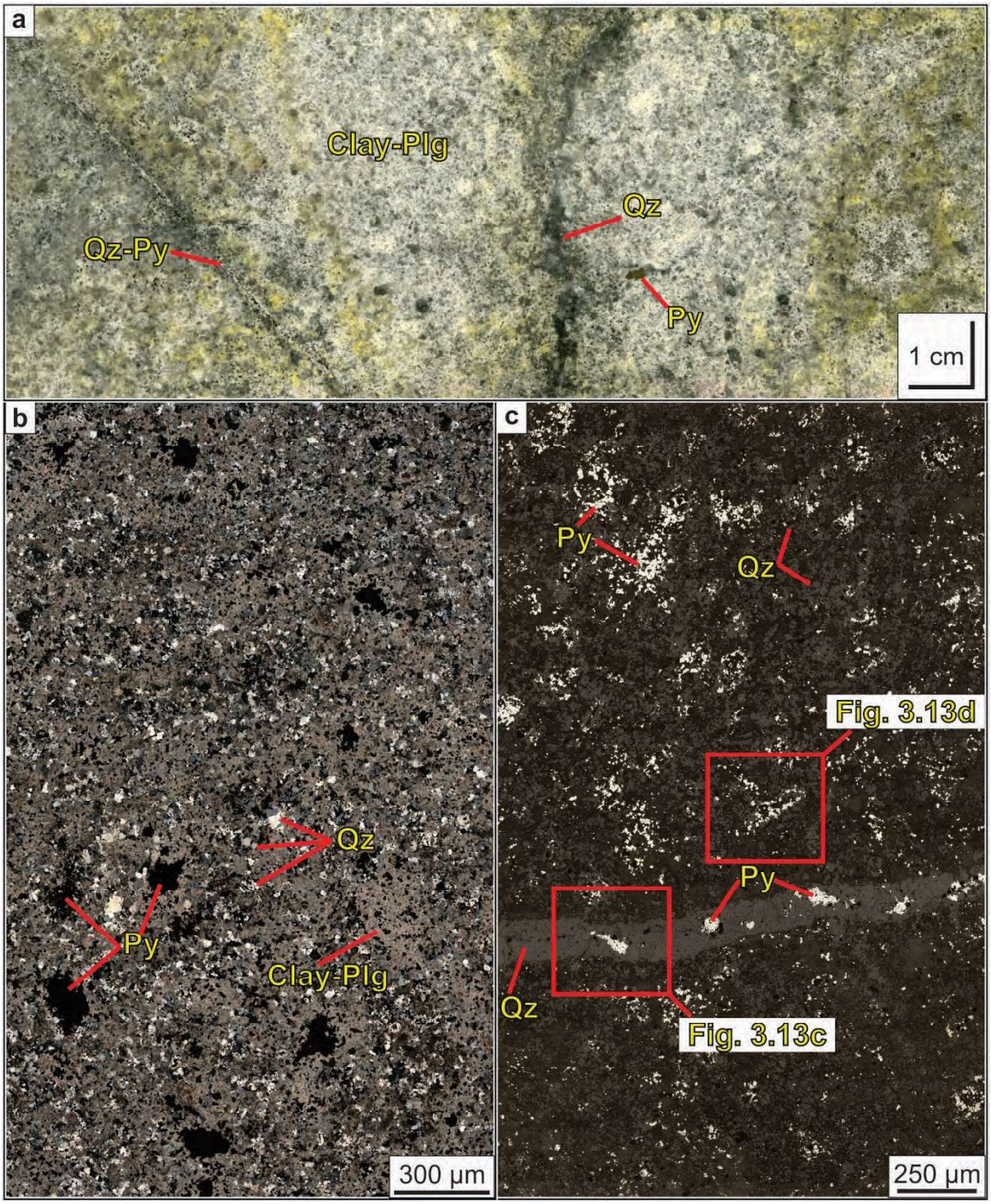

Figure 3.13. Diorite porphyry. a. Hand sample, polished slab, Wavy, incipient quartz-pyrite veinlet cross-cuts the sample (BTG-006; 630 m). **b.** Cross-polarised photomicrograph mosaic. Anhedral quartz crystals in a fine-grained muscovite groundmass; pyrite is anhedral, fine grained, and also occurs in clusters; clay and micas have completely replaced plagioclase crystals (BTG-006; 690 m). **c.** Reflected light photomicrograph mosaic. Fine grained pyrite occurs disseminated and in clusters; wavy quartz vein with pyrite grains; red squares are panels 3.13c and 3.13d (BTG-006; 620 m). Abbreviations: Plg: plagioclase; Py: pyrite; Qz: quartz.

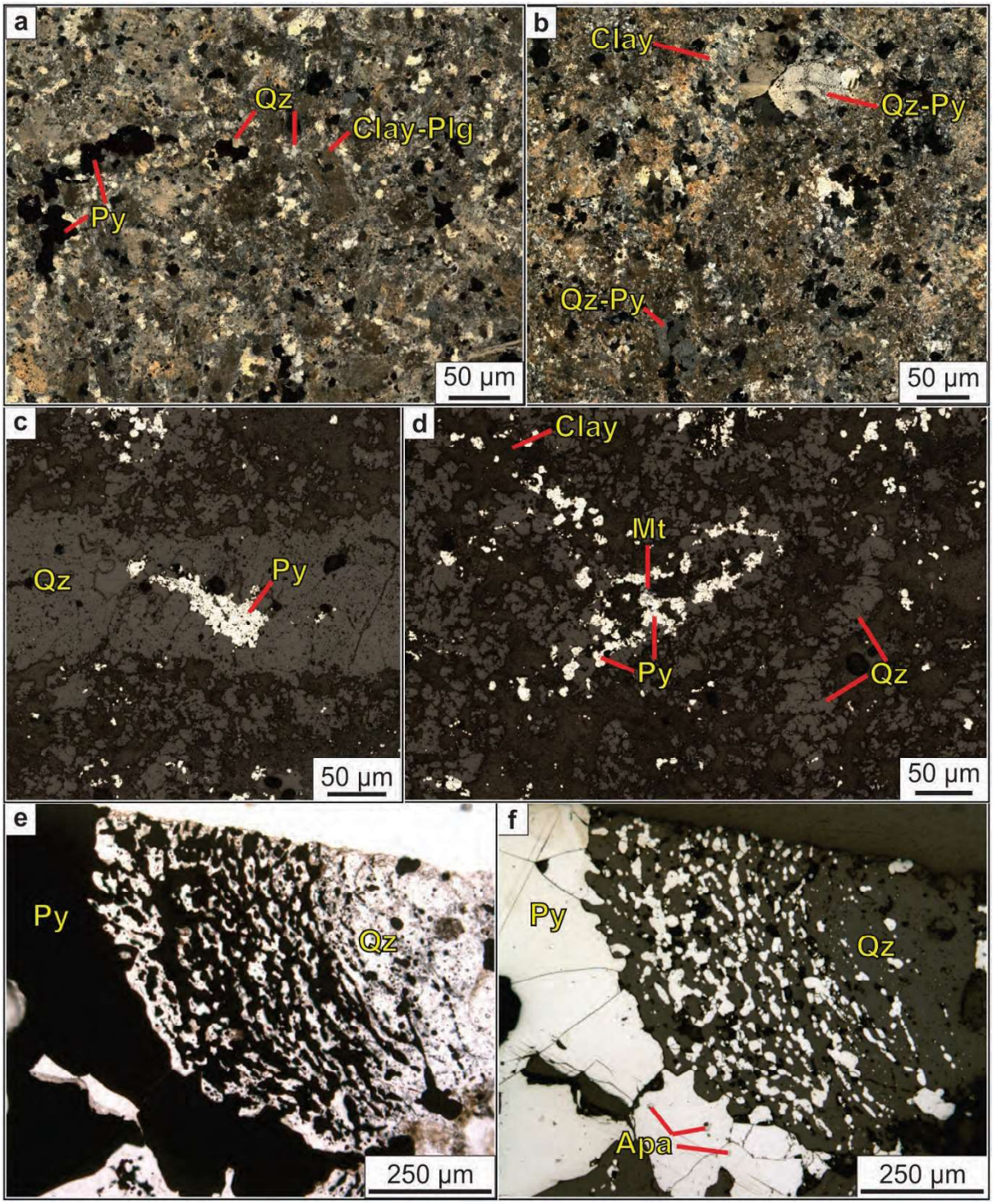

Figure 3.14. Diorite porphyry. a-b. Cross-polarised photomicrographs mosaics. Porphyritic texture overprinted by phyllic alteration, former plagioclase crystal outlines can be recognised and are replaced by clay minerals. Pyrite is disseminated, it occurs in clusters, and cavities with quartz (BTG-006; 588.1 m). **c.** Reflected light photomicrograph. Detail from panel 3.12c. Wavy quartz vein with pyrite (BTG-006; 620 m). **d.** Reflected light photomicrograph. Detail from panel 3.12c. Pyrite grains in quartz; magnetite is fine grained and occurs as inclusions in pyrite (BTG-006; 620 m). **e.** Transmitted light photomicrograph. Pyrite and quartz intergrown in miarolitic cavity (BTG-006; 620 m). **f.** Reflected light photomicrograph. Pyrite and quartz intergrown in miarolitic cavity. Pyrite contains fine grained apatite inclusions (BTG-006; 620 m). Abbreviations: Apa: apatite; Mt: magnetite; Plg: plagioclase; Py: pyrite; Qz: quartz.

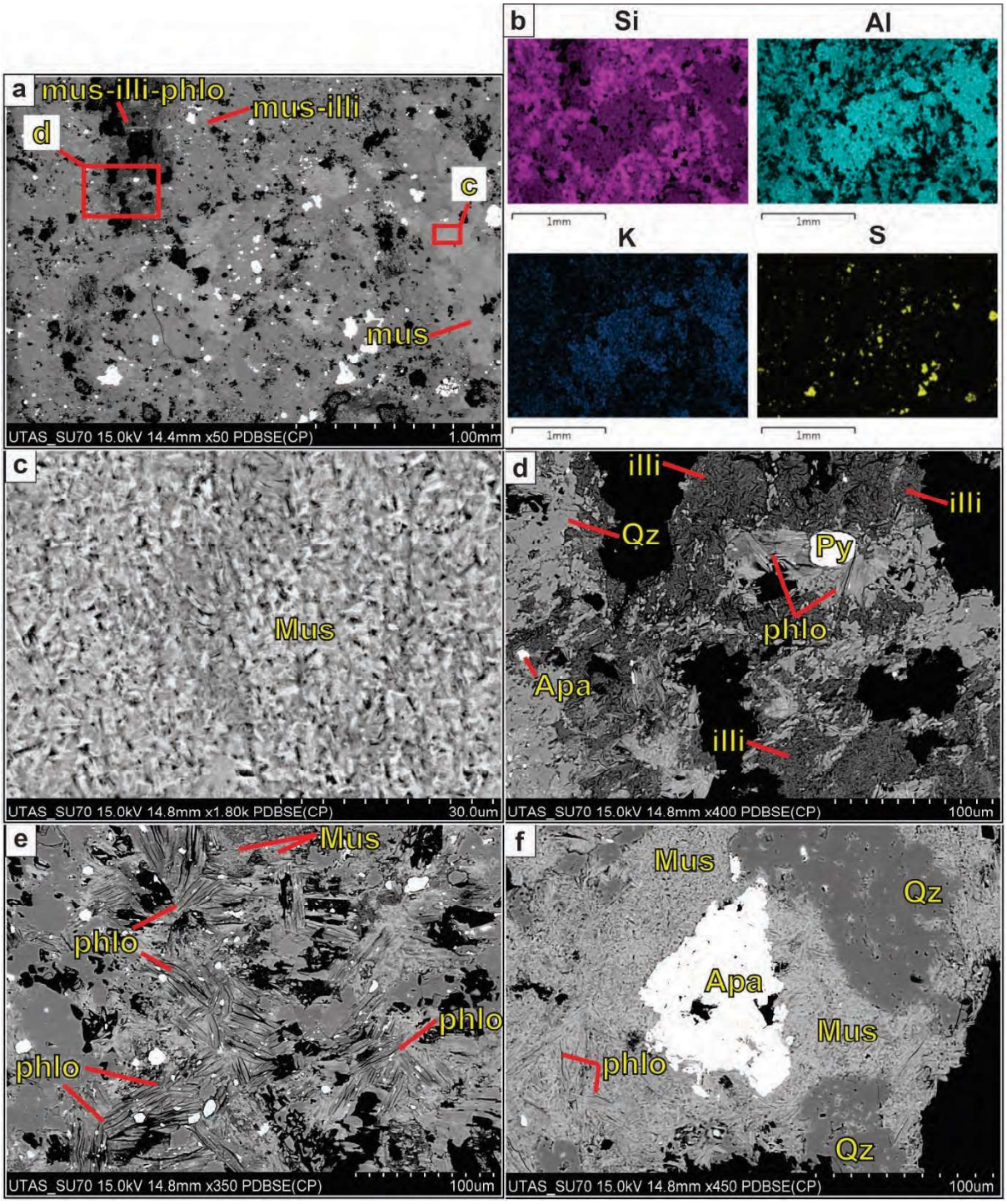

Figure 3.15. Diorite porphyry. a. SEM-BSE image. Quartz and pyrite crystals in a illite-muscovite-phlogopite groundmass. Red squares are details in panels c and d (BTG-006; 665 m). **b.** EDS maps from panel a. Elements depicted are: silicon (Si), aluminium (Al), potassium (K), and sulphur (S). High intensity colour in maps indicates higher concentration of each element. **c.** SEM-BSE image. Detail from panel a. Muscovite crystals (BTG-006; 665 m). **d.** SEM-BSE image. Detail from panel a. Phlogopite, quartz, and pyrite crystals on an illite groundmass. Fine apatite crystals are disseminated (BTG-006; 665 m). **e.** SEM-BSE image. Coarser phlogopite crystals (~60 µm) intergrown with pyrite and muscovite (BTG-006; 665 m). **f.** SEM-BSE image. Coarse apatite crystal (~100 µm) on a muscovite-phlogopite groundmass (BTG-006; 665 m). Abbreviations: Apa: apatite; illi: illite; Mt: magnetite; Mus: muscovite; Phlo: phlogopite; Py: pyrite; Qz: quartz.

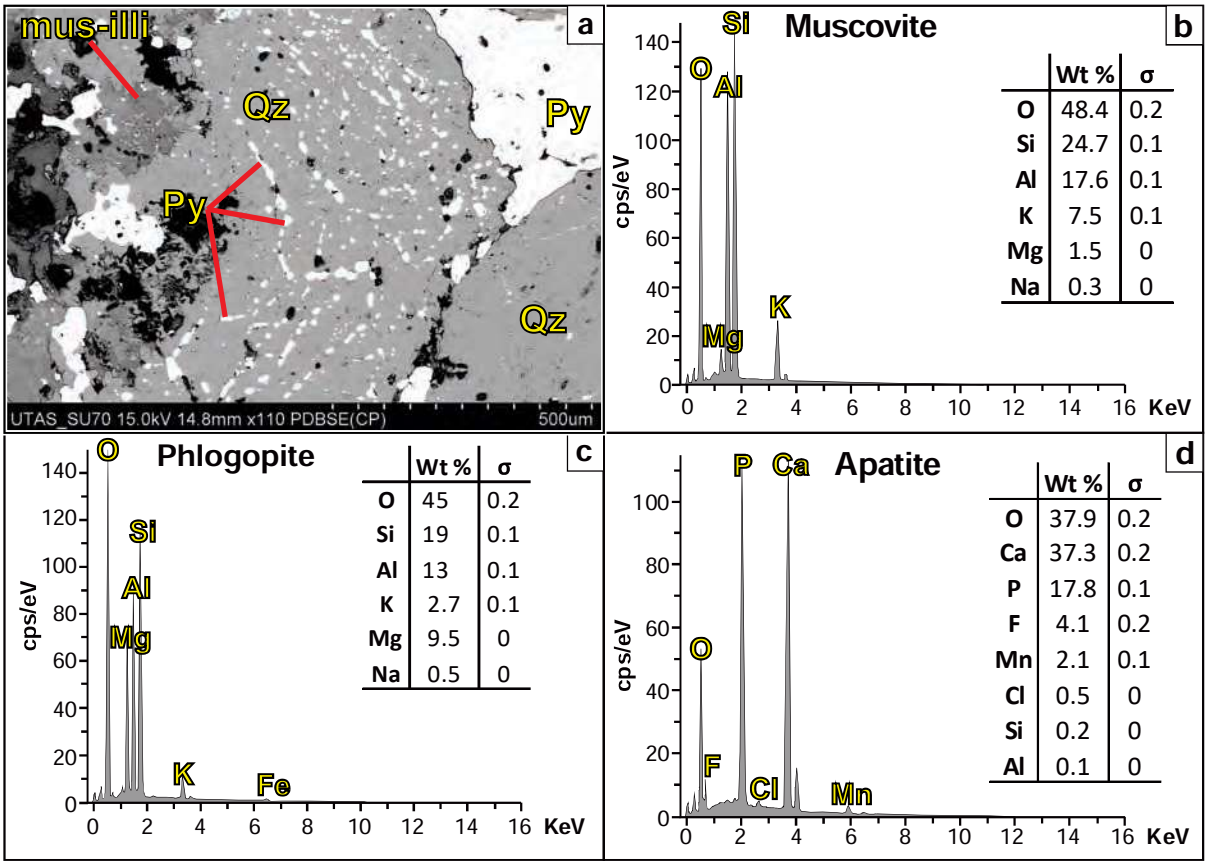

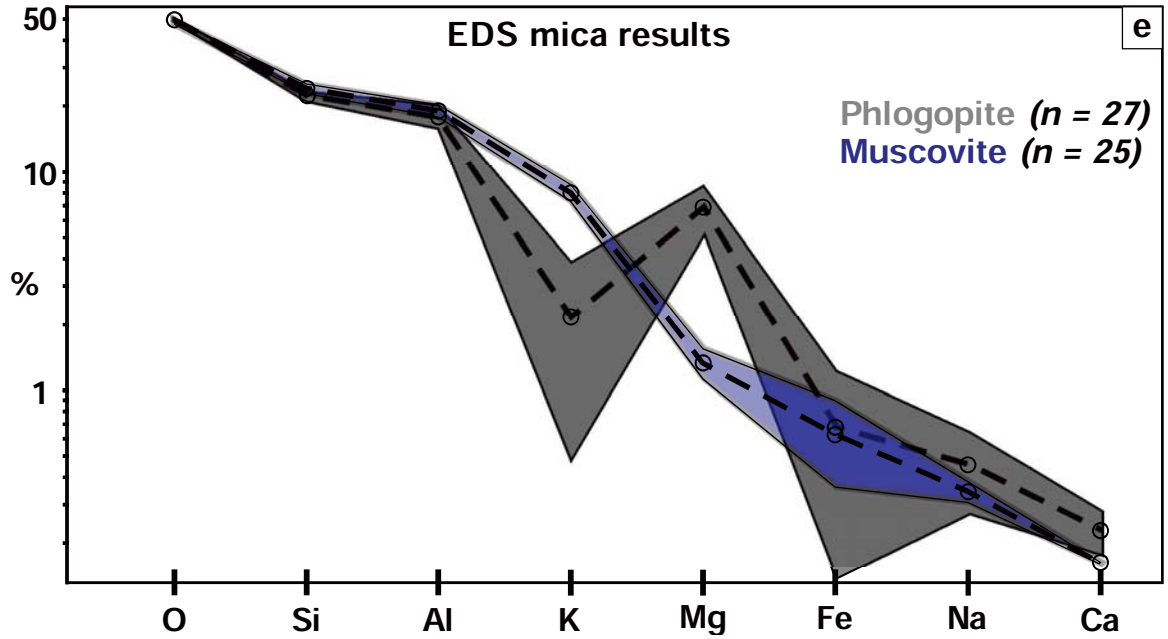

Figure 3.16. Diorite porphyry. a. SEM-BSE image. Quartz and pyrite intergrown (BTG-006; 588.1 m). **b.** SEM-EDS spectra from muscovite crystals in panel l (BTG-006; 665 m). **c.** EDS spectra from phlogopite crystals in panel 3.14e (BTG-006; 665 m). **d.** SEM-EDS spectra from apatite crystal in panel 3.14f (BTG-006; 665 m). **e.** SEM-EDS mica results. Phlogopite in red, and muscovite in blue. Dashed line represents the mean value, shaded area contains results from n-number of analyses (BTG-006; 665 m). Abbreviations: illi: illite; Mus: muscovite; Py: pyrite; Qz: quartz; Al: aluminium; Ca: calcium, Cl: chlorine; F: fluorine; Fe: iron; K: potassium; Mg: magnesium; Mn, manganese; O: oxygen; P: phosphorus; Si: silicon.

3.3.5.2. Pyroxene-plagioclase phyric, miarolitic diorite porphyry (DPD I)

This rock type was intersected by drill hole BTG-003 from 253.9 m to 270.0 m (Figs. 3.3 and 3.5). It is characterised by porphyritic texture defined by sparse pyroxene and plagioclase crystals set in a microcrystalline to granular groundmass (Figs. 3.16 to 3.17). Circular to elliptical cavities of <2 mm in diameter, partially filled with epidote and quartz, were recognized in this intrusion (5-7 vol %; Figs. 3.16a to 3.16c, and 3.18d). Keary (2001) defined miarolitic cavities as small, crystal-lined cavities, in an intrusive igneous rock, product of the segregation of small gas pockets. The cavities observed in DPD I during this study match the description provided by Keary (2001), and are interpreted to be miarolitic cavities.

Pyroxene occurs as euhedral to subhedral phenocrysts from 500 μm to 2 mm in diameter (<15 vol %; Figs. 3.16a, 3.16b, 3.16d, and 3.17a). Some grains are broken, subrounded, and their margins have been weakly altered to clay minerals (Fig. 3.16d). FE-SEM-EDS analyses revealed the pyroxenes to be diopside (Figs. 3.19a and 3.19e; Appendix F). Diopsides have been cut by epidote-quartz veins that are 60-180 μm thick (Figs. 3.18a and 3.18c). Diopside crystals contain quartz, magnetite, and apatite inclusions (Figs. 3.16d and 3.18e). Plagioclase phenocrysts (15 vol %) are euhedral, 1 mm to 2 mm in size, and are weakly to moderately altered to clay minerals (Figs. 3.16, and 3.17a). Plagioclase phenocrysts also contain minor amounts of magnetite inclusions (Figs. 3.16d). Epidote and quartz have filled miarolitic cavities (5-7 vol %). The epidote crystal habit is acicular (~500 μm long) to prismatic, and its aggregate is radiating to drusy (Figs. 3.16a to 3.16c, and 3.18d). Euhedral quartz crystals (<1 vol %; ~400 μm) occur in drusy aggregates with epidote (Figs. 3.16c, and 3.18d).

Magnetite (5 vol %) is disseminated in the groundmass; crystals are fine grained (50-100 μm), and anhedral to subhedral (Fig. 3.17b to 3.17d, and 3.18e). Magnetite also occurs locally in the groundmass as coarser euhedral grains (~500 μm; Fig. 3.17d), and as coarse inclusions in diopside (<20 μm; Fig. 3.16d). Pyrite is rare (<1 vol %); it occurs mostly as fine grains (<10 μm) disseminated in the groundmass and as inclusions in pyroxene (Figs. 3.17c, and 3.18f). Apatite is rare (<1 %), fine grained (<75 μm), and occurs as inclusions in diopside and magnetite crystals (Figs. 3.16d, and 3.18e).

The presence of pyroxene in DPDI and DPDII should not be taken as a discouraging sign for potential porphyry-style mineralisation, as pyroxene-phyric intrusions can be genetically associated with porphyry-style mineralisation (e.g., Northparkes, Australia; Lickfold, 2002; Lickfold et al., 2003; and Lickfold et al., 2007).

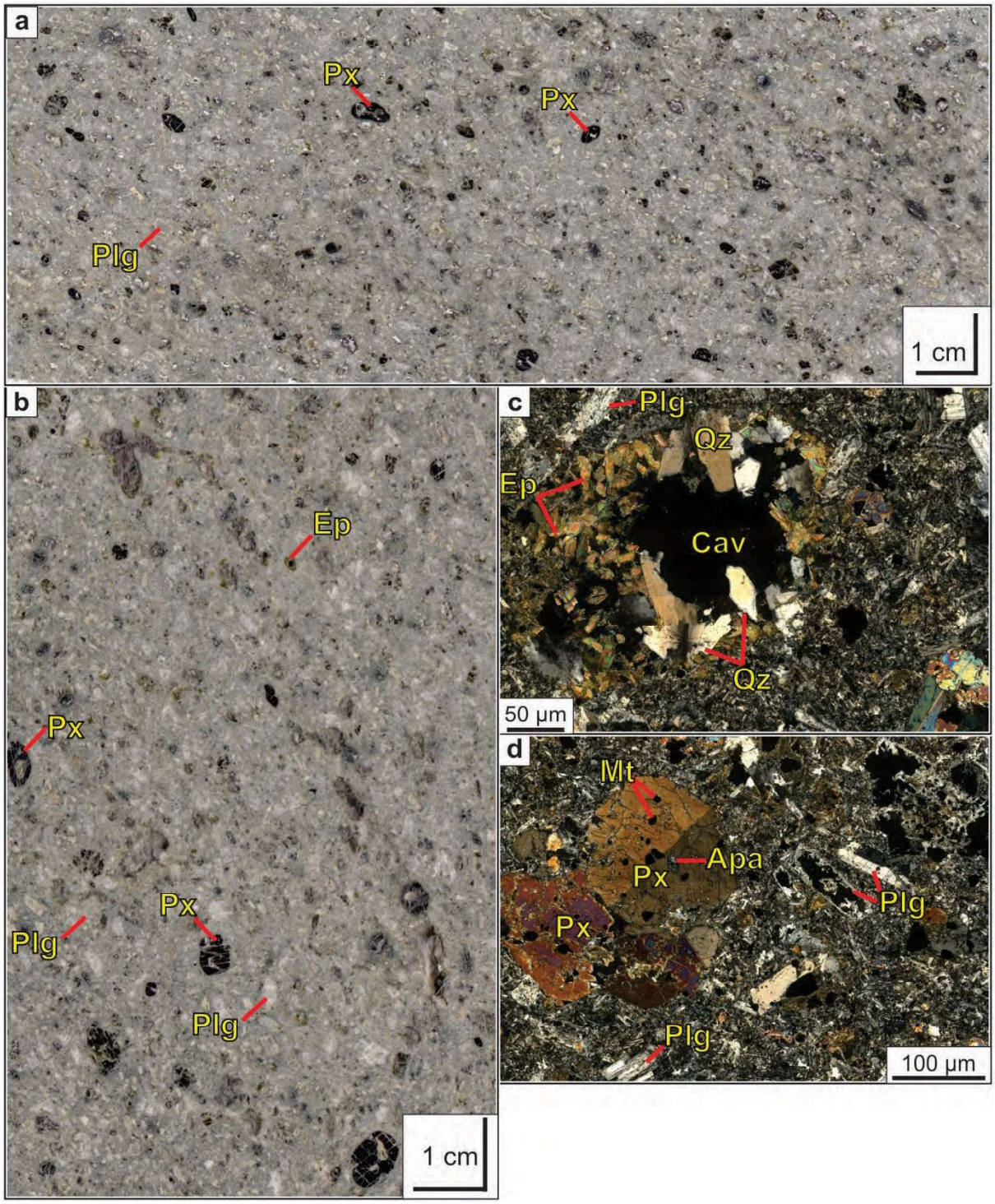

Figure 3.17. Pyroxene-plagioclase phyric, miarolitic diorite porphyry (DPD I). a. Hand sample, polished slab. Sparsely packed porphyritic texture defined by plagioclase and pyroxene phenocrysts (BTG-003; 263 m). **b.** Hand sample, polished slab. Sparsely packed porphyritic texture defined by plagioclase and pyroxene phenocrysts (BTG-003; 268 m). **c.** Cross-polarised photomicrograph. ~150 µm diameter cavity partially filled with quartz and epidote crystals (BTG-003; 263 m). **d.** Cross-polarised photomicrograph. Pyroxene phenocrysts with magnetite and apatite inclusions in a fine-grained groundmass; plagioclase phenocrysts are partially replaced by magnetite (BTG-003; 268 m). Abbreviations: Apa: apatite; Cav: cavity; Ep: epidote; Plg: plagioclase; Px: pyroxene; Qz: quartz.

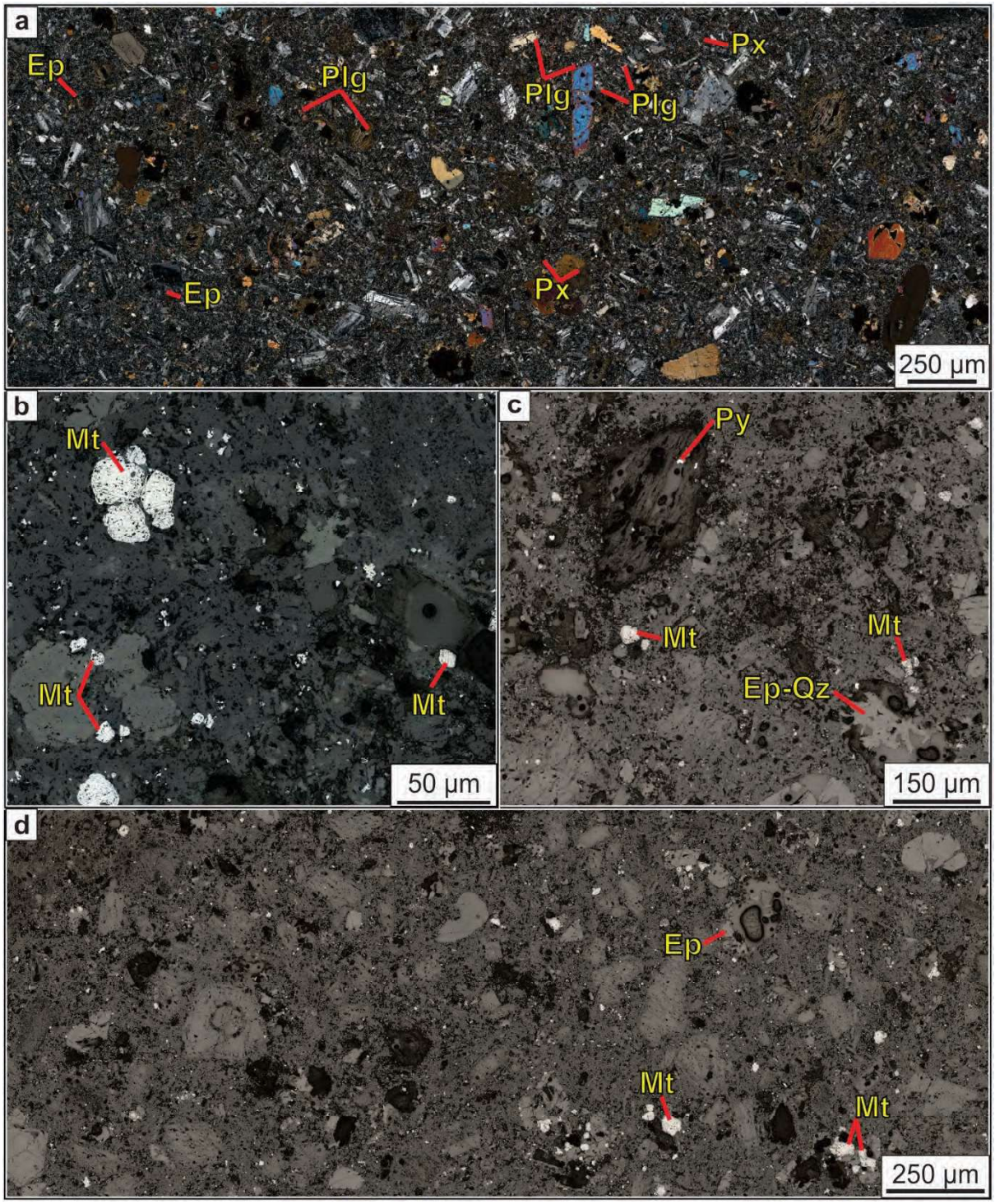

Figure 3.18. Pyroxene-plagioclase phyric, miarolitic diorite porphyry (DPD I). a. Cross-polarised photomicrograph mosaic. Plagioclase and pyroxene phenocrysts in a fine-grained groundmass, and cavities partially filled with epidote and quartz (BTG-003; 268 m). **b.** Reflected light photomicrograph. Coarse and fine grained magnetite disseminated, fine grained magnetite as inclusions in pyroxene (BTG-003; 268 m). **c.** Reflected light photomicrograph. Rare fine grained pyrite as inclusion in partially altered pyroxene (BTG-003; 268 m). **d.** Reflected light photomicrograph mosaic. Coarse and fine grained magnetite disseminated, and replacing pyroxene, throughout the sample (BTG-003; 268 m). Abbreviations: Cav: cavity; Ep: epidote; Mt: magnetite; Plg: plagioclase; Px: pyroxene; Py: pyrite; Qz: quartz.

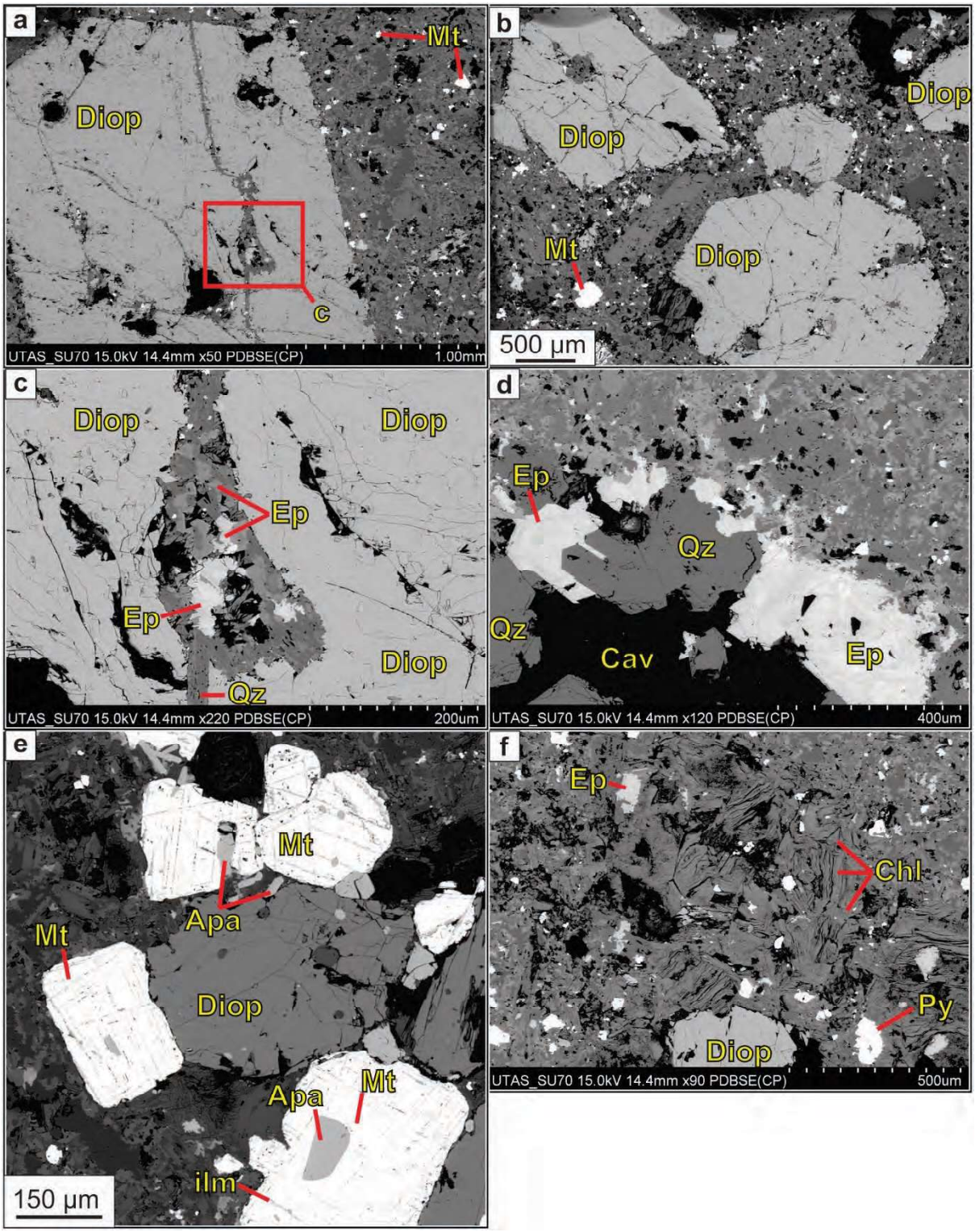

Figure 3.19. Pyroxene-plagioclase phyric, miarolitic diorite porphyry (DPD I). a. SEM-BSE image. Diopside phenocryst in a fine-grained groundmass, a fracture in the phenocryst has been filled with epidote-quartz. Red square is panel c (BTG-003; 268 m). **b.** SEM-BSE image. Diopside phenocrysts in a fine-grained groundmass (BTG-003; 268 m). **c.** SEM-BSE image. Detail from panel a. Fracture in diopside filled with epidote and quartz (BTG-003; 268 m). **d.** SEM-BSE image. Magnetite crystals with apatite inclusions intergrown with diopside phenocrysts (BTG-003; 268 m). **e.** SEM-BSE image. Quartz and epidote crystals partially filling a cavity (BTG-003; 268 m). **f.** SEM-BSE image. Chlorite, pyrite, and epidote crystals around diopside phenocryst (BTG-003; 268 m). Abbreviations: Apa: apatite; Cav: cavity; Chl: chlorite: Diop: diopside; Ep: epidote; ilm: ilmenite; Mt: magnetite; Py: pyrite; Qz: quartz.

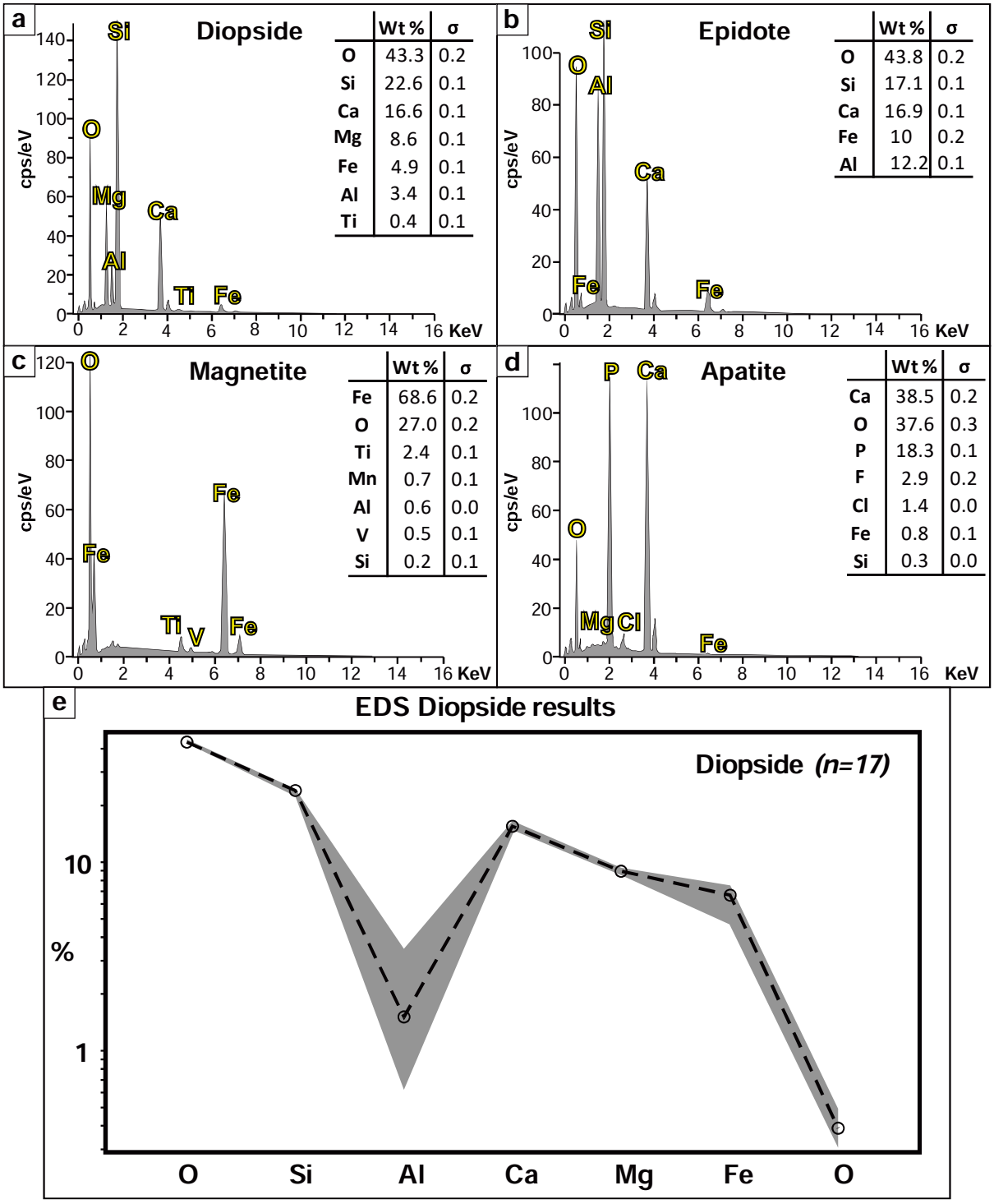

Figure 3.20. Pyroxene-plagioclase phyric, miarolitic diorite porphyry (DPD I). a. SEM-EDS spectra from diopside. Analysis from crystals in panel 3.18a (BTG-003; 268 m). **b.** SEM-EDS spectra from epidote. Analysis from crystals in panel 3.18e (BTG-003; 268 m). **c.** SEM-EDS spectra from magnetite. Analysis from crystals in panel 3.18d (BTG-003; 268 m). **d.** SEM-EDS spectra from apatite. Analysis from crystals in panel 3.18e (BTG-003; 268 m). **e.** SEM-EDS composition spectra from diopside crystals (BTG-003; 268 m). SEM-EDS results are presented in Appendix F. Abbreviations: Al: aluminium; Ca: calcium, Cl: chlorine; F: fluorine; Fe: iron; K: potassium; Mg: magnesium; Mn, manganese; O: oxygen; P: phosphorus; Si: silicon; Ti: titanium; V: vanadium.

3.3.5.3. Plagioclase-pyroxene phyric, crystal crowded diorite porphyry (DPD II)

This rock-type was intercepted by drill hole BTG-003 from 270.3 m to 366.6 m (Figs. 3.3 and 3.5). It is characterised by porphyritic texture made of plagioclase and pyroxene phenocrysts in a granular groundmass (Figs. 3.20 and 3.21a). Plagioclase phenocrysts are abundant (50 vol %), 1-3 mm in size, and closely packed (Fig. 3.20a and 3.21a). Pyroxene phenocrysts (15 vol %) are euhedral, <60 μm in diameter, and sparsely packed (Figs. 3.20 and 3.21a). Most pyroxene crystals have been completely or moderately altered to chlorite (Fig. 3.21b). The alteration process was selective, localised along cracks in pyroxene crystals (Figs. 3.22e and 3.22f). SEM-EDS analyses revealed that most of the pyroxenes are diopside (Ca-Mg) and some are augite (Ca-Na; Figs. 3.22, 3.23c, and 3.23e; Appendix F).

Rare, pale brown micas (<1 vol %) occur as anhedral phenocrysts which range in size from 125 μm to 2 mm (Figs. 3.21a, 3.23a, 3.23d, 3.23f). These crystals are weakly altered to chlorite on their margins, and contain magnetite-apatite inclusions <250 μm (Fig. 3.23a). SEM-EDS analyses revealed the micas to be enriched in Mg, and with a significant K content. These are most likely to be phlogopite (Figs. 3.23d and 3.23f; Appendix F).

Euhedral magnetite grains are disseminated in the groundmass and have replaced pyroxene crystals (7 vol %; 100 μm-500 μm; Fig. 3.21c). Magnetite is intergrown with ilmenite (Figs. 3.21d, and 3.22a to 3.22c) and contains anhedral apatite inclusions (<60 μm; Fig. 3.22c). Chalcopyrite is anhedral, fine grained, and it occurs as inclusions in magnetite and disseminations in the groundmass (1 vol %, <25 μm; Figs. 3.21c and 3.21e). Pyrite is mostly subhedral to anhedral, and it occurs as fine grains disseminated in the groundmass (5 vol %; 10 μm-250 μm; Figs. 3.21c and 3.21e). Pyrite also occurs in veinlets (Fig. 3.20b), and replacing pyroxenes (Fig. 3.21c).

The presence of pyroxene in DPDII and DPDI should not be taken as a discouraging sign for potential porphyry-style mineralisation, as pyroxene-phyric intrusions can be genetically associated with porphyry-style mineralisation (e.g., Northparkes, Australia; Lickfold, 2002; Lickfold et al., 2003; and Lickfold et al., 2007).

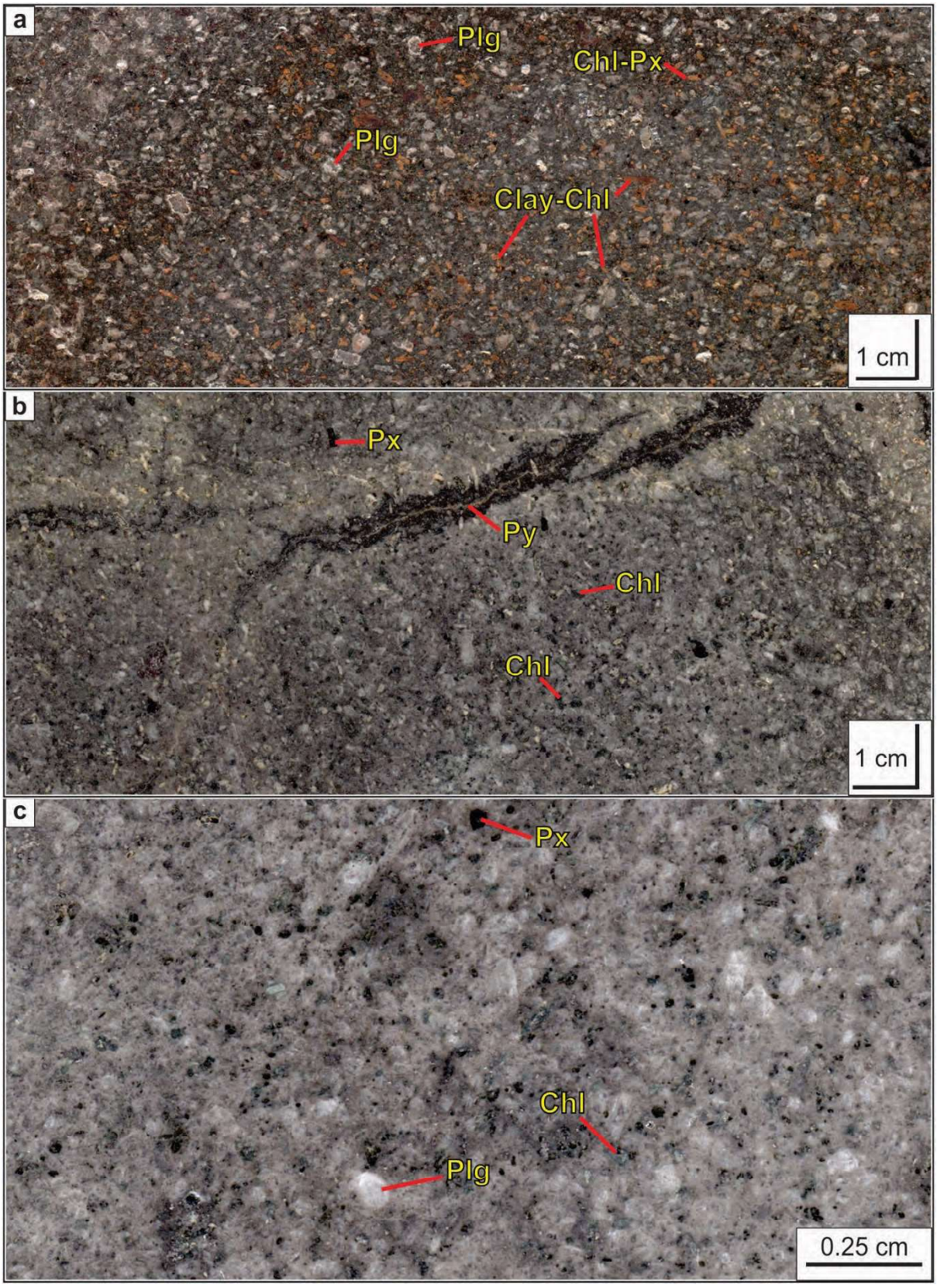

Figure 3.21. Plagioclase-pyroxene phyric, crystal crowded diorite porphyry (DPD II). a. Hand sample, polished slab (BTG-003; 369 m). **b.** Hand sample, polished slab (BTG-003; 374 m). **c.** Hand sample, polished slab (BTG-003; 376 m). Abbreviations: Chl: chlorite; Plg: plagioclase; Px: pyroxene; Py: pyrite.

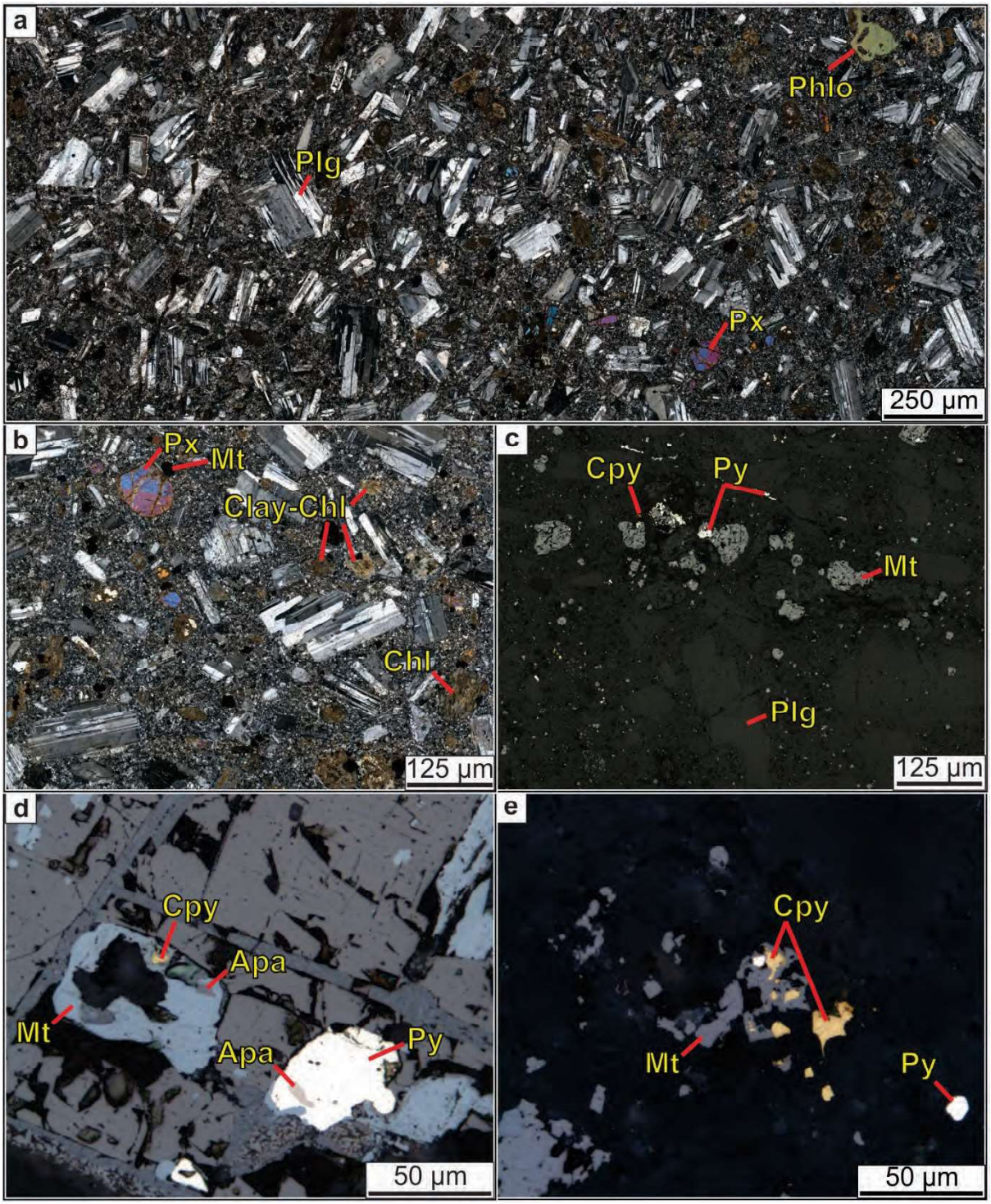

Figure 3.22. Plagioclase-pyroxene phyric, crystal crowded diorite porphyry (DPD II). a. Cross-polarised photomicrograph mosaic. Packed plagioclase phenocrysts with subordinate pyroxene phenocrysts in a fine-grained crystal groundmass (BTG-003; 374 m). **b.** Cross-polarised photomicrograph mosaic. Pyroxene phenocrysts are selectively altered to chlorite through cracks (BTG-003; 374 m). **c.** Reflected light photomicrograph mosaic. Coarse (~100 µm) magnetite crystals disseminated and intergrown with pyroxene. Magnetite crystals are intergrown with pyrite; rare, fine grained chalcopyrite crystals are disseminated (BTG-003; 374 m). **d.** Reflected light photomicrograph. Chalcopyrite and apatite inclusions (<5 µm) in magnetite crystal (left). Apatite inclusion (<10 µm) in pyrite crystal (BTG-003; 374 m). **e.** Reflected light photomicrograph. Chalcopyrite intergrown with magnetite and pyrite (BTG-003; 374 m). Abbreviations: Apa: apatite; Chl: chlorite; Cpy: chalcopyrite; Mt: magnetite; Phlo: phlogopite; Plg: plagioclase; Px: pyroxene; Py: pyrite.

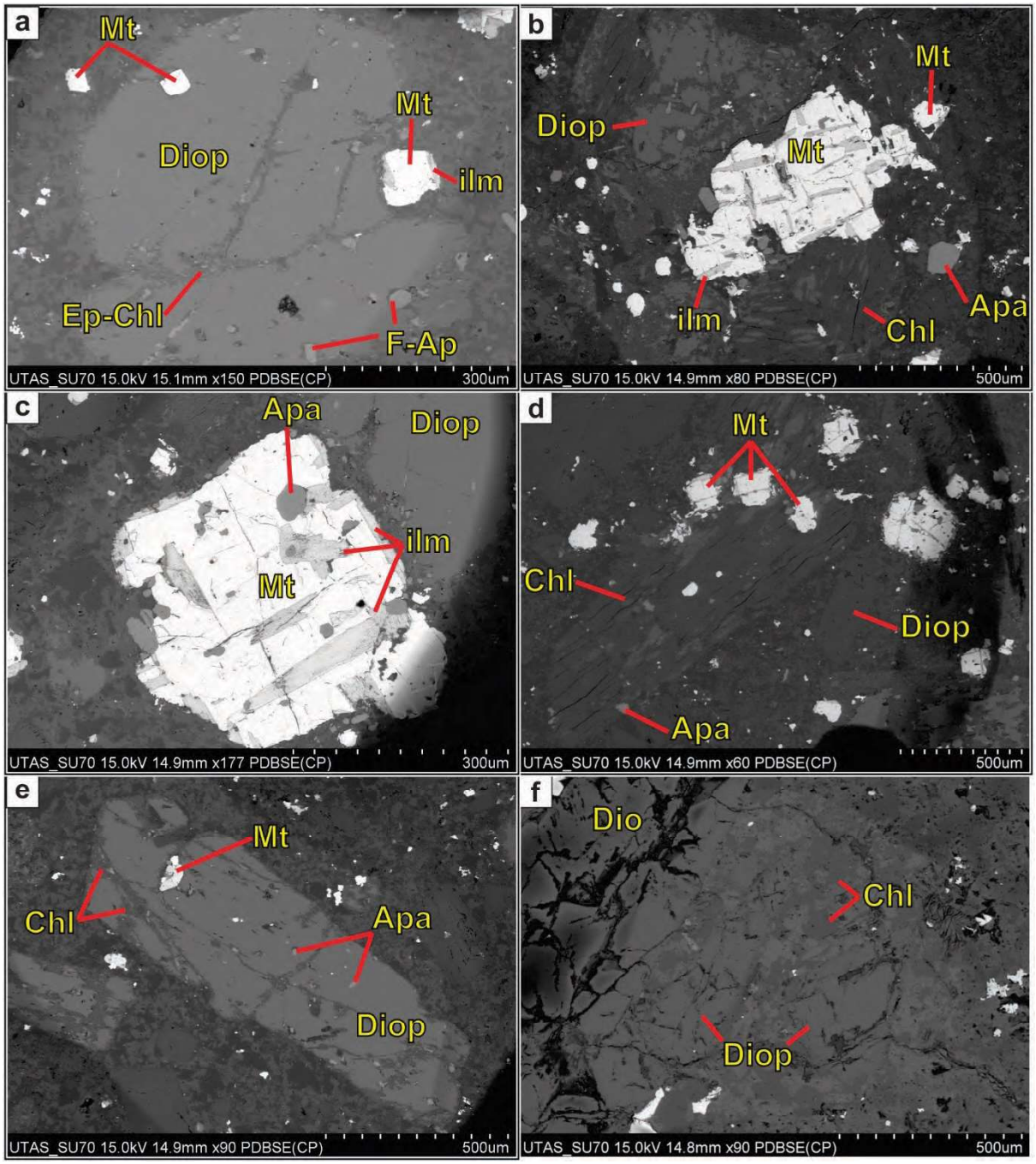

Figure 3.23. Plagioclase-pyroxene phyric, crystal crowded diorite porphyry (DPD II). a. SEM-BSE image. Magnetite and fluorapatite inclusions in diopside. Epidote and chlorite occur in cracks in diopside phenocryst (BTG-003; 374 m). **b.** SEM-BSE image. Magnetite crystal with ilmenite exolution intergrown with diopside; chlorite replaced diopside. Apatite crystals are disseminated throughout the sample (BTG-003; 374 m). **c.** SEM-BSE image. Magnetite crystal with ilmenite exolution and apatite inclusions (BTG-003; 374 m). **d.** SEM-BSE image. Chlorite after diopside. Apatite and magnetite occur with chlorite (BTG-003; 374 m). **e.** SEM-BSE image. Diopside crystal; chlorite replaced diopside through cracks. Magnetite and apatite inclusions occur with diopside (BTG-003; 374 m). **f.** SEM-BSE image. Chlorite replaced diopside (BTG-003; 374 m). Abbreviations: Apa: apatite; Chl: chlorite; Diop: diopside; ilm: ilmenite; Mt: magnetite.

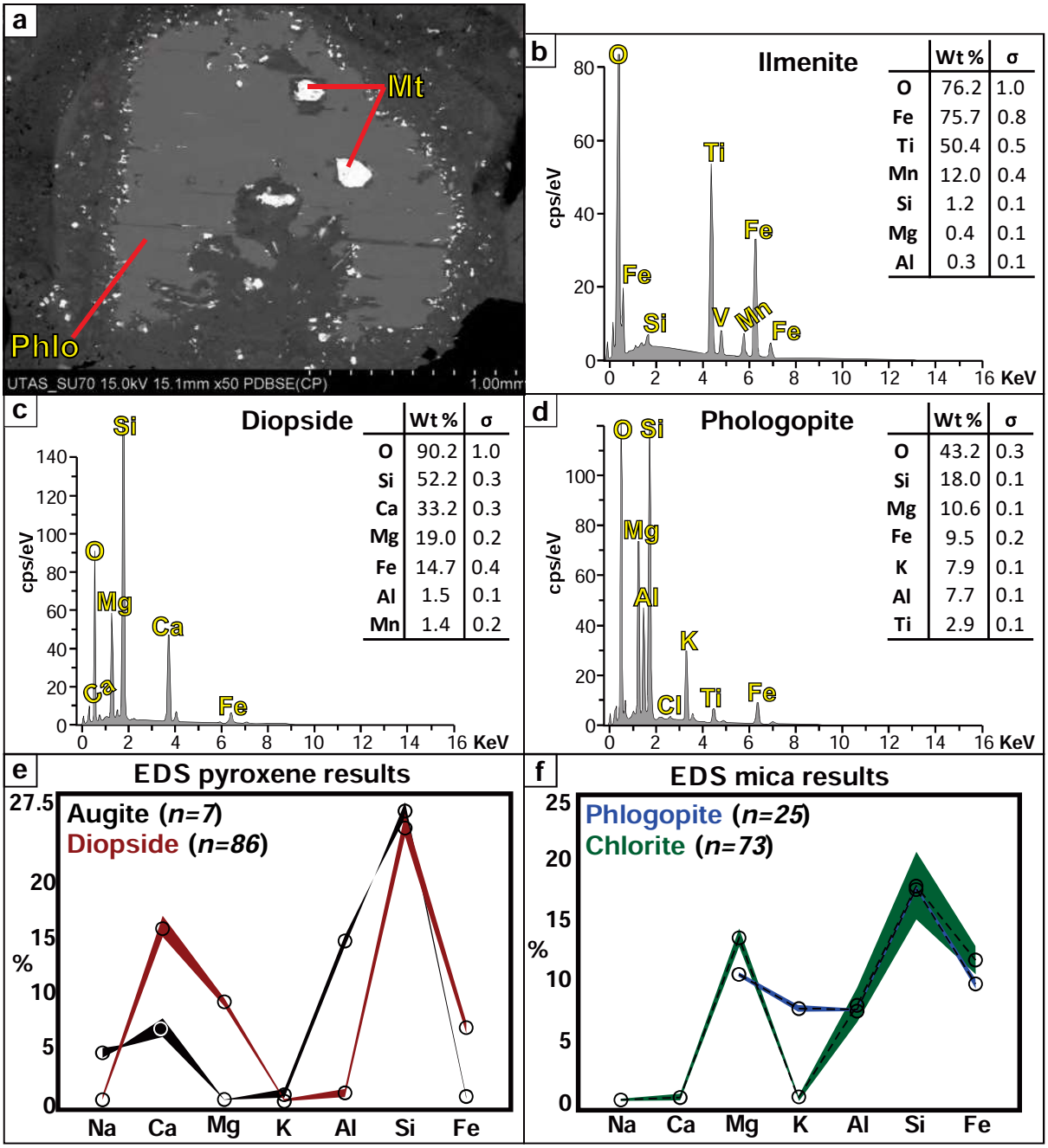

Figure 3.24. Plagioclase-pyroxene phyric, crystal crowded diorite porphyry (DPD II). a. SEM-BSE image. Phlogopite crystal weakly altered; chlorite replaced the border. Phlogopite contains magnetite and apatite inclusions (BTG-003; 374 m). **b.** SEM-EDS spectra from ilmenite in panel 3.22c. **c.** SEM-EDS spectra from diopside crystals in panel 3.22a. **d.** SEM-EDS spectra from phlogopite in panel 3.23a. **e.** SEM-EDS results summary from diopside and augite crystals (BTG-003; 374 m). **f.** SEM-EDS results summary from phlogopite and chlorite crystals (BTG-003; 374 m). FE-SEM-EDS analyses are presented in Appendix F. Abbreviations: Mt: magnetite; Phlo: phlogopite; Al: aluminium; Ca: calcium, Cl: chlorine; F: fluorine; Fe: iron; K: potassium; Mg: magnesium; Mn, manganese; Na: sodium; O: oxygen; P: phosphorus; Si: silicon; Ti: titanium; V: vanadium.

3.3.5.4. Plagioclase-phyric, miarolitic diorite porphyry (DPD III)

This rock type was observed in several segments of drill hole BTG-006 between ~90 m and ~480 m (Figs. 3.3 and 3.6). Individual intercepts are between 20 and 30 m thick. DPD III is characterised by a porphyritic texture defined by hydrothermally altered plagioclase phenocrysts (20 vol %; 1-2 mm), and cavities filled with quartz-pyrite or pyrite-anhydrite (7 vol %; Figs. 3.24, 3.25, and 3.26).

Plagioclase phenocrysts are euhedral, ~200 μm diameter, and are closely packed in a fine-grained groundmass. Plagioclase phenocrysts have been partially (Fig. 3.25c) to completely (Figs. 3.24b, 3.25a, 3.26a, 3.26b) replaced by fine grained (<10 μm) micas and clay minerals (i.e., muscovite and kaolinite).

Cavities are partially to completely filled with quartz-pyrite (Figs. 3.25a and 3.26b), and pyrite-anhydrite (Fig. 3.27a). Quartz and anhydrite in cavities are subhedral to euhedral, and crystals are ~300 μm and <100 μm in size, respectively (Figs. 3.26b and 3.27a). Some quartz crystals in cavities have undulatory extinction when viewed under crossed polarisers (Figs. 3.25a and 3.26b).

Pyrite is mostly fine grained, disseminated, and subhedral (15 vol %, ~20 μm; Figs. 3.25b and 3.27e). Coarser pyrite crystals occur in miarolitic cavities with quartz and anhydrite (1 vol %, 200-500 μm; Figs. 3.26b and 3.27a). Magnetite and chalcopyrite are rare, fine grained, and occur as inclusions in coarser pyrite grains (<1 vol %, <50 μm; Fig. 3.27b).

Figure 3.25. Plagioclase-phyric, miarolitic diorite porphyry (DPD III). a. Hand sample, polished slab. Cavities are partially filled with quartz crystals (BTG-003; 436 m). **b.** Cross-polarised photomicrograph mosaic. A crystal crowded texture is inferred from former plagioclase phenocrysts; plagioclase has been replaced by fine grained clay minerals. Cavities are partially to completely filled with quartz-pyrite (BTG-003; 436 m). Abbreviations: Plg: plagioclase; Py: pyrite; Qz: quartz.

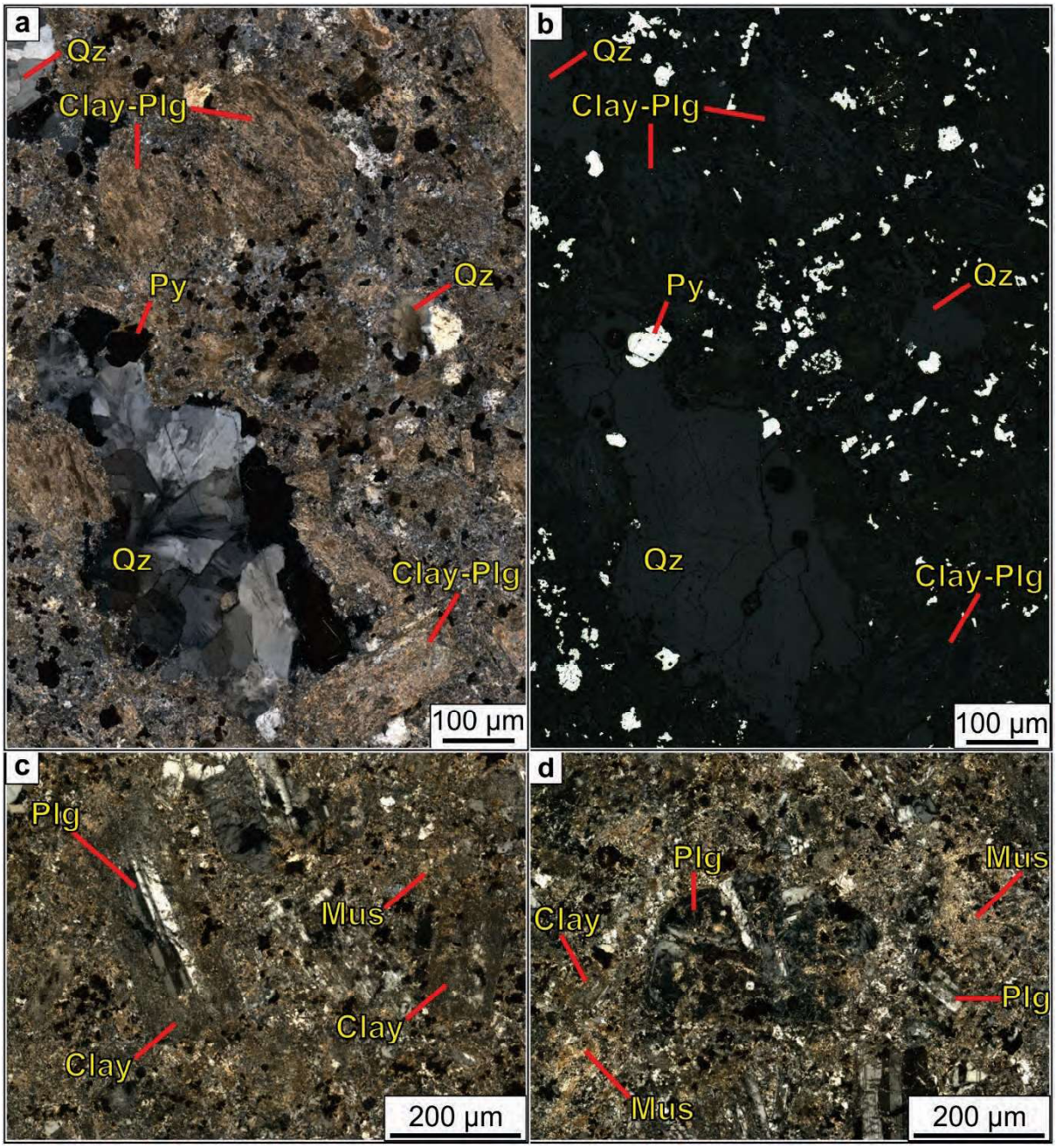

Figure 3.26. Plagioclase-phyric, miarolitic diorite porphyry (DPD III). a. Cross-polarised photomicrograph mosaic. Detail from quartz in cavity. Clay minerals after plagioclase phenocryst (BTG-003; 436 m). **b.** Reflected light photomicrograph mosaic. Field of view as in panel a (BTG-003; 436 m). **c.** Cross-polarised photomicrograph. Plagioclase phenocrysts partially or completely replaced by clay minerals (BTG-006; 460 m). **d.** Cross-polarised photomicrograph. Plagioclase replaced by clay minerals (BTG-006; 460 m). Abbreviations: Mus: muscovite; Plg: plagioclase; Py: pyrite; Qz: quartz.

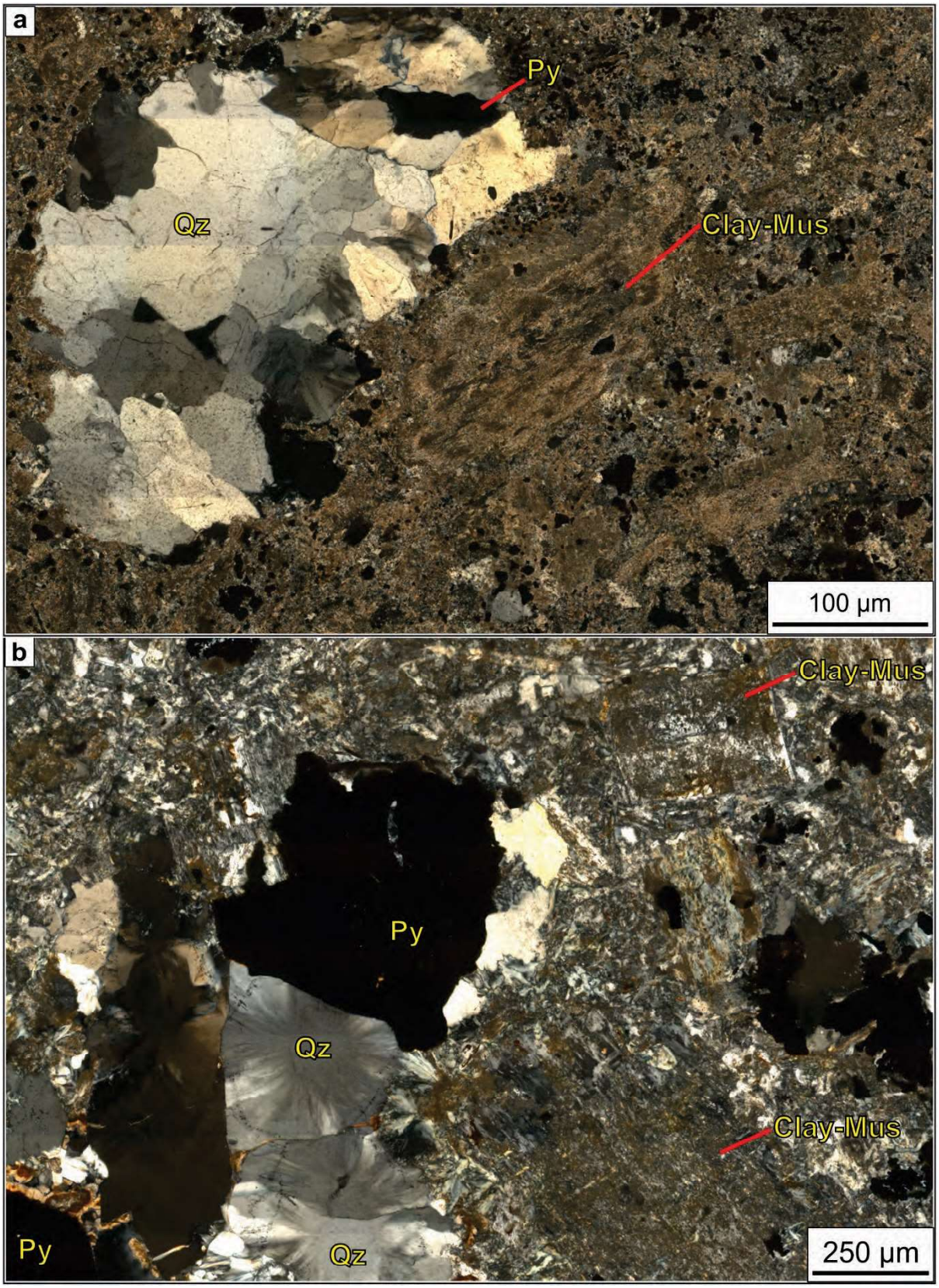

Figure 3.27. Plagioclase-phyric, miarolitic diorite porphyry (DPD III). a. Cross-polarised photomicrograph mosaic. Detail from quartz and pyrite in cavity; fine grained clay minerals and muscovite have replaced former plagioclase phenocrysts (BTG-003; 436 m). **b.** Cross-polarised photomicrograph mosaic. Quartz and pyrite filled in cavity. Quartz exhibits undulose extinction; fine grained clay minerals and muscovite have replaced plagioclase phenocrysts (BTG-006; 192.3 m). Abbreviations: Mus: muscovite; Py: pyrite; Qz: quartz.

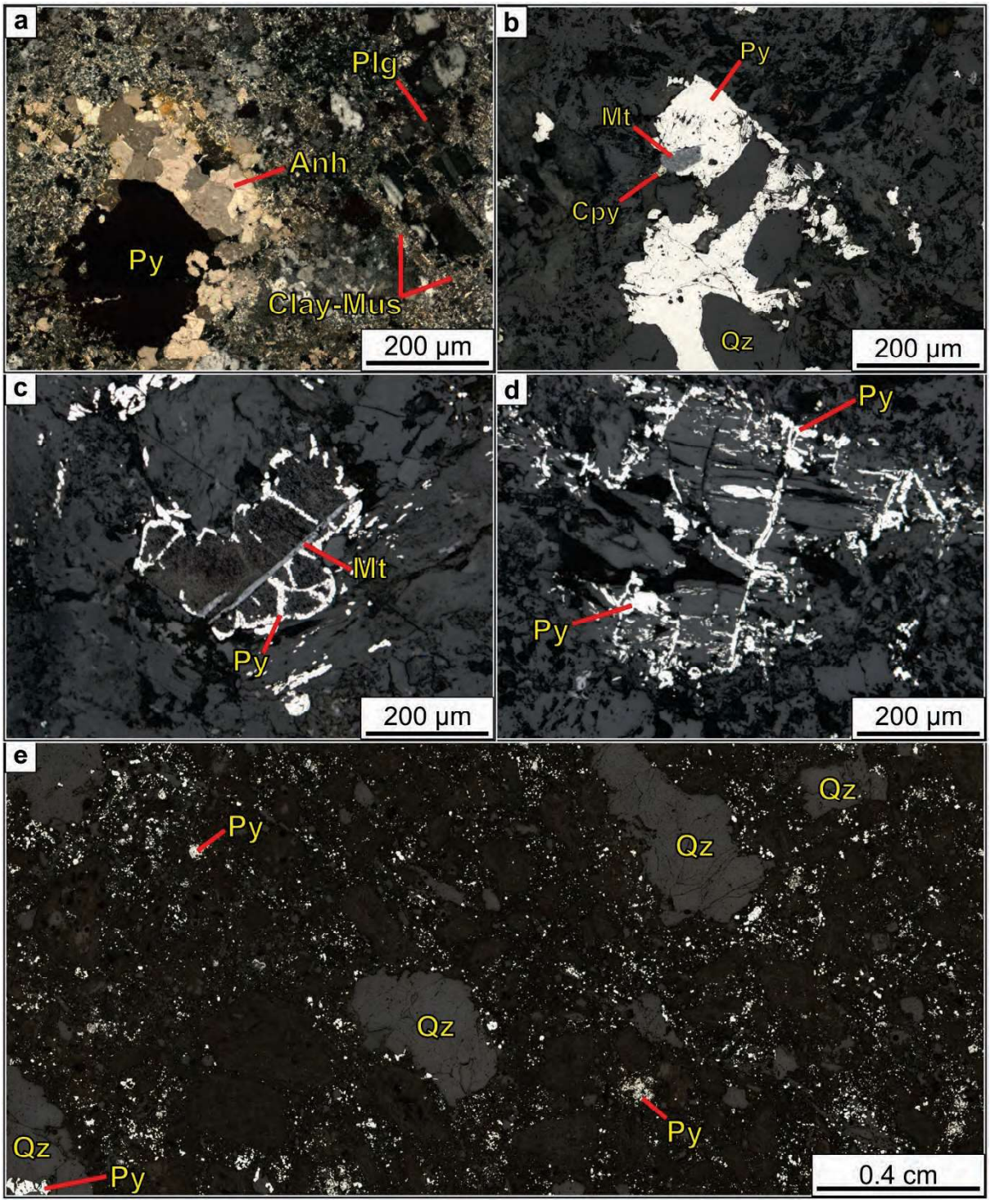

Figure 3.28. Plagioclase-phyric, miarolitic diorite porphyry (DPD III). a. Cross-polarised microphotograph. Anhydrite and pyrite filling cavity (BTG-006; 460 m). **b.** Reflected light photomicrograph. Pyrite and quartz intergrown; minor magnetite and chalcopyrite inclusions (BTG-006; 192.3 m). **c.** Reflected light photomicrograph. Pyrite and magnetite replacing plagioclase crystal border (BTG-006; 192.3 m). **d.** Reflected light photomicrograph. Pyrite replacing plagioclase through (BTG-006; 192.3 m). **e.** Reflected light photomicrograph mosaic. Pyrite is fine grained and mostly disseminated in the groundmass (BTG-003; 436 m). Abbreviations: Anh: anhydrite; Cpy: chalcopyrite; Mt: magnetite; Mus: muscovite; Plg: plagioclase; Py: pyrite; Qz: quartz.

3.4. Geology summary

The geology of the Bantug area comprises: sedimentary rocks from the Pliocene-Pleistocene Caliling Formation, overlain by volcanic rocks from the Pleistocene Canlaon Volcanic Complex (CVC), and cut by intrusive rocks from the Late Pleistocene Bantug Intrusive Complex (BIC). There are two major structural trends in the district, NE and NW; and two minor structural trends, NS and EW. Figure 3.29 presents a schematic summary of the geology in the Bantug area.

The sedimentary rocks at Bantug from the Pliocene-Pleistocene Caliling Formation at Bantug are characterised by centimetre-scale laminations and have been hydrothermally altered. Chlorite and magnetite are the most abundant hydrothermal minerals; chalcopyrite is rare.

Volcanic rocks from the Pleistocene Canlaon Volcanic Complex (CVC) at Bantug are predominantly plagioclase-phyric andesites; although aphyric andesites and andesitic volcaniclastic rocks were also identified. Most volcanic rocks at Bantug have been intensely altered to advanced-argillic assemblages and some have been silicic altered.

The Late Pleistocene Bantug Intrusive Complex (BIC) is made of four intrusions and two hydrothermal breccias. The intrusions are characterised by porphyritic textures and dioritic composition. The intrusions are intensely altered, and for the diorite porphyry (DP) and the diorite porphyry III (DPD III) the original texture has been obliterated and abundant pyrite is disseminated. Diorite porphyry I (DPD I) and diorite porphyry II (DPD II) are pyroxene-phyric, weakly altered, and contain abundant magnetite with little or no pyrite. Hornblende was not recognised in any of the intrusions. Minor phlogopite was recognised in diorite porphyry II.

Hydrothermal breccias part of the Bantug Intrusive Complex (BIC) have been subdivided based on their cement. A natroalunite-pyrite cemented, polymict, hydrothermal breccia contains intensely silicic and advanced-argillic altered clasts; and a quartz-pyrite cemented, polymict hydrothermal breccia contains intensely silicic and advanced argillic altered clasts, as well as clasts with truncated pyrite veins and patchy textured clasts. Hydrothermal breccias are described in detail in Chapter 4.

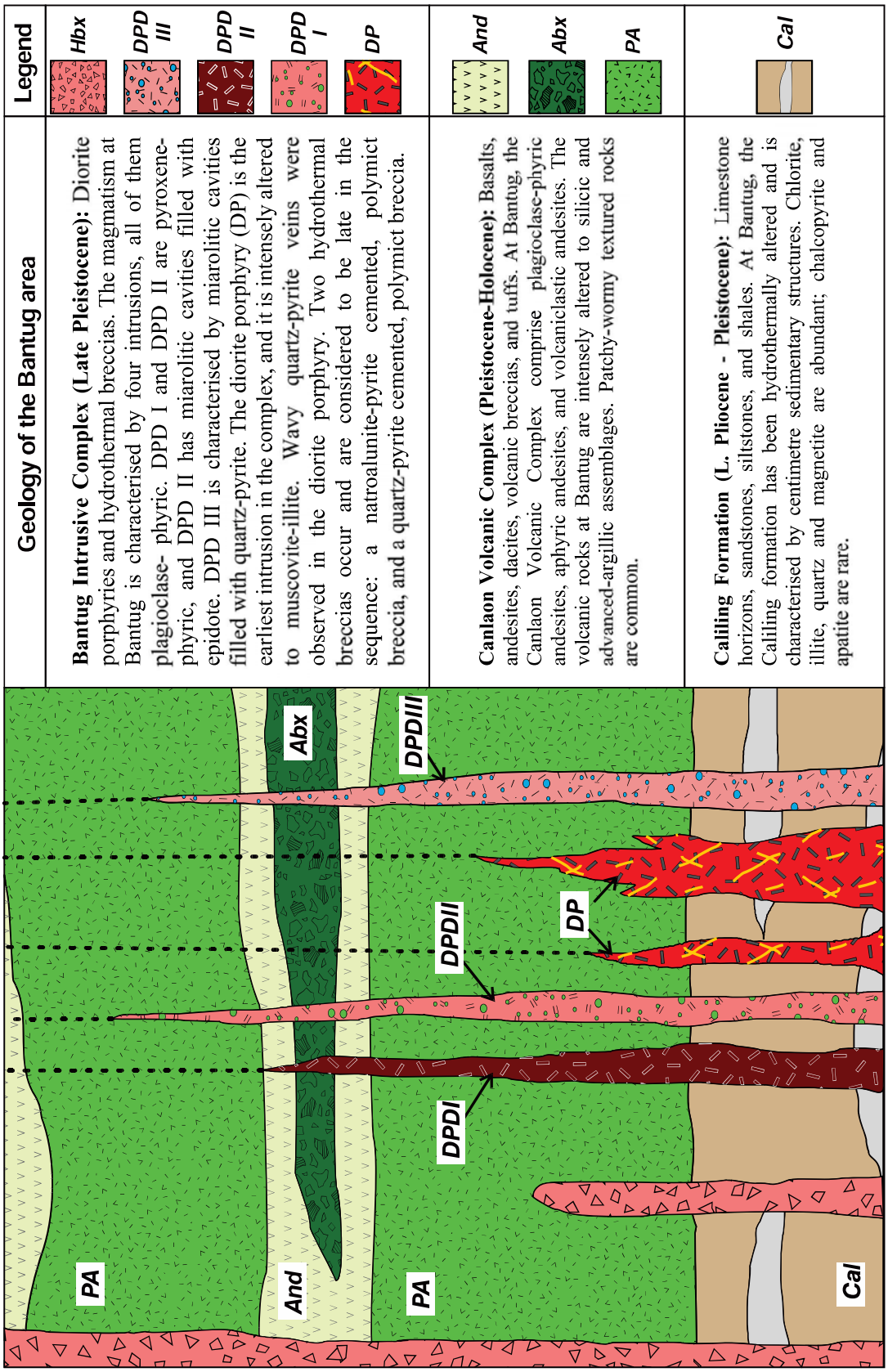

Figure 3.29. Schematic geology of the Bantug area. Diagram not to scale. The horizontal dimension represents ~2.5 km, and the vertical dimension ~850 m. Abbreviations: And: andesite; Abx: andesitic volcaniclastic breccia; Cal: Caliling Formation; DP: diorite poprhyry; DPD: diorite porphyry dike (I to III); PA: plagioclase-phyric andesite; SW: southwest; NE: northeast; BIC: Bantug Intrusive Com plex; CVC: Canlaon Volcanic Complex.

3.5. Objectives of geochronology and geochemistry studies

Drill hole and surface rock samples of key rock types at Bantug were collected in order to determine their geochemical compositions and ages. This section presents results of U-Pb zircon LA-ICP-MS dating and whole rock geochemistry of the volcanic host rocks of the Pleistocene Canlaon Volcanic Complex (CVC) and the Pleistocene Bantug Intrusive Complex (BIC).

3.5.1. Igneous geochemistry

In order to account for the effects of hydrothermal alteration on volcanic and intrusive rocks, several variables were considered. These include SiO_2 content, lost on ignition (LOI), and alteration indexes. Whole rock geochemistry results with SiO_2 contents greater than 88 wt % are interpreted to be silicic altered. Samples with LOI results greater than 10 % were considered as strongly altered. Samples identified as least-altered were considered for tectonic classification.

3.5.1.1. Alteration indices

Alteration indices are multi-component or normalised ratios of geochemical compositional data (Gifkins et al., 2005). They are usually calculated from composition data expressed as weight percentages (wt %) or parts per million (ppm). Alteration indices provide geochemical representations of hydrothermal mineral assemblages and are designed to facilitate discrimination of alteration styles, quantification of alteration intensity, and exploration vectors (Gifkins et al., 2005).

The following alteration indices were considered for discrimination of least-altered rocks from Bantug. The chlorite-carbonate-pyrite index (CCPI) of Large et al. (2001), which was developed to reflect chlorite predominance, as well as Fe-Mg carbonates and pyrite, all of which are ubiquitous in the proximal zones of VHMS deposits (Equation 3.1). The alteration index of Ishikawa et al. (1976), which was defined to quantify the intensity of chlorite and sericite alteration that occurs in the footwall volcanic rocks proximal to the Kuroko deposit (Equation 3.2). The advanced-argillic alteration index of Williams and Davidson (2004) quantifies SiO_2 enrichment and destruction of chlorite, carbonate, and feldspar (Equation 3.3).

$$CCPI = \frac{100\ (MgO + FeO)}{(MgO + FeO + Na_2O + K_2O)} \tag{3.1}$$

$$AI = \frac{100\ (K_2O + MgO)}{(K_2O + MgO + Na_2O + CaO)} \quad (3.2)$$

$$AAAI = 100\times\frac{SiO_2}{SiO_2 + (10\times MgO) + (10\times CaO) + (10\times Na_2O)} \quad (3.3.)$$

3.5.1.2. Volcanic rocks

Three volcanic rock-types were recognised at Bantug in this study, namely: aphyric andesite, plagioclase-phyric andesite, and volcaniclastic andesitic breccia. These rocks belong to the Quaternary Canlaon Volcanic Complex (CVC), and are intensely hydrothermally altered (i.e., silicic, and advanced argillic alteration).

Figure 3.30 presents the discrimination criterion for selection of least-altered volcanic rocks. High LOI results are indeed indicative of components such as H2O and S, clearly products of hydrothermal alteration. However, at Bantug some intensely hydrothermally-altered samples yielded LOI results below 5 % as well as SiO_2 results greater than 88.9 wt % (Figs. 3.30a, 3.30b, 3.30c). This clearly demonstrates that LOI exclusively should not be used to assess hydrothermal alteration effects and intensity in volcanic rocks. Figures 3.30d and 3.30e present the alteration box plots of Large et al. (2001) and Williams and Davidson (2004) respectively. The alteration box plots make use of the alteration indices in order to screen least altered samples. Figure 3.30e reveals that the majority of volcanic rocks have undergone advanced-argillic alteration.

From the alteration box plots, four samples from the CVC are classified as least altered (Fig. 3.30e). These samples plot in the andesite fields of trace element diagrams for classification of volcanic rocks (Figs. 3.31a and 3.31b; Winchester and Floyd, 1977; Pearce, 1996). Least altered samples plot in the calc-alkaline and transitional fields of the tectonic classification diagram of mafic igneous rocks (Fig. 3.31c; Cabanis and Lecolle, 1989). Least altered samples also plot in the calc-alkaline andesite field of the Th-Co discrimination diagram for volcanic rocks (Fig. 3.31d; Hastie et al., 2007). On the Th/Yb versus Nb/Yb discrimination diagram for basalts, least altered samples plot in the continental arc field (Fig. 3.31e; Pearce, 2008).

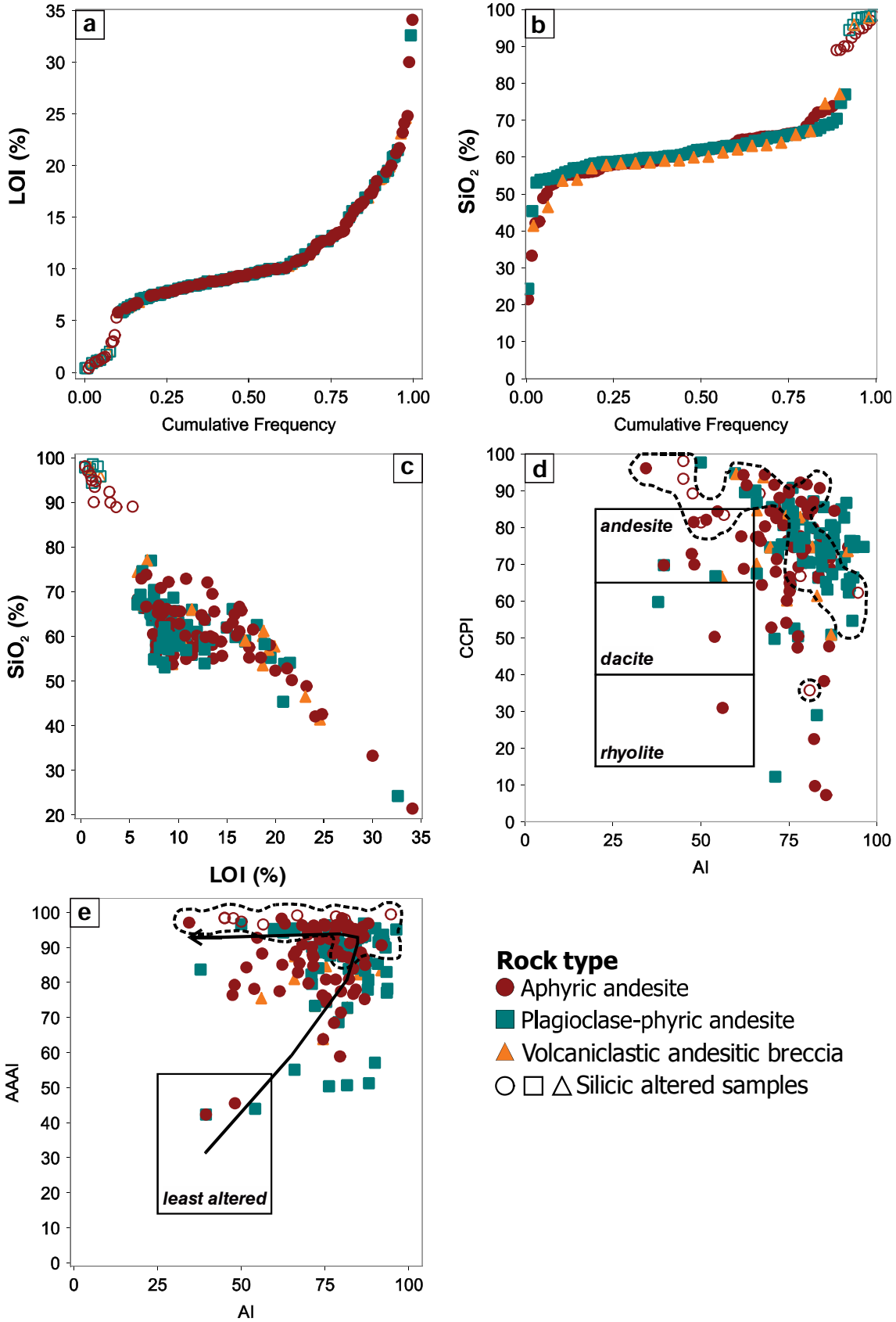

Figure 3.30. Filtering criterion for least-altered volcanic rocks at Bantug. a. Probability plot for lost on ignition (LOI; %). **b.** Probability plot for SiO_2 (wt %). **c.** Bivariate diagram for LOI (%) and SiO_2 (wt %). **d.** Alteration box plot: CCPI and AI (Large et al., 2001). **e.** Alteration box plot: AI and AAAI (Williams and Davidson, 2004). Diagrams contain surface and drill hole data. Dashed line contains silicic-altered samples.

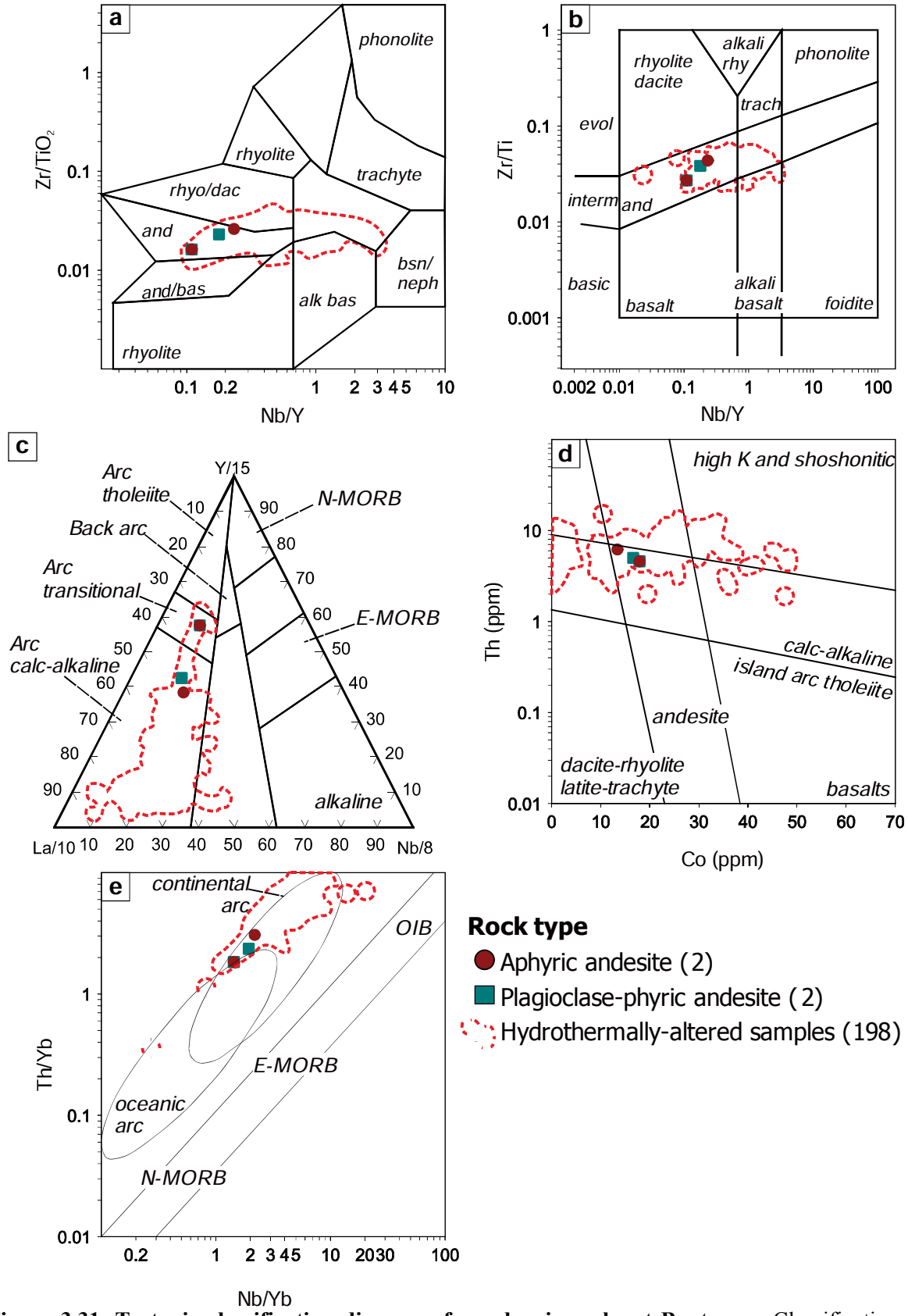

Figure 3.31. Tectonic classification diagrams for volcanic rocks at Bantug. a. Classification of volcanic rocks (Winchester and Floyd, 1977). **b.** Classification of volcanic rocks (Pearce, 1996). **c.** Tectonic classification of mafic igneous rocks (Cabanis and Lecolle, 1989). **d.** Th-Co discrimination diagram for volcanic rocks (Hastie et al., 2007). **e.** Th/Yb versus Nb/Yb discrimination diagram for basalts (Pearce, 2008). Red dashed line contains 198 hydrothermally altered samples.

3.5.1.3. Intrusive rocks

Four intrusive events were recognised at Bantug during this study, namely: diorite porphyry (DP), plagioclase-pyroxene-phyric, miarolitic diorite porphyry (DPD I), plagioclase-pyroxene-phyric, crystal crowded diorite porphyry (DPD II); and plagioclase-phyric, miarolitic diorite porphyry (DPD III). These are described in section 3.3.5.

Intrusive rocks at Bantug yielded lost on ignition values between 5 and 11.6 %, with a mean value of 8.4 % (Fig. 3.32a). Lost on ignition is not considered as an indicator for hydrothermal alteration. Most intrusive rock samples yielded SiO_2 results between 54.5 and 64.5 wt %, and three samples yielded results between 78.9 and 80.9 wt %. The latter are considered silicic altered (Figs. 3.32b and 3.32c).

Figures 3.32d and 3.32e present the alteration box plots of Large et al. (2011) and Williams and Davidson (2004) for intrusive rocks; respectively. From these figures it can be inferred that 12 samples are least-altered, and that 21 samples from the diorite porphyry are hydrothermally altered. Least altered diorite porphyry dike I, II, and III samples plot in the dioritic gabbro and diorite fields of the TAS diagrams for plutonic rocks (Figs. 3.33a and 3.33b; Cox et al., 1979; Middlemost, 1994; respectively). Least altered intrusive rock samples also plot in the diorite fields of the trace element classification diagrams for volcanic rocks adapted for intrusive rocks (Figs. 3.33c and 3.33d; Winchester and Floyd, 1977). Figure 3.33e presents the tectonic setting discrimination diagram for granites of Harris et al. (1986), in which diorite porphyry dike I, II, and III samples plot in the volcanic arc field.

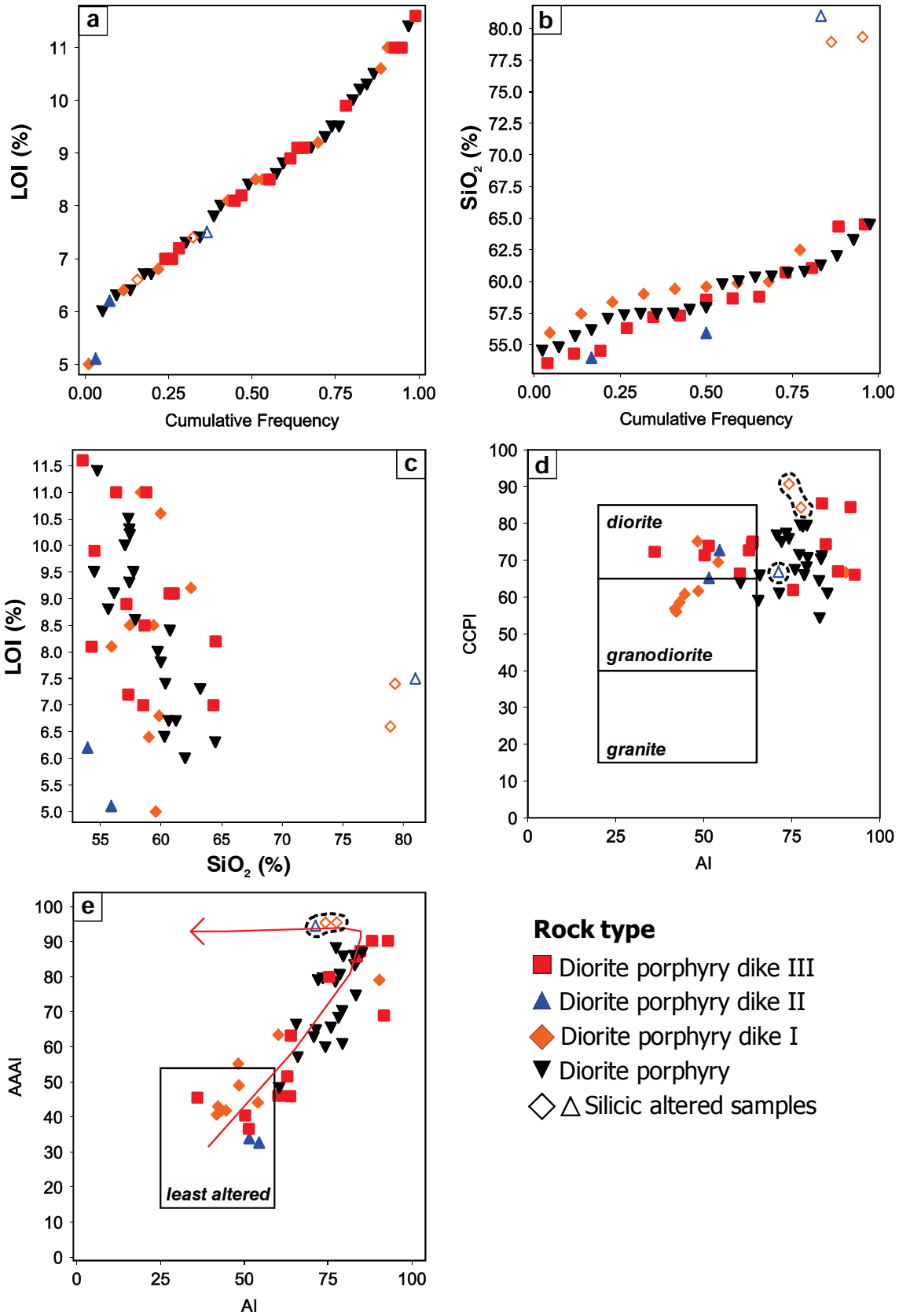

Figure 3.32. Filtering criterion for least-altered intrusive rocks at Bantug. a. Probability plot for lost on ignition (LOI; %). **b.** Probability plot for SiO_2 (wt %). **c.** Bivariate diagram for LOI (%) and SiO_2 (wt %). **d.** Alteration box plot: CCPI and AI (Large et al., 2001). **e.** Alteration box plot: AI and AAAI (Williams and Davidson, 2004). Dashed line contains silicic-altered samples.

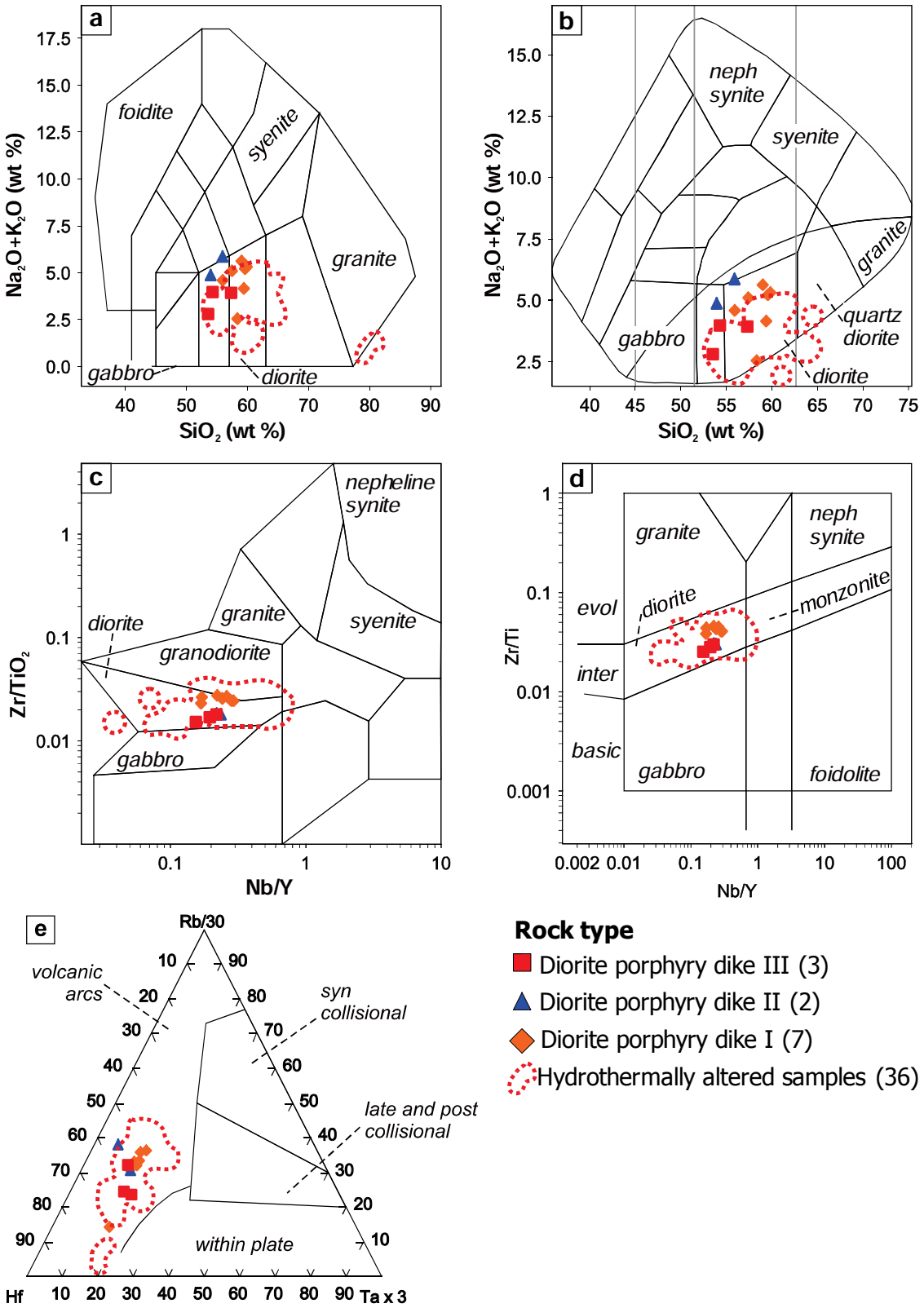

Figure 3.33. Tectonic classification diagrams for intrusive rocks at Bantug. a. Total alkalis versus silica (Na_2O+K_2O vs SiO_2) igneous rocks classification diagram from Middlemost (1994). **b.** Total alkalis versus silica (Na_2O+K_2O vs SiO_2) igneous rocks classification diagram from by Cox et al. (1979). **c.** Volcanic rock classification diagram adapted to intrusive rocks (Winchester and Floyd, 1977). **d.** Volcanic rock classification diagram adapted to intrusive rocks (after Winchester and Floyd, 1977). **e.** Discrimination diagram for granites (Harris et al., 1986). Red dashed line contains hydrothermally altered rocks.

3.5.2. Geochronology

3.5.2.1. U-Pb dating of zircon

Ten rock samples, including two samples from volcanic rocks and 8 from intrusive rocks from Bantug were dated using LA-ICP-MS at CODES, University of Tasmania. Samples from the CVC and the BIC were selected for dating in order to constrain the timing of volcanism, magmatism, and hydrothermal activity. Figure 3.34 presents the locations of samples analysed, and Table 3.2 presents results and details of the samples. Results of individual LA-ICP-MS analyses are presented in Appendix H. Samples from the volcanic host rocks (i.e., plagioclase-phyric andesite) returned the oldest ages obtained in this study, including ages of 1.82 ± 0.11 Ma and 1.71 ± 0.16 Ma. These ages are the first U-Pb zircon crystallisation ages to be reported for the Pleistocene CVC. Two samples from the diorite porphyry (DP), which is thought to mark the beginning of the magmatism at Bantug, returned crystallisation ages of 1.37 ± 0.1 Ma and 1.35 ± 0.3 Ma. One sample from the pyroxene-plagioclase phyric, miarolitic diorite porphyry (DPD I), returned a calculated zircon crystallisation age of 1.46 ± 0.15 Ma. This rock type is interpreted to be younger than DP because of observed crosscutting relations, and differences in mineralogy and hydrothermal alteration style and intensity. Two samples from the plagioclase-pyroxene phyric, crystal crowded diorite porphyry (DPD II), yielded crystallisation ages of 1.25 ± 0.31 Ma and 1.19 ± 0.63 Ma. Although these ages are within error of the DP and DPD I, DPD II is interpreted to be younger than these and the host volcanic rocks based on observed crosscutting relations, differences in mineralogy, and hydrothermal alteration style and intensity. The calculated errors for DPD II are the largest within the suite of analysed samples, this is due to the presence of high common Pb in analysed zircons from these samples (Fig. 3.35)

Table 3.2. Summary of LA-ICP-MS U-Pb dating of zircons

Drill hole	Depth (m)	Age (Ma)	n	Rock Type	Easting (m)[1]	Northing (m)[1]	Elevation (m)
BTG-005	399	1.71 ± 0.16	10	PA	501,926.4	1,105,881.0	736.3
BTG-005	493	1.82 ± 0.11	15	PA	501,875.5	1,105,881.0	657.8
BTG-006	600	1.37 ± 0.10	9	DP	504,847.9	1,107,714.0	514.3
BTG-006	663	1.35 ± 0.30	6	DP	504,815.2	1,107,714.0	463.9
BTG-006	172	1.24 ± 0.05	13	DPD III	505,080.8	1,107,714.0	872.9
BTG-006	376	1.06 ± 0.29	2	DPD III	504,973.5	1,107,714.0	707.7
BTG-003	370	1.25 ± 0.31	14	DPD I	504,290.4	1,106,935.7	875.0
BTG-003	325	1.19 ± 0.63	10	DPD I	504,317.6	1,106,935.7	917.0
BTG-003	265	1.46 ± 0.15	13	DPD II	504,345.9	1,106,935.7	960.5
Surface	0	1.23 ± 0.39	4	DPD III	504,804.0	1,107,788.0	1,065.0

[1]Coordinate system: WGS 1984, UTM zone 51 N. Abbreviations: PA: Plagioclase-phyric andesite; DP: diorite porphyry; DPD I: diorite porphyry I; DPD II: diorite porphyry II; DPD III: diorite porphyry III; n: number of zircons analysed.

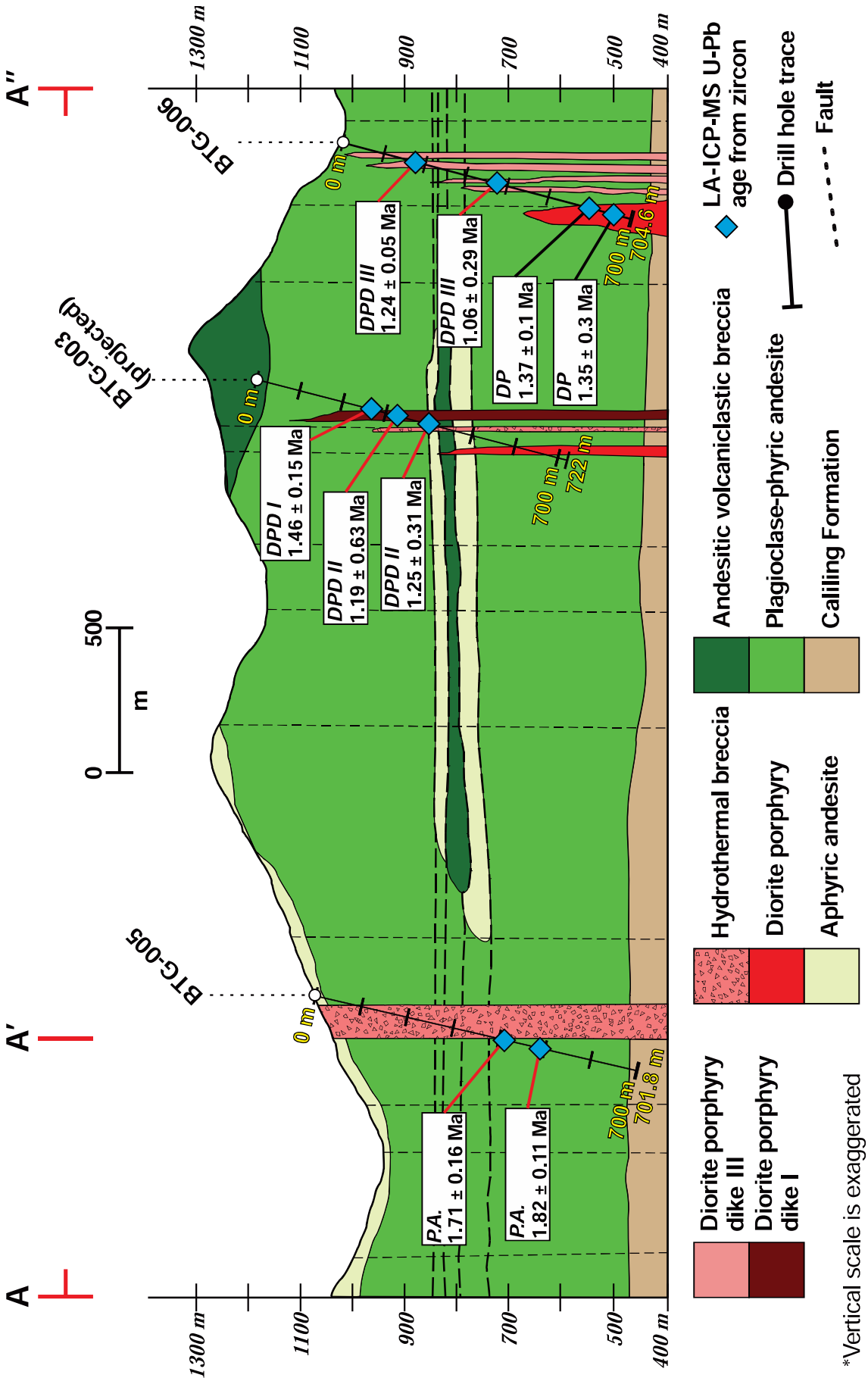

Figure 3.34. Geochronology sample location.

Three plagioclase-phyric, miarolitic diorite porphyry (DPD III) samples returned calculated ages between 1.24 ± 0.05 Ma and 1.06 ± 0.29 Ma. Although two of the ages obtained from this rock type are similar to those obtained from samples of DPD II (Fig. 3.35), the rock types are considered to be different based on textural and mineralogical characteristics. The youngest age from this unit (i.e., 1.06 ± 0.29 Ma) was obtained from each two zircons, and so this age must be treated with caution (Fig. 3.35). The age obtained from an outcropping sample of DPD III (i.e., 1.23 ± 0.39 Ma) was calculated from four zircon analyses. This age is similar to that obtained from a drill-core sample of DPD III in BTG-006 (i.e., 1.24 ± 0.05 Ma), calculated from 13 zircon analyses (Table 3.2; Fig. 3.35). The latter age is considered to be representative for the crystallisation age of DPD III.

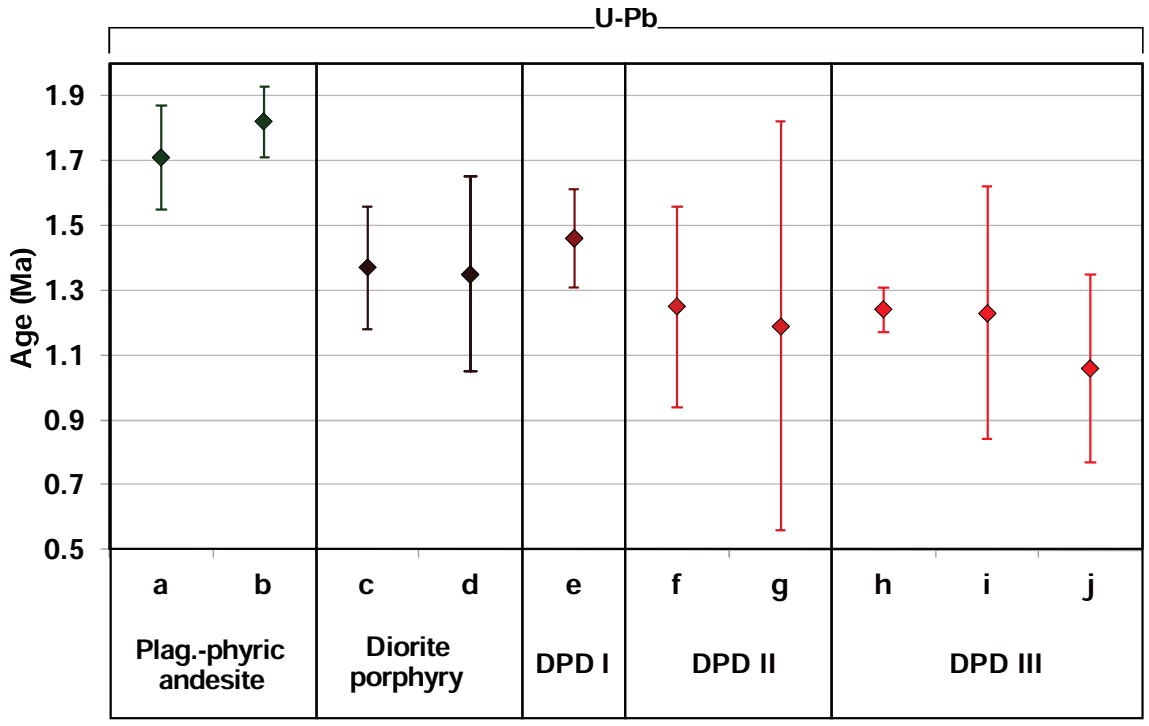

Figure 3.35. Geochronology summary. a. Sample at 399 m depth in BTG-005. **b.** Sample at 493 m depth in BTG-005. **c.** Sample at 600 m depth in BTG-006. **d.** Sample at 663 m depth in BTG-006. **e.** Sample at 265 m depth in BTG-003. **f.** Sample at 370 m depth in BTG-003. **g.** Sample at 325 m depth in BTG-003. **h.** Sample at 172 m depth BTG-006. **i.** Sample on surface (X: 504,804; Y: 1,107,788; WGS84-51N). **j.** Sample at 376 m depth in BTG-006.

3.5.3. Discussion

3.5.3.1. Volcano-sedimentary facies architecture at Bantug

Volcanism and magmatism are ubiquitous at Negros Island, and well defined volcanic edifices makeup the most prominent topographic features in the island. Currently, active volcanism takes place in the north and south portions of Negros (i.e., Mt. Canlaon and Cuernos de Negros volcanoes, respectively. Fig. 3.2a). Circular topographic features in the east-central part of Negros (i.e., the Ayungon and the Bantug areas; Figs. 3.2a and 3.2b), suggest the presence of ancient, eroded volcanic edifices (Fig. 3.2).

The geology of the Bantug area consist of the Pliocene-Pleistocene Caliling Formation, the Pleistocene-Holocene Canlaon Volcanic Complex (i.e., CVC), and the Pleistocene Bantug Intrusive Complex (i.e., BIC; Fig. 3.8). MGB (2004) divided the Caliling Formation into a lower limestone member and an upper clastic member. The latter, is comprised of coarse sandstones with coral fragments and molluscs; it represents the back-reef zone of a continental reef (MGB, 2004). Rock types in the Caliling Formation are indicative of an early marine depositional environment, to a later back-reef and/or continental reef environment. The CVC is composed of basalts, andesites, dacite flows, volcanic breccias, and tuffs (von Biedersee and Pichler, 1995; Sajona et al., 2000; Solidum et al., 2002; MGB, 2004; Rae, 2002; Rae et al., 2003, 2004, 2011). Pillow or marine-depositional textures for the CVC have not been reported previously, and were not observed by the author while core logging at Bantug. Hence, volcanic rocks from the CVC at Bantug are very likely to have deposited above sea level. The most abundant volcanic rock observed in drill core at Bantug was the plagioclase-phyric andesite (Figs. 3.4 to 3.8). Volcanic rocks indicative of fragmentation processes were intercepted by drill hole BTG-003 by <50 m (i.e., andesitic volcaniclastic breccia; Fig. 3.4). Based on drill core logging, the drill holes logged during this study are unlikely to have been placed at the centre of the volcanic system at Bantug.

District-scale volcanic stratigraphy studies at Bantug will contribute to the broader understanding of the geology of the district. The author recommends to carry out these studies as they will aid and profoundly impact the future exploration efforts in the area.

3.5.3.2. Adakitic volcanism and magmatism in Negros

"Adakites" is the term used by Defant and Drummond (1990) to refer to magnesian-rich andesites found near Adak Island in the Aleutians previously studied by Kay (1978). Adakites are characterised by high La/Yb ratios (i.e., high ratios of LREE/HREE), high strontium concentrations (i.e., ~1,800 ppm), relatively high Mg, Cr, and Ni concentrations compared with normal andesites, and nonradiogenic Pb and Sr isotope composition (Kay, 1978; Defant and Drummond, 1990; Richards and Kerrich, 2007). Kay (1978) suggested that adakites formed as partial melts of subducted, garnetiferous (i.e., eclogitized) oceanic crust, which had then reacted and partially equilibrated with the peridotitic asthenospheric mantle wedge during ascent (Richards and Kerrich, 2007).

Kay (1978) noted that the Mg-rich andesites from Adak Island were geochemically unusual, and that this petrogenetic model could not be generally applied to island-arc magmatism. Instead, normal tholeiitic to calc-alkaline arc magmas are thought to be derived from partial melting of hydrated peridotite in the asthenospheric mantle wedge above a dehydrating subducting slab (e.g., Ringwood, 1977; Gill, 1981; Plank and Langmuir, 1988; Hawkesworth et al., 1993; Pearce and Peate, 1995; Schmidt and Poli, 1998; Poli and Schmidt, 2002; Gaetani and Grove, 2003; Richards and Kerrich, 2007).

Richards and Kerrich (2007), based on Defant and Drummond (1990) and Defant and Drummond (1993) proposed the geochemical criteria in Table 3.3 for distinguishing adakitic magmas from normal island-arc basalt-andesite-dacite-rhyolite suites.

Table 3.3. Geochemical criteria for recognition of adakitic magmas

Criteria	Geochemical range[1,2]
SiO_2	≥56 wt %
Al_2O_3	≥15 wt %
MgO	<3 wt %
Mg no.[3]	~0.5
Na_2O	≥3.5 wt %
K_2O	≤3 wt %
K_2O/Na_2O	~0.42
Rb	≤65 ppm
Sr	≥400 ppm
Y	≤18 ppm
Yb	≤1.9 ppm
Ni	≥20 ppm
Cr	≥30 ppm
Sr/Y	≥20
La/Yb	≥20
$^{87}Sr/^{86}Sr$	≤0.7045
Age of subducted oceanic crust	≤25 m.y.

[1]Defabt and Drummond (1990)
[2]Richards and Kerrich (2007)
[3]Mg no. = Mg/(Mg + Fe), where Mg and Fe are atomic proportions; m.y.: millions of years.

Defant and Drummond (1990, 1993) used a plot of Sr/Y versus Y to highlight the mutually exclusive roles of garnet fractionation in adakites (i.e., high Sr/Y, low Y magmas) versus plagioclase fractionation in normal tholeiitic to calc-alkaline rocks (i.e., low Sr/Y, normal to high Y magmas). Drummond and Defant (1990) also used a plot of La/Yb versus Yb to emphasize the strong HREE depletion relative to LREE in adakitic lavas compared to normal arc rocks. These two diagrams are widely used for the identification of adakites and, by extension, for an origin via slab melting. However, Richards and Kerrich (2007) argued that these criteria are nonunique and are therefore not diagnostic of slab melting. They stated that adakites include a range of magma compositions that broadly overlaps with other more common rock types. And since the term adakite has petrogenetic significance, it must be treated carefully. They suggested to refer to rocks that fall in the compositional range presented in Table 3.3 as adakite-like. Richards and Kerrich (2007), and references therein, showed how melting-assimilation-storage-homogenization (i.e., MASH; Hildreth and Moorbath, 1988) and/or assimilation-fractional crystallization (AFC; DePaolo, 1981) processes that control the crustal evolution of normal tholeiitic to calc-alkaline arc magmas can result in similarities to some of the geochemical characteristics of adakites, such as high Sr/Y and La/Yb ratios.

Adakites were suggested to be related to porphyry and epithermal deposits for the first time by Thiéblemont et al. (1997) and Sajona and Maury (1998) in the Philippines. Oyarzun et al. (2001) suggested that adakites were uniquely responsible for the formation of giant porphyry deposits in northern Chile. Since then, increasing adakite occurrences have been claimed in a number of porphyry districts around the world (Richards and Kerrich, 2007). Many of the claims meet some of the criteria presented in Table 3.3; however, most of the criteria are ignored (Richards and Kerrich, 2007).

Baldwin and Pearce (1982) and López (1982) independently noted that intrusions associated with porphyry deposits in northern Chile had negative Y, Mn, Th, and HREE anomalies compared with barren plutons. They suggested that these characteristics might be due to partial melting processes or fractional crystallization of hornblende, titanite, and/or garnet from hydrous magmas. Depletion of HREE have also been noted in porphyry deposit-related intrusions from Arizona, northern Chile, and northern Argentina (Richards and Kerrich, 2007; and references therein). Richards and Kerrich (2007) attributed HREE depletion to amphibole and/or deep-crustal garnet fractionation.

Sajona and Maury (1998), Sajona et al. (2000a), and Sajona et al. (2000b) have reported the occurrence of adakites in the Philippines, some occurrences are associated with porphyry deposit-districts (i.e., eastern Luzon arc, central Mindanao, and Negros). Sajona et al. (2000b) focused on the geochemistry of volcanic rocks from Negros and Batan islands. They argued that volcanic rocks from Cuernos de Negros volcano are adakites, and derived from a garnet amphibolitic source with N-MORB geochemistry.

Solidum (2002) and Solidum et al. (2003) studied the geochemistry of volcanic rocks from several volcanic centres in Negros island. They found that silicic lavas from Cuernos de Negros volcano have high Sr and moderate Sr/Y ratios, similar to those of adakites. They also found that these volcanic rocks have low La/Yb ratios and did not meet other adakite classification criteria. Solidum et al. (2003) modelling results also indicated that partial melting of the subducting Southeast Sulu Sea crust cannot reproduce the adakite-like characteristics or account for other incompatible trace element ratios in Cuernos de Negros volcanic rocks. Solidum et al. (2003) concluded that fractionation of amphibole (± apatite) together with variable fractionation and accumulation of plagioclase are likely to have produced the adakite-like geochemical signature.

Figure 3.35 compares the geochemistry of least-altered volcanic rocks from volcanic centres in Negros and the Bantug area in discrimination diagrams for adakites and adakite-like rocks (von Biedersee and Pichler, 1995; Sajona et al., 2000; Solidum et al., 2003; Rae et al., 2004; This study). Table 3.4 compares results from volcanic rocks from Negros with the criteria for adakite classification proposed by Defant and Drummond (1990) and Richards and Kerrich (2007). Least-altered volcanic rocks reported by Sajona et al. (2000), Solidum et al. (2003), and this study plot in the "normal andesite" of the La/Yb versus Yb diagram (Fig. 3.36a). These samples plot out of the "adakite-like" field of the La/Yb versus SiO_2 diagram (Fig. 3.36d). Ytterbium was not reported for most samples from the dataset (Table 3.4), and La/Yb ratios from the dataset are ≤9.2. Although all samples in the dataset meet the SiO_2, Al_2O_3, K_2O, Rb, and Sr criteria for adakite classification, most samples do not meet the K_2O/Na_2O, Y, Yb, Ni, Cr, and La/Yb criteria (Table 3.4). Samples from Bantug plot in the medium calc-alkaline "normal andesite" fields of classification diagrams (Figs. 3.36a to 3.36d), cannot be classified as adakites, do not display adakite-like geochemical signature, and are very likely to have formed through MASH or AFC processes. Findings in this study support the hypothesis proposed by Solidum et al. (2003) for an AFC process to the formation of adakite-like rocks at Cuernos de Negros.

Table 3.4. Comparison of least-altered volcanic rocks from Negros with key adakitic geochemical features

	von Bidersee and Pitchler (1996)				Sajona et al. (2000)		Solidum et al. (2003)			Rae et al. (2004)	This study
Adakite criteria[1]	**C.N. (n=10)**	**M.C. (n=24)**	**M.M. (n=3)**	**M.S. (n=3)**	**M.C. (n=11)**	**M.S. (n=6)**	**C.N. (n=9)**	**M.C. (n=7)**	**M.S. (n=3)**	**C.N. (n=8)**	**M.C. (n=3)**
SiO_2 ≥56 wt %	59.35	56.95	61.13	57.13	57.54	57.23	57.58	58.24	58.38	55.14	57.02
Al_2O_3 ≥15 wt %	17.38	17.23	16.90	18.00	17.48	18.50	17.87	17.60	17.27	17.73	18.08
MgO <3 wt %	2.400	3.217	2.733	3.033	3.292	2.872	2.902	3.236	2.983	4.939	2.577
Na_2O ≥3.5 wt %	3.760	3.350	3.667	3.467	3.561	3.780	3.718	3.459	3.477	3.135	2.650
K_2O ≤3 wt %	2.060	2.421	1.967	1.967	1.967	1.547	1.899	2.490	1.767	1.226	1.440
K_2O/Na_2O ~0.42	0.546	0.723	0.535	0.568	0.553	0.409	0.510	0.727	0.510	0.372	0.541
Rb ≤65 ppm	42.30	63.71	52.67	50.00	52.05	33.25	37.78	67.00	44.33	22.34	33.13
Sr ≥400 ppm	672.8	649.0	529.7	631.3	627.7	589.8	597.6	533.3	475.3	693.4	309.9
Y ≤18 ppm	17.20	26.25	21.67	23.33		20.10	19.22	24.43	24.67	17.81	29.60
Yb ≤1.9 ppm						1.988	1.450	1.929	2.250		2.380
Ni ≥20 ppm	9.250	6.136	5.500	5.333			8.556	23.714	8.667	32.53	
Cr ≥30 ppm	13.70	19.73	15.33	3.500			15.56	69.00	11.67	105.9	3.933
Sr/Y ≥20	39.54	26.47	26.24	27.69		29.51	31.43	21.97	20.66	43.16	10.41
La/Yb ≥20						9.223	8.904	7.920	5.378		5.560

n: number of analyses; values represent mean values for groups of samples
C.N.: Cuernos de Negros; M.C.: Mt. Canlaon; M.M.: Mt Mandalagan; M.S.: Mt. Silay
[1]Values from Richards and Kerrich (2007)

Table 3.5. Comparison of least-altered intrusive rocks from Negros with key adakitic geochemical features

	Rae et al. (2004)	Rae et al. (2004)	This study
Adakite criteria	**N.P. (n=17)**	**P.D. (n=9)**	**BIC (n=11)**
SiO_2 ≥56 wt %	60.10	56.90	67.06
Al_2O_3 ≥15 wt %	17.86	18.51	12.39
MgO <3 wt %	2.594	3.630	2.295
Na_2O ≥3.5 wt %	3.956	4.704	2.247
K_2O ≤3 wt %	2.167	2.020	1.784
K_2O/Na_2O ~0.42	0.543	0.446	2.419
Rb ≤65 ppm	38.55	34.94	40.29
Sr ≥400 ppm	677.5	981.2	238.0
Y ≤18 ppm	14.09	16.24	15.91
Yb ≤1.9 ppm			1.791
Ni ≥20 ppm	5.347	11.07	13.50
Cr ≥30 ppm	9.459	22.19	5.713
Sr/Y ≥20	48.01	60.18	12.94
La/Yb ≥20			5.719

n: number of analyses; values represent mean values for groups of samples
N.P.: Nasuji Pluton, P.D.: Puhagan Dikes; BIC: Bantug Igneous Complex
[1]Values from Richards and Kerrich (2007)

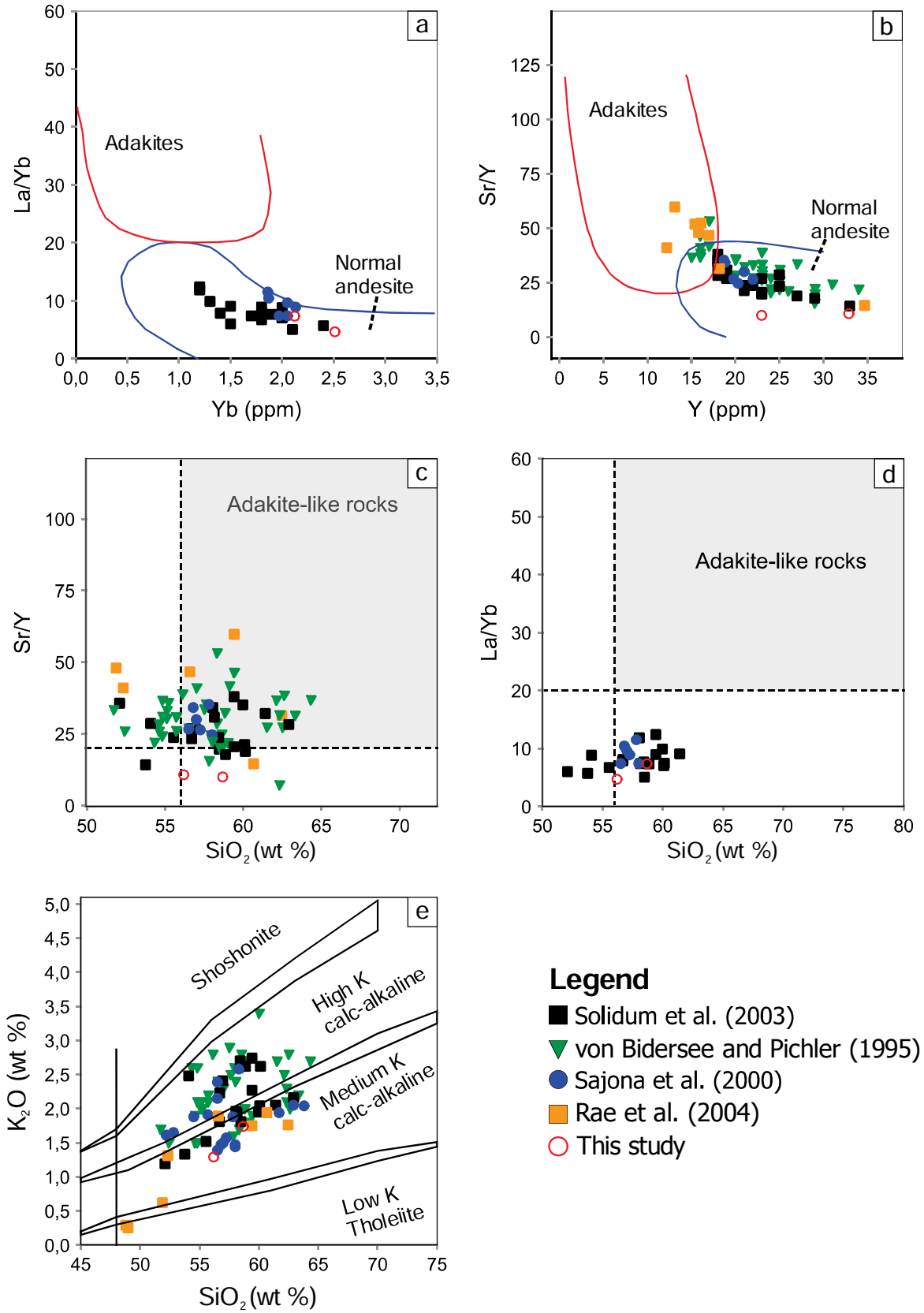

Figure 3.36. Geochemical comparison of volcanic rocks in Negros. a. La/Yb vs Yb diagram for discrimination of adakites (Defant and Drummond, 1990; Castillo et al., 1999). **b.** Sr/Y vs Y diagram for discrimination of adakites (Defant and Drummond, 1990; Castillo et al., 1999). **c.** Sr/Y vs SiO_2 diagram for discrimination of adakite-like rocks (Richards and Kerrich, 2007). **d.** La/Yb vs SiO_2 diagram for discrimination of adakite-like rocks (Richards and Kerrich, 2007). **e.** K_2O vs SiO_2 classification diagram for subalkalic rocks (Rollinson, 1993).

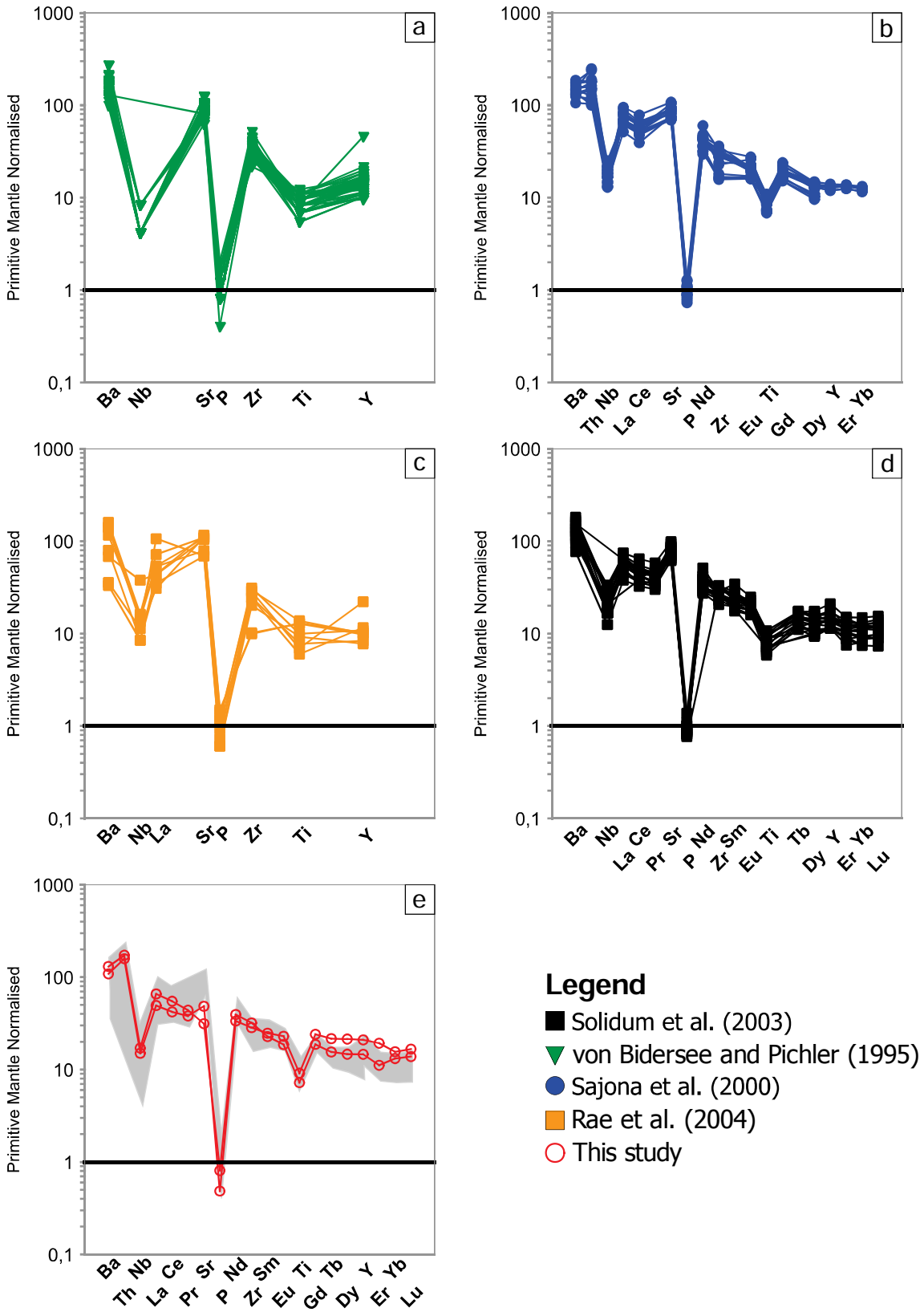

Figure 3.37. Primitive mantle-normalized trace element and rare earth element (REE) diagrams for least-altered volcanic rocks in Negros. a. Diagram for volcanic rocks from Mt. Canlaon, Mt. Mandalagan, Mt. Silay, and Cuernos de Negros volcanoes (von Bidersee and Pichler, 1995). **b.** Diagram for volcanic rocks from Mt. Silay, and Mt. Canlaon volcanoes (Sajona et al., 2000). **c.** Diagram for volcanic rocks from Cuernos de Negros volcano (Rae et al., 2004). **d.** Diagram for volcanic rocks from Mt. Silay, Mt. Canlaon, and Cuernos de Negros volcanoes (Solidum et al., 2003). **e.** Diagram for volcanic rocks from Bantug. Grey shaded area contains results from other studies in Negros.

Figure 3.37 present primitive mantle-normalized trace and rare earth element diagrams for least-altered volcanic rocks from Negros. Not all trace and REE were reported on the datasets from Negros (i.e., Figs. 3.37a to 3.37c); however, enough information was reported by Solidum et al. (2003) and this study. Least-altered volcanic rocks from Negros display significant negative P anomalies, relatively flat LREE and HREE patterns, and negative Gd anomalies (Fig. 3.37). Samples from Bantug present very similar patterns compared to other samples from Negros (Fig.3.37e).

Figure 3.38 compares the geochemistry of least-altered intrusive rocks from the Palinpinon geothermal field (i.e., Cuernos de Negros; Rae et al., 2004) with that of the Bantug Intrusive Complex (i.e., This study) in diagrams for discrimination of adakite and adakite-like rocks. Table 3.5 compares results from the intrusive rocks with the criteria for adakite classification proposed by Defant and Drummond (1990) and Richards and Kerrich (2007). Intrusive rocks from Palinpinon and Bantug fulfil the adakite classification criteria for SiO_2, K_2O, and Y (Table 3.5). Samples from Palinpinon fulfil the criteria for Al_2O_3, Na_2O, and Sr; samples from Bantug do not meet these criteria (Table 3.5). Ytterbium data from intrusive rocks at Palinpinon is not available; hence, assessment of the Yb and La/Yb criteria is not possible (Table 3.5). Least-altered intrusive rocks from Bantug did not meet the La/Yb≥20 criterion. Least-altered intrusive rocks from Palinpinon and Bantug did not meet the Ni≥20 ppm and Cr≥30 ppm criteria for adakite classification (Table 3.5). Least-altered samples from the Nasuji Pluton and the Puhagan Dikes from Palinpinon plot in the adakite and adakite-like fields of diagrams that involve Sr/Y (Fig. 3.38b and 3.38c). Least-altered intrusive rocks from Bantug plot in the "normal andesite" field of adakite and adakite-like classification diagrams (Figs. 3.38a to 3.38d). Most intrusive rocks from Palinpinon plot in the medium-K calc-alkaline field of the K_2O versus SiO_2 diagram for subalkalic rocks (Fig. 3.38e). Some samples from Palinpinon plot in the high-K calc-alkaline and shoshonite fields (Fig. 3.38e). Most samples from the BIC plot in the high-K calc-alkaline field (Fig. 3.38e). Figure 3.39 presents a primitive mantle-normalised trace element and rare earth element diagram for last altered intrusive rocks in Negros. Intrusive rocks from Palinpinon have high Sr contents but do not meet other classification criteria for adakites (Fig. 3.39). Samples from the BIC do not meet several of the classification criteria for adakites, and are significantly depleted in Sr compared to samples from Palinpinon (Fig. 3.39). Strontium contents in intrusive rocks from Palinpinon suggest MASH or AFC formation processes.

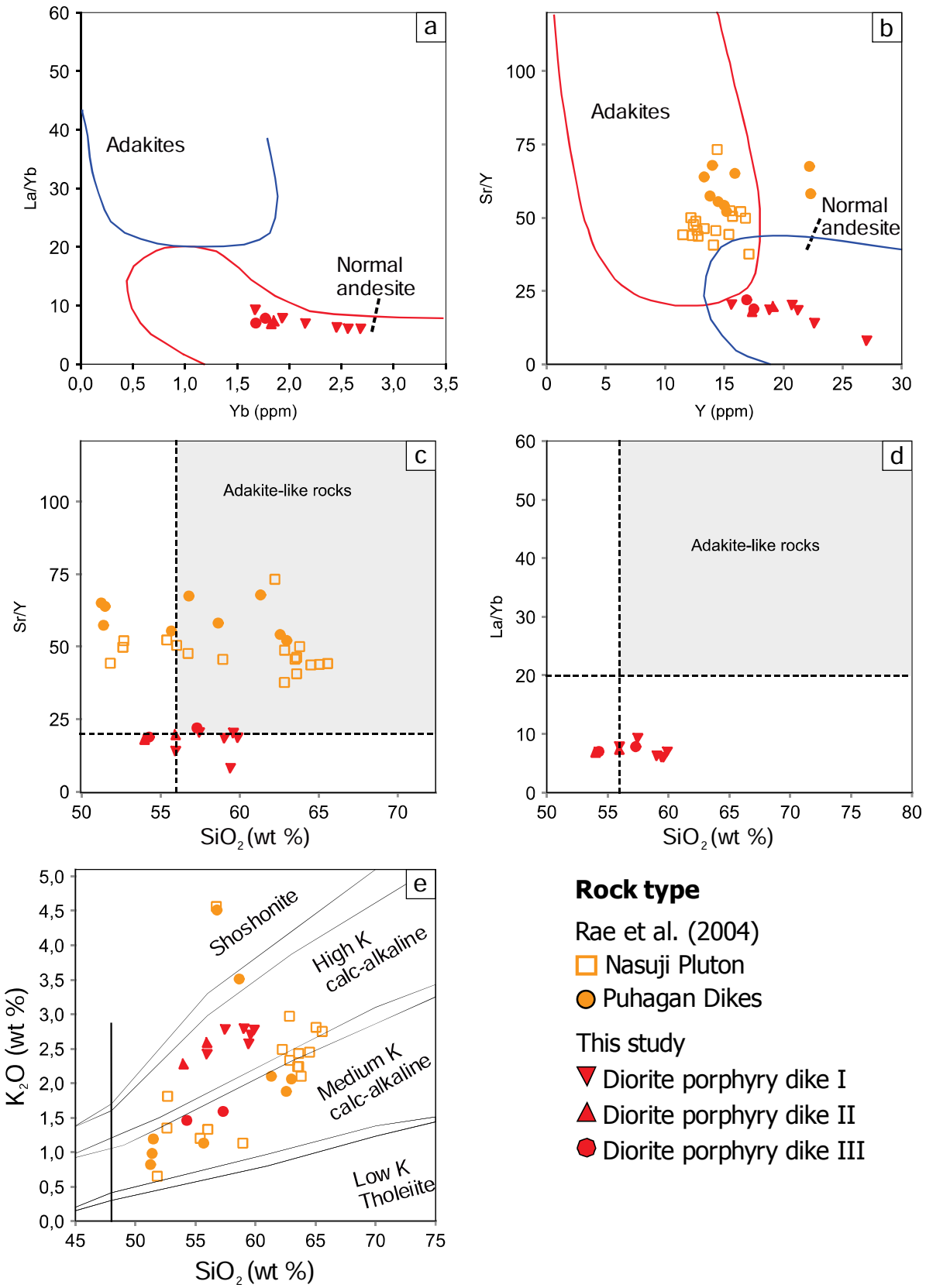

Figure 3.38. Geochemical comparison of least-altered intrusive rocks in Negros. a. La/Yb vs Yb diagram for discrimination of adakites (Defant and Drummond, 1990; Castillo et al., 1999). **b.** Sr/Y vs Y diagram for discrimination of adakites (Defant and Drummond, 1990; Castillo et al., 1999). **c.** Sr/Y vs SiO_2 diagram for discrimination of adakite-like rocks (Richards and Kerrich, 2007). **d.** La/Yb vs SiO_2 diagram for discrimination of adakite-like rocks (Richards and Kerrich, 2007). **e.** K_2O vs SiO_2 classification diagram for subalkalic rocks (Rollinson, 1993).

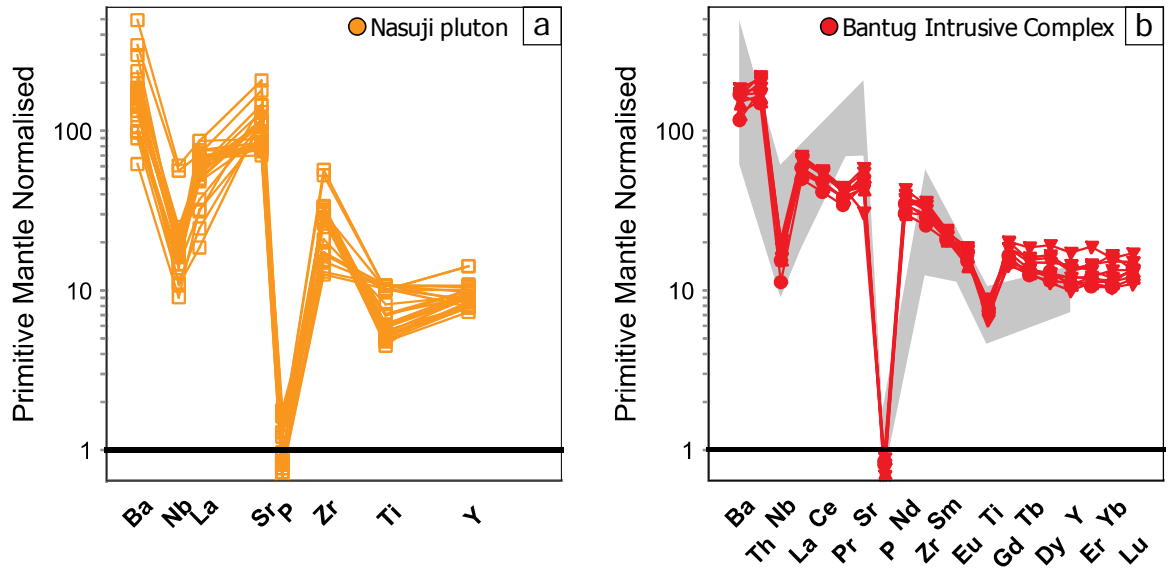

Figure 3.39. Primitive mantle-normalized trace element and rare earth element (REE) diagrams for least-altered intrusive rocks in Negros. a. Diagram for intrusive rocks from the Nasuji pluton in the Palinpinon geothermal field (Rae et al., 2004). **b.** Diagram intrusive rocks from the Bantug Intrusive Complex (BIC; This study). Grey shaded area contains results from the Nasuji Pluton.

3.5.3.3. Pliocene U-Pb ages from zircon

Three zircons from a DPD III sample in drill hole BTG-006 at 376 m depth yielded ages between 3.05 ± 0.35 Ma and 3.78 ± 0.59 Ma and were not included in the calculated crystallisation ages. Five zircons from a diorite porphyry sample in drill hole BTG-006 at 663 m depth also returned individual ages ranging from 3.23 ± 0.72 Ma to 3.44 ± 0.30 Ma. Some of these ages are the result of high common Pb in the analyses, however most were considered to be valid ages (Thompson, pers. commun., 2013). It is possible that these Pliocene-aged zircons may have been inherited, possibly from a Pliocene volcanic host rock or another source. The zircons may have been inherited from the Pliocene Magsinulo Andesite of MGB (2004), which crops out extensively in southeast Negros (Fig. 2.12). Additionally, these Pliocene-aged zircons may suggest that magmatism started at Bantug as early as 3.78 ± 0.59 Ma as the ages are similar to those of the Puhagan dikes at the Palinpinon geothermal field (i.e., ca. 4.2-4.1 Ma Ar^{40}/Ar^{39} in hornblende; Rae et al., 2004).

3.6. Geochronology and geochemistry summary

Least-altered volcanic rocks from the Quaternary Canlaon Volcanic Complex at Bantug plot on the continental arc, calc-alkaline, andesite fields of several trace element classification diagrams (Fig. 3.30). Least altered intrusive rocks from Bantug Intrusive Complex plot in the diorite fields of trace element classification diagrams (Fig. 3.32).

LA-ICP-MS dating of zircons revealed Late Pleistocene ages for the CVC and the BIC (Table 3.2; Figs. 3.33 and 3.34). Least-altered plagioclase-phyric andesites from the CVC returned ages of 1.71 ± 0.16 and 1.82 ± 0.11 Ma. Dioritic porphyries from the BIC returned ages that range from 1.37 ± 0.10 to 1.06 ± 0.29 Ma.

CHAPTER 4:

ALTERATION AND MINERALISATION IN THE LITHOCAP AT BANTUG

4.1. Introduction

This chapter presents the distribution, characterisation, and geochemistry of hydrothermally-altered rocks at Bantug. It begins with an account of the previous sampling work done at Bantug, followed by a description of the methods used (i.e., SWIR, FE-SEM, XRD) and sample distribution. This is followed by a report on the SWIR results and detailed descriptions of each type of alteration encountered at Bantug. Later, a comprehensive documentation of the geochemistry along and through the lithocap is presented. This is followed by a spatial analysis of base and precious metal assays. This chapter finishes with a discussion of the implications of the distribution of trace and rare elements in the lithocap, both in terms of genesis and exploration.

4.2. Methods

4.2.1. Sampling and whole rock geochemistry

In order to understand the geochemical variations, through and along the lithocap at Bantug, surface samples were collected around the three drill holes studied in this project and approximately every 10 m downhole on each drill hole. A total of 261 samples were collected and analysed for whole-rock geochemistry during the AMIRA P1060 project (this study). A total of 46 samples were collected by Professor Dr. Zhaoshan Chang during the AMIRA P765A project in 2009. The current dataset for the Bantug project contains information from 307 samples. Results are presented in Appendix G. The number of samples is presented in Table 4.1. Surface sample locations are presented in Figure 4.1. Surface sample locations were obtained using a GPS, and drill hole sample locations were determined using the drill hole survey information. Sample coordinates are provided in WGS 84 (i.e., latitude, longitude), and UTM (i.e., UTM Zone 51 North) formats (Appendix G). Whole rock analyses were undertaken at ACME Analytical Laboratory, Vancouver, Canada, using Method G4A-G4B described in section 3.6.

Table 4.1. Number of whole rock geochemical analyses

Drill-hole	AMIRA Project	Number of samples
BTG-003	P1060	74
BTG-005	P1060	71
BTG-006	P1060	71
Surface	P1060	45
Surface	P765A	46

4.2.2. Shortwave Infrared Spectroscopy (SWIR)

SWIR data was acquired from surface and down hole samples from Bantug. The 53 surface samples from the AMIRA P765A project were analysed by Professor Zhaoshan Chang using a PIMA instrument. The 45 surface samples from the AMIRA P1060 project were analysed by the author using a Terraspec® instrument at CODES-University of Tasmania. The 590 drill hole samples were analysed in the core shed at Tayasan, Negros, by Ingemar Arellano from Freeport-McMoRan, Doctor Lejun Zhang from CODES, and the author. The data were collected with a Terraspec® instrument. Terraspec® readings were acquired on drill holes BTG-003, BTG-005, and BTG-006, every five meters. Surface and down hole data collected were analysed with The Spectral Geologist (TSG) software® from CSIRO in order to extract the alunite peak position (~1,480 nm), depth of the water feature (DW= ~1,900 nm), the depth of the Al-OH feature (DA= ~2,200 nm), and index of crystallinity (IC). The IC value is the result of dividing the value of the depth of water feature by the value of the depth of the ALOH feature (IC=DW/DA). SWIR results are presented in Appendix I.

4.2.3. Field Emission - Scanning Electron Microscopy

Thin sections and polished laser mounts from the main rock types at Bantug were prepared in the lapidary facilities of the University of Tasmania. These were analysed with a Hitachi SU-70 field emission scanning electron microscope (FE-SEM) at the Central Science Laboratory, University of Tasmania. Secondary electrons and back-scattered electron images were acquired at a distance of 14.9 to 15 mm from the sample, using 15.0 kV current during the analyses. Energy dispersive X-ray spectroscopy (EDS) was used to recognise and quantify major element composition of various minerals in thin sections and laser sample mounts. The AZtec Software® from Oxford Instruments was used to process the EDS point analyses and to create element maps. The MinIdent – Win 4.0 software® was used to identify the most probable mineral occurrence in thin sections and laser mounts according to the EDS results. FE-SEM results from hydrothermally-altered rocks are presented in Appendix F.

4.2.4. X-ray Diffraction

X-ray diffraction (XRD) analyses were performed at CODES-University of Tasmania on a Bruker D2 Phaser at an operating voltage of 30 kV and 10mA using a cobalt X-ray tube to generate CoKα radiation with wavelength of 1.78897 Å. A 0.6 mm (0.3°) fixed divergence slit, 2.5° soller slit and an Fe-filter were used. Each scan ranged from 5 to 90° (2θ) with a 0.02° step size and a measurement time of 0.6 seconds per step. Mineral phases were identified using

a Bruker DIFFRAC.EVA Software® package with the PDF-2 (2012 release) powder diffraction file mineral database. XRD results from hydrothermally-altered rocks are presented in Appendix J.

4.3. Hydrothermal events at Bantug

Figure 4.1 presents a hydrothermal alteration map for the Bantug area; hydrothermal alteration domains overlay the geology. The geology and hydrothermal alteration maps are modified from Subang et al. (2009). Silicic alteration domains in the Bantug area are elongated northwest and northeast. At the centre of the lithocap, silicic alteration covers an elongated area of ~6 km by <1 km in northwest direction. Silicic alteration domains are elongated along the main structural trends (i.e., northeast, northwest; Figs. 4.1a and 4.1b). Advanced argillic, argillic, and propylitic hydrothermally-altered zones surround the silicic-altered domains. Propylitic alteration is the most abundant by surface area (Fig. 4.1; 12.9 km^2) at Bantug, followed by advanced argillic alteration (Fig. 4.1; 12.8 km^2), and argillic alteration (Fig. 4.1; 7.9 km^2). Advanced argillic alteration is abundant in the northern part of the Bantug area, whereas propylitic alteration is common in the southern part. The middle area of the lithocap has been explored with seven drill holes. To the south, a northwest trending area of advanced argillic alteration of ~3.2 km by <0.5 km is surrounded by a small halo of argillic alteration and by a larger halo of propylitic alteration (Fig. 4.1a). A large silicic-altered area (i.e., 2.6 km by 1 km) is located in the northern part of the lithocap (Fig. 4.1a). The northern and southern parts of the lithocap at Bantug remain untested by drilling.

4.3.1. Hydrothermal alteration distribution based on SWIR studies

Figure 4.2 presents sample distribution and SWIR results from surface samples; details of SWIR analyses are presented in Appendix I. Most samples were classified as advanced argillic-altered and contain alunite. Samples with abundant quartz were classified as silicic-altered. Two types of argillic alteration were defined based on the predominance of kaolinite (i.e., argillic 1) and montmorillonite (i.e., argillic 2), and advanced argillic alteration was defined based on the presence of dickite, alunite, pyrophyllite, and natroalunite.

Surface SWIR analyses identified a cluster of samples containing alunite, pyrophyllite, natroalunite, and muscovite over an area of 700 m by 700 m, at 100 m northeast of drill hole collar BTG-006 (Fig. 4.2). Three muscovite-bearing surface samples were identified in this cluster; these were classified as phyllic-altered (Fig. 4.2).

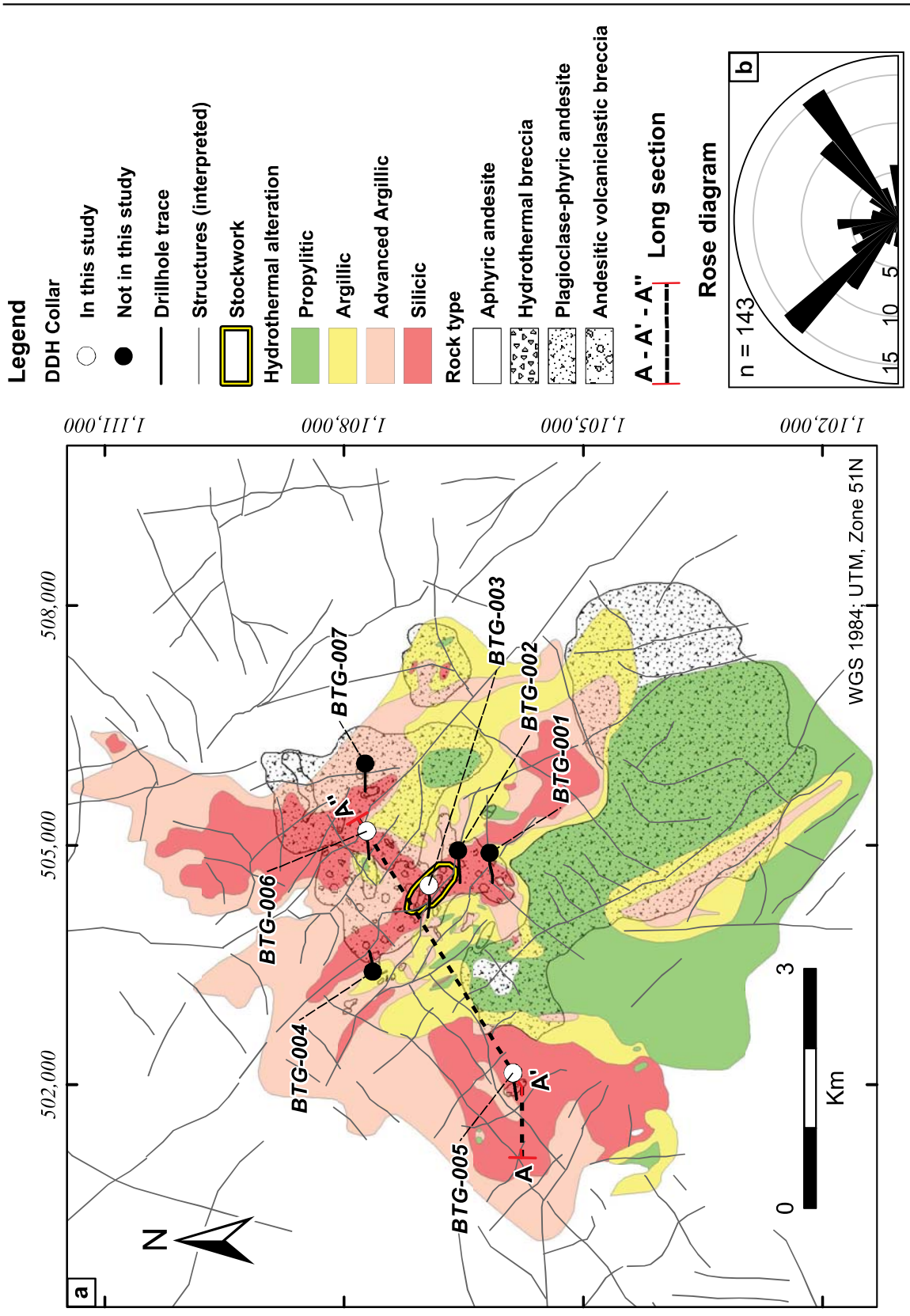

Figure 4.1. Hydrothermal alteration map of the Bantug area. a. Distribution of hydrothermal alteration domains at the Bantug area; after Subang et al. (2009). **b.** Rose diagram from structures at the Bantug area; the two main structural trends are northeast and northwest.

Figure 4.3 presents the alunite peak position and index of crystallinity (IC) results from surface samples. Most alunite-bearing samples are located around drill hole BTG-003. The highest alunite peak position value is 1,490 nm. It came from analyses of a natroalunite-altered plagioclase-phyric andesite sample, that was collected at 500 m northeast of drill hole BTG-006. Other high peak position values are: 1,488 nm (246 m south from BTG-003) and 1,487 nm (680 m southeast from BTG-003). Alunite-bearing samples with peak position values between 1,483 nm and 1,486 nm (n = 23) are located between 300 and 600 m around drill hole BTG-003. These samples surround the stockwork zone documented by Subang et al. (2009). Samples around drill holes BTG-002 and BTG-003 contain alunite. Peak position values define a zonation pattern on the surface; high values occur around BTG-002 and low values are located to the west of BTG-003 (Fig. 4.3).

Three muscovite-bearing surface samples were collected 300 m, 450 m, and 655 m northeast from drill hole collar BTG-006 (Fig. 4.2). IC values range from 0.71 to 1.17; the highest IC value (i.e., 1.17) was detected 318 m to the northeast of drill hole collar BTG-006, close to the sample with the highest alunite peak position value (i.e., 1,490 nm; Fig. 4.3).

Figures 4.4, 4.5, and 4.6 present results from SWIR analyses on drill holes BTG-005, BTG-003 and BTG-006, respectively. SWIR data points were collected every five meters down-hole using a Terraspec® instrument at Tayasan, Negros. Down hole SWIR results are presented in Appendix I. Table 4.2 presents a summary of alunite 1,480 nm peak position and IC values from surface and down hole samples.

SWIR analyses on drill hole BTG-005 (Fig. 4.4) revealed abundant pyrophyllite and montmorillonite. Pyrophyllite is abundant between 240.0 m and 268.6 m depth in the hydrothermal breccia intersect, as well as between 396.7 m and 501.3 m in the contact between the plagioclase-phyric andesite and the hydrothermal breccia (Fig. 4.4). Montmorillonite is abundant between 0 m and 100 m at the contact between the plagioclase-phyric andesite and the hydrothermal breccia, and from 600 m to 678 m depth at the contact between the plagioclase-phyric andesite and the hornfels (Fig. 4.4). Quartz, diaspore, and kaolinite occur sporadically but are mostly concentrated in the hydrothermal breccia (Fig. 4.4).

Table 4.2. Alunite peak position and IC values summary

	Alunite pp		IC	
	Min	**Max**	**Min**	**Max**
Surface	1478.6	1490.8	0.71	1.17
BTG-005	1477.2	1489.0	0.50	3.07
BTG-003	1476.2	1486.3	0.01	2.64
BTG-006	1477.2	1483.9	0.50	4.42

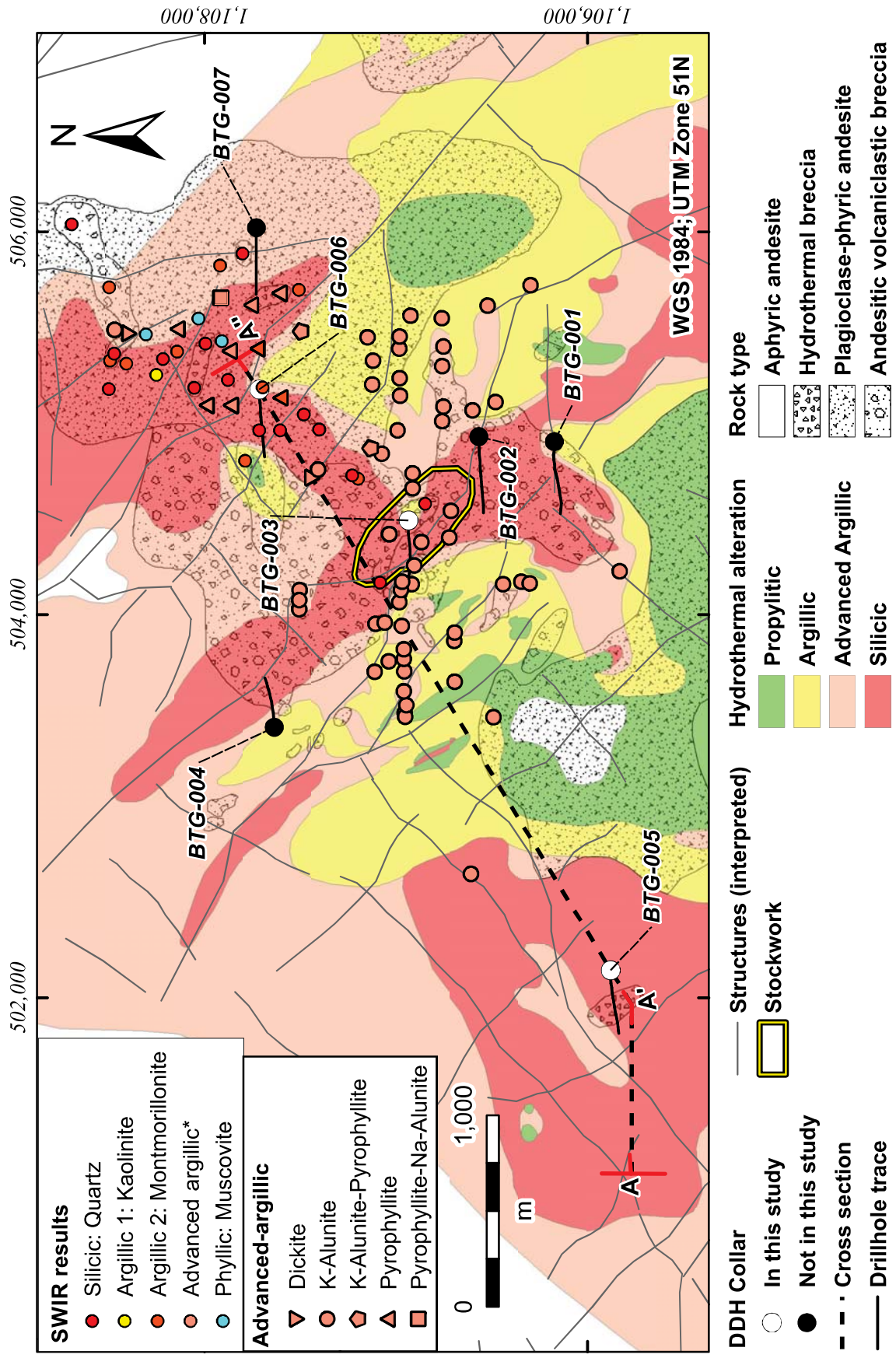

Figure 4.2. SWIR results from surface samples. Surface sample SWIR results overlaying the hydrothermal alteration and geology map (modified from Subang et al., 2009).

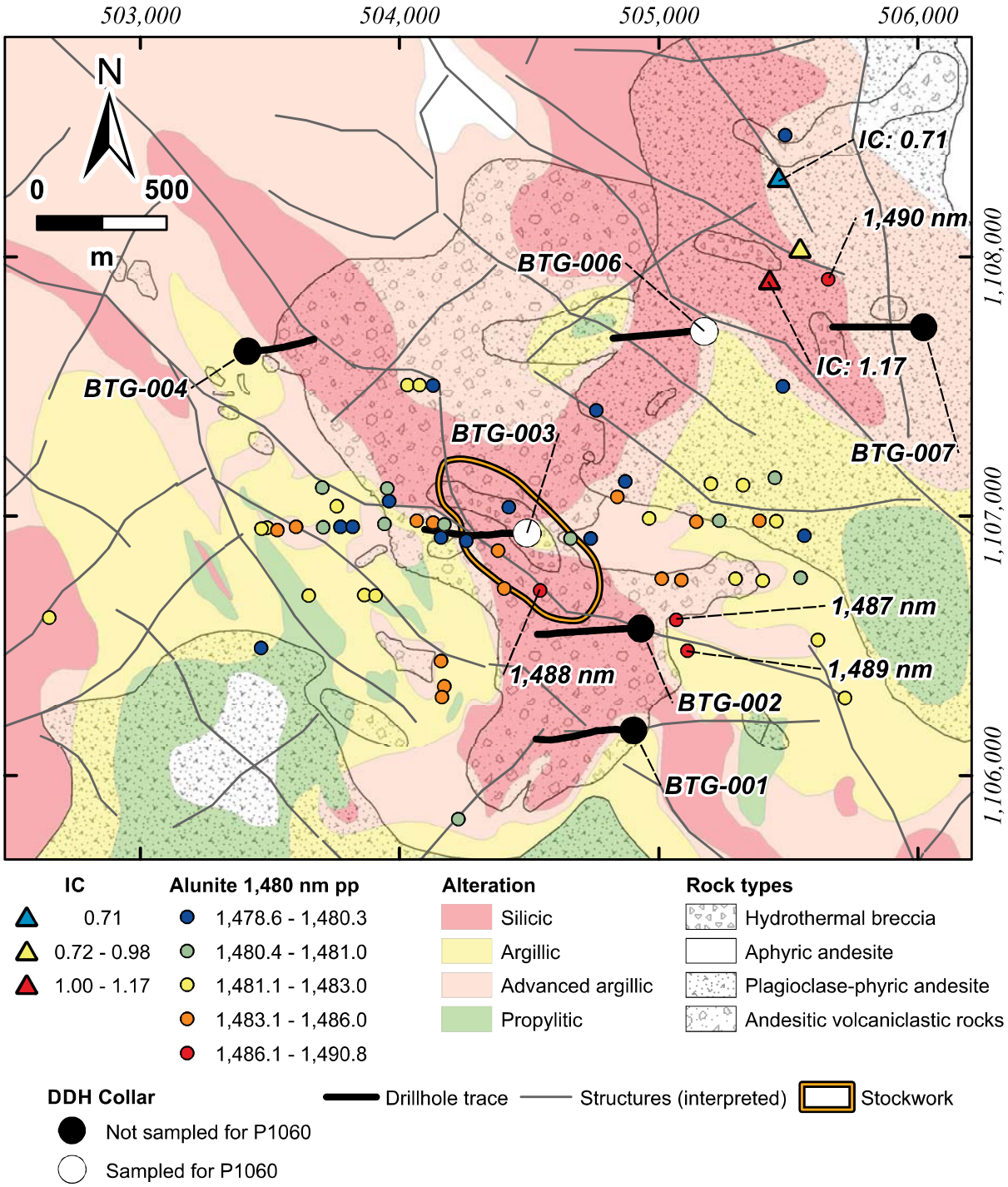

Figure 4.3. SWIR alunite peak position and IC results from surface samples. Surface sample SWIR results; alunite 1,480 nm peak position and index of crystallinity (IC) overlaying the hydrothermal alteration and geology map (modified from Subang et al., 2009).

Muscovite in BTG-005 also occurs sporadically but mostly between 514.4 m and 550.0 m depth in the plagioclase-phyric andesite (Fig. 4.4). Quartz, diaspore, and kaolinite occur sporadically but are mostly concentrated in the hydrothermal breccia (Fig. 4.4). The hydrothermal breccia in drill hole BTG-005 is characterised by alunite and natroalunite cement (Fig. 4.4).

Peak position values from the alunite cement in the hydrothermal breccia range from 1,477.2 nm to 1,482.1 nm, and peak position values from the natroalunite cement range from 1,484.5 nm to 1,489.0 nm (Fig. 4.4). The highest alunite peak position (i.e., 1,489.0 nm) was located at 120 m depth. Index of crystallinity (IC) values range from 0.50 to 3.07. IC values range from 0.50 to 1.11 between 15.4 m and 352.1 m depth, respectively (Fig. 4.4.). IC values between 455 m and 550 m, in the plagioclase-phyric andesite, range between 0.65 and 3.07 (Fig. 4.4.). Two muscovite-bearing samples located at 678 m depth have IC values of 0.93 and 1.05 (Fig. 4.4.).

SWIR analyses of drill hole BTG-003 detected abundant alunite, montmorillonite, and muscovite (Fig. 4.5). Alunite is abundant between 210.1 m and 254.0 m depth, at the contact between the plagioclase-phyric andesite and the diorite porphyry dike I (Fig. 4.5). Montmorillonite occurs mostly between 255.9 m and 374.4 m depth, and is associated with hydrothermal alteration of the diorite porphyry dikes (Fig. 4.5). Montmorillonite also occurs sporadically in the plagioclase-phyric andesite between 50 m and 200 m (Fig. 4.5).

Muscovite mostly occurs between 530 m and 722 m in drill hole BTG-003 (Fig. 4.5). It is the product of hydrothermal alteration of the diorite porphyry and the plagioclase-phyric andesite. Muscovite also occurs in the andesitic volcaniclastic breccia between 380 m and 410 m depth (Fig. 4.5). Quartz, pyrophyllite, and dickite occur sporadically, and most dickite occurs in the aphyric andesite intruded by the hydrothermal breccia at 440 m depth (Fig. 4.5). Kaolinite occurs sporadically and most of it occurs between 0 m and 50 m, and 700 m and 722 m depth (Fig. 4.5). Peak position values from alunite between 210.1 m and 254 m depth range between 1,476.2 nm and 1,479.8 nm; higher peak position values occur at 461.3 m and 470.4 m, respectively: 1,483.81 nm and 1,486.29 nm.

IC values in drill hole BTG-003 range between 0.01 and 2.64 (Fig. 4.5). IC values between 1 and 1.14 occur at 400 m and are associated with hydrothermal alteration of the andesitic volcaniclastic breccia (Fig. 4.5). IC values between 1.34 and 2.64 occur from 610 m to 720 m and are associated with the diorite porphyry (Fig. 4.5).

SWIR analyses of drill hole BTG-006 detected abundant pyrophyllite and muscovite (Fig. 4.6). Pyrophyllite occurs between 0 m and 550 m depth, and is associated with the plagioclase-phyric andesite (Fig. 4.6). Muscovite occurs sporadically at 86.6 m, 90.3 m, 108.2 m, 164.5 m, 256.6 m, and 381.3 m depth in drill hole BTG-006 (Fig. 4.6). However, muscovite is most abundant between 536.1 m and 700.3 m (Fig. 4.6). Quartz, K-alunite, dickite, diaspore, natroalunite, and gypsum occur sporadically (Fig. 4.6). These minerals occur within the first 350 m of drill hole BTG-006; except for gypsum which occurs at 481.8 m and 485.3 m depth (Fig. 4.6). The above mentioned minerals occur as secondary minerals in the plagioclase-phyric andesite. Kaolinite and montmorillonite occur sporadically, the latter is abundant between 431.2 m and 466.1 m depth (Fig. 4.6). Montmorillonite is associated with the diorite porphyry dike III (Fig. 4.6). Alunite peak position values from drill hole BTG-006 vary from 1,477.2 nm to 1,483.9 nm between 0 m and 340.2 m (Fig. 4.6). The highest values occur within the first 35 m of the drill hole (Fig. 4.6). IC values range from 0.50 to 4.42. Most IC values occur between 536.1 m and 704.6 m depth, and are associated with the diorite porphyry (Fig. 4.6). The highest values in drill hole BTG-006 (i.e., 2.77 to 4.42) occur between 566.5 m and 635.1 m, at the contact between the plagioclase-phyric andesite and the diorite porphyry (Fig. 4.6).

In summary, higher alunite peak position values occur on surface to the northeast of drill hole collar BTG-006 and in drill hole BTG-005 associated with the hydrothermal breccia cement. Higher IC values are associated with the diorite porphyry in drill hole BTG-006.

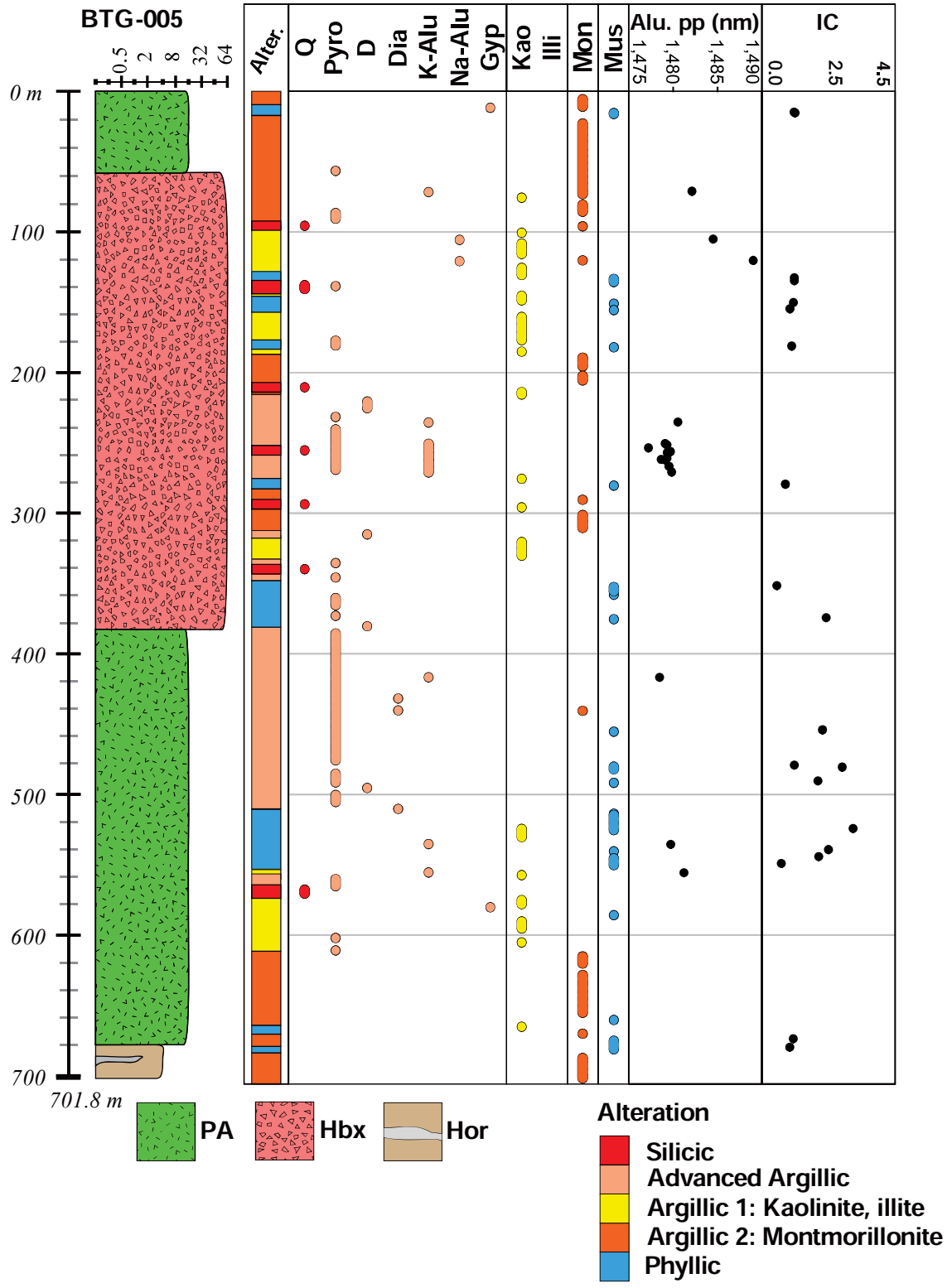

Figure 4.4. Short wave infrared results from drill hole BTG-005. Abbreviations: Alu: k-alunite; Alu. pp: alunite peak position; D: dickite; Dia: diaspore; Gyp: gypsum; Hbx: hydrothermal breccia; Hor: hornfels; IC: Index of crystallinity; Illi: illite; K-; Kao: kaolinite; Mon: montmorillonite; Mus: muscovite; Na-Alu: natroalunite; PA: plagioclase-phyric andesite; Pyro: pyrophyllite; Q: quartz. Collar location: X: 502144; Y: 1105881 (WGS84-51N). Elevation: 1071.3 m; Azimuth: 270°; Dip: 57°.

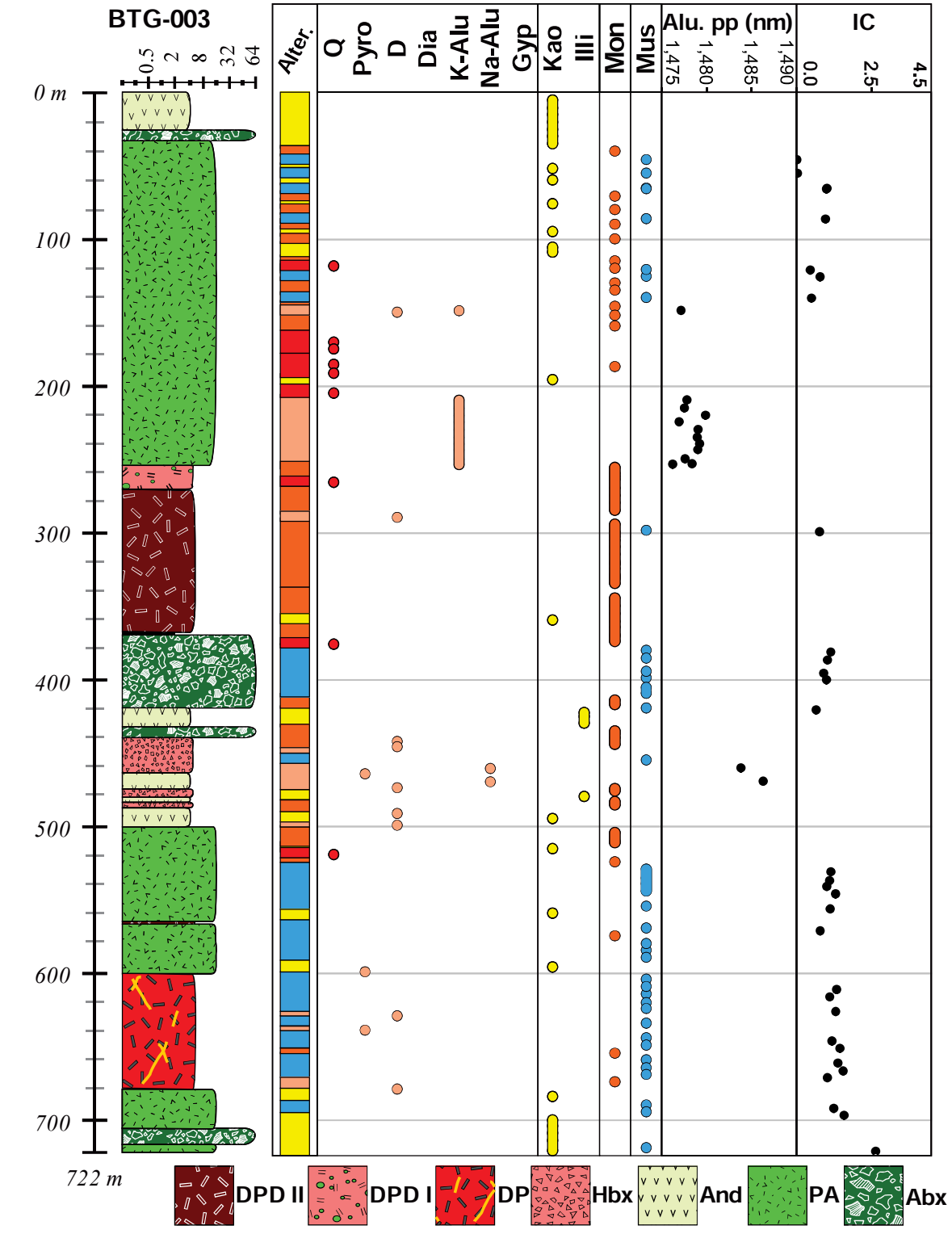

Figure 4.5. Short wave infrared results from drill hole BTG-003. Alteration legend as in Figure 4.4. Abbreviations: Abx: andesitic volcaniclastic breccia; Alu. pp: alunite peak position; And: aphyric andesite; D: dickite; Dia: diaspore; DP: diorite porphyry; DPD I: diorite porphyry I; DPD II: diorite porphyry II; Gyp: gypsum; IC: Index of crystallinity; Illi: illite; Hbx: hydrothermal breccia; K-Alu: k-alunite; Kao: kaolinite; Mon: montmorillonite; Mus: muscovite; Na-Alu: natroalunite; PA: plagioclase-phyric andesite; Pyro: pyrophyllite; Q: quartz. Collar location: X: 504942; Y: 1106935 (WGS84-51N). Elevation: 1186.1 m; Azimuth: 270°; Dip: 57°.

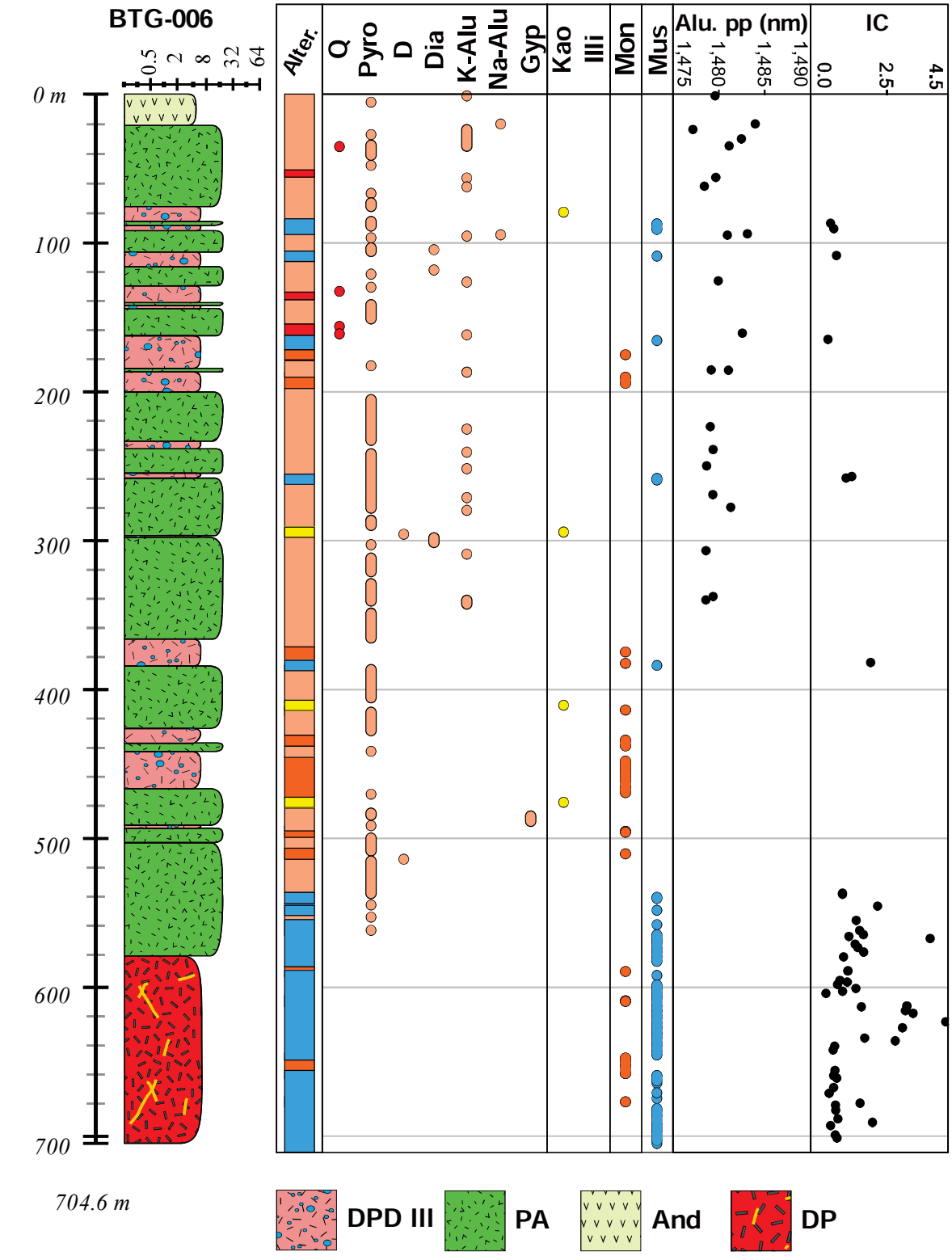

Figure 4.6. Short wave infrared results from drill hole BTG-006. Alteration legend as in Figure 4.4. Abbreviations: Abx: andesitic volcaniclastic breccia; Alu. pp: alunite peak position; And: aphyric andesite; PA: plagioclase-phyric andesite. D: dickite; Dia: diaspore; DPD III: diorite porphyry III; DP: diorite porphyry; Gyp: gypsum; Hbx: hydrothermal breccia; IC: Index of crystallinity; Illi: illite; K-Alu: k-alunite; Kao: kaolinite; Mon: montmorillonite; Mus: muscovite; Na-Alu: natroalunite; Pyro: pyrophyllite; Q: quartz. Collar location: X: 505175; Y: 1107714 (WGS84-51N). Elevation: 1018.0 m; Azimuth: 270°; Dip: 57°.

Figures 4.8 to 4.10 present interpretative alteration cross-sections for the three drill holes studied at Bantug. Interpretations are based on SWIR results and logging observations. The cross-section from drill hole BTG-005 is characterised by a large halo of advanced argillic alteration around the hydrothermal breccia, also by the hornfels at the end of the drill hole. Cross-sections from drill holes BTG-003 and BTG-006 are characterised by the large halos of phyllic alteration around the diorite porphyry intersects. Also, hydrothermal alteration of host rocks transitions from argillic (i.e., kaolinite dominated) in BTG-003, to advanced argillic in BTG-006.

Figure 4.11 presents an interpretative long section of the hydrothermal alteration at Bantug. The long section is defined by the line A-A" in Figure 4.2, and it includes drill holes BTG-005, BTG-003, and BTG-006. Drill hole BTG-003 is projected to the line, which crosses 200 m to the northwest of the drill hole collar. Figure 4.11 highlights a southwest to northeast transition in hydrothermal alteration, from montmorillonite-dominated argillic in BTG-005, to kaolinite-dominated argillic in BTG-003, to advanced argillic in BTG-006. Also, it denotes the presence of higher temperature hydrothermal mineral assemblages (i.e., pyrophyllite and alunite in advanced argillic alteration; muscovite in phyllic alteration) to the northeast.

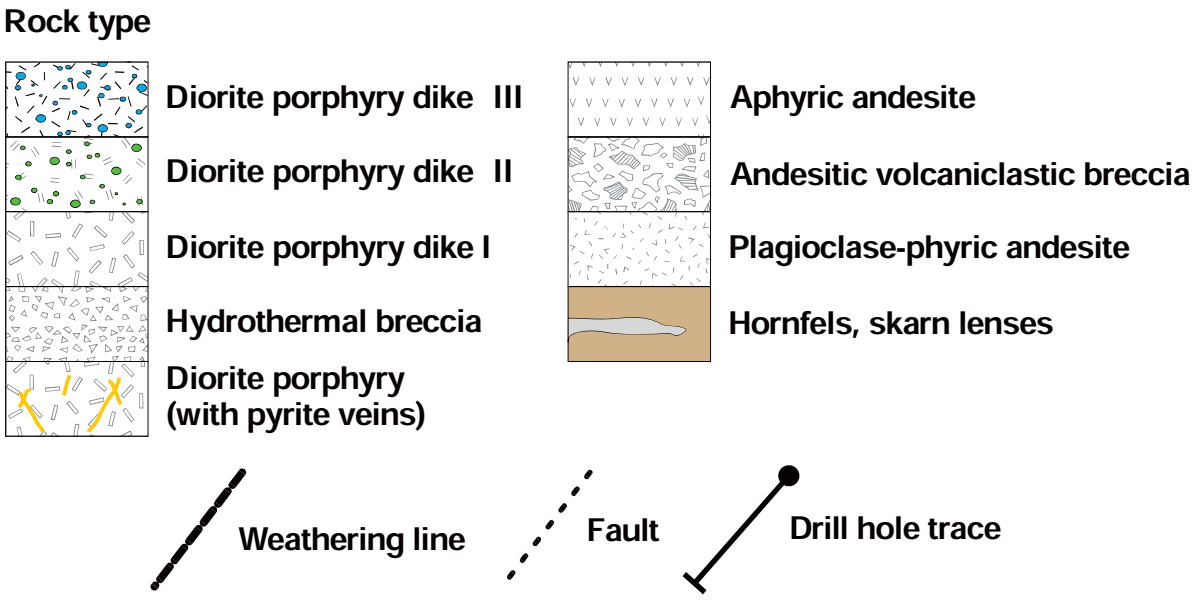

Figure 4.7. Legend for interpretative alteration cross-sections (Figures 4.8 to 4.10).

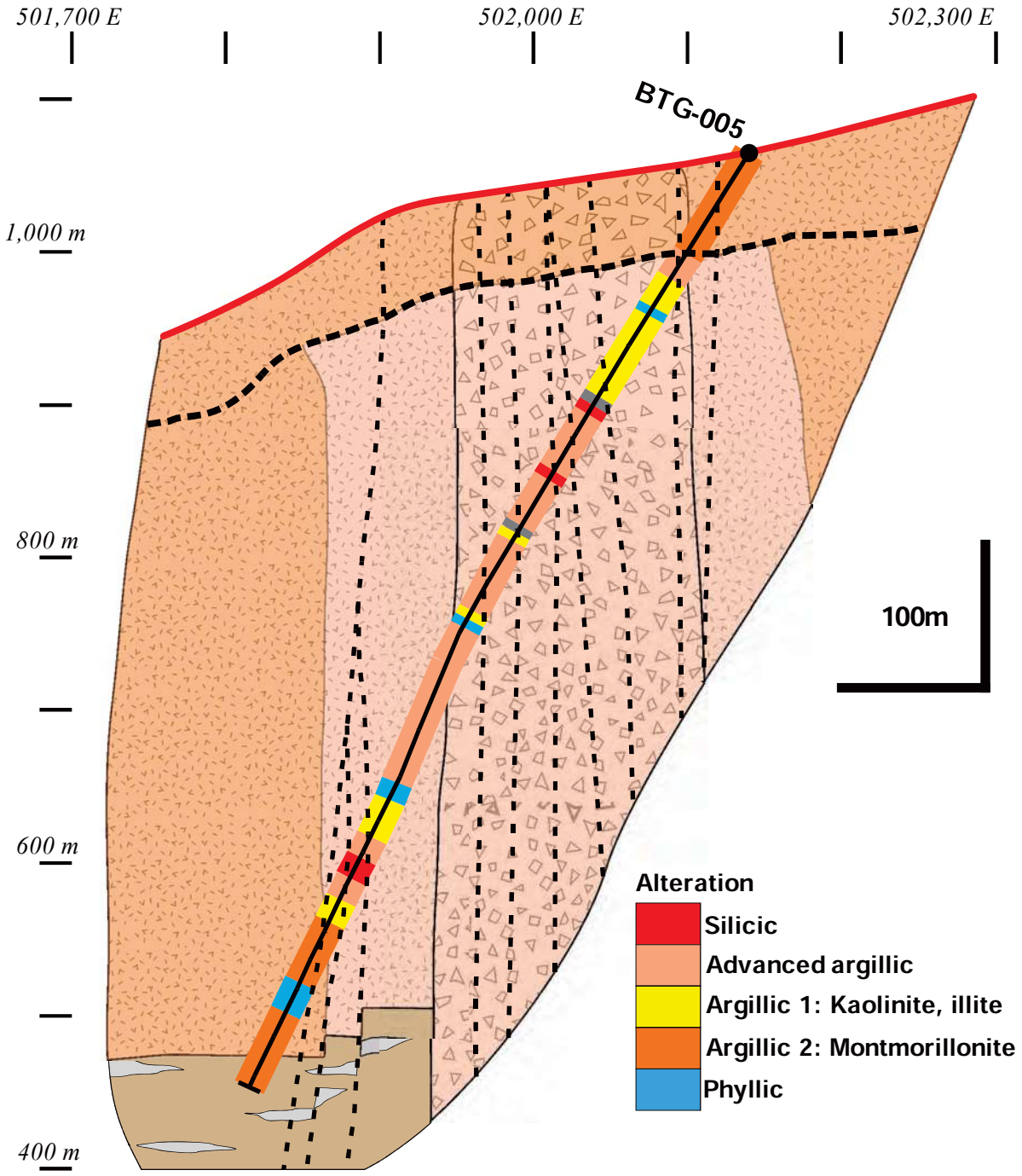

Figure 4.8. Interpretative alteration cross section for drill hole BTG-005. Rock type legend is in Figure 4.7.

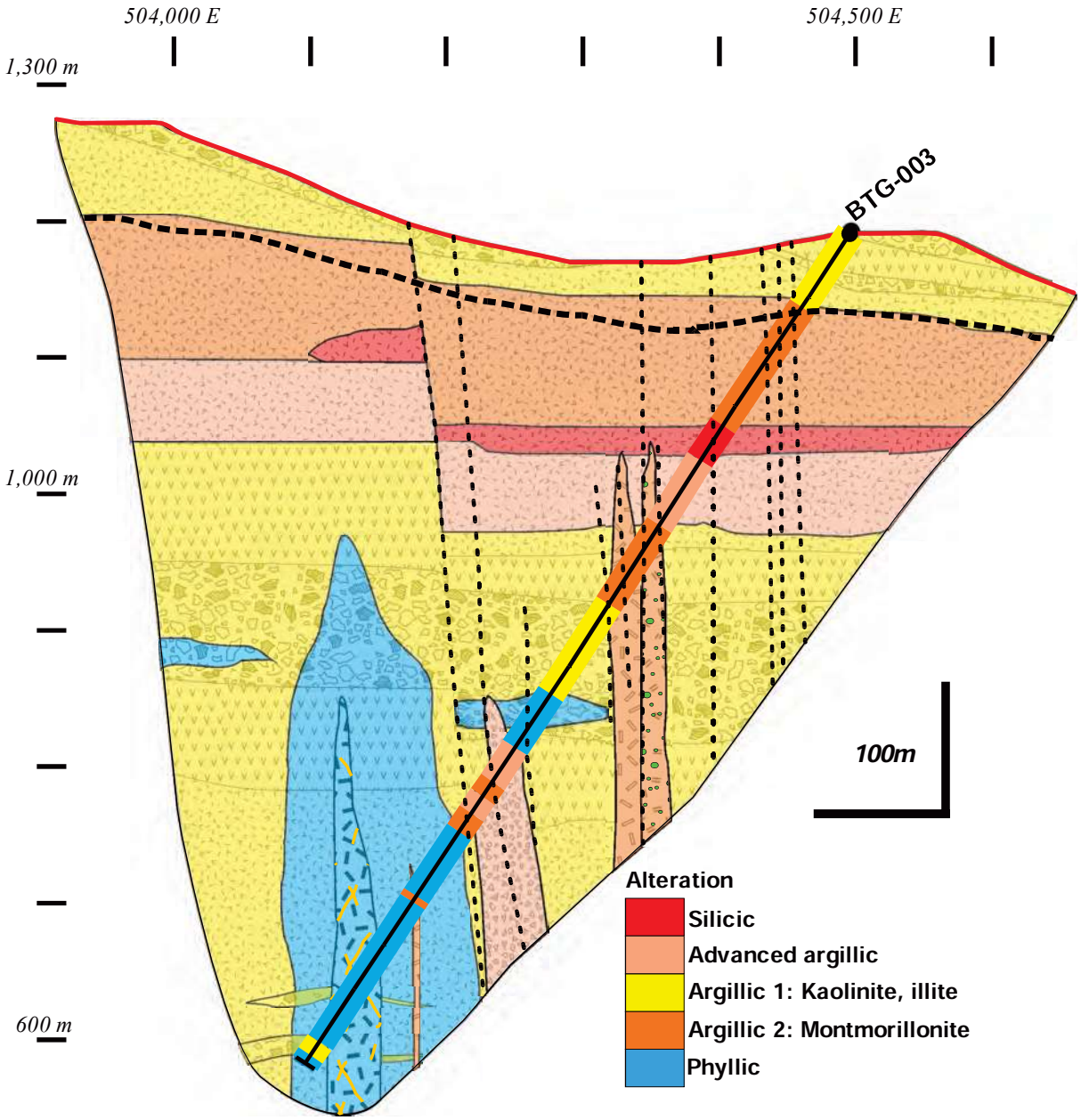

Figure 4.9. Interpretative alteration cross section for drill hole BTG-003. Rock type legend is in Figure 4.7.

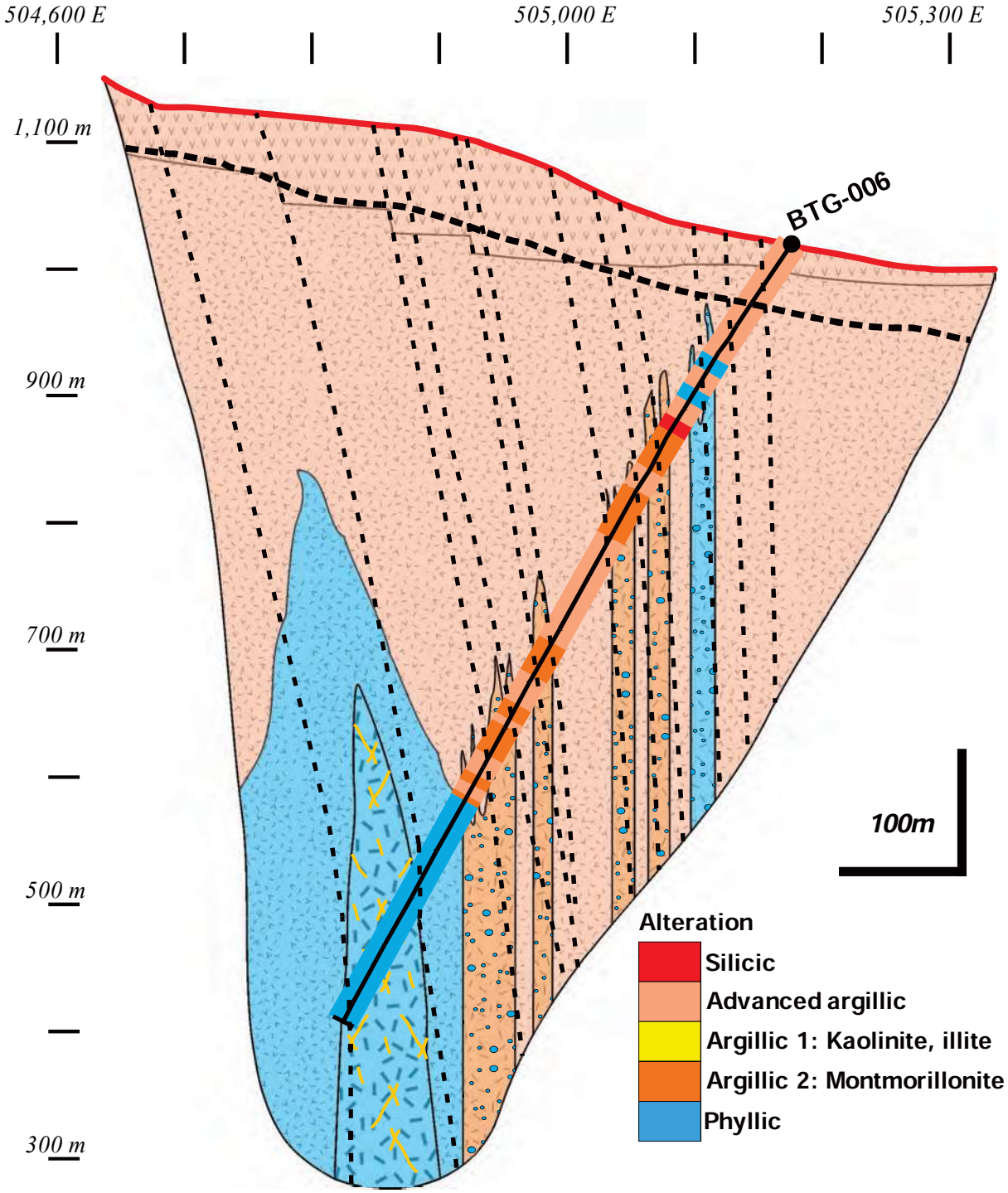

Figure 4.10. Interpretative alteration cross section for drill hole BTG-006. Rock type legend is in Figure 4.7.

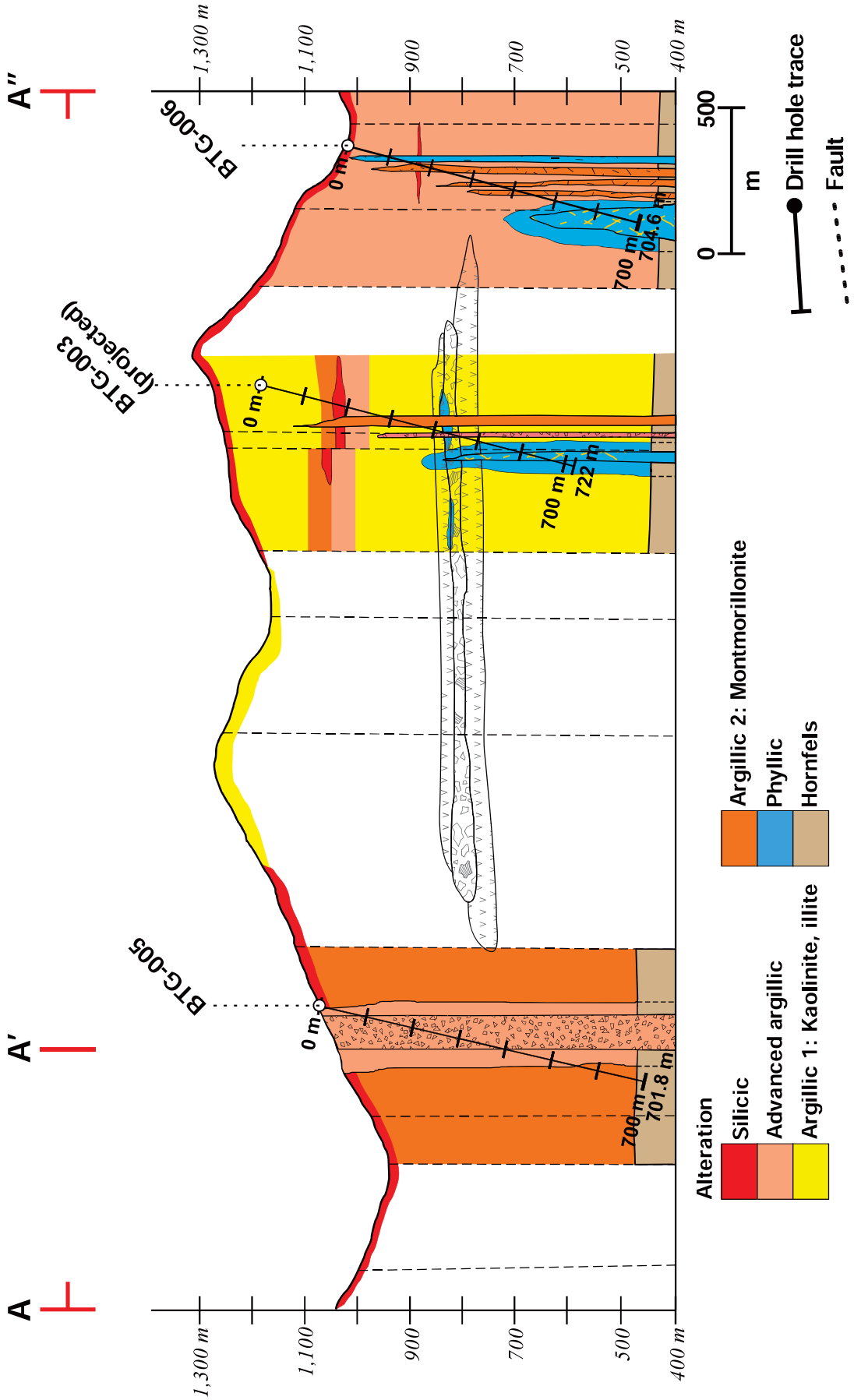

Figure 4.11. Interpretative alteration long section. Rock type legend is in Figure 4.7.

4.3.2. Hornfels

Fine- to medium-grained clastic rocks from the Late Pliocene-Pleistocene Caliling Formation (MGB, 2004) have been altered to hornfels facies. Hornfels was recognised in drill hole BTG-005 from 628.2 m to 701.7 m depth (i.e., end of drill hole; Figs. 4.8 and 4.11). Petrography and SEM analyses revealed that the hornfels at Bantug is characterised by the presence of chlorite-group minerals (i.e., chamosite), montmorillonite, albite, and kaolinite. Also, petrographic and SEM analyses revealed trace amounts (i.e., <1%) of apatite, magnetite, and chalcopyrite. A detailed description of textures and secondary minerals in hornfels at Bantug is presented in Chapter 3, section 3.3.2. Figure 4.12 presents XRD results from hornfels samples from drill hole BTG-005. XRD analyses revealed hornfels samples from Bantug are predominantly made of chlorite-group minerals (i.e., chamosite), albite, and quartz.

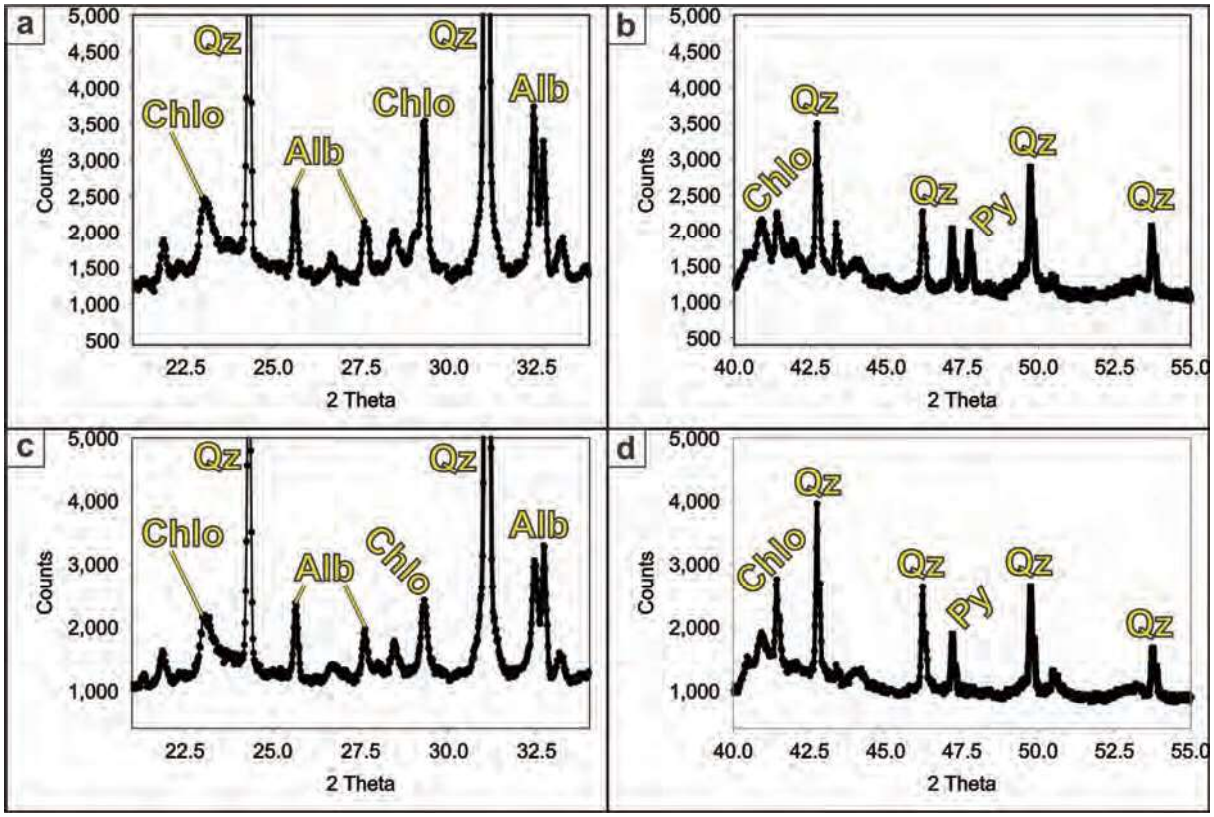

Figure 4.12. XRD results from hornfels. a. XRD profile between 22 and 33 2-theta (687.3 m; BTG-005). **b.** XRD profile between 40 and 55 2-theta (687.3 m; BTG-005). **c.** XRD profile between 22 and 33 2-theta (701.8 m; BTG-005). **d.** XRD profile between 40 and 55 2-theta (701.8 m; BTG-005). Abbreviations: Alb: albite; Chl: chlorite; Py: pyrite; Qz: quartz.

4.3.3. Silicic alteration

Silicic alteration at Bantug is characterised by vuggy-quartz texture, massive texture, and SiO_2 values greater than 87.83 wt % (Figs. 4.13 and 4.14a). Silicic alteration was detected in many surface and drill hole samples from Bantug (Figs. 4.14 and 4.15). Some silicic-altered rocks display vuggy texture (Fig. 4.13). High SiO_2 values on surface samples follow a northeast trending pattern (Fig. 4.14b), and match the hydrothermal alteration map of Subang et al. (2009). Silicic alteration, vuggy texture, and high SiO_2 occur sporadically in drill holes (Fig. 4.15). These are best developed in plagioclase-phyric andesites (Fig. 4.15). The highest SiO_2 values (Table 4.3; 90.06 to 96.99 wt %) occur in drill hole BTG-003 between 151.0 m and 202.3 m depth (Fig. 4.15b), where vuggy texture is well developed.

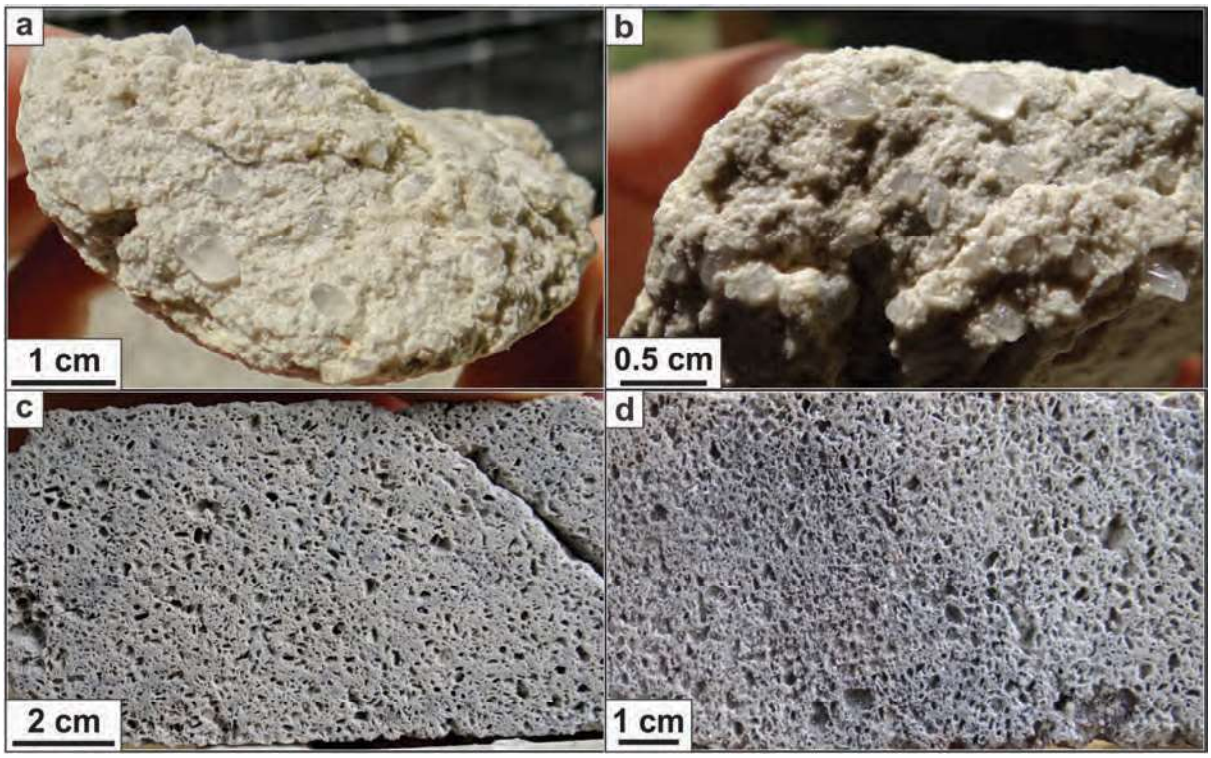

Figure 4.13. Silicic alteration and vuggy quartz texture. a. Vuggy texture after plagioclase-phyric andesite; vugs are filled with quartz crystals (BTG-003; 170 m). **b.** Vuggy texture after plagioclase-phyric andesite; vugs are filled with quartz crystals (BTG-003; 171 m). **c.** Vuggy texture after plagioclase-phyric andesite (BTG-003; 241 m). **d.** Vuggy texture after plagioclase-phyric andesite (BTG-003; 251 m).

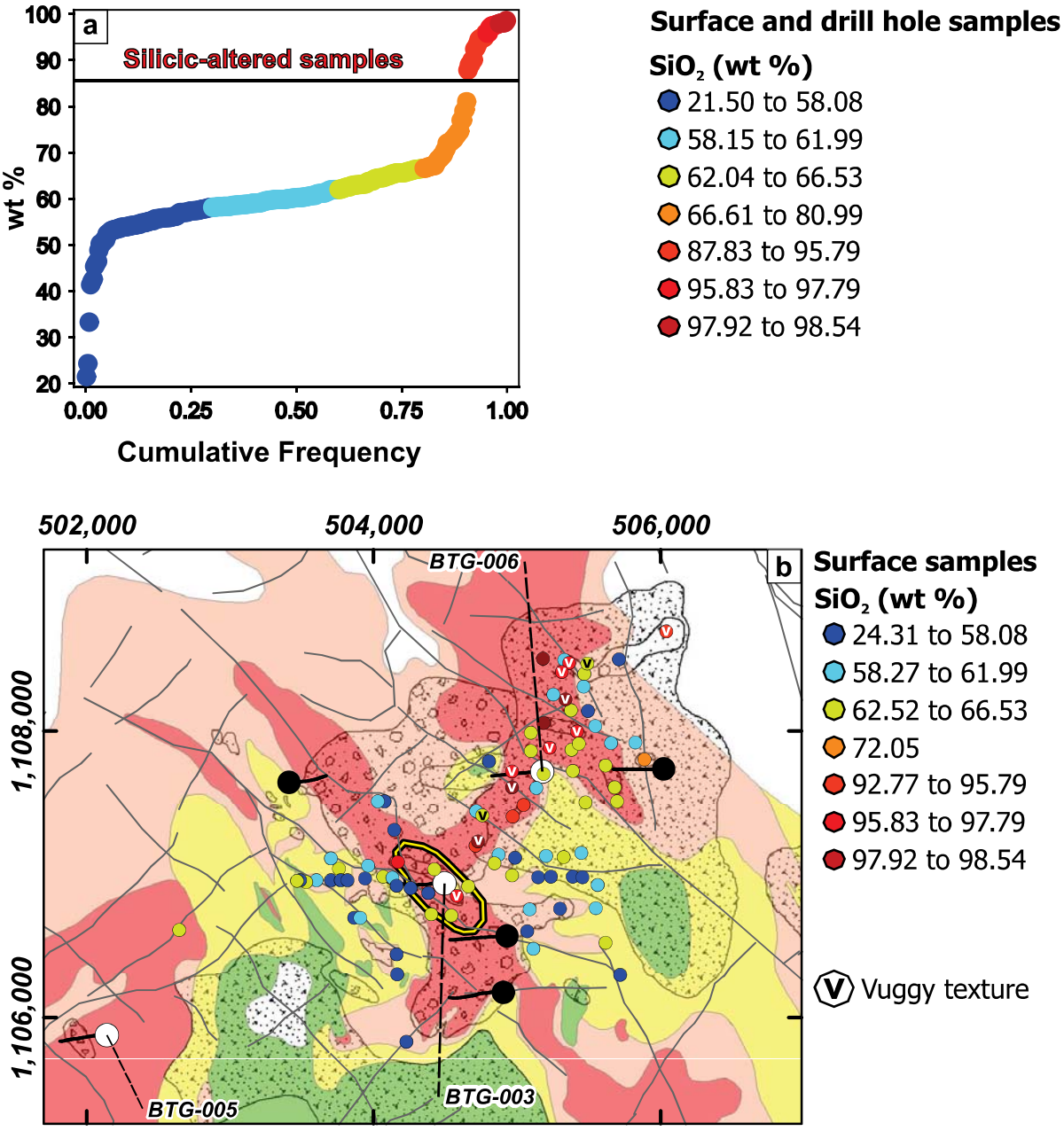

Figure 4.14. Silicic alteration. a. Cumulative frequency diagram from SiO_2 (wt %), based on surface and drill hole samples. **b.** Surface distribution of SiO_2 (wt %) values. Rock types and hydrothermal alteration legend as in Figure 4.1. V: vuggy texture.

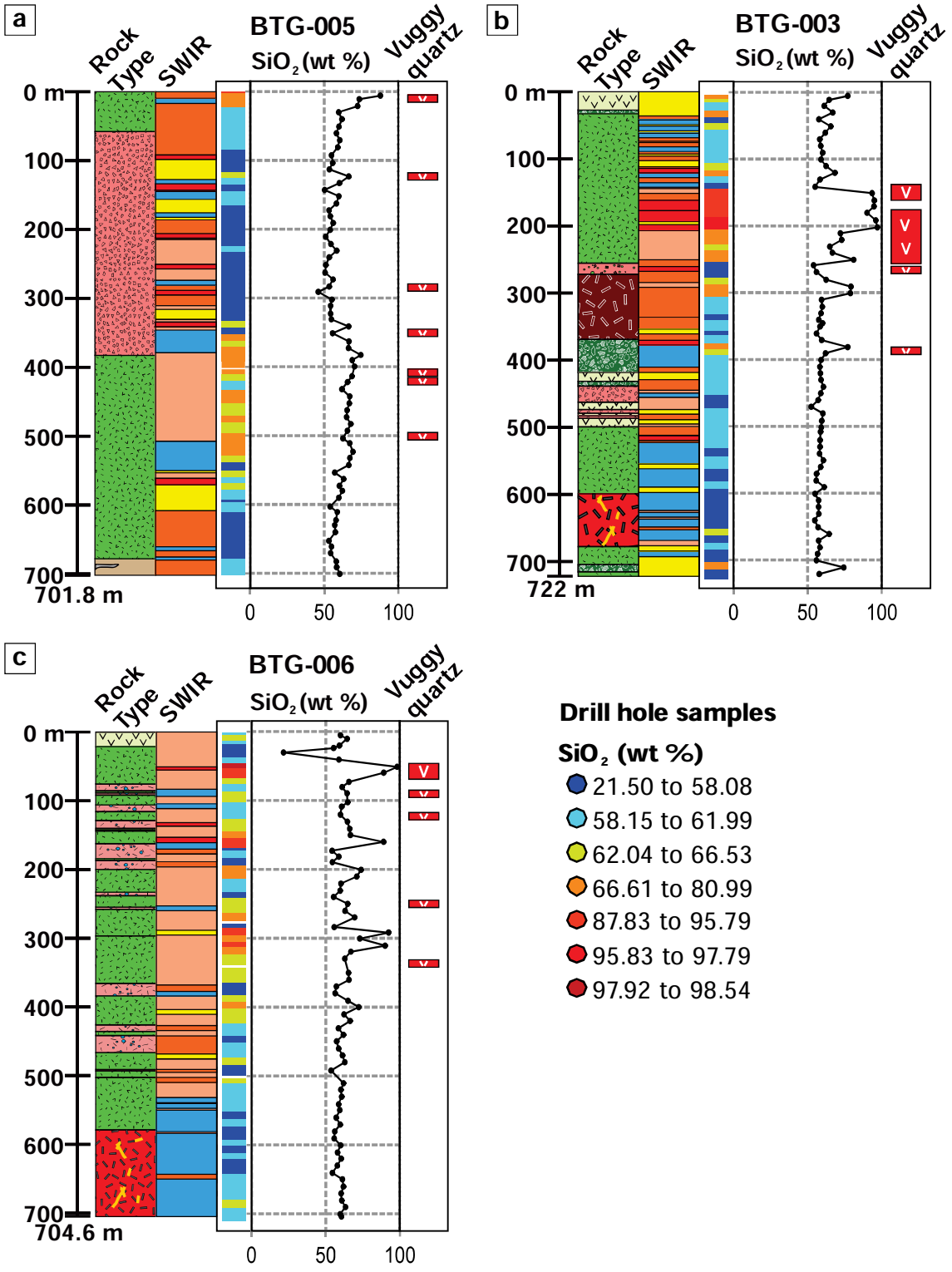

Figure 4.15. Silicic alteration in drill holes. Diagrams include rock type, SWIR results, SiO_2 (wt %) results, and vuggy texture distribution. SiO_2 (wt %) content is presented in a colour coded log and a down-hole line graph. **a.** Drill hole BTG-005. **b.** Drill hole BTG-003. **c.** Drill hole BTG-006. Rock type and hydrothermal alteration legend is the same as in Figures 4.4, 4.5, and 4.6.

4.3.4. Advanced argillic alteration

Advanced argillic alteration mineral assemblages, determined by SWIR and SEM analyses, were recognised in the three drill holes studied. Advanced argillic alteration predominates in BTG-005 and BTG-006 (Figs. 4.8 to 4.11). Pyrophyllite, dickite, diaspore, and alunite occur as secondary minerals in clasts from the hydrothermal breccia in drill hole BTG-005. The hydrothermal breccia cement is predominantly made of natroalunite. Plagioclase-phyric andesites hosting the hydrothermal breccia have been altered to pyrophyllite, dickite, diaspore, and alunite mineral assemblages (Figs. 4.4, 4.8, and 4.11). Advanced argillic alteration in drill hole BTG-003 occurs between 200 m and 250 m depth, and it is characterised by the presence of alunite in vuggy texture (Fig. 4.15b). Advanced argillic alteration is ubiquitous in drill hole BTG-006, and it is most abundant between 30 m and 270 m depth (Figs. 4.6, 4.10, and 4.11). Advanced argillic alteration in drill hole BTG-006 is characterised by abundant pyrophyllite and alunite, as well as minor dickite, diaspore, and natroalunite (Fig. 4.6).

4.3.5. Argillic alteration

Two types of argillic alteration have been defined based on the presence of montmorillonite and kaolinite. Montmorillonite-rich argillic alteration occurs mostly in plagioclase-phyric andesite in drill hole BTG-005 as a halo around the hydrothermal breccia (Fig. 4.8). It is also related to the hornfels. Montmorillonite-rich argillic alteration is abundant in plagioclase-phyric andesites in BTG-003 (Figs. 4.5 and 4.9). However, montmorillonite-rich argillic alteration in drill holes BTG-003 and BTG-006 is most abundant in the diorite porphyry dikes (Figs. 4.5, 4.6, 4.9, and 4.10). Kaolinite-rich alteration is most abundant in drill hole BTG-003. It occurs in the aphyric andesite and andesitic volcaniclastic breccia (Figs. 4.5 and 4.9).

4.3.6. Phyllic alteration

Phyllic alteration at Bantug is defined by the presence of muscovite, which was recognised using SWIR and SEM. It is predominantly related to the porphyry diorite (Figs. 4.4 to 4.11). Phyllic alteration is best developed in drill hole BTG-006 between 540 m and 704.6 m depth. It is also developed in drill hole BTG-003 between 540 m and 700 m depth. Phyllic alteration is intense and pervasive in the diorite porphyry, commonly masking the primary igneous texture (Figs. 3.12 to 3.15). Figure 4.16 presents results from XRD analyses of 6 phyllic-altered diorite porphyry samples. All the analyses indicate the ubiquitous presence of muscovite, quartz, and pyrite; some analyses indicate the presence of albite (Fig. 4.16).

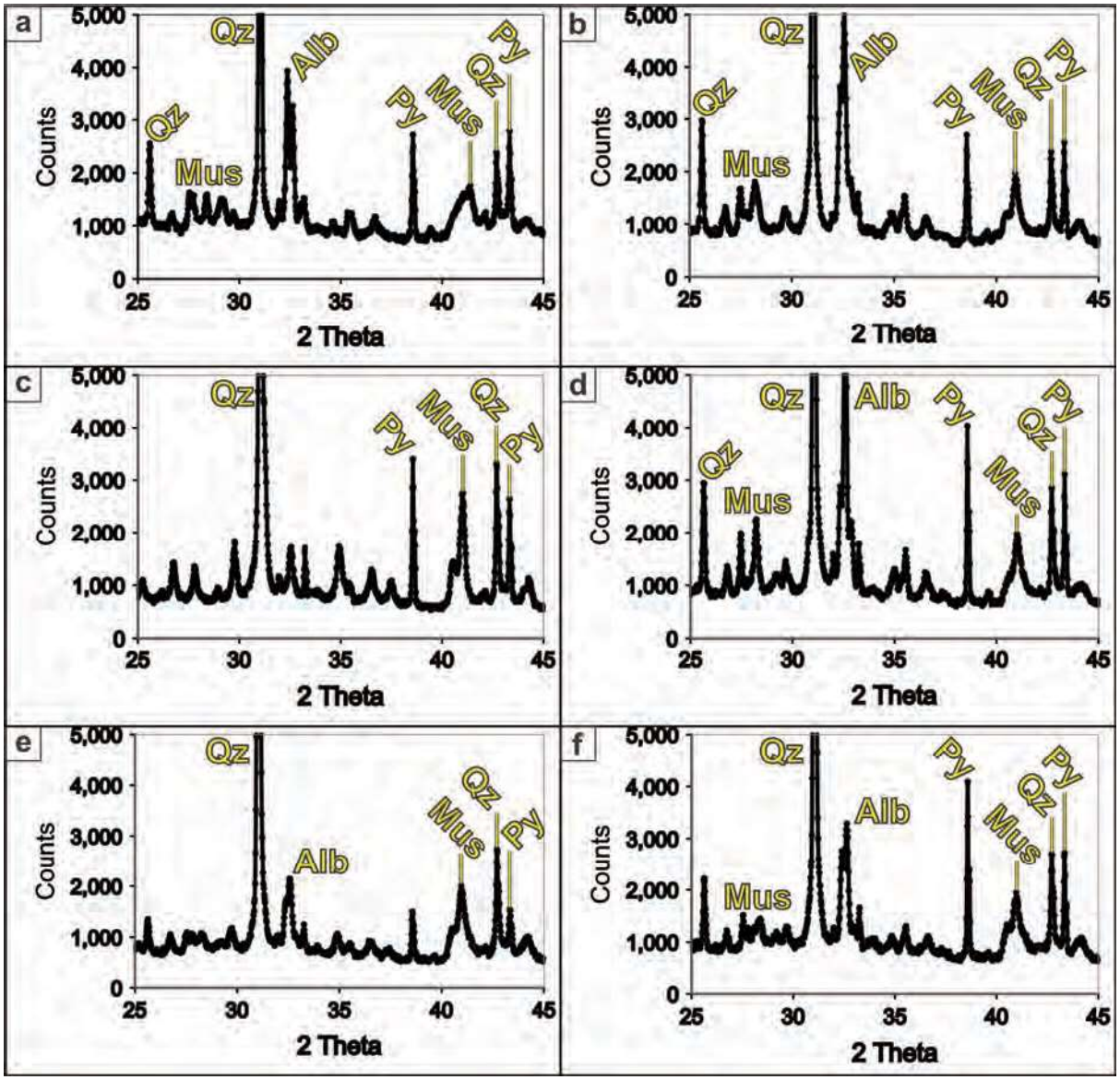

Figure 4.16. XRD results from phyllic-altered diorite porphyry samples. a. Sample from BTG-006 at 585.1 m depth. **b.** Sample from BTG-006 at 601.3 m depth. **c.** Sample from BTG-006 at 620.0 m depth. **d.** Sample from BTG-006 at 661.1 m depth. **e.** Sample from BTG-006 at 663.1 m depth. **f.** Sample from BTG-006 at 665.1 m depth. All panels present XRD profiles between 25 and 45 2-theta. Abbreviations: Alb: albite; Chl: chlorite; Mus: muscovite; Py: pyrite; Qz: quartz

4.3.7. Propylitic alteration

Propylitic alteration at Bantug is defined by the presence of epidote filling vesicules in the pyroxene-plagioclase phyric, miarolitic diorite porphyry dike, observed from 256 m to 275 m depth in drill hole BTG-003 (i.e., DPD I; Figs. 3.20 to 3.23). Propylitic alteration at Bantug is also characterised by chlorite replacement of pyroxene phenocrysts. Figure 4.17 presents examples of <150 µm miarolitic cavities lined with epidote and quartz crystals, and chlorite replacing phenocrysts.

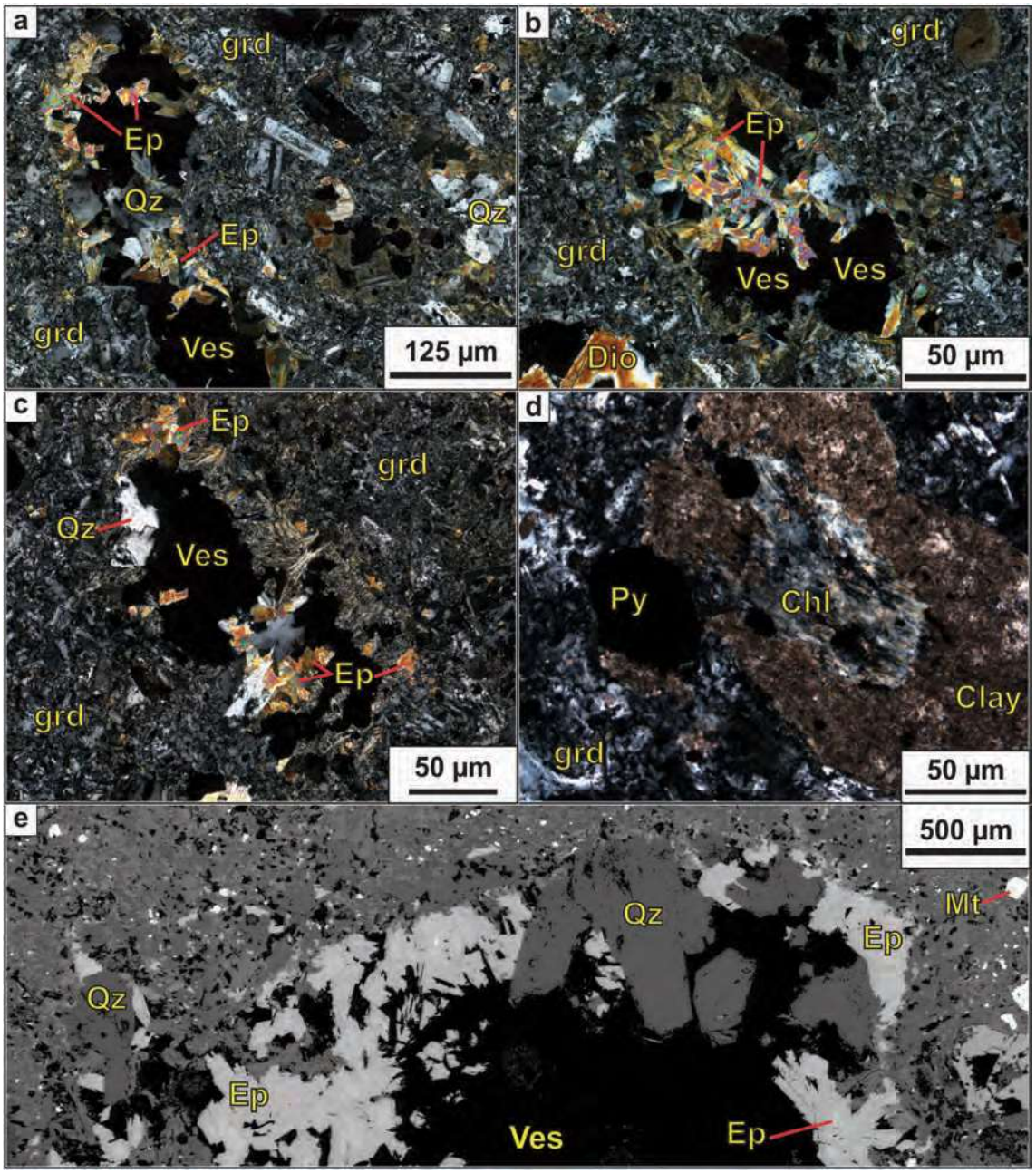

Figure 4.17. Propylitic alteration. a. b. c. Crossed polarisers micrographs of vesicules lined with quartz and epidote. **d.** Crossed polarisers micrograph of chlorite and clay minerals replacing a phenocryst. **e.** Back scattered FE-SEM image of a vesicule lined with epidote and quartz, and the fine-grained groundmass. All images are from a sample at 265.0 m depth in BTG-003. Abbreviations: Chl: chlorite; Ep: epidote; grd: groundmass; Mt: magnetite; Py: pyrite; Qz: quartz; Ves: vesicule

4.3.8. Hydrothermal breccias

4.3.8.1. Natroalunite-pyrite cemented, polymict, hydrothermal breccia

This breccia type was observed in drill holes BTG-003 and BTG-005. The breccia intersects are <50 m thick in BTG-003 and ~250 m thick in BTG-005 (Figs. 4.4, 4.5, 4.8, 4.9). The breccia is clast-supported, with angular to sub-rounded clasts (Fig. 4.18a). Most clasts (~60 %) are <0.5 cm in length, and some clasts (~40 vol %) are up to 4 cm long (Figs. 4.18a). Most clasts are elongated in one dimension, defining tabular shapes that are typically sub-parallel to other clasts (Fig. 4.18a).

Most clasts display intense silicic alteration, and some clasts intense advanced argillic alteration (Fig. 4.18a). Some of the larger and rounded clasts exhibit patchy and vuggy quartz alteration textures (Fig. 4.18a). Due to the variety of textures exhibited by the clasts, this breccia type is interpreted to be polymict, although intense alteration prevents unambiguous identification of clast types.

The breccia cement is predominantly made of natroalunite and pyrite (Figs. 4.18b and 4.18d). SEM analyses also revealed significant amounts of kaolinite in the cement (Figs. 4.18b and 4.18c). Pyrite occurs as euhedral, coarse (2-3 mm) crystals in the cement, and as fine grained (<1 mm) disseminations in the clasts (Fig. 45.18b).

4.3.8.2. Quartz-pyrite cemented, polymict hydrothermal breccia

This cement-supported breccia type was observed in drill hole BTG-005 from 59.6 m to 137 m depth (Figs. 4.4 and 4.8). The breccia also crops out at the surface (Figure 4.1). The cement consists of quartz and pyrite (15 vol %). Pyrite grains are euhedral, <1 mm in size, and are disseminated in quartz. Clasts are polymict, rounded to subrounded, and vary in size from small to large (i.e., 1 cm to 10 cm; Fig. 4.19). Most clasts (~70 %) are silicic-altered and some (~30 %) are advanced argillic-altered. Most of the clasts are aphyric volcanic rocks, but some are plagioclase-phyric volcanic rocks (Fig. 4.19c). Truncated pyrite veins have been observed in some clasts (Figs. 4.19a and 4.19b), as well as patchy and vuggy-textured clasts (Fig. 4.19c).

Juvenile clasts are the product of subsurface interaction of magma with ground water or hydrothermal fluids (Sillitoe, 1985; McPhie et al., 1993; Davies et al., 2008). These clasts are characterised by a distinctive ragged-shape ("wispy"), they occur in the root zones of diatremes, and provide evidence of direct magmatic contribution to breccia formation (Sillitoe, 1985; Davies et al., 2008). Juvenile clasts were recognised in the quartz-pyrite cemented

polymict breccia at Bantug (Fig. 4.19a), implying a magmatic-hydrothermal or volcanic-hydrothermal origin for this breccia.

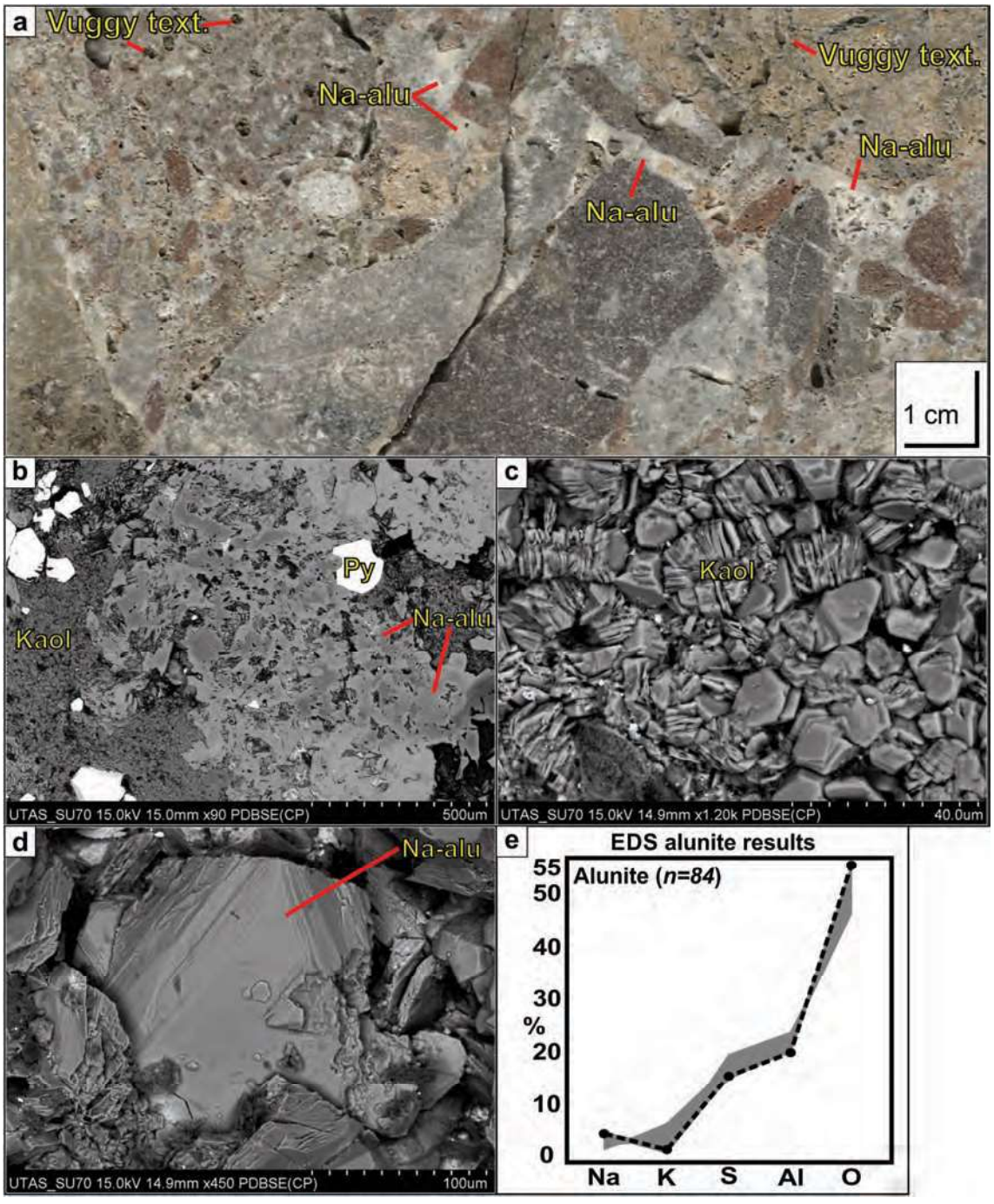

Figure 4.18. Natroalunite-pyrite cemented, polymict, hydrothermal breccia. a. Hand sample, polished slab. Silicic-altered clasts with diverse textures, including vuggy quartz, supported by a natroalunite cement (BTG-003; 260.3 m). **b.** BSE image. Natroalunite crystals intergrown with pyrite and very fine grained kaolinite in a kaolinite groundmass (BTG-003; 470.6 m). **c.** BSE image. Kaolinite crystals in hydrothermal cement (BTG-003; 470.6 m). **d.** BSE image. Large natroalunite crystal (BTG-003; 470.6 m). **e.** EDS results summary diagram. (n: 84 analyses; BTG-003; 470.6 m). Abbreviations: n: number of analyses; Kaol: kaolinite; Na-alu: natroalunite; Py: pyrite; text: texture.

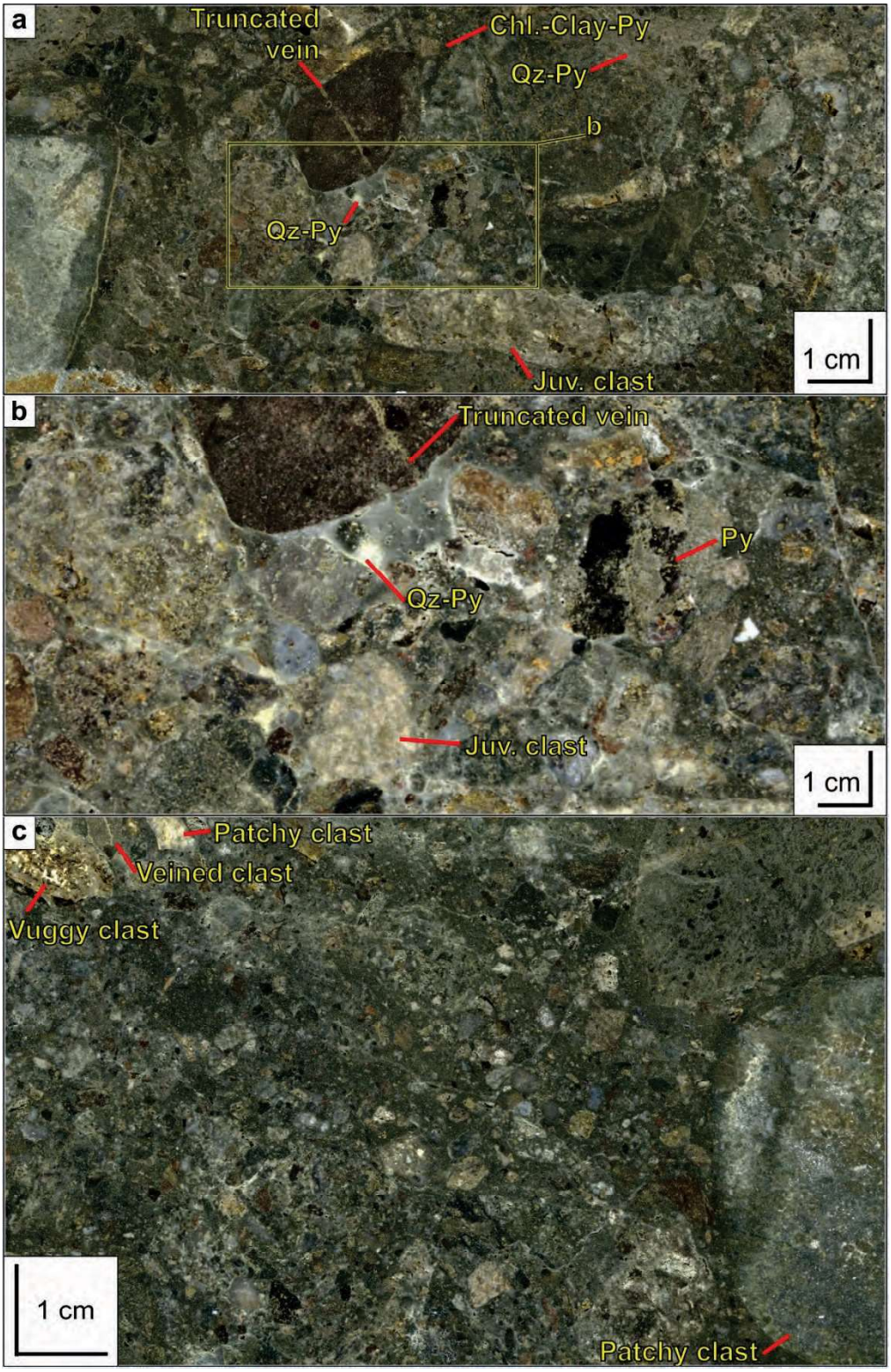

Figure 4.19. Quartz-pyrite cemented hydrothermal breccia. a. Polished slab. Polymict clasts, rounded to subrounded, exhibit different alteration assemblages (e.g., quartz-pyrite, chlorite-clay-pyrite). Clast with a truncated pyrite vein is located on the central left side of the panel. A juvenile clast is located in the central lower part of the panel (BTG-005, 136.5 m). **b.** Detail from panel a. Truncated pyrite vein (top), massive pyrite (right), juvenile clast (bottom), and quartz-pyrite cement. **c.** Polished slab. Large (<5 cm) clasts of pyroxene-phyric (top right) and patchy-altered volcaniclastic rock (right) in a matrix of fine (<1 cm) quartz-clay altered clast, some of them present vuggy texture, patchy texture, and truncated pyrite veins (BTG-005, 136.6 m). **Abbreviations:** Chl: chlorite; Juv: juvenile; Py: pyrite; Qz: quartz.

4.4. Alteration geochemistry of the Bantug lithocap

This section presents the whole rock geochemistry results from surface and drill hole samples from Bantug. A total of 91 results from surface sampling and 216 results from drill hole sampling, collected during AMIRA projects P765A and P1060, make up the dataset available from Bantug. Details from samples are presented in Table 4.1 and whole rock geochemistry results are presented in Appendix G. The dataset was used to create surface and downhole plots from the major elements, high-field strength elements, large-ion lithophile elements, rare earth elements, transition metals, base metals, precious metals, and pathfinder elements. Mass balance calculations and alteration indices, derived from the major elements, are also presented. Results are presented and discussed in terms protolith, hydrothermal alteration, and spatial relation to drill holes. Whole rock geochemistry results are discussed in relation to the spatial distribution of drill holes because of the lithologic and hydrothermal alteration knowledge gained from drill core logging and SWIR analyses. Significant figures are reported consistently throughout this dissertation in accordance with Cooke et al. (2014).

4.4.1. Major elements, mass balance, and alteration indices

4.4.1.1. Major elements

Table 4.3 presents a summary of major element results. Surface and drill hole results from SiO_2 are presented in Figures 4.14 and 4.15. Results from other major elements and total sulphur are presented in Figures 4.20 to 4.23.

Most major elements, as well as total sulphur, present a similar concentration pattern at surface: depletion in the silicic-altered areas, and enrichment in the surrounding argillic and advanced argillic-altered areas (Figs. 4.21 and 4.22). SiO_2 and TiO_2 are the exception; high values are associated with intense silicic alteration.

Results from major elements do not differ significantly between drill holes, as well as between drill hole and surface samples (Table 4.3; Figures 4.20 to 4.23). However, it is worth highlighting that Fe_2O_3 is slightly depleted in surface samples compared with drill hole samples (Table 4.3). This is considered to be the result of weathering of advanced argillic-altered rocks. SiO_2, Al_2O_3, Fe_2O_3, K_2O, and TiO_2 present little variation between rock types (Fig. 4.23). MgO, CaO, Na_2O, P_2O_5, and MnO present the most variations between rock types (Fig. 4.23). The diorite porphyry dike II has the highest MgO, CaO, and Na_2O values compared with other rock types (Fig. 4.23). This is considered to be the result of propylitic alteration. Hornfels presents

a distinctive composition, and contains some of the highest K_2O, P_2O_5, and MnO results (Fig. 4.23).

Table 4.3. Summary of major elements results

	SiO_2	Al_2O_3	Fe_2O_3	MgO	CaO	Na_2O	K_2O	TiO_2	P_2O_5	MnO	Total S
All results											
n	307	307	306	283	302	290	305	307	307	103	307
Min	21.50	0.15	0.20	0.01	0.01	0.01	0.01	0.13	0.01	0.01	0.02
Max	98.54	33.78	19.59	5.03	5.63	3.26	5.33	3.57	0.67	0.24	15.09
Mean	63.36	15.60	6.29	0.63	0.42	0.58	1.84	0.64	0.21	0.05	4.94
Surface											
n	91	91	90	70	87	75	89	91	91	15	91
Min	24.31	0.15	0.20	0.01	0.01	0.02	0.01	0.13	0.01	0.01	0.02
Max	98.54	33.78	10.25	2.24	2.87	2.55	4.75	1.00	0.61	0.06	10.75
Mean	65.64	14.01	4.42	0.32	0.22	0.69	1.85	0.58	0.19	0.03	4.16
BTG-003											
n	74	74	74	74	74	73	74	74	74	33	74
Min	52.43	0.33	0.27	0.02	0.05	0.01	0.03	0.45	0.02	0.01	0.13
Max	96.99	22.15	13.97	5.03	4.74	3.26	3.74	3.57	0.48	0.23	13.19
Mean	63.91	14.90	6.73	0.83	0.68	0.73	1.91	0.75	0.23	0.06	4.85
BTG-005											
n	71	71	71	71	71	71	71	71	71	35	71
Min	45.95	5.90	1.99	0.01	0.05	0.03	0.18	0.36	0.04	0.01	0.27
Max	87.83	23.45	19.59	4.25	2.12	2.78	3.85	1.08	0.48	0.24	15.09
Mean	60.34	17.51	7.62	0.69	0.33	0.36	1.84	0.64	0.23	0.07	5.27
BTG-006											
n	71	71	71	68	70	71	71	71	71	20	71
Min	21.50	0.19	0.50	0.01	0.01	0.01	0.02	0.43	0.04	0.01	0.18
Max	98.09	30.64	10.93	4.12	5.63	2.51	5.33	0.90	0.67	0.17	11.13
Mean	62.91	16.43	6.87	0.67	0.46	0.55	1.74	0.61	0.20	0.06	5.70

Major elements results are in wt % and total sulphur in %. Abbreviations: n: number of analyses; Min: minimum; Max: maximum.

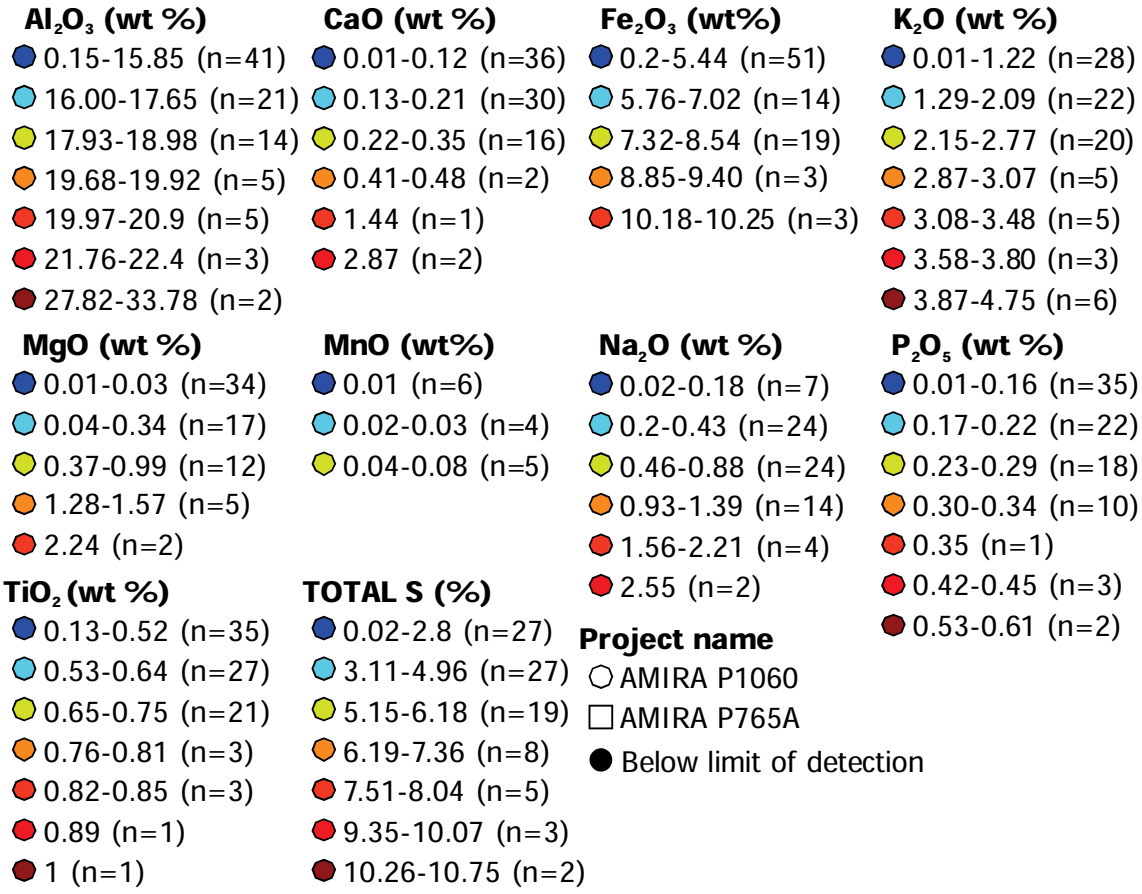

Figure 4.20. Major elements from surface samples. Legend.

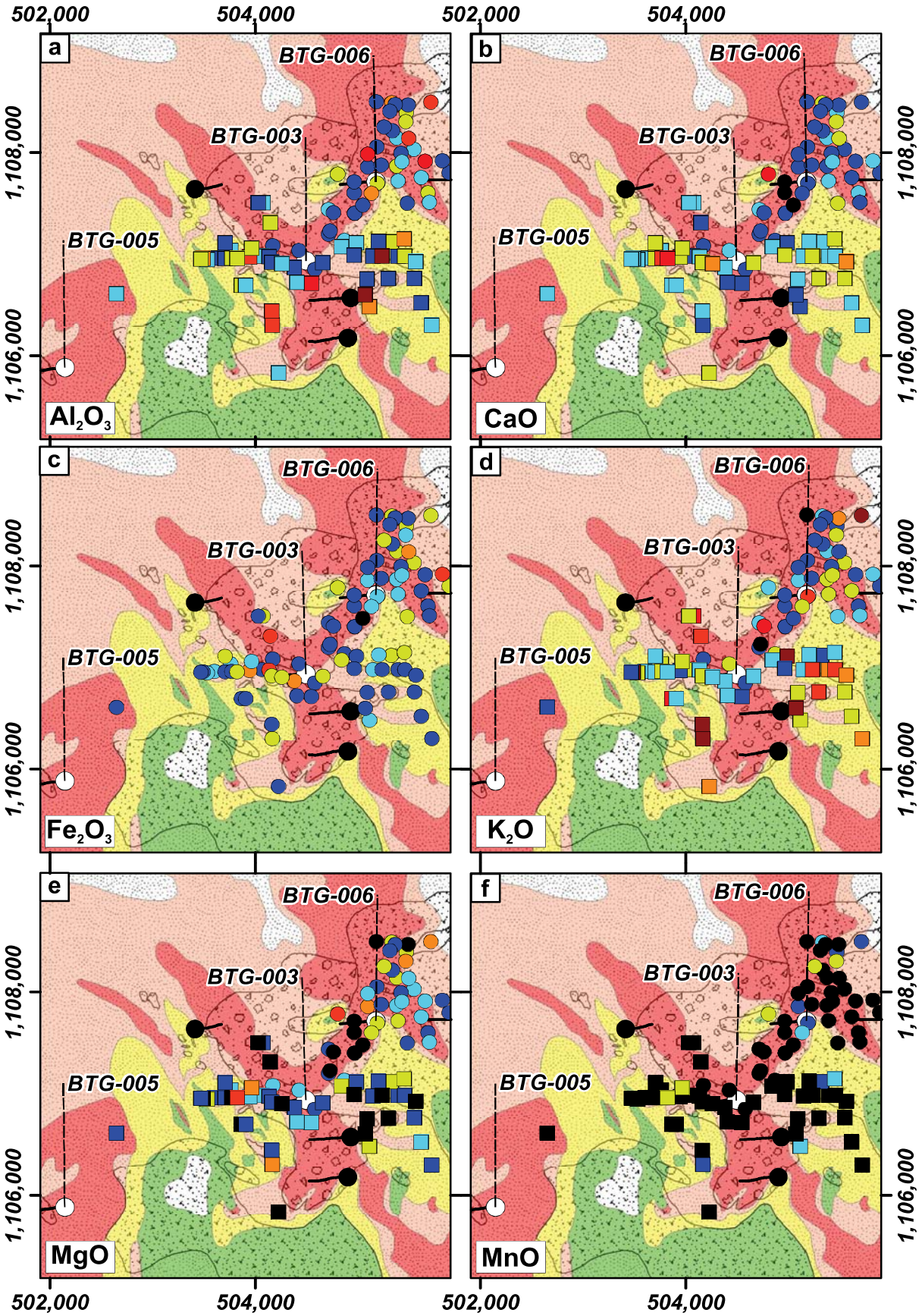

Figure 4.21. Major elements from surface samples. a. Al_2O_3 (wt %). **b.** CaO (wt %). **c.** Fe_2O_3 (wt %). **d.** K_2O (wt %). **e.** MgO (wt %). **f.** MnO (wt %). A legend for the results is presented in Figure 4.20. White drill hole collars indicate drill holes studied in this project. Samples in black indicate values below limit of detection. Rock types and hydrothermal alteration legend as in Figure 4.1.

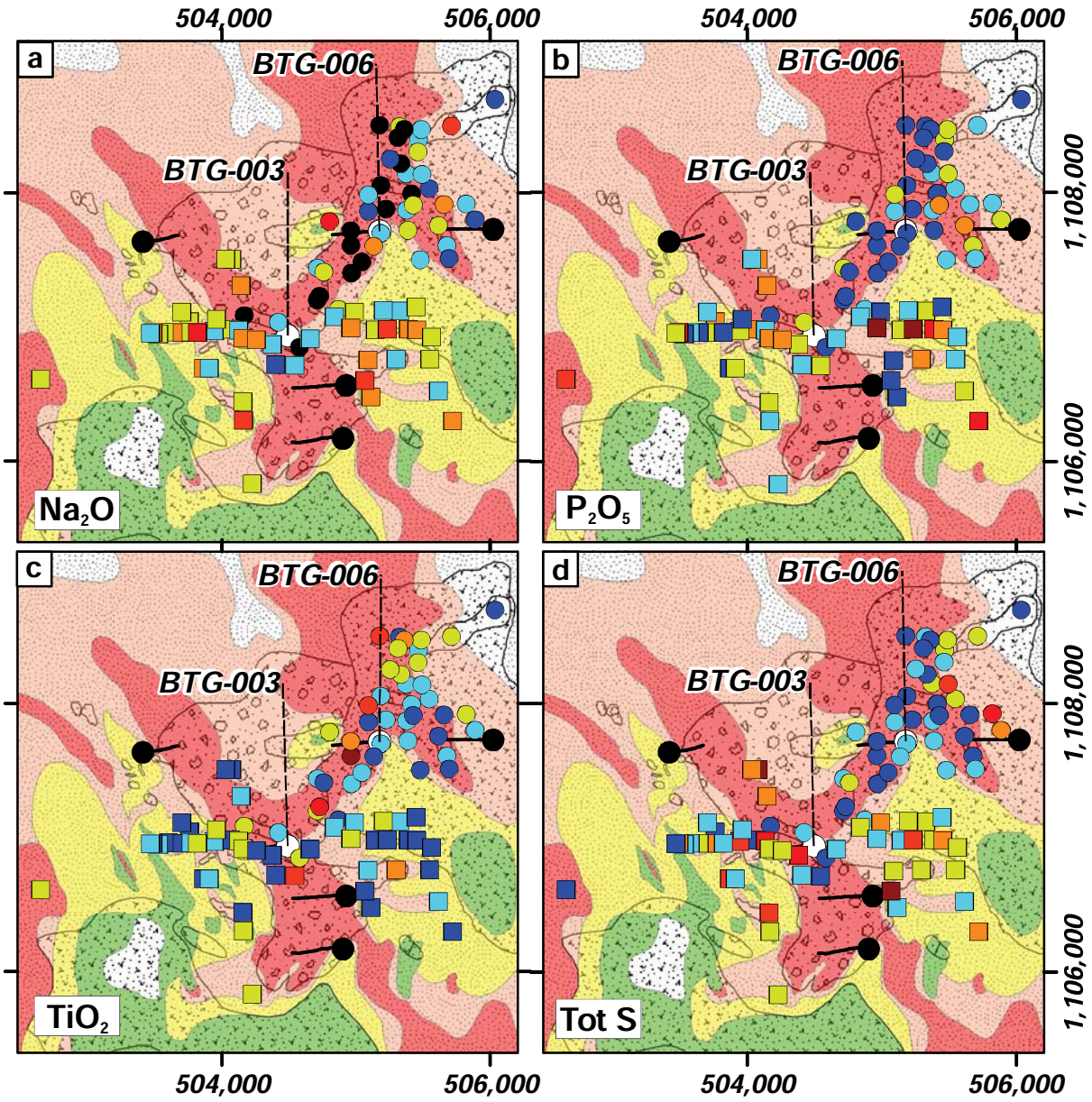

Figure 4.22. Major elements from surface samples (Continued). a. Na_2O (wt %). **b.** P_2O_5 (wt %). **c.** TiO_2 (wt %). **d.** Total sulphur (%). A legend for the results is presented in Figure 4.20. White drill hole collars indicate drill holes studied in this project. Samples in black indicate values below limit of detection. Rock types and hydrothermal alteration legend as in Figure 4.1.

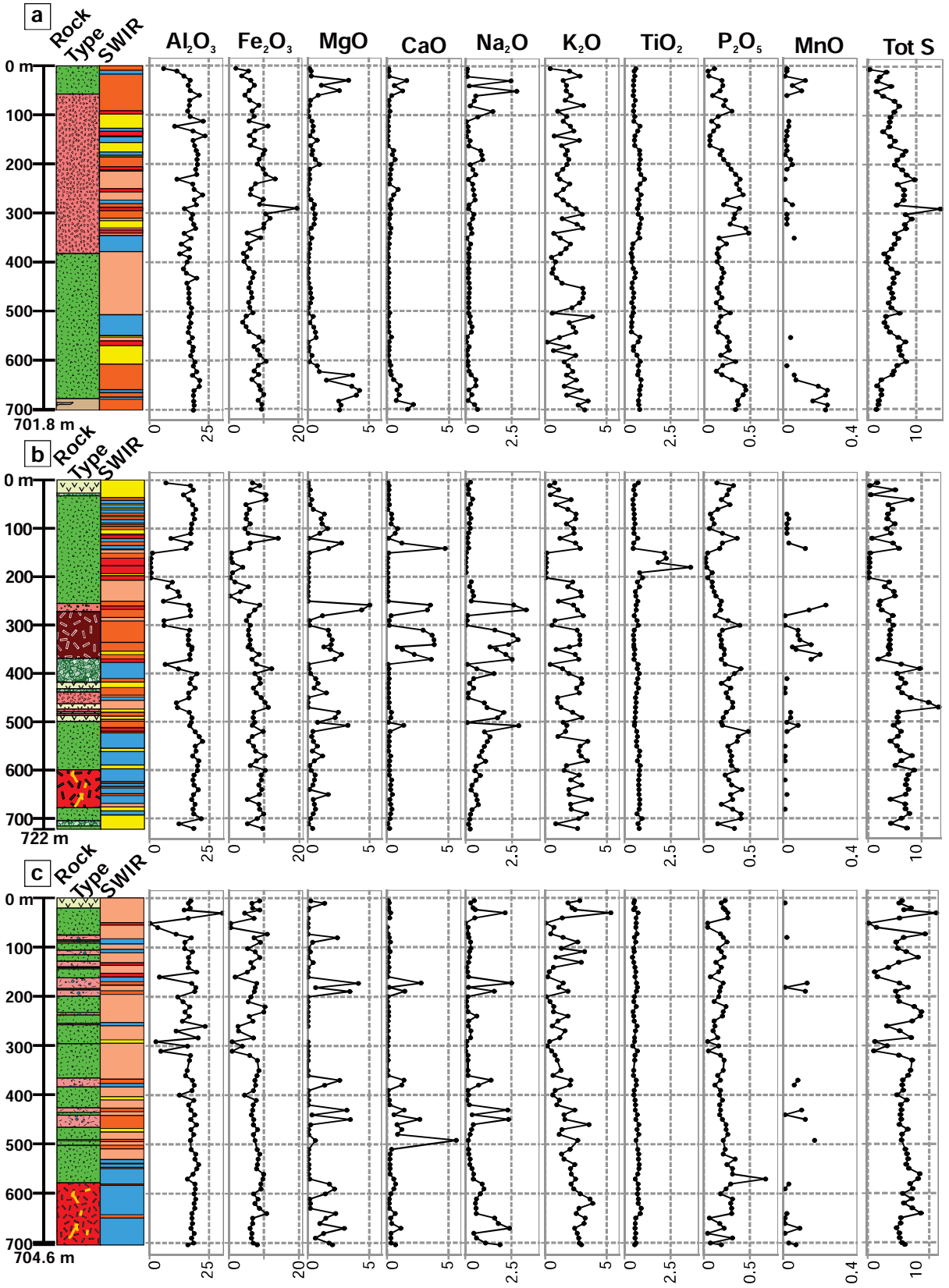

Figure 4.23. Major elements in drill hole whole rock analyses. a. Drill hole BTG-005. **b.** Drill hole BTG-003. **c.** Drill hole BTG-006. Results are in wt % and total sulphur is in %. Rock type and SWIR legend as in Figures 4.4 to 4.6.

4.4.1.2. Mass transfer

Mass transfer techniques aim to quantify the amounts of individual elements added to and subtracted from the rock during alteration in order to overcome the distortions of closure that are inherent in composition data (Gresens, 1967; Grant, 1986; Gifkins et al., 2005). Also, spatial patterns of mass transfer can be used as quantitative exploration vectors (Gifkins et al., 2005).

Mass transfer was calculated following the single precursor method described by MacLean and Barrett (1993), also outlined in detail by Gifkins et al. (2005). Immobile elements were tested on x-y bivariate diagrams with origins at zero, following the method outlined by Barrett and MacLean (1994a) and Gifkins et al. (2005). Zirconium has been used as a monitor element for mass balance calculations by several authors due to its considered least mobility (e.g., Barrett et al., 1990; Barret and MacLean, 1991; Barrett et al., 1993; Barrett and MacLean, 1994a; Barrett and MacLean, 1994b; Barrett and MacLean, 1999; Barrett et al., 2001; Gifkins et al., 2005; Herrmann et al., 2009). Zirconium, Nb, Ti, and TiO_2 results from plagioclase-phyric andesites from Bantug and other areas in the central-eastern Negros (e.g., Sajona et al., 2000; Solidum et al., 2003) were compared in x-y bivariate diagrams. An r value of 0.78 resulted from the Nb-Zr diagram, and an r value of 0.76 resulted from the Zr-Ti and Zr-TiO_2 diagrams. Given its least mobility, zirconium was the immobile elements used for calculations in this section. A composite precursor composition was calculated from 109 analyses available of the plagioclase-phyric andesites from the Quaternary Canlaon Volcanic Complex (Table 4.4; von Biedersee et al., 1995; Sajona et al., 2000; Rae, 2002; Solidum et al., 2003). Mass balance was calculated using Equation 4.1.

$$\Delta^a = \frac{Z^0}{Z^a} \times C^a - C^0 \tag{4.1}$$

Where Δ^a is the absolute mass change in g/100g, C^a is the proportion (wt %) of the component in the altered rock, C^0 is the proportion (wt %) of the component in the precursor, Z^a is the proportion of immobile element in the altered rock, and Z^0 is the proportion of immobile element in the precursor. Table 4.4 presents a summary of mass transfer calculations. Results are presented in Appendix G. Figures 4.24 and 4.25 present results from surface samples, and Figure 4.26 presents results from drill hole samples. Silicic-altered surface samples presented losses in most elements except for SiO_2 and TiO_2 (Figs. 4.2 and 4.25). Samples with mass gains in SiO_2 and TiO_2 are located in the northeast part of the silicic-altered area, ~780 m north of drill hole collar BTG-006 (Figs. 4.24a and 4.25d). Silicic-altered rocks on surface also have

undergone total sulphur gains (Fig. 4.25d). Argillic-altered plagioclase-phyric andesites on surface gained most elements except for Fe_2O_3 and TiO_2 (Figs. 4.24d and 4.25d). Drill core samples from drill hole BTG-005 have the most gains in SiO_2, Al_2O_3, Fe_2O_3, and K_2O (Table 4.4; Fig. 4.26). Enrichment of these elements in plagioclase-phyric andesites in BTG-005 is likely to be due to emplacement of the hydrothermal breccia and its associated alteration. Drill core samples from drill hole BTG-003 presents the greatest losses of Al_2O_3, and Fe_2O_3 due to silicic alteration (Table 4.4; Fig. 4.26). Plagioclase-phyric andesite samples from drill hole BTG-006 present the most gains in total sulphur (Table 4.4; Fig. 4.26). This is likely to be due to emplacement of the diorite porphyry. A major finding, of great value for mineral exploration within lithocaps, is that significant TiO2 enrichment can be detected in silicic-altered rocks using mass transfer calculations. These enriched areas are indicative of a Ti-rich high-temperature fluid. TiO2-rich anomalies may be valuable vectors towards concealed intrusions, potentially mineralised. Mass transfers were only calculated for major elements because whole rock geochemistry results from von Biedersee et al. (1995), Sajona et al. (2000), Rae (2002), Solidum et al. (2003) do not include all groups of elements. Hence, mass transfer calculations of groups of elements, other than the major elements, would have been inaccurate.

Table 4.4. Summary of mass transfer calculations

	SiO_2	Al_2O_3	Fe_2O_3	MgO	CaO	Na_2O	K_2O	TiO_2	P_2O_5	MnO	TOTAL S	Zr (ppm)
All results												
n	151	151	151	151	151	151	151	151	151	151	151	151
Min	-42.25	-18.11	-6.02	-2.95	-7.33	-3.79	-1.93	-0.28	-0.22	-0.11	-0.04	
Max	182.8	33.00	4.87	0.62	-3.24	-0.38	7.62	0.99	0.71	0.04	19.85	
Mean	-3.61	-5.48	-1.45	-2.61	-7.11	-3.46	-0.56	-0.07	-0.07	-0.10	3.89	136.4
BTG-003												
n	36	36	36	36	36	36	36	36	36	36	36	36
Min	-37.72	-18.11	-6.02	-2.95	-7.31	-3.79	-1.93	-0.28	-0.22	-0.11	-0.02	
Max	-6.75	-2.92	3.00	-0.28	-3.24	-1.44	0.50	0.30	0.02	-0.01	7.04	
Mean	-19.91	-8.82	-2.40	-2.51	-7.02	-3.52	-0.70	-0.11	-0.10	-0.10	2.83	184.8
BTG-005												
n	36	36	36	36	36	36	36	36	36	36	36	36
Min	-25.57	-13.39	-4.53	-2.94	-7.28	-3.77	-1.78	-0.21	-0.19	-0.11	0.16	
Max	24.63	1.33	2.82	0.62	-5.64	-0.92	1.56	0.18	0.06	0.04	6.88	
Mean	-0.66	-3.24	-0.31	-2.26	-7.07	-3.49	-0.32	-0.07	-0.05	-0.08	3.96	116.2
BTG-006												
n	42	42	42	42	42	42	42	42	42	42	42	42
Min	-42.25	-17.75	-5.36	-2.95	-7.32	-3.78	-1.89	-0.21	-0.18	-0.11	0.38	
Max	182.8	5.23	4.87	-2.69	-6.52	-2.14	2.14	0.99	0.18	-0.09	9.64	
Mean	4.38	-5.38	-0.82	-2.92	-7.19	-3.57	-0.96	-0.02	-0.07	-0.10	4.72	123.0
Surface												
n	37	37	37	37	37	37	37	37	37	37	37	37
Min	-24.45	-18.10	-5.98	-2.95	-7.33	-3.79	-1.93	-0.22	-0.21	-0.11	-0.04	
Max	93.97	33.00	2.74	-0.85	-4.64	-0.38	7.62	0.24	0.71	-0.06	19.85	
Mean	0.32	-4.52	-2.34	-2.69	-7.13	-3.27	-0.21	-0.07	-0.05	-0.10	3.91	124.33
Precursor composition												
n	109	109	109	109	109	109	109	109	109	109	109	
Mean	58.71	18.22	6.16	2.96	7.33	3.79	1.94	0.56	0.22	0.11	0.06	97.44

Results are absolute mass changes in g/100g (i.e., Δ^a)
Precursor composition calculated from 109 analyses from von Biedersee et al. (1995); Sajona et al. (2000); Rae (2002); Solidum et al. (2003).

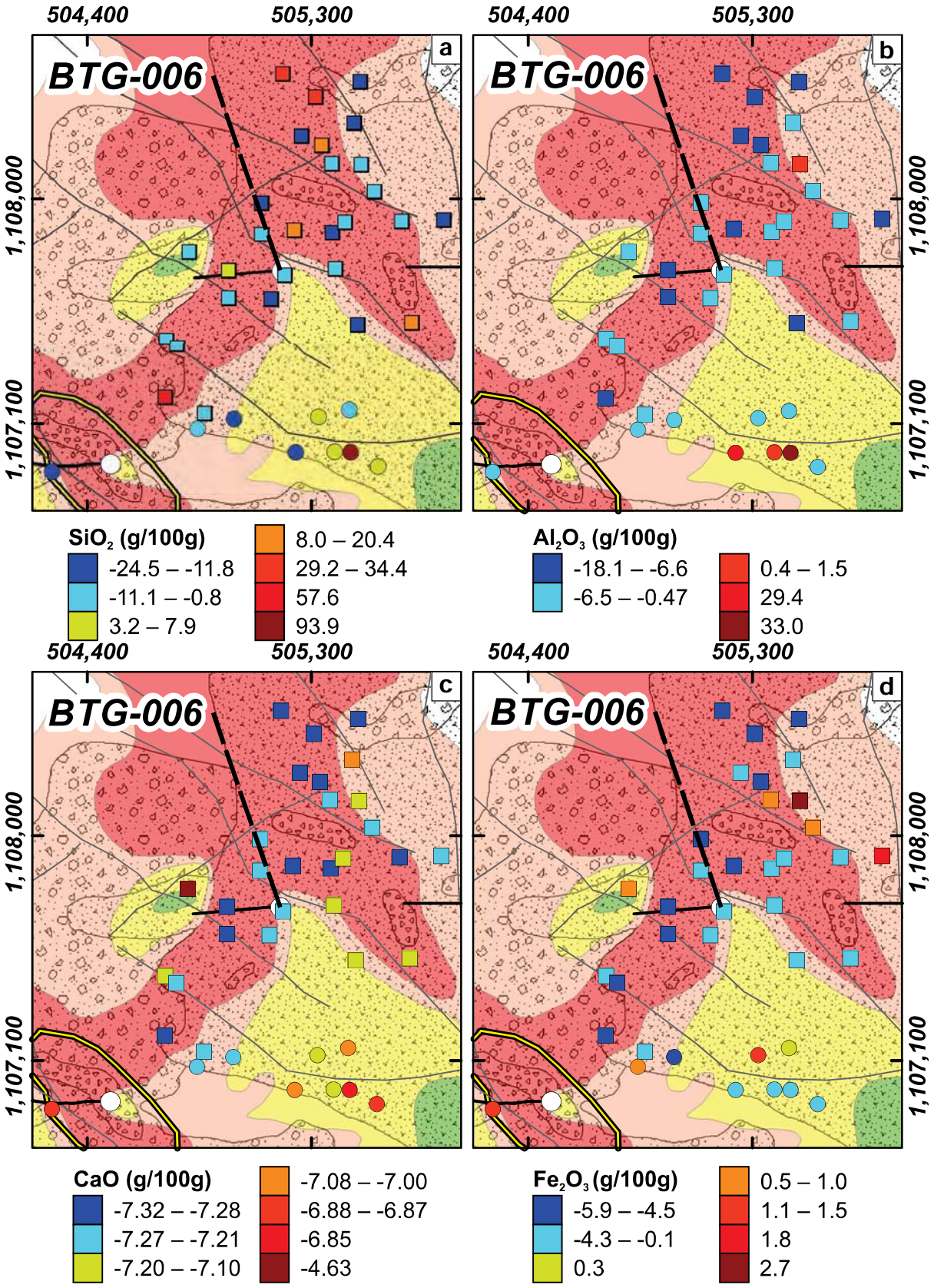

Figure 4.24. Mass transfer calculations of surface samples. Results are in g/100g (i.e., Δ^a). **a.** Al_2O_3. **b.** CaO. **c.** Fe_2O_3. **d.** K_2O. **e.** MgO. **f.** MnO. Rock type and hydrothermal alteration legend as in Figure 4.1.

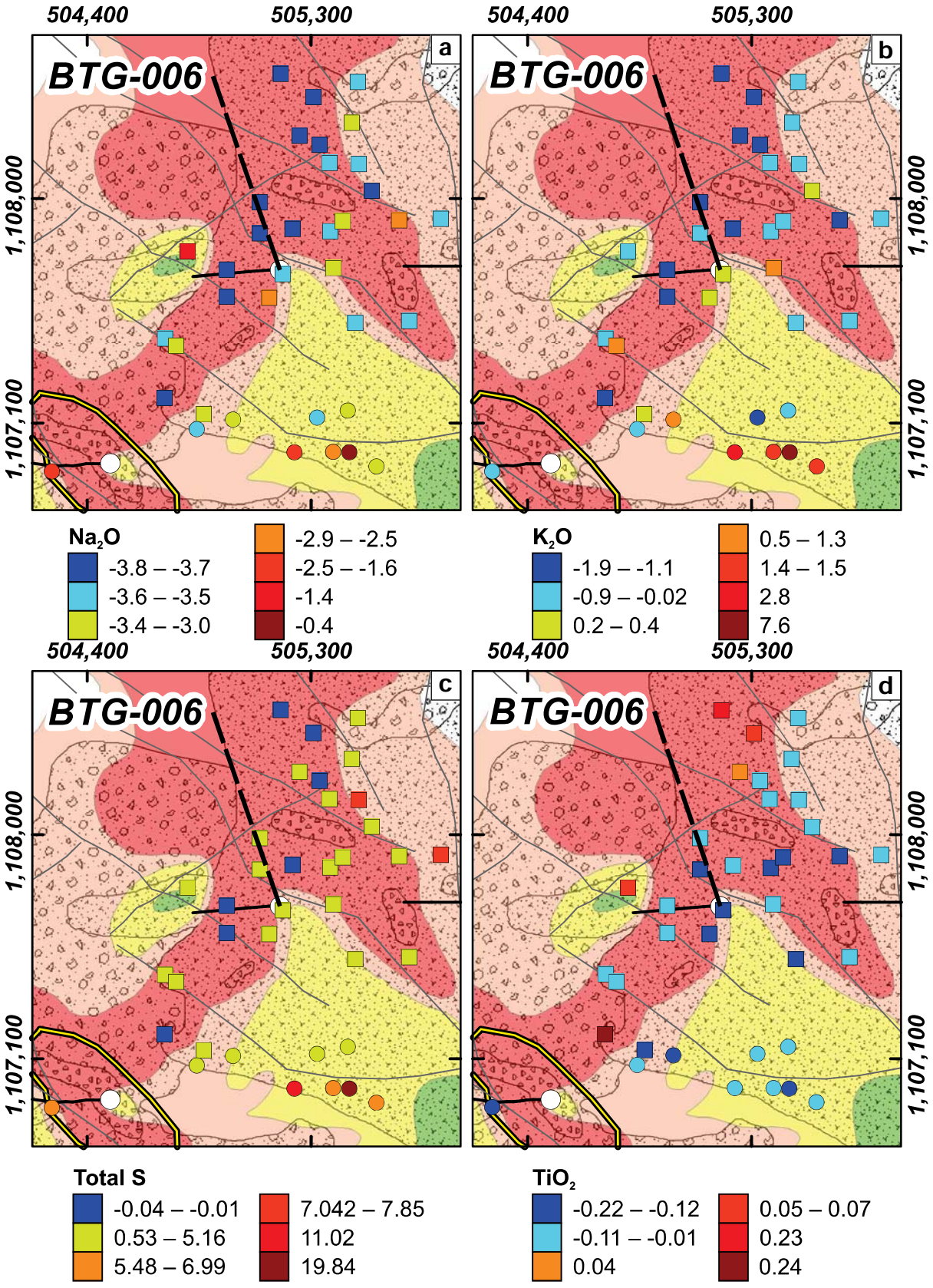

Figure 4.25. Mass transfer calculations of surface samples. Results are in g/100g (i.e., Δ^a). **a.** Na_2O. **b.** K_2O. **c.** Total sulphur. **d.** TiO_2. Rock type and hydrothermal alteration legend as in Figure 4.1.

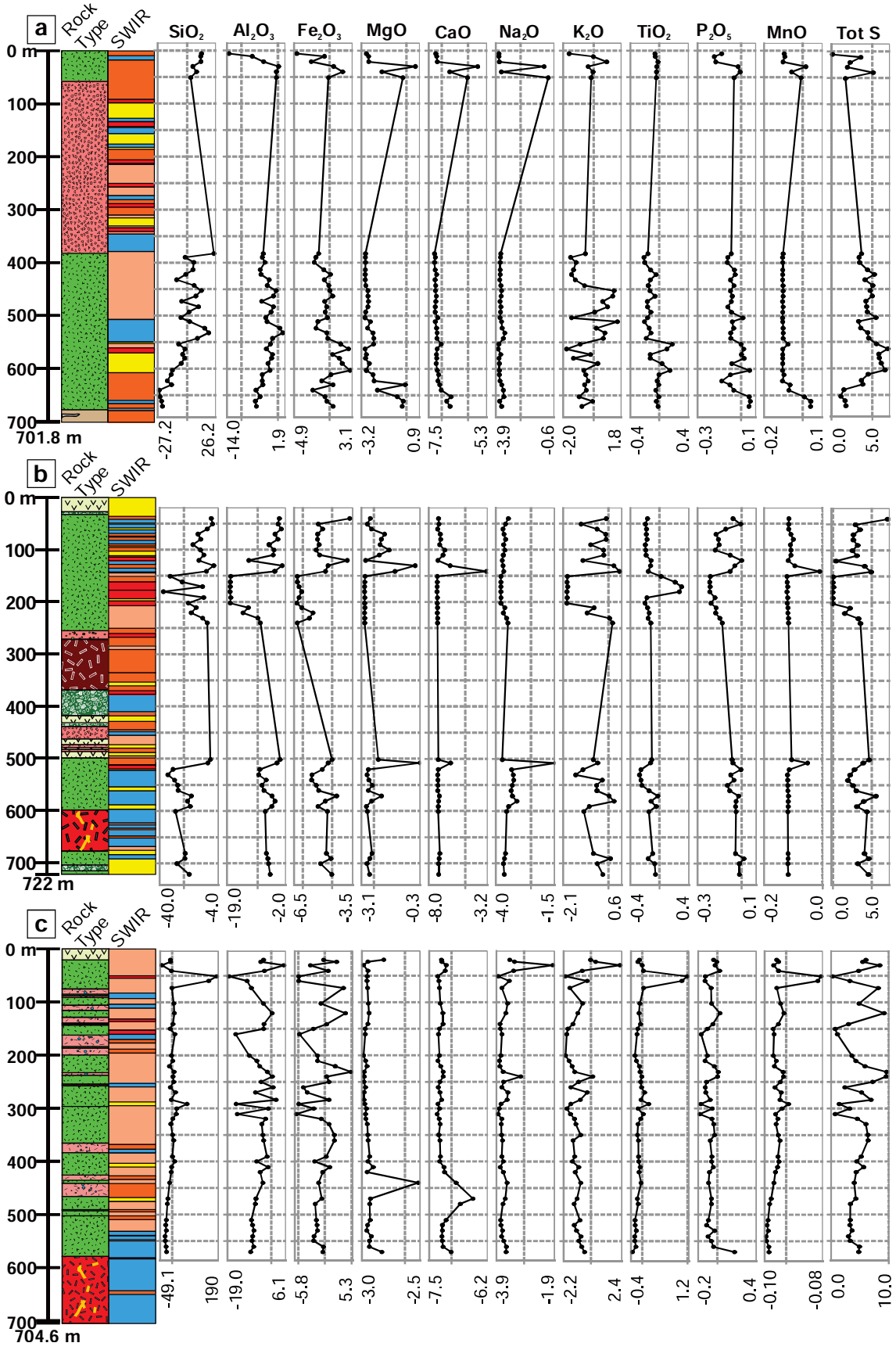

Figure 4.26. Mass transfer in drill hole samples. Results are in g/100g (i.e., Δ^a). **a.** BTG-005. **b.** BTG-003. **c.** BTG-006. Rock type and SWIR legend as in Figures 4.4 to 4.6.

4.4.1.3. Alteration indices

Alteration indices are geochemical representations of hydrothermal mineral assemblages designed to facilitate discrimination of alteration styles, quantification of alteration intensity, and exploration vectors (Gifkins et al., 2005). Details on alteration indices are presented in Chapter 3, section 3.5.1. Section 4.4.1.3. presents surface and drill hole results from the alteration index (AI; Ishikawa et al.,1976), and the advanced argillic alteration index (AAAI; Williams and Davidson, 2014). The two indices were calculated from whole rock geochemistry results. Table 4.5 presents a summary of the results. Complete results are presented in Appendix G. Figure 4.28 presents results from surface samples, and Figure 4.29 presents results from drill hole samples.

High AI values (i.e., 90.9-96.3; Fig. 4.27) came from silicic-altered rocks immediately to the northeast of drill hole collar BTG-006 (Fig. 4.28a). These results define a surface area of 670 m by 650 m (Fig. 4.28a). High AAAI values (i.e., 94.9-96.9; Fig. 4.27) on surface are associated with advanced argillic and silicic-altered plagioclase-phyric andesites (Fig. 4.28b). The highest AAAI value (i.e., 96.9) occurs 200 m west from drill hole collar BTG-007 (Fig. 4.28b). Most surface samples have low AAAI values (i.e., 42.3-78.2), except for those samples northeast of drill hole collar BTG-006 (Fig. 4.28b). The lowest LOI values (i.e., 0.4-8.1 %) on surface clearly denote the silicic-altered area to the northeast and southwest of drill hole collar BTG-006 (Fig. 4.28c). The highest LOI values (i.e., 30.0-32.63 %) on surface are associated with argillic and advanced argillic-altered plagioclase-phyric and aphyric andesites, which surround the silicic-altered area (Fig. 4.28c).

Table 4.5 presents a summary of the AI, AAAI, and LOI (%) results by rock type, surface, and drill hole. Figure 4.29 presents AI, AAAI, and LOI (%) drill hole results coupled with rock types and SWIR results. The highest AI values came from advanced argillic-altered plagioclase-phyric andesites from drill holes BTG-005 and BTG-006, AI: 84.41 and 79.60 respectively (Table 4.5; Figs. 4.29a and 4.29c). The highest AAAI results came from advanced argillic-altered aphyric and plagioclase-phyric andesites from drill hole BTG-006, AAAI: 94.28 and 88.53 respectively (Table 4.5; Figs. 4.29c). High AAAI values are also associated with advanced argillic-altered andesitic volcaniclastic breccia in BTG-003 (i.e., 88.10; Table 4.5; Fig. 4.29b). Plagioclase-phyric andesite and hydrothermal breccia samples from BTG-005 also yielded high AAAI results, 86.12 and 84.03 respectively (Table 4.5; Fig. 4.29a).

The highest LOI values resulted from advanced argillic-altered hydrothermal breccia samples from drill holes BTG-003 and BTG-005 (i.e., 14.98 and 11.96, respectively; Table 4.5; Figs. 4.29b and 4.29a).

Table 4.5. Summary of alteration indices and LOI results

	Surface				BTG-003			BTG-005			BTG-006			
AI	**n**	**Min**	**Max**	**Mean**	**n**	**Min**	**Max**	**Mean**	**n**	**Min**	**Max**	**Mean**	**n**	**Min**	**Max**	**Mean**
All values	59	24.14	96.26	73.39	73	41.77	93.41	70.31	71	38.04	95.24	78.65	67	34.37	94.64	73.18
And	19	39.44	83.38	69.65	33	45.00	91.84	73.87					30	34.38	94.64	71.68
PA	25	37.84	96.26	77.33	8	54.12	93.41	74.68	30	50.00	93.04	82.41	10	72.98	87.74	79.60
Abx	11	65.84	87.01	76.09	7	55.99	91.77	72.11								
Hbx	4	24.14	82.42	59.15	4	45.66	78.63	61.48	38	38.04	95.24	75.92				
DP					7	72.07	83.62	77.81					14	60.43	85.15	75.14
DPD I					11	41.77	90.27	56.78								
DPD II					3	51.48	71.24	59.06								
DPD III													13	36.02	92.84	69.56
Horn									3	67.58	87.39	75.54				
AAAI	**n**	**Min**	**Max**	**Mean**	**n**	**Min**	**Max**	**Mean**	**n**	**Min**	**Max**	**Mean**	**n**	**Min**	**Max**	**Mean**
All values	59	42.31	96.91	84.35	73	32.60	99.16	77.93	71	44.70	96.88	83.77	67	36.61	99.45	82.30
And	19	42.31	92.79	82.99	33	45.51	99.16	83.59					30	79.30	99.45	94.29
PA	25	42.31	95.11	84.54	8	43.96	95.41	78.58	30	50.38	96.88	86.13	10	77.96	92.60	88.54
Abx	11	63.83	94.89	83.70	7	75.45	96.73	88.10								
Hbx	4	84.63	96.91	91.40	4	58.30	94.99	78.89	38	44.70	96.38	84.04				
DP					7	68.19	88.09	80.08					14	48.20	86.78	69.19
DPD I					11	40.63	95.43	58.94								
DPD II					3	32.60	94.52	53.66								
DPD III													13	36.61	90.21	63.95
Horn									3	52.24	62.99	56.82				
LOI (%)	**n**	**Min**	**Max**	**Mean**	**n**	**Min**	**Max**	**Mean**	**n**	**Min**	**Max**	**Mean**	**n**	**Min**	**Max**	**Mean**
All values	91	0.400	32.60	11.94	74	0.7000	20.90	9.070	71	2.600	19.50	10.28	71	0.400	34.10	9.325
And	25	6.500	30.00	15.97	34	0.7000	16.30	8.912					34	0.400	34.10	10.03
PA	37	0.4000	32.60	10.96	8	7.200	12.70	9.375	30	5.800	12.70	8.503	10	8.200	13.20	9.420
Abx	17	1.000	24.60	13.58	7	5.800	10.50	8.343								
Hbx	12	0.4000	16.50	4.217	4	7.700	20.90	14.98	38	2.600	19.50	11.96				
DP					7	6.300	11.40	9.714					14	6.000	9.500	7.871
DPD I					11	5.000	11.00	8.009								
DPD II					3	5.100	7.500	6.267								
DPD III													13	7.000	11.60	8.969
Horn									3	6.400	7.300	6.766				

Abbreviations: AI: Alteration index (Ishikawa et al., 1976); AAAI: Advanced argillic alteration index (Williams and Davidson, 2004); LOI: lost on ignition; n: number of analyses; Min: minimum value; Max: maximum value; Mean: mean value. AI and AAAI are dimensionless and LOI results are in percent (%); And: aphyric andesite; PA: plagioclase phyric andesite; Abx: andesitic volcaniclastic breccia; Hbx: hydrothermal breccia; DP: diorite porphyry; DPD I to III: diorite porphyry dike I to III; Horn: hornfels. .

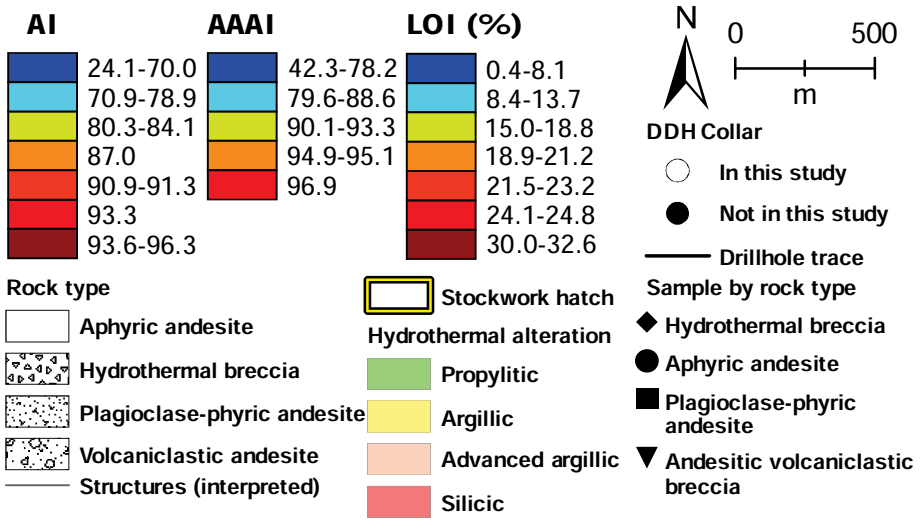

Figure 4.27. AI, AAAI, and LOI results from surface samples. Legend.

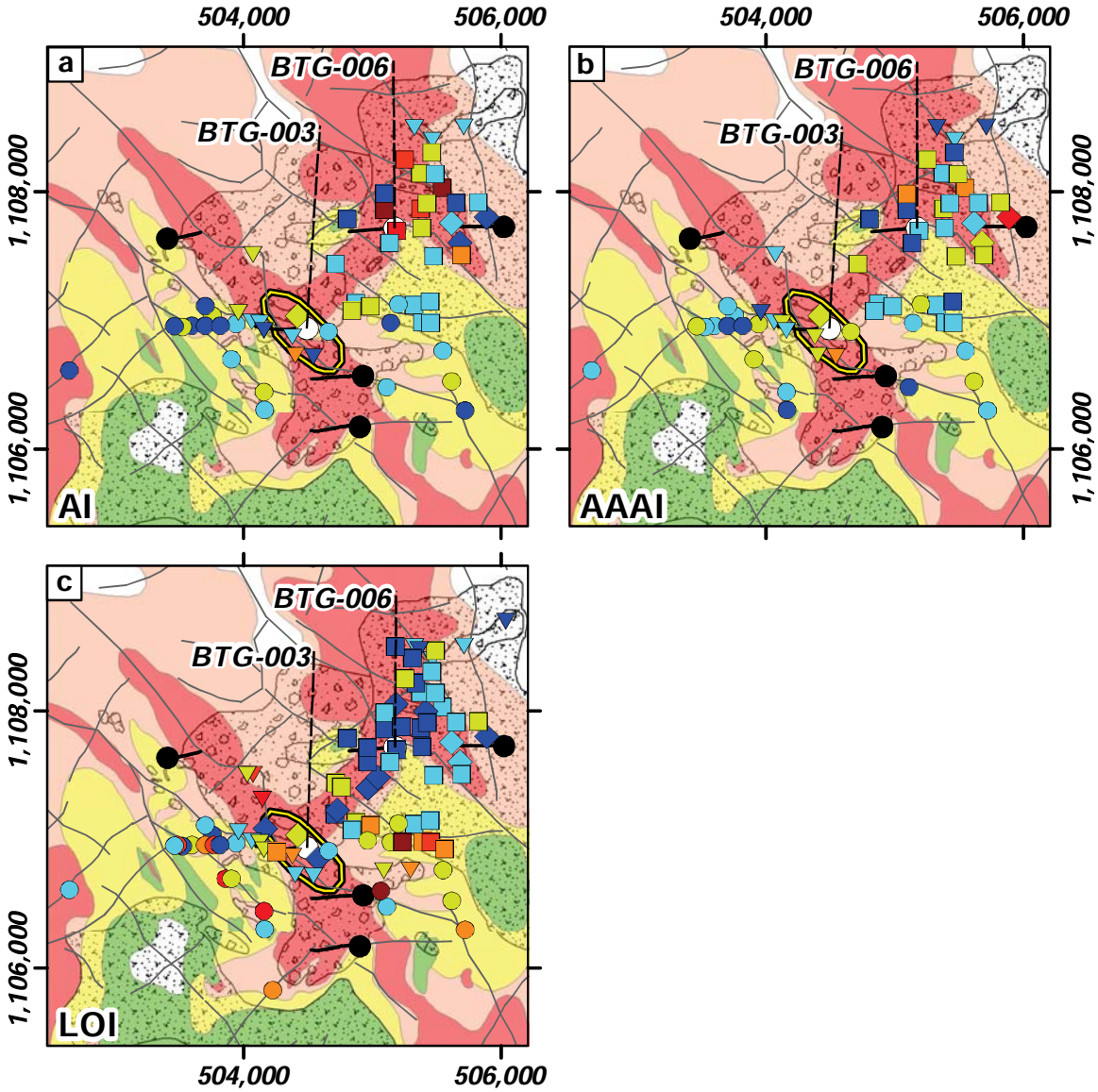

Figure 4.28. AI, AAAI, and LOI results from surface samples. a. Alteration index (AI) of Ishikawa et al. (1976). **b.** Advanced argillic alteration index (AAAI). **c.** Lost on ignition (LOI). AI and AAAI are dimensionless and LOI results are in percent (%). Rock type and hydrothermal alteration legend as in Figure 4.1.

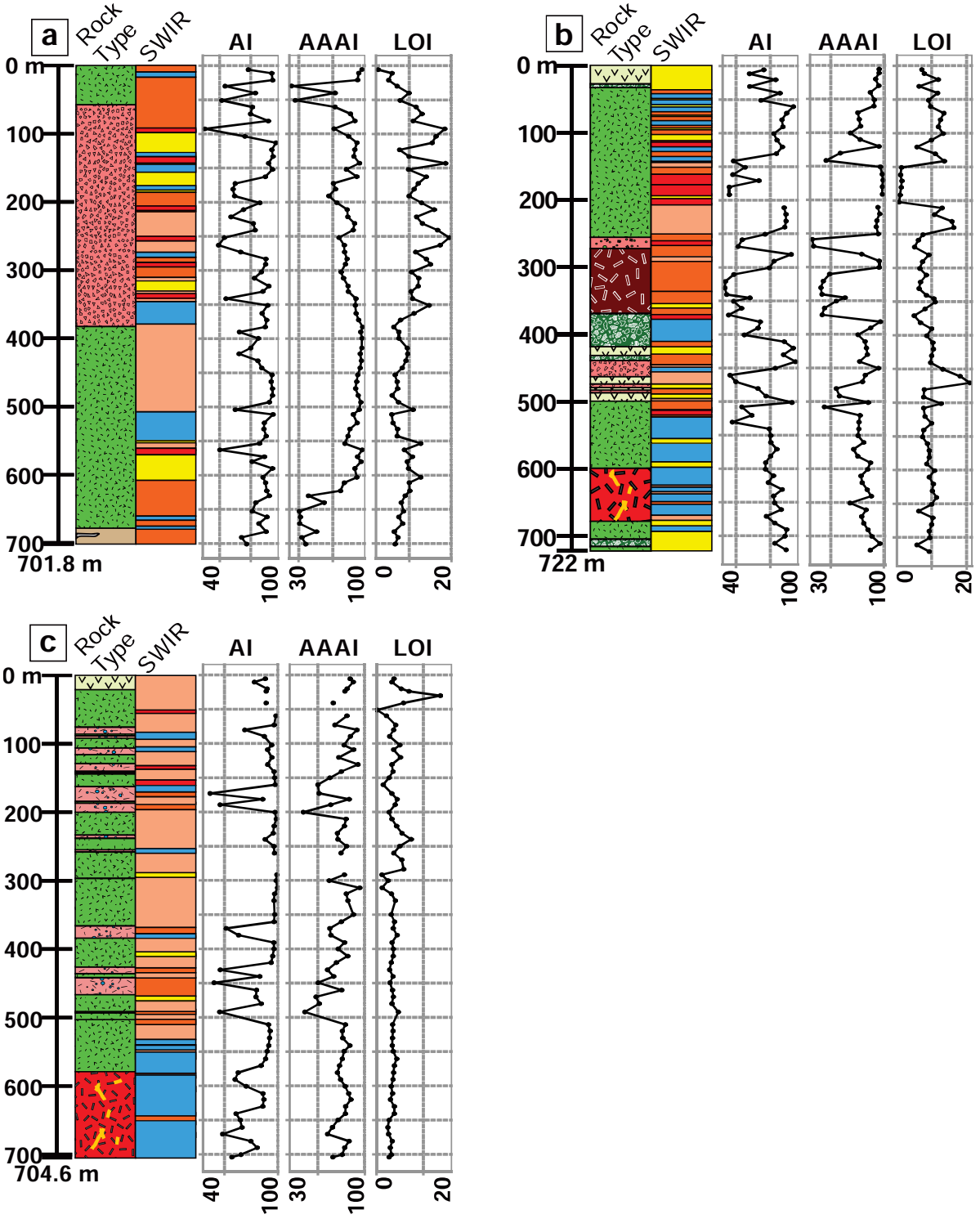

Figure 4.29. AI, AAAI, and LOI results from drill hole samples. a. Drill hole BTG-005. **b.** Drill hole BTG-005. **c.** Drill hole BTG-006. AI and AAAI are dimensionless, and LOI is in %. Rock type and SWIR legend as in Figures 4.4 to 4.6.

4.4.2. High-field strength elements (HFSE)

Table 4.6 summarises the results of the HFSE (i.e., Hf, Nb, Ta, Y, and Zr). Figures 4.31 and 4.32 present surface and drill hole results, respectively. Whole rock geochemistry results are presented in Appendix G.

Silicic-altered plagioclase-phyric andesites at 660 m northeast of drill hole collar BTG-006 make up a cluster of high Nb and Ta, and low Y and Zr (Fig. 4.31). Niobium and Ta values range from 6.6 to 7.5 ppm, and 0.4 and 0.7 ppm, respectively (Figs. 4.30 and 4.31). Most Y and Zr results in this cluster are low (i.e., 1.7 to 5.6 ppm, and 40.5 to 113.7 ppm, respectively; Table 4.6; Figs. 4.30 and 4.31). The HFSE geochemical signature of this cluster is likely to be the surface expression of the diorite porphyry at depth.

The cluster of samples over the surface trace of drill hole BTG-003 presents low value results of most elements (Fig. 4.31). Samples surrounding drill hole collar BTG-003 present high Hf, Nb, Ta, and Zr results (Fig. 4.31). This is interpreted to be due to emplacement of the diorite porphyry dikes at depth. A cluster of argillic-altered plagioclase-phyric samples at 840 m east of drill hole collar BTG-003 presents low value results for all HFSE (Table 4.6; Figs. 4.30 and 4.31).

High Hf, Nb, and Ta results are associated with silicic and advanced argillic-altered aphyric andesites in BTG-003, and hornfels in BTG-005 (Table 4.6; Figs. 4.32a and 4.32b). Advanced argillic-altered plagioclase-phyric andesite and phyllic-altered diorite porphyry samples from BTG-006 also returned high Hf, Nb, and Ta values (Table 4.6; Fig. 4.32c). Phyllic-altered diorite porphyry and argillic-altered diorite porphyry dike III samples from BTG-006 yielded the highest Y mean values (i.e., 24.5 and 22.6 ppm, respectively; Table 4.6; Fig. 4.32c). Phyllic-altered diorite porphyry and argillic-altered diorite porphyry dike I samples from BTG-003 returned significantly high Y values (i.e., 21.7 and 20.9 ppm, respectively; Table 4.6; Fig. 4.32c). Hornfels from BTG-005 and silicic-altered aphyric andesite from BTG-003 yielded the highest Zr mean values (i.e., 192.2 ppm and 188.4 ppm, respectively; Table 4.6; Fig. 4.32c and 4.32a).

Table 4.6. Summary of HFSE results.

	Surface				BTG-003				BTG-005				BTG-006			
Hf (ppm)	**n**	**Min**	**Max**	**Mean**	**n**	**Min**	**Max**	**Mean**	**n**	**Min**	**Max**	**Mean**	**n**	**Min**	**Max**	**Mean**
All values	91	0.9000	112.8	4.619	74	1.800	11.30	4.209	71	2.300	5.900	3.462	71	1.100	6.100	3.270
And	25	1.900	4.800	3.408	34	3.100	11.30	4.847					34	1.100	4.400	2.965
PA	37	0.9000	5.100	3.405	8	2.900	3.900	3.500	30	2.500	4.700	3.247	10	3.000	5.300	4.250
Abx	17	2.400	5.000	3.582	7	1.800	4.200	3.414								
Hbx	12	1.900	112.8	12.35	4	2.500	3.800	3.300	38	2.300	5.900	3.526				
DP					7	3.000	4.600	4.071					14	2.100	6.100	3.729
DPD I					11	2.800	5.900	3.773								
DPD II					3	2.500	5.500	3.867								
DPD III													13	2.200	4.000	2.823
Horn									3	4.600	5.000	4.800				
Nb (ppm)	**n**	**Min**	**Max**	**Mean**	**n**	**Min**	**Max**	**Mean**	**n**	**Min**	**Max**	**Mean**	**n**	**Min**	**Max**	**Mean**
All values	91	1.600	7.700	4.614	74	3.600	18.90	5.886	71	3.000	7.300	4.437	71	2.400	8.500	4.346
And	25	2.700	6.600	4.368	34	3.900	18.90	6.841					34	2.400	5.400	3.879
PA	37	1.600	7.700	4.597	8	4.100	7.600	4.975	30	3.000	6.100	4.017	10	3.600	6.700	5.330
Abx	17	2.800	7.500	4.765	7	5.000	6.500	5.700								
Hbx	12	3.800	6.400	4.967	4	3.600	4.500	4.175	38	3.400	7.300	4.579				
DP					7	4.600	6.800	5.386					14	3.000	8.500	5.607
DPD I					11	3.800	6.400	4.964								
DPD II					3	3.800	6.000	4.767								
DPD III													13	2.700	5.100	3.454
Horn									3	6.600	7.000	6.833				
Ta (ppm)	**n**	**Min**	**Max**	**Mean**	**n**	**Min**	**Max**	**Mean**	**n**	**Min**	**Max**	**Mean**	**n**	**Min**	**Max**	**Mean**
All values	91	0.1000	0.7000	0.3198	74	0.1000	1.100	0.3878	71	0.2000	0.5000	0.3000	70	0.2000	0.6000	0.3143
And	25	0.2000	0.6000	0.3160	34	0.2000	1.100	0.4647					34	0.2000	0.4000	0.2824
PA	37	0.1000	0.7000	0.3108	8	0.1000	0.4000	0.2875	30	0.2000	0.4000	0.3100	10	0.3000	0.5000	0.3800
Abx	17	0.2000	0.6000	0.3353	7	0.2000	0.5000	0.3143								
Hbx	12	0.2000	0.4000	0.3333	4	0.2000	0.3000	0.2500	38	0.2000	0.5000	0.2816				
DP					7	0.3000	0.6000	0.3857					13	0.2000	0.6000	0.3923
DPD I					11	0.3000	0.5000	0.3455								
DPD II					3	0.1000	0.5000	0.3000								
DPD III													13	0.2000	0.3000	0.2692
Horn									3	0.4000	0.5000	0.4333				

Abbreviations: n: number of analyses; Min: minimum value; Max: maximum value; Mean: mean value. Results are in parts per million (ppm); And: aphyric andesite; PA: plagioclase phyric andesite; Abx: andesitic volcaniclastic breccia; Hbx: hydrothermal breccia; DP: diorite porphyry; DPD I to III: diorite porphyry dike I to III; Horn: hornfels.

Table 4.6. Summary of HFSE results (Continued).

	Surface				BTG-003				BTG-005				BTG-006			
Y (ppm)	**n**	**Min**	**Max**	**Mean**	**n**	**Min**	**Max**	**Mean**	**n**	**Min**	**Max**	**Mean**	**n**	**Min**	**Max**	**Mean**
All values	91	1.700	32.90	9.022	74	2.000	64.90	17.41	71	2.000	178.0	16.05	71	0.2000	77.80	14.08
And	25	2.100	32.90	10.08	34	6.500	64.90	18.26					34	0.2000	16.90	5.282
PA	37	2.100	32.90	9.530	8	2.700	30.10	16.96	30	2.000	178.0	15.03	10	11.00	35.90	18.32
Abx	17	1.700	20.20	8.624	7	2.000	26.60	11.60								
Hbx	12	1.700	15.60	5.808	4	2.700	13.30	5.750	38	5.300	39.50	16.60				
DP					7	11.50	31.40	21.70					14	14.20	69.90	24.45
DPD I					11	15.10	37.30	20.95								
DPD II					3	9.100	19.10	15.17								
DPD III													13	5.500	77.80	22.66
Horn									3	18.30	20.00	19.27				
Zr (ppm)	**n**	**Min**	**Max**	**Mean**	**n**	**Min**	**Max**	**Mean**	**n**	**Min**	**Max**	**Mean**	**n**	**Min**	**Max**	**Mean**
All values	91	40.50	1662	142.3	74	93.30	424.8	163.0	71	86.40	217.2	128.9	71	39.70	232.1	126.7
And	25	74.30	159.6	123.5	34	115.6	424.8	188.4					34	39.70	166.3	111.2
PA	37	40.50	193.8	124.3	8	122.0	155.8	133.9	30	86.40	179.0	118.9	10	113.5	198.7	162.3
Abx	17	77.40	194.3	131.9	7	93.30	169.3	136.4								
Hbx	12	83.00	1662	251.4	4	110.0	133.3	121.2	38	93.40	217.2	131.8				
DP					7	132.3	191.1	158.2					14	101.4	232.1	156.1
DPD I					11	121.9	233.6	147.2								
DPD II					3	113.7	188.8	138.8								
DPD III													13	89.40	151.7	108.0
Horn									3	184.2	196.5	192.2				

Abbreviations: n: number of analyses; Min: minimum value; Max: maximum value; Mean: mean value. Results are in parts per million (ppm); And: aphyric andesite; PA: plagioclase phyric andesite; Abx: andesitic volcaniclastic breccia; Hbx: hydrothermal breccia; DP: diorite porphyry; DPD I to III: diorite porphyry dike I to III; Horn: hornfels.

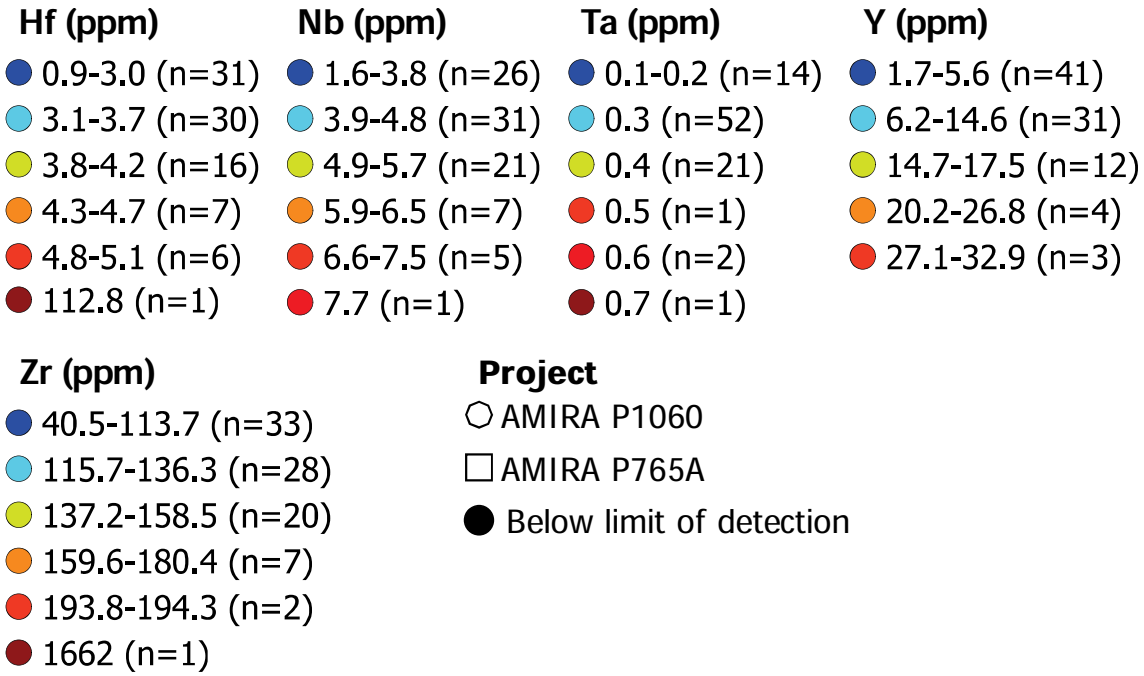

Figure 4.30. HFSE legend for surface samples.

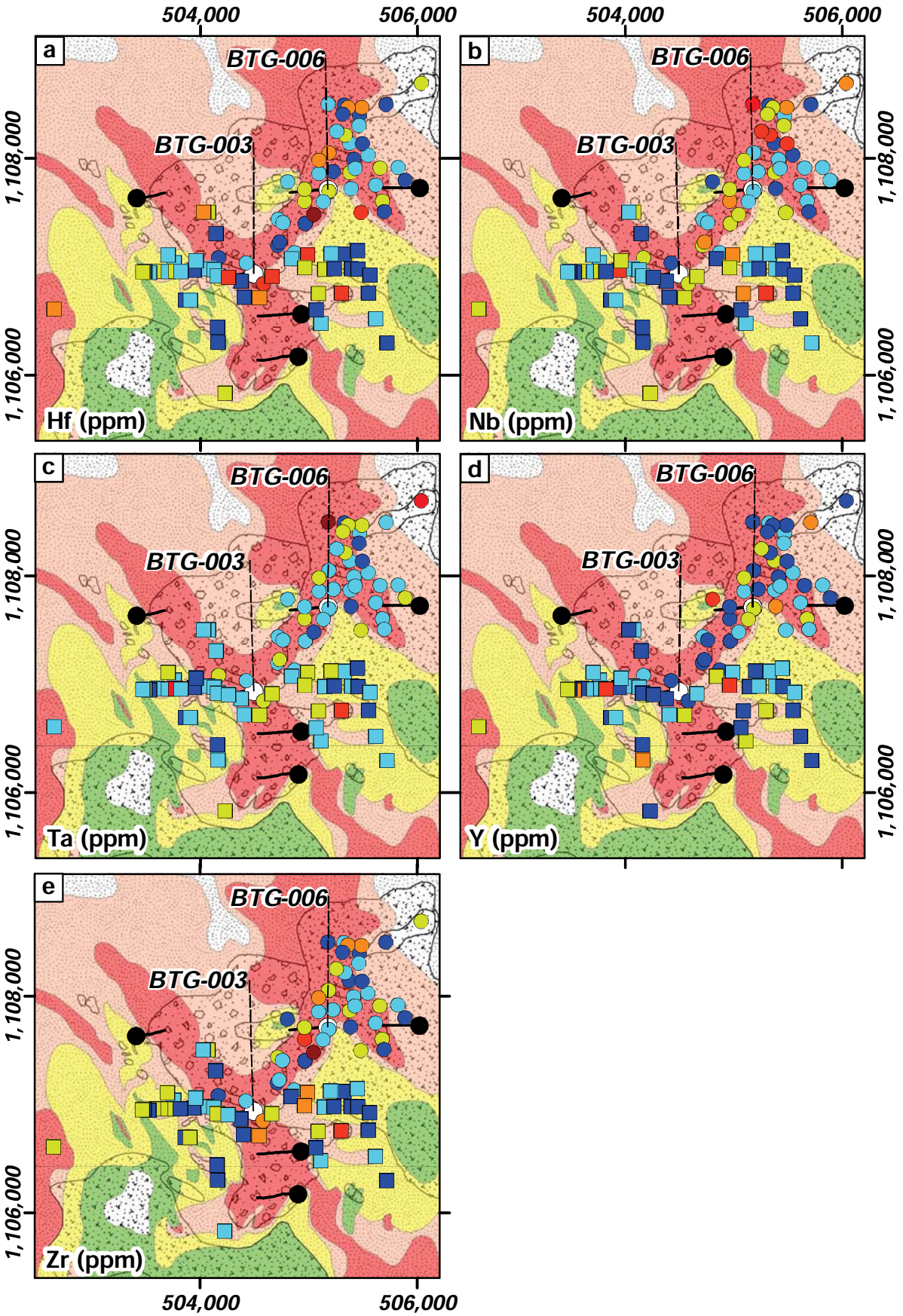

Figure 4.31. HFSE results from surface samples. a. Hafnium (Hf). **b.** Niobium (Nb). **c.** Tantalum (Ta). **d.** Yttrium (Y). **e.** Zirconium (Zr). Legend for the results is in Figure 4.30, all results are in ppm. Rock type and hydrothermal alteration legend as in Figure 4.1.

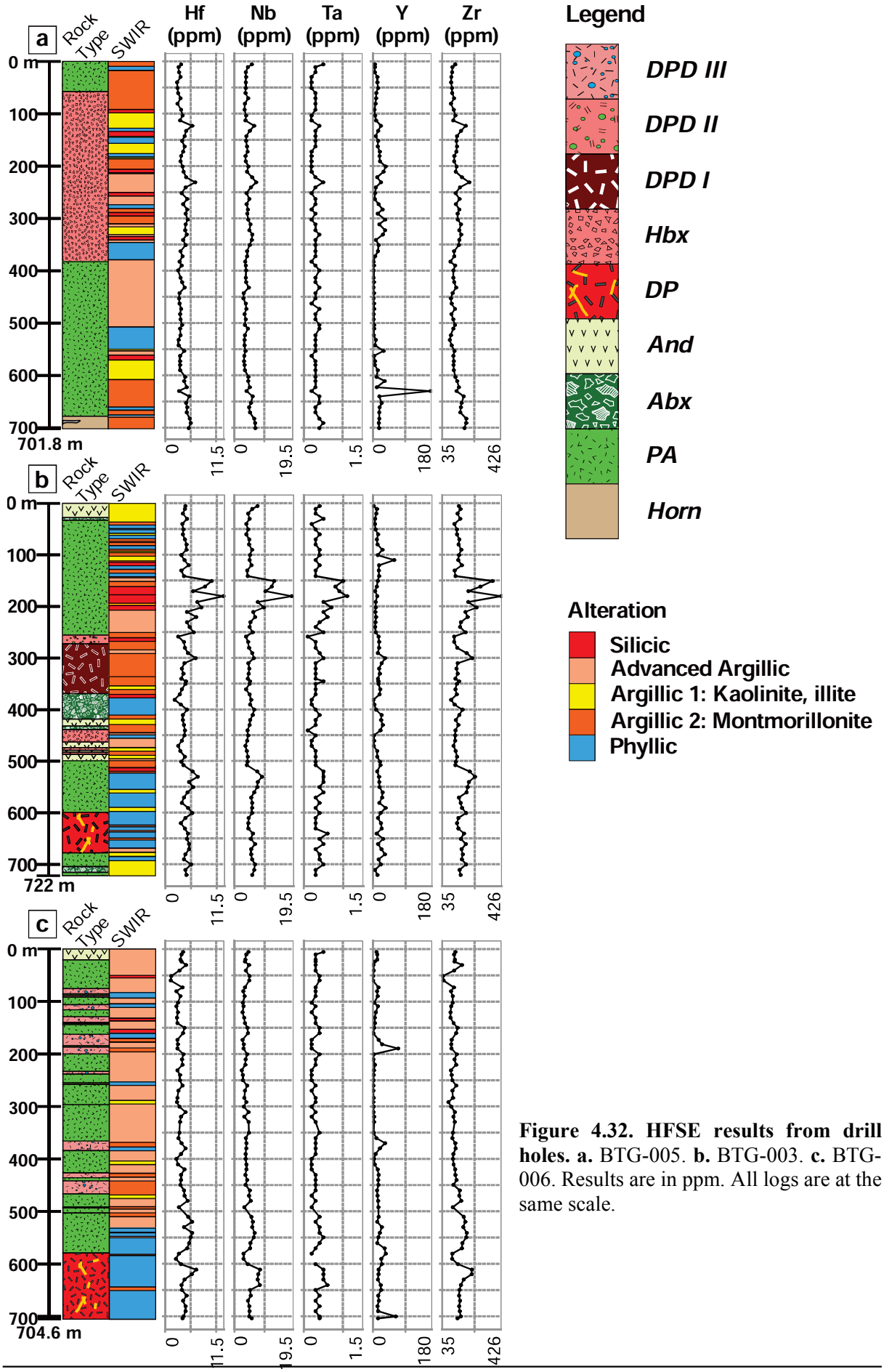

Figure 4.32. HFSE results from drill holes. a. BTG-005. **b.** BTG-003. **c.** BTG-006. Results are in ppm. All logs are at the same scale.

4.4.3. Large-ion lithophile elements (LILE)

Table 4.7 summarises LILE (i.e., Ba, Cs, Rb, Sr, Th, and U). Figures 4.34 and 4.35 present surface and drill hole results respectively. Whole rock geochemistry results are presented in Appendix G.

Advanced argillic-altered hydrothermal breccia samples from surface yielded the lowest LILE results (Table 4.7; Fig. 4.34). Argillic and advanced argillic-altered aphyric andesite surface samples yielded the highest Ba, Sr, Th, and U results (Table 4.7; Fig. 4.34). Samples from drill hole BTG-003 returned the highest LILE results, and samples from BTG-006 the lowest (Table 4.7; Fig. 4.35). Advanced argillic-altered aphyric andesite samples from BTG-006 yielded the lowest Cs, Rb, Th, and U mean value results (i.e.,0.4 ppm, 2.8 ppm, 4.2 ppm, 1.6 ppm, respectively; Table 4.7). Advanced argillic-altered aphyric andesite samples from BTG-003 returned the highest Ba mean value (i.e., 660.6 ppm; Table 4.7; Fig. 4.35). Phyllic and propylitic-altered diorite porphyry and diorite porphyry dike I samples from BTG-003 returned high Cs mean values (i.e., 2.9 and 3.1 ppm, respectively; Table 4.7; Fig. 4.35). Phyllic-altered diorite porphyry samples from BTG-006 and BTG-003 returned the highest Rb mean values (i.e., 76.5 and 70 ppm, respectively; Table 4.7; Fig. 4.35). High Sr concentrations are associated with advanced argillic-altered hydrothermal breccia samples from BTG-003 (i.e., 713.5 ppm; Table 4.7; Fig. 4.35). Hornfels samples from BTG-005 returned the highest Rb, Th, and U results (i.e., 85.7, 10, 4.3 ppm, respectively; Table 4.7; Fig. 4.35).

In summary: high Ba and Sr values resulted from advanced argillic-altered aphyric and plagioclase-phyric andesites. Caesium, Rb, Th, and U are depleted in advanced argillic-altered aphyric andesites from BTG-006. High Sr values resulted from advanced argillic-altered hydrothermal breccias. Hornfels samples from BTG-005 are enriched in Rb, Th, and U, and are depleted in Sr.

Table 4.7. Summary of LILE results

	Surface				BTG-003				BTG-005				BTG-006			
Ba (ppm)	**n**	**Min**	**Max**	**Mean**	**n**	**Min**	**Max**	**Mean**	**n**	**Min**	**Max**	**Mean**	**n**	**Min**	**Max**	**Mean**
All values	91	2.000	1628	414.3	74	204.0	2629	511.1	71	199.0	866.0	462.4	71	92.00	1133	458.4
And	25	209.0	1247	496.2	34	204.0	2629	660.6					34	92.00	1133	506.6
PA	37	6.000	1628	404.0	8	230.0	564.0	354.5	30	230.0	866.0	459.7	10	313.0	961.0	465.7
Abx	17	7.000	1193	485.2	7	209.0	490.0	391.7								
Hbx	12	2.000	738.0	174.8	4	220.0	448.0	358.3	38	199.0	705.0	458.3				
DP					7	215.0	521.0	337.7					14	160.0	778.0	375.7
DPD I					11	259.0	615.0	413.4								
DPD II					3	310.0	767.0	480.0								
DPD III													13	261.0	763.0	415.5
Horn									3	327	836	540.7				
Cs (ppm)	**n**	**Min**	**Max**	**Mean**	**n**	**Min**	**Max**	**Mean**	**n**	**Min**	**Max**	**Mean**	**n**	**Min**	**Max**	**Mean**
All values	55	0.1000	4.600	1.056	73	0.1000	11.90	2.159	66	0.1000	6.800	1.471	44	0.1000	2.700	0.9659
And	16	0.1000	4.600	0.9500	34	0.1000	5.900	1.888					7	0.1000	0.8000	0.3714
PA	23	0.1000	4.100	1.200	8	0.1000	4.700	2.263	27	0.1000	3.100	1.133	10	0.2000	1.200	0.4800
Abx	13	0.1000	4.600	1.062	7	0.2000	4.700	1.971								
Hbx	3	0.1000	1.200	0.5000	3	0.1000	2.000	0.9667	36	0.1000	6.800	1.667				
DP					7	1.000	4.400	2.943					14	0.8000	2.700	1.557
DPD I					11	0.8000	11.90	3.073								
DPD II					3	0.1000	2.900	1.400								
DPD III													13	0.5000	2.000	1.023
Horn									3	1.900	2.500	2.167				
Rb (ppm)	**n**	**Min**	**Max**	**Mean**	**n**	**Min**	**Max**	**Mean**	**n**	**Min**	**Max**	**Mean**	**n**	**Min**	**Max**	**Mean**
All values	90	0.2000	84.00	18.49	74	0.9000	106.2	44.66	71	1.100	107.0	39.78	71	0.2000	106.9	30.18
And	25	1.900	84.00	18.81	34	1.100	102.7	42.13					34	0.2000	21.90	2.821
PA	37	0.2000	70.10	21.55	8	1.700	66.30	38.71	30	1.100	100.3	37.51	10	15.60	64.30	38.34
Abx	17	0.5000	84.00	20.06	7	6.200	92.80	45.14								
Hbx	11	0.3000	40.10	5.009	4	0.9000	73.30	19.70	38	1.300	80.80	37.96				
DP					7	49.50	106.2	70.03					14	55.70	106.9	76.46
DPD I					11	13.90	85.30	51.25								
DPD II					3	2.500	59.60	37.90								
DPD III													13	21.00	67.00	45.59
Horn									3	73.30	107.0	85.70				

Abbreviations: n: number of analyses; Min: minimum value; Max: maximum value; Mean: mean value. Results are in parts per million (ppm); And: aphyric andesite; PA: plagioclase phyric andesite; Abx: andesitic volcaniclastic breccia; Hbx: hydrothermal breccia; DP: diorite porphyry; DPD I to III: diorite porphyry dike I to III; Horn: hornfels.

Table 4.7. Summary of LILE results (Continued)

	Surface				BTG-003				BTG-005				BTG-006			
Sr (ppm)	**n**	**Min**	**Max**	**Mean**	**n**	**Min**	**Max**	**Mean**	**n**	**Min**	**Max**	**Mean**	**n**	**Min**	**Max**	**Mean**
All values	91	2.100	3322	537.9	74	26.90	1465	434.2	71	48.90	1692	405.7	71	6.600	1733	433.6
And	25	91.50	1998	699.3	34	26.90	1465	391.0					34	6.600	1733	576.4
PA	37	4.700	3322	523.5	8	227.4	845.3	493.8	30	81.70	802.7	368.2	10	218.0	1066	490.1
Abx	17	8.100	1521	542.0	7	76.00	1386	580.4								
Hbx	12	2.100	1257	239.8	4	172.4	975.5	713.5	38	95.60	1692	458.5				
DP					7	138.1	660.5	314.9					14	66.20	492.2	177.2
DPD I					11	216.7	1224	414.8								
DPD II					3	316.2	503.7	400.1								
DPD III													13	101.6	716.4	292.7
Horn									3	48.90	142.7	110.6				
Th (ppm)	**n**	**Min**	**Max**	**Mean**	**n**	**Min**	**Max**	**Mean**	**n**	**Min**	**Max**	**Mean**	**n**	**Min**	**Max**	**Mean**
All values	91	0.5000	11.70	5.060	74	1.900	15.20	6.939	71	3.400	12.30	6.728	71	0.2000	14.10	5.380
And	25	2.400	11.70	6.012	34	3.600	15.20	7.665					34	0.2000	8.000	4.203
PA	37	0.6000	9.700	5.003	8	3.700	9.500	6.013	30	4.800	10.70	6.513	10	5.000	11.60	7.700
Abx	17	1.100	9.700	5.347	7	1.900	10.10	6.329								
Hbx	12	0.5000	6.500	2.850	4	4.700	6.100	5.325	38	3.400	12.30	6.642				
DP					7	6.800	9.100	7.757					14	3.000	14.10	7.036
DPD I					11	5.000	8.600	6.255								
DPD II					3	4.500	6.800	5.367								
DPD III													13	3.900	6.600	4.892
Horn									3	9.300	10.90	9.967				
U (ppm)	**n**	**Min**	**Max**	**Mean**	**n**	**Min**	**Max**	**Mean**	**n**	**Min**	**Max**	**Mean**	**n**	**Min**	**Max**	**Mean**
All values	91	0.5000	4.100	1.922	74	1.300	5.500	2.965	71	1.200	5.000	2.659	69	0.4000	5.800	2.277
And	25	0.8000	3.000	2.072	34	2.000	5.500	3.332					32	0.4000	2.900	1.588
PA	37	0.5000	4.100	1.843	8	1.600	3.800	2.538	30	1.400	4.800	2.747	10	2.200	4.700	3.650
Abx	17	1.200	4.100	2.182	7	1.300	3.800	2.814								
Hbx	12	0.6000	2.800	1.483	4	1.400	2.300	1.875	38	1.200	4.200	2.461				
DP					7	2.900	4.100	3.429					14	1.500	5.800	3.107
DPD I					11	1.500	3.500	2.536								
DPD II					3	1.700	3.000	2.233								
DPD III													13	1.200	2.900	2.023
Horn									3	3.700	5.000	4.300				

Abbreviations: n: number of analyses; Min: minimum value; Max: maximum value; Mean: mean value. Results are in parts per million (ppm); And: aphyric andesite; PA: plagioclase phyric andesite; Abx: andesitic volcaniclastic breccia; Hbx: hydrothermal breccia; DP: diorite porphyry; DPD I to III: diorite porphyry dike I to III; Horn: hornfels.

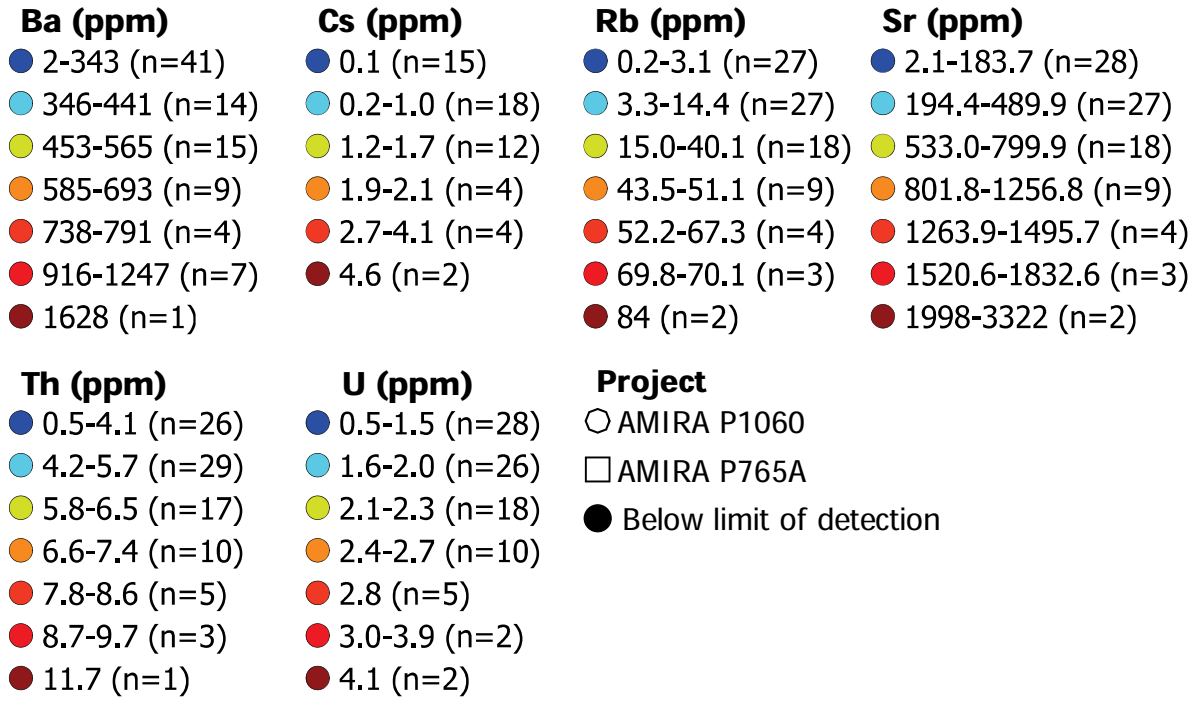

Figure 4.33. LILE legend for surface samples.

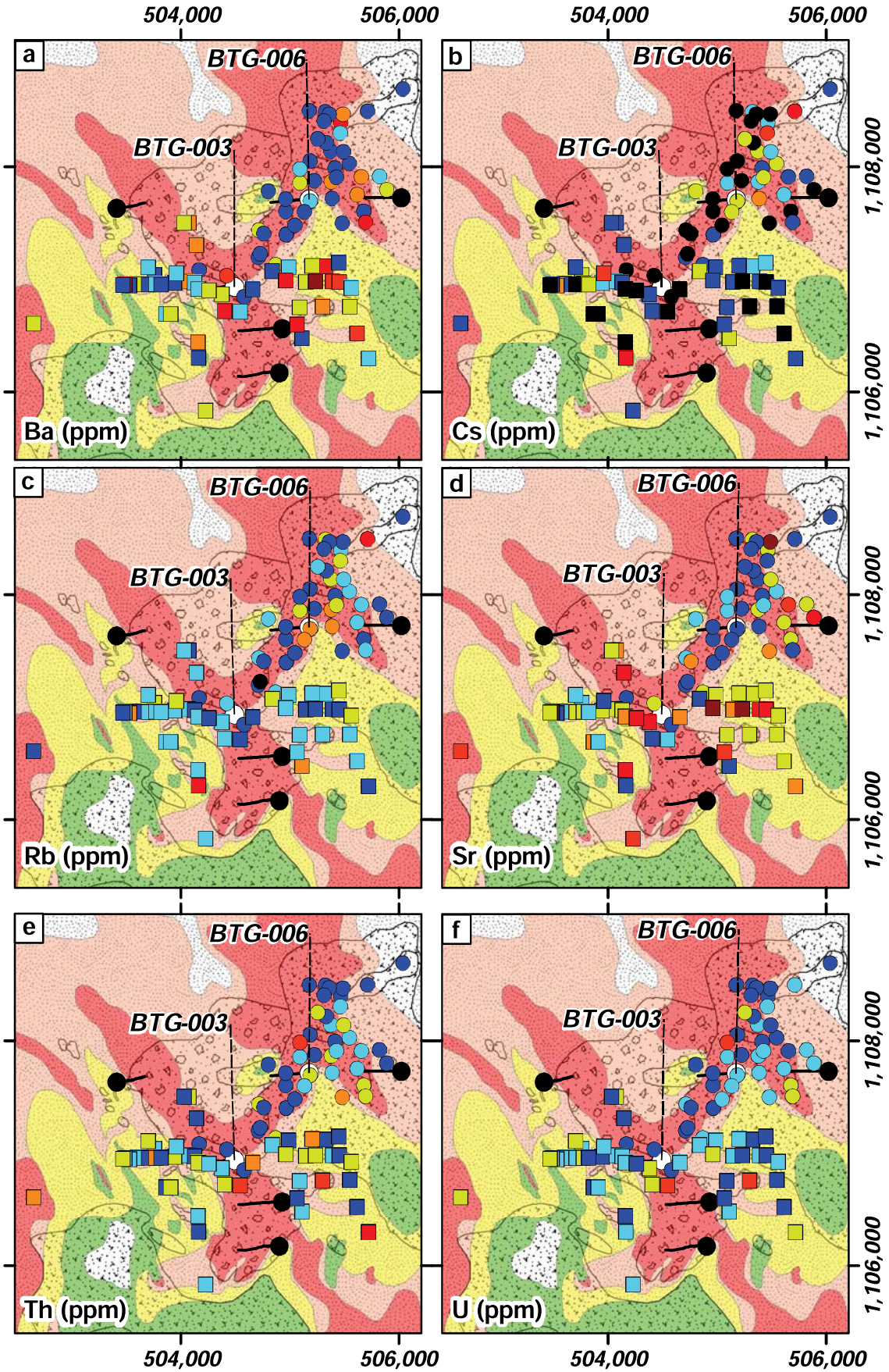

Figure 4.34. LILE results from surface samples. a. Barium (Ba). **b.** Caesium (Cs). **c.** Rubidium (Rb). **d.** Strontium (Sr). **e.** Thorium (Th). **f.** Uranium (U). Legend for the results is presented in Figure 4.33, all results are in ppm. Rock type and hydrothermal alteration legend as in Figure 4.1.

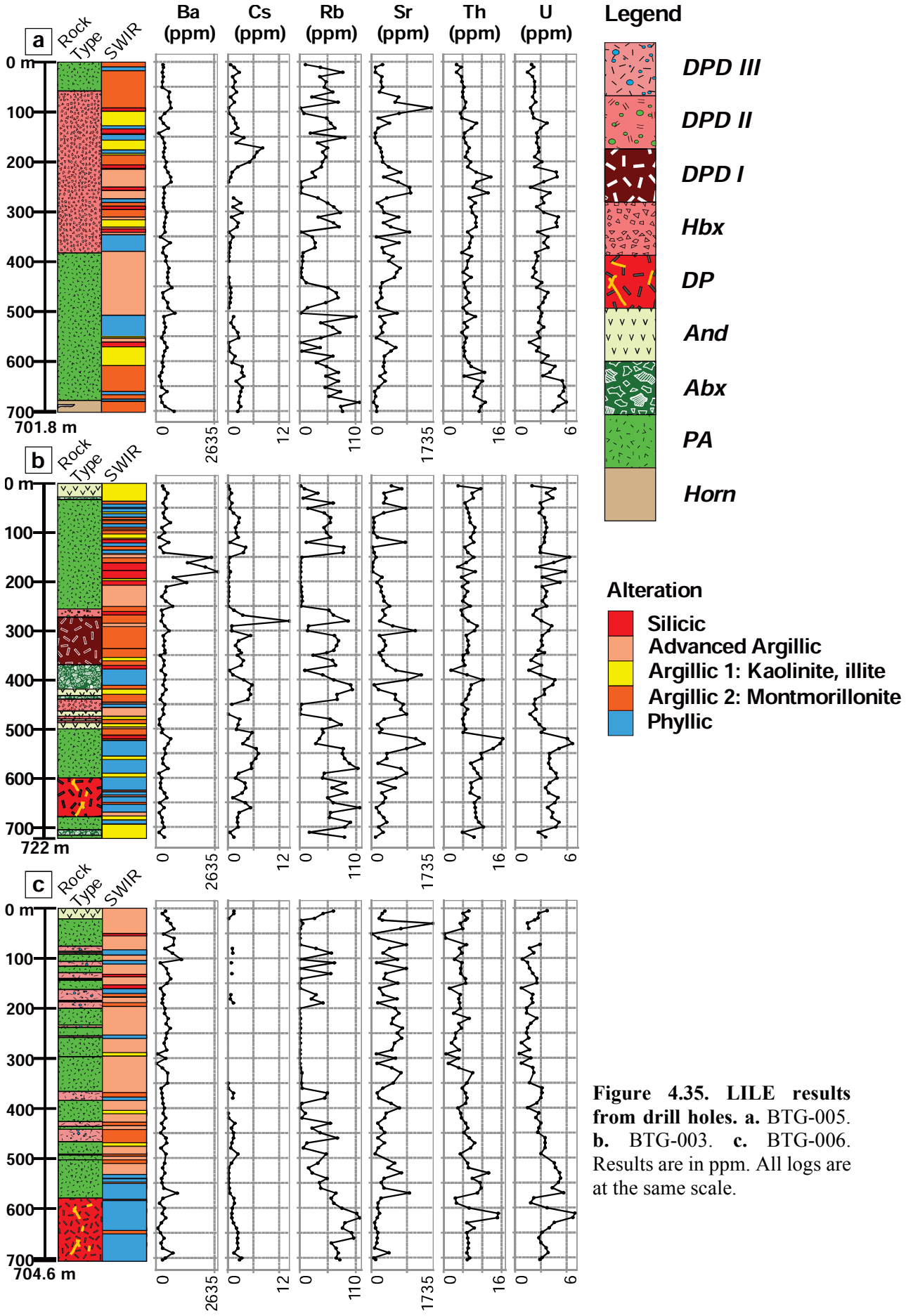

Figure 4.35. LILE results from drill holes. a. BTG-005. **b.** BTG-003. **c.** BTG-006. Results are in ppm. All logs are at the same scale.

4.4.4. Rare earth elements (REE)

Table 4.8 and Figures 4.36 to 3.37 present surface results from three LREE (i.e., La, Ce, Pr) and three HREE (i.e., Tm, Yb, Lu). Table 4.8 and Figure 3.38 present drill hole results from La, Ce, Pr, Eu, Gd, Tb, Tm, Yb, and Lu. Whole rock geochemistry results are presented in Appendix G, and plots from all elements are presented in Appendix K.

REE surface samples mean value results are lower compared to drill hole sample mean value results (Table 4.8). REE are most abundant in argillic and silicic-altered aphyric andesites on surface compared to other rock types (Table 4.8; Fig. 4.37). REE are depleted in advanced argillic-altered hydrothermal breccia samples on surface (Table 4.8; Fig. 4.37).

Lanthanum, Ce, and Eu mean values from drill hole BTG-005 are higher than in other drill holes (i.e., 17.34 ppm, 36.36 ppm, 0.9497 ppm, respectively; Table 4.8). Praseodymium, Gd, Tb, Tm, Yb, and Lu average results are higher in drill hole BTG-003 (Table 4.8). Lanthanum, Ce, and Pr highest values resulted from hornfels samples from BTG-005 (i.e., 20.07 ppm, 43.03 ppm, 5.247 ppm, respectively; Table 4.8; Fig. 4.38a). Advanced argillic-altered plagioclase-phyric andesite and phyllic-altered diorite porphyry samples from drill hole BTG-006 yielded similar La, Ce, and Pr results to those of hornfels samples in BTG-005 (Table 4.8; Figs. 4.38a and 4.38c). Advanced argillic-altered aphyric andesite and argillic-altered diorite porphyry dike III samples from BTG-006 yielded the lowest LREE (Table 4.8; Fig. 4.38).

Phyllic-altered diorite porphyry samples from BTG-003 and BTG-006 returned the highest Eu, Gd, and Tb results (Table 4.8; Figs. 4.38b and 4.38c). Advanced argillic-altered aphyric andesite samples from BTG-006 are depleted in Eu, Gd, and Tb (Table 4.8; Fig. 4.38). Phyllic-altered diorite porphyry samples from BTG-003 and BTG-006, and argillic-altered diorite porphyry dike III returned the highest Tm, Yb, and Lu results (Table 4.8; Figs. 4.38a and 4.38c). Advanced argillic-altered hydrothermal breccias from BTG-003 and aphyric andesites from BTG-006 yielded the lowest HREE results (Table 4.8; Fig. 4.38).

Figure 4.38 revealed an inversed pattern between light and HREE. Specific segments of samples or individual samples that yielded high LREE values returned low HREE results, and vice versa. These phenomena can be explained by the predominant presence of either svanbergite (i.e., Sr-rich APS mineral), and/or florencite (i.e., Ce-rich APS mineral).

Table 4.8. Summary of REE results

	Surface				BTG-003				BTG-005				BTG-006			
La (ppm)	**n**	**Min**	**Max**	**Mean**	**n**	**Min**	**Max**	**Mean**	**n**	**Min**	**Max**	**Mean**	**n**	**Min**	**Max**	**Mean**
All values	91	0.3000	36.90	14.34	74	1.600	33.60	16.99	71	9.200	30.30	17.34	71	0.3000	42.80	15.45
And	25	8.700	32.10	17.15	34	1.600	33.60	16.47					34	0.3000	24.50	13.55
PA	37	0.5000	36.90	14.09	8	13.00	26.80	17.51	30	9.900	25.20	15.65	10	11.70	33.10	18.98
Abx	17	0.5000	36.40	16.28	7	7.600	25.20	18.26								
Hbx	12	0.3000	20.70	6.533	4	14.80	19.60	17.23	38	9.200	30.30	18.46				
DP					7	12.40	22.90	18.41					14	12.50	42.80	19.09
DPD I					11	14.50	23.30	16.77								
DPD II					3	12.80	20.40	15.70								
DPD III													13	10.90	17.50	13.77
Horn									3	19.50	20.70	20.07				
Ce (ppm)	**n**	**Min**	**Max**	**Mean**	**n**	**Min**	**Max**	**Mean**	**n**	**Min**	**Max**	**Mean**	**n**	**Min**	**Max**	**Mean**
All values	91	0.4000	95.30	29.13	74	2.900	69.80	35.61	71	17.10	68.60	36.36	71	0.3	106.0	31.90
And	25	16.40	95.30	36.16	34	2.900	69.80	34.39					34	0.3	45.30	26.35
PA	37	0.9000	79.20	28.33	8	27.70	55.50	36.65	30	17.90	56.80	32.28	10	24.10	84.40	41.66
Abx	17	1.100	70.10	31.88	7	15.80	53.30	37.39								
Hbx	12	0.4000	42.90	13.06	4	30.50	39.90	35.25	38	17.10	68.60	39.06				
DP					7	27.80	46.00	40.19					14	26.50	106.0	40.91
DPD I					11	31.60	50.20	35.65								
DPD II					3	28.00	39.70	32.10								
DPD III													13	23.80	35.00	29.19
Horn									3	41.90	44.90	43.03				
Pr (ppm)	**n**	**Min**	**Max**	**Mean**	**n**	**Min**	**Max**	**Mean**	**n**	**Min**	**Max**	**Mean**	**n**	**Min**	**Max**	**Mean**
All values	91	0.02000	13.59	3.615	74	0.3700	8.760	4.311	71	1.890	8.340	4.252	70	0.2000	14.34	3.860
And	25	1.880	13.59	4.602	34	0.3700	8.760	4.099					33	0.2000	5.160	3.042
PA	37	0.08000	10.69	3.470	8	3.370	6.540	4.469	30	1.890	6.600	3.541	10	3.050	12.74	5.263
Abx	17	0.1500	8.340	3.915	7	2.480	6.790	4.594								
Hbx	12	0.02000	5.630	1.577	4	3.900	5.050	4.462	38	2.000	8.340	4.735				
DP					7	3.640	5.800	5.097					14	2.760	14.34	5.015
DPD I					11	3.480	5.930	4.228								
DPD II					3	3.540	4.590	3.910								
DPD III													13	2.860	4.920	3.615
Horn									3	5.160	5.290	5.247				

Abbreviations: n: number of analyses; Min: minimum value; Max: maximum value; Mean: mean value. Results are in parts per million (ppm); And: aphyric andesite; PA: plagioclase phyric andesite; Abx: andesitic volcaniclastic breccia; Hbx: hydrothermal breccia; DP: diorite porphyry; DPD I to III: diorite porphyry dike I to III; Horn: hornfels.

Table 4.8. Summary of REE results (Continued)

	Surface				BTG-003				BTG-005				BTG-006			
Eu (ppm)	**n**	**Min**	**Max**	**Mean**	**n**	**Min**	**Max**	**Mean**	**n**	**Min**	**Max**	**Mean**	**n**	**Min**	**Max**	**Mean**
All values	88	0.02000	2.140	0.6968	74	0.04000	2.530	0.9395	71	0.1800	2.270	0.9497	69	0.03000	4.410	0.9187
And	25	0.1100	2.140	0.8060	34	0.04000	2.530	0.8571					32	0.03000	1.140	0.5847
PA	36	0.02000	2.090	0.7131	8	0.4600	1.340	0.9888	30	0.1800	1.790	0.7350	10	0.6400	4.350	1.273
Abx	17	0.05000	1.400	0.7024	7	0.6200	1.600	1.017								
Hbx	10	0.03000	1.290	0.3560	4	0.6100	0.8300	0.7425	38	0.3700	2.270	1.105				
DP					7	0.7900	1.850	1.273					14	0.6900	4.410	1.297
DPD I					11	0.7800	1.440	0.9927								
DPD II					3	0.8100	0.9300	0.8500								
DPD III													13	0.4500	2.240	1.061
Horn									3	1.080	1.200	1.127				
Gd (ppm)	**n**	**Min**	**Max**	**Mean**	**n**	**Min**	**Max**	**Mean**	**n**	**Min**	**Max**	**Mean**	**n**	**Min**	**Max**	**Mean**
All values	91	0.08000	6.490	2.090	74	0.5900	10.06	3.236	71	0.4400	9.800	3.106	69	0.1600	13.57	2.980
And	25	0.3200	6.490	2.451	34	0.5900	10.06	3.136					32	0.1600	3.520	1.505
PA	37	0.1400	5.370	2.184	8	1.040	4.630	3.183	30	0.4400	7.120	2.289	10	1.940	11.95	4.142
Abx	17	0.1200	4.590	2.142	7	1.530	5.710	3.136								
Hbx	12	0.08000	4.340	0.9750	4	1.390	2.630	2.048	38	1.120	9.800	3.695				
DP					7	2.260	6.700	4.321					14	2.380	13.57	4.686
DPD I					11	2.500	5.330	3.448								
DPD II					3	2.520	3.450	3.013								
DPD III													13	1.120	10.27	3.883
Horn									3	3.610	3.980	3.820				
Tb (ppm)	**n**	**Min**	**Max**	**Mean**	**n**	**Min**	**Max**	**Mean**	**n**	**Min**	**Max**	**Mean**	**n**	**Min**	**Max**	**Mean**
All values	91	0.02000	0.9000	0.2797	74	0.1000	1.720	0.4712	71	0.06000	2.050	0.4483	69	0.02000	1.720	0.4062
And	25	0.04000	0.9000	0.3212	34	0.1100	1.720	0.4774					32	0.02000	0.4900	0.1753
PA	37	0.04000	0.8700	0.2965	8	0.1000	0.6700	0.4475	30	0.06000	2.050	0.3393	10	0.2500	1.330	0.5490
Abx	17	0.03000	0.6100	0.2812	7	0.1500	0.8200	0.3886								
Hbx	12	0.02000	0.5100	0.1392	4	0.1200	0.3900	0.2175	38	0.1600	1.370	0.5253				
DP					7	0.3400	0.9900	0.6129					14	0.3600	1.720	0.6693
DPD I					11	0.4000	0.9200	0.5400								
DPD II					3	0.2800	0.4900	0.4133								
DPD III													13	0.1600	1.700	0.5815
Horn									3	0.5400	0.5900	0.5633				

Abbreviations: n: number of analyses; Min: minimum value; Max: maximum value; Mean: mean value. Results are in parts per million (ppm); And: aphyric andesite; PA: plagioclase phyric andesite; Abx: andesitic volcaniclastic breccia; Hbx: hydrothermal breccia; DP: diorite porphyry; DPD I to III: diorite porphyry dike I to III; Horn: hornfels.

Table 4.8. Summary of REE results (Continued)

	Surface				BTG-003				BTG-005				BTG-006			
Tm (ppm)	**n**	**Min**	**Max**	**Mean**	**n**	**Min**	**Max**	**Mean**	**n**	**Min**	**Max**	**Mean**	**n**	**Min**	**Max**	**Mean**
All values	91	0.04000	0.4300	0.1800	74	0.04000	0.9700	0.2923	71	0.04000	2.570	0.2711	70	0.01000	1.120	0.2343
And	25	0.05000	0.4300	0.1956	34	0.1400	0.9700	0.3103					33	0.01000	0.3600	0.1161
PA	37	0.06000	0.4200	0.1851	8	0.08000	0.4000	0.2738	30	0.04000	2.570	0.2487	10	0.2300	0.4900	0.2960
Abx	17	0.04000	0.3600	0.1806	7	0.04000	0.4000	0.1943								
Hbx	12	0.05000	0.3100	0.1308	4	0.06000	0.2500	0.1150	38	0.1000	0.6300	0.2847				
DP					7	0.2300	0.5000	0.3600					14	0.2300	0.7900	0.3543
DPD I					11	0.2600	0.5800	0.3427								
DPD II					3	0.2100	0.2900	0.2600								
DPD III													13	0.1400	1.120	0.3577
Horn									3	0.3100	0.3300	0.3233				
Yb (ppm)	**n**	**Min**	**Max**	**Mean**	**n**	**Min**	**Max**	**Mean**	**n**	**Min**	**Max**	**Mean**	**n**	**Min**	**Max**	**Mean**
All values	91	0.1900	2.730	1.266	74	0.2700	6.080	1.985	71	0.3700	15.08	1.766	71	0.07000	7.220	1.592
And	25	0.3300	2.700	1.357	34	0.9900	6.080	2.166					34	0.07000	2.660	0.8694
PA	37	0.4600	2.730	1.280	8	0.5500	2.960	1.911	30	0.3700	15.08	1.628	10	1.270	2.960	1.920
Abx	17	0.1900	2.730	1.279	7	0.2700	2.740	1.316								
Hbx	12	0.4200	2.420	1.014	4	0.3200	1.300	0.6925	38	0.7400	3.760	1.852				
DP					7	1.690	2.980	2.231					14	1.560	5.390	2.409
DPD I					11	1.420	3.520	2.281								
DPD II					3	1.590	1.850	1.753								
DPD III													13	1.010	7.220	2.349
Horn									3	1.890	2.300	2.073				
Lu (ppm)	**n**	**Min**	**Max**	**Mean**	**n**	**Min**	**Max**	**Mean**	**n**	**Min**	**Max**	**Mean**	**n**	**Min**	**Max**	**Mean**
All values	91	0.04000	0.4600	0.2196	74	0.07000	0.9200	0.3165	71	0.08000	2.120	0.2839	71	0.02000	1.090	0.2575
And	25	0.08000	0.4100	0.2360	34	0.2100	0.9200	0.3415					34	0.02000	0.4200	0.1565
PA	37	0.08000	0.4600	0.2241	8	0.1100	0.4600	0.3138	30	0.08000	2.120	0.2610	10	0.2600	0.4400	0.3150
Abx	17	0.04000	0.4600	0.2153	7	0.07000	0.4100	0.2114								
Hbx	12	0.08000	0.4000	0.1775	4	0.0900	0.2600	0.1500	38	0.1400	0.5800	0.3003				
DP					7	0.2500	0.4800	0.3543					14	0.2500	0.7900	0.3593
DPD I					11	0.2700	0.4900	0.3482								
DPD II					3	0.2800	0.3300	0.3033								
DPD III													13	0.1400	1.090	0.3677
Horn										0.2900	0.3200	0.3067				

Abbreviations: n: number of analyses; Min: minimum value; Max: maximum value; Mean: mean value. Results are in parts per million (ppm); And: aphyric andesite; PA: plagioclase phyric andesite; Abx: andesitic volcaniclastic breccia; Hbx: hydrothermal breccia; DP: diorite porphyry; DPD I to III: diorite porphyry dike I to III; Horn: hornfels.

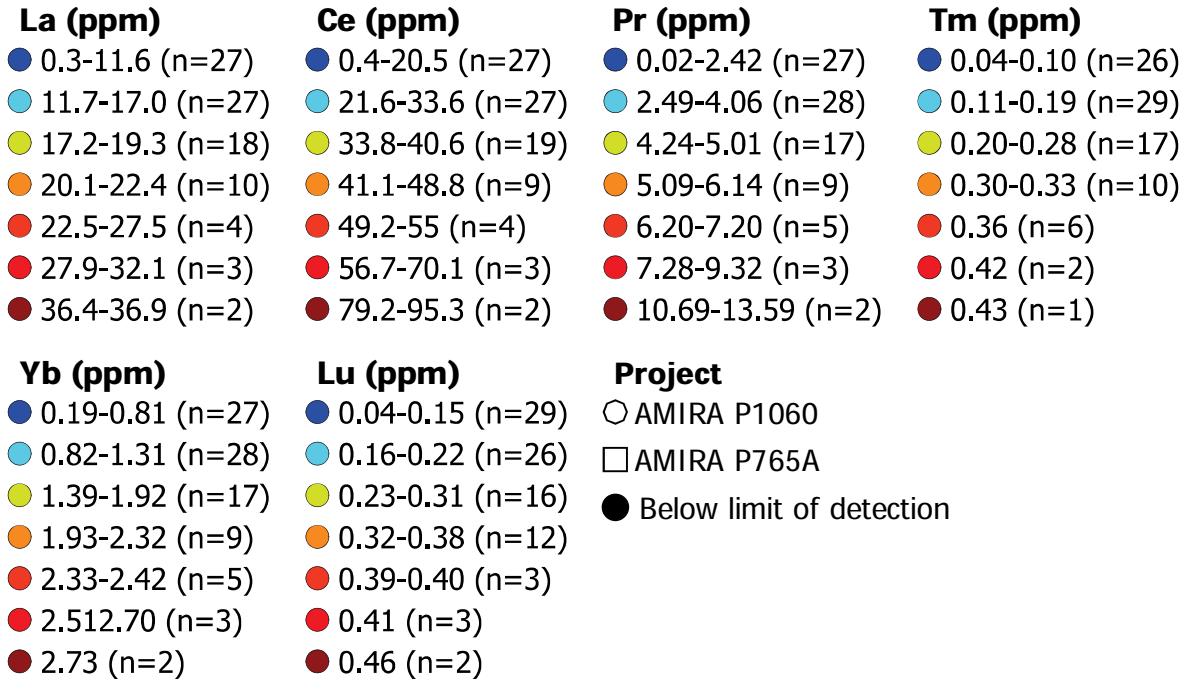

Figure 4.36. REE legend for surface samples.

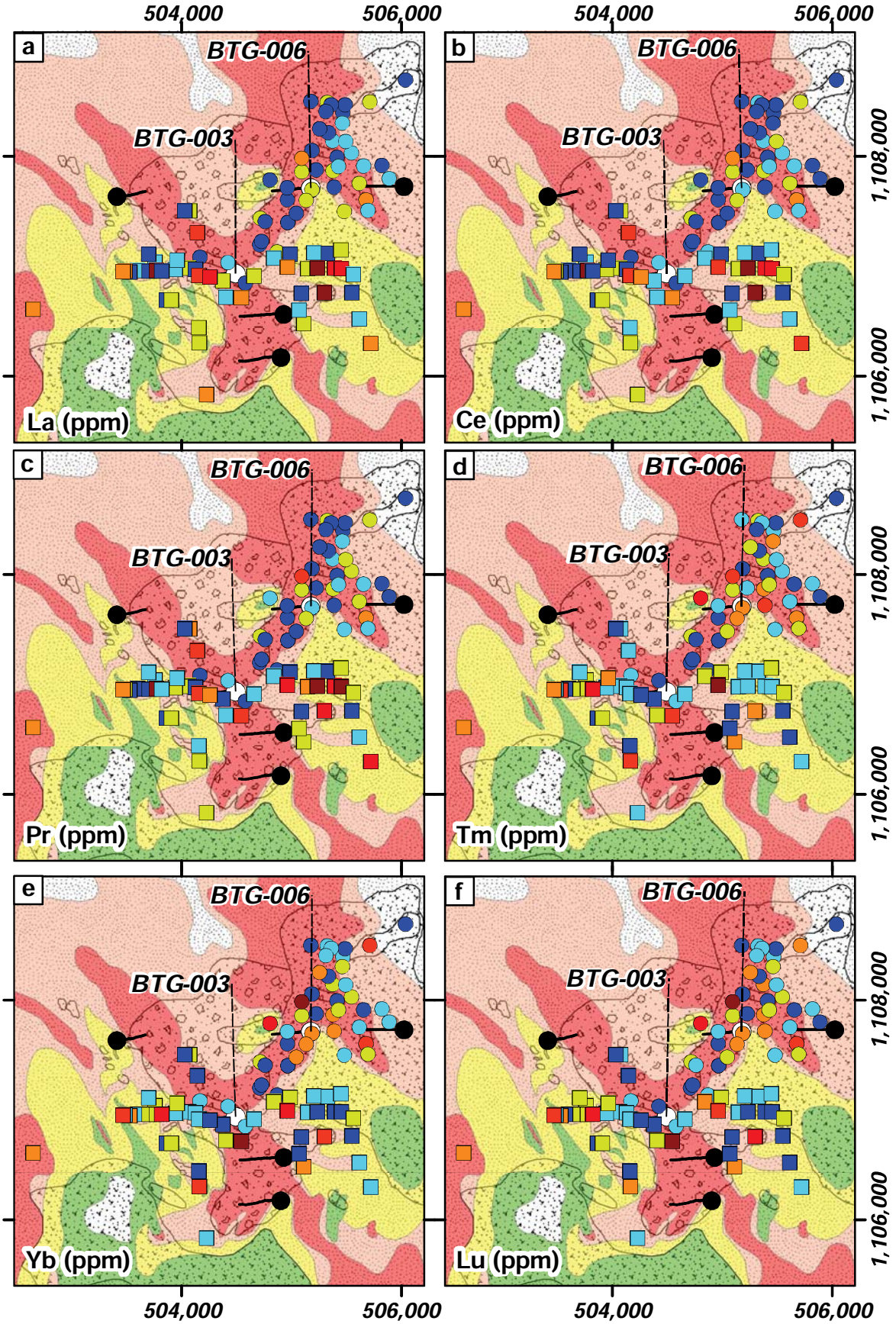

Figure 4.37. REE results from surface samples. a. Lanthanum (La). **b.** Cerium (Ce). **c.** Praseodymium (Pr). **d.** Thulium (Tm). **e.** Ytterbium (Yb). **f.** Lutetium (Lu). Legend for the results is presented in Figure 4.33, all results are in ppm. Rock type and hydrothermal alteration legend as in Figure 4.1.

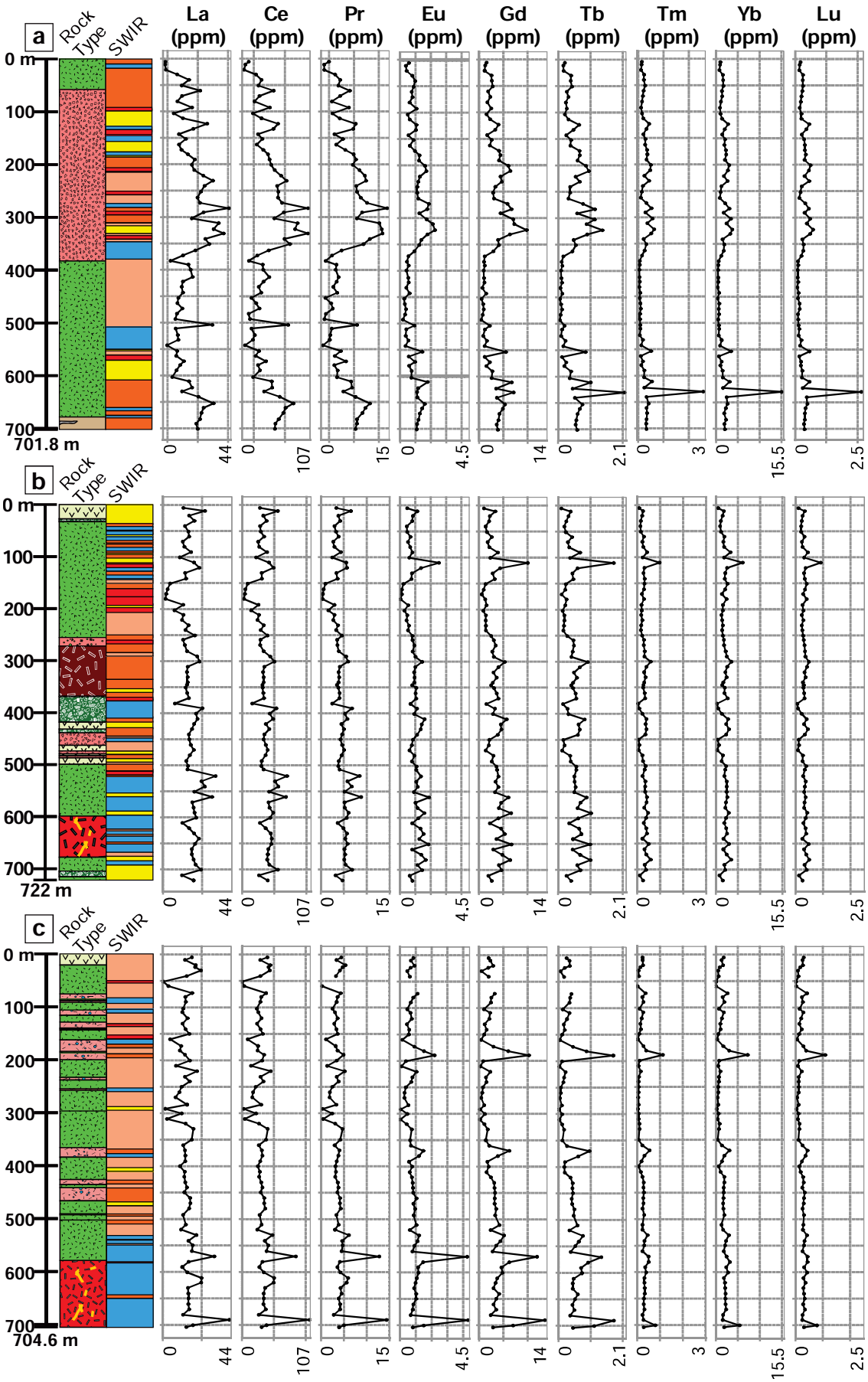

Figure 4.38. REE results from drill holes. a. BTG-005. **b.** BTG-003. **c.** BTG-006. All results are in ppm All logs are at the same scale. Rock type and SWIR legend as in Figures 4.35.

4.4.5. Transition metals

Table 4.9 and Figures 4.39 to 4.41 present surface and drill hole transition metals results (i.e., Co, Cr, Ni, Sc, and V). Whole rock geochemistry results are presented in Appendix G.

Surface samples returned the lowest transition metals results compared to drill hole samples, except for Cr (Table 4.9). Advanced argillic-altered hydrothermal breccia surface samples yielded the lowest Co, Ni, Sc, and V results, and the highest Cr mean values (Table 4.9; Figs. 4.39 and 4.40). Silicic-altered volcaniclastic andesitic breccia surface samples yielded the highest Co mean value (i.e., 9.220 ppm; Table 4.9). Argillic-altered aphyric andesite surface samples returned the highest Sc and V results (i.e., 12.96 and 169.7 ppm, respectively; Table 4.9).

Advanced argillic-altered plagioclase-phyric andesite samples from BTG-006 yielded the highest Co mean value result (i.e., 31.75 ppm; Table 4.9; Fig. 4.41c). Advanced argillic-altered aphyric andesites from BTG-003 returned the lowest mean value (i.e., 14.30 ppm; Table 4.9; Fig. 4.41b). Propylitic-altered diorite porphyry dike II samples from BTG-003 yielded the highest Cr mean value (i.e., 10.37 ppm; Table 4.9; Fig. 4.41b). Phyllic-altered diorite porphyry samples from BTG-003 yielded the lowest Cr mean value (i.e., 1.485 ppm; Table 4.9; Fig. 4.41b). Phyllic-altered diorite porphyry samples from BTG-006 yielded the highest Ni mean value (i.e., 34.25 ppm; Table 4.9), and hornfels samples from BTG-005 returned the lowest (i.e., 11.00 ppm; Table 4.9; Figs. 4.41c and 4.41a, respectively). Phyllic-altered diorite porphyry samples from BTG-003 returned the highest Sc and V mean values (i.e., 25.28 ppm, and 262.5 ppm, respectively; Table 4.9; Figs. 4.41b). Advanced argillic-altered hydrothermal breccia and argillic-altered diorite porphyry dike I samples from BTG-003 returned the lowest Sc and V mean values (Table 4.9; Figs. 4.41b).

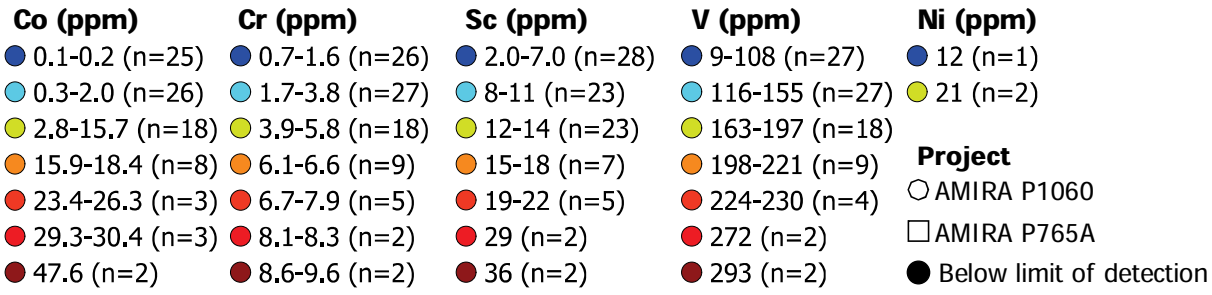

Figure 4.39. Transition metals legend for surface results.

Table 4.9. Summary of transition metals results

	Surface				BTG-003				BTG-005				BTG-006			
Co (ppm)	**n**	**Min**	**Max**	**Mean**	**n**	**Min**	**Max**	**Mean**	**n**	**Min**	**Max**	**Mean**	**n**	**Min**	**Max**	**Mean**
All values	85	0.1000	47.60	7.081	74	0.2000	47.50	18.00	71	3.500	60.90	26.27	71	0.2000	81.90	22.79
And	23	0.1000	29.30	5.265	34	0.2000	34.30	14.30					34	0.2000	49.10	18.68
PA	35	0.1000	47.60	8.471	8	0.3000	29.70	17.15	30	10.90	45.10	24.49	10	16.40	81.90	31.75
Abx	17	0.1000	47.60	9.224	7	0.2000	47.50	27.60								
Hbx	10	0.1000	23.40	2.750	4	17.80	32.50	26.95	38	3.500	60.90	28.05				
DP					7	15.00	28.30	23.77					14	13.40	34.20	21.46
DPD I					11	11.50	31.90	16.97								
DPD II					3	0.5000	30.30	18.20								
DPD III													13	18.80	72.20	28.08
Horn									3	19.70	24.70	21.60				
Cr (ppm)	**n**	**Min**	**Max**	**Mean**	**n**	**Min**	**Max**	**Mean**	**n**	**Min**	**Max**	**Mean**	**n**	**Min**	**Max**	**Mean**
All values	89	0.7000	9.600	3.422	74	0.9000	15.60	3.403	71	2.200	48.20	7.914	71	0.9000	10.00	2.572
And	25	1.000	7.900	2.888	34	0.9000	9.100	2.826					34	1.100	10.00	3.068
PA	36	0.7000	8.600	3.283	8	1.400	6.100	3.863	30	2.200	48.20	8.063	10	0.9000	4.700	1.870
Abx	16	0.7000	6.100	2.956	7	2.500	7.600	5.057								
Hbx	12	1.000	9.600	5.575	4	1.400	4.200	2.975	38	2.300	29.10	7.853				
DP					7	1.000	2.400	1.486					14	1.000	5.600	2.071
DPD I					11	1.700	4.900	3.273								
DPD II					3	5.200	15.60	10.37								
DPD III													13	0.9000	4.500	2.354
Horn									3	5.100	9.000	7.200				
Ni (ppm)	**n**	**Min**	**Max**	**Mean**	**n**	**Min**	**Max**	**Mean**	**n**	**Min**	**Max**	**Mean**	**n**	**Min**	**Max**	**Mean**
All values	3	12.00	21.00	18.00	20	10.00	28.00	17.85	71	10.00	42.00	22.34	14	10.00	54.00	19.93
And					6	10.00	23.00	16.00					5	10.00	19.00	13.60
PA	1	21.00	21.00	21.00					30	13.00	32.00	19.25	4	10.00	24.00	14.50
Abx	1	21.00	21.00	21.00	6	10.00	28.00	21.00								
Hbx	1	12.00	12.00	12.00	3	21.00	22.00	21.33	19	10.00	42.00	24.89				
DP					3	13.00	16.00	14.67					4	13.00	54.00	34.25
DPD I																
DPD II					2	13.00	14.00	13.50								
DPD III													1	16.00	16.00	16.00
Horn									1	11.00	11.00	11.00				

Abbreviations: n: number of analyses; Min: minimum value; Max: maximum value; Mean: mean value. Results are in parts per million (ppm); And: aphyric andesite; PA: plagioclase phyric andesite; Abx: andesitic volcaniclastic breccia; Hbx: hydrothermal breccia; DP: diorite porphyry; DPD I to III: diorite porphyry dike I to III; Horn: hornfels.

Table 4.9. Summary of transition metals results (Continued)

	Surface				BTG-003				BTG-005				BTG-006			
Sc (ppm)	**n**	**Min**	**Max**	**Mean**	**n**	**Min**	**Max**	**Mean**	**n**	**Min**	**Max**	**Mean**	**n**	**Min**	**Max**	**Mean**
All values	90	2.000	36.00	11.03	74	3.000	29.00	15.27	71	6.000	36.00	18.42	70	1.000	29.00	14.11
And	25	4.000	36.00	12.96	34	3.000	29.00	15.59					33	1.000	20.00	9.788
PA	37	2.000	29.00	9.730	8	5.000	23.00	13.38	30	6.000	36.00	16.30	10	12.00	26.00	18.60
Abx	17	4.000	29.00	12.18	7	5.000	24.00	14.57								
Hbx	11	2.000	36.00	9.273	4	6.000	15.00	9.250	38	6.000	33.00	19.84				
DP					7	18.00	29.00	25.29					14	13.00	25.00	17.71
DPD I					11	7.000	13.00	11.45								
DPD II					3	6.000	23.00	17.00								
DPD III													13	13.00	29.00	17.77
Horn									3	20.00	23.00	21.67				
V (ppm)	**n**	**Min**	**Max**	**Mean**	**n**	**Min**	**Max**	**Mean**	**n**	**Min**	**Max**	**Mean**	**n**	**Min**	**Max**	**Mean**
All values	89	9.000	293.0	137.8	74	24.00	310.0	169.5	71	78.00	333.0	189.5	71	21.00	313.0	172.1
And	25	106.0	272.0	169.7	34	24.00	310.0	159.5					34	21.00	313.0	144.1
PA	37	9.000	230.0	122.4	8	85.00	235.0	167.0	30	78.00	333.0	176.3	10	135.0	266.0	217.2
Abx	17	13.000	293.0	160.2	7	104.0	271.0	191.3								
Hbx	10	12.000	272.0	76.40	4	145.0	191.0	161.5	38	78.00	292.0	197.6				
DP					7	234.0	286.0	262.6					14	150.0	235.0	192.6
DPD I					11	96.00	162.0	133.3								
DPD II					3	92.00	202.0	163.7								
DPD III													13	100.0	255.0	188.7
Horn									3	204.0	238.0	219.3				

Abbreviations: n: number of analyses; Min: minimum value; Max: maximum value; Mean: mean value. Results are in parts per million (ppm); And: aphyric andesite; PA: plagioclase phyric andesite; Abx: andesitic volcaniclastic breccia; Hbx: hydrothermal breccia; DP: diorite porphyry; DPD I to III: diorite porphyry dike I to III; Horn: hornfels.

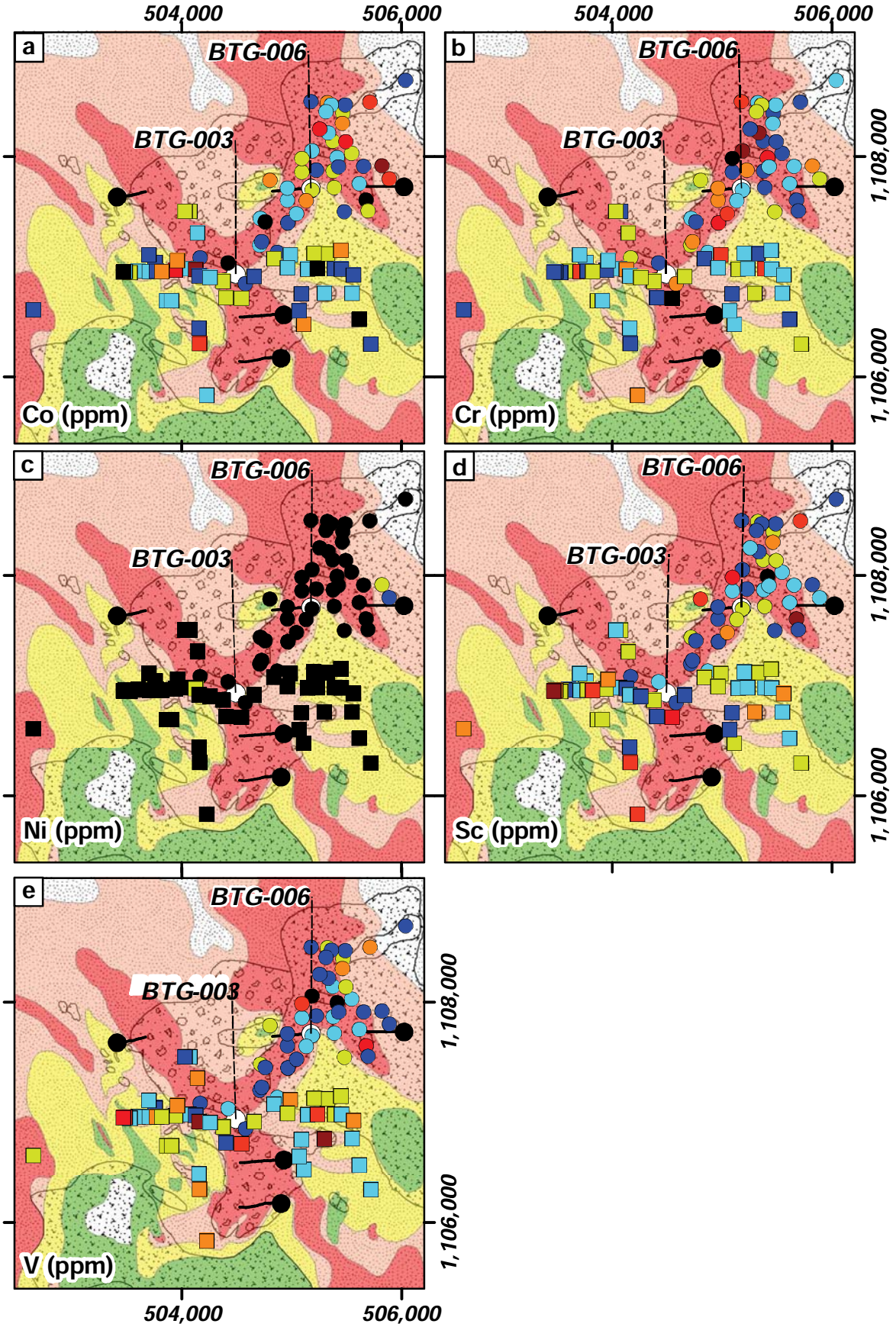

Figure 4.40. Transition metals surface results. a. Cobalt (Co). **b.** Chromium (Cr). **c.** Nickel (Ni). **d.** Scandium (Sc). **e.** Vanadium (V). Legend for the results is in Figure 4.39, all results are in ppm. Rock type and hydrothermal alteration legend as in Figure 4.1.

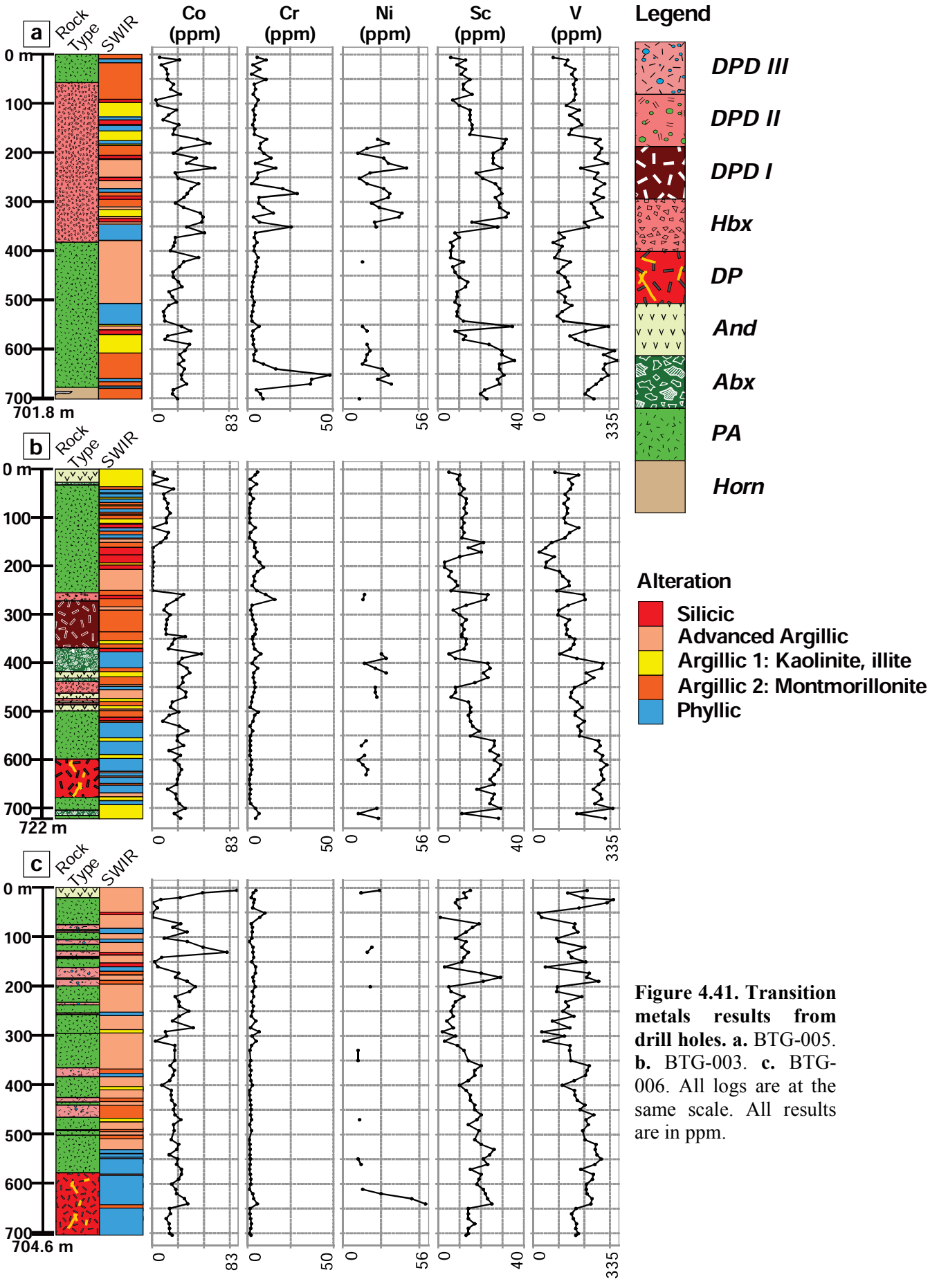

Figure 4.41. Transition metals results from drill holes. a. BTG-005. **b.** BTG-003. **c.** BTG-006. All logs are at the same scale. All results are in ppm.

4.5. Mineralisation

This section addresses the whole rock geochemistry results of base and precious metals from surface and drill hole samples from Bantug. Chalcopyrite was the only ore mineral observed during this study. Chalcopyrite occurs in trace amounts and small size (i.e., <25 μm), it occurs as anhedral inclusions in pyrite and quartz crystals in hornfels (Figs.3.9b and 3.9f) and diorite porphyry (Fig.3.13f) samples. Sulfosalts typically associated with high-sulfidation epithermal deposits (i.e., enargite, luzonite) were not observed while logging or during micro-analytical analyses.

4.5.1. Base metals

Table 4.10 presents a summary of surface and drill hole results for Cu, Mo, Pb, Zn, Sn, and W. Figures 4.43 and 4.44 present surface and drill hole results, respectively. Whole rock geochemistry results are presented in Appendix G.

Surface samples are depleted in base metals in comparison with drill hole samples, except for Sn (Table 4.10). Silicic-altered volcaniclastic andesitic breccia surface samples returned the highest Cu result (i.e., 240.9 ppm; Table 4.10). Advanced argillic-altered hydrothermal breccia surface samples returned the lowest Cu, Pb, and Zn mean values (i.e., 18.70 ppm, 5.788 ppm, 1.066 ppm, respectively). Silicic-altered volcaniclastic andesitic breccia and aphyric andesite surface samples returned the highest Mo results (i.e., 27.55 and 26.39 ppm; Table 4.10; Fig. 4.43b). Advanced argillic-altered plagioclase-phyric andesite surface samples returned the lowest Mo mean result (i.e., 3.593 ppm; Table 4.10). Argillic-altered aphyric andesite surface samples yielded the highest Pb mean value (i.e., 11.81 ppm; Table 4.10). Advanced argillic-altered hydrothermal breccia surface samples returned the lowest mean value (i.e., 5.788 ppm; Table 4.10; Fig. 4.43c). Silicic-altered andesitic volcaniclastic breccia surface samples returned the highest mean Zn value (i.e., 16.33 ppm), and advanced argillic-altered hydrothermal breccia samples the lowest mean value (i.e., 1.066 ppm; Table 4.10; Fig. 4.43d). Silicic-altered plagioclase-phyric andesite and advanced argillic-altered hydrothermal breccia surface samples yielded the highest Sn mean value (i.e., 5.600 ppm, and 4.888 ppm, respectively; Table 4.10; Fig. 4.43e). Silicic-altered aphyric andesite surface samples returned the lowest Sn mean result (i.e., 2.300 ppm; Table 4.10; Fig. 4.43f). Advanced argillic-altered hydrothermal breccia surface samples yielded the highest W mean value (i.e., 1.833 ppm; Table 4.10; Fig. 4.43f), and advanced argillic-altered aphyric andesite samples returned the lowest mean value (i.e., 1.260 ppm; Table 4.10; Fig. 4.43f).

Advanced argillic-altered aphyric andesite samples from BTG-006 returned the highest Cu mean value (i.e., 405.7 ppm; Table 4.10), and the highest Cu value (i.e., 2,517 ppm; Table 4.10; Fig. 4.44c). Propylitic-altered diorite porphyry dike II samples from drill hole BTG-003 returned the lowest Cu mean value (i.e., 40.72 ppm; Table 4.10), and the lowest Cu value (i.e., 8.500 ppm; Table 4.10; Fig. 4.44b). Phyllic-altered diorite porphyry samples from BTG-003 and BTG-006, characterised by incipient stockwork, returned Cu mean values of 159.9 ppm and 115.3 ppm, respectively (Table 4.10; Figs. 4.44b and 4.44c). Phyllic-altered andesitic volcaniclastic breccia samples from drill hole BTG-003 yielded the highest Mo result (i.e., 284.4 ppm; Table 4.10; Fig. 4.44b). A phyllic-altered diorite porphyry sample from BTG-006 returned a similar Mo result (i.e., 214.5 ppm; Table 4.10; Fig. 4.44c). Phyllic-altered diorite porphyry samples from drill holes BTG-003 and BTG-006 returned the highest Zn mean values (i.e., 167.1 ppm, 106.6 ppm, respectively; Table 4.10). Advanced argillic-altered aphyric andesite samples from BTG-006 returned the lowest Zn mean value (i.e., 3.802 ppm; Table 4.10). Advanced argillic-altered aphyric andesite and hydrothermal breccia samples from BTG-003 returned the highest mean Sn values (i.e., 8.062 ppm, and 7.333 ppm, respectively; Table 4.10). Argillic-altered diorite porphyry dike I samples from BTG-003 yielded the lowest Sn mean value (i.e., 1.500 ppm; Table 4.10). Advanced argillic-altered hydrothermal breccia samples from BTG-005 returned the highest W mean value (i.e., 4.710 ppm; Table 4.10). Propylitic-altered diorite porphyry dike II samples from BTG-003 yielded the lowest W mean value (i.e., 1.000 ppm; Table 4.10).

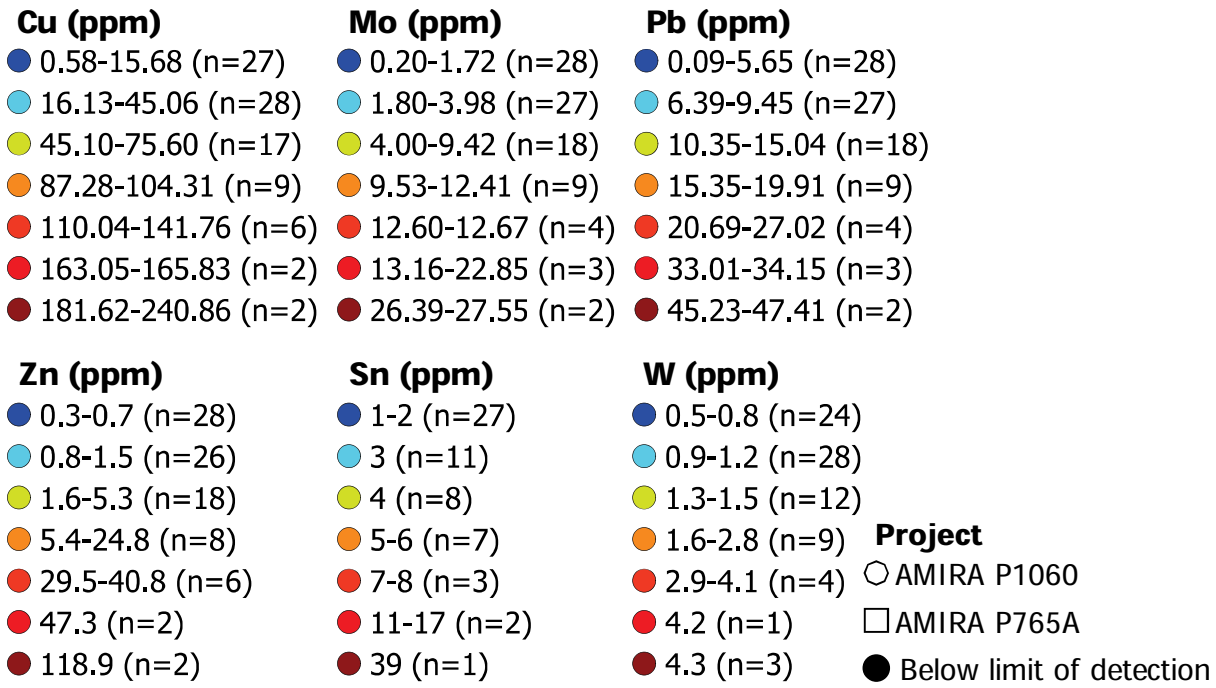

Figure 4.42. Base metals legend for surface results.

Table 4.10. Summary of base metals results

	Surface				BTG-003				BTG-005				BTG-006			
Cu (ppm)	**n**	**Min**	**Max**	**Mean**	**n**	**Min**	**Max**	**Mean**	**n**	**Min**	**Max**	**Mean**	**n**	**Min**	**Max**	**Mean**
All values	91	0.5800	240.9	47.37	74	2.530	1128	109.9	71	28.51	1516	170.0	71	8.440	2517	293.6
And	25	3.160	141.8	45.49	34	2.530	349.8	77.62					34	8.440	2517	405.8
PA	37	0.5800	181.6	48.82	8	56.83	309.89	139.7	30	29.46	241.8	92.49	10	41.82	1744	245.1
Abx	17	1.680	240.9	67.23	7	43.25	1128	279.5								
Hbx	12	0.9000	90.07	18.70	4	46.57	183.9	107.0	38	28.51	1516	232.3				
DP					7	130.0	216.2	160.0					14	55.55	188.4	115.3
DPD I					11	39.70	128.2	68.18								
DPD II					3	8.500	57.26	40.73								
DPD III													13	39.98	1248	229.3
Horn									3	128.0	198.6	155.0				
Mo (ppm)	**n**	**Min**	**Max**	**Mean**	**n**	**Min**	**Max**	**Mean**	**n**	**Min**	**Max**	**Mean**	**n**	**Min**	**Max**	**Mean**
All values	91	0.2000	27.55	5.094	74	1.330	284.4	14.96	71	0.5700	75.86	6.742	71	0.9200	214.5	14.35
And	25	1.400	26.39	7.959	34	1.330	60.52	8.776					34	1.830	124.9	11.80
PA	37	0.2200	13.16	3.594	8	2.030	115.5	29.40	30	1.020	75.86	9.613	10	3.020	62.98	17.37
Abx	17	0.2000	27.55	4.649	7	5.420	284.4	47.76								
Hbx	12	0.4500	12.67	4.382	4	4.440	46.43	23.76	38	0.5700	23.21	3.906				
DP					7	1.970	6.370	3.599					14	2.290	214.5	27.67
DPD I					11	1.980	17.89	6.601								
DPD II					3	2.580	41.43	15.55								
DPD III													13	0.9200	16.07	4.341
Horn									3	2.650	21.22	13.96				
Pb (ppm)	**n**	**Min**	**Max**	**Mean**	**n**	**Min**	**Max**	**Mean**	**n**	**Min**	**Max**	**Mean**	**n**	**Min**	**Max**	**Mean**
All values	91	0.09000	47.41	10.24	74	7.250	1399	106.3	71	2.810	58.46	20.33	71	1.240	189.9	20.37
And	25	2.890	45.23	11.81	34	9.230	1399	180.1					34	2.330	90.13	21.73
PA	37	0.09000	47.41	11.11	8	31.66	150.8	58.40	30	8.010	58.05	21.19	10	1.240	12.45	4.876
Abx	17	0.2700	20.69	9.161	7	9.440	85.75	42.05								
Hbx	12	0.2600	20.69	5.788	4	29.93	45.28	40.38	38	2.810	58.46	19.48				
DP					7	8.430	135.0	57.62					14	2.690	60.93	16.98
DPD I					11	9.630	49.83	22.84								
DPD II					3	7.250	149.1	54.71								
DPD III													13	2.260	189.9	32.39
Horn									3	13.71	35.23	22.46				

Abbreviations: n: number of analyses; Min: minimum value; Max: maximum value; Mean: mean value. Results are in parts per million (ppm); And: aphyric andesite; PA: plagioclase phyric andesite; Abx: andesitic volcaniclastic breccia; Hbx: hydrothermal breccia; DP: diorite porphyry; DPD I to III: diorite porphyry dike I to III; Horn: hornfels.

Table 4.10. Summary of base metals results (Continued)

	Surface				BTG-003				BTG-005				BTG-006			
Zn (ppm)	**n**	**Min**	**Max**	**Mean**	**n**	**Min**	**Max**	**Mean**	**n**	**Min**	**Max**	**Mean**	**n**	**Min**	**Max**	**Mean**
All values	90	0.3000	118.9	8.558	74	0.5000	325.9	70.19	71	1.900	240.1	35.78	71	0.3000	244.7	36.20
And	25	0.3000	118.9	9.444	34	0.5000	325.9	57.08					34	0.3000	33.50	3.803
PA	37	0.3000	47.30	7.027	8	1.900	321.8	97.90	30	4.500	240.1	46.58	10	0.7000	243.0	42.47
Abx	16	0.5000	118.9	16.33	7	1.200	249.1	49.79								
Hbx	12	0.3000	6.900	1.067	4	5.300	46.40	16.33	38	1.900	86.10	23.80				
DP					7	56.30	263.5	167.2					14	28.20	244.7	106.7
DPD I					11	3.600	140.7	67.65								
DPD II					3	1.700	76.00	47.33								
DPD III													13	4.100	81.90	40.22
Horn									3	70.80	88.60	79.53				
Sn (ppm)	**n**	**Min**	**Max**	**Mean**	**n**	**Min**	**Max**	**Mean**	**n**	**Min**	**Max**	**Mean**	**n**	**Min**	**Max**	**Mean**
All values	59	1.000	39.00	4.051	65	1.000	65.00	5.769	63	1.000	15.00	4.143	56	1.000	9.000	3.268
And	20	1.000	7.000	3.000	32	1.000	65.00	8.063					30	1.000	9.000	3.167
PA	20	1.000	39.00	5.600	6	2.000	9.000	4.333	30	2.000	15.00	6.133	8	2.000	9.000	5.375
Abx	10	1.000	4.000	2.300	7	2.000	4.000	3.429								
Hbx	9	2.000	11.00	4.889	3	7.000	8.000	7.333	30	1.000	7.000	2.367				
DP					6	2.000	5.000	3.333					12	1.000	5.000	2.333
DPD I					8	1.000	2.000	1.500								
DPD II					3	1.000	11.00	4.333								
DPD III													6	1.000	6.000	2.833
Horn									3	1.000	3.000	2.000				
W (ppm)	**n**	**Min**	**Max**	**Mean**	**n**	**Min**	**Max**	**Mean**	**n**	**Min**	**Max**	**Mean**	**n**	**Min**	**Max**	**Mean**
All values	81	0.5000	4.300	1.388	73	0.6000	58.20	3.225	68	0.5000	72.80	3.274	70	0.5000	5.600	1.820
And	23	0.5000	4.200	1.261	34	0.6000	58.20	4.209					33	0.7000	5.600	1.615
PA	33	0.5000	4.300	1.324	7	0.8000	14.90	3.471	28	0.5000	4.000	1.543	10	1.800	4.500	2.810
Abx	13	0.5000	4.300	1.362	7	0.8000	14.00	3.543								
Hbx	12	0.8000	4.300	1.833	4	0.9000	2.400	1.800	37	0.8000	72.80	4.711				
DP					7	1.300	3.600	2.114					14	0.8000	5.600	2.407
DPD I					11	0.7000	4.800	1.655								
DPD II					3	0.9000	1.200	1.000								
DPD III													13	0.5000	2.100	0.9462
Horn									3	1.400	2.100	1.700				

Abbreviations: n: number of analyses; Min: minimum value; Max: maximum value; Mean: mean value. Results are in parts per million (ppm); And: aphyric andesite; PA: plagioclase phyric andesite; Abx: andesitic volcaniclastic breccia; Hbx: hydrothermal breccia; DP: diorite porphyry; DPD I to III: diorite porphyry dike I to III; Horn: hornfels.

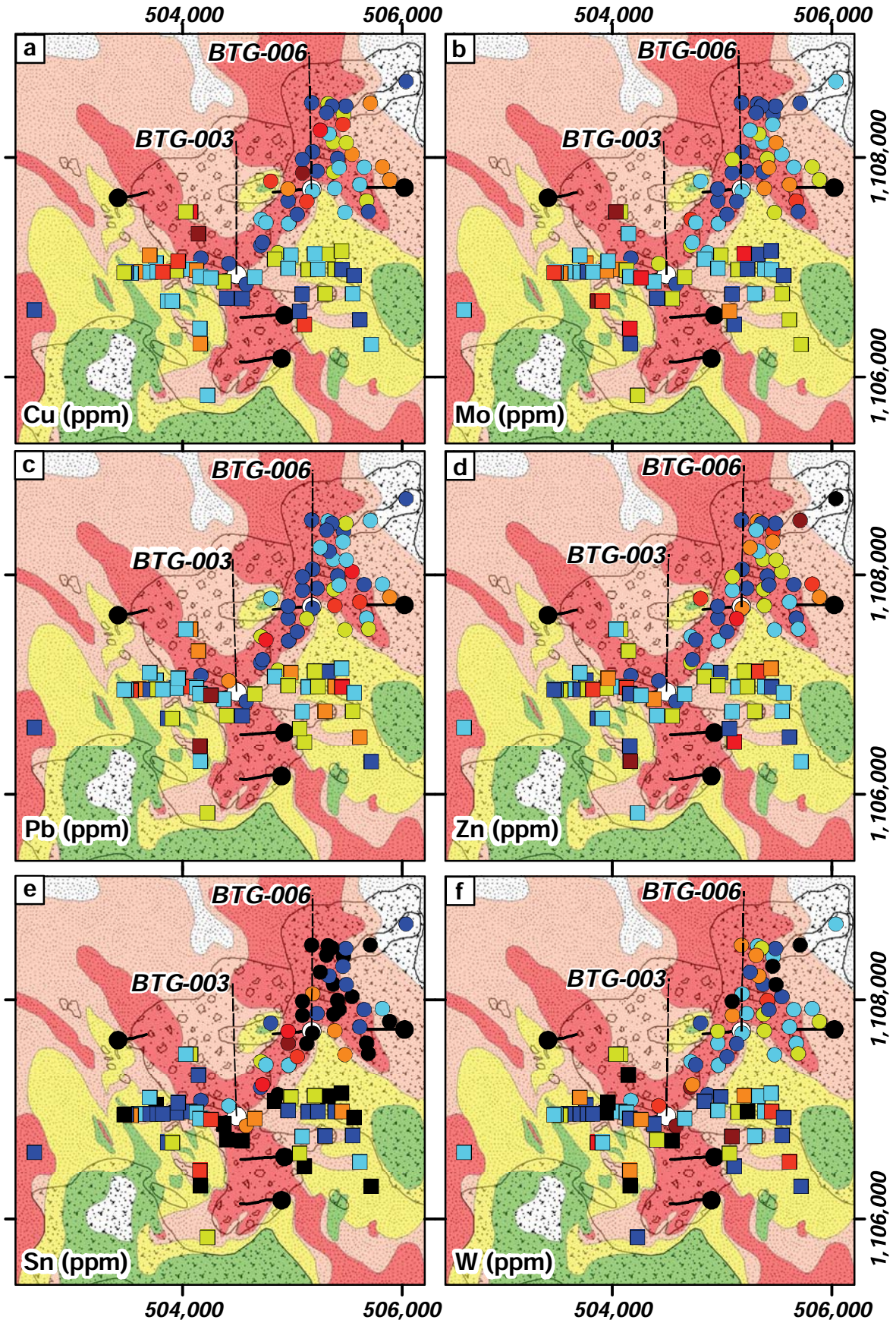

Figure 4.43. Base metals surface results. a. Copper (Cu). **b.** Molybdenum (Mo). **c.** Lead (Pb). **d.** Zinc (Zn). **e.** Tin (Sn). **f.** Tungsten (W). Legend for the results is presented in Figure 4.33, all results are in ppm. Rock type and hydrothermal alteration legend as in Figure 4.1.

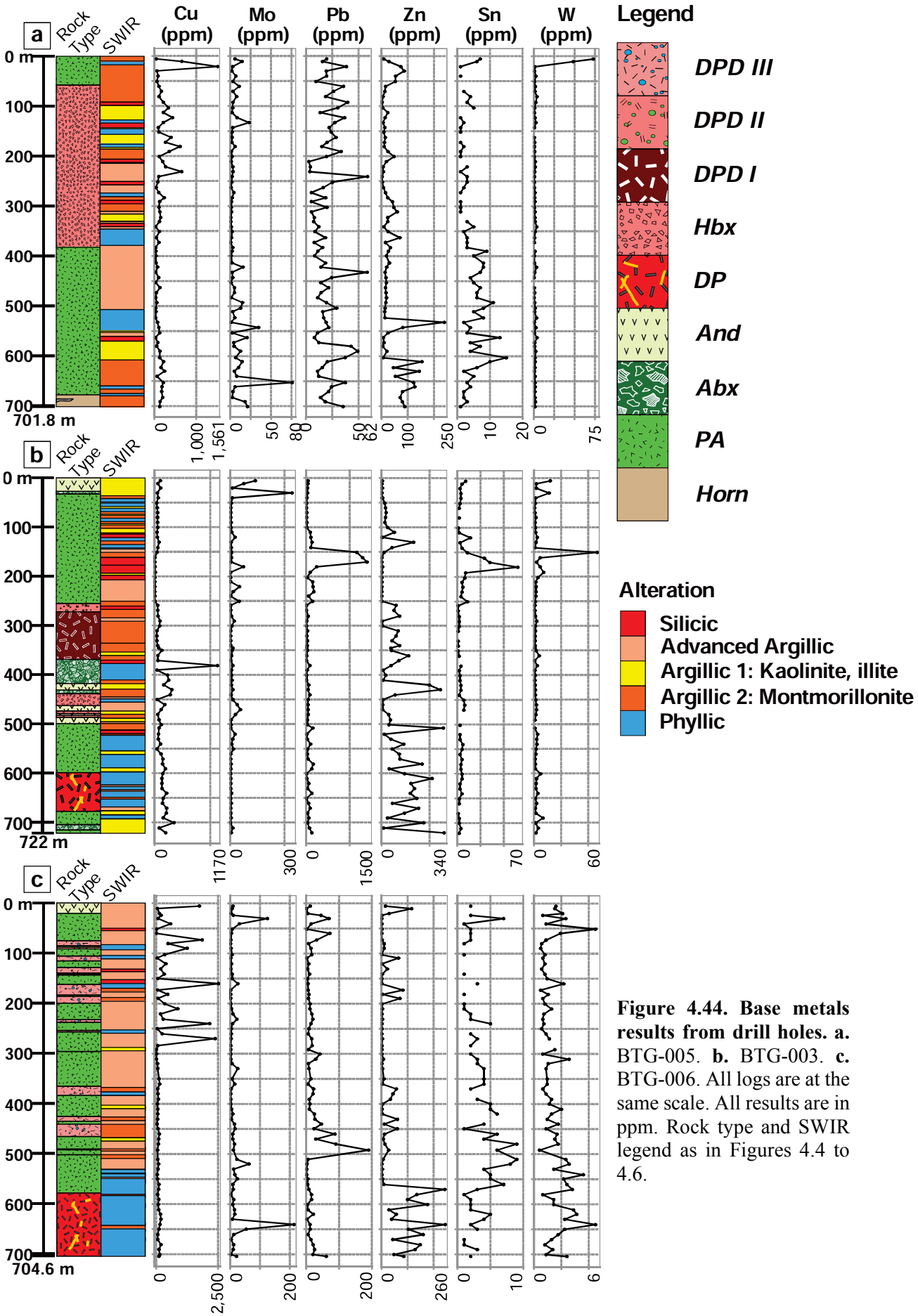

Figure 4.44. Base metals results from drill holes. a. BTG-005. **b.** BTG-003. **c.** BTG-006. All logs are at the same scale. All results are in ppm. Rock type and SWIR legend as in Figures 4.4 to 4.6.

4.5.2. Precious metals

Table 4.11 presents a summary of results for Au, Ag, Pt, and Re. Figures 4.46 and 4.47 present surface and drill hole results, respectively. Whole rock geochemistry results are presented in Appendix G.

Surface samples returned the lowest mean value results for Ag, Pt, and Re compared with drill hole mean value results (Table 4.11). The highest Au value resulted from a silicic-altered plagioclase-phyric andesite surface sample (i.e., 0.5621 ppm; Table 4.11; Fig. 4.46a). The highest surface Ag value resulted from an advanced argillic-altered hydrothermal breccia sample (i.e., 0.87 ppm; Table 4.11; Fig. 4.46b). The highest surface Re value resulted from a silicic-altered andesitic volcaniclastic breccia sample (i.e., 501 ppb; Table 4.11; Fig. 4.46d).

Advanced argillic-altered andesitic volcaniclastic breccia samples from BTG-003 yielded the highest Au mean value (i.e., 0.0389 ppm; Table 4.11). However, an advanced argillic-altered hydrothermal breccia sample at 21.15 m depth in drill hole BTG-005 returned a value of 0.445 ppm Au (Table 4.11; intercept not in scale in Figure 4.47a). Phyllic-altered diorite porphyry dike III and diorite porphyry samples from BTG-006 returned the lowest mean value results (i.e., 0.0015 ppm, and 0.0025 ppm, respectively; Table 4.11).

The highest Ag value resulted from an advanced argillic-altered hydrothermal breccia surface sample (i.e., 0.8700 ppm; Table 4.11; Fig. 4.46b). The highest Ag drill hole value resulted from an advanced argillic-altered aphyric andesite from BTG-003 (i.e., 0.8020 ppm; Table 4.11; Fig. 4.47b). The highest Ag mean value resulted from phyllic-altered diorite porphyry samples from BTG-003 (i.e., 0.254 ppm; Table 4.11), and the lowest mean value from advanced argillic-altered plagioclase phyric andesite samples from BTG-005 (i.e., 0.04267 ppm; Table 4.11).

The highest Pt value, and the highest mean value, resulted from advanced argillic-altered andesitic volcaniclastic breccia samples from BTG-003 (i.e., 11 ppb, 7 ppb, respectively; Table 4.11; Fig. 4.47b). The lowest mean value resulted from hornfels samples from BTG-005 (i.e., 2.66 ppb Table 4.11; Fig. 4.47a). The highest Re result and mean value result came from advanced argillic-altered hydrothermal breccias in BTG-003 (i.e., 925.0 ppb, 433.7 ppb, respectively; Table 4.11; Fig. 4.47b). The lowest mean value resulted from phyllic-altered diorite porphyry samples from BTG-003 (i.e., 16.71 ppb; Table 4.11)

Table 4.11. Summary of precious metals results

	Surface				BTG-003				BTG-005				BTG-006			
Au (ppm)	**n**	**Min**	**Max**	**Mean**	**n**	**Min**	**Max**	**Mean**	**n**	**Min**	**Max**	**Mean**	**n**	**Min**	**Max**	**Mean**
All values	77	0.0005000	0.5621	0.01595	74	0.001100	0.08430	0.01794	70	0.0004000	0.4455	0.02170	67	0.0003000	0.01590	0.0037
And	22	0.0007000	0.02860	0.00869	34	0.001100	0.06980	0.01560					33	0.0003000	0.01590	0.0039
PA	32	0.0005000	0.5621	0.02614	8	0.006900	0.07250	0.02610	30	0.0005000	0.06380	0.01495	10	0.002700	0.01040	0.0066
Abx	14	0.0008000	0.0249	0.00705	7	0.01470	0.08430	0.03890								
Hbx	9	0.0006000	0.0359	0.01127	4	0.005100	0.02200	0.01295	37	0.0004000	0.4455	0.02676				
DP					7	0.003100	0.03130	0.009800					13	0.0008000	0.006400	0.0026
DPD I					11	0.001300	0.04340	0.01652								
DPD II					3	0.001600	0.01000	0.00463								
DPD III													11	0.0003000	0.003400	0.0016
Horn									3	0.02110	0.03000	0.02673				
Ag (ppm)	**n**	**Min**	**Max**	**Mean**	**n**	**Min**	**Max**	**Mean**	**n**	**Min**	**Max**	**Mean**	**n**	**Min**	**Max**	**Mean**
All values	90	0.002000	0.8700	0.04672	74	0.01000	0.8020	0.1208	71	0.00800	0.5280	0.06621	71	0.003000	0.2380	0.05279
And	25	0.002000	0.08800	0.02324	34	0.02500	0.8020	0.1258					34	0.003000	0.2380	0.05038
PA	37	0.003000	0.3640	0.04865	8	0.01000	0.2800	0.1096	30	0.00800	0.2790	0.04267	10	0.009000	0.1410	0.05340
Abx	16	0.003000	0.1590	0.04781	7	0.01000	0.2800	0.1169								
Hbx	12	0.004000	0.8700	0.08825	4	0.03200	0.1150	0.08100	38	0.01100	0.5280	0.08497				
DP					7	0.09900	0.4450	0.2540					14	0.02800	0.09400	0.04614
DPD I					11	0.03700	0.1780	0.06536								
DPD II					3	0.03900	0.05300	0.04800								
DPD III													13	0.03300	0.2190	0.06577
Horn									3	0.03900	0.07700	0.06400				
Pt (ppb)	**n**	**Min**	**Max**	**Mean**	**n**	**Min**	**Max**	**Mean**	**n**	**Min**	**Max**	**Mean**	**n**	**Min**	**Max**	**Mean**
All values	5	2.000	3.000	2.800	38	2.000	11.00	4.789	33	2.000	9.000	4.182	30	2.000	8.000	4.233
And	2	3.000	3.000	3.000	18	2.000	8.000	4.222					7	2.000	6.000	4.000
PA	3	2.000	3.000	2.667	2	3.000	7.000	5.000	11	3.000	7.000	4.545	5	3.000	7.000	4.400
Abx					7	3.000	11.00	7.000								
Hbx					1	6.000	6.000	6.000	19	2.000	9.000	4.211				
DP					7	3.000	5.000	3.833					13	2.000	8.000	4.538
DPD I					4	3.000	7.000	4.500								
DPD II																
DPD III													5	2.000	8.000	3.600
Horn									3	2.000	3.000	2.667				

Abbreviations: n: number of analyses; Min: minimum value; Max: maximum value; Mean: mean value. Results are in parts per million (ppm); And: aphyric andesite; PA: plagioclase phyric andesite; Abx: andesitic volcaniclastic breccia; Hbx: hydrothermal breccia; DP: diorite porphyry; DPD I to III: diorite porphyry dike I to III; Horn: hornfels.

Table 4.11. Summary of precious metals results (Continued)

	Surface				BTG-003				BTG-005				BTG-006			
Re (ppb)	**n**	**Min**	**Max**	**Mean**	**n**	**Min**	**Max**	**Mean**	**n**	**Min**	**Max**	**Mean**	**n**	**Min**	**Max**	**Mean**
All values	65	1.000	501.0	36.28	63	1.000	925.0	67.68	66	1.000	479.0	80.52	65	1.000	660.0	112.4
And	19	1.000	304.0	33.53	26	1.000	382.0	40.15					32	4.000	398.0	98.25
PA	27	1.000	304.0	32.07	7	4.000	231.0	82.43	30	3.000	415.0	98.87	9	11.00	660.0	158.9
Abx	11	1.000	501.0	71.36	7	3.000	114.0	51.43								
Hbx	8	2.000	31.00	8.750	4	32.00	925.0	433.8	33	1.000	262.0	43.94				
DP					7	7.000	27.00	16.71					13	12.00	618.0	148.9
DPD I					10	12.00	60.00	28.10								
DPD II					3	15.00	135.0	75.00								
DPD III													11	1.000	314.0	72.45
Horn									3	25.00	479.0	299.3				

Abbreviations: n: number of analyses; Min: minimum value; Max: maximum value; Mean: mean value. Results are in parts per million (ppm); And: aphyric andesite; PA: plagioclase phyric andesite; Abx: andesitic volcaniclastic breccia; Hbx: hydrothermal breccia; DP: diorite porphyry; DPD I to III: diorite porphyry dike I to III; Horn: hornfels.

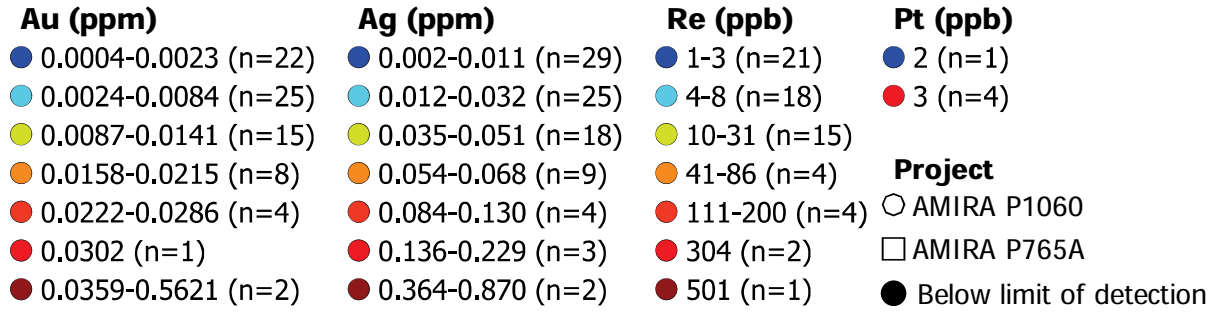

Figure 4.45. Precious metals legend for surface results.

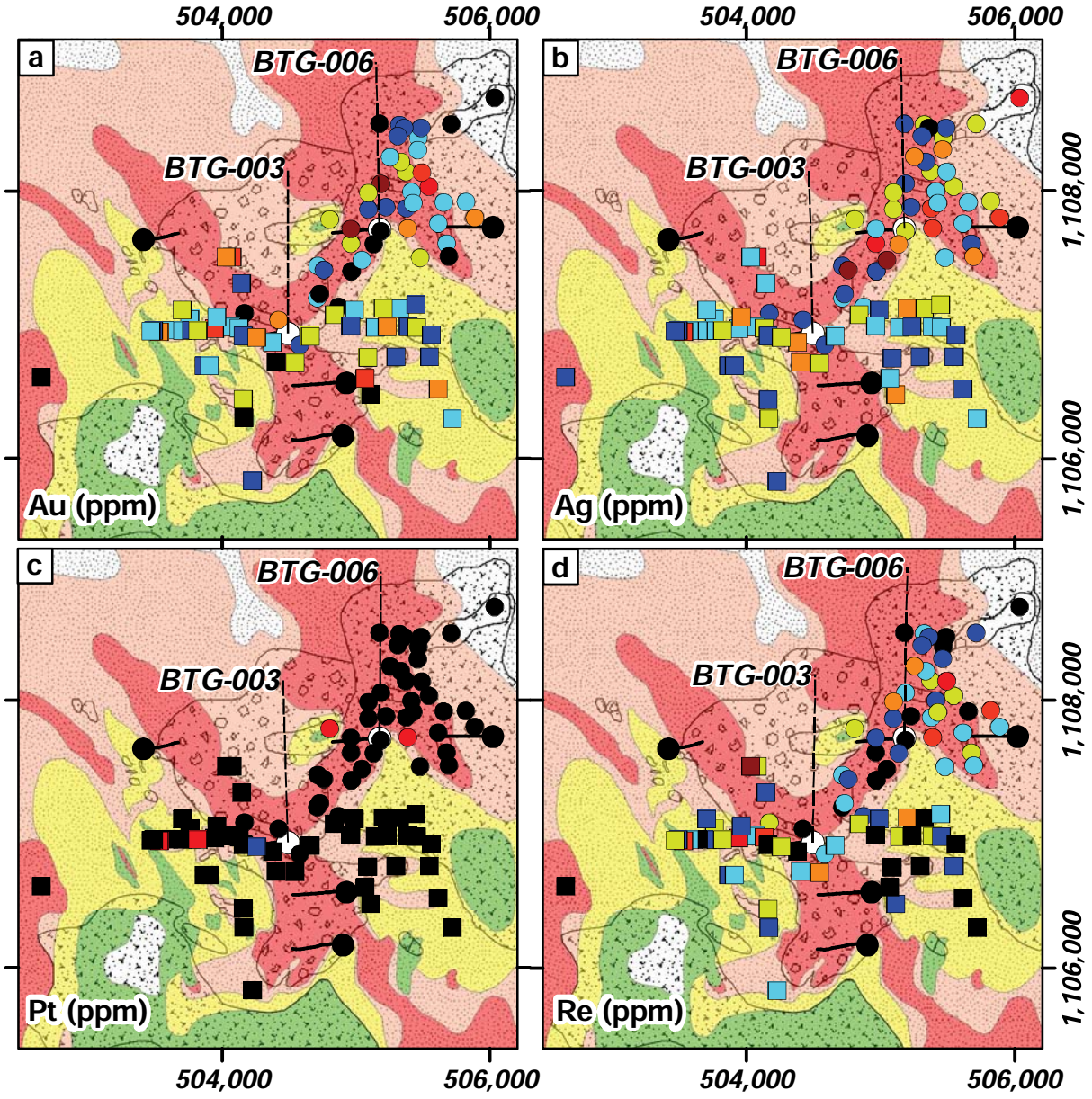

Figure 4.46. Precious metals surface results. a. Gold (Au). **b.** Silver (Ag). **c.** Platinum (Pt). **d.** Rhenium (Re). Legend for the results is presented in Figure 4.33, all results are in ppm. Rock type and hydrothermal alteration legend as in Figure 4.1. Squares symbols indicate samples collected for the AMIRA P765A project, and circles indicate samples collected for the AMIRA P1060 project. Samples coloured in black resulted below the limit of detection (LOD).

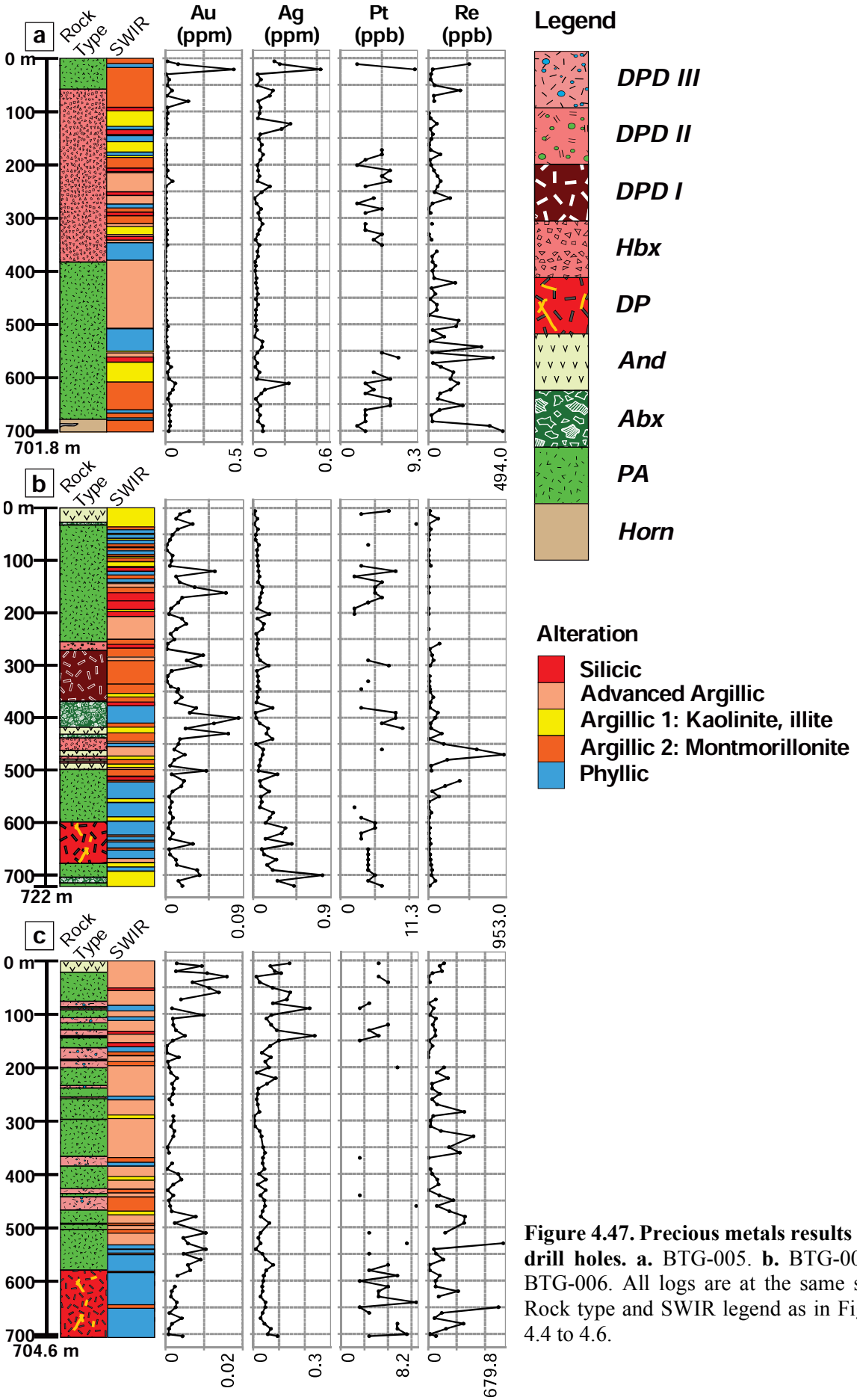

Figure 4.47. Precious metals results from drill holes. a. BTG-005. **b.** BTG-003. **c.** BTG-006. All logs are at the same scale. Rock type and SWIR legend as in Figures 4.4 to 4.6.

4.5.3. Pathfinder elements

Pathfinder elements for porphyry-epithermal deposits include: As, Sb, Bi, Te, Hg (Coope, 1973; Govet, 1983; Mauk and Simpson, 2007; Booden et al., 2011; Cohen and Bowell, 2014). Table 4.12 presents a summary of the results, and Figures 4.48 and 4.50 present surface and drill hole results. Whole rock geochemistry results are presented in Appendix G.

Samples from drill hole BTG-003 yielded the highest mean value results for all pathfinder elements (Table 4.12). Samples from BTG-005 yielded the lowest As mean value result, and samples from BTG-006 returned the lowest Sb, Bi, and Te mean values (Table 4.12). Samples from BTG-005 yielded the lowest Hg mean value result (Table 4.12).

Advanced argillic-altered andesitic volcaniclastic breccia samples from BTG-003 yielded the highest As result and mean value (i.e., 381.5 ppm, 74.32 ppm, respectively; Table 4.12; Fig. 4.50b). Advanced argillic-altered aphyric andesite samples from BTG-003 yielded the highest Sb, Bi, and Te results (i.e., 91.75 ppm, 638.4 ppm, 65.90 ppm, respectively; Table 4.12; Fig. 4.50b). Also, the second highest As and Hg results (i.e., 221.7 ppm, 462.0 ppb, respectively; Table 4.12; Fig 4.50b). Hornfels samples from BTG-005 yielded the lowest mean value As, Sb, Te, and Hg results (i.e., 1.05 ppm, 0.08333 ppm, 0.23 ppm, 7.5 ppb, respectively; Table 4.12). Propylitic-altered diorite porphyry dike II samples from BTG-003 returned the highest Bi mean value (i.e., 41.52 ppm; Table 4.12). Phyllic-altered diorite porphyry samples returned the lowest Bi mean value (i.e., 0.4407 ppm; Table 4.12). Argillic-altered diorite porphyry dike I samples from BTG-003 returned the highest Hg mean value (i.e., 864.6 ppb; Table 4.12).

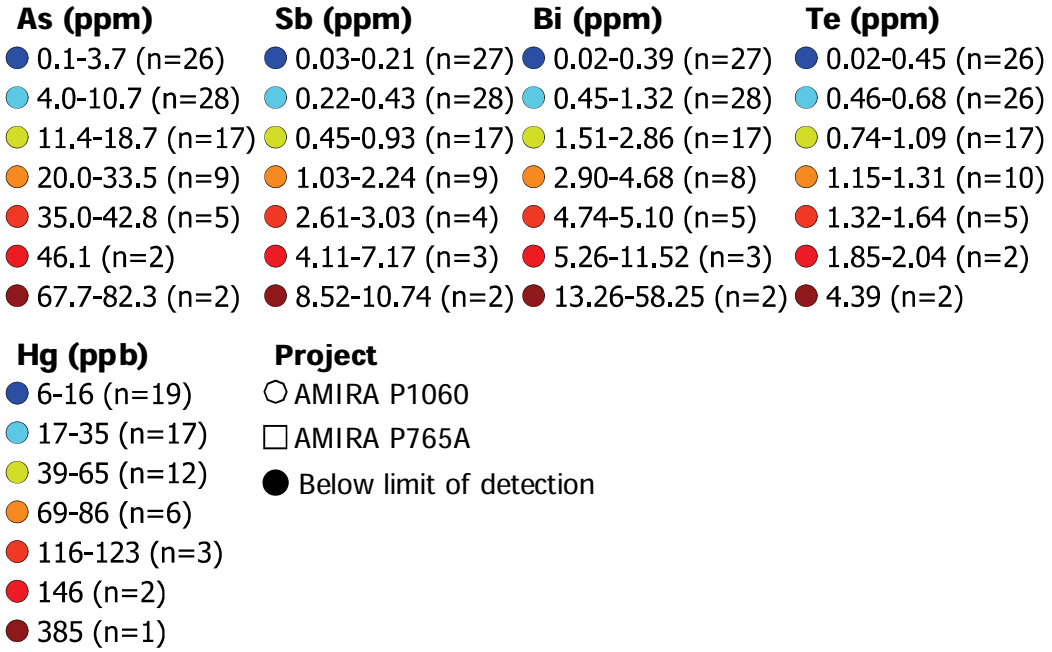

Figure 4.48. Pathfinder elements legend for surface results.

Table 4.12. Summary of pathfinder elements results

	Surface				BTG-003				BTG-005				BTG-006			
As (ppm)	**n**	**Min**	**Max**	**Mean**	**n**	**Min**	**Max**	**Mean**	**n**	**Min**	**Max**	**Mean**	**n**	**Min**	**Max**	**Mean**
All values	89	0.1000	82.30	12.66	74	2.500	381.5	41.86	69	0.4000	108.30	24.68	69	0.5000	229.6	24.44
And	24	0.5000	67.70	14.77	34	2.900	221.7	42.90					34	1.300	229.6	35.98
PA	36	0.3000	46.10	10.85	8	11.30	107.3	37.74	29	0.4000	43.60	14.53	8	0.8000	74.40	17.80
Abx	17	0.3000	82.30	15.01	7	5.900	381.5	74.33								
Hbx	12	0.1000	42.80	10.58	4	22.40	53.40	36.13	38	2.700	108.30	33.66				
DP					7	28.30	75.40	48.20					14	0.5000	16.70	7.986
DPD I					11	7.300	55.60	23.13								
DPD II					3	2.500	65.80	26.97								
DPD III													13	5.600	39.20	16.05
Horn									2	0.4000	1.700	1.050				
Sb (ppm)	**n**	**Min**	**Max**	**Mean**	**n**	**Min**	**Max**	**Mean**	**n**	**Min**	**Max**	**Mean**	**n**	**Min**	**Max**	**Mean**
All values	90	0.03000	10.74	0.9677	74	0.05000	91.75	3.699	71	0.04000	2.500	0.3215	71	0.04000	1.4200	0.3234
And	25	0.07000	7.170	1.168	34	0.07000	91.75	6.726					34	0.05000	1.2900	0.4006
PA	36	0.03000	7.170	0.6456	8	0.1200	4.780	1.348	30	0.04000	0.7300	0.3107	10	0.04000	1.4200	0.3190
Abx	17	0.04000	8.520	1.039	7	0.2100	4.430	1.327								
Hbx	12	0.04000	10.74	1.416	4	0.2500	1.680	0.9025	38	0.06000	2.500	0.3489				
DP					7	0.6700	2.740	1.316					14	0.07000	0.5300	0.2250
DPD I					11	0.1600	1.910	0.5073								
DPD II					3	0.05000	6.430	2.187								
DPD III													13	0.09000	0.5900	0.2308
Horn									3	0.05000	0.1200	0.08333				
Bi (ppm)	**n**	**Min**	**Max**	**Mean**	**n**	**Min**	**Max**	**Mean**	**n**	**Min**	**Max**	**Mean**	**n**	**Min**	**Max**	**Mean**
All values	90	0.02000	58.25	2.343	74	0.1800	638.4	12.11	70	0.03000	3.970	1.353	71	0.03000	2.940	0.6741
And	25	0.08000	58.25	4.588	34	0.1800	638.4	20.48					34	0.03000	2.940	0.7494
PA	36	0.04000	5.260	1.344	8	0.7800	3.610	1.765	30	0.5300	2.630	1.277	10	0.1300	1.950	0.8490
Abx	17	0.02000	11.52	1.847	7	0.4500	3.130	1.650								
Hbx	12	0.08000	5.100	1.368	4	0.6100	0.9000	0.7925	38	0.03000	3.970	1.485				
DP					7	0.4500	1.480	0.9957					14	0.2800	0.6000	0.4407
DPD I					11	0.3800	15.96	3.613								
DPD II					3	0.4300	123.6	41.52								
DPD III													13	0.09000	1.300	0.5938
Horn									3	0.4500	0.5400	0.4867				

Abbreviations: n: number of analyses; Min: minimum value; Max: maximum value; Mean: mean value. Results are in parts per million (ppm); And: aphyric andesite; PA: plagioclase phyric andesite; Abx: andesitic volcaniclastic breccia; Hbx: hydrothermal breccia; DP: diorite porphyry; DPD I to III: diorite porphyry dike I to III; Horn: hornfels.

Table 4.12. Summary of pathfinder elements results (Continued)

	Surface				BTG-003				BTG-005				BTG-006			
Te (ppm)	**n**	**Min**	**Max**	**Mean**	**n**	**Min**	**Max**	**Mean**	**n**	**Min**	**Max**	**Mean**	**n**	**Min**	**Max**	**Mean**
All values	88	0.02000	4.390	0.7615	73	0.07000	65.90	1.854	71	0.06000	4.900	0.8676	68	0.02000	3.860	0.6269
And	25	0.2400	4.390	0.9540	33	0.07000	65.90	2.665					31	0.02000	2.650	0.4187
PA	36	0.03000	4.390	0.7033	8	0.3400	7.460	2.021	30	0.07000	1.030	0.3173	10	0.09000	2.120	1.027
Abx	17	0.04000	1.550	0.7041	7	0.2700	3.300	1.284								
Hbx	10	0.02000	1.640	0.5870	4	0.3300	0.5400	0.4250	37	0.06000	4.900	1.352				
DP					7	0.1700	0.6000	0.4114					14	0.09000	1.390	0.4550
DPD I					11	0.4700	1.960	1.387								
DPD II					3	0.1700	1.610	0.8033								
DPD III													13	0.1600	3.860	1.001
Horn									3	0.1500	0.2700	0.2300				
Hg (ppb)	**n**	**Min**	**Max**	**Mean**	**n**	**Min**	**Max**	**Mean**	**n**	**Min**	**Max**	**Mean**	**n**	**Min**	**Max**	**Mean**
All values	60	6.000	385.0	46.12	56	6.000	7337	184.3	56	5.000	121.0	19.18	56	5.000	168.0	29.04
And	20	8.000	146.0	48.75	24	6.000	462.0	71.83					27	5.000	168.0	31.52
PA	22	6.000	120.0	32.41	7	6.000	142.0	49.57	26	5.000	37.00	17.23	9	5.000	28.00	16.44
Abx	12	7.000	385.0	68.92	5	16.00	39.00	28.40								
Hbx	6	9.000	116.0	42.00	3	18.00	36.00	25.00	28	5.000	121.0	21.82				
DP					7	11.00	41.00	28.71					9	9.000	79.00	22.33
DPD I					9	7.000	7337.0	864.7								
DPD II					1	48.00	48.00	48.00								
DPD III													11	7.000	126.0	38.73
Horn									2	6.000	9.000	7.500				

Abbreviations: n: number of analyses; Min: minimum value; Max: maximum value; Mean: mean value. Results are in parts per million (ppm); And: aphyric andesite; PA: plagioclase phyric andesite; Abx: andesitic volcaniclastic breccia; Hbx: hydrothermal breccia; DP: diorite porphyry; DPD I to III: diorite porphyry dike I to III; Horn: hornfels.

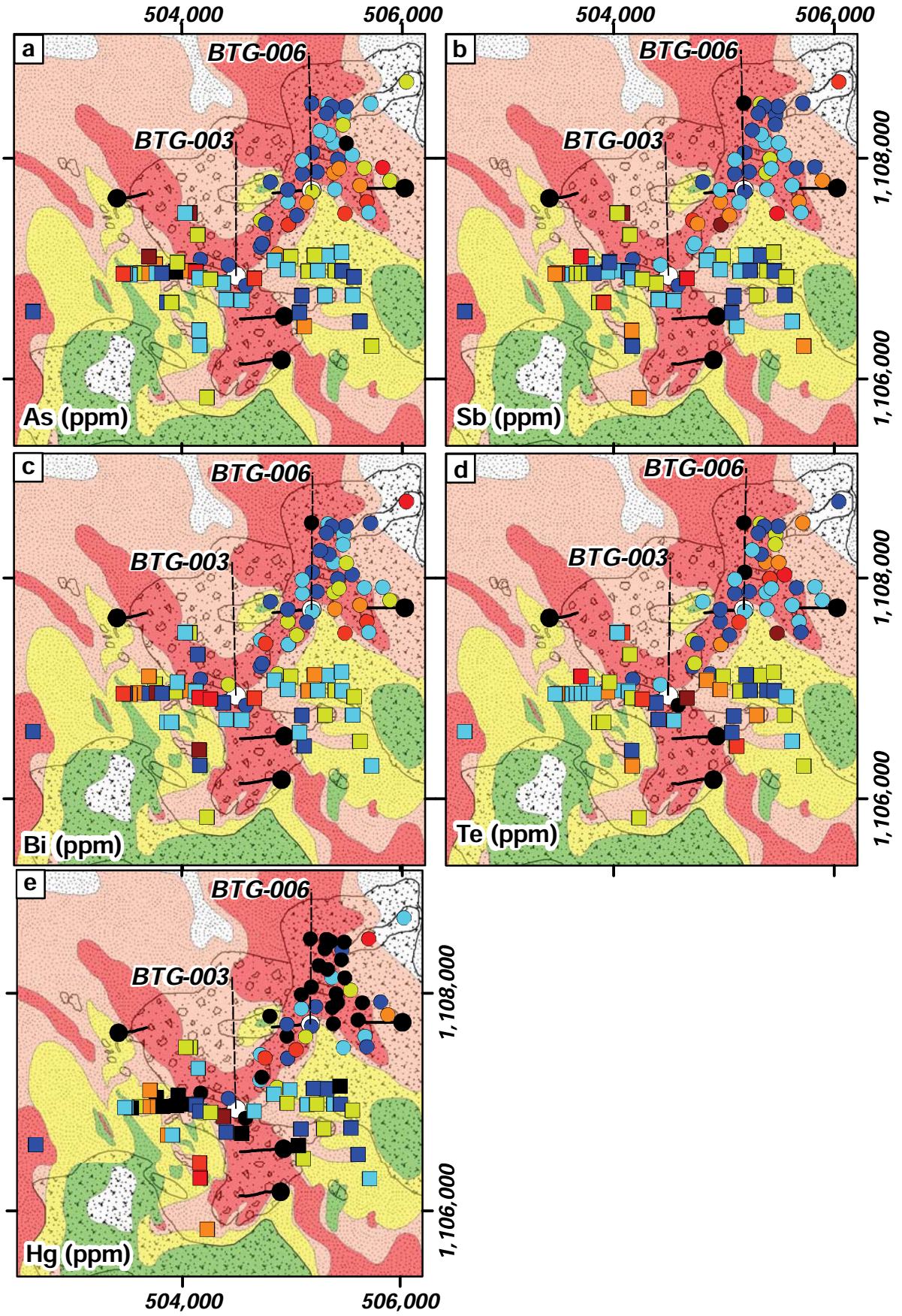

Figure 4.49. Pathfinder elements results from surface samples. a. Arsenic (As). **b.** Antimony (Sb). **c.** Bismuth (Bi). **d.** Tellurium (Te). **e.** Mercury (Hg). Legend for the results is presented in Figure 4.33, all results are in ppm. Rock type and hydrothermal alteration legend as in Figure 4.1.

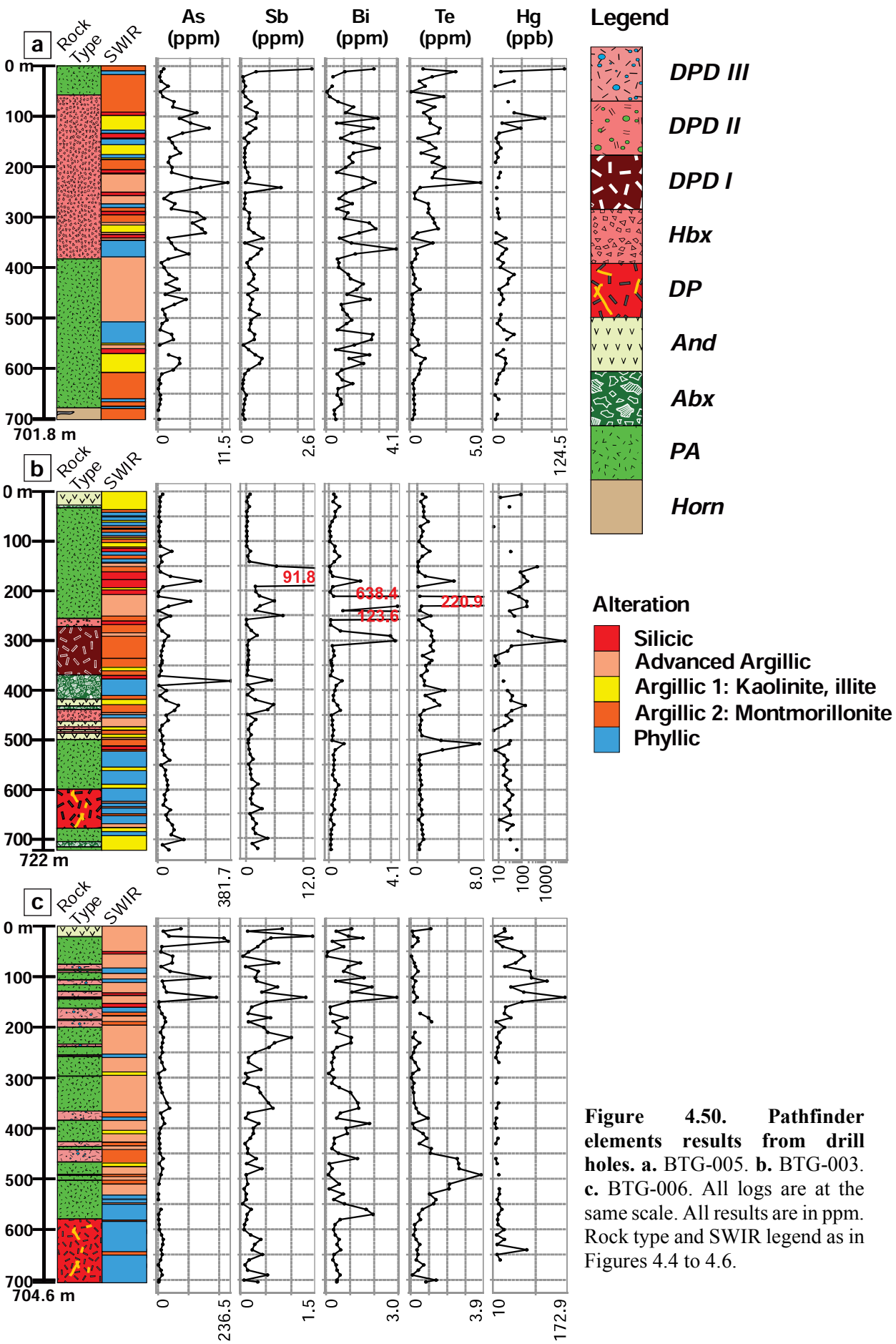

Figure 4.50. Pathfinder elements results from drill holes. a. BTG-005. **b.** BTG-003. **c.** BTG-006. All logs are at the same scale. All results are in ppm. Rock type and SWIR legend as in Figures 4.4 to 4.6.

4.6. Discussion

4.6.1. Geochemical variations due to weathering at the Bantug lithocap

Braxton et al. (2009) found that oxidation profiles in humid tropical porphyry systems are typically subdued, with sulfide oxidation generally less than 100 m below the weathering surface. Hematite and jarosite, formed after weathering of hydrothermal minerals, were observed at the Bantug lithocap at various depths, in some cases greater than 100 m (Fig. 4.51). Appendix D presents graphic logs for drill holes analysed during this study. The depths of weathering determined for drill holes BTG-003, BTG-005, and BTG-006 are 40.45 m, 181 m, and 162 m, respectively. Jarosite was observed between 0 and 8 m depth in BTG-003, and hematite was observed between 8 and 38 m depth; both minerals were found at 120 m and 140 m depth (Fig. 4.51b). Jarosite was observed irregularly from 0 to 52 m depth in drill hole BTG-005, and hematite was observed to ~180 m depth (Fig. 4.51a). Hematite was observed to 160 m depth in drill hole BTG-006 (Fig. 4.51c). Hematite was also observed in short intercepts between 184 and 236.6 m depth in this drill hole (Fig. 4.51c). Hematite and jarosite at depths greater than 100 m in drill holes are interpreted to have been formed due to superficial water flowing downwards through faults and fractures weathering deeper parts of the lithocap (Appendix D).

Figure 4.52 presents box plots comparing major element, precious and base metal, and path finder element concentrations in weathered and fresh rocks. Components that are slightly enriched in weathered rocks are: SiO_2, Ag, Au, Cu, and Mo (Fig. 4.52). Components that are depleted in weathered rocks are: MgO, CaO, Na_2O, K_2O, TiO_2, P_2O_5, MnO, and Zn (Fig. 4.52). Variations for all these components are subtle, and values for each remain within the same order of magnitude. However, these subtle variations should be take into account when generating target areas for future exploration.

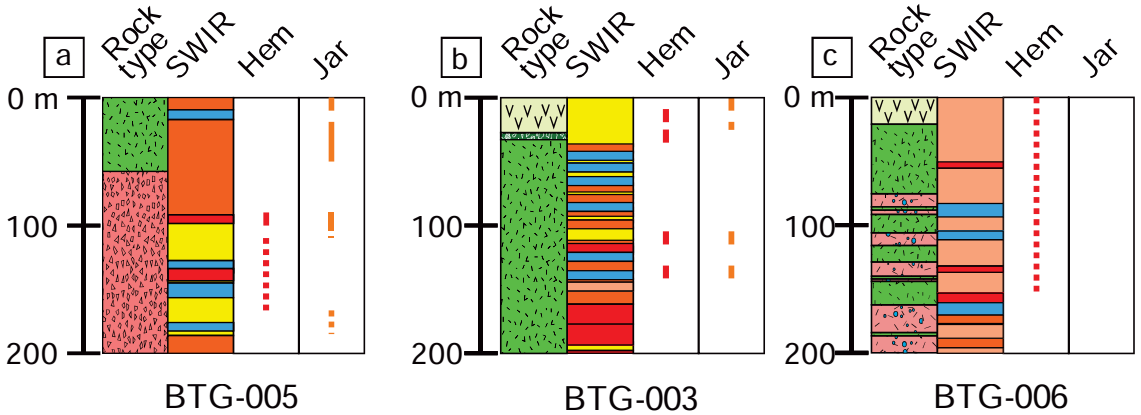

Figure 4.51. Distribution of hematite and jarosite in drill holes. a. BTG-005. **b.** BTG-003. **c.** BTG-006. Legend as in Figure 4.50. Abbreviations: Hem: hematite; Jar: Jarosite.

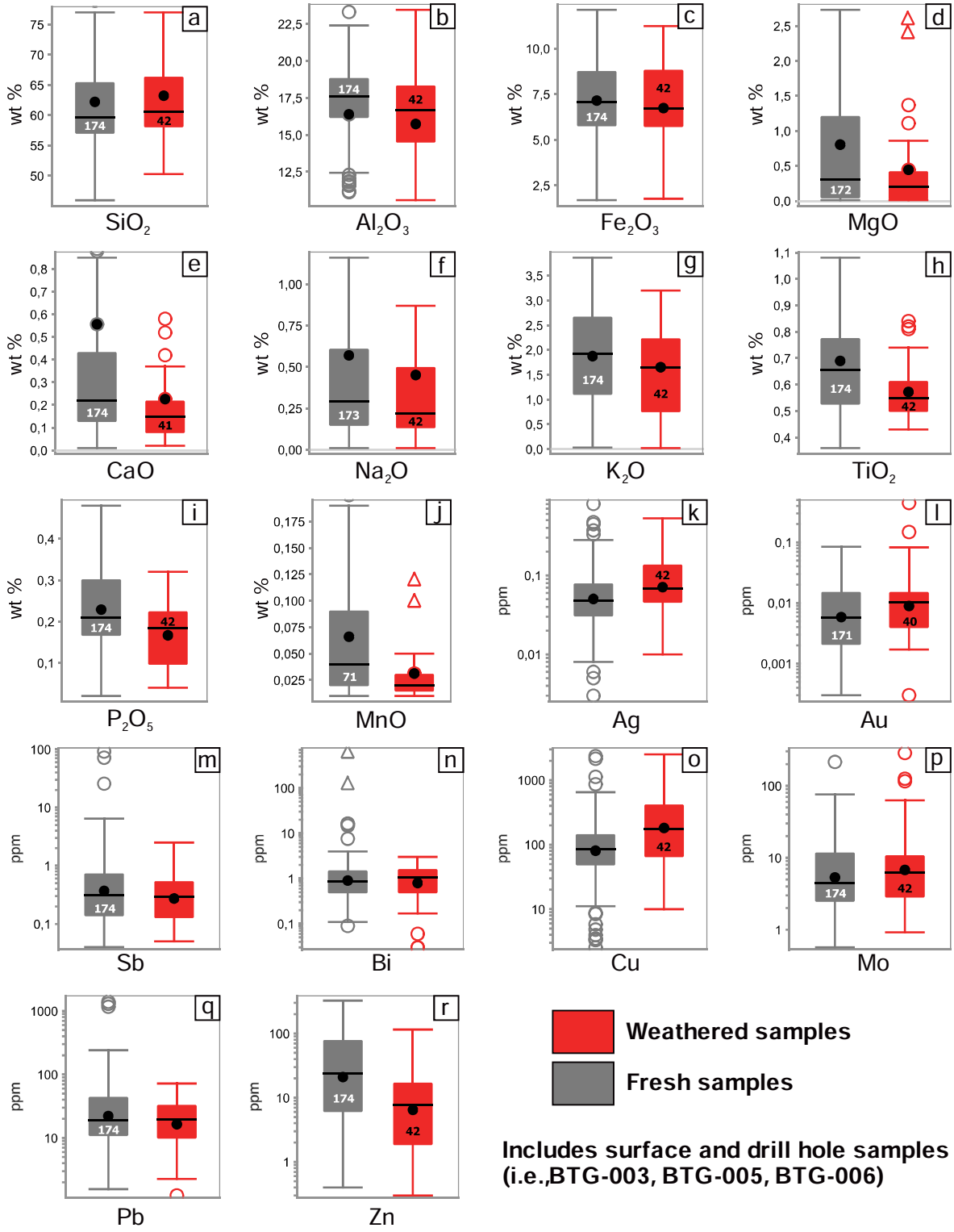

Figure 4.52. Geochemical variations due to weathering in the Bantug lithocap. Depth of weathering for BTG-003 is 40.45 m, 181 m for BTG-005, and 162 m depth for BTG-006. **a.** SiO_2. **b.** Al_2O_3. **c.** Fe_2O_3. **d.** MgO. **e.** CaO. **f.** Na_2O. **g.** K_2O. **h.** TiO_2. **i.** P_2O_5. **j.** MnO. **k.** Silver (Ag). **l.** Gold (Au). **m.** Antimony (Sb). **n.** Bismuth (Bi). **o.** Copper (Cu). **p.** Molybdenum (Mo). **q.** Lead (Pb). **r.** Zinc (Zn).

4.6.2. Implications of mineralogy and geochemical distribution in the lithocap at Bantug

Surface samples at Bantug are predominantly advanced argillic-altered. Most common minerals include: alunite, pyrophyllite, natroalunite, and dickite. Alunite is the most abundant mineral and it occurs predominantly around drill hole collar BTG-003 (Fig.4.2). Pyrophyllite, natroalunite, and muscovite occur northeast of drill hole collar BTG-006. The area northeast of drill hole collar BTG-006 contains minerals that are stable above 200°C (i.e., pyrophyllite, Reyes, 1990; muscovite, Fleet, 2003). The occurrence of these minerals is interpreted to indicate an area of relatively high temperature fluid flow (i.e., >200°C), which has potential to conceal a heat source for the lithocap.

Drill hole SWIR results (i.e., pyrophyllite, natroalunite, muscovite) suggest a similar increase in temperature to the northeast (i.e., from BTG-005 to BTG-006; Fig. 4.2). SWIR results from BTG-006 revealed abundant pyrophyllite (i.e., 200-300°C), and muscovite at depth (300-400°C). Muscovite is the product of hydrothermal alteration of the diorite porphyry in BTG-006 (Fig. 4.11). It is uncertain if the diorite porphyry found at depth in drill hole BTG-006 is the heat source indicated by mineral assemblages on surface. Projection to surface of the diorite porphyry intersect reveals its location 720 m southwest of the high-temperature minerals on surface (Fig. 4.2). It is possible that the diorite porphyry in drill hole BTG-006 may be related to a larger diorite intrusion (i.e., stock) located at depth, to the northeast of BTG-006 collar.

The area located 600 m north of drill hole collar BTG-006 remains unexplored. A silicic-altered area of 1.2 km by 2.0 km has not been tested by SWIR spectroscopy, whole rock geochemistry, or drill holes (Fig. 4.1). It is recommended to prioritise this are in future exploration activities.

Surface geochemistry results define a clear pattern of low value anomalies northeast of drill hole collar BTG-006. SiO_2, TiO_2, Hf, Nb, Co, and Cr are anomalously high results in this area (Figs. 4.14, 4.22, 4.31, 4.40). Mass balance calculations also defined high SiO_2 and TiO_2 anomalous results in this area. Alteration indices (i.e., AI and AAAI) presented similar high results (Fig. 4.28).

Surface results display a marked difference between LREE and HREE. LREE results are associated with silicic-altered rocks, and most high values are located in the periphery of the silicic-altered zone (Fig. 4.37). HREE in surface and drill hole samples do not display any clear distribution patterns (Fig. 4.37). It is very likely that acid hydrothermal fluids may have leached

the LREE from the precursors to the silicic-altered rocks and precipitated them in the surrounding argillic-altered rocks. LREE concentrations of argillic-altered rocks at Bantug are two to three times higher than average andesites elsewhere in the world (i.e., La=18.10 ppm; Ce=37.27 ppm; Pr=4.68 ppm; GEOROC, 2016).

Given the geologic variability encountered in drill holes, identification of distribution patterns proves difficult. However, high Zn, W, U, and Th results are related to the diorite porphyry and may be useful to locate potential heat sources elsewhere in the lithocap.

4.6.3. Mineralisation

Most of the samples collected from Bantug have low precious and base metal concentrations (Tables 4.10 and 4.11). Copper, Mo, Au, and Ag results from diorite porphyry samples in drill hole BTG-006 are particularly low (Tables 4.10 and 4.11). Two hypothesis that may explain this phenomenon are: i) inefficient ore-forming physicochemical conditions, ii) a metal-depleted magma, iii) the centre of mineralisation has not yet been intersected by drill holes.

Inefficient ore-forming and concentration processes could have resulted from shallow depth intrusion emplacement (i.e., <1 km). Shallow depths provide inadequate confining pressures for stockwork formation (Burnham, 1985).

A metal-deficient magmatic system beneath the Bantug lithocap could also explain the lack of metals. Small amounts of copper sulfides were found in the diorite porphyry and hornfels samples.

Vuggy quartz and advanced argillic-altered samples from drill hole BTG-003 present high Sb, Bi, and Te concentrations. The presence of these elements in these rocks indicates potential for high-sulfidation epithermal deposits in the lithocap.

Copper sulfides and significant amounts of magmatic-hydrothermal minerals (i.e., apatite, chlorite) were found in hornfels, underlying the advanced argillic-altered volcanic rocks. This hornfels is the metasomatic product of interaction of hydrothermal fluids from the Quaternary Bantug Intrusive Complex with the Late Pliocene-Pleistocene Caliling Formation. This formation is ~500 m thick, and it is made of limestone, sandstone, siltstone, and shale (MGB, 2004). Members of this formation represent physical and chemical traps through which hydrothermal fluids from the Quaternary Bantug Igneous Complex had to circulate before reaching the Quaternary Canlaon Volcanic Complex. There is the possibility that metals from

hydrothermal fluids may have been sequestered by permeable or organic matter-rich sedimentary rocks from the Late Pliocene-Pleistocene Caliling Formation. This formation represents a potential target for skarn and replacement-type mineral deposits.

4.7. Summary

Figure 4.53 presents a conceptual graphic summary of the distribution of hydrothermal mineral assemblages at Bantug. The lithocap at Bantug has a surface area of 33.6 km^2. Hydrothermal alteration types observed at Bantug include silicic, argillic, advanced argillic, propylitic, phyllic, and hornfels. The lithocap at Bantug is characterised by a northeast-trending elongated silicic-altered area. Alteration textures at Bantug include massive and vuggy quartz in silicic-altered samples, as well as patchy-wormy in advanced argillic-altered samples. Propylitic alteration is characterised by the presence of epidote in vesicules as well as chlorite replacing phenocrysts in the diorite porphyry dike I. Phyllic alteration is characterised by the presence of muscovite replacing the groundmass and plagioclase phenocrysts in the diorite porphyry.

Two hydrothermal breccias have been recognised at Bantug: a natroalunite-pyrite cemented polymict breccia, and a quartz-pyrite cemented polymict breccia. Both hydrothermal breccia types contain silicic and advanced argillic-altered clasts, some of which exhibit patchy textures. The quartz-pyrite cemented breccia contains juvenile clasts, and it is interpreted to be a magmatic hydrothermal breccia (e.g., Sillitoe, 1985).

SWIR spectroscopy results from surface samples revealed the presence of alunite, dickite, pyrophyllite, and muscovite. Alunite samples are common on surface, and pyrophyllite and muscovite-bearing samples are located to the northeast of the studied area. SWIR spectroscopy results from drill hole samples present a similar transition pattern from argillic assemblages in the southwest (i.e., BTG-005) to advanced argillic assemblages in the northeast (i.e., BTG-006). SWIR spectroscopy results from drill hole BTG-006 revealed abundant pyrophyllite in advanced argillic-altered volcanic rocks, and muscovite in a diorite porphyry intrusion at depth.

Whole rock geochemistry results from surface and drill hole samples have shown that most elements were depleted in intensely silicic-altered areas (Fig. 4.22). LREE are enriched in the surrounding advanced argillic-altered rocks (Fig. 4.37). Mass transfer calculations revealed gains in SiO_2 and TiO_2 in the northeastern part of the studied area (Figs. 4.24 and 4.25). Alteration indices of surfaces samples also indicate high values to the northeast of the studied area (Fig.4.28).

Precious and base metals results are anomalous on surface and drill hole samples; however, values are uneconomic. Low base and precious metals contents could be the result of inefficient mineralisation mechanisms, and/or a deficient metal budget in the magmatic system. Copper sulfides were found in hornfels samples from the Late Pliocene-Pleistocene Caliling Formation. Organic matter-rich members of this formation may be effective traps for mineralised hydrothermal fluids.

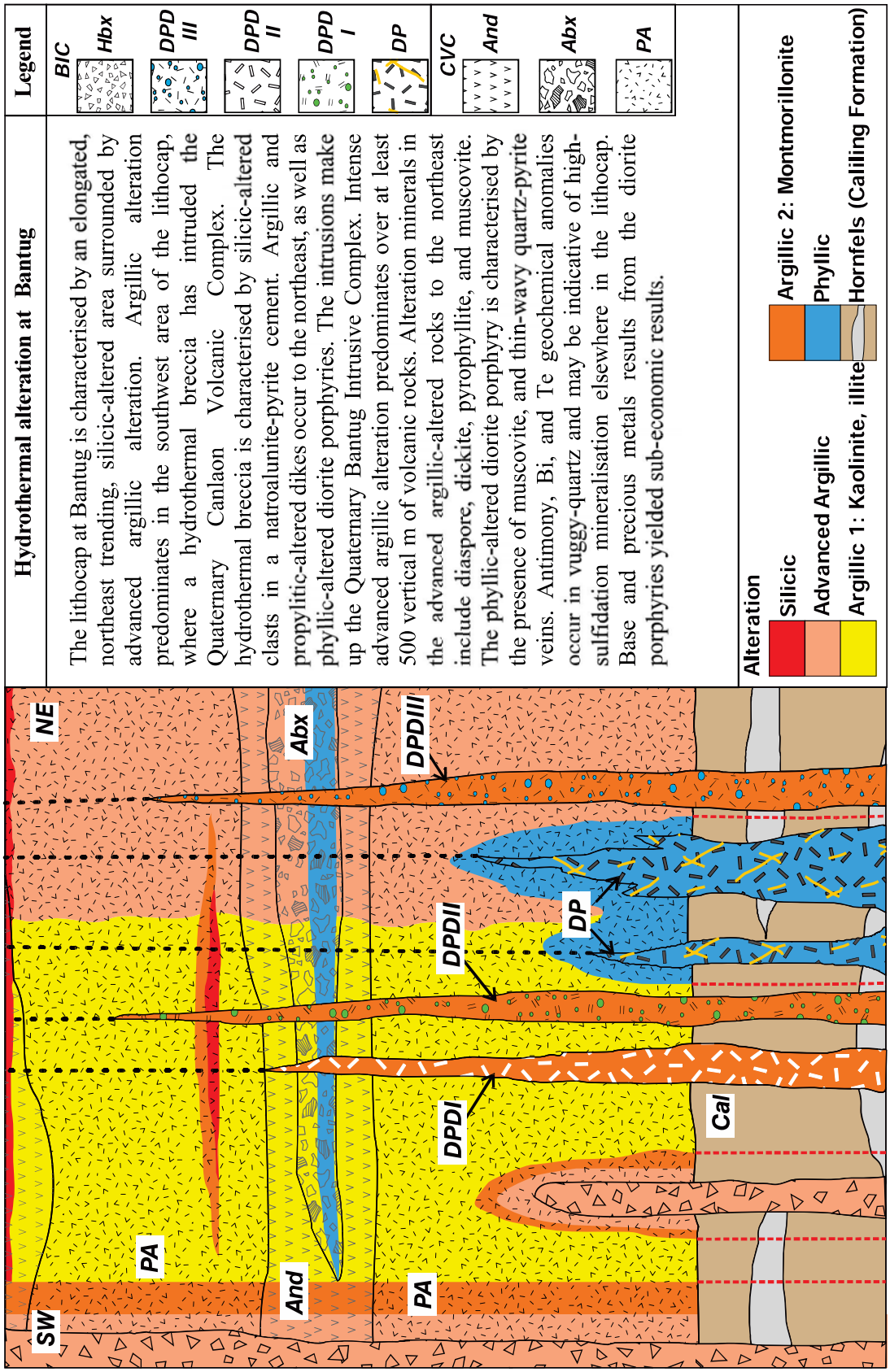

Figure 4.53. Schematic hydrothermal alteration of the Bantug area. Diagram not to scale. The horizontal dimension represents ~2.5 km, and the vertical dimension ~850 m. Abbreviations: And: andesite; Abx: andesitic volcaniclastic breccia; Cal: Caliling Formation; DP: diorite poprhyry; DPD: diorite porphyry dike (I to III); PA: plagioclase-phyric andesite; SW: southwest; NE: northeast; BIC: Bantug Intrusive Com plex; CVC: Canlaon Volcanic Complex.

CHAPTER 5:

MINERAL CHEMISTRY

5.1. Introduction

This chapter presents the results of SEM and LA-ICP-MS analyses of key minerals from surface and drill hole samples from the lithocap at Bantug. The minerals analysed include: alunite, pyrite, epidote, chlorite, and magnetite. Results are presented as major (10,000 ppm ≤ *x*), minor (1,000 ppm < *x* < 10,000 ppm), and trace elements (x ≤ 1,000 ppm). This is followed by data comparison with the Mankayan lithocap, Batu Hijau porphyry Cu-Au deposit, and Baguio district porphyry deposits in order to facilitate discussions about vectoring and fertility assessment.

5.2. Methods

5.2.1. Laser ablation inducted coupled mass spectrometer (LA-ICP-MS)

Two sets of instrumentation were used for LA-ICP-MS analyses in this study: (1) a New Wave 213-nm solid-state laser microprobe coupled to an Agilent 4500 quadrupole ICPMS; and (2) a New Wave 193-nm solid-state laser coupled to an Agilent 7500cs quadrupole ICP-MS, both housed at the CODES LA-ICP-MS analytical facility, University of Tasmania. The laser microprobes were equipped with in-house small volume (~2.5 cm^3) sample chambers. The He gas carrying the ablated aerosol was mixed with Ar (~1.2 L/min) immediately after the ablation chamber. For spot analyses, the aerosol and gas mixture was passed through a pulse-homogenizing device (Laurin Technic, Australia) prior to direct introduction into the torch, where the stream of ablated aerosol is split into 10 tubes with differing residence times before being recombined to one tube before entering the ICP-MS plasma. The ICP-MS was optimized daily to maximize sensitivity on mid- to high-mass isotopes (in the range 130−240 a.m.u.).

Alunite, epidote, and chlorite crystals were analysed using a 34 μm beam diameter, 10 Hz frequency, 3.55 J/cm^2 fluence. Pyrite crystals were analysed using a 35 μm beam diameter, 5 Hz frequency, 3.50 J/cm^2 fluence. Magnetite crystals were analysed using a 34 μm beam diameter, 5 Hz frequency, 3.00 J/cm^2 fluence. Details on the methods used for pyrite and epidote analyses are presented by Large et al. (2009), and Cooke et al. (2014), respectively.

The LA-ICP-MS results were reduced using an XLS macro created by Professor Leonid Danyushevsky and Dr Sarah Gilbert at CODES in 2014. The macro was used to screen laser analyses that intercepted mineral inclusions and to convert counts per second (cps) to parts per

million (ppm). Laser analyses had a duration of 90 seconds. The macro allowed the selection of inclusion-free periods in order to ensure analyses quality. Alunite, epidote, chlorite, magnetite and pyrite individual analyses from Bantug were manually filtered using the XLS macro of Danyushevsky and Gilbert (2014) to avoid large inclusions of different minerals. Counts per second were converted to ppm with the macro using major elements contents previously acquired using EDS analyses with a Hitachi SU-70 field emission scanning electron microscope (FE-SEM). Major elements used from alunite, epidote, chlorite, and magnetite are Al, Ca, Mg, and Fe respectively. A stoichiometric Fe value of 465,000 ppm was used to convert counts per second to parts per million from pyrite analyses. Two standards were analysed to calibrate alunite, epidote, magnetite, and chlorite analyses. The primary standard NIST612 was analysed using an 89 μm spot size at a 10 Hz frequency and 3.5 J/cm^2 fluence. The secondary standard GSD-1G was analysed using a 34 μm spot size at a 10 Hz frequency and 3.5 J/cm^2 fluence. Primary and secondary standards used for pyrite analyses are STDGL2b2 and GSD-1G (Danyushevsky et al., 2011).

5.2.2. Detection limits

The limit of detection for the alunite analyses is 0.01 ppm. Analyses which resulted below the limit of detection were not considered for statistical purposes.

5.3. Results

5.3.1. Sample distribution

A total of 19 LA-ICP-MS samples were prepared from surface and drill hole rock samples from Bantug. Table 5.1 and Figure 5.1 present information about sample distribution. Alunite was analysed from surface samples and drill hole BTG-005, BTG-003, and BTG-006. Pyrite samples were prepared from the same drill holes; but pyrite was not analysed from surface samples. Magnetite was analysed from samples from drill holes BTG-003 and BTG-006. Chlorite was analysed from samples from drill hole BTG-003. Epidote analysed from samples from drill holes BTG-003 and BTG-006.

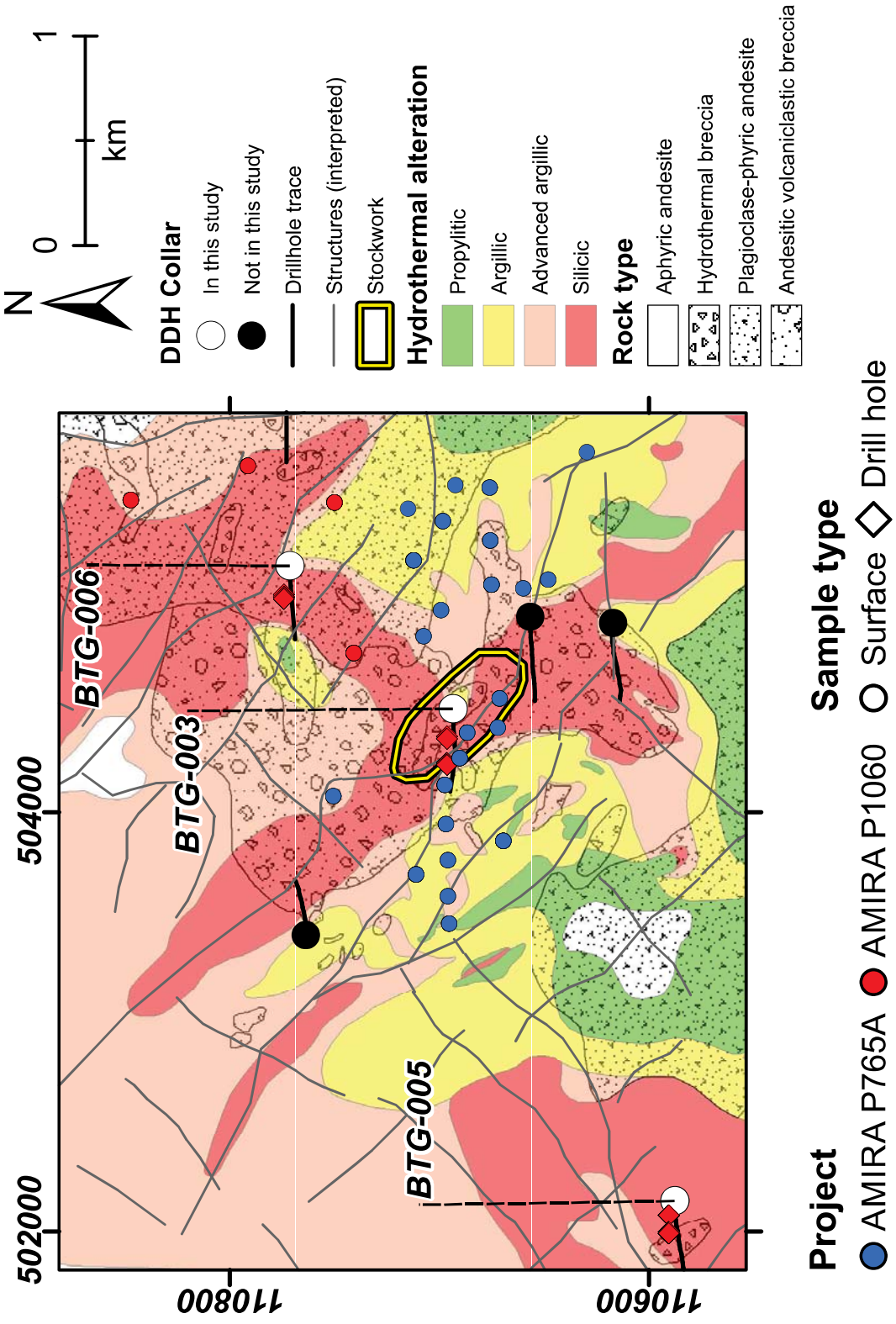

Figure 5.1. Surface sample distribution. Geology and hydrothermal alteration after Subang et al. (2012).

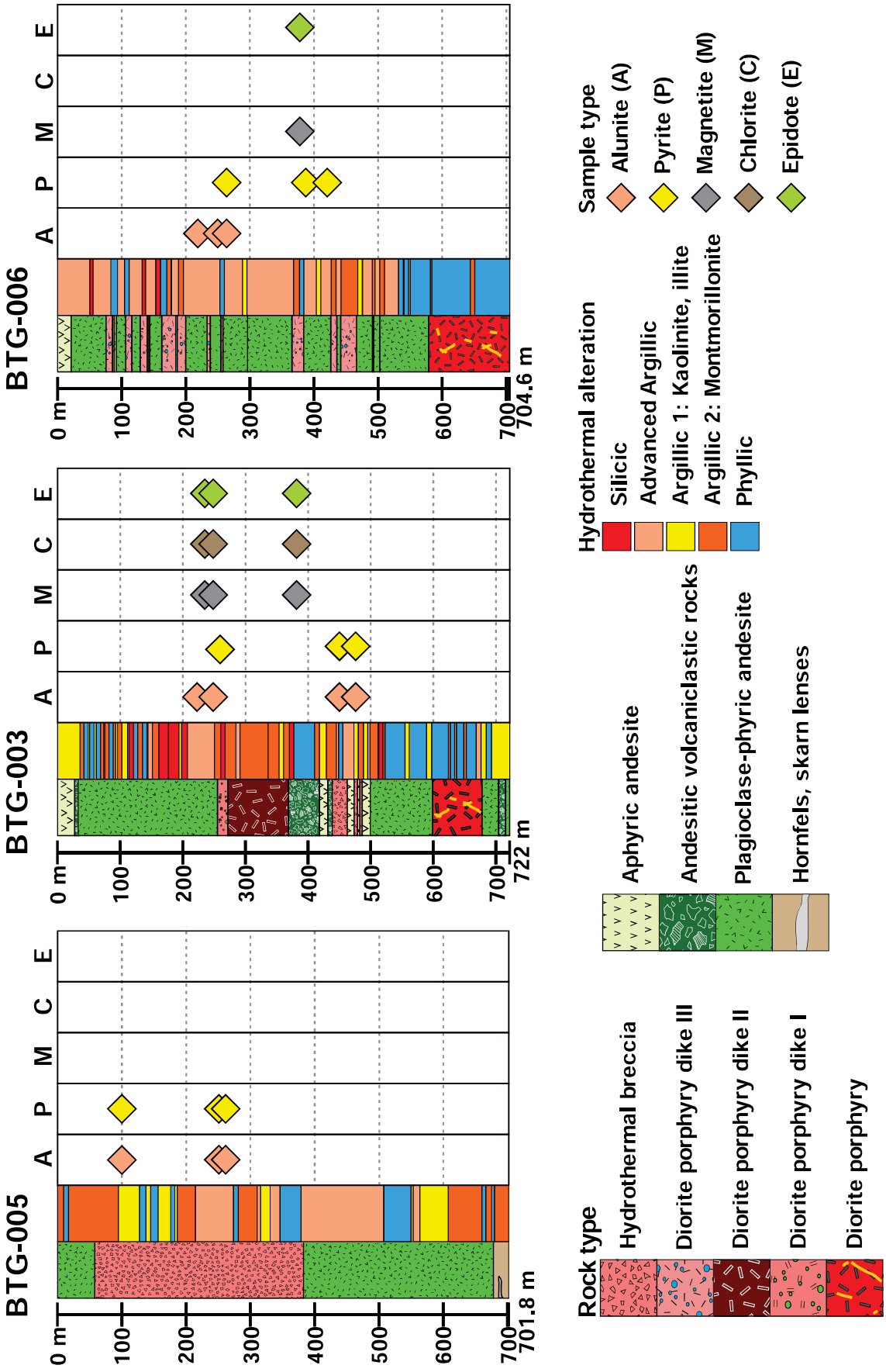

Figure 5.2. Drill hole sample distribution.

Table 5.1 Summary of LA-ICP-MS analyses

	Surface			BTG-005				BTG-003				BTG-006			
	Rock type	Sample ID	n	Rock type	Depth (m)	Sample ID	n	Rock type	Depth (m)	Sample ID	n	Rock type	Depth (m)	Sample ID	n
	PA	BN13CJ221	12	Hbx	103.7	BN13CJ156	22	PA	220.9	BN13CJ94	17	PA	231.2	BN13CJ25	15
	PA	BN13CJ232	17	Hbx	252.0	BN13CJ171	18	PA	240.1	BN13CJ96	24	PA	250	BN13CJ27	16
	PA	BN13CJ247	12	Hbx	263.0	BN13CJ172	18	Hbx	450.5	BN13CJ118	18	PA	269.9	BN13CJ29	12
Alunite	PA	BN13CJ253	15					Hbx	470.7	BN13CJ120	20				
				Hbx	103.7	BN13CJ156	10	DPD I	269	BN13CJ99	12	PA	269.9	BN13CJ29	12
				Hbx	252	BN13CJ171	15	Hbx	450.5	BN13CJ118	10	PA	390.7	BN13CJ40	10
Pyrite				Hbx	263	BN13CJ172	15	Hbx	470.7	BN13CJ120	10	PA	420	BN13CJ43	10
								DPD I	258.7	BN13CJ98	27	DPD III	380	BN13CJ39	4
								DPD I	269	BN13CJ99	4				
Magnetite								DPD II	371	BN13CJ110	19				
								DPD I	258.7	BN13CJ98	89				
								DPD I	269	BN13CJ99	19				
Chlorite								DPD II	371	BN13CJ110	47				
								DPD I	258.7	BN13CJ98	5	DPD III	380	BN13CJ039	23
								DPD I	269	BN13CJ99	3				
Epidote								DPD II	371	BN13CJ110	3				

5.3.2. Alunite geochemistry

5.3.2.1. Sample description

Three occurrences of alunite were identified (Fig. 5.2): *i*) as replacement in patches in patchy-wormy texture, *ii*) in the cement of hydrothermal breccias, and *iii*) replacing plagioclase phenocrysts in plagioclase-phyric andesites. Table 5.2 presents LA-ICP-MS filtering criteria for alunite proposed by Chang et al. (2011). These filters were applied to identified ablation of pyrite, apatite, APS minerals, rutile, quartz, and zircons inclusions (Table 5.2)

Table 5.2. LA-ICP-MS filtering criteria for alunite

Filter	n
K > 90,000 ppm	56
Na > 25,000 ppm	80
Ca > 6,000 ppm	32
Fe > 10,000 ppm	15
P > 10,000 ppm	0
Ti > 250 ppm	20
Zr > 40 ppm	10
Si > 25,000 ppm	33

n: number of analyses rejected

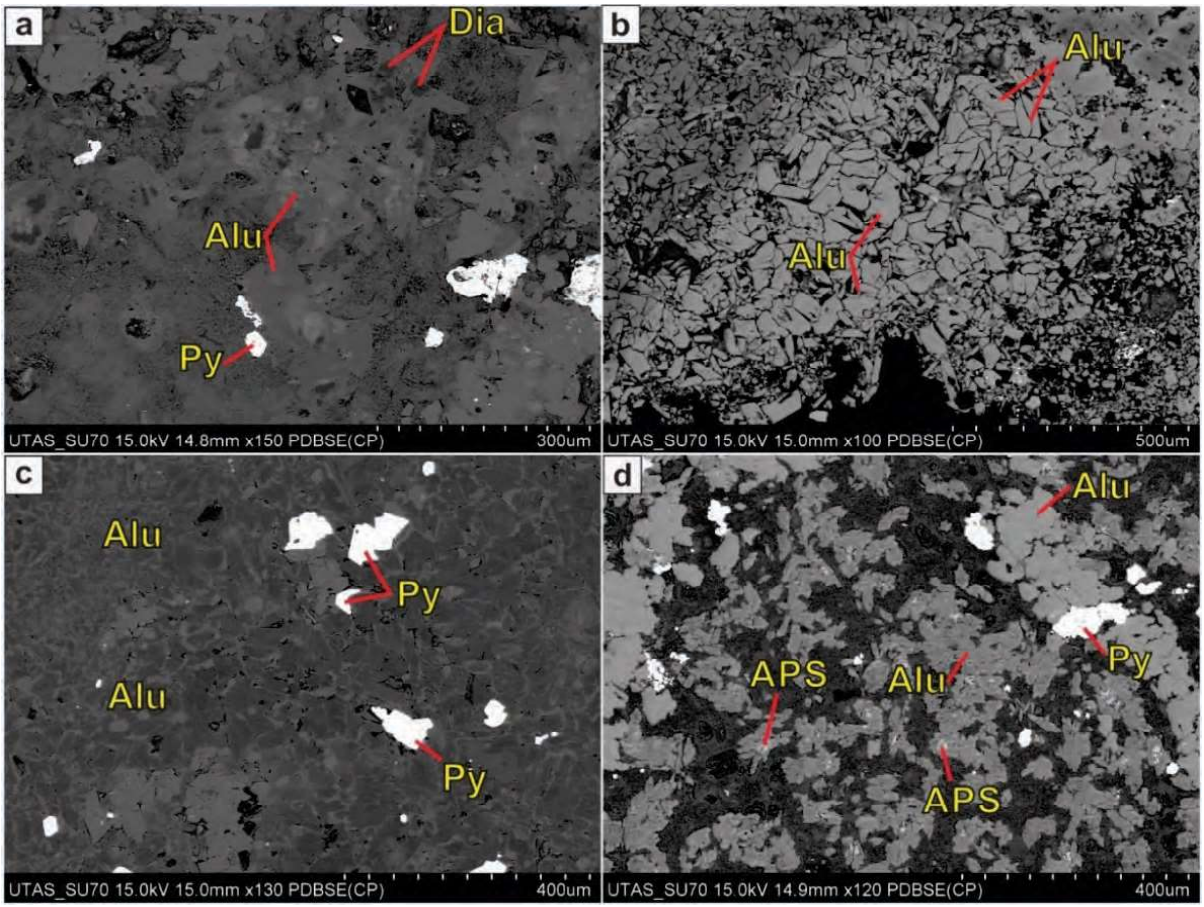

Figure 5.3. Alunite-bearing samples. a. Alunite in hydrothermal breccia cement (263 m; BTG-005). **b.** Alunite replacing plagioclase phenocrysts in plagioclase-phyric andesite (240.1 m; BTG-003). **c.** Plagioclase-phyric andesite (269.9 m; BTG-006;). **d.** Plagioclase-phyric andesite (surface sample; X: 505478 m, Y: 1107500 m). Abbreviations: Alu: alunite; APS: aluminium-phosphate-sulphate mineral; Dia: diaspore; Py: pyrite.

5.3.2.2. Major elements in alunite

Major elements analysed in alunite from Bantug are Al, K, and Na. Table 5.3 and Figure 5.3a present a summary from major elements results. Results from surface, BTG-005, and BTG-003 satisfied the filtering criteria. Results from BTG-006 did not. Complete results are presented in Appendix L.

Potassium contents in alunite from the hydrothermal breccia in BTG-005 are ~20,000 ppm higher than in alunite from surface samples or from drill hole BTG-003. Alunite from surface andesitic volcaniclastic breccia samples have higher Na contents compared with the surface aphyric andesite and plagioclase-phyric andesite samples (Fig. 5.3b).

Figure 5.5 presents K and Na results from alunite in surface samples. The highest K value (i.e., 87,360 ppm) occurs 1,050 m to the east of drill hole collar BTG-003 and it is associated with argillic alteration (Fig. 5.5). The highest Na value (i.e., 21,970 ppm) occurs 400 m to the east of drill hole collar BTG-003 and it is associated with advanced-argillic alteration. Low K and Na values occur to the northeast of drill hole collar BTG-006, and are associated with silicic and advanced argillic alteration (Fig. 5.5).

Table 5.3. Summary of LA-ICP-MS major elements results from alunite

	Al (ppm)	K (ppm)	Na (ppm)
All results			
n	12	86	86
Min	187,000	3,553	2,578
Max	208,100	89,280	24,710
Mean	189,600	65,100	14,340
Surface			
n	4	77	77
n (And)	31	31	31
n (Hbx)	0	0	0
n (Abx)	30	30	30
n (PA)	16	16	16
Min	187,000	3,553	2,578
Max	204,200	89,280	23,760
Mean	188,000	65,140	14,220
BTG-005			
n	2	2	2
n (Hbx)	2	2	2
Min	201,200	78,600	10,100
Max	208,100	84,180	13,100
Mean	204,700	81,390	11,600
BTG-003			
n	7	7	7
n (Hbx)	3	3	3
n (PA)	4	4	4
Min	200,200	23,880	6,652
Max	207,900	77,790	24,710
Mean	203,600	59,930	16,510

n: number of analyses; Min: minimum; Max: maximum; Mean: mean value. Abbreviations: Abx: andesitic volcaniclastic breccia; And: aphyric andesite; Hbx: hydrothermal breccia; PA: plagioclase-phyric andesite.

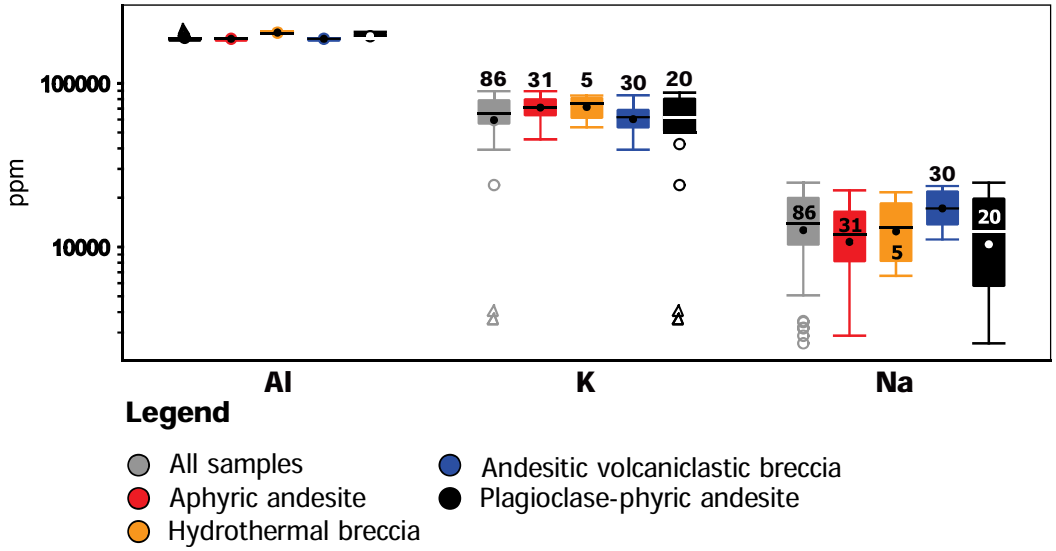

Figure 5.4. LA-IPC-MS major elements results from alunite. Colour coded by rock-type. Boxes include surface and drill hole results. Numbers in and above bins are number of analyses. Circles are outliers, and triangles are far-outliers. The median is represented by lines and the mean is represented by circles inside the boxes.

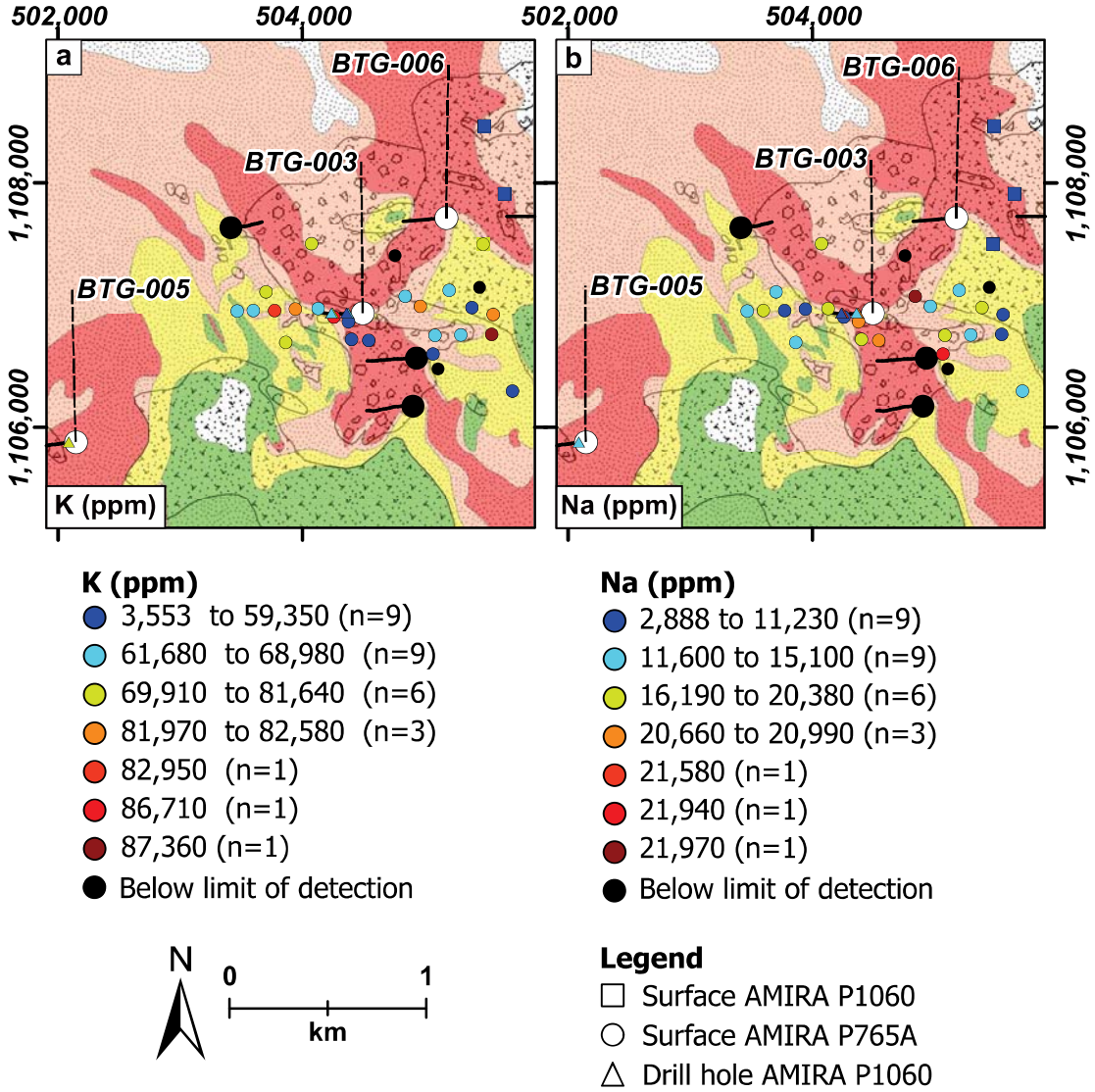

Figure 5.5. Major elements in alunite from surface samples. a. Potassium. **b.** Sodium. Grid marks are spaced 2 km. Geology and hydrothermal alteration map after Subang et al. (2012).

5.3.2.3. Minor elements in alunite

Minor elements in alunite from Bantug include Si, Ca, P, Sr, and Ba (Table 5.4, Figures 5.6 and 5.7; Appendix L). Calcium, P, and Ba concentrations are higher in alunite from hydrothermal breccia cement compared with other alunite types. Strontium is significantly high in alunite from aphyric andesites and plagioclase-phyric andesites compared with other alunite-types (Table 5.4, Figure 5.6; Appendix L).

High calcium values occur in surface samples at 500 m to the east of drill hole collar BTG-003 (i.e., 4,258 ppm) and at 75 m to the west of drill hole collar BTG-005 (i.e., 4,380 ppm). The highest Ba surface value in alunite (i.e., 3,641 ppm) occurs 367m southeast of drill hole collar BTG-006 (Table 5.4; Fig. 5.7). This sample also has high P and Sr contents (3,739 ppm and 3,495 ppm, respectively). Other high Ba values, as well as P and Sr, occur on surface above the trace of drill hole BTG-003.

Table 5.4. Summary of LA-ICP-MS minor elements results from alunite

	Si (ppm)	Ca (ppm)	P (ppm)	Sr (ppm)	Ba (ppm)
All results					
n	11	72	86	86	86
Min	447.5	289.5	49.02	41.4	38.29
Max	24,360	5,408	7,609	13,660	5,866
Mean	4,579	2,889	1,490	1,388	1,239
Surface					
n	3	63	77	77	77
n (And)	0	25	31	31	31
n (Abx)	0	28	30	30	30
n (PA)	3	10	16	16	16
Min	447.5	289.5	49.02	41.4	38.29
Max	3,391	4,774	5,853	4,399	5,866
Mean	2,053	2,731	1,233	1,229	1,148
BTG-005					
n	2	2	2	2	2
n (Hbx)	2	2	2	2	2
Min	1,280	3,352	1,480	769.8	457.4
Max	1,814	5,408	4,625	1,903	4,348
Mean	1,547	4,380	3,052	1,336	2,403
BTG-003					
n	6	7	7	7	7
n (Hbx)	2	3	3	3	3
n (PA)	4	4	4	4	4
Min	672.5	2,751	2,573	409.2	175
Max	24,360	5,385	7,609	13,660	3,784
Mean	6,853	3,881	3,873	3,153	1,908

n: number of analyses; Min: minimum; Max: maximum; Mean: mean value. Abbreviations: Abx: andesitic volcaniclastic breccia; And: aphyric andesite; Hbx: hydrothermal breccia; PA: plagioclase-phyric andesite.

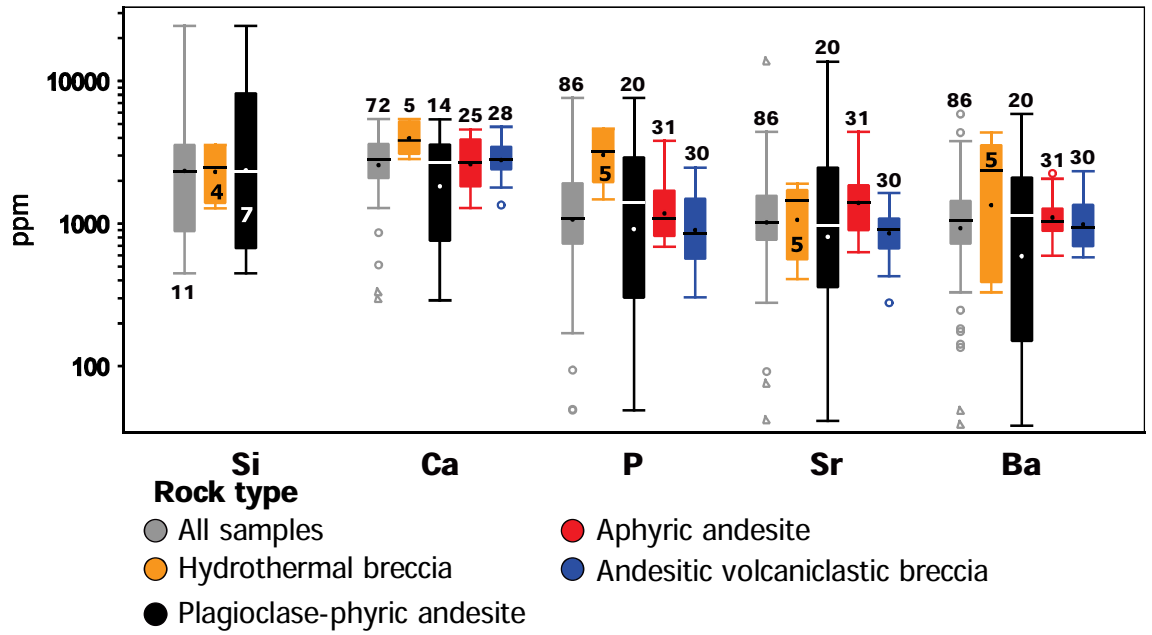

Figure 5.6. LA-ICP-MS minor elements results in alunite. a. Box plots for minor elements in alunite. Boxes include surface and drill hole results. Numbers in and above bins are number of analyses. Circles are outliers, and triangles are far-outliers. The median is represented by lines and the mean is represented by circles inside the boxes. Data is presented in Appendix L.

5.3.2.4. Trace elements in alunite

Trace elements in alunite from Bantug include Fe, Pb, Ti, Ce, Bi, Cr, La, As, Se, Nd, Cu, Rb, Mn, Zn, Zr, Gd, Sm, Sb, Y, Eu, Ag, Au, Hf, Yb, Cs, Lu, and Ta. Table 5.5, Figures 5.8, 5.9 and 5.10 present a summary of the results. Complete results are presented in Appendix L.

From Figure 5.8a it can be inferred that trace elements in alunite from the hydrothermal breccia and plagioclase-phyric andesite have similar concentrations. The aphyric andesite and andesitic volcaniclastic breccia samples are similar to each other. The alunite from hydrothermal breccia and plagioclase-phyric andesite samples are significantly enriched in Bi, As, and Cu, compared with other rock types (Figs. 5.8a, 5.8c to 5.8 g). Alunite from aphyric andesite and andesitic volcaniclastic breccia samples are depleted in Bi and As compared with alunite in other rock types (Figs. 5.8a, 5.8c, 5.8d). Manganese, Zn, and Au results are higher in alunite from andesitic volcaniclastic breccia samples compared with alunite in other rock types (Figs. 5.8a, 5.8f).

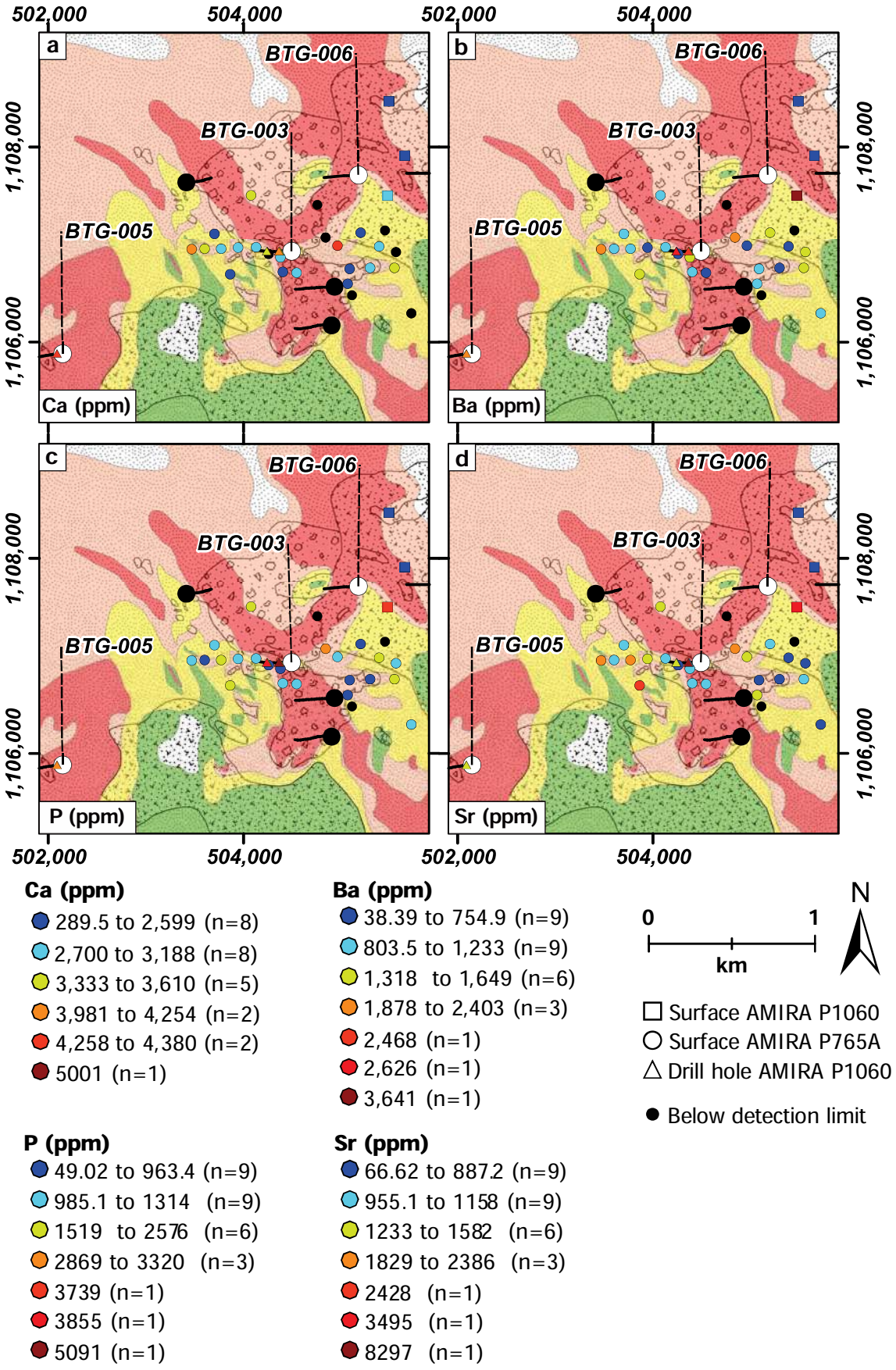

Figure 5.7. Minor elements in alunite from surface samples. a. Calcium. **b.** Barium. **c.** Phosphorus. **d.** Strontium. Grid marks are spaced 2 km.

Table 5.5 Summary of LA-ICP-MS trace elements results from alunite

ppm	Fe	Pb	Ti	Ce	Bi	Cr	La	As	Se	Nd	Cu	Rb	Mn	Zn
n	58	86	14	86	64	10	86	35	3	86	36	86	35	46
min	25.12	15.82	0.522	1.072	0.01287	0.4343	0.5113	0.2965	10.72	0.2894	0.2543	0.1503	0.1731	0.3689
max	9,445	1,276	248.1	585.4	797.5	59.05	318.8	148.6	17.30	180.3	237.2	55.91	31.03	42.88
mean	758.3	182.4	81.06	40.75	32.48	23.52	20.33	13.68	13.06	11.88	10.48	10.06	3.903	3.492
Surface														
n	49	77	5	77	56	3	77	28		77	31	77	29	41
n (And)	22	31		31	18		31	11		31	11	31	6	14
n (Abx)	19	30		30	24		30	11		30	15	30	17	19
n (Pa)	8	16	5	16	14	3	16	6		16	5	16	6	8
min	25.12	15.82	0.522	1.072	0.01287	0.4343	0.5113	0.2965		0.2894	0.2543	0.1503	0.1731	0.3689
max	1,943	789.7	60.03	212.5	130.8	14.31	118.6	25.61		45.27	24.2	55.91	31.03	42.88
mean	257.2	147.8	16.80	30.88	4.471	5.102	15.02	2.842		8.472	3.773	10.47	4.294	3.645
BTG-005														
n	2	2	2	2	2	1	2	2	1	2	1	2	1	
n (Hbx)	2	2	2	2	2	1	2	2	1	2	1	2	1	
min	319.4	300.5	205.6	15.55	0.04673	59.05	3.754	3.844	10.72	10.05	6.303	9.207	1.214	
max	8,962	542.0	242.8	22.94	576.9	59.05	11.99	116.8	10.72	12.77	6.303	9.467	1.214	
mean	4,641	421.3	224.2	19.25	288.5	59.05	7.874	60.32	10.72	11.41	6.303	9.337	1.214	
BTG-003														
n	7	7	7	7	6	6	7	5	2	7	4	7	5	5
n (Hbx)	3	3	3	3	3	3	3	2	1	3	2	3	2	2
n (Pa)	4	4	4	4	3	3	4	3	1	4	2	4	3	3
min	198.4	81.52	19.04	12.70	0.04665	5.155	3.606	3.199	11.17	9.445	3.297	1.265	1.515	0.6797
max	9,445	1,276	248.1	585.4	797.5	55.89	318.8	148.6	17.30	180.3	237.2	11.64	3.353	3.781
mean	3,156	495.0	86.06	155.4	208.5	26.81	82.35	55.70	14.23	49.47	63.54	5.708	2.173	2.244

Table 5.5 Summary of LA-ICP-MS trace elements results from alunite (Continued)

ppm	Zr	Gd	Sm	Sb	Y	Eu	Ag	Au	Hf	Yb	Cs	Lu	Ta
n	10	13	75	38	14	80	10	3	5	6	28	1	2
min	0.016	0.01877	0.03033	0.04947	0.02	0.02715	0.02146	0.04518	0.02594	0.01807	0.02018	0.03803	0.01903
max	13.15	5.329	22.93	5.902	2.250	5.100	1.202	0.4973	0.3843	0.1616	0.1734	0.03803	0.02895
mean	3.381	1.742	1.685	1.295	0.5838	0.5361	0.2505	0.2145	0.1916	0.07097	0.06000	0.03803	0.02399
Surface													
n	4	4	66	34	5	71	10	2		3	27		1
n (And)			27	22	0	28	1			0	8		
n (Abx)			27	8	0	29	6	1		0	12		
n (Pa)	4	4	12	4	5	14	3	1	1	3	7		1
min	0.01600	0.01877	0.03033	0.04947	0.02000	0.02715	0.02146	0.1010	0.02594	0.01807	0.02018		0.01903
max	1.116	1.397	5.630	5.902	0.4248	1.705	1.202	0.4973	0.02594	0.07523	0.1734		0.01903
mean	0.5756	0.4811	1.136	1.329	0.1491	0.394	0.2505	0.2992	0.02594	0.03906	0.05768		0.01903
BTG-005													
n	1	2	2	2	2	2				1			
n (Hbx)	1	2	2	2	2	2				1			
min	0.2164	0.4898	1.457	0.3256	0.2524	0.5887				0.07369			
max	0.2164	1.453	3.225	1.079	0.2777	1.546				0.07369			
mean	0.2164	0.9713	2.341	0.7024	0.265	1.067				0.07369			
BTG-003													
n	5	7	7	2	7	7		1	4	2	1	1	1
n (Hbx)	2	3	3	1	3	3		1	2	1			
n (Pa)	3	4	4	1	4	4			2	1	1	1	1
min	0.09039	0.9838	2.022	1.137	0.1359	0.4714		0.04518	0.03985	0.0733	0.1227	0.03803	0.02895
max	13.15	5.329	22.93	1.468	2.250	5.100		0.04518	0.3843	0.1616	0.1227	0.03803	0.02895
mean	6.257	2.683	6.679	1.303	0.9854	1.826		0.04518	0.2330	0.1175	0.1227	0.03803	0.02895

Figure 5.10 presents results from key trace elements (i.e., As, Bi, Cu, Pb, Sb, and Zn) in alunite from surface samples. Most high values occur above the trace of drill hole BTG-003, and are associated with silicic and advanced-argillic alteration (Fig. 5.10).

Most low values occur to the east of drill hole collar BTG-003, and to the northeast of drill hole collar BTG-006 (Fig. 5.10). Arsenic and Bi are also high (i.e., 60.32 ppm and 288.46 ppm, respectively) in the sample located 75 m to the west of drill hole collar BTG-005 (Figs. 5.10a and 5.10b). Samples between collars BTG-003 and BTG-006 also have higher concentrations of Pb and Zn (Figs. 5.10d and 5.10f).

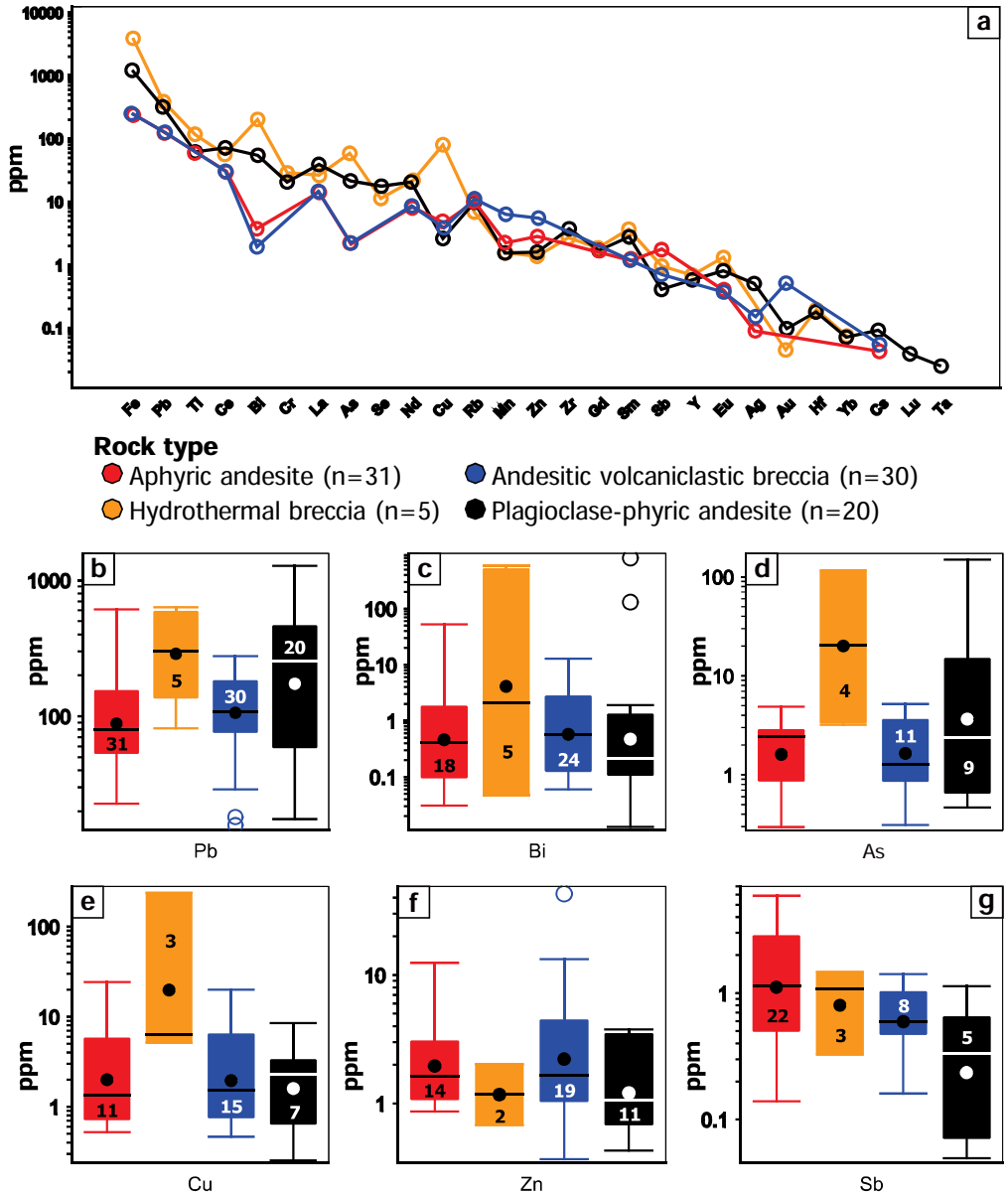

Figure 5.8. Trace elements in alunite from surface and drill hole samples. a. Parallel coordinate plot from trace elements in alunite. Lines represent mean values. Number of analyses (n) is indicated in the legend. **b.** Lead (Pb). **c.** Bismuth (Bi). **d.** Arsenic (As). **e.** Copper (Cu). **f.** Zinc (Zn). **g.** Antimony (Sb). Boxes include surface and drill hole results. Numbers in and above bins are number of analyses. Circles are outliers, and triangles are far-outliers. The median is represented by lines and the mean is represented by circles inside the boxes.

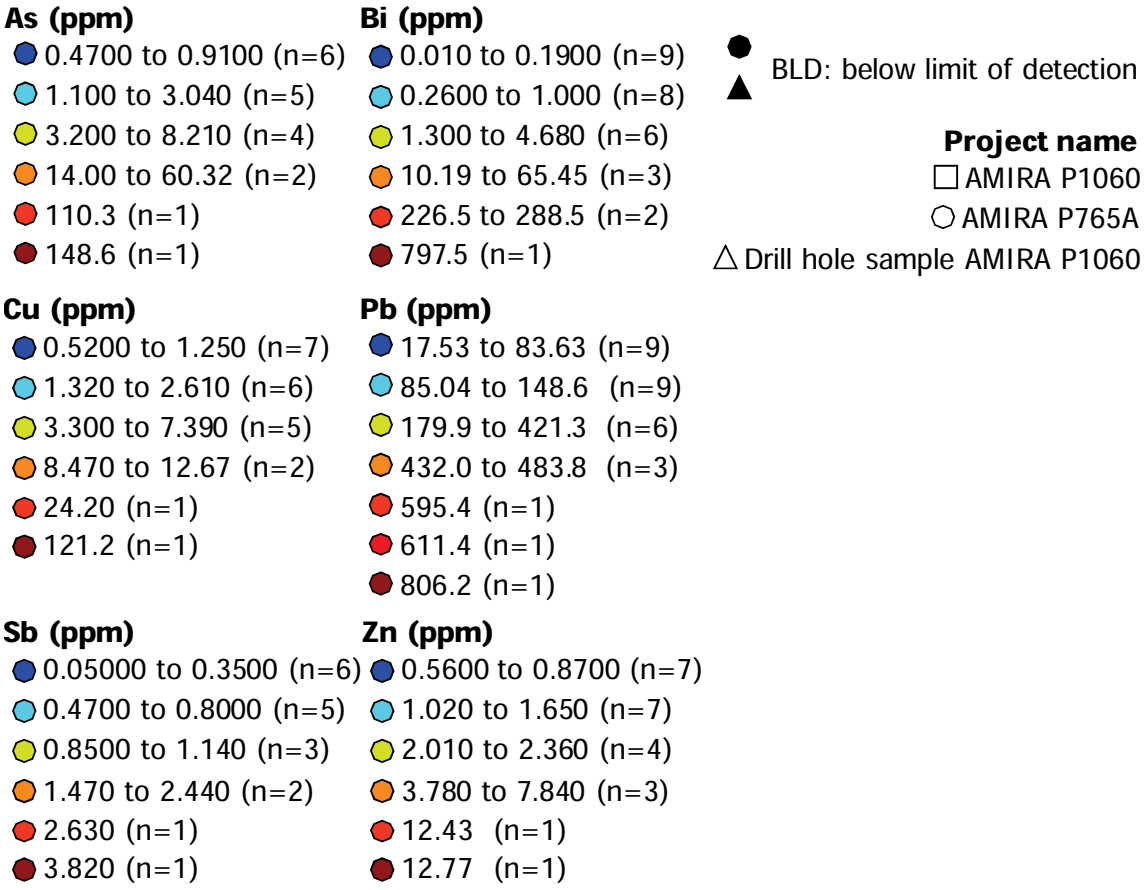

Figure 5.9. Legend for trace elements in alunite from surface samples. Abbreviations: n: number of analyses; BDL: below limit of detection.

5.3.2.5. Discussion

5.3.2.5.1. Comparison with alunite from Mankayan lithocap, Philippines

Late Cretaceous to middle Miocene metavolcanic and volcaniclastic rocks from the Lepanto and Apaoan Formations at Mankayan in northern Luzon, Philippines, have been altered to silicic and advanced argillic mineral assemblages (Hedenquist et al., 1998; Arribas et al., 1995; Chang et al., 2011). Hydrothermal alteration and mineralisation are considered to have been caused by intrusion of the ~1.4 Ma Far Southeast porphyry (Chang et al., 2011). Extensive advanced argillic alteration at Mankayan have formed a 4 km long and <100 m thick, northwest-trending lithocap (Chang et al., 2011). The lithocap at Mankayan hosts the Lepanto high-sulfidation and the Far Southeast porphyry deposits (650 Mt Au; Chang et al., 2011), as well as many other porphyry prospects and intermediate-sulfidation veins (Chang et al., 2011).

Alunite from Mankayan was analysed during the AMIRA project P765, completed in December 2006. Results are presented in Chang et al. (2011) and Gemmell et al. (2014).

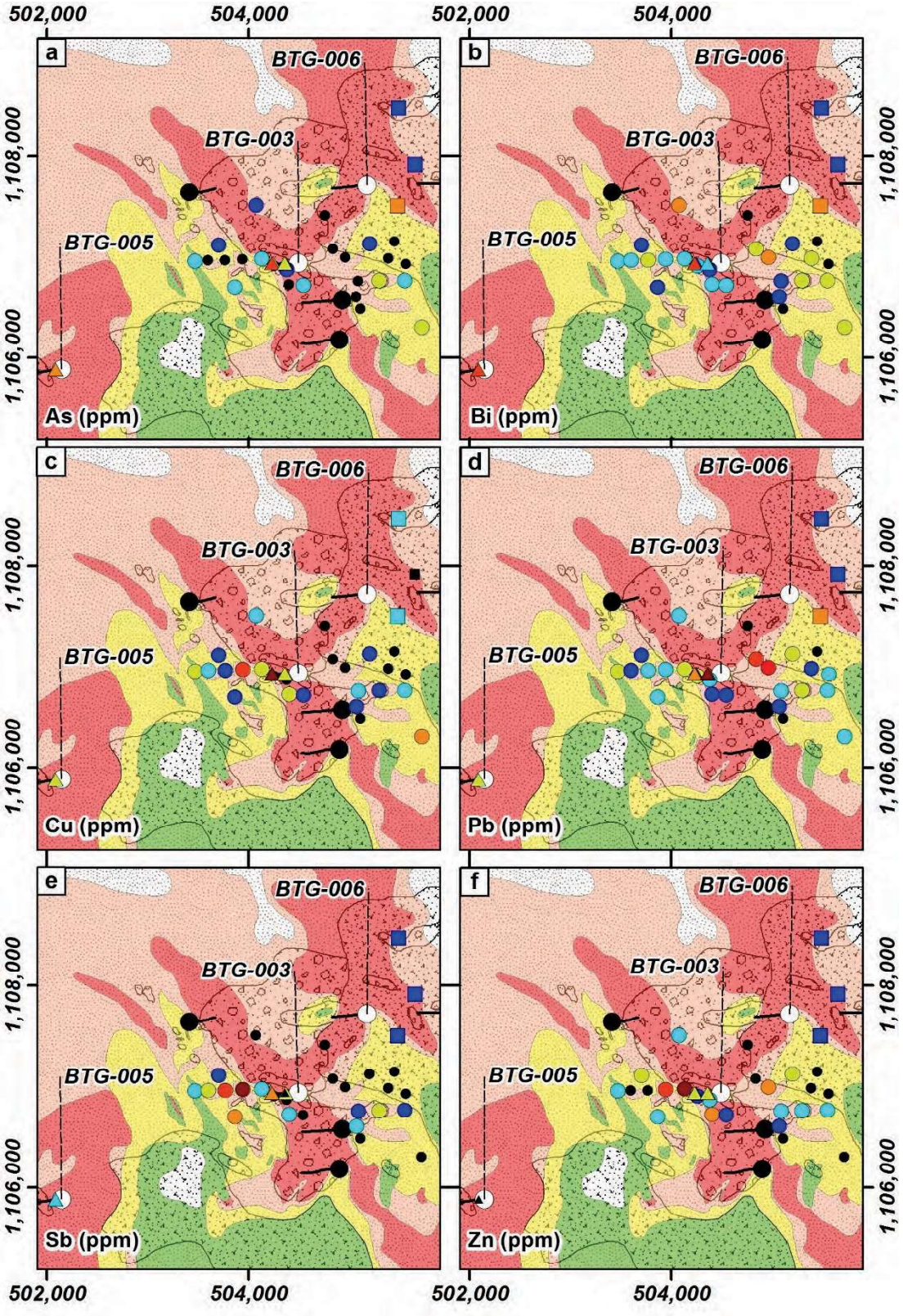

Figure 5.10. Selected trace elements in alunite from surface samples. a. Arsenic. **b.** Bismuth. **c.** Copper. **d.** Lead. **e.** Antimony. **f.** Zinc. Legend is in Figure 5.9. Black circles and triangles are values below the limit of detection (BLD). Geology and alteration legend is the same as in Figure 5.1. Grid marks are spaced 2 km. Legend is in Figure 5.9.

Figures 5.11 and 5.12 present comparisons of LA-ICP-MS alunite results from Bantug and Mankayan. Results from Mankayan are presented by distance to the centre of the Far Southeast (FSE) porphyry deposit which is considered to be the heat source for the hydrothermal fluids. Distance groups were determined according to slope variations on a probability plot for the Pb/La vector of Chang et al. (2011). Results from Bantug are presented by drill hole and surface (Fig. 5.11). Elements in alunite from Mankayan whose concentration decrease with increasing distance from the centre of the deposit are Na and Sr (Fig. 5.11; Chang et al., 2011). Also, Pb concentration in alunite from Mankayan increases with increasing distance from the centre of the deposit (Fig. 5.11; Chang et al., 2011). These outcomes, and element ratios such as Sr/Pb, 100 La/Pb, Pb/La, and Pb/Sr are useful vectors towards potential heat sources (Fig. 5.11; Chang et al., 2011). Sodium and Pb results from Bantug are comparable to those located between 1.4 and 2.5 km away from the FSE porphyry deposit at Mankayan (Figs. 5.11a and 5.11d). Lanthanum and Sr results indicate that alunite from Bantug are more likely to be within 1.8 km of proximity to a potential heat source. Ratio results from Bantug indicate that alunite samples analysed may located between 0.9 and 1.8 km distance from a potential heat source (Figs. 5.11e to 5.11h).

Figure 5.12a presents a Pb/La vs Pb/Sr diagram (Chang et al., 2011) in which most proximal samples to FSE are located in the lower-left part of the diagram, and most distal samples to FSE are located in the upper-right part of the diagram. Most Bantug surface and BTG-003 samples plot on top of or near Mankayan samples located between 0.9 and 1.8 km away from FSE (Fig. 5.12a). Bantug samples were colour coded to distance to FSE based on their similar Pb/La and Pb/Sr results (Fig. 5.12b). Most samples indicating a distance of 0.9 – 1.4 km and 1.4 – 1.8 km to a potential heat source are located to the south and west of drill hole BTG-003 (Fig. 5.12b). Samples which ratio values indicated a distance of 0.9 – 1.4 km to a potential heat source are located to the east of drill hole BTG-003 (Fig. 5.12b).

The occurrence of both range of values south and west of BTG-003 can be attributed to the presence of intrusions encountered in drill holes BTG-003 and BTG-006. Distance between the samples and the intrusions is within 0.9 – 1.8 km. Samples located east of BTG-003 and south of BTG-006 are mostly within 0.9 – 1.4 km. These samples are very likely to indicate the presence of the diorite porphyry encountered in BTG-006 or similar concealed intrusions further north or northwest of BTG-006.

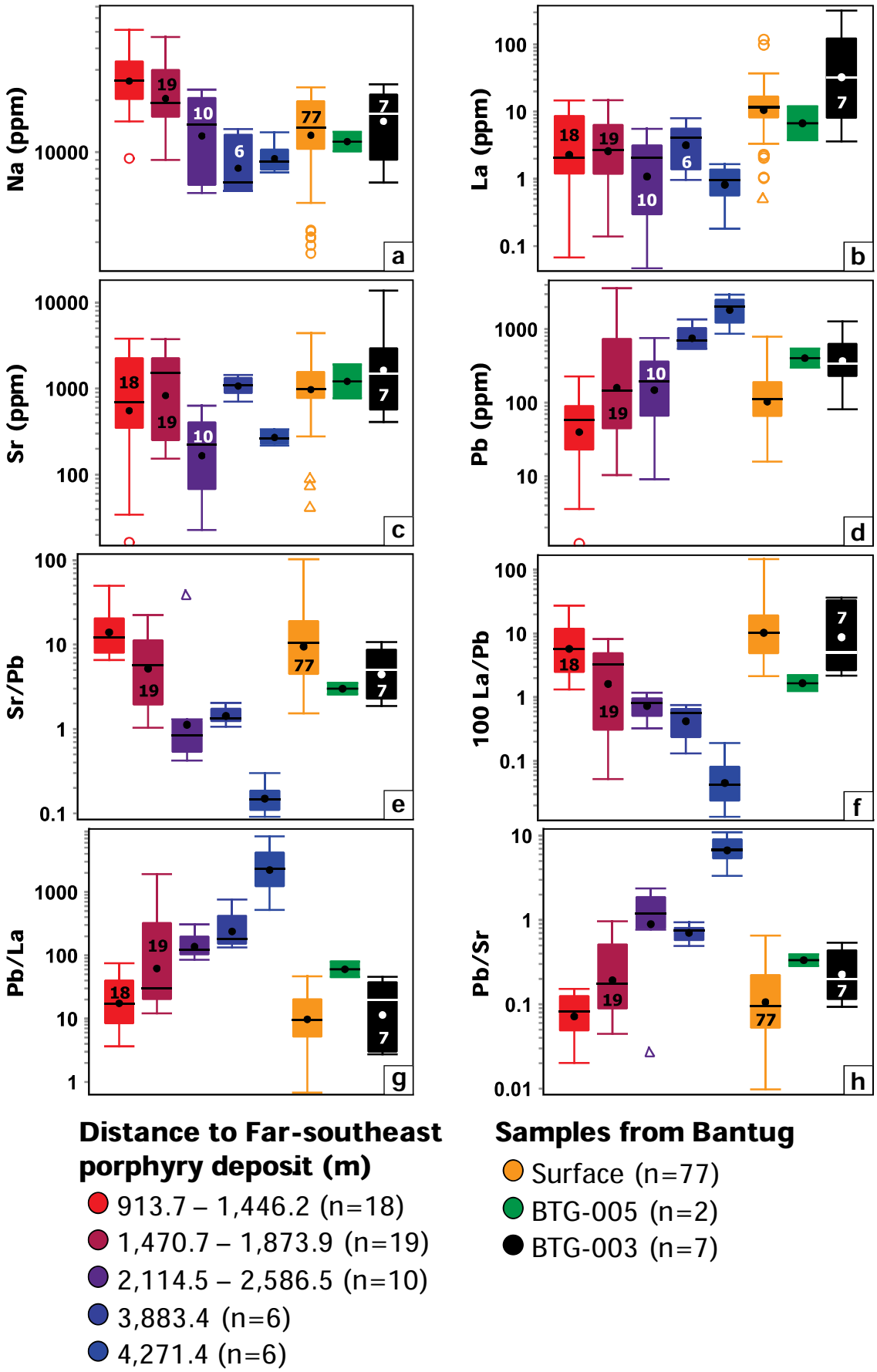

Figure 5.11. Comparison of LA-ICP-MS alunite results from Mankayan and Bantug. a. Sodium (Na). **b.** Lanthanum (La). **c.** Strontium (Sr). **d.** Lead (Pb). **e.** Sr/Pb. **f.** 100 La/Pb. **g.** Pb/La. **h.** Pb/Sr.

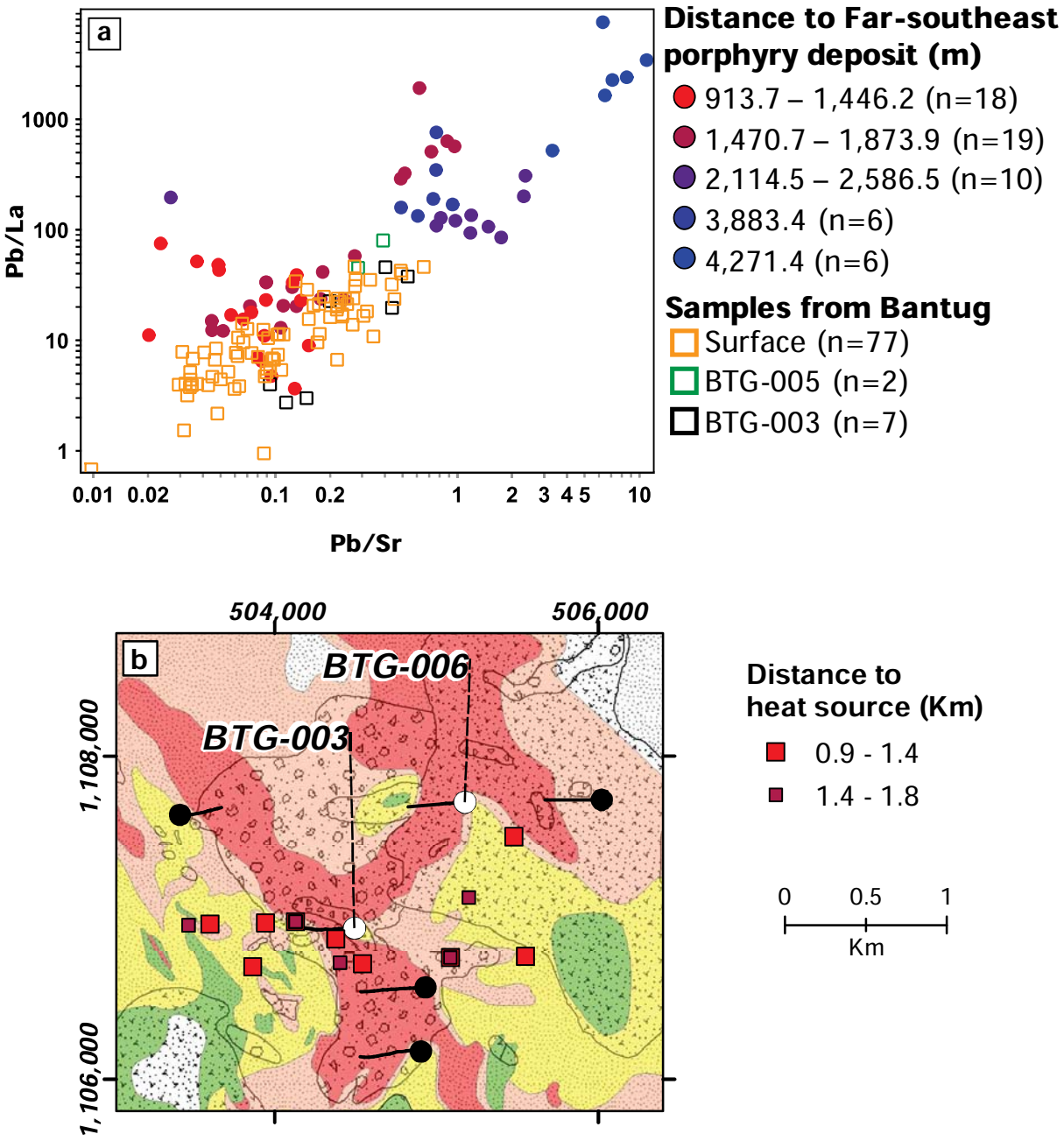

Figure 5.12. Comparison of LA-ICP-MS alunite results from Mankayan and Bantug. a. Pb/La versus Pb/Sr diagram from LA-ICP-MS results from Mankayan and Bantug samples. Results from Mankayan are colour coded to indicate distance to the Far Southeast porphyry deposit (Chang et al., 2011; Gemmell et al., 2014). **b.** Bantug surface alunite samples colour coded based on similar Pb/La and Pb/Sr LA-ICP-MS results from Mankayan.

5.3.3. Pyrite geochemistry

5.3.3.1. Sample description

Pyrite was analysed from drill hole samples from drill holes BTG-003, BTG-005, and BTG-006 (Table 5.1; Fig. 5.2). Pyrite crystals were not found in surface samples. Details of sample location and number of analyses are presented in Table 5.1. Pyrite results are presented in Appendix L.

Pyrite-bearing samples include: advanced argillic-altered hydrothermal breccias from drill hole BTG-005, argillic-altered diorite porphyry dike I and advanced argillic-altered hydrothermal breccias from drill hole BTG-003, advanced argillic-altered, patchy textured, plagioclase-phyric andesites from drill hole BTG-006.

Pyrite grains in hydrothermal breccia samples from drill hole BTG-005 (i.e., 5-7 vol %) occur as subhedral to anhedral coarse grains from 100 μm to ~1 mm, in the alunite-natroalunite cement (Figs. 5.13a and 5.13b). Crystals occur in clusters, are disseminated in the cement, and frequently contain rutile and apatite inclusions (Figs. 5.13a and 5.13b). Pyrite crystals in diorite porphyry dike I samples from drill hole BTG-003 (i.e., 5 vol %) are anhedral, coarse (i.e., 2 mm), contain abundant inclusions, and occur in the groundmass and in miarolitic cavities (Figs. 5.13c and 5.13d). A second generation of pyrite occurs as fine-grained (i.e., ~100 μm) anhedral crystals disseminated in the groundmass (Figs. 5.13c). Coarse pyrite crystals from argillic-altered porphyry dike I samples complied with the size requirements for LA-ICP-MS analyses (Fig. 5.13c). Pyrite crystals in hydrothermal breccia samples from drill hole BTG-003 (i.e., 10-20 vol %) occur as clusters of anhedral crystals and as fine-grained disseminations (Fig. 5.13d). Pyrite in plagioclase-phyric andesite samples from drill hole BTG-006 (i.e., 10-20 vol %) occurs as anhedral, massive, masses disseminated in the alunite-pyrophyllite-quartz groundmass (Figs. 5.13e and 5.13f). Table 5.6 presents the filtering criteria used for screening LA-ICP-MS results. Ablation of apatite, diaspore, and rutile inclusions produced anomalous Ca, Al, and Ti results respectively. A total of 104 LA-ICP-MS pyrite results from Bantug comply with the filtering criteria.

Table 5.6. Number of LA-ICP-MS pyrite analyses rejected

Filter	n
S>561,000	4
Ca>10,000	5
Al > 20,000	12
Ti > 10,000	4

n: number of analyses.

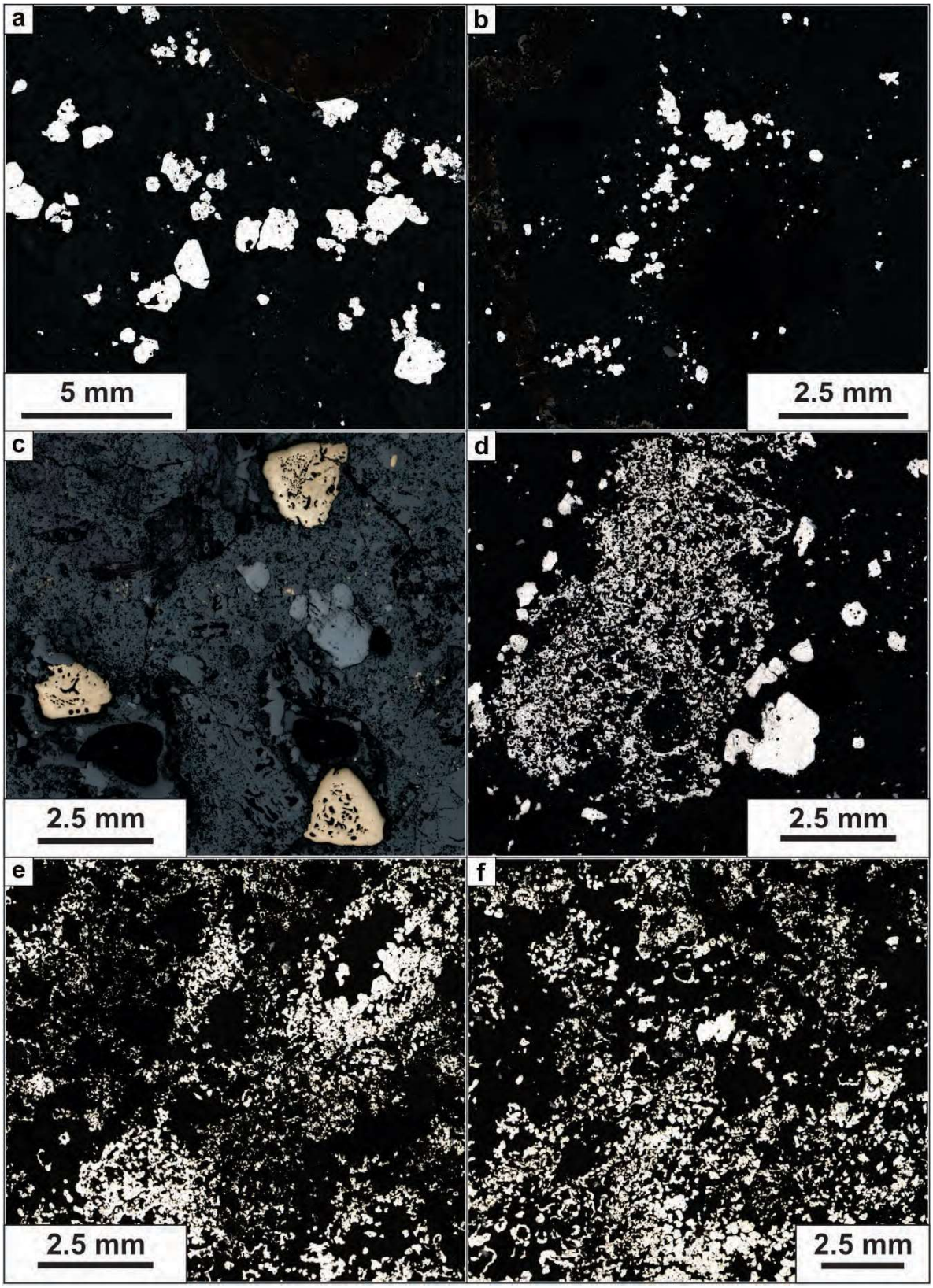

Figure 5.13. Pyrite-bearing samples. Reflected light photomicrographs. **a.** Hydrothermal breccia (252 m depth; BTG-005). **b.** Hydrothermal breccia (252 m depth; BTG-005). **c.** Diorite porphyry dike I (269 m depth; BTG-003). **d.** Hydrothermal breccia (450.5 m depth; BTG-003). **e.** Aphyric andesite (269.9 m depth; BTG-006). **f.** Patchy-textured plagioclase-phyric andesite (269.9 m depth; BTG-006).

5.3.3.2. Major elements in pyrite

The major element analysed in pyrite from Bantug is S. A fixed value of 465,000 ppm Fe was used for all the compositional calculations. Table 5.7 and Figure 5.14 present a summary of sulphur results. Complete results are presented in Appendix L. Sulphur content from pyrites in diorite porphyry dike I and hydrothermal breccia samples in BTG-003 is higher compared with other samples (Table 5.7; Fig. 5.14).

Table 5.7. Summary of LA-ICP-MS major elements results from pyrite

	S (ppm)
All results	
n	87
Min	412,100
Max	537,800
Mean	473,900
BTG-005	
n	35
n (Hbx)	35
Min	412,100
Max	537,800
Mean	473,900
BTG-003	
n	32
n (DPD I)	12
n (Hbx)	20
Min	412,100
Max	537,800
Mean	473,900
BTG-006	
n	20
n (PA)	20
Min	412,100
Max	537,800
Mean	473,900

n: number of analyses; Min: minimum; max: Maximum; Mean: mean value. Abbreviations: Abx: andesitic volcaniclastic breccia; And: aphyric andesite; Hbx: hydrothermal breccia; PA: plagioclase-phyric andesite.

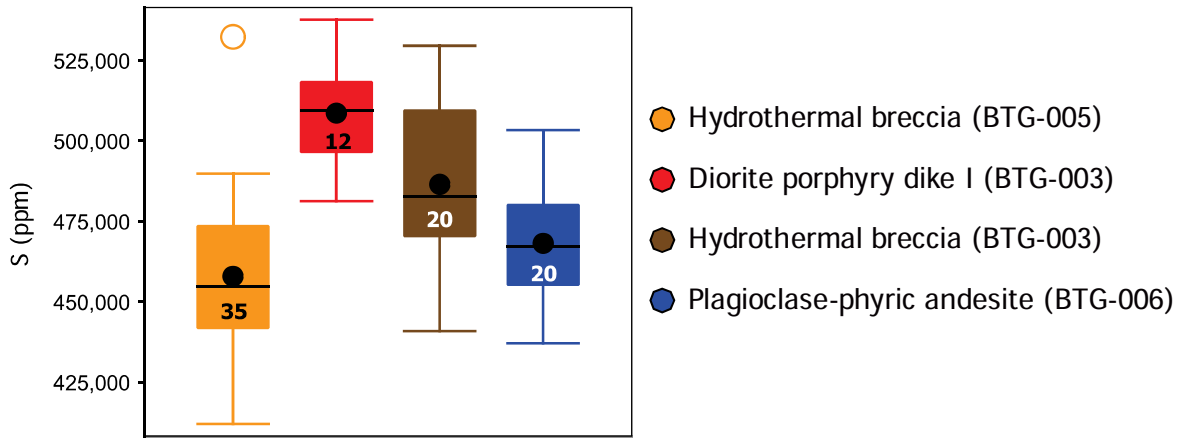

Figure 5.14. LA-ICP-MS major elements results from pyrite. Box plot. Sulphur (S).

5.3.3.3. Minor elements in pyrite

Minor elements analysed in pyrite include Al, Ti, and Ca. Table 5.8 and Figure 5.15 present a summary of the results. Complete results are presented in Appendix L. Aluminium and Ti results are particularly high in plagioclase-phyric andesites compared with other samples (Table 5.8; Fig. 5.15). These high results are followed by those from hydrothermal breccias in BTG-005 and BTG-003.

Table 5.8. Summary of LA-ICP-MS minor elements results from pyrite

	Al (ppm)	Ti (ppm)	Ca (ppm)
All results			
n	52	64	5
Min	0.8910	0.3565	191.0
Max	16,220	19,320	844.5
Mean	4,271	2,039	368.3
BTG-005			
n	21	17	2
n (Hbx)	21	17	2
Min	78.19	4.059	191.0
Max	7,063	19,320	198.5
Mean	1,444	2,442	194.8
BTG-003			
n	11	27	3
n (DPD I)	3	10	
n (Hbx)	8	17	3
Min	0.8910	0.3565	263.1
Max	7,089	7,629	844.5
Mean	1,169	285.5	483.9
BTG-006			
n	20	20	
n (PA)	20	20	
Min	127	557.60	
Max	16,220	15,030	
Mean	8,946	4,063	

n: number of analyses; min: minimum; max: maximum; mean: mean value. Abbreviations: Abx: andesitic volcaniclastic breccia; And: aphyric andesite; Hbx: hydrothermal breccia; PA: plagioclase-phyric andesite.

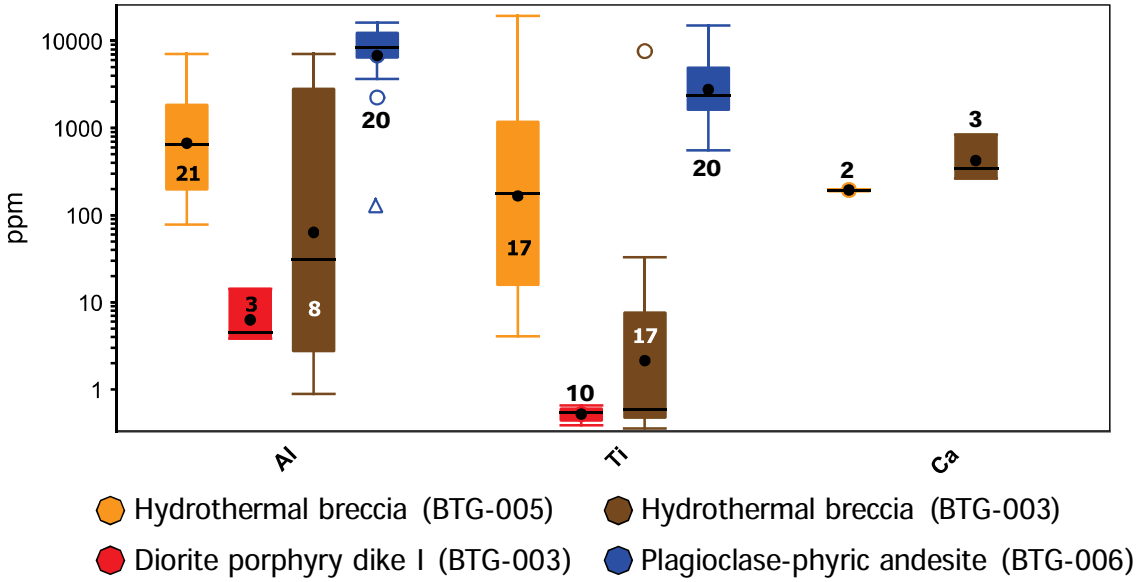

Figure 5.15. LA-ICP-MS minor elements results from pyrite. Box plots. Includes Aluminium (Al), Titanium (Ti), Calcium (Ca).

5.3.3.4. Trace elements in pyrite

Trace elements analysed in pyrite are presented in Table 5.9, Figures 5.16 and 5.17. Pyrites from hydrothermal breccia samples from BTG-005 exhibit higher concentration of most trace elements compared with other samples (Table 5.9; Figs. 5.16 and 5.17), particularly Mg, Zn, Tl, and Gd. Pyrites from plagioclase-phyric andesite samples from BTG-006 exhibit similar results; highly concentrated elements include Pb, Te, Ba, Zr, Mo, Sn, Hf, and U (Table 5.9; Figs. 5.16 and 5.17). Pyrites in diorite porphyry dike I samples from BTG-003 yielded the majority of lower results (Table 5.9; Figs. 5.16 and 5.17). Cobalt, Ni, and La results are very similar in all samples.

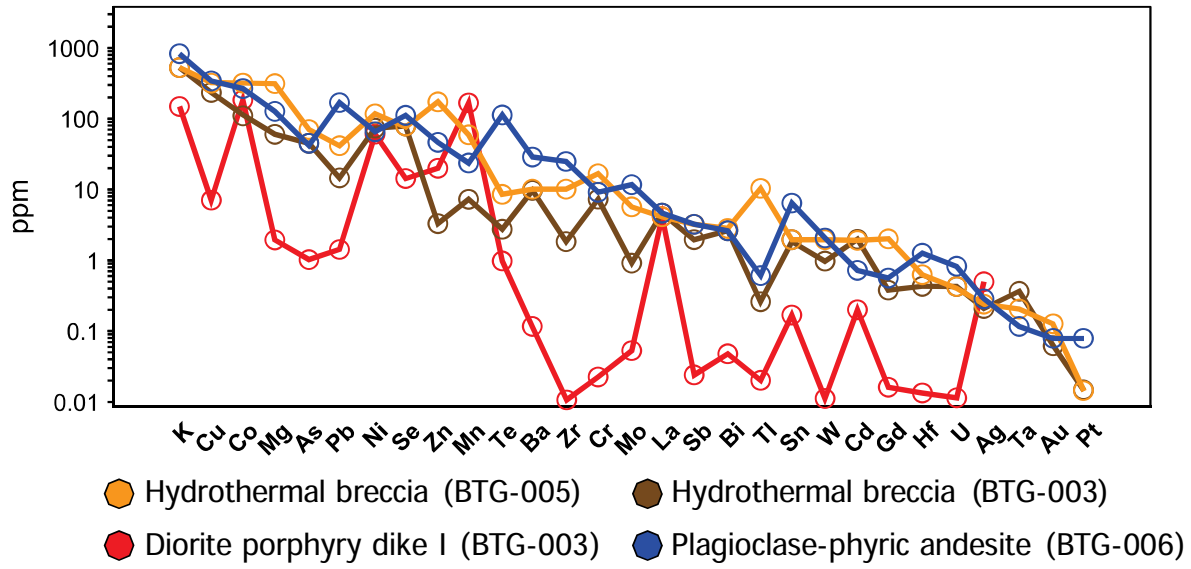

Figure 5.16. LA-ICP-MS trace elements results from pyrite. Line graph. Lines represent mean values.

5.3.3.5. Discussion

5.3.3.5.1. Comparison with pyrite from Batu Hijau and Mankayan

LA-ICP-MS pyrite results from Bantug were compared with pyrite results from the Batu Hijau porphyry deposit in Indonesia (Garwin, 2000, 2002; Wilkinson et al., 2015) and Mankayan in the Philippines (Chang et al., 2011). Results were compiled in the AMIRA P1060 project (Cooke et al., 2014). Pyrite in porphyry dike I (DPD I) samples from Bantug were compared with samples from Batu Hijau; pyrite in plagioclase-phyric and hydrothermal breccia samples were compared with samples from Mankayan.

Table 5.9. Summary of LA-ICP-MS trace elements results from pyrite

ppm	K	Cu	Co	Mg	As	Pb	Ni	Se	Zn	Mn	Te	Ba	Zr	Cr	Mo
All results															
n	40	82	87	35	61	72	87	83	58	48	45	46	46	20	32
Min	3.291	0.1591	2.305	0.2639	0.4721	0.01000	2.332	4.118	0.1690	0.09958	0.1304	0.01340	0.01000	0.8241	0.03739
Max	2,993	2,034	938.8	2,058	454.4	934.3	346.8	293.8	1,361	374.6	1,196	224.4	157.8	36.91	42.39
Mean	598.3	278.6	209.1	174.2	54.86	57.88	83.26	77.48	55.89	41.22	41.93	14.58	14.32	10.03	7.053
BTG-005															
n	13	34	35	12	27	24	35	31	13	19	12	14	20	5	10
n (Hbx)	13	34	35	12	27	24	35	31	13	19	12	14	20	5	10
Min	66.30	2.688	2.305	9.657	2.042	0.4336	2.332	4.686	1.907	0.9286	0.8243	0.4183	0.02208	5.685	0.05160
Max	1,910	2,034	938.8	2,058	454.4	359.3	346.8	250.6	1,361	365.7	24.04	47.44	56.18	36.91	23.55
Mean	523.5	355.1	258.0	324.8	75.01	36.05	117.2	81.45	163.3	55.95	8.385	9.937	10.65	15.87	5.021
BTG-003															
n	9	28	32	7	14	28	32	32	26	10	18	14	6	4	7
n (DPD I)	4	12	12	2	4	9	12	12	8	3	10	7	1	0	1
n (Hbx)	5	16	20	5	10	19	20	20	18	7	8	7	5	4	6
Min	3.291	0.1591	3.804	0.2639	0.4721	0.01000	2.974	4.118	0.1690	0.09958	0.1304	0.01340	0.01000	0.8241	0.03739
Max	1,121	1,310	644.1	234.3	279.2	71.42	263.4	212.5	75.52	374.6	8.078	38.85	8.645	12.40	1.615
Mean	337.8	139.7	134.7	39.76	33.15	10.16	56.76	50.97	8.040	49.70	1.707	4.975	1.450	6.549	0.6595
BTG-006															
n	18	20	20	16	20	20	20	20	19	19	15	18	20	11	15
n (PA)	18	20	20	16	20	20	20	20	19	19	15	18	20	11	15
Min	82.91	13.46	2.316	7.180	4.411	1.237	5.911	20.39	2.242	1.289	8.167	0.8241	0.1938	3.684	0.5300
Max	2,993	1,213	745.4	315.6	173.1	934.3	196.0	293.8	142.9	66.58	1,196	224.4	157.8	18.08	42.39
Mean	782.5	342.9	242.4	120.1	42.87	150.9	66.28	113.8	47.87	22.03	117.0	25.67	21.85	8.638	11.39

Table 5.9. Summary of LA-ICP-MS trace elements results from pyrite (Continued)

ppm	La	Sb	Bi	Tl	Sn	W	Cd	Gd	Hf	U	Ag	Ta	Au	Pt
All results														
n	87	43	66	47	87	27	16	16	22	37	32	16	17	6
Min	4	0.02216	0.0100	0.0100	0.08726	0.01000	0.06987	0.01433	0.02824	0.01000	0.01000	0.01000	0.01216	0.01000
Max	4	22.99	14.00	103.3	34.13	10.00	8.693	7.591	4.599	2.002	1.598	0.4943	0.4462	0.06994
Mean	4	2.738	2.301	3.199	2.617	1.614	1.347	0.8866	0.8910	0.5651	0.2503	0.1494	0.08049	0.02291
BTG-005														
n	35	14	29	13	35	6	5	5	10	14	7	6	6	1
n (Hbx)	35	14	29	13	35	6	5	5	10	14	7	6	6	1
Min	4	0.2139	0.1609	0.04494	0.2097	0.03737	1	0.01491	0.02824	0.06779	0.03272	0.01	0.01216	0.01381
Max	4	22.99	8.577	103.3	18.84	4.019	3.305	7.591	2.324	0.655	0.3581	0.4943	0.4462	0.01381
Mean	4	3.135	2.293	10.76	1.526	1.585	1.762	1.921	0.6	0.3344	0.1742	0.1867	0.1165	0.01381
BTG-003														
n	32	10	18	20	32	6	7	4	1	5	12	1	7	4
n (DPD I)	12	1	5	10	12	1	2	1	0	1	4	0	0	0
n (Hbx)	20	9	13	10	20	5	5	3	1	4	8	1	7	4
Min	4	0.02216	0.01000	0.01000	0.08726	0.01000	0.06987	0.01433	0.3717	0.01000	0.01000	0.3580	0.02864	0.01000
Max	4	13.95	14.00	1.897	34.13	4.080	8.693	0.5890	0.3717	1.637	1.598	0.3580	0.08833	0.01925
Mean	4	1.693	1.946	0.1335	1.255	0.7107	1.437	0.2665	0.3717	0.3459	0.2860	0.3580	0.05717	0.01342
BTG-006														
n	20	19	19	14	20	15	4	7	11	18	13	9	4	1
n (PA)	20	19	19	14	20	15	4	7	11	18	13	9	4	1
Min	4	0.1465	0.5317	0.03267	0.9830	0.2714	0.4897	0.02388	0.09203	0.1715	0.07824	0.01832	0.05014	0.06994
Max	4	10.89	6.386	1.377	22.93	10.00	0.7400	1.594	4.599	2.002	0.4959	0.3256	0.08381	0.06994
Mean	4	2.997	2.651	0.5541	6.703	1.988	0.6709	0.5021	1.203	0.8055	0.2584	0.1013	0.06734	0.06994

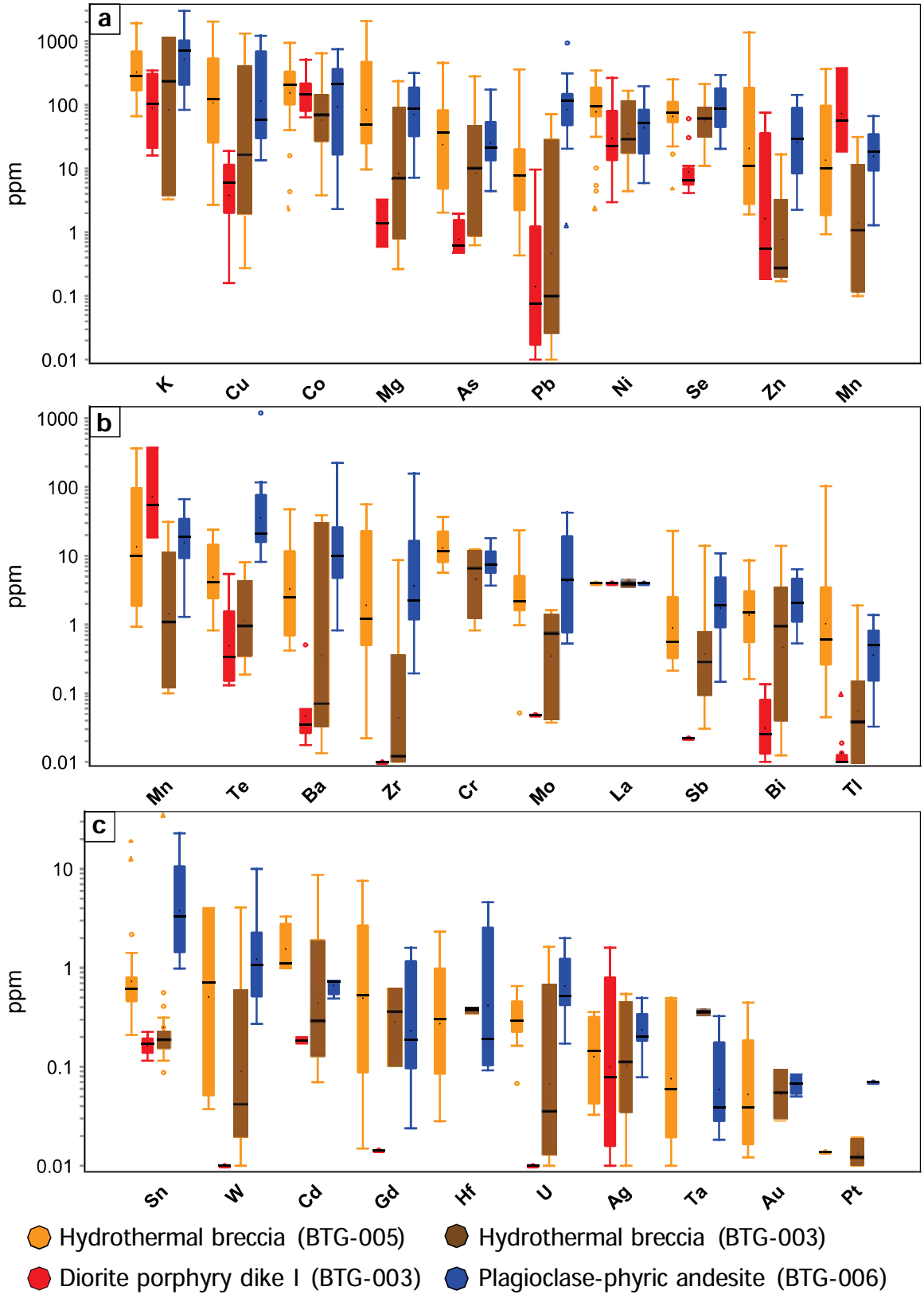

Figure 5.17. LA-ICP-MS trace elements results from pyrite. Box-plot diagrams. **a.** Most abundant trace elements; includes: K, Cu, Co, Mg, As, Pb, Ni, Se, Zn, and Mn. **b.** Moderately abundant trace elements; includes: Mn, Te, Ba, Zr, Cr, Mo, La, Sb, Bi, and Tl. **c.** Least abundant trace elements; includes: Sn, W, Cd, Gd, Hf, U, Ag, Ta, Au, and Pt.

High Ni concentrations in hydrothermal pyrite crystals, located in close proximity to the Batu Hijau ore deposit, were found to be indicative of high temperature (Gemmell et al., 2014; Wilkinson et al., 2015). Nickel results from pyrite in DPD I are comparable to results from pyrites at 0.5 – 1 km distance from the Batu Hijau deposit (Fig. 5.18a). Nickel content in those pyrites is considered indicative of high temperature (i.e., 100-400 ppm). However, W results from pyrite in DPD I are significantly lower than results from pyrite at 2 – 2.5 km distance from Batu Hijau (Fig. 5.18b). Thus, an accurate location of a potential heat source, based on pyrite results from DPD I is not recommended.

Nickel results from pyrite in hydrothermal breccia (BTG-005) samples are comparable to those of pyrites at 2 – 2.5 km away from the FSE porphyry deposit in the Mankayan lithocap (Fig. 5.18c). Nickel results from pyrite in hydrothermal breccia (BTG-003) and plagioclase-phyric andesite (BTG-006) samples are comparable to results from pyrites at 1 – 2 km distance from FSE (Fig. 5.18c). Cobalt results from pyrite in these samples are also comparable to those at 1 – 2 km distance from FSE (Fig. 5.18d).

Comparison of pyrite results with samples from Batu Hijau and Mankayan suggest the location of a potential heat source somewhere between 0.5 and 2.5 km distance. Although pyrite results from Bantug are encouraging, the conclusion that be drawn from them is ambiguous. It is recommended to perform more analyses, particularly in advanced argillic-altered samples to the north of drill hole BTG-006.

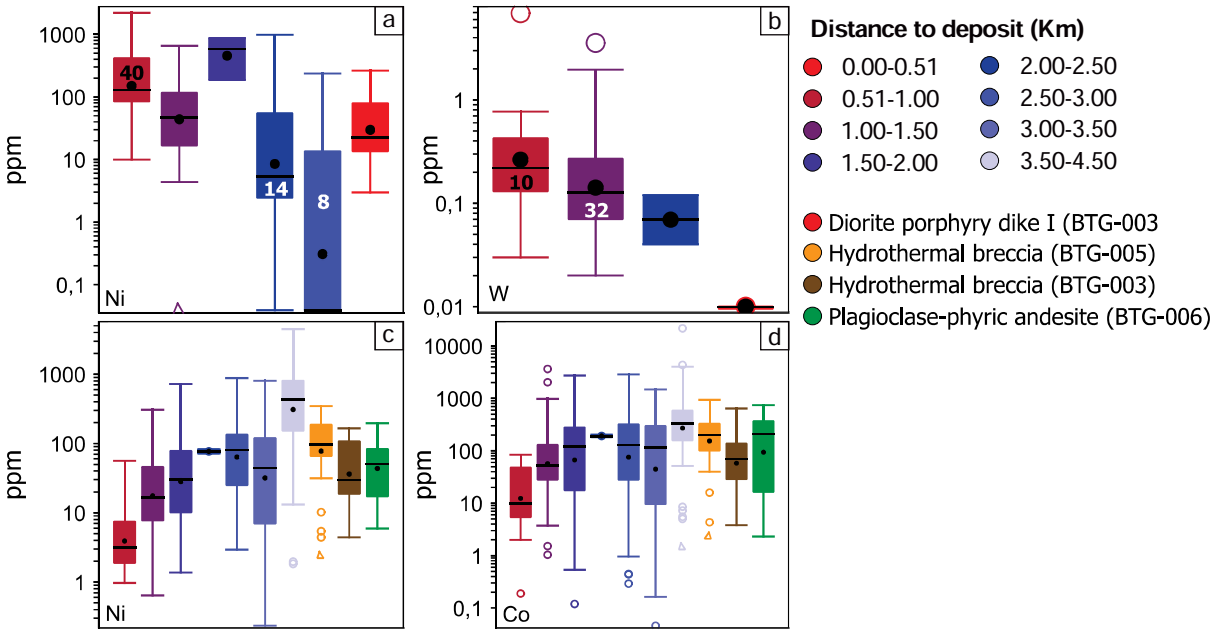

Figure 5.18. Comparison of LA-ICP-MS pyrite results from Batu Hijau and Bantug. Box plots. **a.** Nickel results from Batu Hijau and Bantug. b. Tungsten results from Batu Hijau and Bantug. c. Nickel results from Mankayan and Bantug. d. Cobalt results from Mankayan and Bantug. Results from Batu Hijau and Mankayan from Cooke et al. (2014).

5.3.4. Epidote geochemistry

5.3.4.1. Sample description

Epidote was analysed from diorite porphyry dike I and III samples from drill holes BTG-003 and BTG-006 respectively. Results were filtered in order detect ablation of quartz, diaspore, pyrite, and rutile inclusions (Table 5.10). Tables 5.11 to 5.13, as well as Figures 5.19 to 5.22. present summaries of the results. Complete results are presented in Appendix L.

Epidote occurs as anhedral, acicular crystals of ~500 μm length filling miarolitic cavities (5-7 vol %). Euhedral quartz crystals (i.e., <1 vol %; ~400 μm) occur with epidote in cavities (Fig. 5.19). Zonation was commonly observed within epidote crystals on FE-SEM images (Figs. 5.19e and 5.19f). Zonation is very likely to be due to twinning and small compositional differences.

Table 5.10. Filtering criteria for epidote

Filter	n
Si>370,000	3
Al>160,000	1
Fe>165,000	1
Ti>2,000	2

n: number of analyses

5.3.4.2. Major elements

Major elements analysed on epidote crystals include Si, Ca, Al, and Fe. Table 5.11 and Figure 5.20 present a summary of the results. Major element mean contents of epidotes from DPD I and DPD III are similar, and small differences in Al and Fe contents were observed between samples (Fig. 5.20).

Table 5.11. Summary of LA-ICP-MS major elements results from epidote

	Si (ppm)	Ca (ppm)	Al (ppm)	Fe (ppm)
All results				
n	25	25	25	25
Min	190,900	156,500	102,100	95,910
Max	282,300	167,800	129,900	130,700
Mean	211,300	164,500	116,400	112,600
BTG-003				
n (DPD I)	7	7	7	7
Min	190,900	156,500	102,100	101,300
Max	211,600	167,800	124,000	130,700
Mean	200,300	163,000	111,100	116,600
BTG-006				
n (DPD III)	18	18	18	18
Min	198,400	164,200	107,800	95,910
Max	282,300	166,100	129,900	122,600
Mean	215,600	165,100	118,500	111,100

n: number of analyses; Min: minimum; Max: maximum; Mean: mean value. Abbreviations: DPD I: diorite porphyry dike I; DPD III: diorite porphyry dike III.

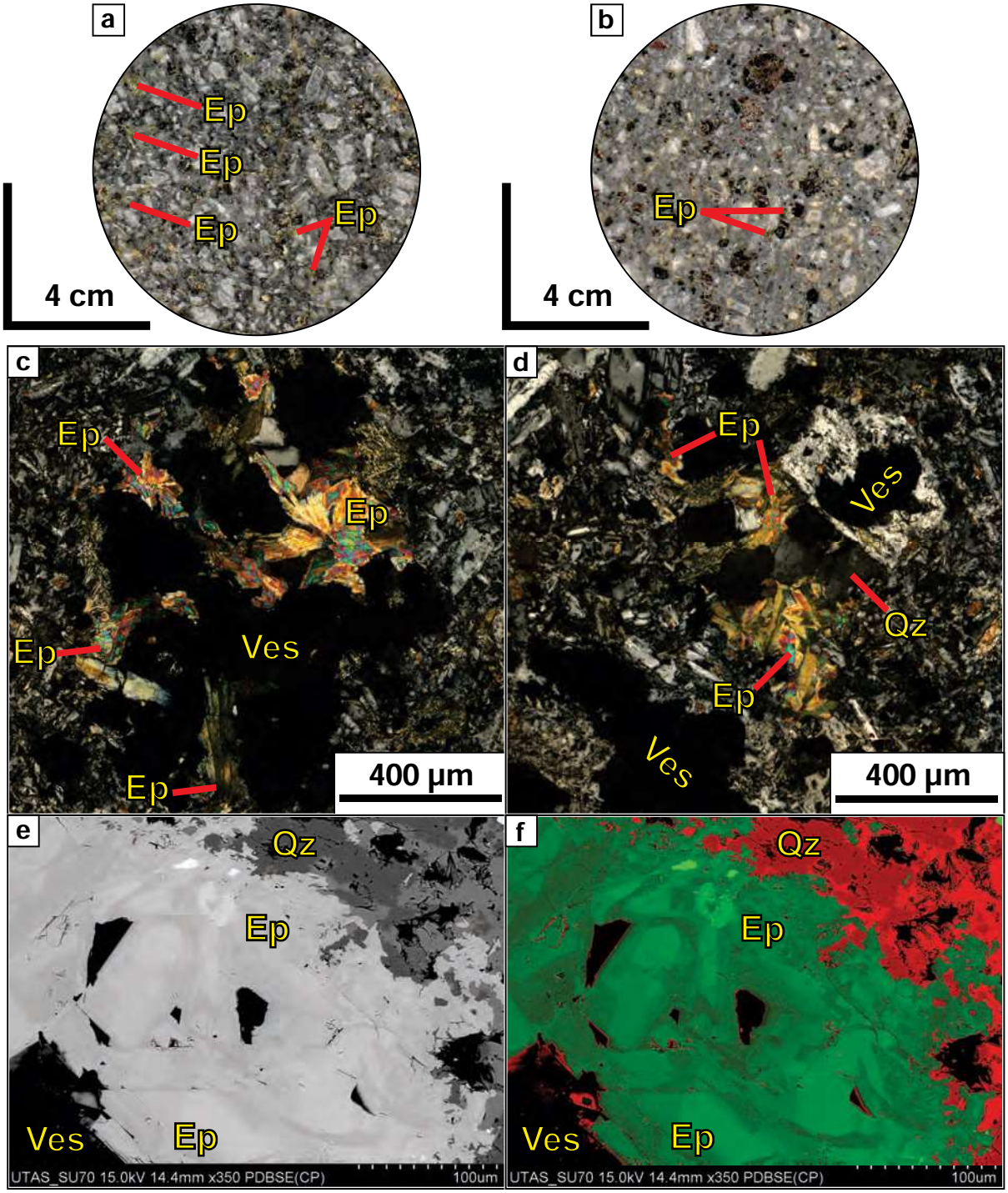

Figure 5.19. Epidote-bearing samples. a. Diorite porphyry dike III hand sample (380 m depth; BTG-006). **b.** Diorite porphyry dike I hand sample (269 m depth; BTG-003). **c.** Crossed-polarised photomicrograph, diorite porphyry dike I (268 m depth; BTG-003). **d.** Crossed-polarised photomicrograph, diorite porphyry dike I (268 m depth; BTG-003). **e.** BSE image, diorite porphyry dike I (268 m depth; BTG-003). **f.** Pseudo-coloured BSE image from panel e. Notice the zonation within epidote crystals. Abbreviations: Ep: epidote; Qz: quartz; Ves: vesicule.

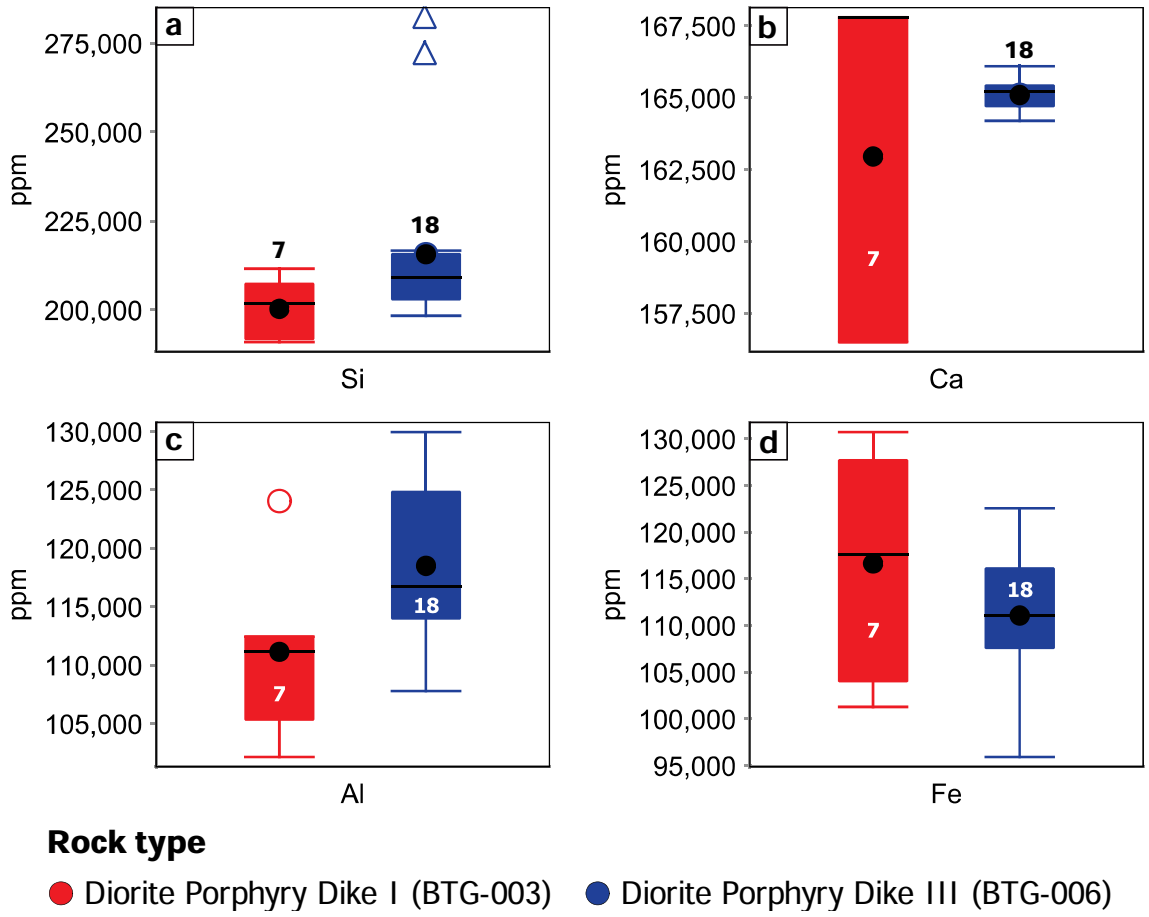

Figure 5.20. LA-ICP-MS major elements results from epidote. Box plots. **a.** Silicon (Si). **b.** Calcium (Ca). **c.** Aluminium (Al). **d.** Iron (Fe).

5.3.4.3. Minor elements

Minor elements analysed include Mn and Sr. Table 5.12 and Figure 5.21 present a summary of the results.

Table 5.12. Summary of LA-ICP-MS minor elements results from epidote

	Mn (ppm)	Sr (ppm)
All results		
n	25	25
Min	672.3	676.2
Max	5,809	4,091
Mean	2,143	1,814
BTG-003		
n (DPD I)	7	7
Min	1,094	1,483
Max	2,843	3,027
Mean	1,991	2,372
BTG-006		
n (DPD III)	18	18
Min	672.3	676.2
Max	5,809	4,091
Mean	2,202	1,597

n: number of analyses; Min: minimum; Max: maximum; Mean: mean value. Abbreviations: DPD I: diorite porphyry dike I; DPD III: diorite porphyry dike III.

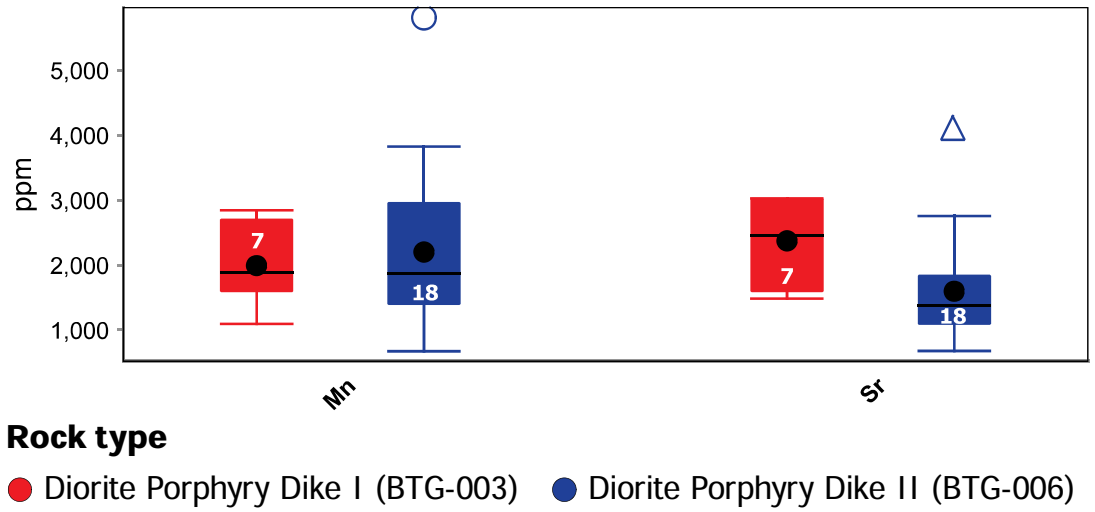

Figure 5.21. LA-ICP-MS minor elements results from epidote. Box plots. Manganese (Mn) and strontium (Sr).

Manganese contents of epidotes from DPD I and DPD III are similar; Sr epidote contents are higher in DPD I compared with DPD II.

5.3.4.4. Trace elements

Trace elements analysed in epidotes include Eu, Gd, Sb, Sn, Yb, Th, U, Hf, Co, Mo, Lu, Bi, Ag, Au, Ta, and Tl. Table 5.13, Figures 5.22 and 5.23 present a summary of the results. Complete results are presented in Appendix L.

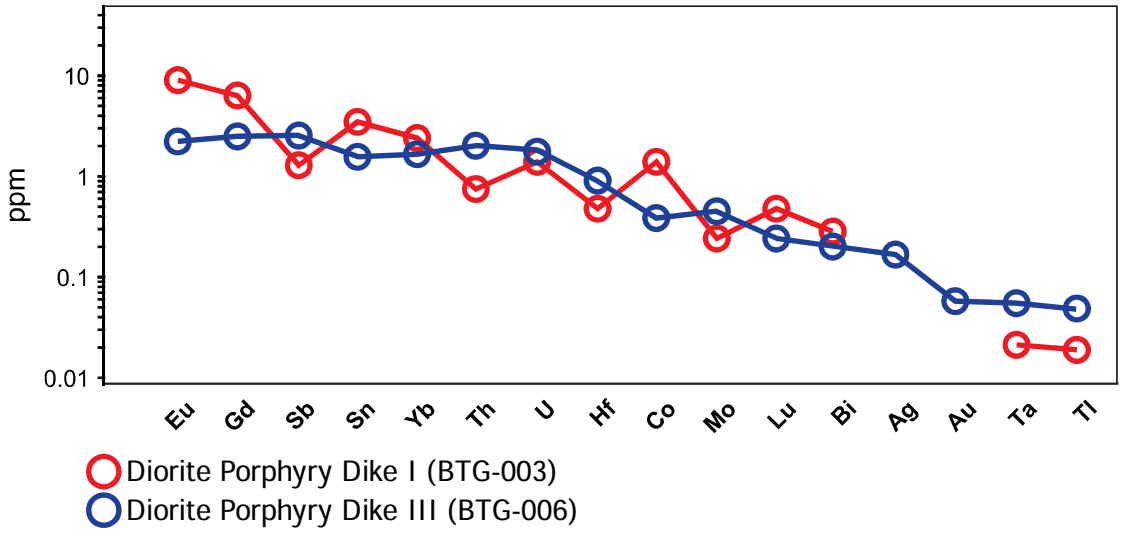

Figure 5.22. LA-ICP-MS trace elements results from epidote. Line graph. Lines represent mean values.

Epidote crystals from DPD I contain higher Eu, Gd, Sn, Co, and Lu than epidotes from DPD III (Table 5.13; Figs. 5.21 and 5.22). Epidote crystals from DPD III contain higher Sb, Th, Hf, Ta, and Tl than epidotes from DPD I (Table 5.13; Figs. 5.21 and 5.22).

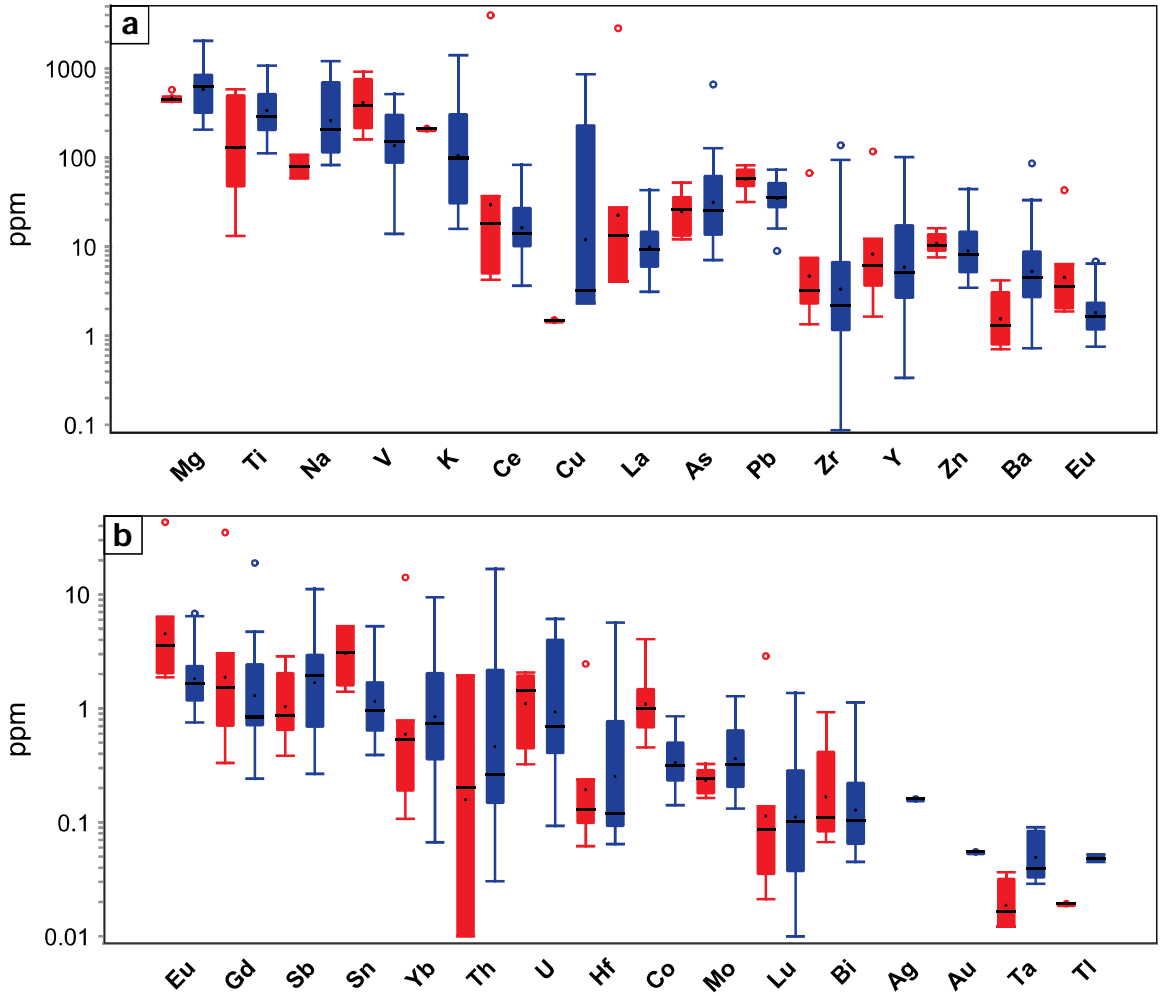

Figure 5.23. LA-ICP-MS trace elements results from epidote. Box plots. **a.** Most abundant trace elements; includes: Mg, Ti, Na, V, K, Ce, Cu, La, As, Pb, Zr, Y, Zn, Ba, and Eu. **b.** Least abundant trace elements; includes: Eu, Gd, Sb, Sn, Yb, Th, U, Hf, Co, Mo, Lu, Bi, Ag, Au, Ta, and Tl.

5.3.4.5. Discussion

5.3.4.5.1. Comparison with epidote from the Baguio district, Philippines

Cooke et al. (2014) used LA-ICP-MS to analyse epidote in propylitic-altered rocks from the Baguio district, Philippines. The Baguio district contains several porphyry, epithermal, and skarn deposits formed over the last 3 million years when the Scarborough Ridge subducted under northern Luzon (Hollings et al., 2011a; Waters et al., 2011; Cooke et al., 2014).

Table 5.13. Summary of LA-ICP-MS trace elements results from epidote

ppm	Mg	Ti	Na	V	K	Ce	Cu	La	As	Pb	Zr	Y	Zn	Ba	Eu
All results															
n	25	25	16	25	17	25	5	25	25	25	23	25	25	23	25
Min	206.5	13.21	58.73	13.97	15.86	3.652	1.5	3.118	7.1	8.948	0.08717	0.3371	3.466	0.7063	0.7538
Max	2056	1077	1215	924.8	1414	3971	862.4	2844	664.2	81.54	137.4	117.5	44.25	86.35	43.18
Mean	628.3	372.2	343	282	234.5	178.6	174.6	125.7	60.07	45.07	17.48	16.33	11.25	8.714	4.132
BTG-003															
n (DPD I)	7	7	2	7	1	7	1	7	7	7	7	7	7	7	7
Min	422.4	13.21	58.73	160.3	211.8	4.244	1.5	4.085	12.15	31.88	1.351	1.641	7.596	0.7063	1.877
Max	578.7	586.5	107.5	924.8	211.8	3971	1.5	2844	52.55	81.54	67.26	117.5	16.17	4.176	43.18
Mean	468	259.9	83.09	499	211.8	581.9	1.5	417	27.51	60.12	12.58	22.31	11.23	1.884	9.075
BTG-006															
n (DPD III)	18	18	14	18	16	18	4	18	18	18	16	18	18	16	18
Min	206.5	111.7	82.65	13.97	15.86	3.652	2.318	3.118	7.1	8.948	0.08717	0.3371	3.466	0.7245	0.7538
Max	2056	1077	1215	518.8	1414	83.42	862.4	43.11	664.2	73.28	137.4	101.2	44.25	86.35	6.825
Mean	690.7	415.8	380.2	197.6	235.9	21.73	217.9	12.45	72.74	39.21	19.62	14	11.26	11.7	2.21

Table 5.13. Summary of LA-ICP-MS trace elements results from epidote (Continued)

ppm	Gd	Sb	Sn	Yb	Th	U	Hf	Co	Mo	Lu	Bi	Ag	Au	Ta	Tl
All results															
n	24	24	25	23	19	25	19	21	16	24	22	1	1	11	4
Min	0.2424	0.2668	0.3904	0.06671	0.01	0.09301	0.0618	0.1417	0.1323	0.01	0.04501	0.1607	0.05511	0.0122	0.01934
Max	35.01	11.15	5.275	14.13	16.81	6.104	5.678	4.055	1.283	2.882	1.129	0.1607	0.05511	0.09058	0.05245
Mean	3.577	2.164	2.084	1.881	1.802	1.705	0.7405	0.7145	0.3741	0.3093	0.2209	0.1607	0.05511	0.04229	0.04131
BTG-003															
n (DPD I)	7	7	7	7	3	7	7	7	6	7	6			4	1
Min	0.3328	0.3839	1.401	0.1073	0.01	0.3235	0.0618	0.4547	0.1638	0.02124	0.06702			0.0122	0.01934
Max	35.01	2.863	5.275	14.13	1.947	2.073	2.46	4.055	0.3258	2.882	0.9278			0.03656	0.01934
Mean	6.228	1.286	3.448	2.397	0.7201	1.33	0.47	1.386	0.2403	0.4812	0.2712			0.02077	0.01934
BTG-006															
n (DPD III)	17	17	18	16	16	18	12	14	10	17	16	1	1	7	3
Min	0.2424	0.2668	0.3904	0.06671	0.03043	0.09301	0.06432	0.1417	0.1323	0.01	0.04501	0.1607	0.05511	0.0289	0.04519
Max	18.92	11.15	5.262	9.482	16.81	6.104	5.678	0.8538	1.283	1.363	1.129	0.1607	0.05511	0.09058	0.05245
Mean	2.485	2.526	1.553	1.656	2.005	1.851	0.8982	0.3787	0.4544	0.2385	0.2021	0.1607	0.05511	0.05458	0.04864

Waters et al. (2011) estimated an endowment of over 35 million ounces of Au and 3 million metric tons of Cu contained in the porphyry and epithermal deposits. Cooke et al. (2014) found that epidote chemistry varies with respect to distance from porphyry deposit centres. The highest concentrations of proximal pathfinder elements (e.g., Cu, Mo, Au, Sn) were detected in epidote from close to the potassic alteration zone. Distal pathfinder elements (e.g., As, Sb, Pb, Zn, Mn) are most enriched in epidote located more than 1.5 km away from the deposit centre.

Cooke et al. (2014) concluded that epidote geochemistry has the capacity to help explorers to detect productive porphyry systems for more than 1 km beyond the pyrite halo to the ore deposits. They also suggested that low-level trace element analyses can be combined with mapping of simple textural features, such as epidote vein intensity, to provide explorers with new tools that provide indications of proximity to ore zones in near-mine and far-field environments.

Figure 5.24 presents a comparison between epidote proximal and distal pathfinder results from the Baguio district (Cooke et al., 2014) and Bantug (this study). Copper and Mo results from Bantug are comparable to those results from Baguio located at, or beyond, 1.1 km from any ore deposit (Figs. 5.24a and 5.24b). Only one analysis from Bantug yielded a result above detection limit (Fig. 5.24c). This result is comparable to two results from Baguio located within 500 m of proximity to an ore deposit (Fig. 5.24c). Tin results from DPD I at Bantug are comparable with those located at <1 km from an ore deposit at Baguio (Fig. 5.24d). Tin results from DPD III at Bantug are very similar to those from Baguio located beyond 1.1 km distance from an ore deposit (Fig. 5.24d). Arsenic and Pb results from Bantug are comparable to the most distal results from Baguio (Figs. 524e and 5.24). Antimony results from Bantug are similar to those located within 1 km from an ore deposit at Baguio (Fig. 5.24f).

Small quantities of epidote at Bantug were observed to replace mafic minerals and fill in cavities. The propylitic alteration observed while logging drill core in this study can be best described as weak and categorised as distal. The distal character of the propylitic alteration is supported by the comparison of LA-ICP-MS results from Bantug with those from the Baguio district. Due to the small number and restricted location of LA-ICP-MS epidote analyses, it is inaccurate to make suggestions. However, results indicate a heat source at depth or in any direction located at more than 1 km distance. The author recommends targeting of epidote-bearing samples for LA-ICP-MS analyses in further exploration efforts.

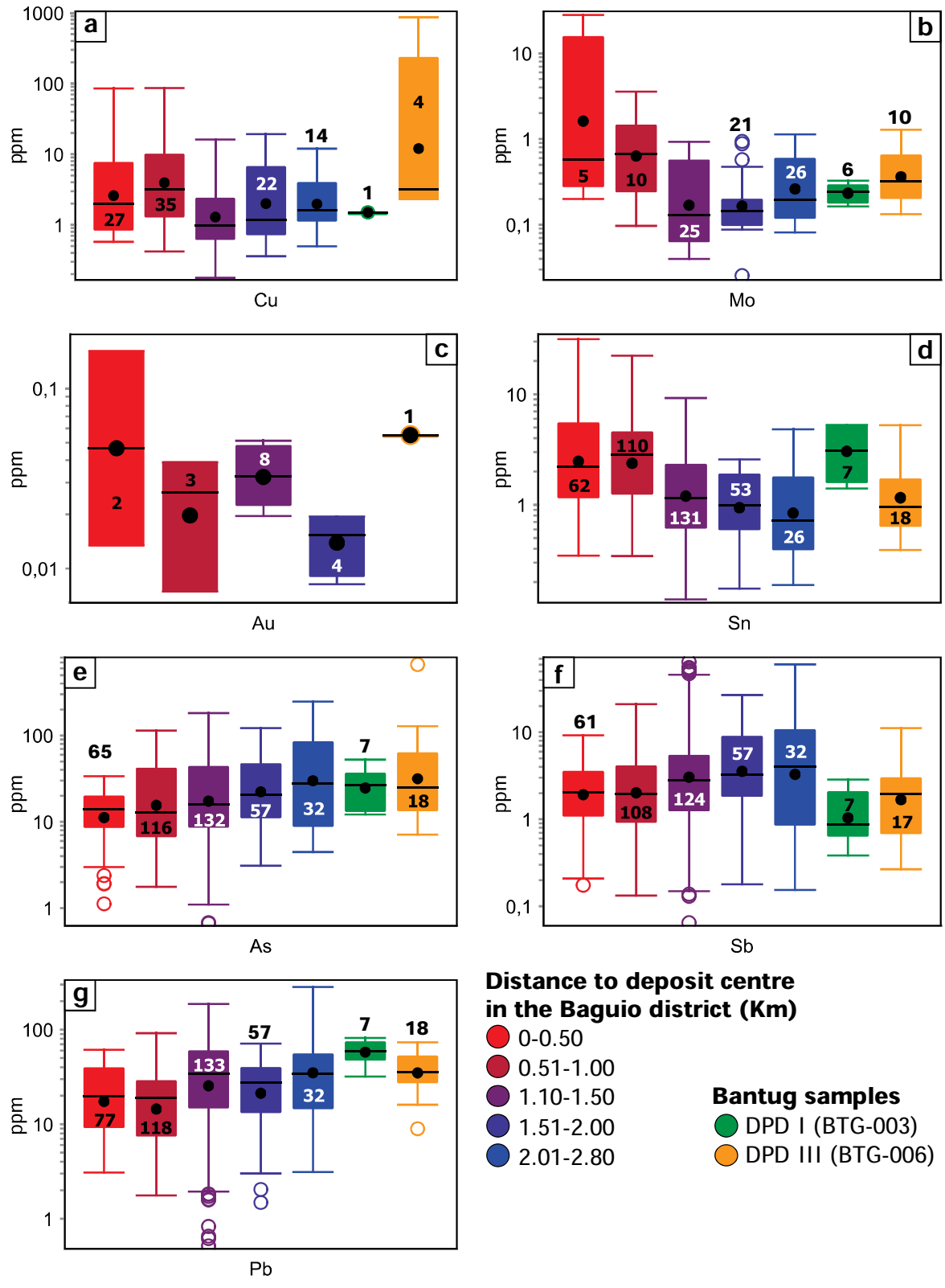

Figure 5.24. Comparison of pathfinder elements in epidote from the Baguio district and Bantug. Box and whisker diagram. **a.** Copper (Cu). **b.** Molybdenum (Mo). **c.** Gold (Au). **d.** Tin (Sn). **e.** Arsenic (As). **f.** Antimony (Sb). **g.** Lead (Pb).

5.3.5. Chlorite geochemistry

5.3.5.1. Sample description

LA-ICP-MS analyses were carried on two samples from the propylitic-altered, chlorite-bearing diorite porphyry dike I, encountered by drill-hole BTG-003. The samples were collected at 258.7 m and 269.0 m down-hole. Both samples are characterised by porphyritic texture defined by plagioclase (15-20 vol %.), and pyroxene (5 vol %.) phenocrysts (Figs. 5.25a and 5.25b). Chlorite was observed to replace pyroxene phenocrysts (Fig. 5.25); epidote inclusions in chlorite were ubiquitous (<100 µm; Fig. 5.25d).

Table 5.14. Filtering criteria for chlorite

Filter	n
Ca>20,000	1
K>130	1
Ti>40	1

n: number of analyses

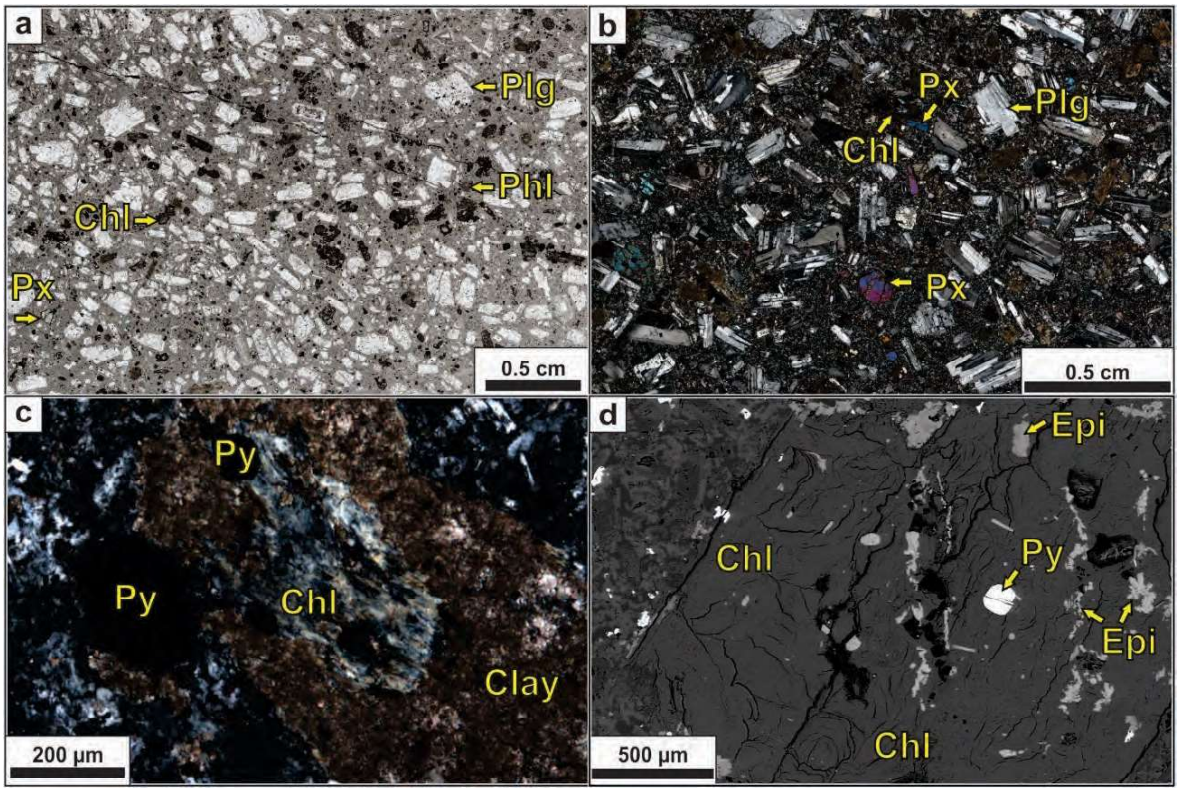

Figure 5.25. Chlorite-bearing diorite porphyry dike I. a. Parallel-polarised photomicrograph (258.7 m depth; BTG-003). **b.** Cross-polarised photomicrograph (258.7 m depth; BTG-003). **c.** Cross-polarised photomicrograph (269 m depth; BTG-003). **d.** SEM-BSE image (269 m depth; BTG-003). Abbreviations: Chl: chlorite; Ep: epidote; Plg: plagioclase; Px: pyroxene; Py: pyrite.

5.3.5.2. Major elements

Major elements analysed from chlorite include Si, Mg, Fe, and Al. Table 5.15 and Figure 5.25 present a summary of the results. Complete results are presented in Appendix L. Silicon and Mg results from chlorites at 269 m depth are higher compared with chlorites at 258.7 m depth (Fig. 5.25). Iron and Al results are higher in chlorites from 258.7 m depth compared with chlorites at 269 m depth (Fig. 5.25).

Table 5.15. Summary of LA-ICP-MS major elements results from chlorite

	Si (ppm)	Mg (ppm)	Fe (ppm)	Al (ppm)
All results				
N	26	26	26	26
Min	173,900	149,500	101,100	84,040
Max	203,100	191,900	137,100	89,080
Mean	190,100	176,500	113,700	86,770
258.7 m				
N	8	8	8	8
Min	173,900	149,500	129,500	88,950
Max	191,100	162,100	137,100	89,080
Mean	179,100	157,200	133,500	89,030
269 m				
n	18	18	18	18
Min	183,700	170,100	101,100	84,040
Max	203,100	191,900	108,200	87,980
Mean	195,000	185,100	104,800	85,770

n: number of analyses; Min: minimum; Max: maximum; Mean: mean value.

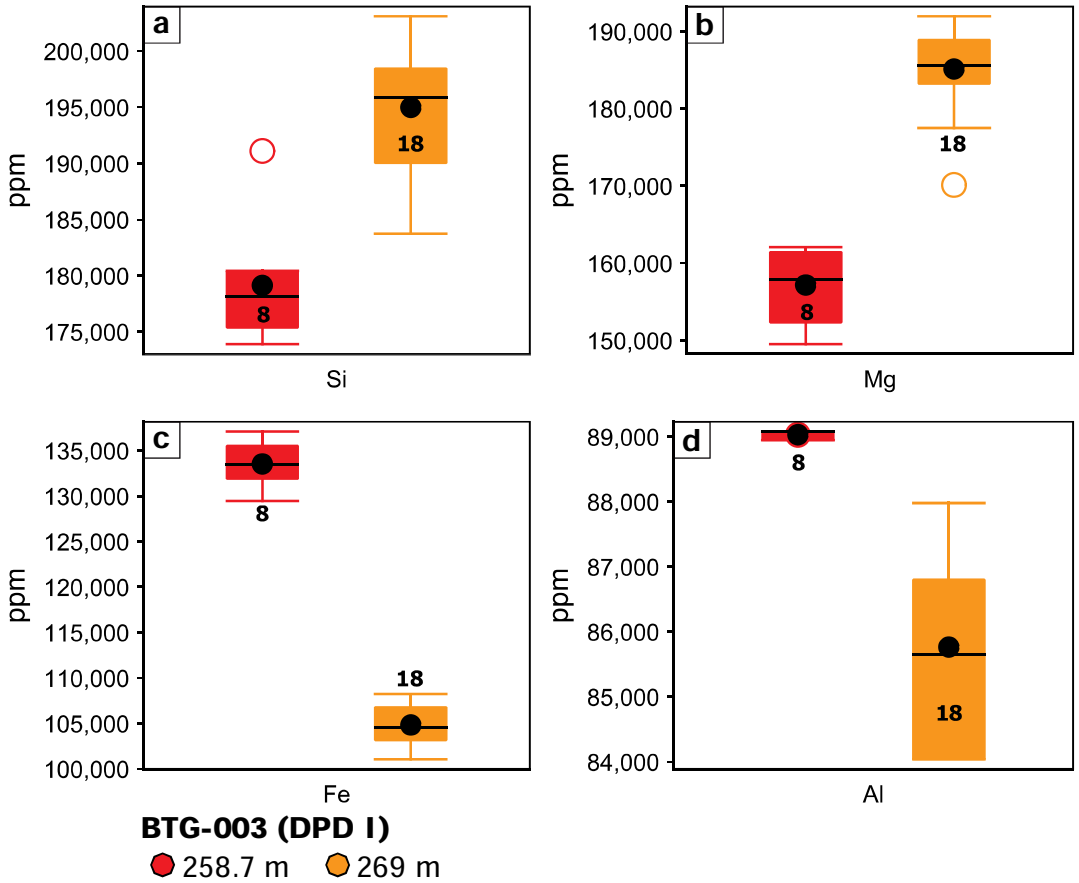

Figure 5.26. LA-ICP-MS major elements results from chlorite. Box plots. **a.** Silicon (Si). **b.** Magnesium (Mg). **c.** Iron (Fe). **d.** Aluminium (Al).

5.3.5.3. Minor elements

Minor elements analysed in chlorite are Ca and Mn. Table 5.16 and Figure 5.26 present a summary of the results. Complete results are presented in Appendix L. Minor element contents of both samples are very similar; however, chlorites from the sample collected at 269 m depth contain slightly higher mean values and high value outliers (Table 5.16; Fig. 5.26.).

Table 5.16. Summary of LA-ICP-MS minor elements results from chlorite

	Ca (ppm)	Mn (ppm)
All results		
n	26	26
Min	1,832	4,020
Max	17,000	4,955
Mean	4,194	4,473
258.7 m		
n	8	8
Min	1,832	4,020
Max	2,403	4,595
Mean	2,097	4,369
269 m		
n	18	18
Min	2,554	4,327
Max	17,000	4,955
Mean	5,126	4,520

n: number of analyses; Min: minimum; Max: maximum; Mean: mean value.

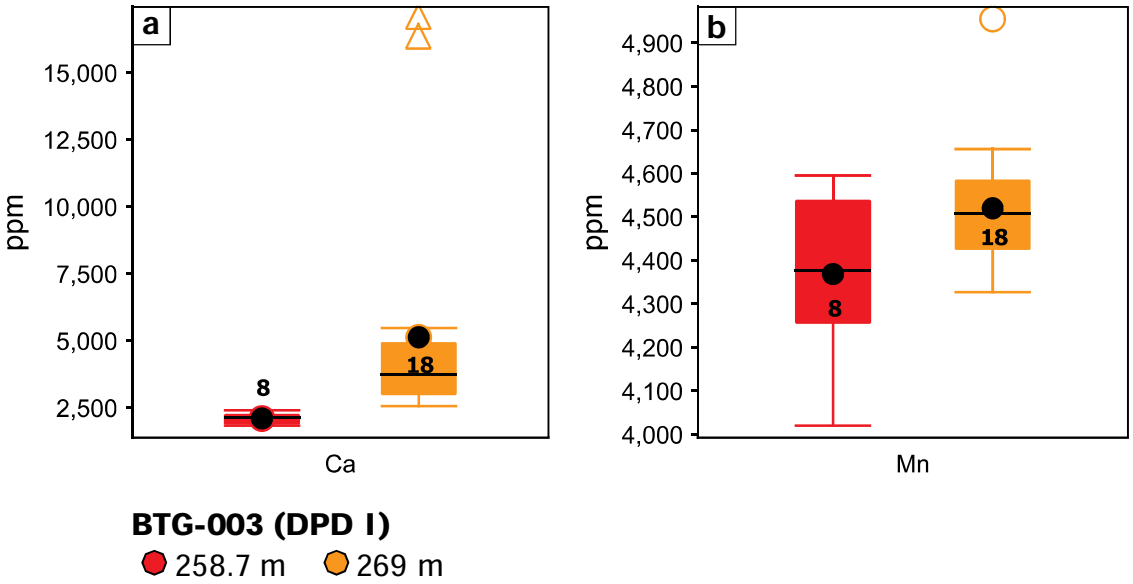

Figure 5.27. LA-ICP-MS minor elements results from chlorite. Box plots. **a.** Calcium (Ca). **b.** Manganese (Mn).

5.3.5.4. Trace elements

Trace elements analysed in chlorites are listed in Table 5.17. Figures 5.27 and 5.28 present a summary of the results. Complete results are presented in Appendix L.

Chlorites from 258.7 m depth are depleted in Cu, Pb, Ce, Y, La, As, U, and Sb compared with chlorites from 269 m depth (Table 5.17; Figs. 5.27 and 5.28). Chlorites from 258.7 m depth are significantly enriched in Cr and Ba, and chlorites from 269 m depth are significantly enriched in Sb (Table 5.17; Figs. 5.27 and 5.28).

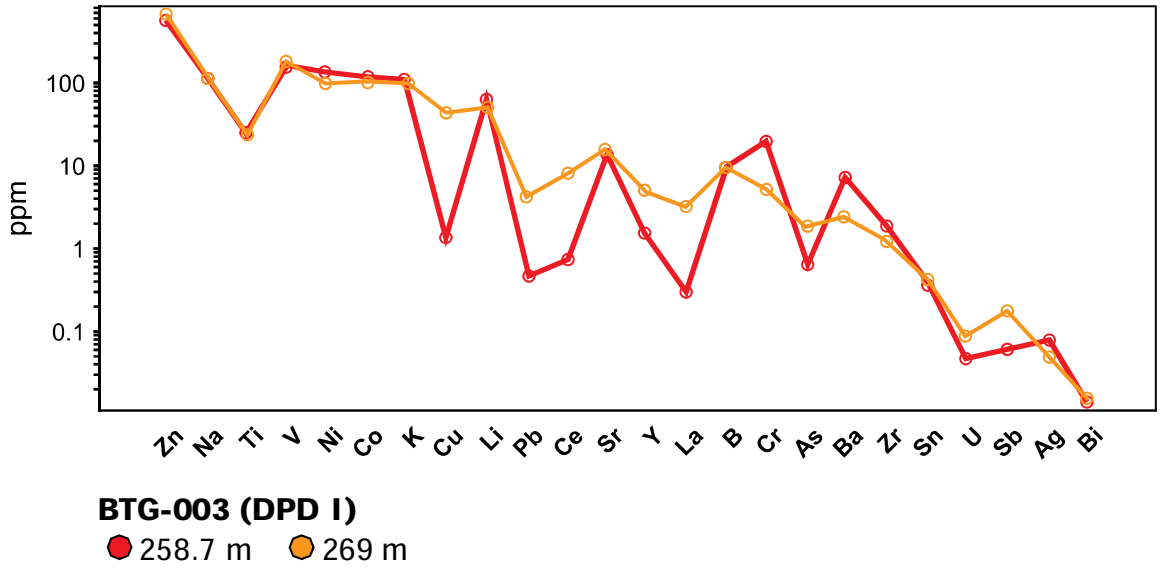

Figure 5.28. LA-ICP-MS trace elements results from chlorite. Line graph. Lines represent mean values.

Table 5.17. Summary of LA-ICP-MS trace elements results from chlorite

ppm	Zn	Na	Ti	V	Ni	Co	K	Cu	Li	Pb	Ce	Sr
All results												
n	26	26	26	26	26	26	26	23	26	26	26	26
Min	475.2	59.17	16.52	142.2	36.71	88.42	66.51	0.5309	42.81	0.2146	0.1137	7.949
Max	690.8	399.6	37.67	205.6	290.6	125.6	126.2	75.39	72.22	12.67	69.82	121.4
Mean	617.3	113.8	23.20	164.3	108.8	108.0	98.66	34.22	54.97	3.039	5.527	16.23
258.7 m												
n	8	8	8	8	8	8	8	5	8	8	8	8
Min	475.2	59.17	18.52	148.8	58.15	103.0	69.34	0.5309	59.15	0.2146	0.1137	11.58
Max	588.4	399.6	37.67	205.6	290.6	125.6	116.0	2.998	72.22	1.000	2.318	17.73
Mean	549.1	119.4	26.46	170.0	137.7	118.6	100.4	1.332	65.62	0.4798	0.6870	13.48
269 m												
n	18	18	18	18	18	18	18	18	18	18	18	18
Min	591.7	80.40	16.52	142.2	36.71	88.42	66.51	18.26	42.81	1.553	0.1337	7.949
Max	690.8	162.5	35.90	186.2	246.1	122.2	126.2	75.39	58.47	12.67	69.82	121.4
Mean	647.6	111.4	21.75	161.8	95.97	103.3	97.88	43.36	50.24	4.177	7.678	17.45

Table 5.17. Summary of LA-ICP-MS trace elements results from chlorite (continued)

ppm	Y	La	B	Cr	As	Ba	Zr	Sn	U	Sb	Ag	Bi
All results												
n	26	26	26	18	15	26	25	25	13	3	1	2
Min	0.9508	0.04404	5.634	1.246	0.5117	1.503	0.1438	0.1756	0.01265	0.1230	0.07800	0.01332
Max	32.00	26.85	33.15	33.33	5.803	8.914	13.06	1.047	0.4072	0.2210	0.07800	0.01623
Mean	3.844	2.193	9.581	8.502	1.53	3.962	1.481	0.4107	0.08303	0.1771	0.07800	0.01477
258.7 m												
n	8	8	8	4	3	8	8	8	2	0	1	1
Min	1.128	0.04568	6.837	14.88	0.5117	5.907	0.7779	0.2456	0.04120		0.07800	0.01332
Max	2.202	1.014	13.46	33.33	0.8270	8.914	3.771	0.5918	0.05229		0.07800	0.01332
Mean	1.529	0.2924	10.11	20.16	0.6508	7.198	1.940	0.3911	0.04674		0.07800	0.01332
269 m												
n	18	18	18	14	12	18	17	17	11	3	0	1
Min	0.9508	0.04404	5.634	1.246	0.5509	1.503	0.1438	0.1756	0.01265	0.1230		0.01623
Max	32.00	26.85	33.15	19.71	5.803	3.371	13.06	1.047	0.4072	0.2210		0.01623
Mean	4.873	3.038	9.347	5.170	1.750	2.524	1.265	0.4199	0.08963	0.1771		0.01623

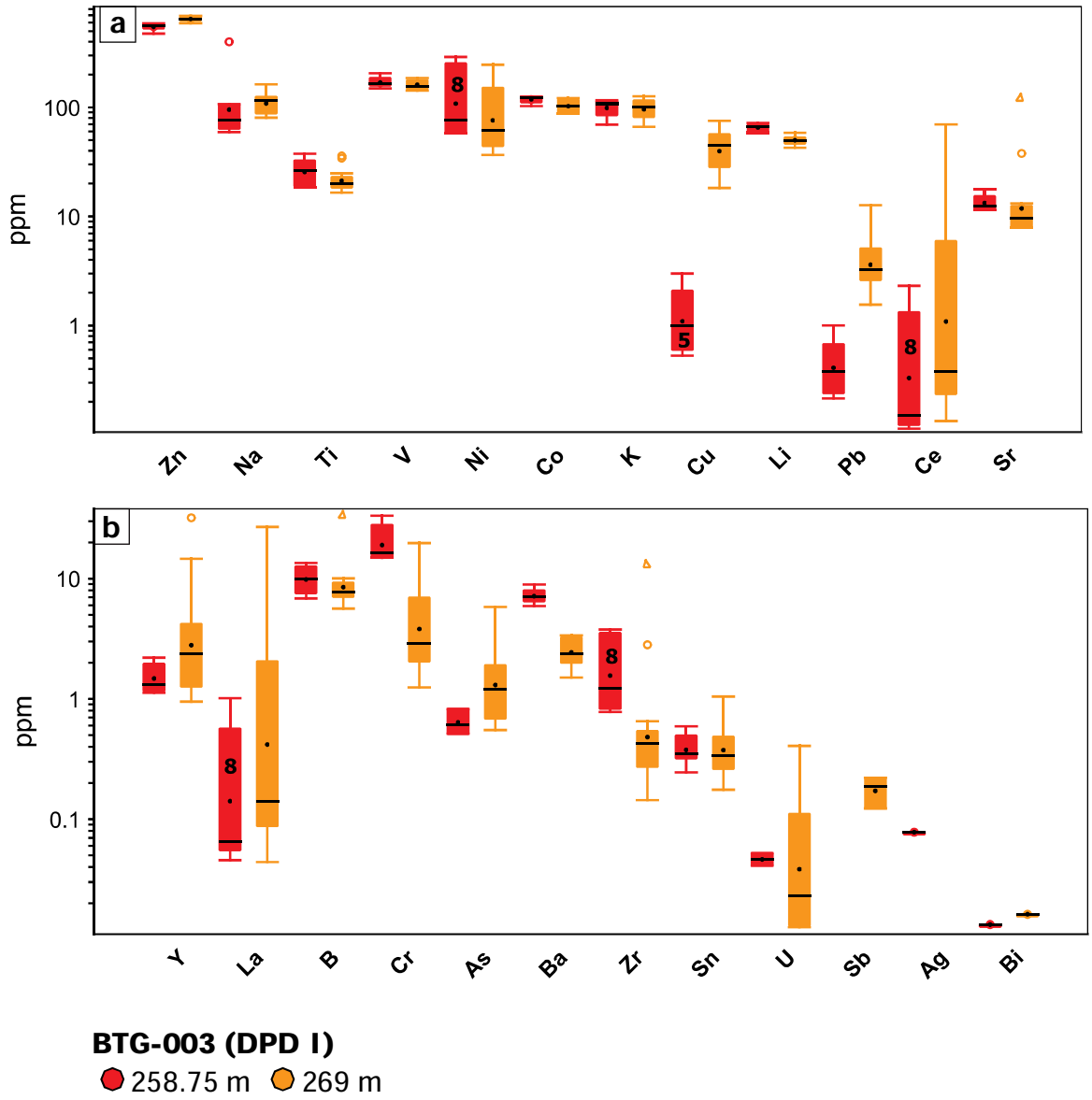

Figure 5.29. LA-ICP-MS trace elements results from chlorite. Box plots. **a.** Most abundant trace elements; includes: Zn, Na, Ti, V, Ni, Co, K, Cu, Li, Pb, Ce, and Sr. **b.** Least abundant trace elements; includes: Y, La, B, Cr, As, Ba, Zr, Sn, U, Sb, Ag, and Bi.

5.3.5.5. Discussion

5.3.5.5.1. Comparison with chlorites from the Batu-Hijau Cu–Au porphyry

The Batu Hijau Cu-Au porphyry deposit in Sumbawa Island, Indonesia, is one of the largest porphyry deposits in the world (Garwin, 2002; Sinclair, 2007; Singer et al., 2008; Wilkinson et al., 2015). Batu Hijau contains 1,644 Mt of ore at 0.35 g/t Au and 0.44 wt % Cu, for a total of 572 t Au and 7.23 Mt Cu (Garwin, 2002). Batu Hijau formed at ~3.7 Ma during collision between the Indian-Australian plate and the Timorese segment of the Banda arc, and its genesis is possibly linked to subduction of the Roo Rise (Garwin, 2002).

Wilkinson et al. (2015) presented results from 97 LA-ICPMS analyses from 15 hydrothermally-altered samples bearing chlorite from the Batu Hijau porphyry Cu-Au deposit. Samples were collected from 120 m to 4,762 m away from the orebody, defining a clear transect into the Batu Hijau orebody.

Wilkinson et al. (2015) found that K, Li, Ca, Sr, Ba, Co, Ni and Pb concentrations in chlorite increase with increasing distance from the centre of the orebody. Titanium, V, Zn and Mg decrease exponentially with increasing distance. Also, they were able to distinguish chemically metamorphic chlorite from hydrothermal-related chlorite. Wilkinson et al. (2015) proposed the chlorite proximitor (Equation 5.1) to predict the distance to a deposit centre; where x is the distance to the deposit centre, R is an element ratio, and a and b are exponential fit parameters.

$$x = \frac{\ln\left(R/a\right)}{b} \quad \textbf{(5.1)}$$

Figure 5.30 presents a comparison of hydrothermal chlorites from Batu Hijau (Wilkinson et al., 2014) and Bantug (This study), and metamorphic chlorites the Georgetown inlier (Baker et al., 2010). Table 5.18 present results from the chlorite proximitor for Bantug using the Ti/Sr ratio.

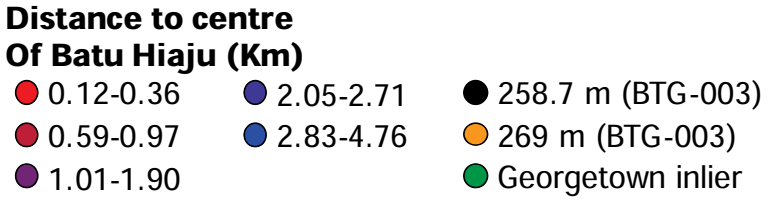

Figure 5.30. Comparison of chlorite LA-ICP-MS results from Batu Hijau, Bantug, and the Georgetown Inlier. Legend. Results from Batu Hijau are from Wilkinson et al. (2014), and results from the Georgetown Inlier are from Baker et al. (2010).

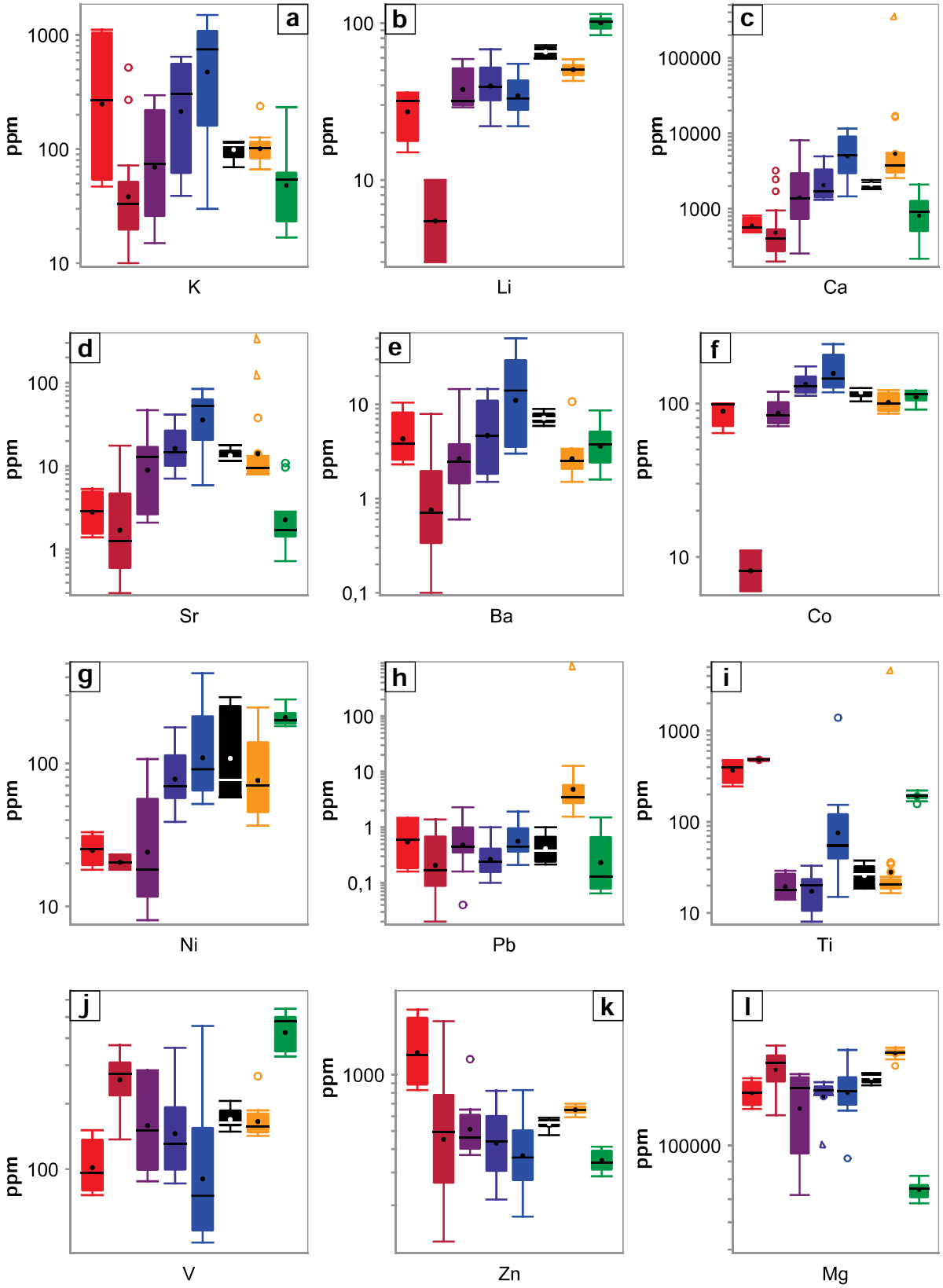

Figure 5.30. Comparison of chlorite LA-ICP-MS results from Batu Hijau, Bantug, and the Georgetown Inlier *(Continued).* Box and whisker diagrams. **a.** Potassium (K). **b.** Lithium (Li). **c.** Calcium (Ca). **d.** Strontium (Sr). **e.** Barium (Ba). **f.** Cobalt (Co). **g.** Nickel (Ni). **h.** Lead (Pb). **i.** Titanium (Ti). **j.** Vanadium (V). **k.** Zinc (Zn). **l.** Magnesium (Mg). Results from Batu Hijau are from Wilkinson et al. (2014), and results from the Georgetown Inlier are from Baker et al. (2010).

Table 5.18. Chlorite proximitor results for Bantug

	Ti/Sr	x (m)
258.7 m (n=8)		
Min	1.48	1,580.9
Max	2.72	1,649.9
Mean	1.97	1,620.5
269.0 m (n=19)		
Min	0.30	1,400.2
Max	13.36	1,833.2
Mean	2.63	1,616.6

R values for equation 5.1 are Ti/Sr ratios in Table 5.18, *a* is 3.0 x 10^6, and *b* is -0.0088.

From Figure 5.30 it can be concluded that chlorites from Bantug have a hydrothermal geochemical signature rather than a metamorphic one. Also, that the composition of chlorite from Bantug is similar to that of chlorites from samples located between 2.05 – 2.71 km away from the Batu Hijau orebody. Results from the chlorite proximitor using the Ti/Sr ratio indicate a potential heat source at 1.4 – 1.8 km in any direction.

5.3.6. Magnetite geochemistry

5.3.6.1. Sample description

Hydrothermal magnetite was analysed from DPD I and DPD II samples from drill hole BTG-003, and DPD III samples from drill hole BTG-006 (Fig. 5.2). Magnetite crystals are subhedral to anhedral, ~50 μm, and occur with pyroxene, epidote, and pyrite (Figs. 5.31). Ilmenite intergrowth and apatite inclusions are ubiquitous (Figs. 5.31d and 5.31e). McQueen and Cross (1998) and Nadoll et al. (2015) provided textural criteria for the discrimination of hydrothermal and igneous magnetite. These criteria include: (i) area of occurrence (vein vs. disseminated in host rock), (ii) habit (euhedral vs. massive), (iii) associated minerals (mafic minerals vs. secondary hydrothermal minerals), and (iv) the occurrence and type of exsolutions and mineral inclusions. Magnetite crystals from Batung share both igneous and hydrothermal characteristics mentioned by McQueen and Cross (1998) and Nadoll et al. (2015). However, given the intimate relation between magnetite crystals and hydrothermal minerals, magnetite crystals from Bantug are considered of hydrothermal origin.

Table 5.19 presents the filtering criteria in order to screen for ablation of inclusions. LA-ICP-MS spot analyses were placed in inclusion free areas within magnetite crystals, and particular attention was devoted to ilmenite intergrowth zones. Table 5.20 to 5.22, and Figures 5.32 to 5.35 present a summary of the results. Complete results are presented in Appendix L.

Table 5.19. Filtering criteria for magnetite

Filter	n
Ti>101,000	1
Si>100,000	2
Ca>55,000	1
Al>22,000	1
K>420	6
Ni>115	1
Cu>20	2

n: number of analyses

5.3.6.2. Major elements

Major elements analysed in magnetite include Fe, Ti, Si, and Ca. Table 5.20 and Figure 5.32 present a summary of the results. Complete results are presented in Appendix L. Magnetite crystals from DPD II yielded the highest Fe results, and crystals from DPD III the lowest (Fig. 5.32a). DPD I and DPD III Ti results are very similar, and DPD II yielded the lowest results (Fig. 5.32b). Silicon and Ca results for all samples are alike (Figs. 5.32c and 5.32d); DPD I and DPD II yielded similar results, and DPD III yielded the highest results. Iron variations on magnetite crystals are likely to be due to ilmenite inclusions or variations in iron across samples (i.e. rock types).

Table 5.20. Summary of LA-ICP-MS major element results from magnetite

	Fe (ppm)	Ti (ppm)	Si (ppm)	Ca (ppm)
All results				
N	47	47	47	42
Min	448,000	8,223	1,094	535.9
Max	715,600	100,600	70,830	54,960
Mean	632,600	45,650	11,890	11,790
BTG-003				
n (DPD I)	30	30	30	28
Min	600,000	17,770	1,094	1,424
Max	648,500	100,600	34,420	54,960
Mean	622,300	54,340	8,067	11,490
n (DPD II)	13	13	13	10
Min	710,000	8,223	1,111	535.9
Max	715,600	65,680	20,290	21,070
Mean	713,000	21,380	6,478	4,521
BTG-006				
n (DPD III)	4	4	4	4
Min	448,000	33,020	39,630	21,480
Max	448,000	76,590	70,830	45,380
Mean	448,000	59,410	58,200	32,030

n: number of analyses; Min: minimum; Max: maximum; Mean: mean value. Abbreviations: DPD I: diorite porphyry dike I; DPD II: diorite porphyry dike II; DPD III: diorite porphyry dike III.

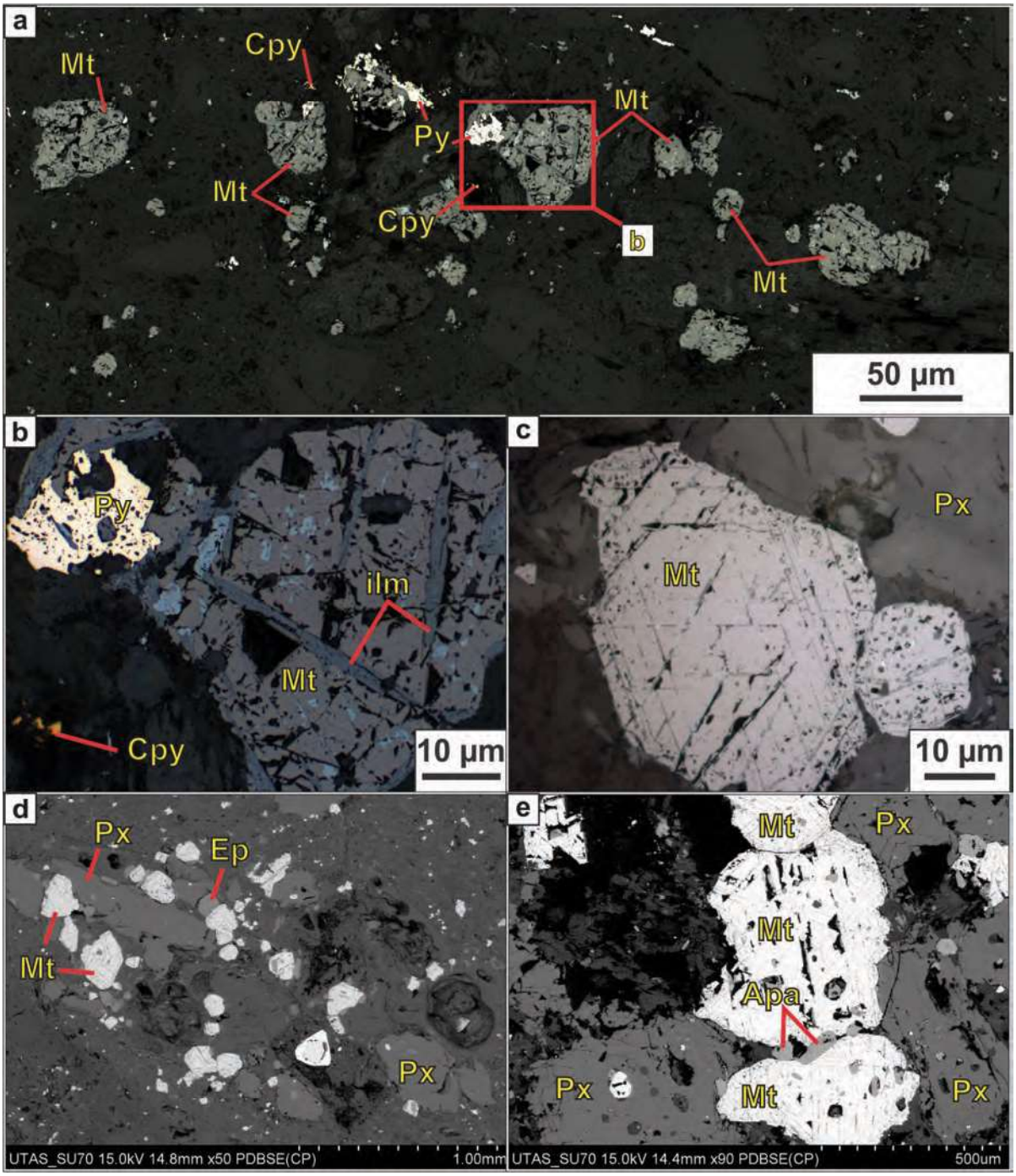

Figure 5.31. Magnetite-bearing samples. a. Reflected light photomicrograph, diorite porphyry dike II (370 m depth; BTG-003). **b.** Reflected light photomicrograph, diorite porphyry dike II (370 m depth; BTG-003). **c.** Reflected light photomicrograph, diorite porphyry dike I (263 m depth; BTG-003). **d.** FE-SEM BSE image, diorite porphyry dike II (370 m depth; BTG-003). **e.** FE-SEM BSE image, diorite porphyry dike II (370 m depth; BTG-003). Abbreviations: Apa: apatite; Cpy: chalcopyrite; Ep: epidote; ilm: ilmenite; Mt: magnetite; Px: pyroxene; Qz: quartz.

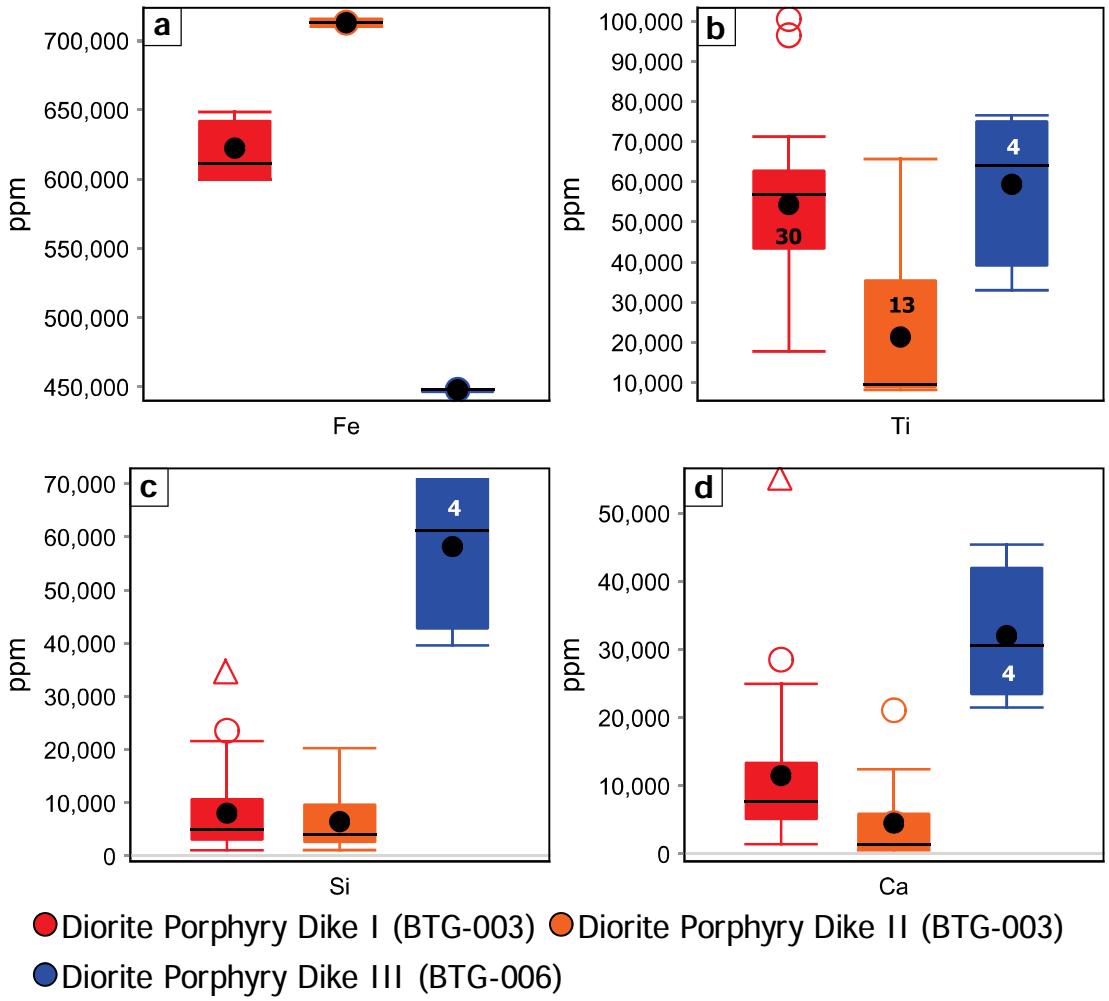

Figure 5.32. LA-ICP-MS major elements results from magnetite. Box plots. **a.** Iron (Fe). **b.** Titanium (Ti). **c.** Silicon (Si). **d.** Calcium (Ca).

5.3.6.3. Minor elements

Minor elements analysed in magnetite include Mn, Al, V, Mg, Zn, and Na (Table 5.21; Fig. 5.33). Magnetite from DPD I and DPD II samples yielded similar Al, V, Mg, and Na results (Fig. 5.33). Magnetite from DPD I and DPD III samples yielded similar Mn results; magnetite from DPD II samples yielded the lowest Mn results (Fig. 5.33a). Magnetite from DPD III samples yielded the highest Al, V, and Mg results (Fig. 5.33). Magnetite from DPD II samples yielded the highest Zn results (Fig. 5.33e)

Table 5.21. Summary of minor elements LA-ICP-MS results from magnetite

	Mn (ppm)	Al (ppm)	V (ppm)	Mg (ppm)	Zn (ppm)	Na (ppm)
All results						
n	47	47	47	47	47	8
Min	1,466	2,722	3,049	756.4	173.5	103.1
Max	28,770	20,970	5,275	18,210	6,409	2,628
Mean	7,774	7,231	4,103	2,581	1,536	1,179
BTG-003						
n (DPD I)	30	30	30	30	30	4
Min	1,466	2,722	3,049	756.4	173.5	103.1
Max	28,770	17,460	4,908	11,150	5,539	2,628
Mean	9,331	6,239	4,024	1,888	798.1	1,293
n (DPD II)	13	13	13	13	13	3
Min	2,703	3,128	3,849	805.1	1,116	465.9
Max	5,277	9,492	4,571	4,287	6,409	1,721
Mean	3,763	6,398	4,166	2,226	3,117	1,210
BTG-006						
n (DPD III)	4	4	4	4	4	1
Min	2,954	13,920	3,863	5,198	1,785	630.3
Max	14,890	20,970	5,275	18,210	2,149	630.3
Mean	9,125	17,380	4,496	8,936	1,934	630.3

n: number of analyses; Min: minimum; Max: maximum; Mean: mean value. Abbreviations: DPD I: diorite porphyry dike I; DPD II: diorite porphyry dike II; DPD III: diorite porphyry dike III.

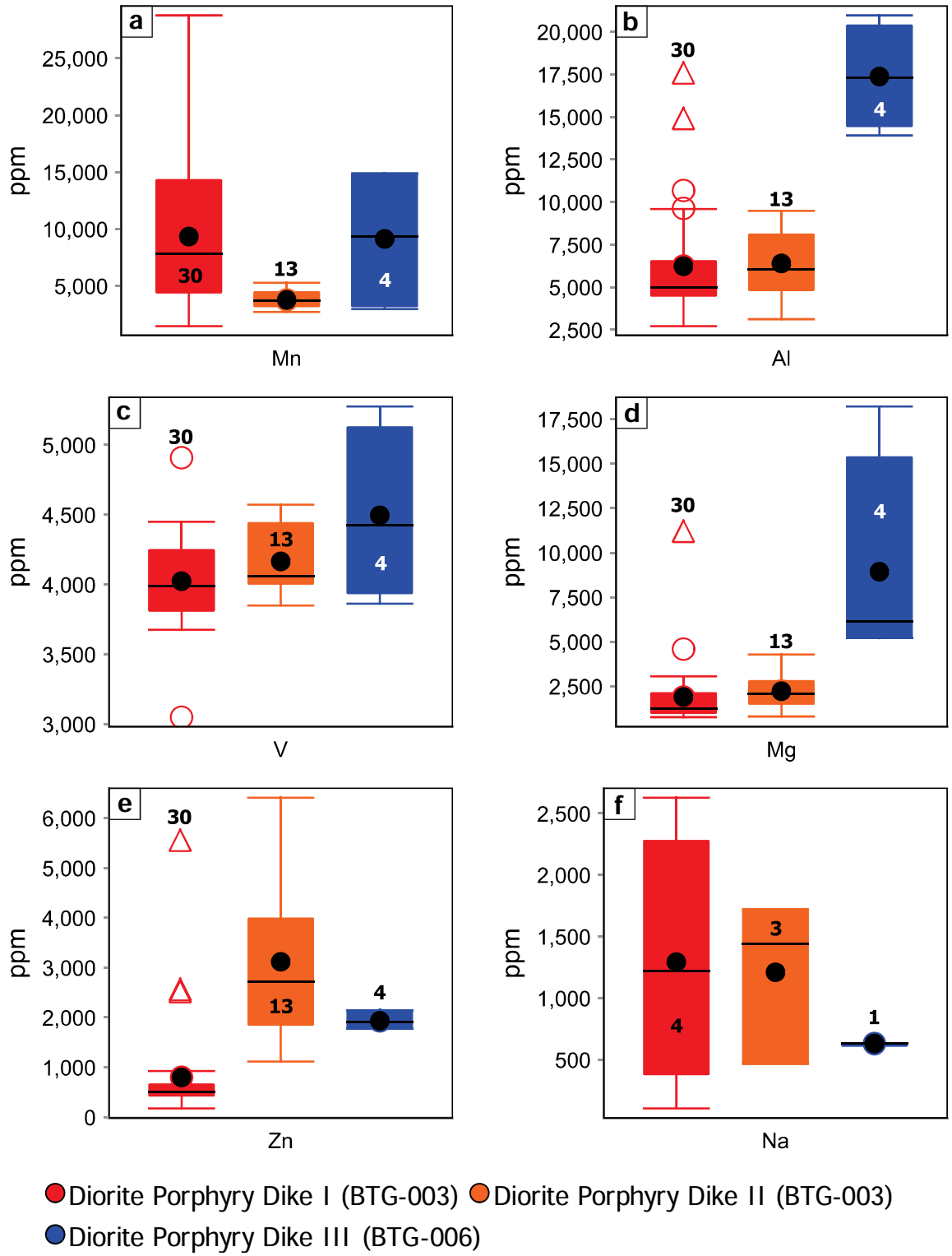

Figure 5.33. LA-ICP-MS minor elements results from magnetite. Box plots. **a.** Manganese (Mn). **b.** Aluminium (Al). **c.** Vanadium (V). **d.** Magnesium (Mg). **e.** Zinc (Zn). **f.** Sodium (Na).

5.3.6.4. Trace elements

Table 5.22 and Figures 5.33 and 5.34 present a summary of the LA-ICP-MS trace elements results from magnetite. Mean value results of magnetite from DPD I and DPD II samples are very similar compared with results from DPD III. Magnetite from DPD I and DPD II samples are enriched in Co, Ni, Ga, and Ce compared with magnetite from DPD III (Table 5.21; Figs. 5.33 and 5.34). Magnetite from DPD III samples are enriched in Sc, Pb, Y, Sn, and Cu compared with magnetite from DPD III samples (Table 5.22; Figs. 5.34 and 5.35).

Table 5.22. Summary of trace elements LA-ICP-MS results from magnetite

ppm	K	Cr	Co	Ni	Ga	Zr	Sc	Pb	Sr	Ce
All results										
N	34	47	47	47	47	46	47	47	47	47
Min	14.45	53.73	6.084	9.441	17.71	0.2493	6.390	0.3591	0.2360	0.1140
Max	419.1	160.9	138.6	106.5	54.97	98.54	109.8	187.1	143.9	192.7
Mean	100.5	96.67	75.18	64.57	43.62	37.23	23.78	22.28	19.23	18.84
BTG-003										
n (DPD I)	19	30	30	30	30	30	30	30	30	30
Min	14.45	53.73	29	51.28	32.65	8.877	9.463	0.3591	0.8560	1.296
Max	103.0	114.9	138.6	97.36	54.66	98.54	51.39	52.63	143.9	192.7
Mean	38.52	89.17	91.18	61.42	47.18	49.81	24.77	11.73	24.09	21.96
n (DPD II)	11	13	13	13	13	12	13	13	13	13
Min	49.02	89.25	45.41	55.92	29.48	0.2493	6.390	0.5988	0.2360	0.114
Max	393.5	160.9	84.10	106.5	54.97	39.16	34.55	187.1	17.00	62.02
Mean	153.0	108.7	59.26	88.24	42.75	9.094	12.44	35.23	5.354	16.65
BTG-006										
n (DPD III)	4	4	4	4	4	4	4	4	4	4
Min	188.2	99.03	6.084	9.441	17.71	22.68	32.19	46.75	15.28	1.838
Max	419.1	137.6	8.027	13.23	21.93	33.21	109.8	69.15	41.66	3.843
Mean	250.8	113.7	6.901	11.26	19.78	27.28	53.23	59.31	27.88	2.557

Table 5.22. Summary of trace elements LA-ICP-MS results from magnetite (Continued)

ppm	Y	As	Sn	Cu	Li	U	Sb	Bi
All results								
n	47	47	47	41	46	45	25	10
Min	0.06066	0.3558	1.514	0.8583	0.6958	0.03408	0.1139	0.01407
Max	83.83	21.15	20.86	13.81	4.622	7.786	2.672	0.07868
Mean	13.07	7.521	7.060	3.914	2.061	0.9865	0.6878	0.03175
BTG-003								
n (DPD I)	30	30	30	28	30	30	14	3
Min	1.016	0.5393	1.514	0.8583	0.9072	0.03408	0.1155	0.01918
Max	83.83	21.15	15.61	8.911	4.622	1.901	0.3851	0.02953
Mean	13.71	8.071	5.753	3.069	2.116	0.3835	0.2166	0.02507
n (DPD II)	13	13	13	9	13	11	7	7
Min	0.06066	0.3558	3.359	1.126	0.8862	0.1315	0.1139	0.01407
Max	34.22	19.84	14.91	9.284	3.152	7.786	2.672	0.07868
Mean	8.488	5.294	7.179	3.800	2.122	1.901	1.173	0.03462
BTG-006								
n (DPD III)	4	4	4	4	3	4	4	0
Min	17.56	9.603	14.43	6.768	0.6958	2.079	1.294	
Max	28.97	11.88	20.86	13.81	1.847	4.317	1.758	
Mean	23.21	10.64	16.47	10.09	1.253	2.993	1.489	

n: number of analyses; min: minimum; max: maximum; mean: mean value. Abbreviations: DPD I: diorite porphyry dike I; DPD II: diorite porphyry dike II; DPD III: diorite porphyry dike III.

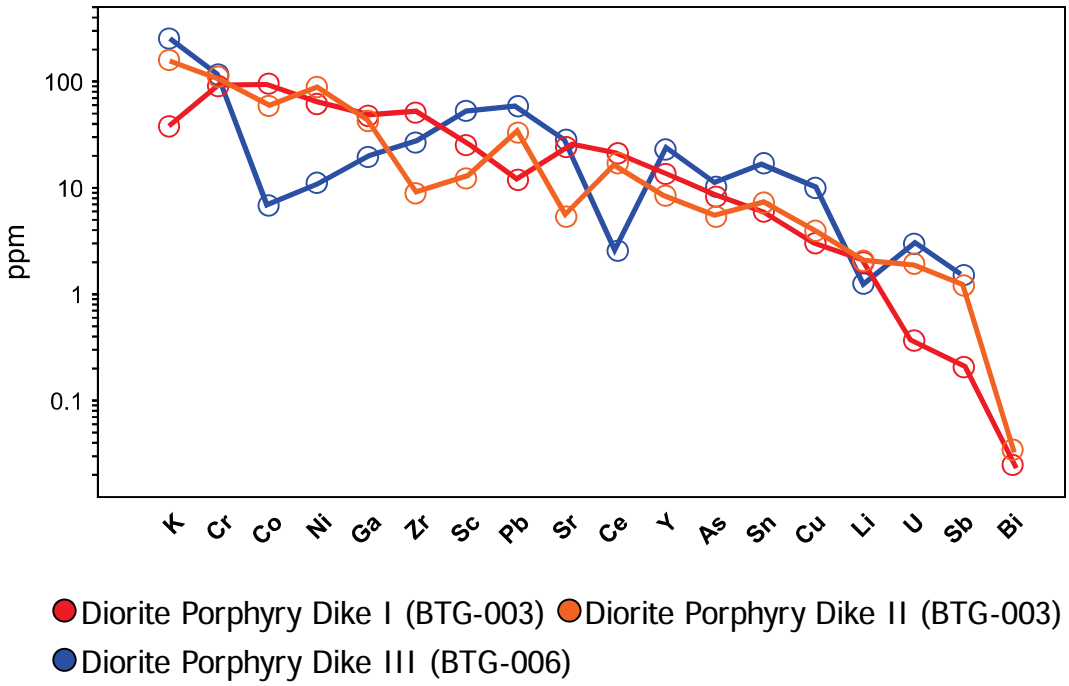

Figure 5.34. LA-ICP-MS trace elements results from magnetite. Line graph. Lines represent mean values.

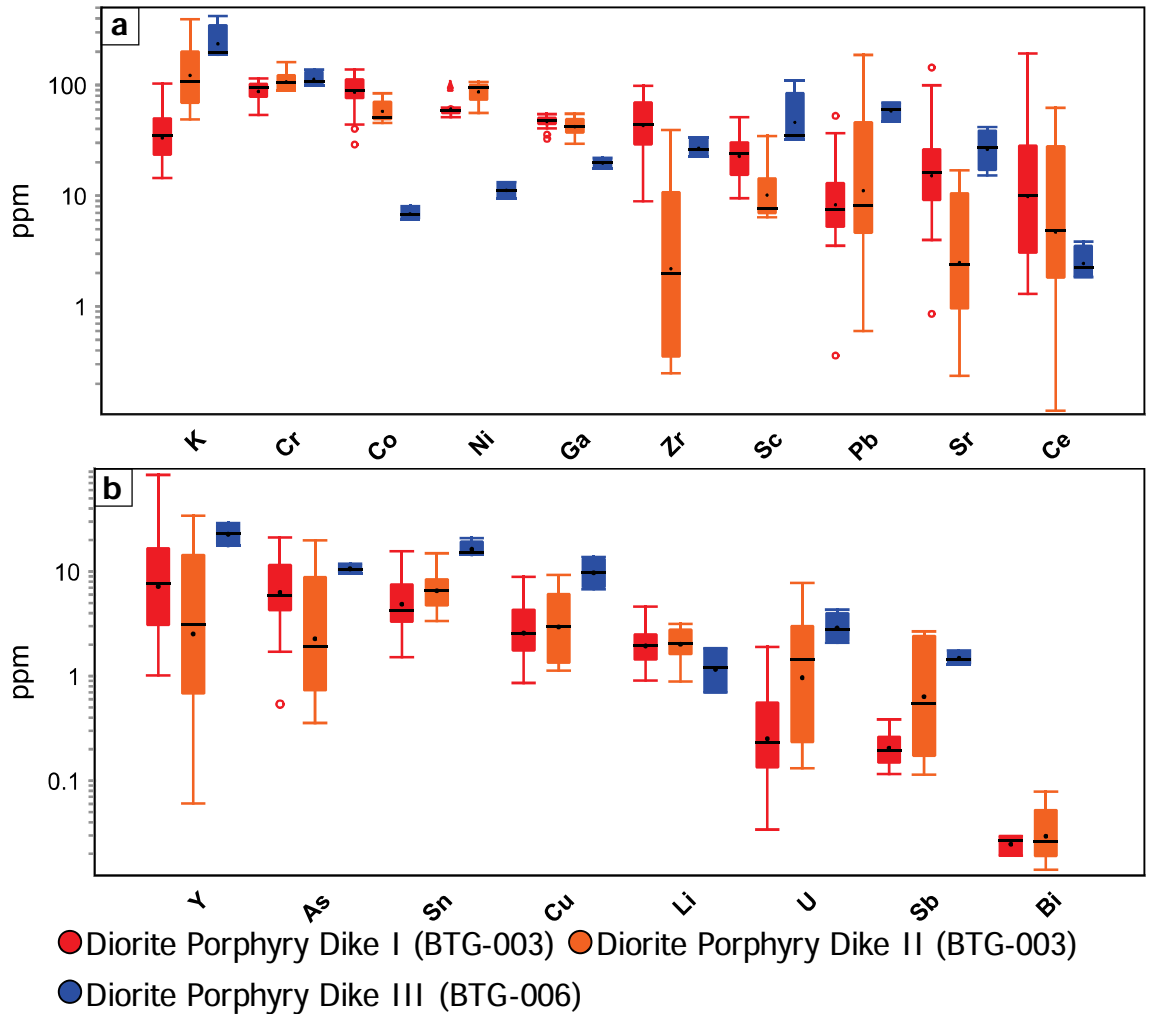

Figure 5.35. LA-ICP-MS trace elements results from magnetite. Box plots. **a.** Most abundant trace elements; includes: K, Cr, Co, Ni, Ga, Zr, Sc, Pb, Sr, Ce. **b.** Least abundant trace elements; includes: Y, As, Sn, Cu, Li, U, Sb, and Bi.

5.3.6.5. Discussion

5.3.6.5.1. Comparison with magnetite from the Batu-Hijau Cu–Au porphyry

Magnetite crystals from Batu Hijau were analysed in the AMIRA project P1060 (Cooke et al., 2014). The magnetite dataset from the Batu Hijau porphyry Au-Cu deposit includes 895 results, from which 281 were collected from igneous rocks. Figure 5.36 compares magnetite LA-ICP-MS results from igneous rocks at Bantug (n=47) with results from igneous rocks at Batu Hijau (n=281). Figure 5.36 presents some of the elements which define clear vectors to the mineralised centre at Batu Hijau. Chromium presented the most encouraging comparison results (Fig. 5.36b); samples from Bantug yielded similar results to those from Batu Hijau located between 0.5 and 1 km distance from the orebody. Comparison of As, Li, V, and Zr results suggests that samples from Bantug may be located at 2 or more kilometres from a mineralised centre (Fig. 5.36).

Magnesium, Pb, and Sr results from Bantug are significantly higher than those from Batu Hijau (Figs. 5.36d to 5.36f). These results are not comparable to those proximal nor distal to the mineralised centre at Batu Hijau. Given the distal signal interpreted from other elements (i.e., As, Li, V, and Zr), the author interprets Mg, Pb, and Sr to indicate a distal signature to a potential mineralised heat source.

5.3.7. Conclusions

The following points summarise the key findings related to mineral chemistry results from the lithocap at Bantug.

- Alunite chemistry indicates a potential tool for vectoring at Bantug. Sodium, La, Sr, Pb, Sr/Pb, 100 La/Pb, Pb/La, and Pb/Sr results from Bantug are comparable to those at Mankayan most proximal to the FSE deposit. Geochemical anomalism of surface alunite-bearing samples indicates the presence of the intrusions intercepted by drill holes BTG-003 and BTG-006
- Nickel results from pyrites in intrusive rocks from Bantug are comparable to those of pyrite-bearing intrusive rocks at 1 to 1.5 km from the Batu Hijau orebody. Nickel and Co results from pyrite-bearing advanced argillic-altered rocks from Bantug are analogous to those from Mankayan located at 1.5 to 2.5 km from the FSE orebody

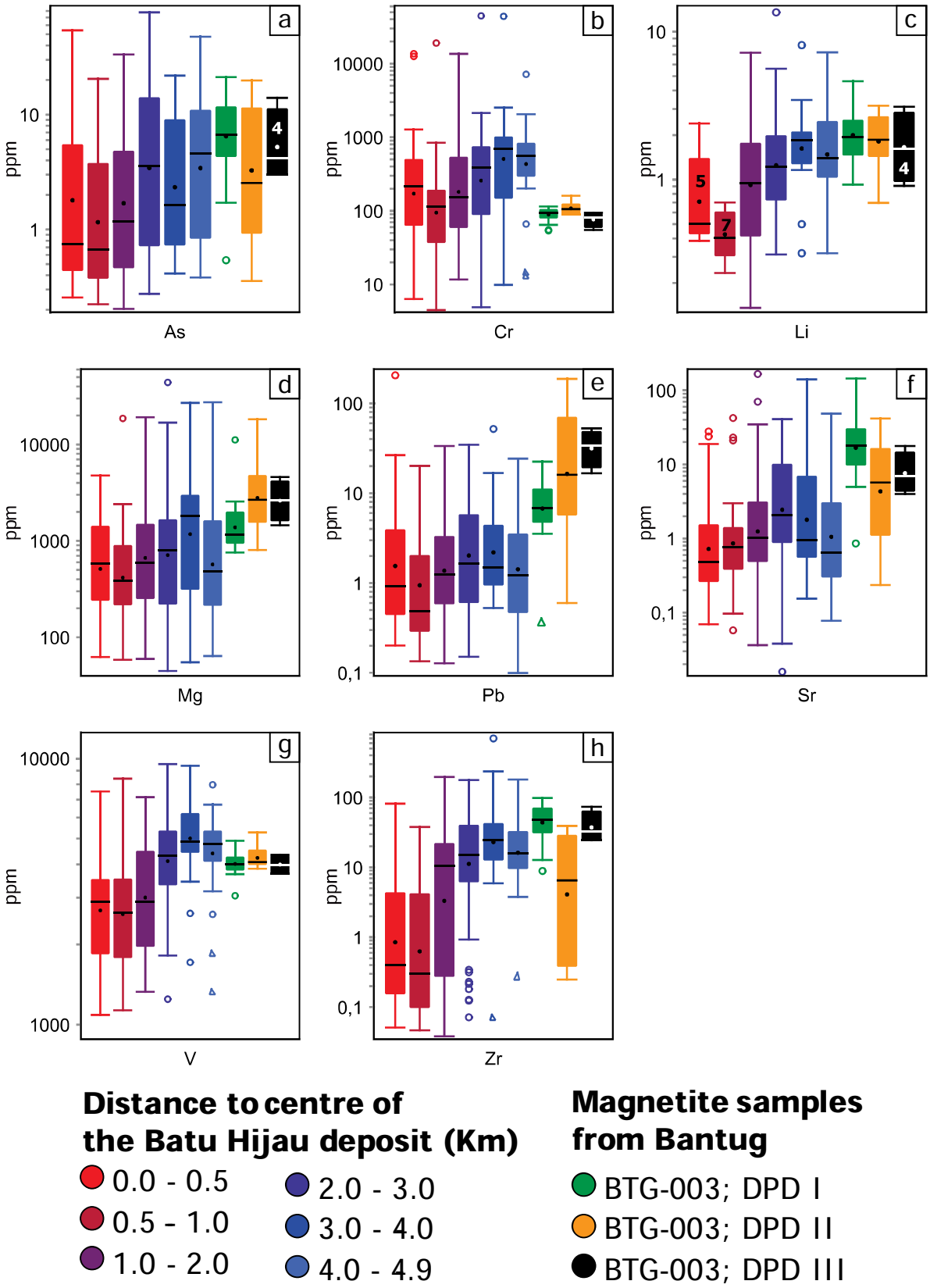

Figure 5.36. Comparison of magnetite LA-ICP-MS results from Batu Hijau and Bantug. Box plot diagrams. **a.** Arsenic (As). **b.** Chromium (Cr). **c.** Lithium (Li). **d.** Magnesium (Mg). **e.** Lead (Pb). **f.** Strontium (Sr). **g.** Vanadium (V). **h.** Zirconium (Zr).

- Comparison of pathfinder elements (i.e., Mo, Sn, As, Sb, and Pb) in epidote from Bantug with epidote from the Baguio district revealed that samples from Bantug may be located at or beyond 1 km distance from a potential heat source
- Chlorites from intrusive rocks at Bantug exhibit a hydrothermal signature rather than metamorphic. Pathfinder element results from Bantug compared with Batu Hijau suggest the presence of a heat source at 2.05 to 2.71 km. Results from the chlorite proximitor using the Ti/Sr ratio suggest a distance of 1.4 to 1.8 km to a potential heat source
- Magnetite analyses from Bantug yielded results comparable to those from Batu Hijau located at 2 or more kilometres away from the orebody.

Mineral chemistry results acquired during this study suggest a potential heat source beyond 1.5 km from the samples. Given the constrained spatial distribution of the samples, it is not possible to determine the direction in which the potential heat source may be located. Given the preservation of the lithocap at Bantug, the author suggest that the potential heat source may located at or beyond 1.5 km depth.

CHAPTER 6:
PATCHY-WORMY TEXTURES AT BANTUG

6.1. Introduction

This chapter addresses the rock textures that have been found near the base of several lithocaps around the world and that are present in the lithocap at Bantug. These are known as wormy-patchy or gusano textures (Tosdal, 1996; Vidal et al., 1997; Pinto, 2002; Gustafson et al., 2004; Teal and Benavides, 2010).

Detailed descriptions and characterisation of the wormy-patchy textures at Bantug are provided based on field and petrographic observations, coupled with SWIR spectroscopy, microanalyses (i.e., FE-SEM and EPMA), and XRD analyses. These data are combined with a review of other occurrences of similar textures to produce a model for the formation of wormy-patchy textures.

6.2. Previous work

Patchy-wormy textured rocks have been identified in lithocaps from several locations around the world (Table 6.1; Fig. 6.1). Some of those lithocaps host high-sulfidation epithermal deposits, and show evidence of transition to deep-seated porphyry style-mineralisation (e.g., Kupfertal, Peru; Pinto, 2002; Gustafson et al., 2004).

Patchy textures are characterized by amoeboid-like patches of clays, sulphate, and sulfide minerals in a fine-grained quartz groundmass (Pinto, 2002; Gustafson et al., 2004; Teal and Benavides; 2010; Noble et al., 2011; This study). The patches are the key defining characteristic of patchy texture (Figs. 6.2 and 6.3). Contorted dark-grey quartz veins have been observed to cross-cut clay-sulphate patches at La Zanja, Peru, (Pinto, 2002; Gustafson et al., 2004; Teal and Benavides; 2010; Noble et al., 2011; Fig. 6.3a and 6.3c). The contorted appearance of these dark-grey quartz veins bears a strong resemblance to worms, and their presence defines the wormy texture (Fig. 6.3a and 6.3c). Patchy-wormy textures are also known as gusano textures (e.g., Gustafson et al., 2004).

Gusano is the Spanish word for worm. The term ‘gusano’ was used during the first studies of the textures in Peru by Dilles (1996) at Tantahuatay and Vidal et al. (1997) at Arco Punco. Pinto (2002) followed this work at Kupfertal, Yanacocha district, Peru, where she documented the transition from wormy-patchy textures in advanced-argillic altered to rocks to porphyry style mineralisation (i.e., quartz-stockwork) in potassic altered rocks (Fig. 6.4). Aquino (1993) described advanced argillic altered rocks at Dizon, Philippines, with striking similarities to patchy-textured rocks elsewhere.

Gustafson et al. (2004) highlighted the importance of distinguishing between 'gusano' and patchy textures in the Yanacocha district. They defined gusano textures as soft, white, rounded blobs or patches of alunite ± pyrophyllite ± diaspore in a moderately hard matrix of granular quartz with interstitial pyrophyllite ± diaspore ± alunite (e.g., Fig. 6.2d and 6.2e). They defined patchy texture as irregular, sub-angular to angular, hard granular quartz within a generally interconnected matrix of pyrophyllite ± diaspore ± alunite. Gustafson et al. (2004) considered both textures to be the product of textural destruction of the precursor rock.

Garcia (2009) reported the presence of patchy textures at the Milagros prospect in the Alto Chicama district, northern Peru. The geology of the district consists of Mesozoic sandstone, siltstone, shale, and coal horizons. These are unconformably overlain by Eocene to Lower Miocene andesitic to dacitic volcanic rocks. Hydrothermal alteration has overprinted the volcanic rocks at Milagros, and hydrothermal breccias have intruded the sedimentary and volcanic sequences (Garcia, 2009). $^{40}Ar/^{39}Ar$ dating of alunite samples from Milagros by Garcia (2009) yielded Lower Miocene ages (15.82 ± 0.11 Ma to 15.67 ± 0.14 Ma). The Milagros prospect is located 3 km southeast of the Lagunas Norte high sulfidation Au-Cu deposit, and 500 m east from the Lagunas Sur gold prospect. Hydrothermal alteration at Milagros extends over an area of 800 by 600 m (Garcia, 2009). Intense, pervasive advanced argillic alteration has overprinted volcanic rocks at Milagros and has developed patchy textures (Garcia, 2009). Advanced argillic-altered patchy-textured rocks at Milagros are characterised by quartz, kaolinite, dickite, pyrophyllite, and diaspore (Garcia, 2009). Petrography and microanalyses of patchy-textured rocks from Milagros revealed abundant pyrophyllite at the core of patchy features and at the contact with the quartz groundmass (Garcia, 2009). Patchy textures at Milagros are considered to be the result of retrograde alteration from white mica to pyrophyllite, to kaolinite, to alunite as part of an upward-cooling system (Garcia, 2009).

Noble et al. (2011) described advanced-argillic altered rocks from Yanacocha, Tantahuatay, and La Zanja. The authors used the terms ovoidal and mottled to refer to wormy and patchy textural features respectively. Noble et al. (2011) defined the ovoidal features as spherical, ovoid to irregular masses of hydrous aluminium-silicate and/or aluminium-sulphate minerals, containing variable amounts of quartz, pyrite, enargite, and native sulphur within a matrix of very fine-grained silica, either chalcedony or quartz. Noble et al. (2011) considered both textures to be the product of liquid immiscibility of melted material at the upper levels of a magmatic chamber.

Table 6.1. Global occurrences of wormy-patchy textures

Deposit	Lat.	Long.	Reference
Bantug, Philippines	123.14°	10.02°	This study
Caspiche, Chile	69.02°	27.10°	Sillitoe et al. (2013)
Milagros, Peru	7.58°	78.14°	Garcia (2009)
Escondida, Chile	69.05°	24.25°	Padilla-Garza (2001)
Kupfertal, Peru	6.96°	78.50°	Pinto (2002); Gustafson et al. (2004)
La Zanja, Peru	6.96°	78.50°	Gustafson et al. (2004)
Oyu Tolgoi, Mongolia	107.89°	42.80°	Khashgerel et al. (2008); Khashgerel et al. (2009)
Tampakan, Philippines	125.04°	6.45°	Rohrlach (2002)
Yanacocha, Peru	6.96°	78.50°	Gustafson et al. (2004); Teal and Benavides (2010)

Lat.: latitude; Long.: longitude

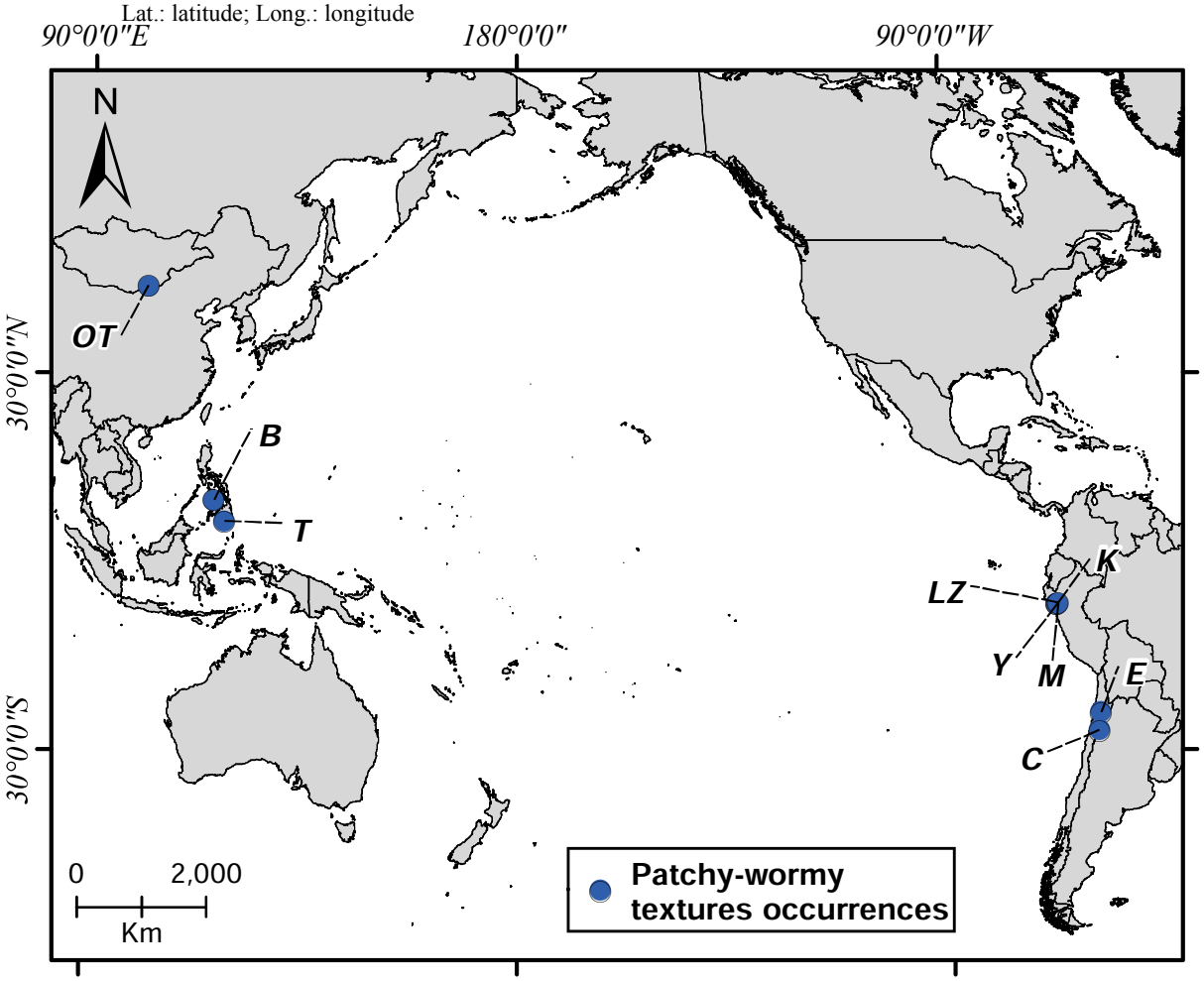

Figure 6.1. Patchy-wormy texture global occurrences. See Table 6.1 for details. Abbreviations: B: Bantug; C: Caspiche; E: Escondida; K: Kupfertal; LZ: La Zanja; M: Milagros; OT: Oyu Tolgoi; T: Tampakan; Y: Yanacocha.

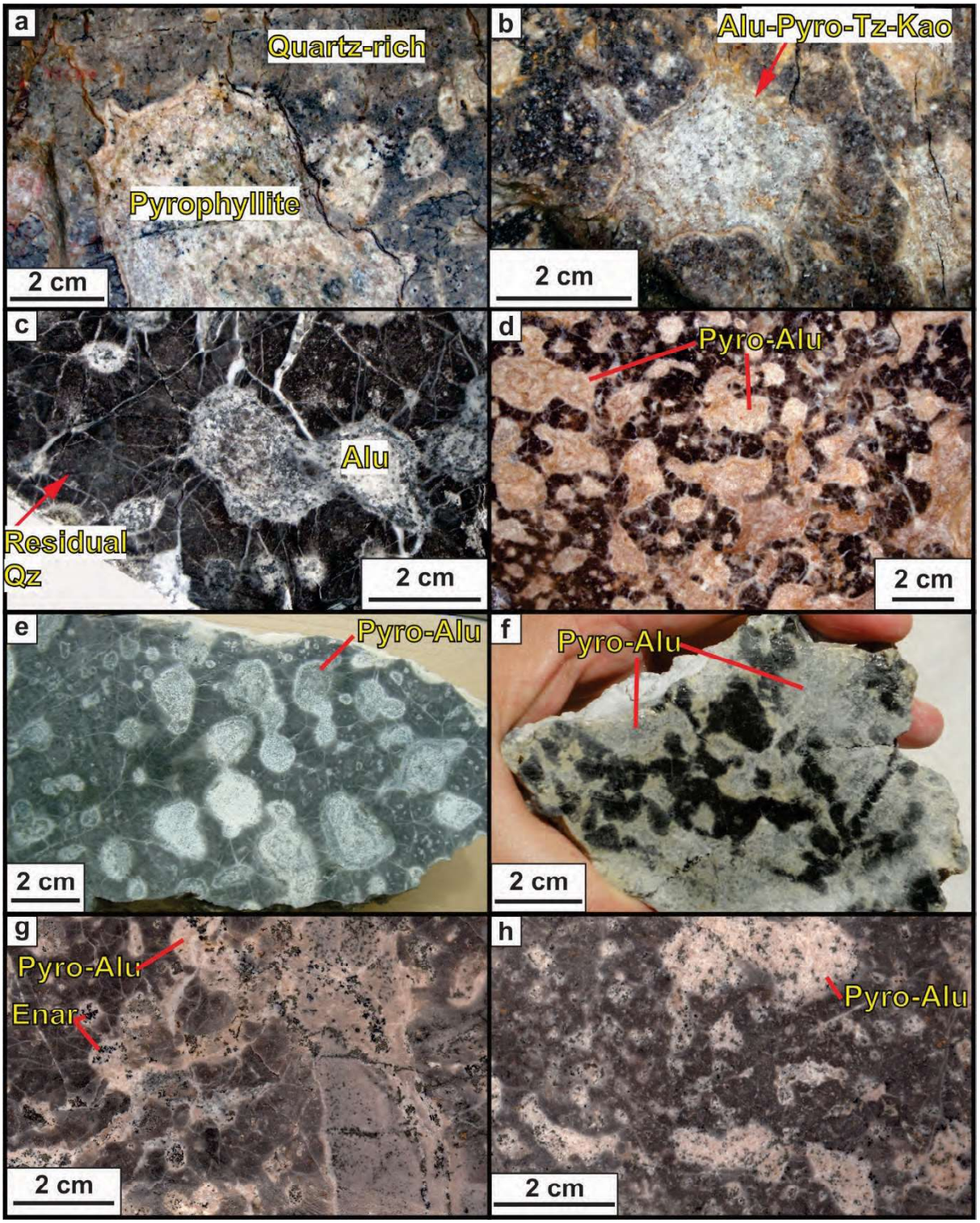

Figure 6.2. Wormy-patchy textures in hand specimens. a to **d.** Patches (red triangles) of <4 cm diameter, made of pyrophyllite, alunite, topaz, and kaolinite in a quartz-rich groundmass. Bornite is disseminated in the patches and in the quartz-groundmass in panel a. Samples from Oyu Tolgoi, Mongolia. Images courtesy of Imants Kavalieris. **e.** Pyrophyllite patches of ~4 cm in a quartz-rich groundmass; sample from Kupfertal in the Yanacocha district, Peru. Image courtesy of Eugenio Espada. **f.** Patchy-wormy textured rock from Kupfertal, Yanacocha district, Peru. Image courtesy of Eugenio Espada. **g** to **h.** Patches of ~2 cm diameter, made of alunite, pyrophyllite, and diaspore in a quartz-rich groundmass. Bornite and pyrite are disseminated in the patches. Samples from La Zanja, Yanacocha district, Peru. Samples provided by Bruce Gemmell. Abbreviations: Alu: alunite; Enar: enargite; Kao: kaolinite; Pyro: pyrophyllite; Qz: quartz; Tz: topaz.

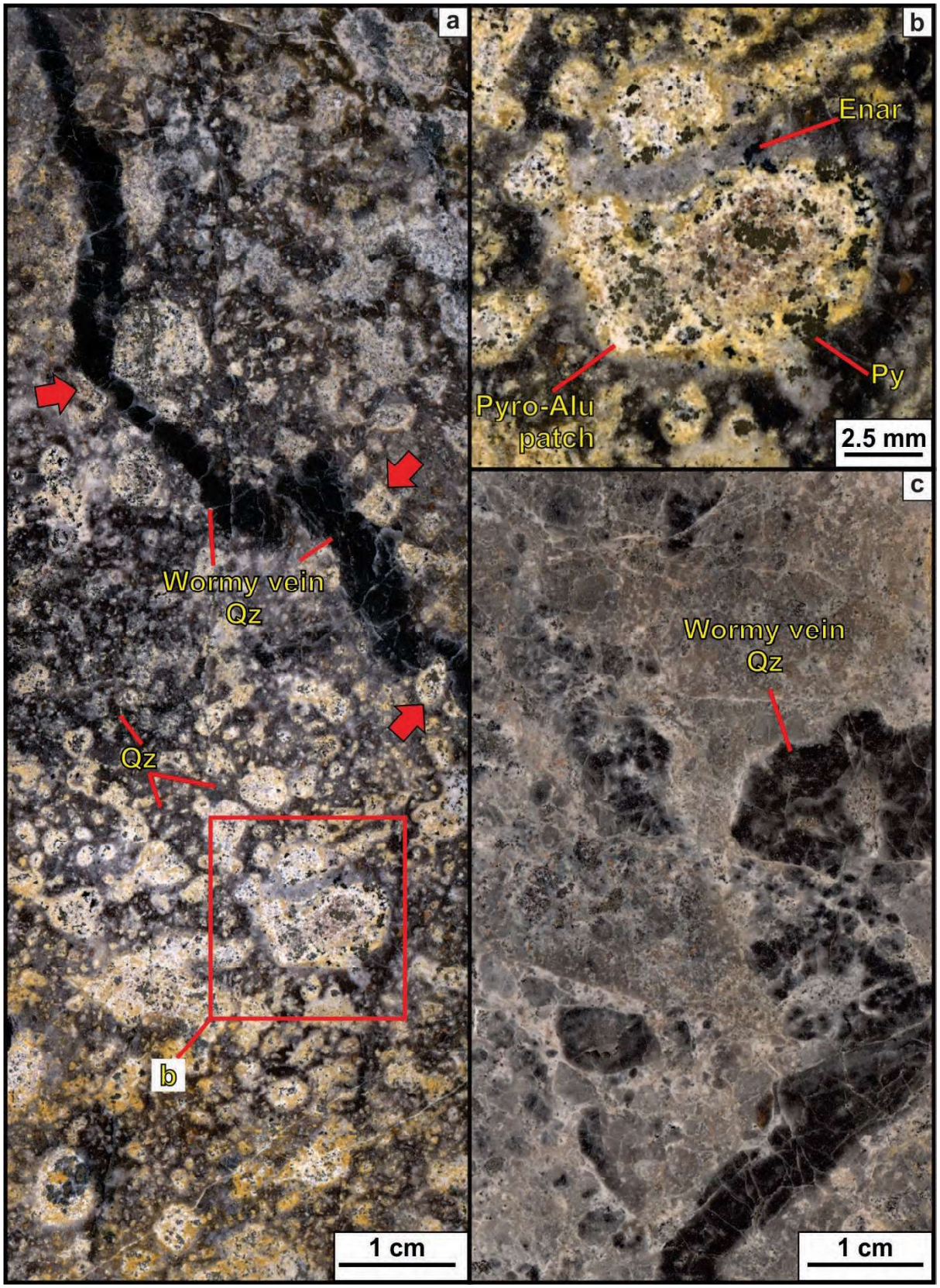

Figure 6.3. Wormy-patchy textures in hand specimens from La Zanja, Peru. a. Pyrophyllite-alunite-pyrite-enargite patches in quartz-altered groundmass; a wormy quartz vein is located across the sample. Patches developed into the wormy quartz vein (red arrows). **b.** Detail from panel i. Pyrophyllite-alunite-pyrite-enargite patch. **c.** Wormy vein. Samples provided by Bruce Gemmell. Abbreviations: Alu: alunite; Py: pyrite; Pyro: pyrophyllite; Qz: quartz.

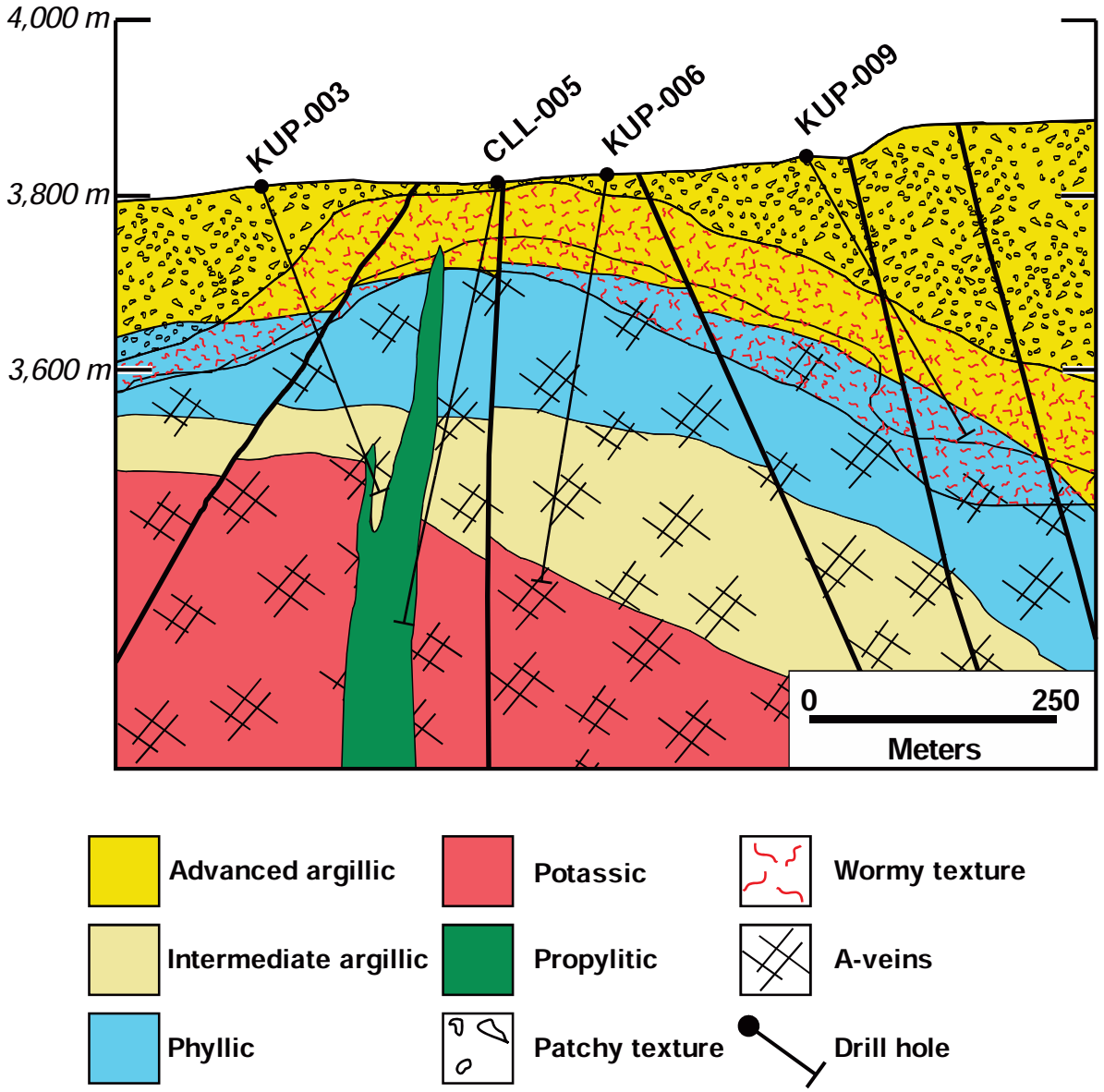

Figure 6.4. Wormy-patchy texture transition to A-veins at Kupfertal, Yanacocha district, Peru. Modified from Pinto (2002) and Gustafson et al. (2004).

6.3. Methods

6.3.1. Core logging

Patchy-wormy texture occurrences were documented systematically during lithologic and hydrothermal alteration logging at Bantug. The density (i.e., vol %) and size (i.e., cm) of patches was logged from drill holes BTG-003, BTG-005, and BTG-006. Details of core logging are presented in Appendix D.

6.3.2. Shortwave Infrared Spectroscopy (SWIR)

A Terraspec® instrument belonging to Freeport-McMoRan was used in the field at Tayasan, Negros, Philippines for determining the mineral compositions of patchy features. TSG software® at CODES-University of Tasmania was used to interpret the data collected in the field.

6.3.3. Petrography

Five polished thin sections and twenty-two polished laser mounts from patchy-wormy textured rocks at Bantug were prepared at the lapidary facilities of CODES, University of Tasmania. Thin sections were studied with a Leica DM 4000 M automated microscope. Sets of three mosaic images (i.e., transmitted light with crossed polarisers, transmitted light with parallel polarisers, and reflected light with parallel polarisers) using a 5x magnification lens were prepared from each thin section. Mosaic images from the thin sections are provided in Appendix E. Photomicrographs were acquired with the same microscope using 10x and 20x magnification lenses.

6.3.4. Field Emission - Scanning Electron Microscopy

Thin sections and polished laser mounts from patchy-wormy textured rocks at Bantug were analysed with a Hitachi SU-70 field emission scanning electron microscope (FE-SEM) at the Central Science Laboratory of the University of Tasmania. Secondary electrons (SE) and back-scattered electron images (BSE) were acquired at a distance of 14.9 to 15 mm from the sample, using 15.0 kV voltage during the analyses. Energy dispersive X-ray spectroscopy (EDS) was used to detect the most abundant elements in selected minerals from thin sections and laser sample mounts. The AZtec Software® was used to process the EDS point analyses. The MinIdent-Win 4.0 Software® was used to identify the most probable mineral occurrence in thin sections and mounts according to the EDS results. A total of 1,920 FE-SEM EDS results from thin sections and laser mounts from patchy-textured rocks from Bantug are presented in Appendix F.

6.3.5. Cathodoluminescence-SEM

Thin sections and polished laser mounts from patchy-wormy textured rocks at Bantug were analysed with a Gatan PanaCLF panchromatic cathodoluminescence (CL) detector with RGB filters attached to a FEI MLA 650 E-SEM. Detectors were located at 10 to 12.2 mm distance from the sample, and a voltage of 15.0 kV was used during analyses. Contrast and balance were modified from images using ImageJ® and GIMPS® software. A total of 162 CL images and 10

mosaic images were prepared using the MosaicJ script for ImageJ. All images are presented in Appendix M.

6.3.6. Electron Probe Micro Analyser

Polished laser mounts from patchy-wormy textured rocks at Bantug were analysed with a Cameca SX100 (TCP/IP Socket) electron probe micro analyser (EPMA) equipped with a Cameca CL detector. Trace elements analysed in quartz are Al, Fe, and Ti. The Cameca SX100 EPMA was used at 40° take-off angle, beam energy of 15 keV, beam current of 200 nA, beam diameter of 5 µm. Elements were acquired using analysing crystals LLIF for Fe ka, LPET for Ti ka, and TAP for Al ka. The standards were corundum synthetic NMNH 135602 (I14) for Al ka, hematite (Astimex block) for Fe ka, and rutile (Astimex block) for Ti ka. The counting and off peak time were both 300 seconds for Fe ka, Ti ka, and Al ka. The off peak correction method was linear for all elements. Unknown and standard intensities were corrected for deadtime. Results are the average of 4 points and detection limits ranged from 0.000 weight percent for Al ka and for Ti ka, to 0.002 weight percent for Fe ka. A quantitative blank correction was utilized. The aggregate intensity option was selected. The matrix correction method was ZAF or Phi-Rho-Z Calculations, and the mass absorption coefficients dataset was LINEMU (Armstrong, 1988; Donovan et al.; 2011). The ZAF or Phi-Rho-Z algorithm utilized was Armstrong/Love Scott (Armstrong, 1988; Donovan et al.; 2011). A total of 21 EPMA trace element results are presented in Appendix N.

6.3.7. X-ray Diffraction

A total of nine patchy-textured samples were analysed with X-ray diffraction (XRD) at CODES, University of Tasmania. The instrument used was a Bruker D2 Phaser at an operating voltage of 30 kV and 10mA current using a cobalt X-ray tube to generate Co Kα radiation with wavelength of 1.78897 Å. A 0.6 mm (0.3°) fixed divergence slit, 2.5° soller slit and an Fe-filter were used. Each scan ranged from 5 to 90° (2θ) with a 0.02° step size and a measurement time of 0.6 seconds per step. Mineral phases were identified using Bruker DIFFRAC.EVA software® package with the PDF-2 (2012 release) powder diffraction file mineral database. XRD results from hydrothermally altered rocks are presented in Appendix J.

6.4. Wormy-patchy textures at Bantug

6.4.1. Description

Some of the intensely advanced argillic-altered rocks at Bantug display patchy-wormy textures. These textures are characterised by soft, amoeboid-like, sub-rounded, patches of <5 cm of

alunite ± pyrophyllite ± muscovite ± diaspore ± APS minerals ± zunyite ± pyrite ± rutile in a fine-grained clay-quartz groundmass. Figures 6.5, 6.6, and 6.7 illustrate several drill hole and surface samples from Bantug displaying patchy-wormy textures. These textures vary from patchy-dominated (e.g., Figs. 6.5a, 6.5c, 6.6c, 6.6d, and 6.7a) to groundmass-dominated (e.g., Figs. 6.5b).

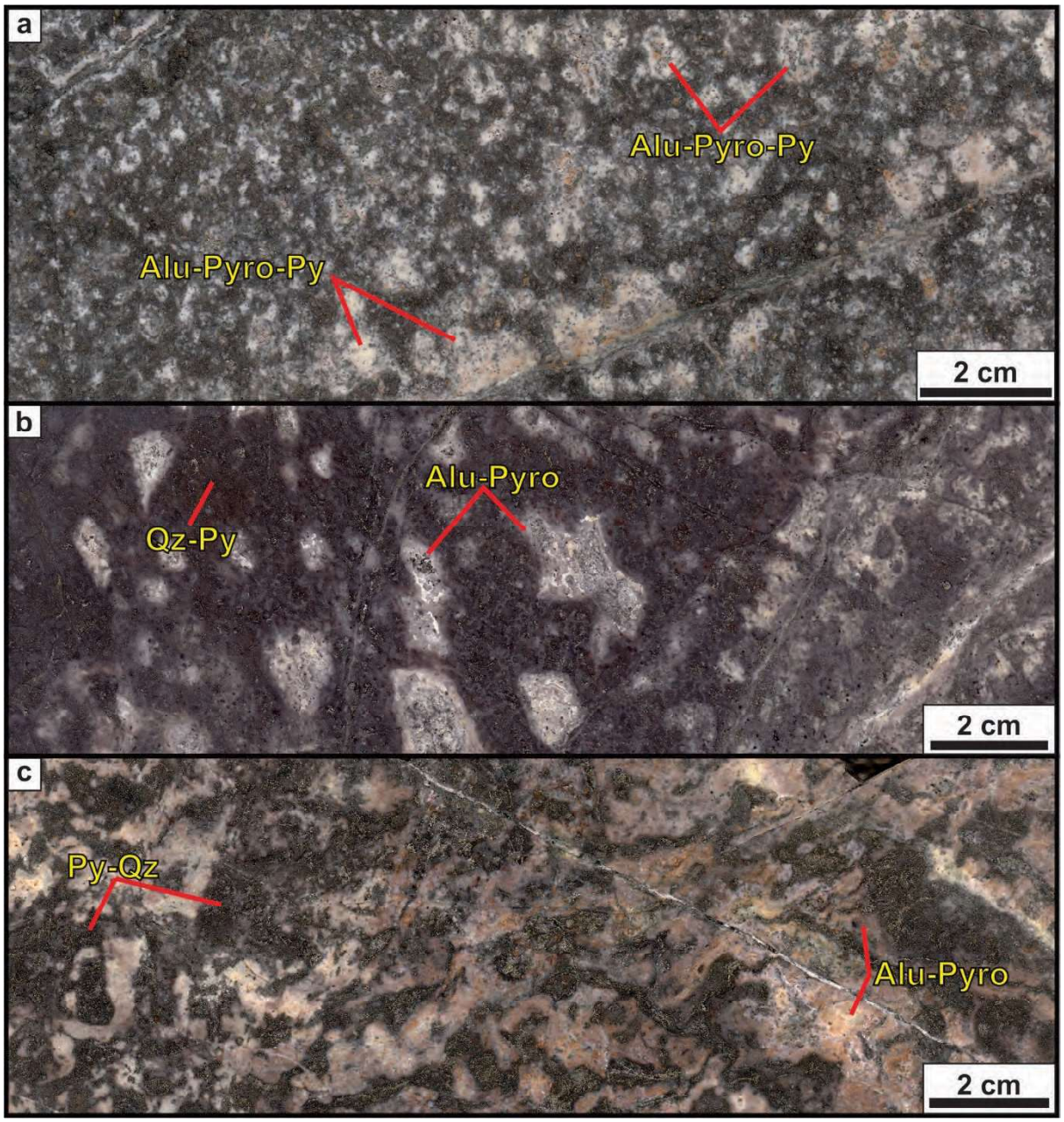

Figure 6.5. Patchy-textured rocks from Bantug. a. Patchy-textured plagioclase-phyric andesite. Alunite-pyrophyllite-pyrite patches of <2 cm in a fine-grained quartz groundmass (BTG-006; 541 m). **b.** Patchy-textured plagioclase-phyric andesite. Fine-grained quartz-dominated groundmass which contains alunite-pyrophyllite patches up to ~2cm diameter (BTG-003; 590 m). **c.** Patchy-textured plagioclase-phyric andesite. Alunite-pyrophyllite patches in a quartz-pyrite groundmass (BTG-003; 595.6 m). Abbreviations: Alu: alunite; Py: pyrite; Pyro: pyrophyllite; Qz: quartz.

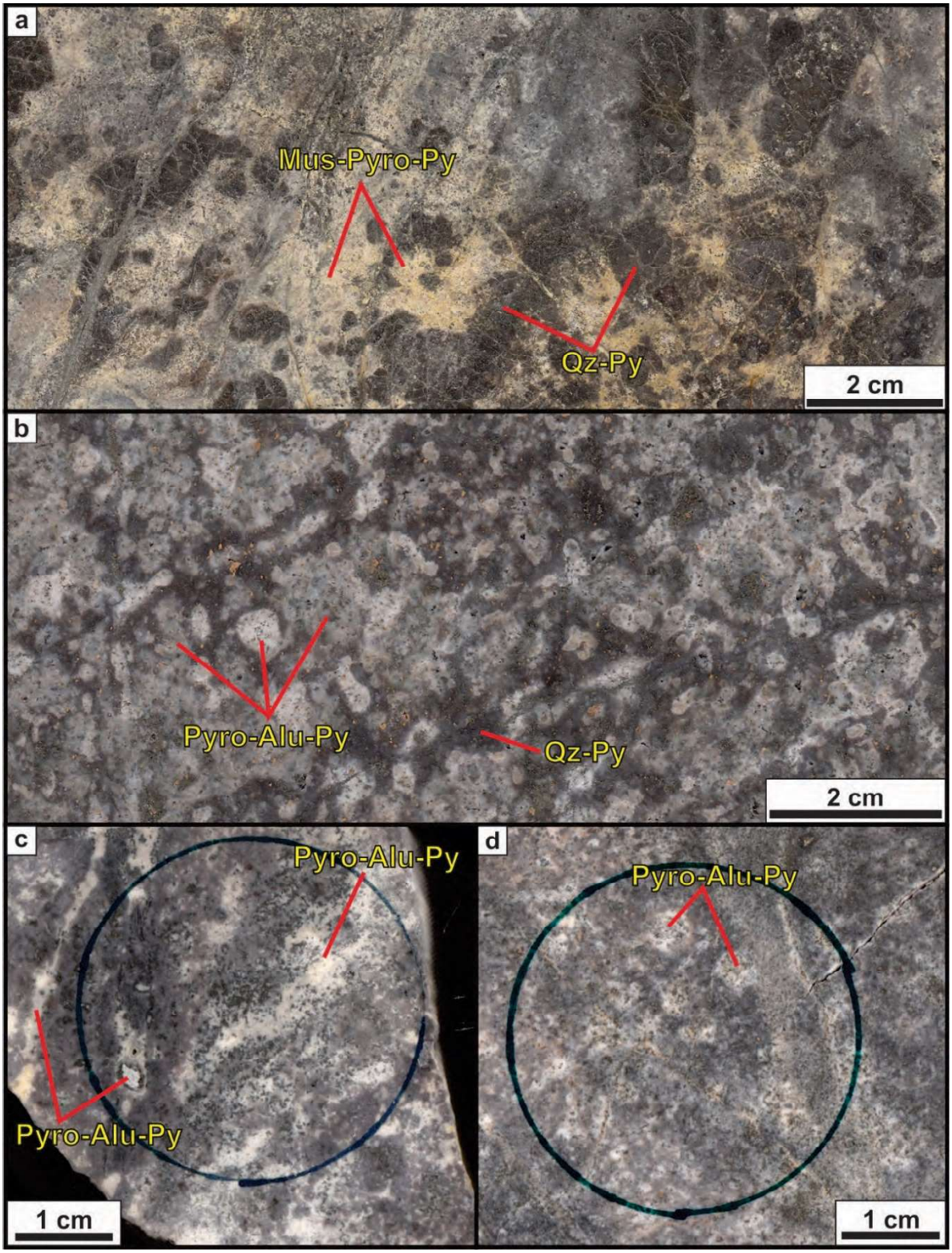

Figure 6.6. Patchy-textured rocks from Bantug. a. Patchy-textured andesitic volcaniclastic breccia. Wormy quartz-pyrite veins in a muscovite-pyrophyllite-pyrite groundmass (BTG-003; 383 m). **b.** Patchy-textured plagioclase-phyric andesite. Pyrophyllite-alunite-pyrite patches in a fine-grained quartz-pyrite groundmass (BTG-006; 518 m). **c.** Surface sample located at X: 505,388, Y: 1,107,721 (UTM-51N). Pyrophyllite-alunite-pyrite patches of <1 cm occur in a fine-grained quartz groundmass. The circle marks a SWIR spot analysis. **d.** Surface sample located at X: 505,491, Y: 1,108,140 (UTM-51N). Pyrophyllite-alunite-pyrite patches of <1 cm occur in a fine-grained quartz groundmass. The circle marks a SWIR spot analysis. Abbreviations: Alu: alunite; Mus: muscovite; Py: pyrite; Pyro: pyrophyllite; Qz: quartz.

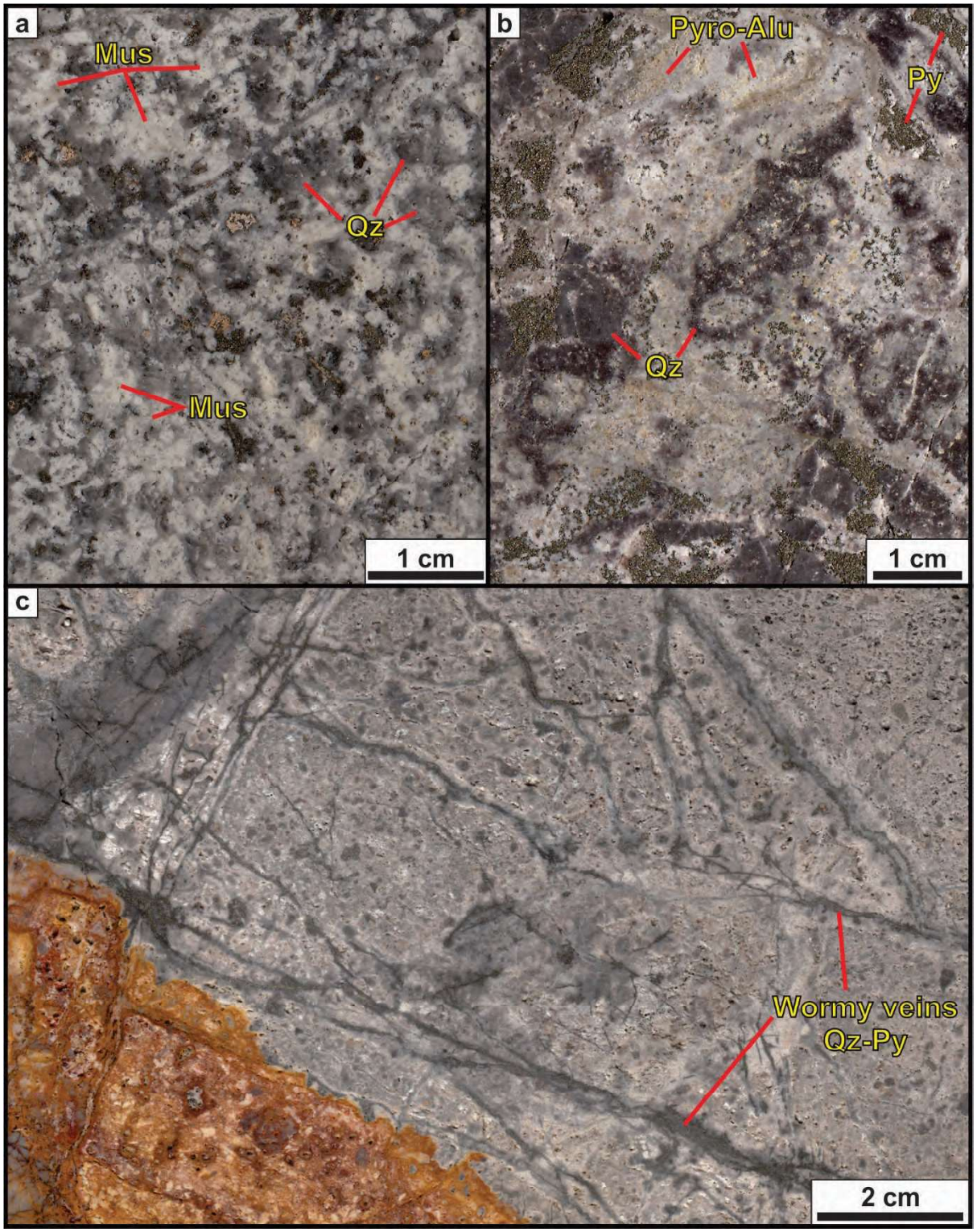

Figure 6.7. Patchy-textured rocks from Bantug. a. Patchy-textured diorite porphyry dike III. Patches are made of muscovite-montmorillonite replacing former plagioclase phenocrysts, groundmass is made of quartz (BTG-006; 381.3 m). **b.** Patchy-textured andesitic volcaniclastic breccia. Pyrophyllite-alunite-pyrite patches in a fine-grained quartz groundmass (BTG-003; 438 m). **c.** Surface sample. Wormy veins in intensely advanced argillic-altered patchy-textured rock. Surface sample displaying wormy and patchy texture (**X:** 504276.5 m, **Y:** 1106526.8 m; WGS 84, 51 N); sample courtesy of Ingemar Arellano from Freeport-McMoRan. Abbreviations: Alu: alunite; Mus: muscovite; Py: pyrite; Pyro: pyrophyllite; Qz: quartz.

6.4.2. SWIR spectroscopy from patchy textures

6.4.2.1. Introduction

This section presents the results of SWIR spectroscopy analyses on patchy-textured rocks from surface and drill holes studied at Bantug (i.e., BTG-005, BTG-003, BTG-006). Logs from drill holes are presented from the most westward (i.e., BTG-005) to the most eastward (i.e., BTG-006). SWIR spectroscopy analyses were collected down hole every five meters. Details of the SWIR analyses are presented in Chapter 4.

6.4.2.2. Results

6.4.2.2.1. Surface

Of the 45 surface samples collected during this study, 18 samples display patchy texture and 1 displays wormy texture (Fig. 6.8). Patchy-textured rocks occur within a 500-m radius from drill hole collar BTG-006. Most patchy-textured samples define isolated spots, and some samples define strips of <250 m length. Also, a group of 5 samples located at 186 m northeast from BTG-006 defines a ~600 m long strip of patchy-textured rocks (Fig. 6.8). The most frequent mineral detected in patchy-textured samples on surface is quartz, followed by pyrophyllite, alunite, montmorillonite, and muscovite (Fig. 6.8). Quartz and alunite-bearing samples occur southwest of drill hole BTG-006. Pyrophyllite and muscovite-bearing samples occur to the northeast of drill hole BTG-006. Alunite-bearing samples to the southwest have 1,480 nm peak position values of 1,479.0 nm and 1,479.8 nm. The alunite bearing sample located ~820 m to the northeast of BTG-006 has a peak position value of 1,478.6 nm (Fig. 6.8). The muscovite-bearing sample located ~663 m northeast of drill hole BTG-006 has an IC value of 0.71. The wormy-textured sample is located ~262 m southwest of drill hole BTG-006. Appendix I presents details on SWIR analyses on surface samples.

6.4.2.2.2. Drill hole BTG-005

Table 6.2 and Figures 6.9 and 6.10 present information about patchy textures observed in drill hole BTG-005. Patches were mostly observed in the plagioclase-phyric andesite, and some were observed in clasts from the quartz-pyrite cemented hydrothermal breccia. Pyrophyllite and diaspore were the predominant minerals detected by SWIR spectroscopy, and advanced-argillic is the predominant alteration type. Patch density ranges from 5 to 20 vol%, and the average is 10 vol%. Patch size ranges from 1 to 2 cm, and the average is 1.9 cm. Patch density increases from 10 vol% at 390 m to a maximum of 20 vol% between 410 and 550 m, and decreases to 15 vol% at 678 m. Rock type between 390 and 678 m is plagioclase-phyric

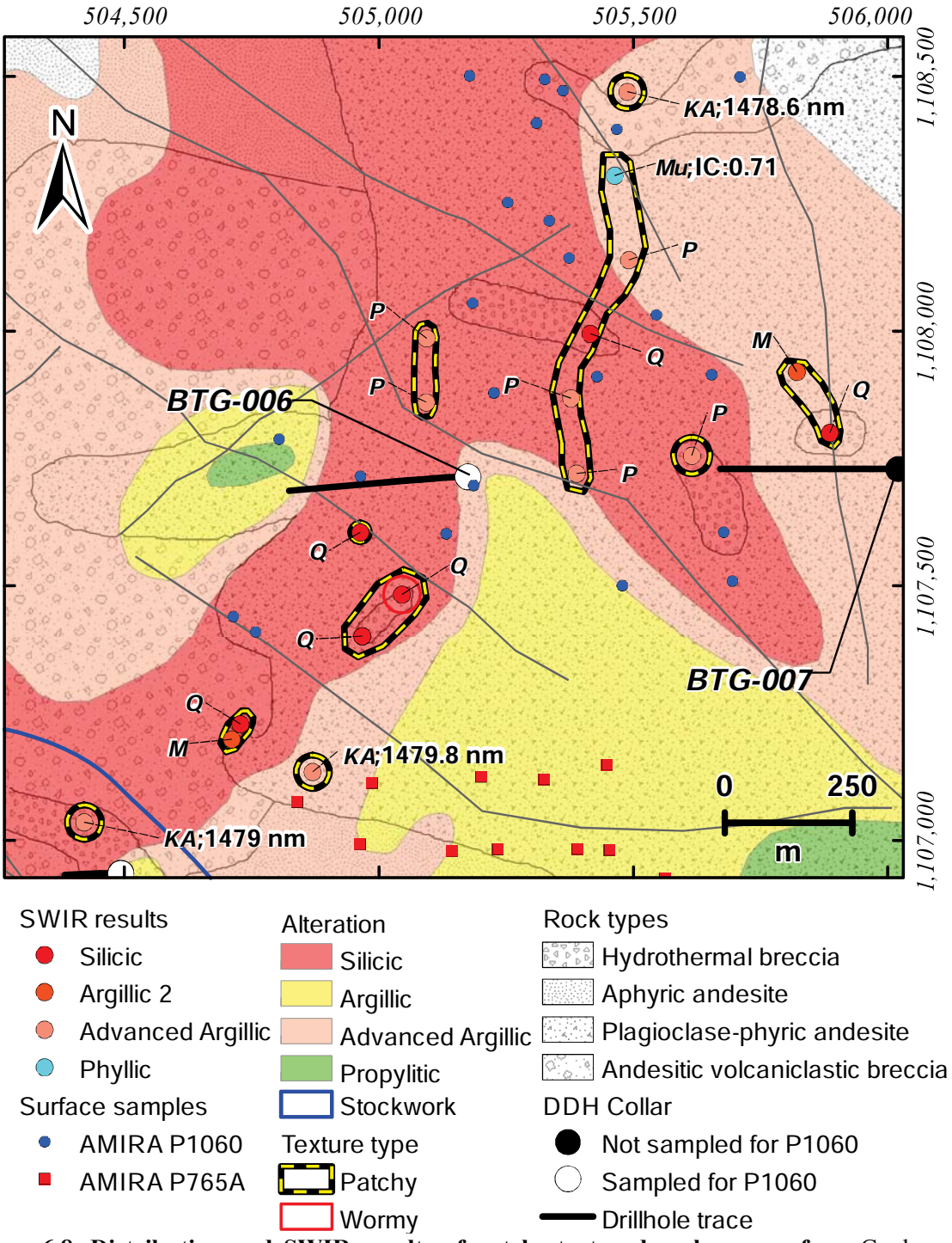

Figure 6.8. Distribution and SWIR results of patchy-textured rocks on surface. Geology and alteration map after Subang et al. (2009) with patchy texture occurrence areas (i.e., yellow dashed lines). Potassium alunite-bearing samples are labelled with their respective 1480 nm peak position; a paragonite-bearing sample is labelled with its respective IC value. Coordinate system: WGS84; 51N. Abbreviations: KA: potassium alunite; M: montmorillonite; P: pyrophyllite; Mu: muscovite; Q: quartz.

andesite, and the predominant alteration type is advanced-argillic. Alunite and muscovite were not identified in patchy-textured rocks in BTG-005, 1,480 nm peak position values or IC values were not recorded from this drill hole.

6.4.2.2.3. Drill hole BTG-003

Table 6.2, and Figures 6.11 and 6.12 present information about patchy textures observed in drill hole BTG-003. Patchy textures were mostly observed in the andesitic volcaniclastic breccia and plagioclase-phyric andesite. Muscovite was the predominant mineral detected by SWIR spectroscopy, and phyllic is the predominant alteration type. Patch density ranges from 6 to 16 vol % (average=10 vol %). Patch sizes range from 2 to 4 cm (average=2.6 cm). Patch density is particularly high between 336 and 337 m, in the plagioclase-pyroxene-phyric, crystal crowded diorite porphyry (DPD II). Patches in DPD II are predominantly made of montmorillonite. Larger patches were observed between 370 and 420 m, and from 432 to 440 m, in the andesitic volcaniclastic breccia. Patches in the andesitic volcaniclastic breccia are predominantly made of muscovite. SWIR spectroscopy did not detect alunite in patchy-textured rocks in drill hole BTG-003. IC values in the plagioclase-phyric andesite range from 0.65 to 1.08 (average= 0.84; Fig. 6.12), and IC values in the andesitic volcaniclastic breccia range from 0.65 to 0.94 (average=0.79; Fig. 6.12).

6.4.2.2.4. Drill hole BTG-006

Table 6.2, and Figures 6.13 and 6.14 summarise the SWIR results from patchy-textured rocks observed in drill hole BTG-006. Patchy textures in this drill hole were best developed in the plagioclase-phyric andesite. Patchy textures were also observed in the diorite porphyry dike III (DPD III; Fig. 6.7a) and in the diorite porphyry (DP). Pyrophyllite and alunite were the most abundant minerals detected with SWIR spectroscopy, and the predominant alteration type is advanced-argillic. Patch density ranges from 2 to 20 vol% (average=7 vol%). Patch density varies from 299 to 502 m (i.e., 10 vol %), and from 502 to 580 m (i.e., 20 vol %). The intrusive contact between the plagioclase-phyric andesite and the diorite porphyry was observed at 580 m depth (Fig. 6.13). Patch size ranges from 0.5 cm in the diorite porphyry to 6 cm in the plagioclase-phyric andesite. Patches are particularly large between 141 and 142 m (6 cm), 240 and 257 m, 260 and 298 m (5.2 cm; Fig. 6.13). Alunite 1,480 nm peak position values range from 1,479.0 to 1,480.5 nm (average=1,480.1 nm; Fig. 6.14). The mean IC value between 87 and 90 m in the plagioclase-phyric andesite is 0.9 (Fig. 6.14). The mean IC value between 580 and 704.6 m in the diorite porphyry is 1.4 (Fig. 6.14).

Table 6.2. Summary of patchy texture logs and SWIR results from drill holes studied at Bantug

From (m)	To (m)	Rock type	Alteration type	Density (vol%)	Size (cm)	SWIR mineralogy	1,480 nm peak position	IC
Drill hole BTG-005								
159	170	Hbx	Argillic 1	5	2	Kao		
215	242	Hbx	AA	5	2	Pyro, Dia		
386	390	PA	AA	2	1	Pyro		
390	395	PA	AA	10	2	Pyro		
395	410	PA	AA	15	2	Pyro		
410	550	PA	AA	20	2	Pyro, D, Dia		
550	678	PA	Argillic 2	15	2	Mon		
Drill hole BTG-003								
36	150	PA	Phyllic	6	2	Mus, Mon, Kao		0.6
336	337	DPD II	Argillic 2	16	2	Mon		
370	420	Abx	Phyllic	10	4	Mus		0.9
432	440	Abx	Phyllic	10	4	Mus		0.6
500	563	PA	Phyllic	10	2	Mus		1.1
564	600	PA	Phyllic	10	3	Mus		0.8
650	660	DP	Argillic 2	10	2	Mon		
708	720	Abx	Argillic 1	10	2	Kao		
Drill hole BTG-006								
21	78	PA	AA	5	4	Pyro, K-Alu	1480.5	
87	90	PA	Phyllic	5	4	Mus		0.9
95	108	PA	AA	5	4	Pyro, K-Alu	1482.0	
118	130	PA	AA	7	4	Pyro, Dia		
141	142	PA	AA	5	6	Pyro		
143	163	PA	AA	6	4	Pyro		
187	188	PA	AA	5	2	Pyro		
200	235	PA	AA	6	2	Pyro		
240	257	PA	AA	10	5.2	Pyro, K-Alu	1479.0	
260	298	PA	AA	6	5.2	Pyro, K-Alu	1480.3	
299	370	PA	AA	10	2.5	Pyro, K-Alu	1478.8	
385	429	PA	AA	10	2.5	Pyro		
439	442	PA	AA	10	2	Pyro		
469	495	PA	AA	10	2	Pyro		
496	502	PA	AA	10	2	Pyro		
502	580	PA	AA	20	1	Pyro		
580	704.6	DP	Phyllic	2	0.5	Mus		1.4

Rock types: Abx: andesitic volcaniclastic breccia; DP: diorite porphyry; DPDII: diorite porphyry dike II; Hbx: hydrothermal breccia; PA: plagioclase-phyric andesite. **Hydrothermal alteration:** AA: advanced argillic; Argillic 1: kaolinite, illite; Argillic 2: montmorillonite; Phyllic: muscovite. **Mineralogy:** D: dickite; Dia: diaspore; K-Alu: potassium alunite; Mon: montmorillonite; Mus: muscovite; Pyro: pyrophyllite.

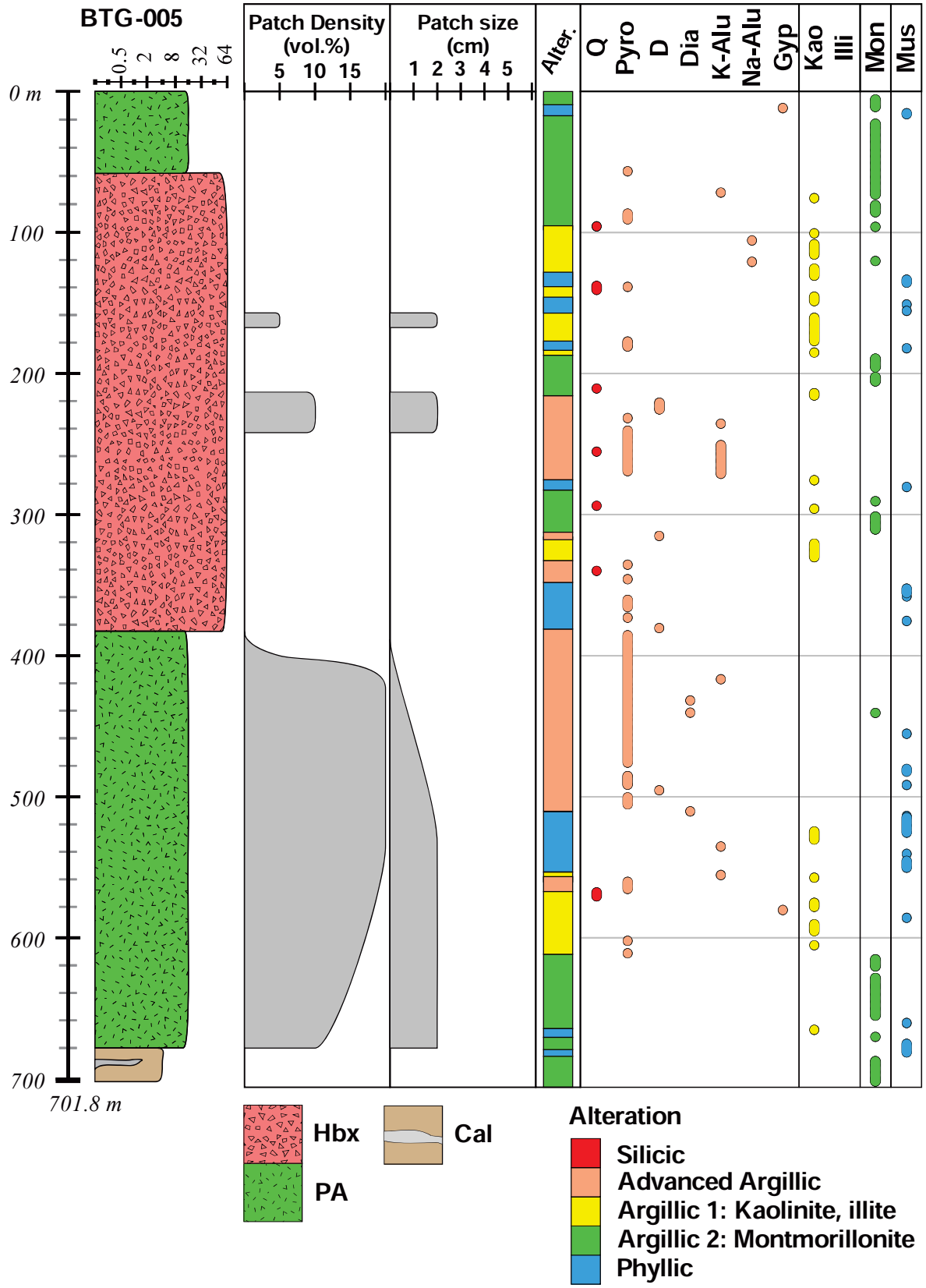

Figure 6.9. Patchy texture and SWIR results strip log from drill hole BTG-005. Geology log, patchy texture density (vol %) and size (cm), hydrothermal alteration, SWIR mineralogy. Abbreviations: Alter.: alteration type; Hbx: hydrothermal breccia; PA: plagioclase-phyric andesite; Cal: sandstones and mudstones of the Cretaceous Caliling Formation; D: dickite; Dia: diaspore; Gyp: gypsum; Illi: illite; K-Alu: K-alunite; Kao: kaolinite; Na-Alu: natroalunite; Mon: montmorillonite; Mus: muscovite; Pyro: pyrophyllite; Q: quartz.

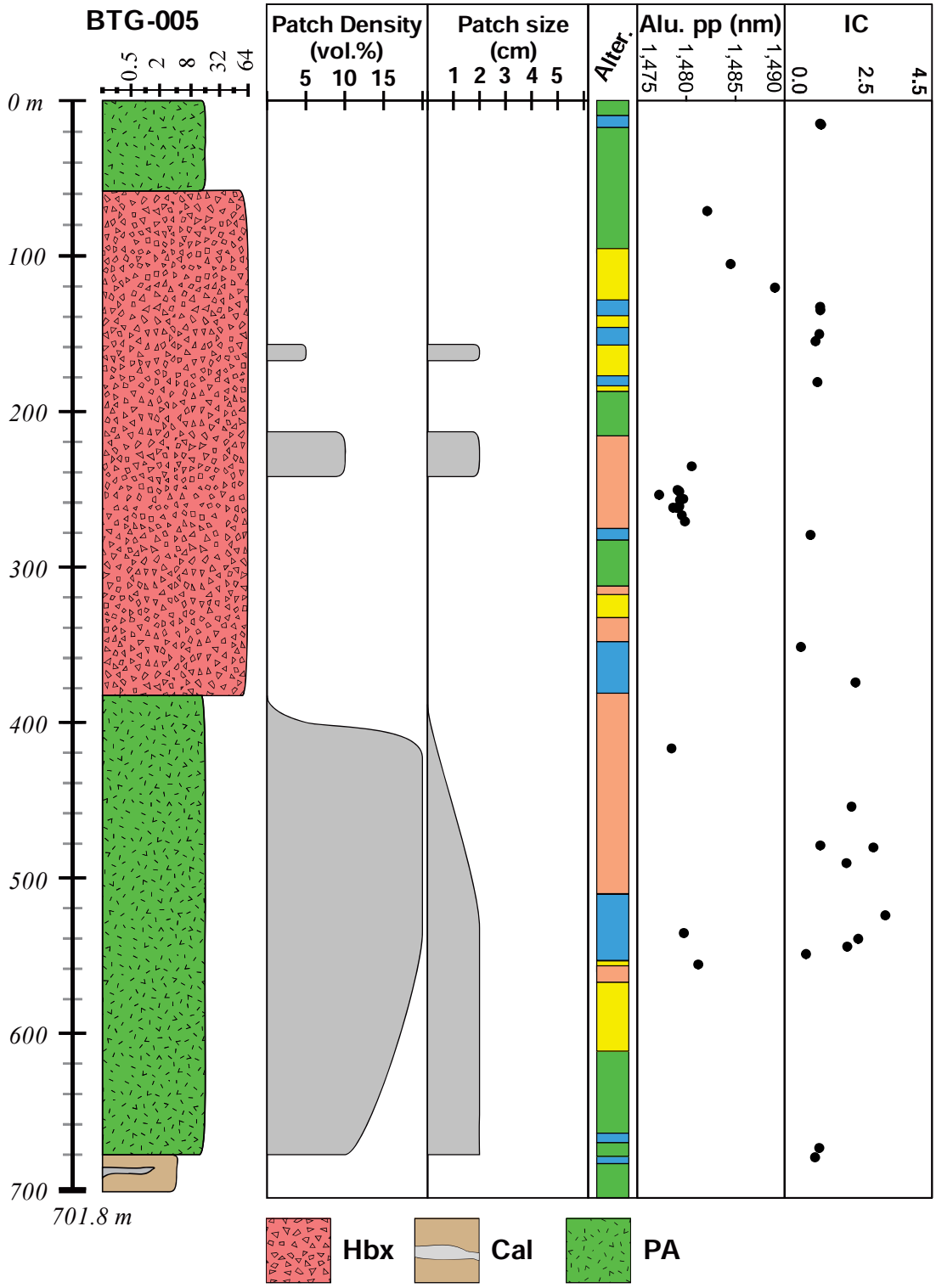

Figure 6.10. Patchy texture and SWIR results strip log from drill hole BTG-005. Geology log patchy texture density (vol %) and size (cm), hydrothermal alteration (Alter.), alunite 1,480 nm peak position value, index of crystallinity (IC). Abbreviations: Alter.: alteration; Alu. pp: alunite 1,480 peak position; IC: index of crystallinity; Hbx: hydrothermal breccia; PA: plagioclase-phyric andesite; Cal: sandstones and mudstones of the Cretaceous Caliling Formation. Alteration legend as in Figure 6.9.

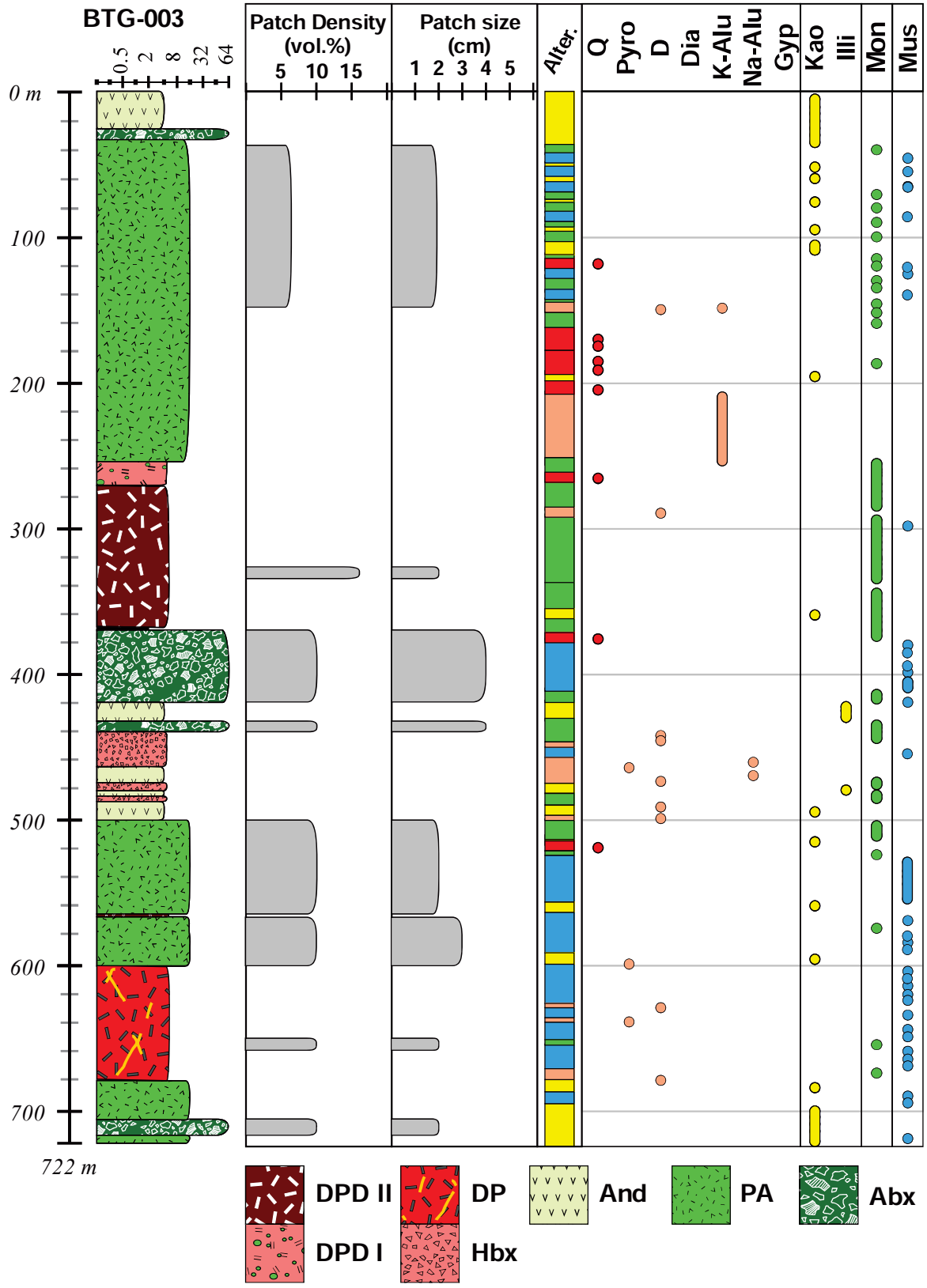

Figure 6.11. Patchy texture and SWIR results strip log from drill hole BTG-003. Geology log, patchy texture density (vol %) and size (cm), hydrothermal alteration (Alter.), SWIR mineralogy. Abbreviations: Alter.: hydrothermal alteration; DPD: diorite porphyry dikes (I and II); DP: diorite porphyry; Hbx: hydrothermal breccia; And: aphyric andesite; PA: plagioclase-phyric andesite; Abx: andesitic volcaniclastic breccia; D: dickite; Dia: diaspore; Gyp: gypsum; Illi: illite; K-Alu: K-alunite; Kao: kaolinite; Na-Alu: natroalunite; Mon: montmorillonite; Mus: muscovite; Pyro: pyrophyllite; Q: quartz. Alteration legend as in Figure 6.9.

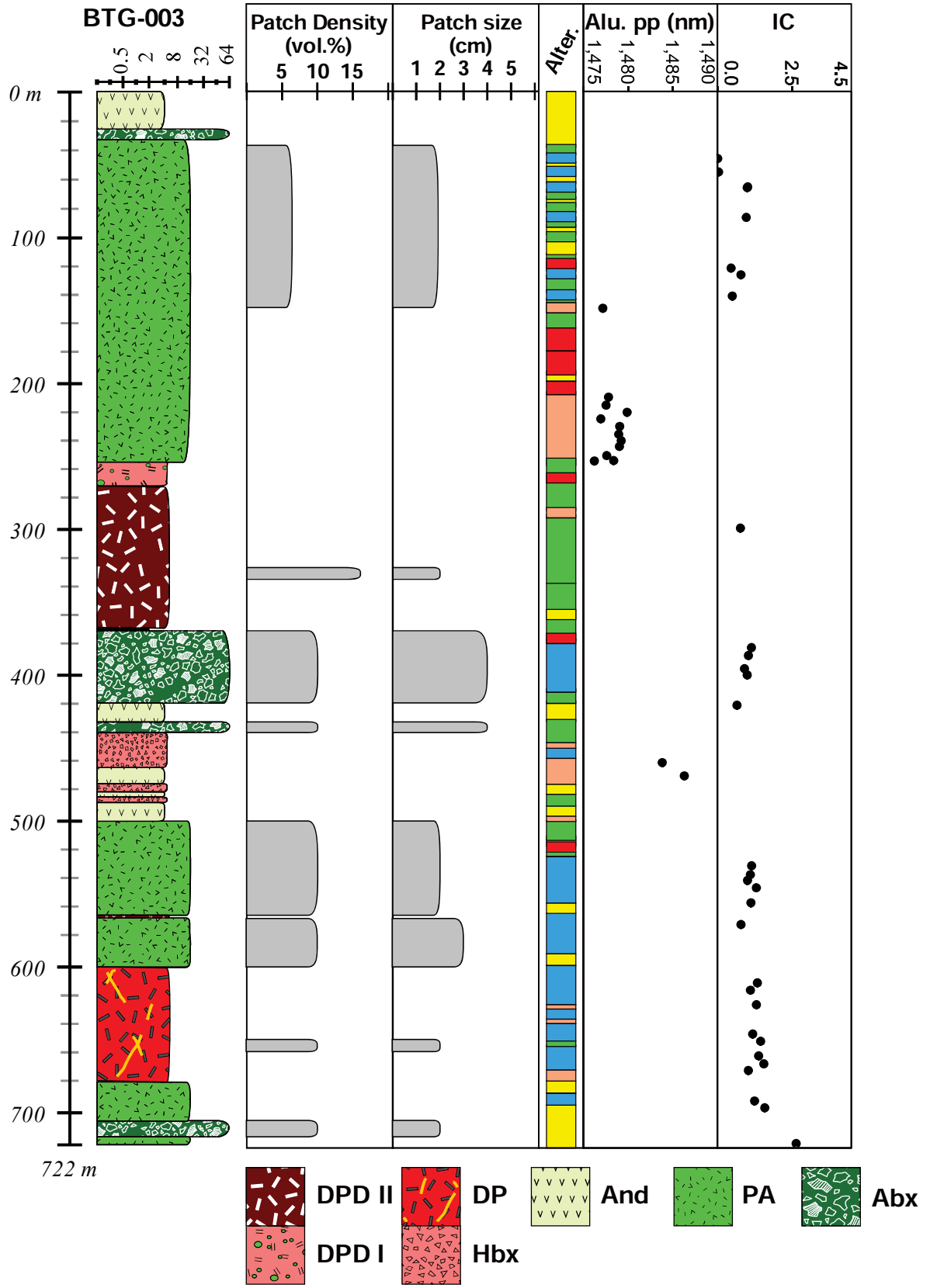

Figure 6.12. Patchy texture and SWIR results strip log from drill hole BTG-003. Geology log patchy texture density (vol %) and size (cm), hydrothermal alteration, alunite 1,480 nm peak position value, index of crystallinity (IC). Abbreviations: Alter.: alteration; Alu. pp: alunite 1,480 peak position; IC: index of crystallinity; DPD: diorite porphyry dikes (I and II); DP: diorite porphyry; Hbx: hydrothermal breccia; And: aphyric andesite; PA: plagioclase-phyric andesite; Abx: andesitic volcaniclastic breccia. Alteration legend as in Figure 6.9.

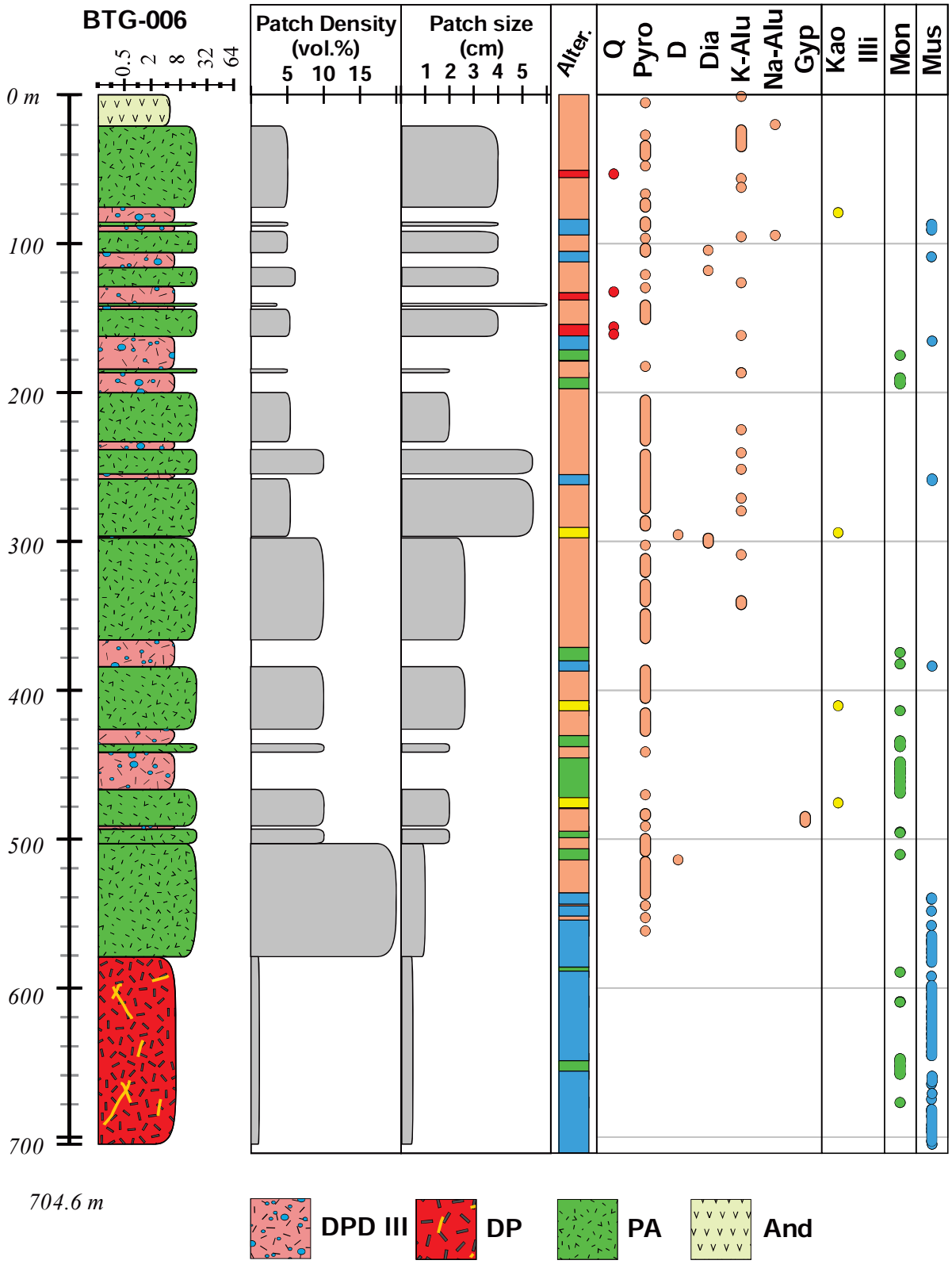

Figure 6.13. Patchy texture and SWIR results strip log from drill hole BTG-006. Drill hole BTG-006. Geology log, patchy texture density (vol %) and size (cm), hydrothermal alteration (Alter.), SWIR mineralogy. Abbreviations: Alter.: alteration; DPD III: diorite porphyry dike III; DP: diorite porphyry; And: aphyric andesite; PA: plagioclase-phyric andesite; D: dickite; Dia: diaspore; Gyp: gypsum; Illi: illite; K-Alu: K-alunite; Kao: kaolinite; Na-Alu: natroalunite; Mon: montmorillonite; Mus: muscovite; Pyro: pyrophyllite; Q: quartz. Alteration legend as in Figure 6.9.

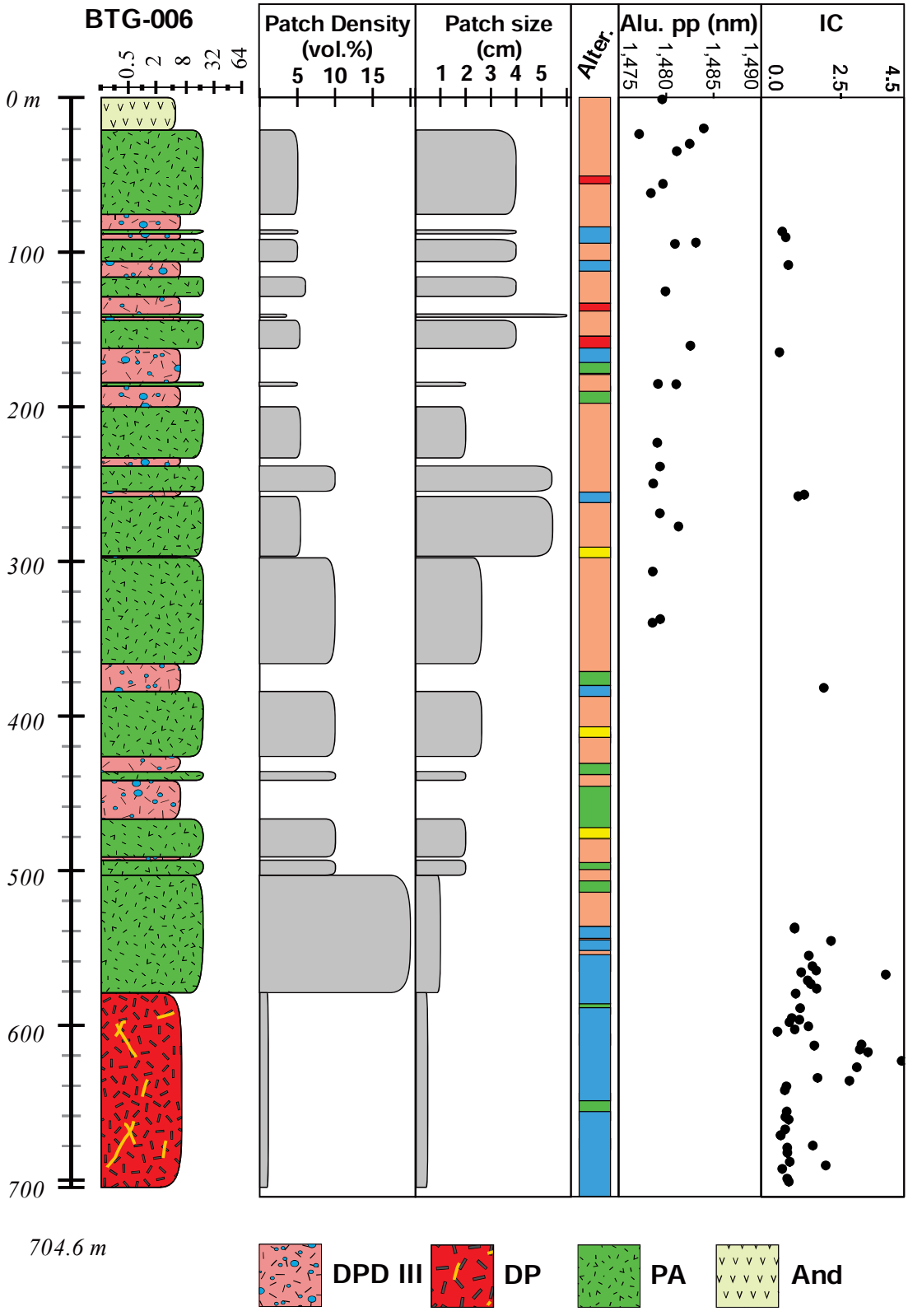

Figure 6.14. Patchy texture and SWIR results strip log from drill hole BTG-006. Drill hole BTG-006. Geology log patchy texture density (vol %) and size (cm), hydrothermal alteration (Alter.), alunite 1480 nm peak position value, index of crystallinity (IC). Abbreviations: Alter.: alteration; Alu. pp: alunite 1,480 peak position; IC: index of crystallinity DPD III: diorite porphyry dike III; DP: diorite porphyry; And: aphyric andesite; PA: plagioclase-phyric andesite. Alteration legend as in Figure 6.9.

6.4.3. Petrography and microanalyses

6.4.3.1. Petrography

The patchy textures from Bantug contain quartz, alunite, APS, diaspore, pyrophyllite, zunyite, rutile, and pyrite (Figs. 6.15 and 6.16). Petrographic observations revealed that patchy features have four components: a core, a fine-grained halo, sinuous radiating fractures, and groundmass (Figs. 6.15a, 6.15b, and 6.16a). The core of the patchy features can be best described as a mosaic of fine-grained pyrophyllite and muscovite. This mosaic also contains coarse diaspore and alunite grains (i.e., 100 μm), as well as pyrite crystals and APS minerals (Figs. 6.15 and 6.16). The fine-grained halos surrounding patchy features are <3 mm thick. These are predominantly made of quartz and pyrophyllite generally <10 μm. Lesser pyrite, diaspore, and alunite were also observed in the halos (Figs. 6.15a, 6.15b, and 6.15e). Sinuous radiating fractures extend outward from the contact between the core and the fine-grained halo of patchy features (Fig. 6.15a, b and c). These fractures are <5 mm long and are filled with coarse diaspore, alunite, and pyrite crystals, as well as fine-grained pyrophyllite (Fig. 6.15a, 6.15b, and 6.15c). The groundmass in which patchy features occur is mostly made of fine-grained granular quartz. Lesser pyrophyllite, muscovite, and fine-grained pyrite were also observed in the groundmass. Coarse alunite and pyrite, and broken quartz phenocrysts are also disseminated in the groundmass (Fig. 6.16.a).

Alunite, APS minerals, diaspore, and pyrite are intimately and complexly related, both in the core and groundmass of patchy features. In a plagioclase-phyric andesite sample collected at 264 m depth in drill hole BTG-006, diaspore and alunite crystals of ~50 μm were observed to nucleate on subhedral-anhedral, <20 μm, pyrite grains (Fig. 6.15d). In the same sample, alunite and diaspore grains were observed to be interlocked with APS minerals, and to contain abundant pyrite and APS inclusions (Figs. 6.15d and 6.15e). In other plagioclase-phyric andesite samples, coarser (i.e., 2 to 3 mm) euhedral pyrite crystals were observed in the core of patchy features. Alunite and diaspore crystals nucleated on pyrite (Figs. 6.16b and 6.16c). Pyrite is the most abundant (i.e., ~99%) opaque mineral observed in thin sections (Figs. 6.15 and 6.16). It occurs as fine-grained disseminations, in veins, and as coarse euhedral to subhedral grains in the groundmass and at the core of patches (Figs. 6.16a, 6.16b, and 6.16d). Trace amounts of fine-grained rutile were also observed in patchy features as clusters of needle-like crystals in the core of patches and in the pyrophyllite-muscovite mosaics. Variations on pyrite size and grain shape were observed, and are indicative of several precipitation stages.

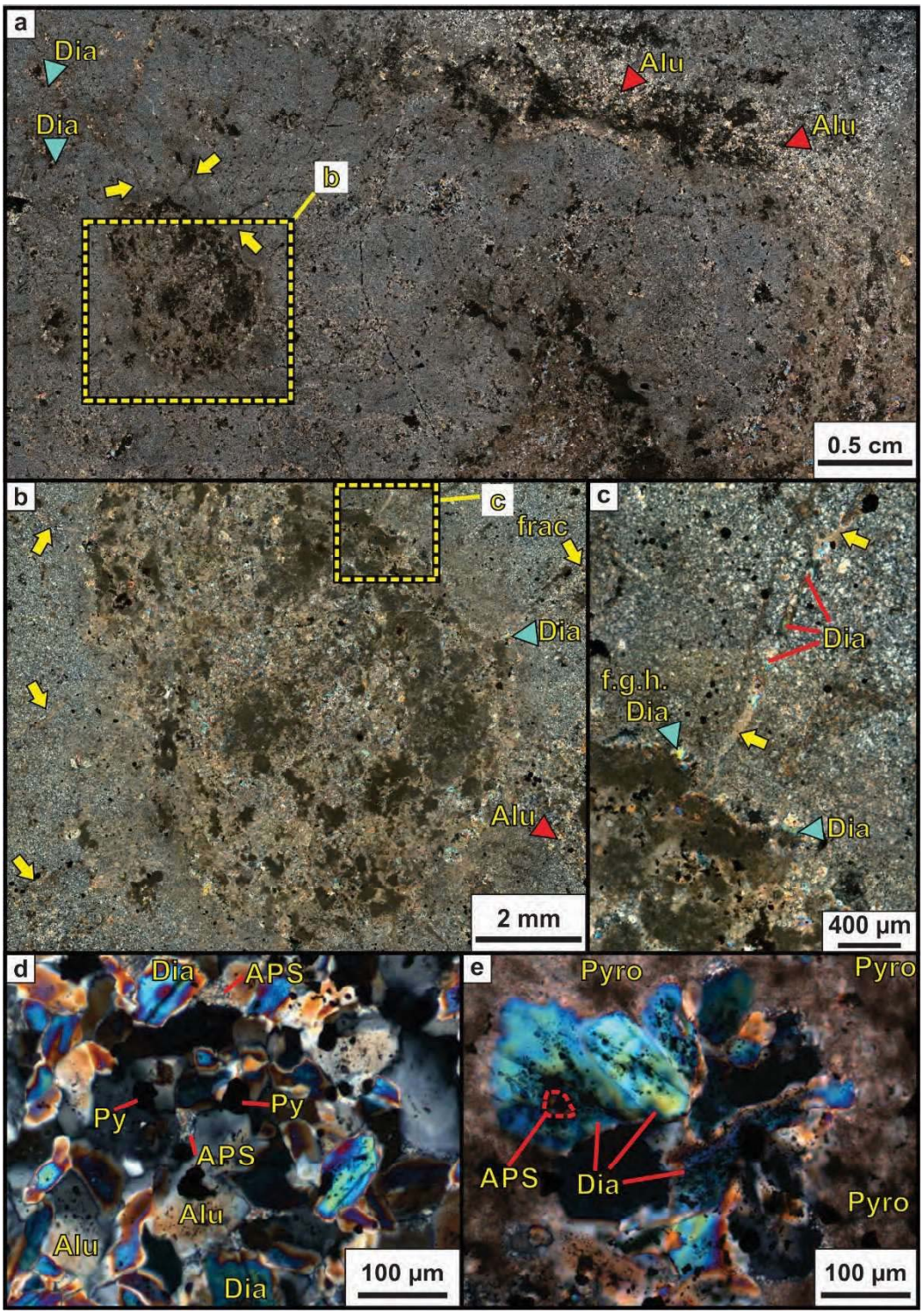

Figure 6.15. Photomicrographs from patchy-textured rocks from Bantug. a. Transmitted light micrograph; imaged area: 4.4 cm by 2.3 cm. Patches are made of diaspore, alunite, pyrophyllite, APS, and pyrite. Notice fine-grained patch halo. Sinuous cracks (yellow arrows), filled with alunite and diaspore, irradiate from patch. **b.** Detail from panel a. Transmitted light mosaic micrograph; imaged area: 1.7 cm by 0.9 cm. Fine-grained halo surrounding patchy feature. Sinuous cracks (yellow arrows), filled with alunite and diaspore, irradiate from patch. **c.** Detail from panel b. Patchy feature, fine-grained halo (f.g.h.), and sinuous radial crack stemming from patchy feature. **d.** Detail at the core of a patchy feature; pyrite, alunite, APS minerals, and diaspore occur in equilibrium. **e.** Diaspore and APS minerals occur in a pyrophyllite groundmass. Sample from plagioclase-phyric andesite at 264 m in drill hole BTG-006. Blue triangles: diaspore; red triangles: alunite. Abbreviations: Alu: alunite; APS: aluminium-phosphate-sulphate minerals; Dia: diaspore; f.g.h.: fine grain halo; Py: pyrite; Pyro: pyrophyllite.

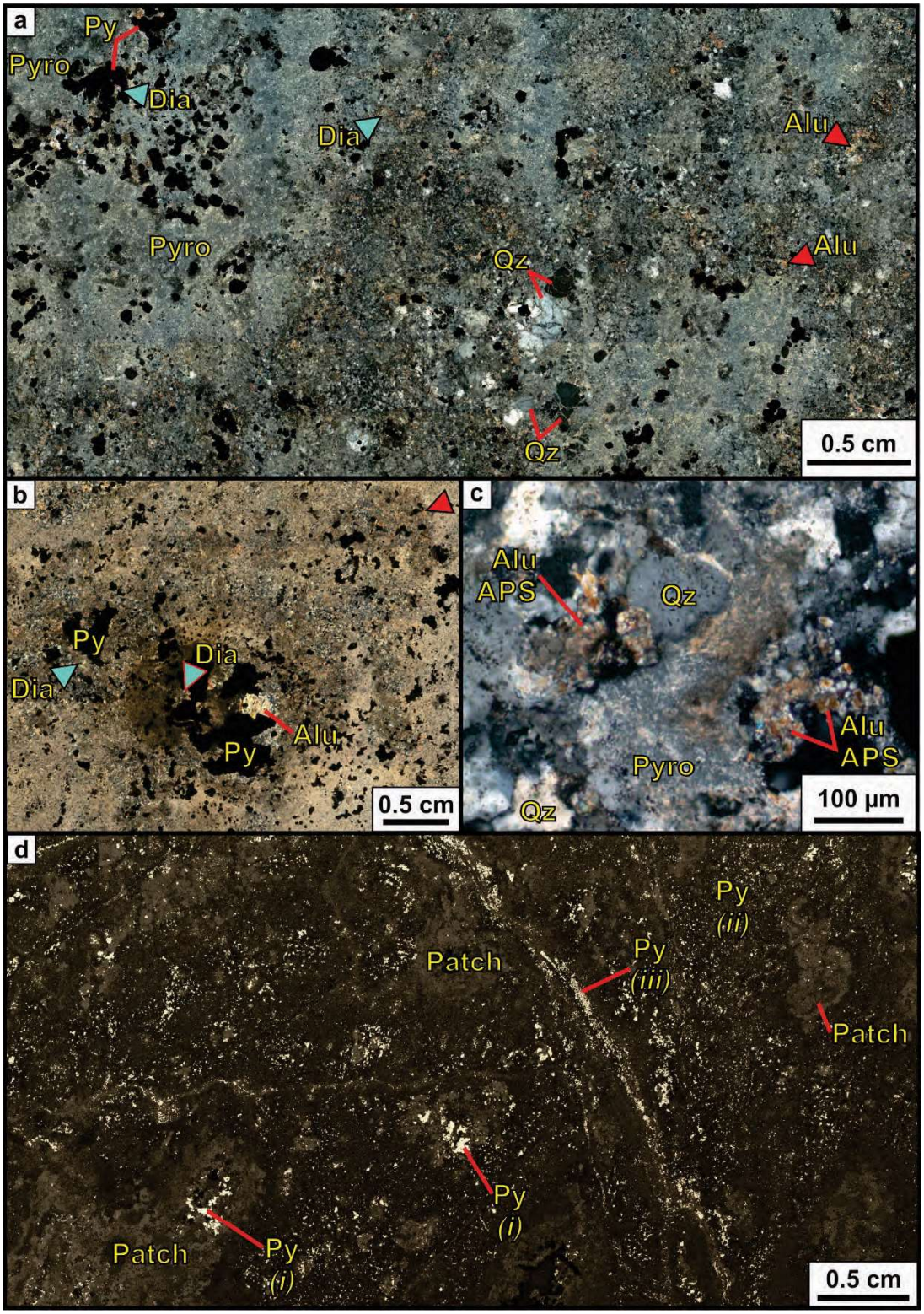

Figure 6.16. Photomicrographs from patchy-textured rocks from Bantug. a. Transmitted light photomicrograph, imaged area: 4.4 cm by 2.3 cm. Patches are made of pyrophyllite (BTG-006; 540 m). **b.** Transmitted light photomicrograph; imaged area: 3.5 cm by 2.7 cm. Pyrite and alunite crystals at the core of a patchy feature (BTG-003; 590 m). **c.** Transmitted light micrograph. Detail of a patchy feature; alunite and APS minerals in a pyrophyllite groundmass. (BTG-005; 485.8 m). **d.** Reflected light micrograph. Imaged area: 5 cm by 2.6 cm. Coarse pyrite crystals are at the core of patchy features, fine-grained pyrite occurs in the groundmass and veins (BTG-003; 580 m). Thin sections are from plagioclase-phyric andesites. Abbreviations: Alu: alunite; APS: aluminium-phosphate-sulphate minerals; Dia: diaspore; f.g.h.: fine grain halo; Py: pyrite; Pyro: pyrophyllite; Qz: quartz.

6.4.3.2. Field-emission scanning electron microscopic analyses of patchy-textured rocks

FE-SEM analyses revealed the presence of several hydrothermal minerals in patchy-textured rocks. These include alunite, APS minerals (i.e., svanbergite, woodhouseite, weilerite, and florencite), pyrite, diaspore, muscovite, pyrophyllite, quartz, rutile, and zunyite (Figs. 6.17, 6.18, and 6.19).

FE-SEM analyses at the core of patchy features revealed the presence of coarse (i.e., <300 μm diameter) subhedral to anhedral pyrite grains with quartz and diaspore inclusions (Figs. 6.17b, 6.18b, and 6.19b). Pyrite crystals in the core of patchy features are typically intergrown with anhedral diaspore grains <100 μm diameter (Fig. 6.17b). Diaspore occurs with quartz, alunite, APS minerals, and fine-grained muscovite-pyrophyllite (Figs. 6.17b, 6.18b, and 6.19b). Pyrite also occurs as fine grains disseminated in the muscovite-pyrophyllite groundmass (Fig. 6.17c).

The fine-grained halos surrounding patchy features contains granular quartz (Figs. 6.17a, and 6.17d to 6.17f). Granular quartz occurs as anhedral masses in a pyrophyllite-dominated groundmass (Fig. 6.17f). Pyrite, APS minerals, and diaspore also occur in the fine-grained halos surrounding patchy features (Fig. 6.17d and 6.17e). Pyrite occurs as anhedral, embayed, crystals <100 μm diameter; these contain quartz and diaspore inclusions (Fig. 6.17d). APS minerals in the fine-grained halos are complexly zoned, <10 μm diameter, and are intergrown with quartz (Fig. 6.17e).

Diaspore, alunite, and APS minerals in the core of patchy features are abundant and have complex growth relationships (Fig. 6.18c, 6.18d, and 6.18f). APS minerals have nucleated on anhedral diaspore and alunite crystals. Florencite, a cerium-rich APS mineral, was also observed in the core of alunite crystals (Fig. 6.18f). Euhedral, coarse, zunyite grains were also observed in the core of some patchy features.

Rutile also occurs in the core of patchy features. It occurs as clusters of needle-like crystals, <10 μm long, intergrown with pyrite, both in a pyrophyllite-muscovite groundmass (Fig. 6.18c).

The fine-grained core of the patchy features is mostly composed of pyrophyllite; however, some samples were predominantly composed of muscovite. Pyrophyllite-rich samples, typically had ~70 μm muscovite grains in cavities (Fig. 6.18c, 6.19c to 6.19e).

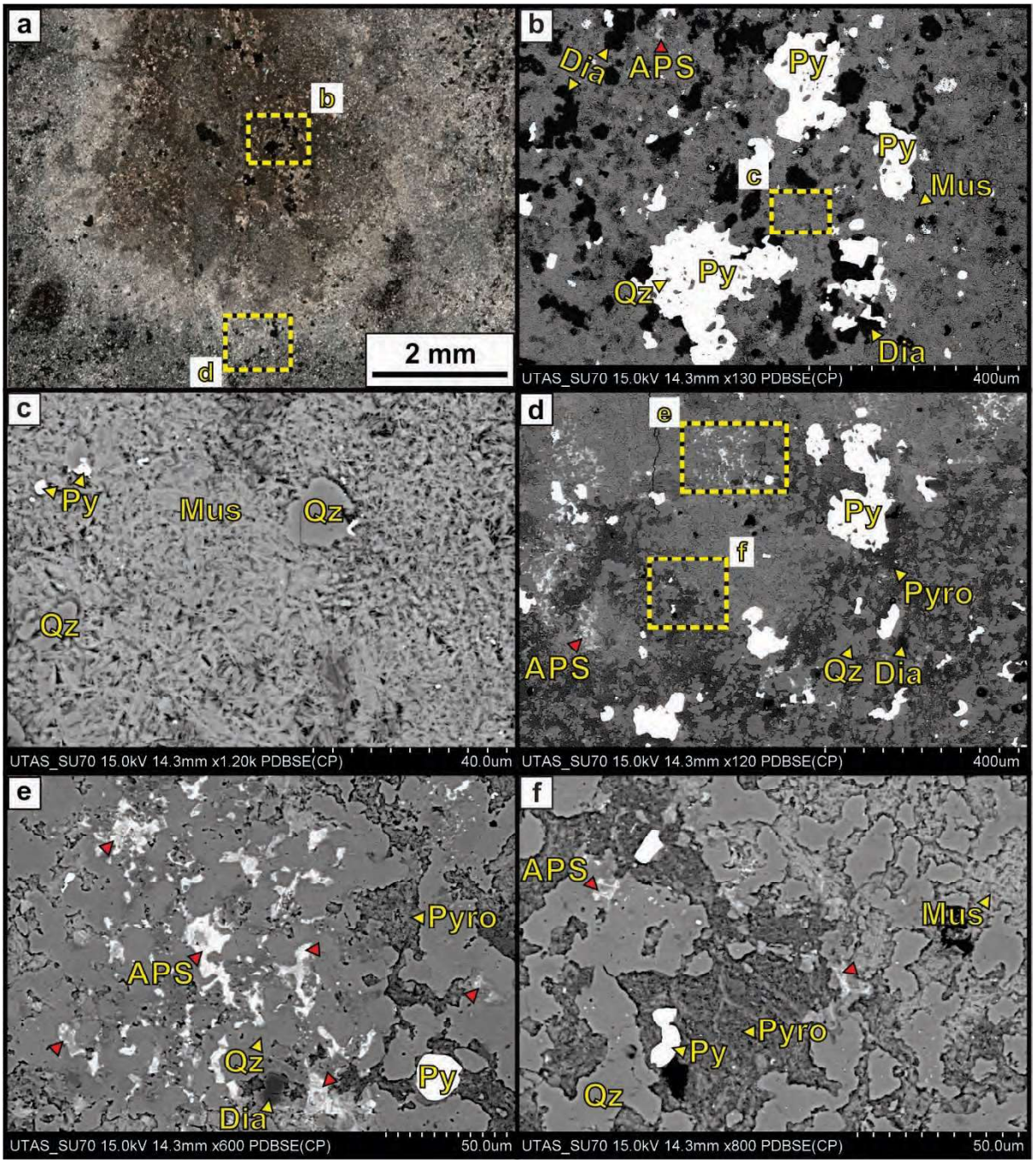

Figure 6.17. FE-SEM images from patchy-textured rocks from Bantug. a. Transmitted light photomicrograph. Patchy feature characterised by a ~1 mm thick fine-grain quartz-pyrophyllite-muscovite halo. **b.** BSE image. Detail from panel a; border of a patchy feature. Pyrite, diaspore, quartz, and APS in a pyrophyllite-muscovite groundmass. **c.** and **d.** BSE images. Details from panel b. APS minerals intergrown with quartz in a pyrophyllite-muscovite groundmass. **e.** BSE image. Detail from panel a; core of the patchy feature. Pyrite and diaspore crystals in a muscovite groundmass. **f.** BSE image. Detail from panel e; muscovite groundmass at the core of the patchy feature. Thin section from plagioclase-phyric andesite (BTG-006; 690 m). Abbreviations: APS: aluminium-phosphate-sulphate minerals; Dia: diaspore; Mus: muscovite; Py: pyrite; Pyro: pyrophyllite; Qz: quartz.

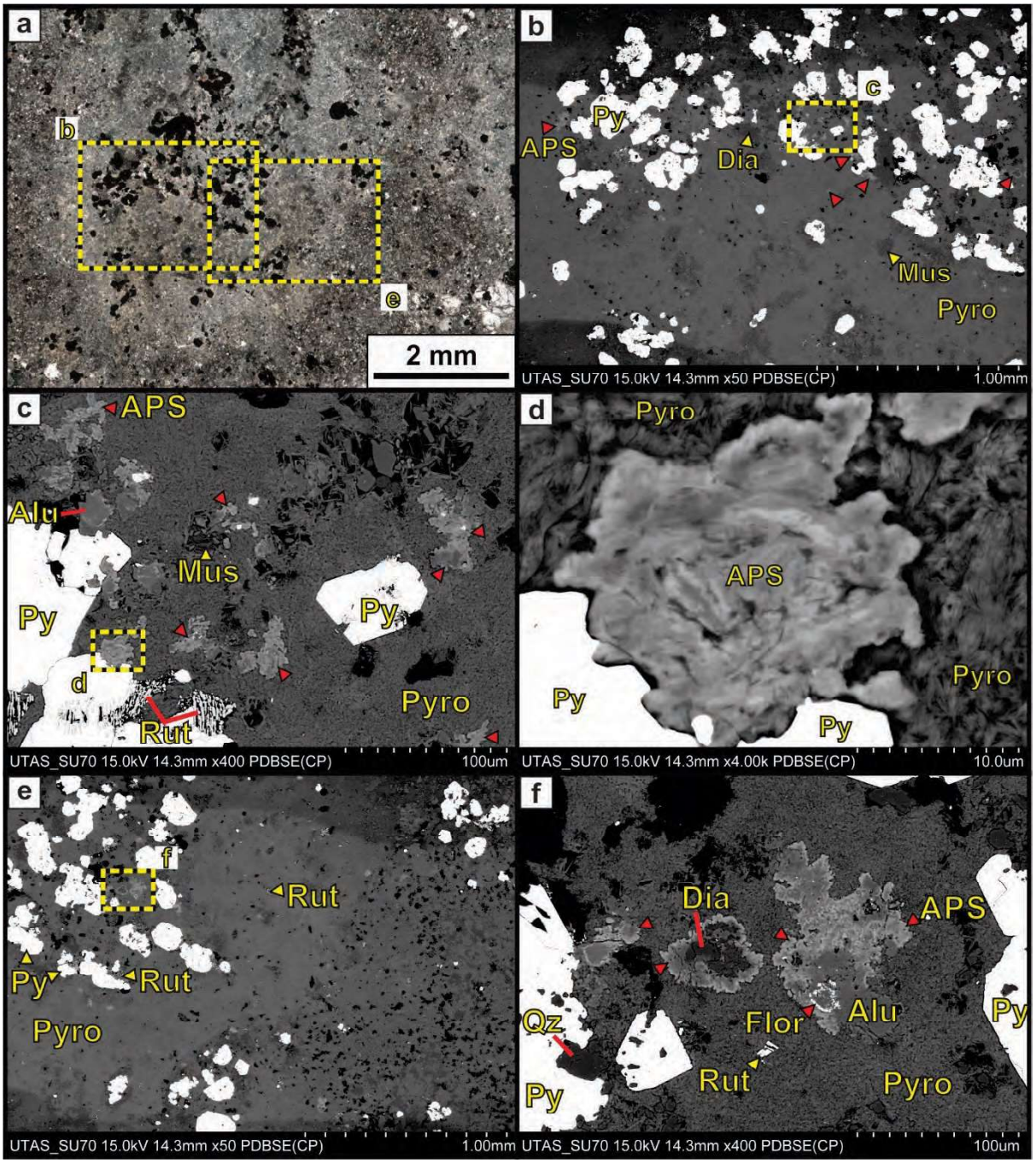

Figure 6.18. FE-SEM images from patchy-textured rocks from Bantug. a. Transmitted light photomicrograph of a patchy feature. **b.** BSE image. Detail from panel a; core of a patchy feature. Pyrite grains and APS minerals in a pyrophyllite-muscovite groundmass. **c.** BSE image. Detail from panel b; core of a patchy feature. Pyrite, rutile, APS, alunite, quartz crystals in a pyrophyllite groundmass; muscovite and quartz occur in cavities. **d.** BSE image. Detail from panel c. APS mineral in a pyrophyllite groundmass at the core of a patchy feature. **e.** BSE image. Detail from panel a. Pyrite, rutile, diaspore, and APS minerals in a pyrophyllite groundmass at the core of a patchy feature. **f.** BSE image. Detail from panel e. APS minerals nucleate on diaspore, florencite, and alunite crystals; these occur in a pyrophyllite groundmass. muscovite and quartz occur in cavities. Thin section from plagioclase-phyric andesite (BTG-006; 540 m). Abbreviations: APS: aluminium-phosphate-sulphate minerals; Flor: florencite; Dia: diaspore; Mus: muscovite; Py: pyrite; Pyro: pyrophyllite; Qz: quartz; Rut: rutile.

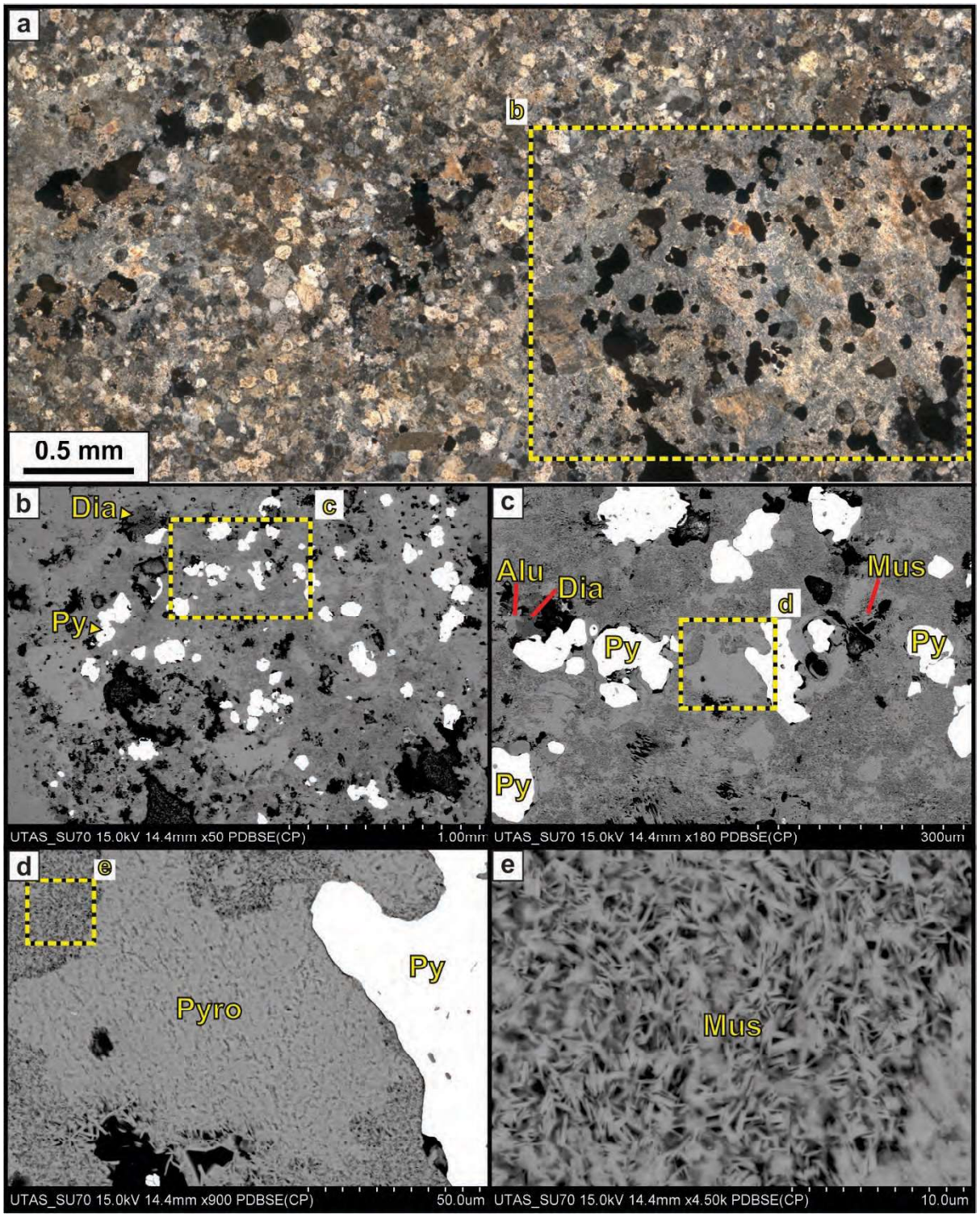

Figure 6.19. FE-SEM images from patchy-textured rocks from Bantug. a. Transmitted light photomicrograph of patchy feature. **b.** BSE image. Detail from panel a. Pyrite, diaspore, and APS minerals occur in a pyrophyllite groundmass. **c.** BSE image. Detail from panel b. Pyrite, diaspore, and alunite occur in a pyrophyllite groundmass. Muscovite occurs in cavities. **d.** BSE image. Detail from panel c. Pyrophyllite and muscovite groundmass at the core of a patchy feature. **e.** BSE image. Detail from panel d. Muscovite crystals in the groundmass of a patchy feature. Thin section from plagioclase-phyric andesite (BTG-005; 485.8 m). Abbreviations: Dia: diaspore; Mus: muscovite; Py: pyrite; Pyro: pyrophyllite.

6.4.3.3. Aluminium-phosphate-sulphate (APS) minerals in patchy-textured rocks

APS minerals were observed in the cores and fine-grained halos surrounding patchy features in the hydrothermally altered plagioclase-phyric andesites from Bantug. Four types of APS minerals were recognised: svanbergite ($Sr\ Al_3\ [PO_4]\ [SO_4]\ [OH_6]$), woodhouseite ($Ca\ Al_3\ [PO_4]\ [SO_4]\ [OH_6]$), weilerite ($Ba\ Al_3\ [PO_4]\ [OH_6]$), and florencite ($Ce\ Al_3\ [PO_4]\ [OH_6]$). Svanbergite and woodhouseite are the most common APS minerals in samples from Bantug; florencite and weilerite are rare.

APS minerals from the core of patchy features occur as anhedral zoned grains <40 µm diameter (Fig. 6.20c). APS mineral zonation typically follows distinct crystal facets (Fig. 6.21a to 6.21f). APS minerals were observed to nucleate on rutile (Fig. 6.20f), natroalunite (Fig. 6.21a and 6.21b), diaspore (Fig. 6.21e), and pyrite (Fig. 6.22a and 6.22b). Svanbergite is characterised by intense brightness on back-scattered electron (BSE) images, whereas woodhouseite is characterised by lower intensity to dull BSE brightness (Fig. 6.21e). Svanbergite was most frequently found in the core of APS minerals, and it is often characterised by rhythmic intergrowths with woodhouseite (Figs. 6.21a to 6.21f). Svanbergite-woodhouseite bands on APS minerals are <3 µm thick. Woodhouseite was also observed in the core of APS minerals, upon which svanbergite nucleated (Fig. 6.22f). Other APS mineral occurrences from the core of patchy features include anhedral woodhouseite masses of <40µm with abundant alunite inclusions of <5 µm, and weilerite inclusions of <1 µm (Figs. 6.22c and d). Florencite is rare, <10 µm diameter, and alunite was observed to nucleate on it. Florencite was also observed to nucleate on woodhouseite and anhydrite crystals (Figs. 6.22e and 6.22f; BTG-006 at 540 m).

Svanbergite is the dominant APS minerals in the fine-grained halos surrounding patchy features. It occurs as anhedral masses interlocked with anhedral quartz in a fine-grained pyrophyllite groundmass (Figs. 6.21a, 6.21b, and 6.21d).

Table 6.3 and Figure 6.23 summarize the energy dispersive X-ray spectroscopy (EDS) results from APS minerals in plagioclase-phyric andesite samples. These are compared with natroalunite results from patchy-textured plagioclase phyric andesites.

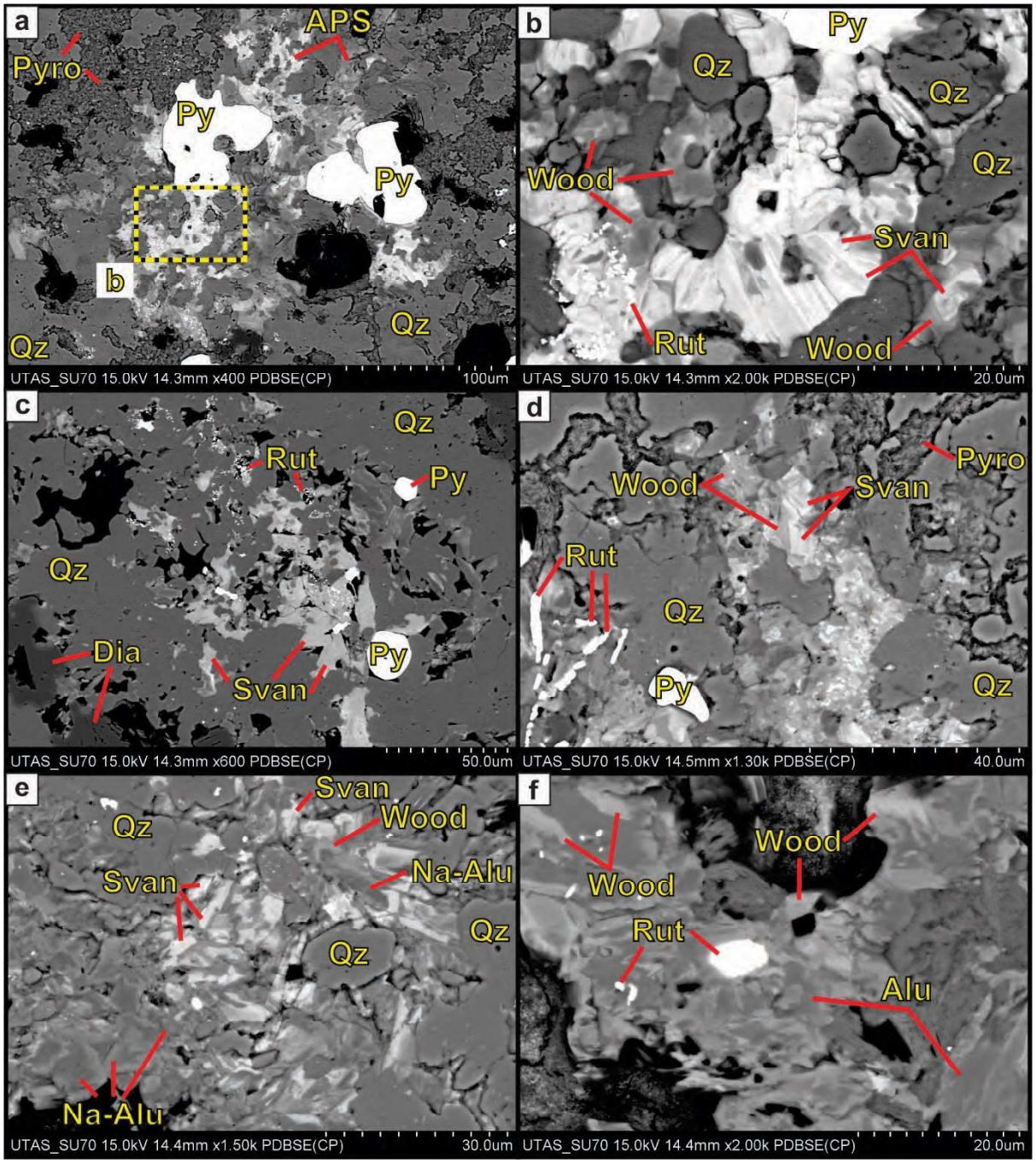

Figure 6.20. BSE images of APS minerals in patchy-textured rocks from Bantug. a. BSE image. Pyrite, APS minerals, and quartz in a pyrophyllite groundmass (BTG-003; 590 m). **b.** BSE image. Detail from a. APS minerals zonation varies from woodhouseite (dark; Ca-rich) to svanbergite (bright; Sr rich). APS minerals contain rutile inclusions, and are interlocked with quartz and pyrite crystals (BTG-003; 590 m). **c.** BSE image. Svanbergite crystals contain rutile inclusions; these are intergrown with quartz, pyrite and diaspore (BTG-003; 590 m). **d.** BSE image. Woodhouseite and svanbergite intergrown with quartz, pyrophyllite, and pyrite (BTG-003; 590 m). **e.** Svanbergite, woodhouseite, and natroalunite intergrown with quartz (BTG-003; 595.6 m). **f.** Woodhouseite intergrown with alunite; both contain rutile inclusions (BTG-003; 595.6 m). Thin sections from plagioclase-phyric andesites. Abbreviations: Alu: alunite; APS: aluminium-phosphate-sulphate mineral; Dia: diaspore; Na-alu: natroalunite; Py: pyrite; Pyro: pyrophyllite; Qz: quartz; Rut: rutile; Svan: svanbergite; Wood: woodhouseite.

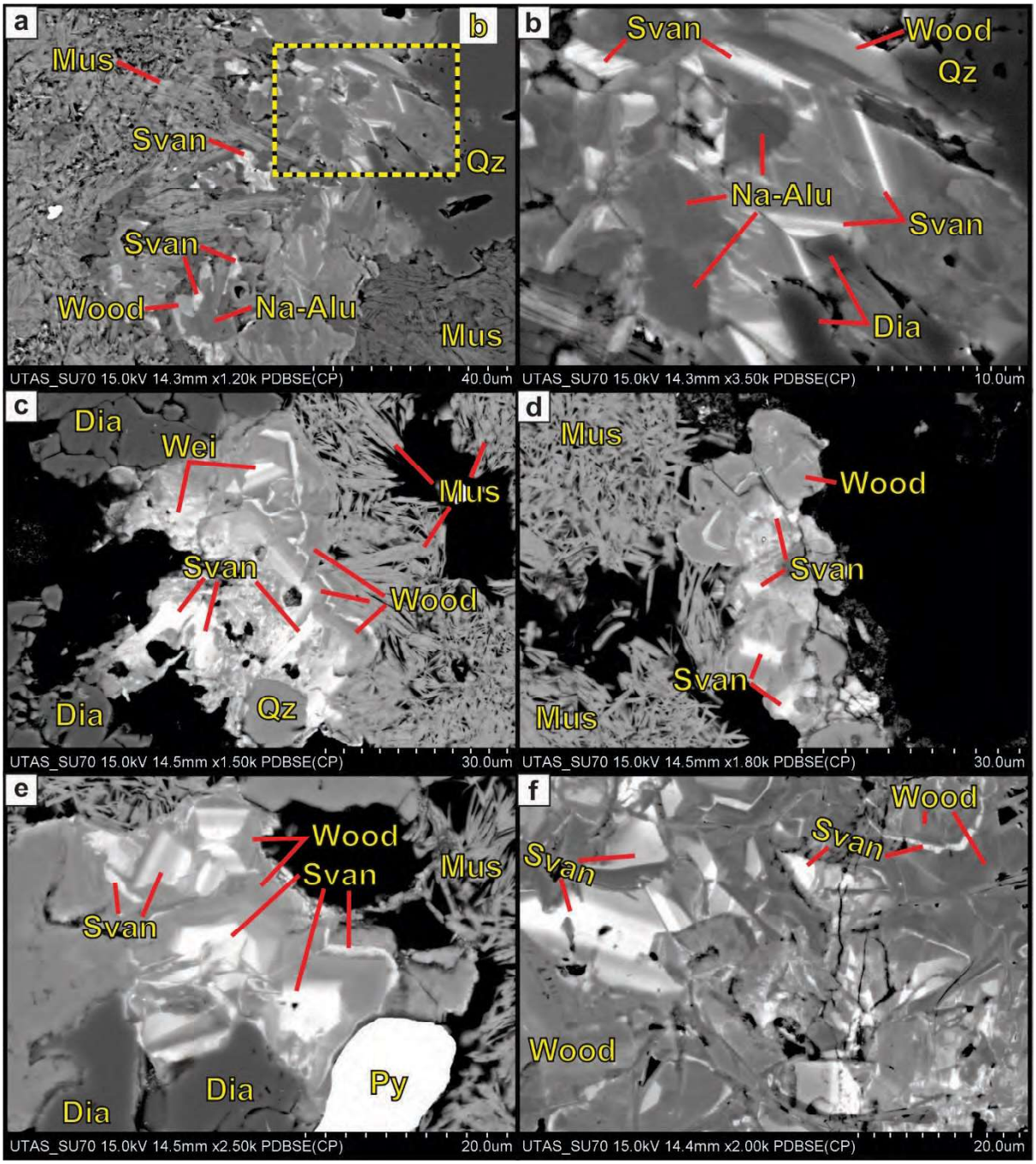

Figure 6.21. BSE images of APS minerals in patchy-textured rocks from Bantug. a. BSE image. Natroalunite, svanbergite, and woodhouseite intergrown with muscovite and quartz (BTG-003; 590 m). **b.** BSE image. Detail from g. svanbergite, woodhouseite, and natroalunite intergrown with quartz and diaspore (BTG-003; 590 m). **c.** BSE image. Weilerite (bright; Ba-rich APS mineral) intergrown with svanbergite and woodhouseite (BTG-005; 485.8 m). **d.** BSE image. Svanbergite-woodhouseite in a muscovite groundmass (BTG-005; 485.8 m). **e.** Svanbergite and woodhouseite intergrown with diaspore and pyrite in a muscovite groundmass (BTG-005; 485.8 m). **f.** Svanbergite and woodhouseite (BTG-005; 485.8 m). Thin sections from plagioclase-phyric andesites. Abbreviations: Alu: alunite; APS: aluminium-phosphate-sulphate mineral; Dia: diaspore; Mus: muscovite; Na-alu: natroalunite; Py: pyrite; Pyro: pyrophyllite; Qz: quartz; Svan: svanbergite; Wood: woodhouseite.

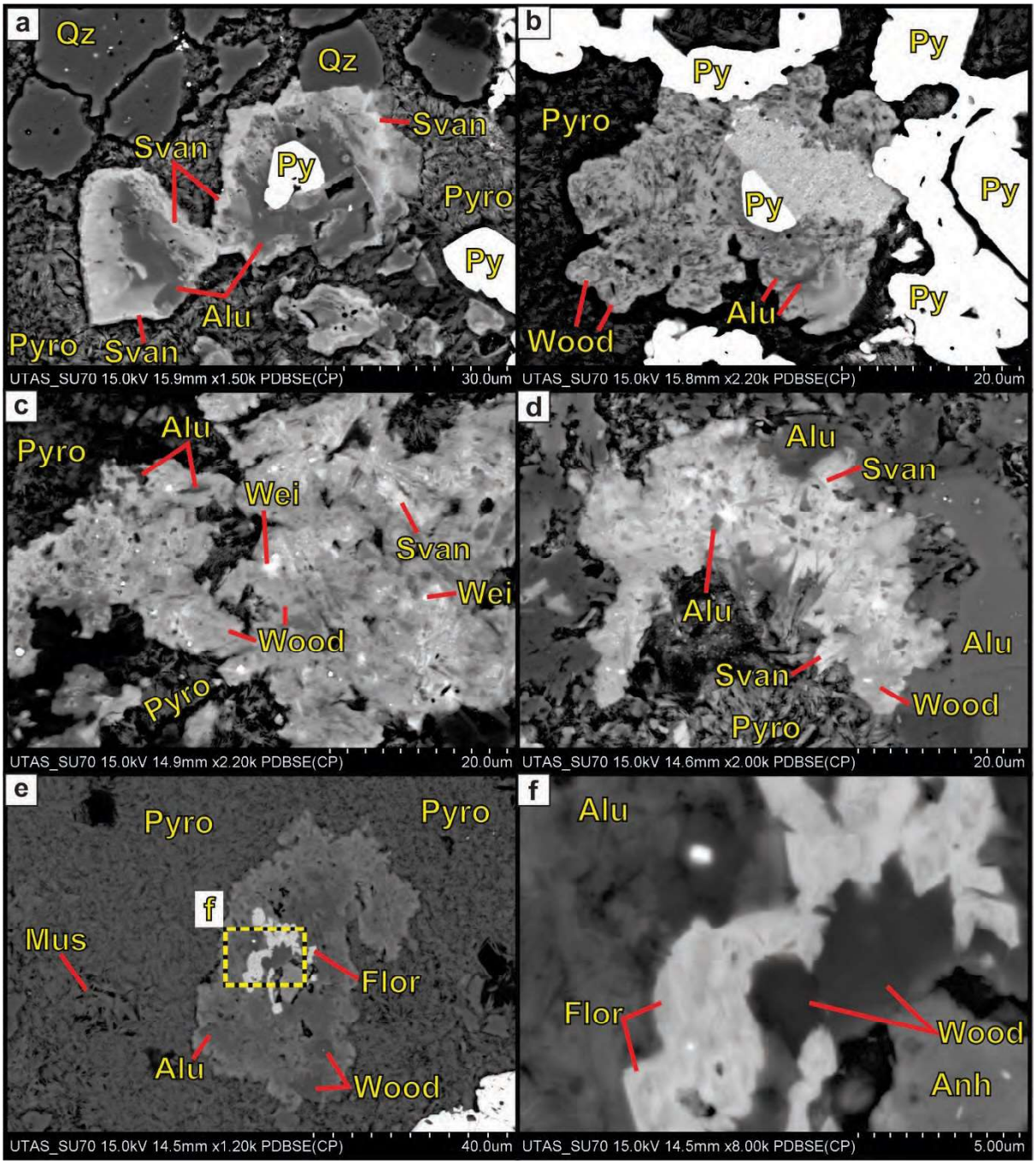

Figure 6.22. BSE images of APS minerals in patchy-textured rocks from Bantug. a. BSE image. Alunite and svanbergite nucleating on a pyrite crystal, these are in a pyrophyllite groundmass (BTG-006; 240.7 m). **b.** BSE image. Alunite-woodhouseite nucleated on a pyrite crystal, both in a pyrophyllite groundmass. (BTG-006; 240.7 m). **c.** BSE image. Alunite intergrown with woodhouseite, svanbergite, and weilerite; all in a pyrophyllite groundmass (BTG-006; 394 m). **d.** BSE image. Svanbergite intergrown with alunite in a pyrophyllite groundmass. (BTG-006; 394 m). **e.** BSE image. APS minerals in a pyrophyllite groundmass; muscovite crystals occur on cavities (BTG-006; 540 m). **f.** BSE image. Woodhouseite, florencite, and alunite nucleated on an anhydrite crystal (BTG-006; 540 m). Abbreviations: Alu: alunite; Anh: anhydrite; APS: aluminium-phosphate-sulphate mineral; Dia: diaspore; Flor: florencite; Mus: muscovite; Py: pyrite; Pyro: pyrophyllite; Qz: quartz; Svan: svanbergite; Wood: woodhouseite.

Strontium and Ba are ~10 times higher in svanbergite and weilerite, respectively, compared to other APS minerals (Table 6.3; Figures 6.23a, 6.23e, and 6.23f). APS minerals from BTG-005 contain higher Ca and Ba concentrations compared to those from other drill holes (Table 6.3; Fig. 6.23g). APS minerals from BTG-003 yielded the highest Sr results, and APS minerals from BTG-006 yielded slightly lower results than those from BTG-003 (Table 6.3; Fig. 6.23g).

Table 6.3. EDS Ca, Sr, and Ba results from APS minerals in patchy-textured rocks at Bantug

		Ca (%)				Sr (%)				Ba (%)		
Drill hole	***n***	**Min**	**Max**	**Mean**	***n***	**Min**	**Max**	**Mean**	***n***	**Min**	**Max**	**Mean**
BTG-003	*56*	0.2	6.8	1.5	*55*	0.5	13.8	7.3	*53*	0.1	5.0	1.4
BTG-005	*15*	1.6	7.9	3.8	*11*	0.7	1.8	1.1	*14*	0.5	13.6	4.8
BTG-006	*37*	0.8	9.2	3.3	*31*	0.2	12.7	5.5	*35*	0.1	26.8	4.1
		Ca				**Sr**				**Ba**		
Drill hole	***n***	**Min**	**Max**	**Mean**	***n***	**Min**	**Max**	**Mean**	***n***	**Min**	**Max**	**Mean**
Woodhouseite												
BTG-003	*12*	0.2	6.8	3.0	*13*	0.5	7.7	3.8	*13*	0.1	2.6	1.0
BTG-005	*8*	2.9	7.9	4.5	*5*	0.9	1.3	1.1	*7*	0.5	2.8	1.8
BTG-006	*20*	0.8	9.2	4.0	*14*	0.2	9.6	3.7	*19*	0.1	9.3	2.0
Svanbergite												
BTG-003	*44*	0.3	2.6	1.1	*42*	4.3	13.8	8.3	*40*	0.2	5.0	1.5
BTG-005												
BTG-006	*12*	1.3	5.3	2.6	*12*	5.0	12.7	8.2	*11*	0.2	3.3	1.3
Weilerite												
BTG-003												
BTG-005	*7*	1.63	4.33	3.02	*6*	0.7	1.76	1.01	*7*	1.19	13.6	7.8
BTG-006	*5*	1.49	2.66	1.93	*5*	3.42	4.54	4.12	*5*	13.3	26.8	18.3

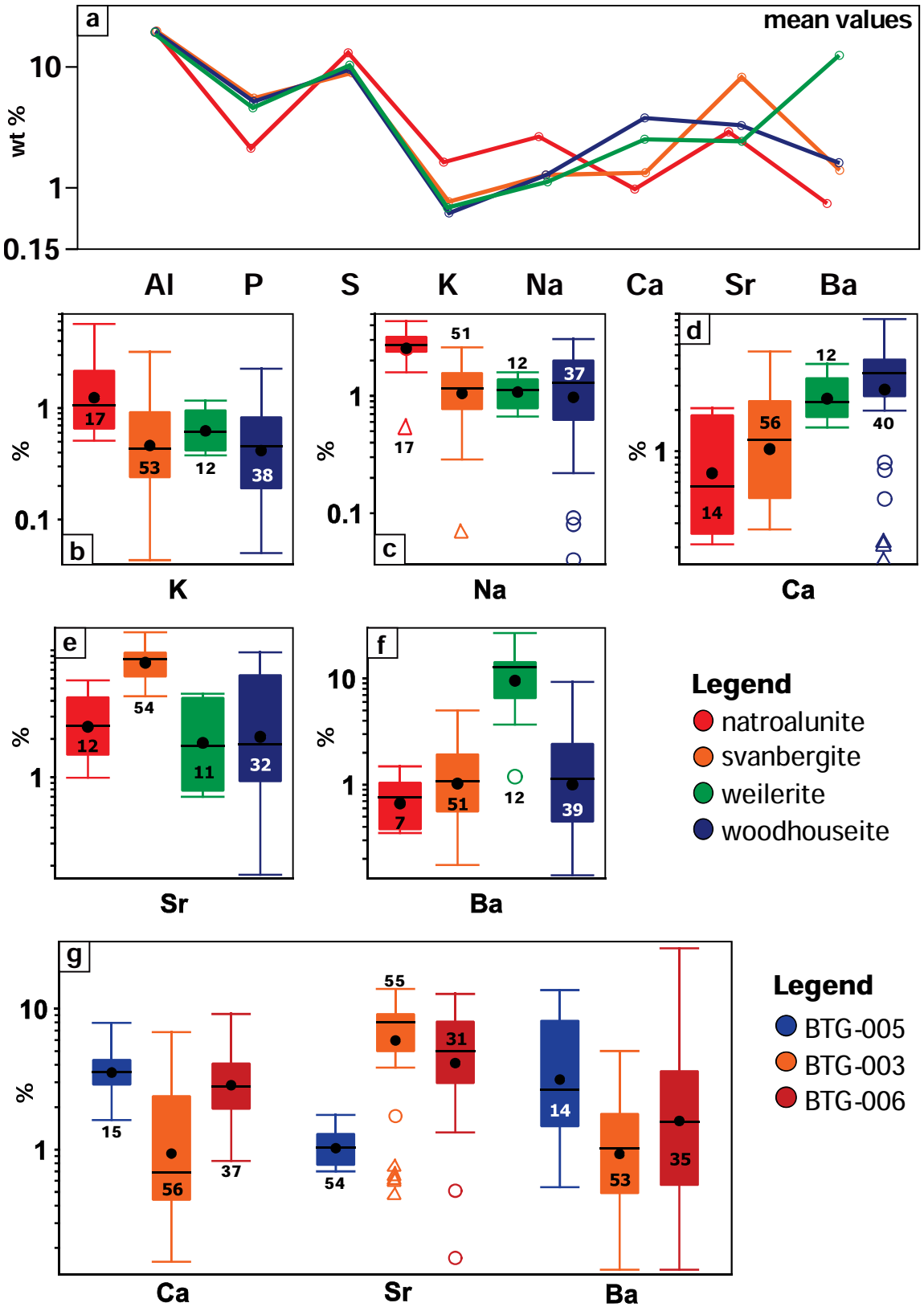

Figure 6.23. EDS results from APS minerals in patchy-textured rocks at Bantug. a. Parallel plot for mean values from different APS minerals. **b.** Box-plot for potassium (K) in APS minerals. **c.** Box-plot for sodium (Na) in APS minerals. **d.** Box-plot for calcium (Ca) in APS minerals. **e.** Box-plot for strontium (Sr) in APS minerals. **f.** Box-plot for barium (Ba) in APS minerals. **g.** Comparative box-plot for Ca, Sr, and Ba EDS results from APS minerals by drill hole. Numbers in boxes are number of analyses. Abbreviations: Ba: barium; Ca: calcium; K: potassium; Na: sodium; Sr: strontium.

6.4.3.4. Zunyite in patchy-textured rocks

Zunyite (Al_{13} Si_5 O_{20} [OH, F]$_{18}$ Cl) is a cubic mineral that can occur as tetrahedral or pseudo-octahedral crystals exclusively in advanced argillic-altered rocks. It is typically colourless, but can fluoresce red under UV light (Hsu, 1986; Keary, 2001). Zunyite may occur in altered rocks with fluorite, topaz, and sulfides (Meyer and Hemley, 1967).

Hsu (1986) conducted experiments on zunyite at 1 kb, 300°C to 600°C, with HCl concentrations of 1 m, and HF concentrations between 0.1 and 20 moles. He observed that zunyite was only stable below 450°C, and when HF concentrations of 0.1 to 2.0 moles were available. Hsu (1986) also observed that zunyite was replaced by topaz above 450°C when HF concentrations were greater than 2 moles. Hydrous aluminosilicates such as pyrophyllite, boehmite, gibbsite, and diaspore grew metastably during the early stages of the experiments. Hsu (1986) concluded that F and Cl are essential for zunyite formation but that higher F concentrations inhibit zunyite formation. This implies that the association of zunyite and topaz in some hydrothermal deposits may reflect fluctuations of HF and Cl concentrations in hydrothermal fluids, as well as temperature variations (Hsu, 1986).

Zunyite was observed in patchy-textured rocks from Bantug (Figs. 6.24 and 6.25). Zunyite crystals were found only in plagioclase-phyric andesite thin sections and mounts from drill hole BTG-006. These samples (i.e., two thin sections and eleven mounts), were collected between 204 m and 418 m depth in drill hole BTG-006. Zunyite occurs in the core of patchy features together with alunite, diaspore, APS minerals, pyrite, and rutile. These minerals occur in a fine-grained pyrophyllite-muscovite-altered groundmass (Figs. 6.24 and 6.25). Zunyite crystals are characterised by their high-relief (Fig. 6.24), are colourless, euhedral (i.e., isometric-hextetrahedral), and <200 μm in size (Figs. 6.24 and 6.25). Zunyite crystals were observed to contain pyrite inclusions (Figs. 6.24e and 6.24f), as well as diaspore and svanbergite inclusions (Fig.6.25b). Alunite and svanbergite had nucleated on zunyite crystals (Figs. 6.25a to 6.25e).

Table 6.4 and Figure 6.26 present EDS results from zunyite crystals on patchy textured rocks at Bantug. Fluorine content on zunyite crystals was observed to increase with depth in drill hole BTG-006 (Table 6.4; Fig. 6.26a). EDS analyses also detected chlorine in zunyite crystals, but no obvious variations in concentration were observed (Table 6.4; Fig. 6.26b).

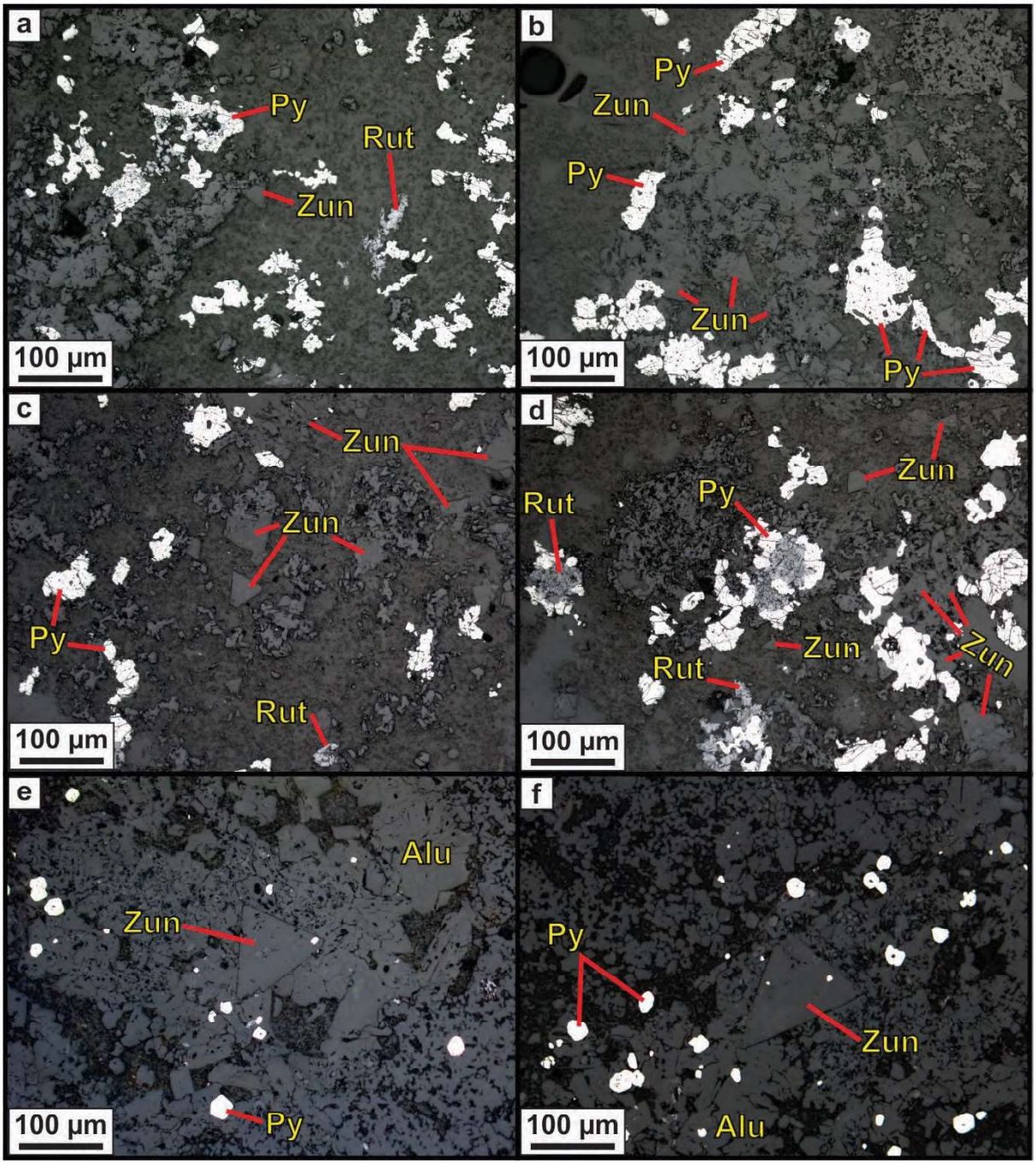

Figure 6.24. Zunyite crystals in patchy-textured rocks from Bantug. a. Reflected light micrograph. Zunyite, pyrite, and rutile crystals in a pyrophyllite-altered groundmass (BTG-006; 204 m). **b.** Reflected light micrograph. Zunyite and pyrite crystals in a pyrophyllite-altered groundmass (BTG-006; 204 m). **c.** Reflected light micrograph. Zunyite, pyrite, and rutile crystals in a pyrophyllite groundmass (BTG-006; 204 m). **d.** Reflected light micrograph. Pyrite nucleated on rutile crystals; these occur with zunyite in a pyrophyllite-altered groundmass (BTG-006; 204 m). **e.** Reflected light micrograph. Zunyite, alunite, and pyrite occur in a pyrophyllite-altered groundmass (BTG-006; 261 m). **f.** Reflected light micrograph. Zunyite, alunite, and pyrite occur in a pyrophyllite-altered groundmass (BTG-006; 261 m). Abbreviations: Alu: alunite; Py: pyrite; Rut: rutile; Zun: zunyite.

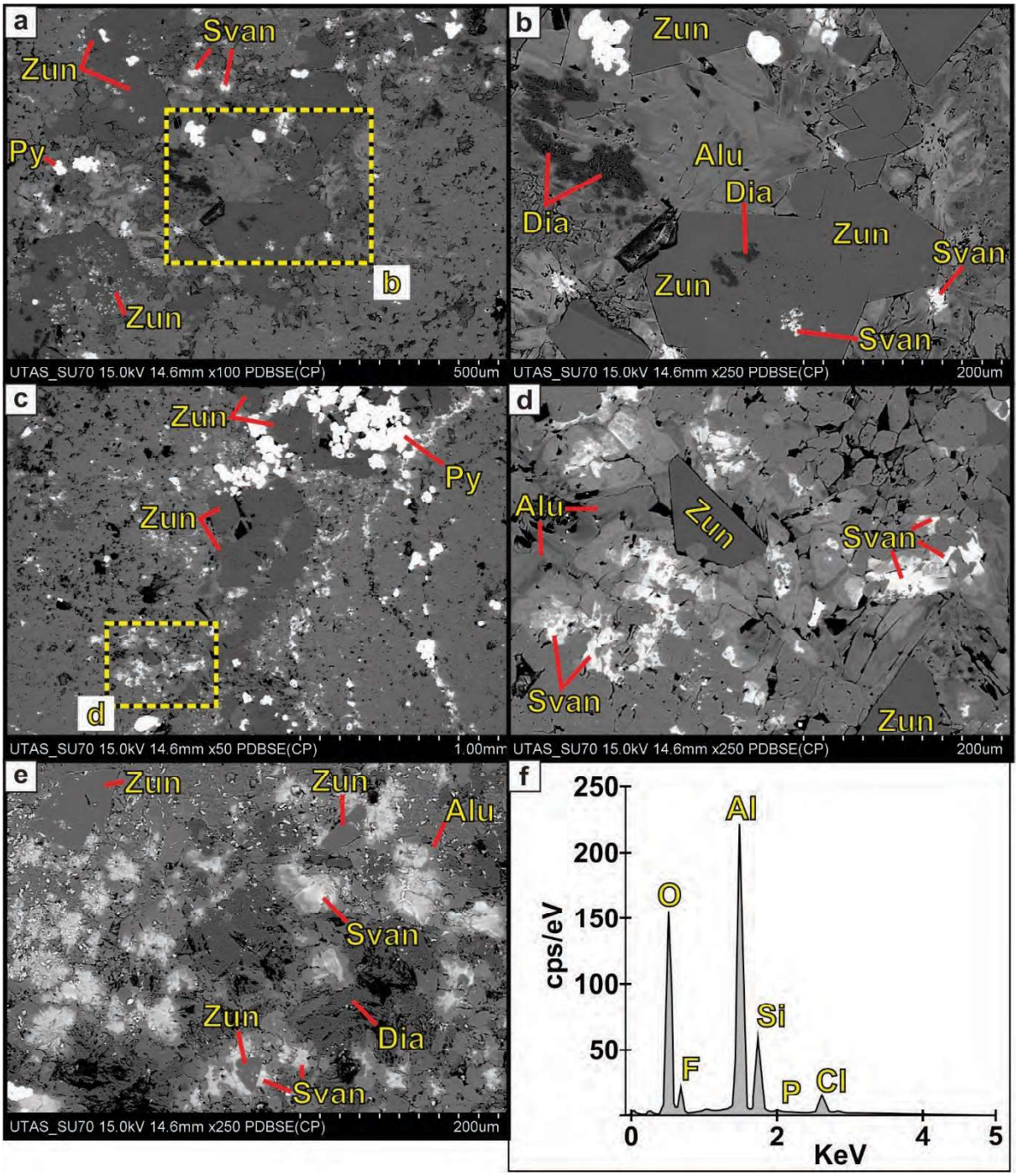

Figure 6.25. FE-SEM BSE images and EDS spectra from zunyite crystals in patchy-textured rocks from Bantug. a. BSE image. Zunyite crystals in an alunite-altered groundmass; alunite contains svanbergite (BTG-006; 241 m). **b.** BSE image. Detail from panel a. **c.** BSE image. Zunyite and pyrite crystals in an alunite-quartz-altered groundmass (BTG-006; 241 m). **d.** BSE image. Detail from panel c. Alunite and svanbergite nucleated on zunyite crystals. **e.** BSE image. Alunite and svanbergite nucleated on zunyite crystals. (BTG-006; 418 m). **f.** EDS spectra of zunyite crystal in panel j. Abbreviations: Alu: alunite; Py: pyrite; Rut: rutile; Svan: svanbergite; Zun: zunyite; Al: aluminium; Cl: chlorine; F: fluorine; O: oxygen; P: phosphorus; Si: silicon.

Table 6.4. FE-SEM EDS analyses of zunyite crystals from patchy-textured plagioclase-phyric andesites at Bantug

Spot ID	O (%)	F (%)	Na (%)	Al (%)	Si (%)	P (%)	S (%)	Cl (%)	Total
BTG-006; 250 m									
C1-S6	47.8	6.7	0.0	32.0	10.1	0.6	0.0	2.8	100
C1-S12	47.6	6.5	0.0	32.0	10.3	0.6	0.0	3.0	100
C4-S76	48.2	6.3	0.0	31.3	9.7	0.9	0.8	2.9	100
C5-S89	50.1	4.6	0.0	31.9	7.4	0.9	2.9	2.2	100
BTG-006; 269.9 m									
C1-S101	48.1	6.4	0.0	31.8	10.7	0.0	0.0	3.0	100
C1-S106	47.5	6.8	0.0	31.7	11.0	0.0	0.0	3.0	100
C2-S118	47.7	6.7	0.0	0.0	31.9	10.8	0.0	2.9	100
C2-S126	47.3	7.0	0.0	0.0	31.4	11.3	0.0	3.0	100
C3-S136	46.9	7.1	0.0	31.8	11.3	0.0	0.0	2.9	100
C3-S135	46.4	8.0	0.0	32.3	10.0	0.6	0.0	2.7	100
BTG-006; 418.5 m									
C1-S246	45.3	9.0	0.3	31.6	10.0	0.8	0.5	2.6	100
C1-S251	46.0	8.0	0.2	32.9	9.9	0.5	0.0	2.5	100
C6-S327	45.8	6.7	0.2	32.1	11.6	0.4	0.3	2.9	100
C7d-S349	45.6	8.4	0.0	31.6	10.8	0.5	0.3	2.9	100
C7d-S350	45.8	7.5	0.2	32.1	10.9	0.4	0.3	2.8	100
C7d-S351	45.6	7.5	0.2	32.1	11.0	0.4	0.3	3.0	100
C7d-S353	45.7	7.7	0.2	31.8	11.1	0.3	0.3	2.9	100
C7-S339	44.5	8.8	0.2	32.8	10.2	0.6	0.2	2.7	100

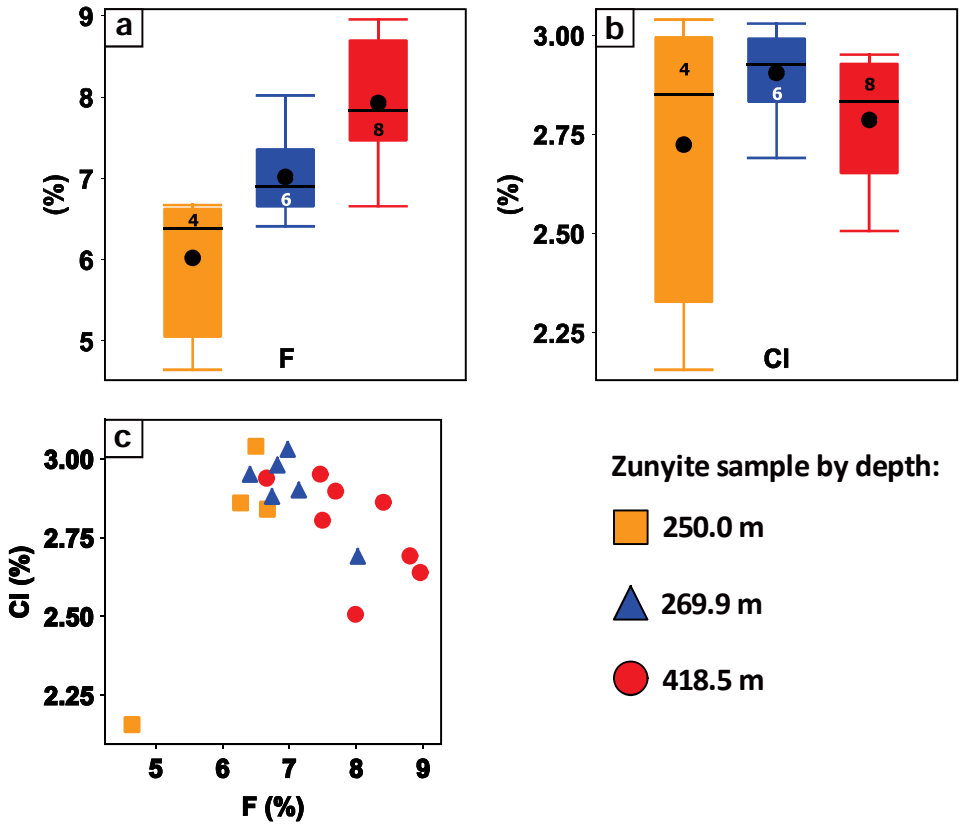

Figure 6.26. FE-SEM EDS results from zunyite crystals in patchy-textured plagioclase-phyric andesites from Bantug. a. Box-plot for fluorine. **b.** Box-plot for chlorine. **c.** Chlorine vs fluorine diagram. Numbers in boxes are number of analyses. Abbreviations: Cl: chlorine; F: fluorine.

6.4.3.5. Rutile in patchy-textured rocks

Rutile was commonly observed in thin sections and polished mounts from patchy-textured plagioclase-phyric andesites from Bantug. Rutile occurs in the core of patchy features with alunite, diaspore, APS minerals, pyrite, and zunyite. Rutile was observed disseminated in the pyrophyllite-muscovite-altered groundmass and as inclusions in pyrite grains. Rutile in patchy textures is very fine-grained (<10 μm), and its habit is acicular or anhedral (Figs. 6.27 and 6.28). Anhedral masses of rutile are <10 μm diameter (Figs. 6.27a to 6.27c), whereas acicular rutile occur as clusters of <60 μm (Figs. 6.27c and 6.27d). Individual rutile crystals are <30 μm long and ~1 μm thick (Figs. 6.28a, 6.28b, and 6.28e). Acicular rutile was commonly observed as clusters in the pyrophyllite-altered groundmass (Figs. 6.28a and 6.28e), and in some cases intergrown with pyrite (Figs. 6.27d, 6.28a, 6.28b). Alunite and svanbergite were observed to nucleate on anhedral masses of rutile (Figs. 6.28c and 6.28d).

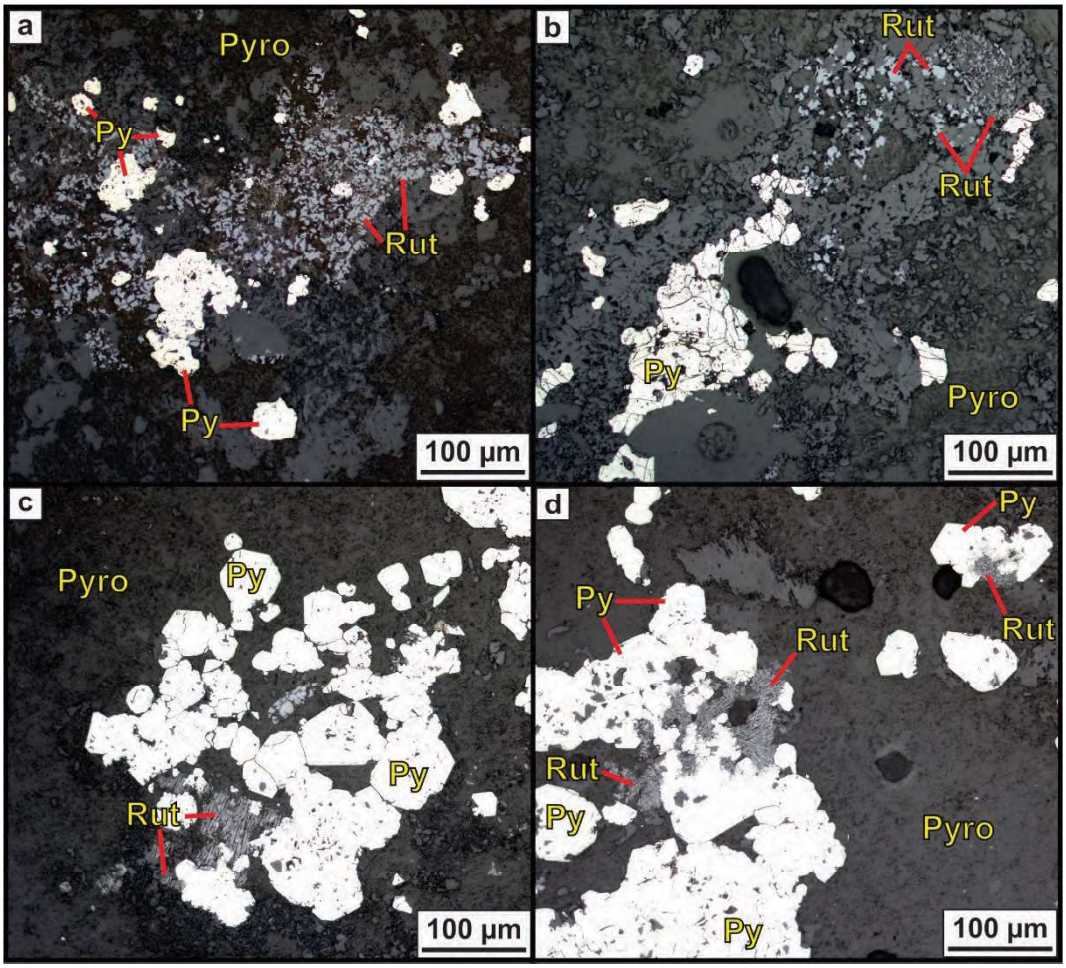

Figure 6.27. Rutile in patchy-textured rocks from Bantug. a. Reflected light micrograph. Pyrite and rutile in a pyrophyllite groundmass (BTG-006; 261 m). **b.** Reflected light micrograph. Pyrite and rutile in a pyrophyllite groundmass (BTG-006; 204 m). **c.** Reflected light micrograph. Euhedral pyrite crystals and rutile in a pyrophyllite groundmass (BTG-006; 204 m). **d.** Reflected light micrograph. Euhedral pyrite crystals and rutile in a pyrophyllite groundmass (BTG-006; 204 m). Abbreviations: Py: pyrite; Pyro: pyrophyllite; Qz: quartz; Rut: rutile.

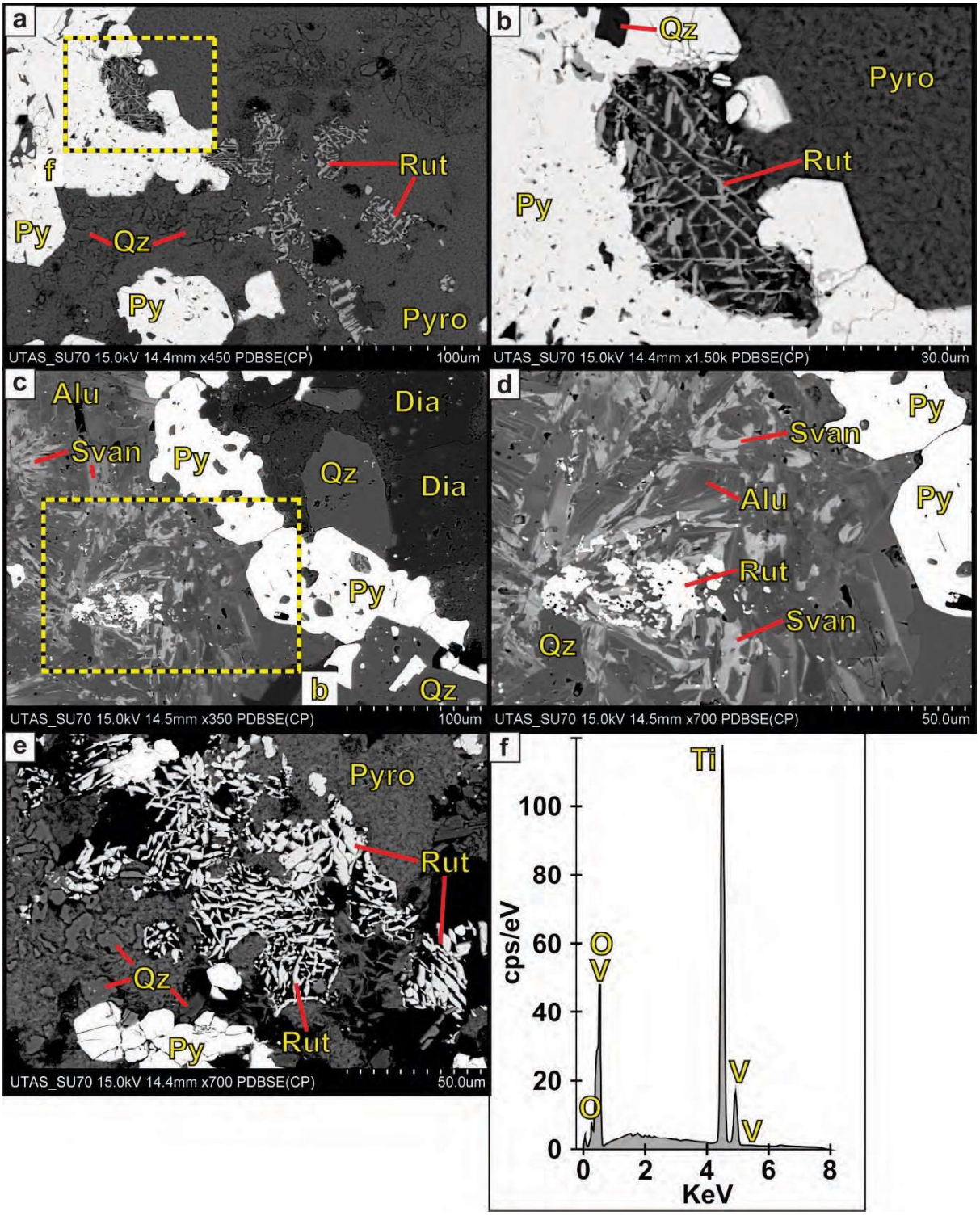

Figure 6.28. FE-SEM BSE images from rutile in patchy-textured rocks from Bantug. a. BSE image. Pyrite and rutile in a pyrophyllite-quartz-altered groundmass (BTG-006; 204 m). **b.** BSE image. Detail from panel a. Rutile and pyrite in a pyrophyllite-altered groundmass (BTG-006; 204 m). **c.** BSE image. Rutile intergrown with alunite and svanbergite; these, quartz, and diaspore occur in a pyrophyllite-altered groundmass (BTG-003; 590 m). **d.** BSE image. Detail from panel c. Rutile intergrown with alunite and svanbergite. **e.** BSE image. Rutile and pyrite in a pyrophyllite-quartz-altered groundmass. (BTG-006; 540 m). **f.** EDS spectra. Data acquire from crystal in panel e (BTG-006; 540 m). Abbreviations: Alu: alunite; Dia: diaspore; O: oxygen; Py: pyrite; Pyro: pyrophyllite; Qz: quartz; Rut: rutile; Svan: svanbergite; Ti: titanium; V: vanadium.

6.4.3.6. Cathodoluminescence analyses of quartz in patchy textured-rocks

Cathodoluminescence (CL) studies revealed that the quartz groundmass of patchy-textured plagioclase-phyric andesites from Bantug is made of clusters of quartz grains (Fig. 6.29). These clusters are made of large amounts of individual, very fine-grained (<10 μm), zoned quartz crystals (Fig. 6.29).

Individual quartz crystals are subhedral-anhedral, subrounded, mostly <10 μm diameter, and some are between 20 μm and 50 μm diameter (Figs. 6.29c and 6.30). Despite their subrounded appearance, quartz crystals also display defined euhedral crystals facets (Figs. 6.30a and 6.30b). Zonation varies from CL-dark cores to CL-bright rims (Figs. 6.29 and 6.30).

Figure 6.30 presents detailed images of quartz crystals together with interpretative sketches. The images revealed that single quartz crystals are in contact with each other along euhedral-subhedral facets. Quartz crystals nucleated on anhedral pyrite grains of <50 μm. Some quartz crystals have CL- dark cores close to or in contact with anhedral pyrite grains (Fig. 6.30).

Single quartz crystals can have complex and variable internal zonation. At least five stages of quartz were identified (Fig. 6.30e and 6.30f). Most quartz crystals are characterised by an anhedral CL-dark core mostly <10 μm diameter (i.e., Qz II; Figs. 6.30e and 6.30f). Qz II commonly contains anhedral CL-bright, <5 μm diameter quartz inclusions (i.e., Qz I; Figs. 6.30e and 6.30f). Qz II and Qz I are followed by a CL-bright quartz stage, Qz III which is characterised by distinctive subrounded-euhedral-subhedral crystal facets (Figs. 6.30e and 6.30f). Qz III makes up most of the volume of individual quartz crystals. Thin CL-dark lines within Qz III denote distinctive crystal facets (Figs. 6.30e and 6.30f). Later quartz stages (i.e., Qz IV and Qz V), are thin (i.e., <2 μm), exhibit CL-dark responses, and are located along the margins of Qz III.

Pyrite in the groundmass is ubiquitous, and at least two stages were identified: i) anhedral pyrite, and ii) pyrite veins. Anhedral pyrite occurred early and Qz I is nucleated onto it (Figs. 6.29 and 6.30). Pyrite veins cross-cut the groundmass (Fig. 6.29), and in some samples at least two stages of pyrite veins can be identified (Fig. 6.29b).

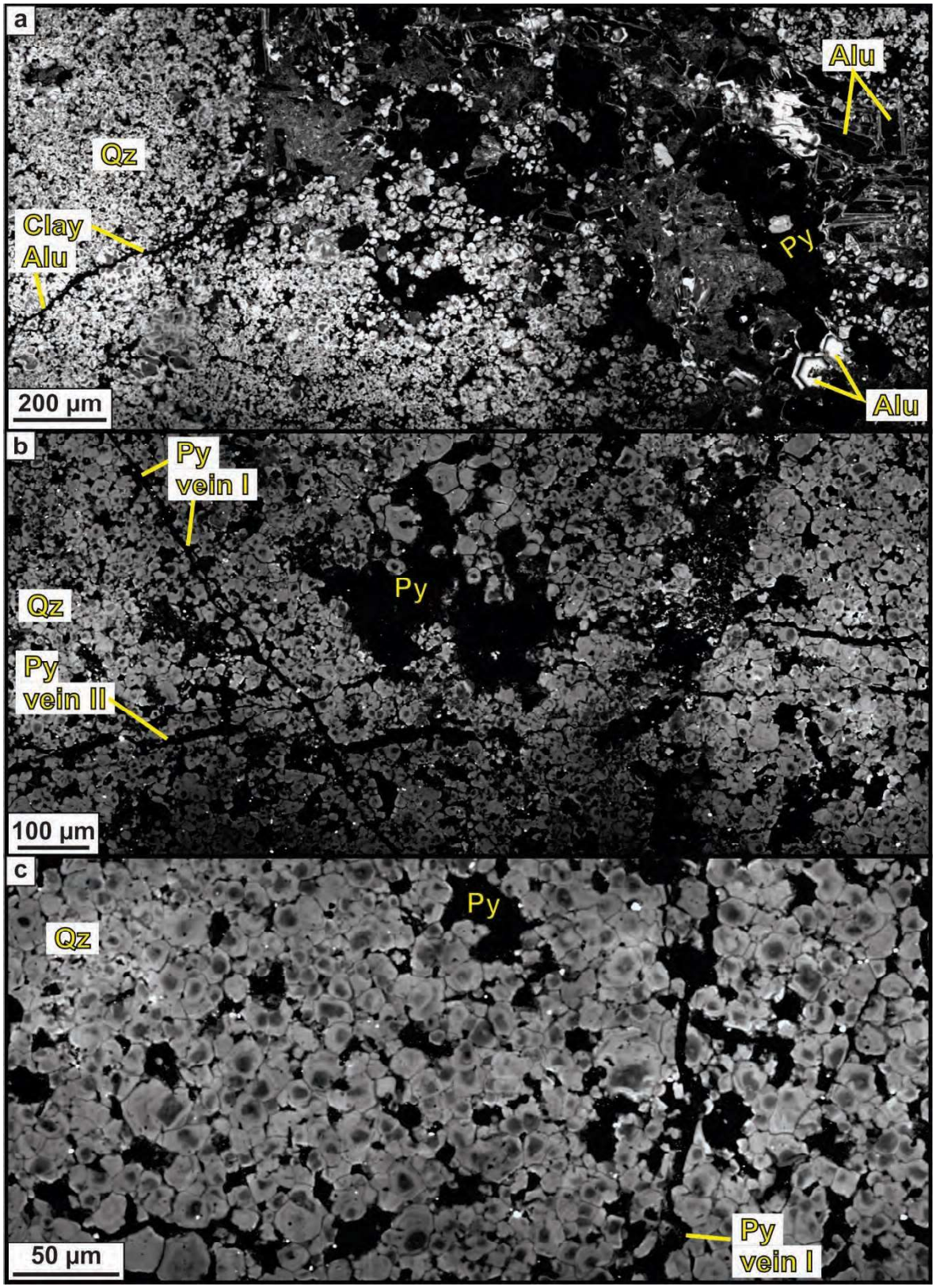

Figure 6.29. Cathodoluminescence images of fine-grained granular quartz groundmass in patchy-textured plagioclase-phyric andesites from Bantug. a. Alunite and pyrite on a fine-grained, granular quartz-groundmass. Imaged area: 1.9 mm by 0.9 mm (BTG-006; 241 m). **b.** Pyrite, alunite and pyrophyllite in a fined-grained, granular, quartz-groundmass; pyrite-pyrophyllite veins cross-cut the groundmass. Imaged area: 1.3 mm by 0.6 mm (BTG-006; 241 m). **c.** fined-grained, granular, quartz groundmass. Imaged area: 434 µm by 200 µm (BTG-003; 383 m). Abbreviations: Alu: alunite; Py: pyrite; Qz: quartz.

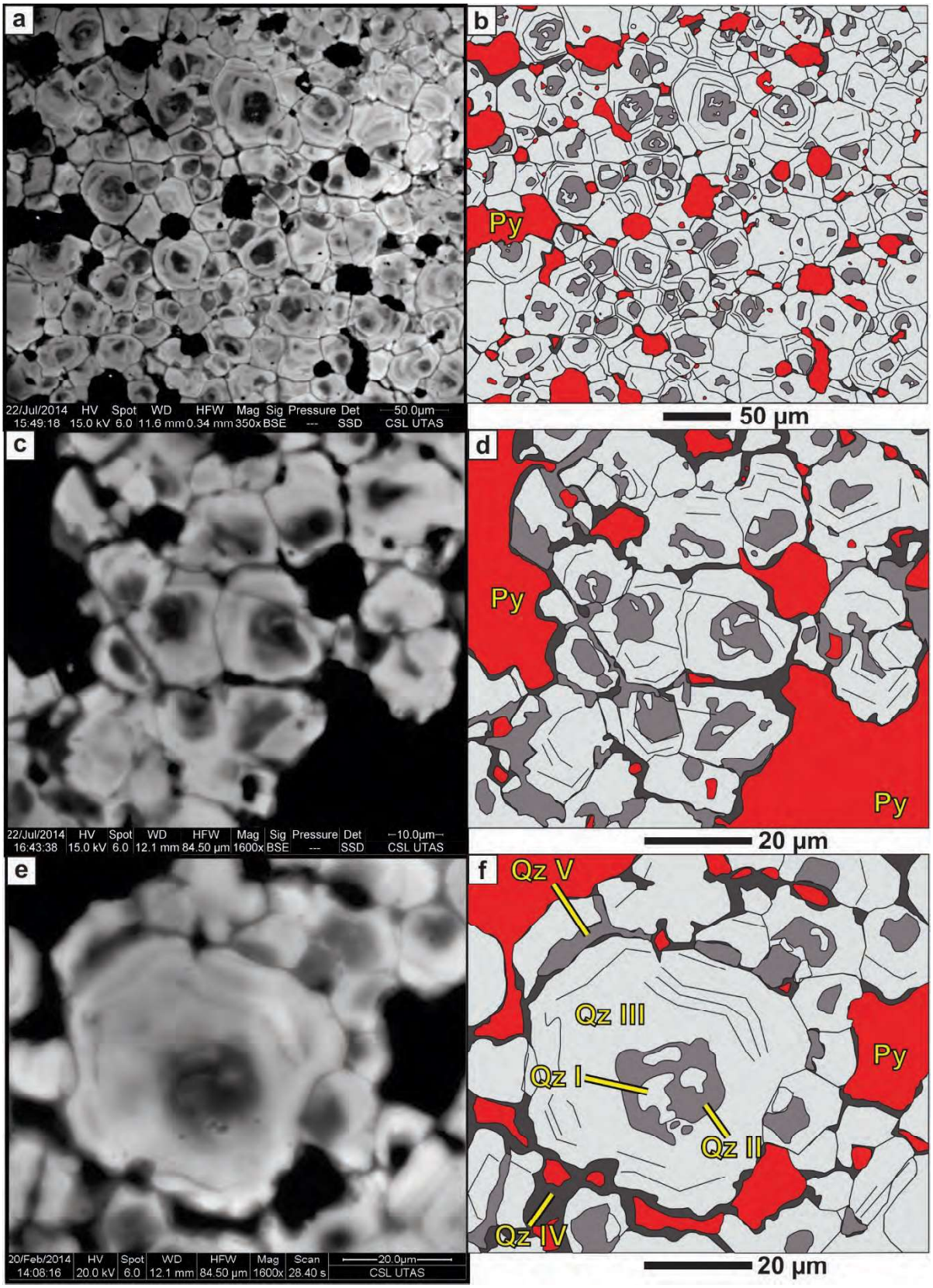

Figure 6.30. Cathodoluminescence images and interpretative sketches of groundmass quartz in patchy-textured plagioclase-phyric andesites from Bantug. a. CL image. Zoned quartz crystals nucleated on pyrite (BTG-006; 241 m). **b.** Sketch of CL image on panel a. **c.** CL image. Zoned quartz crystals nucleated on pyrite (BTG-003; 383.1 m). **d.** Sketch of CL image on panel c. **e.** CL image. Detail of zoned quartz crystal (BTG-006; 241 m). **f.** Sketch of CL image on panel e. At least five stages of quartz were recognized during analyses, I to V. Abbreviations: Py: pyrite; Qz: quartz.

6.4.3.7. X-ray diffraction analyses of patchy texture mineralogy

Nine patchy-textured plagioclase-phyric andesite samples from the lithocap at Bantug were analysed using X-ray diffraction (XRD). A summary of the results is presented in Table 6.5 and Figure 6.31. Figure 6.31 presents XRD profiles from selected samples, and Appendix J contains results and XRD profiles from all samples.

Five patchy-textured samples were analysed from drill hole BTG-006, one sample from BTG-005, and another one from BTG-003. Two types of samples were prepared for XRD analyses: whole rock crushed powders, and selective powders from patchy features (Table 6.5). Patchy features were selectively analysed from three samples (Table 6.5; Fig. 6.31c). Alunite was the most common mineral detected in all samples. The XRD profile peak at 31 2θ (degrees) was the distinctive feature which aided alunite identification (Fig. 6.31). Other minerals commonly detected include quartz, pyrite, pyrophyllite, and muscovite (Fig. 6.31).

XRD analyses aimed to characterise the type of quartz present in the groundmass of patchy-textured rocks. Results suggest the groundmass is made of quartz; no evidence for the presence of opal was found.

Table 6.5. XRD results from patchy-textured plagioclase-phyric andesites from Bantug

Sample ID	Drill hole	Depth (m)	Alteration type	XRD results
68969	BTG-005	506.5	Advanced argillic	Alunite, pyrophyllite, quartz, pyrite
67900[1]	BTG-003	595.7	Phyllic	Alunite, muscovite, quartz pyrite
67028	BTG-006	261	Advanced argillic	Alunite, quartz, pyrite
67826	BTG-006	270.1	Advanced argillic	Alunite, quartz, pyrite
67040a	BTG-006	390.75	Advanced argillic	Alunite, quartz, pyrophyllite, pyrite
67040b[1]	BTG-006	391.1	Advanced argillic	Alunite, quartz, pyrophyllite, pyrite
67055b[1]	BTG-006	541	Phyllic	Alunite, pyrophyllite, muscovite, pyrite, quartz

[1]Whole rock and selective samples were prepared and analysed from this rock samples

6.4.3.8. Electron probe micro analyser results from groundmass quartz

Squared rock-chips of approximately 0.5 cm by 0.5 cm were prepared from the granular quartz-altered groundmass of patchy-textured plagioclase-phyric andesites from drill hole BTG-006. The rock-chips were mounted on epoxy for EPMA analyses. CL images were collected, as well as Al, Fe, and Ti concentrations. CL images from mounts are presented in Appendix M. Details and results from EPMA analyses are presented in Appendix N.

Table 6.6 and Figures 6.32 to 6.34 present CL images and a EPMA results from the quartz-altered groundmass. Concentric zoned quartz crystals from the groundmass were selected for EPMA spot analyses, and a 5 μm beam size was used.

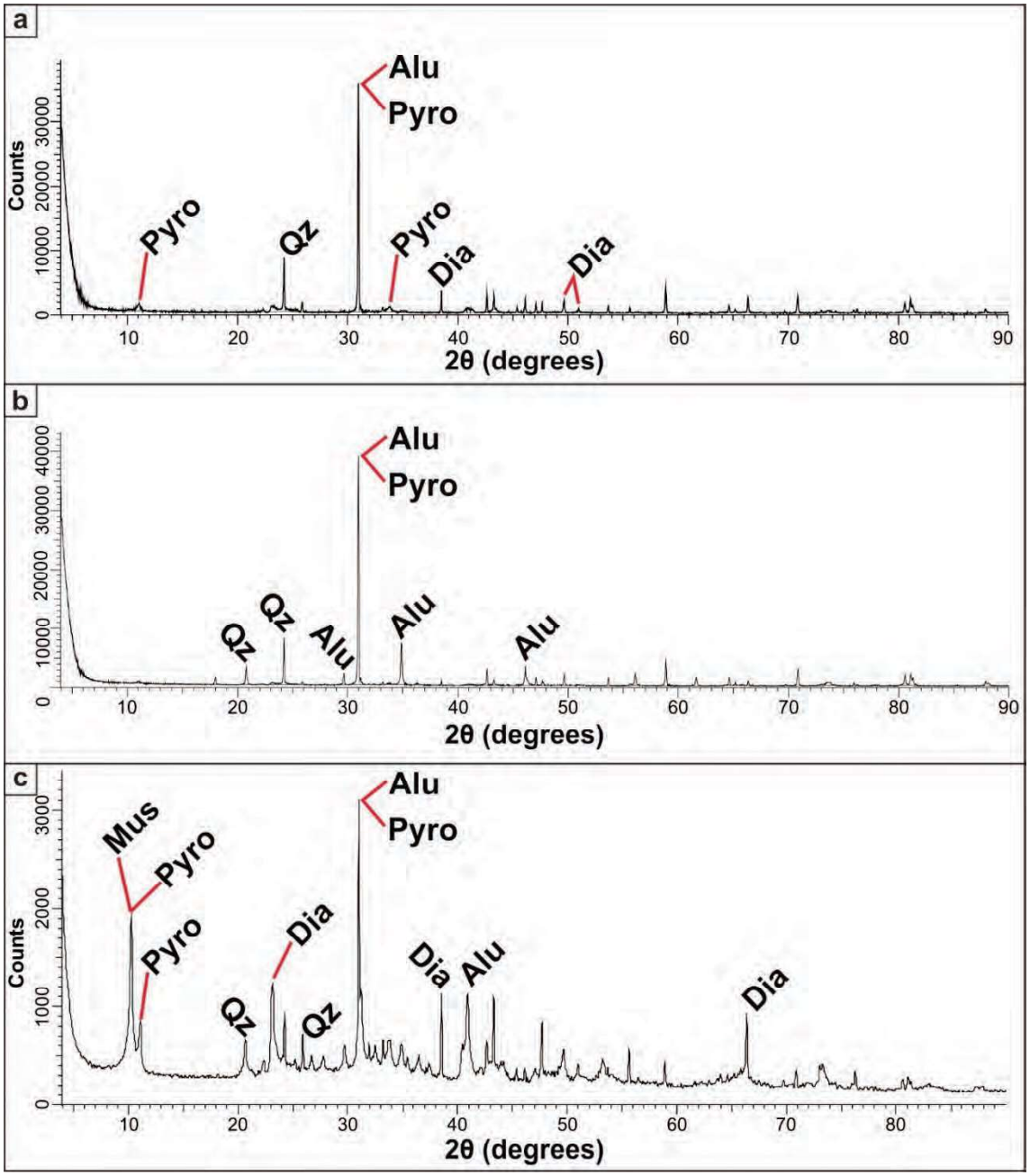

Figure 6.31. XRD profiles from patchy-textured rocks from Bantug. a. Analysis of patchy feature (BTG-006, 391.5 m; analysis 67040). **b.** Whole rock sample (BTG-006, 261 m; analysis 67028). **c.** Analysis patchy feature (BTG-006, 541 m; analysis 67055). All samples are plagioclase-phyric andesites. Abbreviations: Alu: alunite; Dia: diaspore; Mus: muscovite; Pyro: pyrophyllite; Py: pyrite; Qz: quartz.

Granular quartz grains from the sample collected from 204 m depth in BTG-006 are <15 µm diameter, anhedral to subrounded, and display concentric zonation (Figs. 6.32a, 6.32b, and 6.32c). The core of quartz crystals display CL-dark response and contains few CL-bright inclusions (Fig. 6.32c). Most of quartz-altered groundmass area in this sample has CL-bright response (Fig. 6.32a).

Quartz grains from the sample collected from 241 m depth are anhedral, elongated, <30 μm in the longer dimension, and have concentric zonation pattern (Fig. 6.33). Most of the quartz-altered groundmass in this sample has a CL-dark response (Figs. 6.33a and 6.33d). The crystals in this samples are characterised by CL-dark responses in their cores (Fig. 6.33c and 6.33e). Quartz crystals in the sample located at 261 m depth are anhedral, rounded to subrounded, and < 20 μm diameter (Fig. 6.34). Quartz grains display concentric zonation, and cores have both dark and CL-bright responses (Figs. 6.34b and 6.34e). Most of the quartz-altered groundmass area on this sample has a CL-bright response (Figs. 6.34a and 6.34d).

EPMA results revealed that aluminium concentrations in CL-dark zones are higher than in CL-bright zones (Table 6.6; Figure 6.35a and 6.345b). Also, that iron contents are very similar in CL-dark and CL-bright zones (Table 6.6; Figure 6.35c and 6.345d). However, iron results from CL-dark zones at 241 m depth are slightly higher than those from CL-bright zones (Table 6.6; Figure 6.35c and 6.345d). Titanium EPMA results revealed that concentrations in CL-bright zones are significantly higher than in CL-dark zones (Table 6.6; Figure 6.35e and 6.345f). EPMA results also revealed that Al, Fe, and Ti concentrations decrease with depth in drill hole BTG-006 (Table 6.6; Figure 6.35a to 6.345f).

Table 6.6. EMPA results from quartz in patchy-wormy textures

Spot ID	CL response	Al (ppm)	Fe (ppm)	Ti (ppm)
BTG-006; depth: 204 m				
67818g-3-1a	Dark	4,987	1,816	151
67818g-3-1b	Bright	3,030	1,749	375
67818g-3-1c	Bright	3,745	1,573	462
67818g-4-1a	Dark	2,460	1,640	151
67818g-4-1b	Bright	2,456	2,856	427
67818g-4-1c	Bright	1,206	1,158	321
BTG-006; depth: 241 m				
67026g-3-1a	Dark	3,521	1,594	13
67026g-3-1b	Bright	2,639	1,937	636
67026g-3-1c	Bright	1,213	1,148	273
67026g-3-1d	Dark	2,626	2,257	31
67026g-3-2a	Dark	1,318	2,761	38
67026g-3-2b	Dark	2,645	2,741	31
67026g-3-2c	Dark	3,275	2,103	22
BTG-006; depth: 261 m				
67028g-3-1a	Bright	23,674	1,389	221
67028g-3-1b	Bright	593	2,043	220
67028g-3-1c	Bright	750	1,216	235
67028g-3-2a	Bright	471	276	122
67028g-3-2b	Dark	443	284	123
67028g-3-2c	Bright	694	338	128
67028g-3-2d	Bright	1,125	446	383

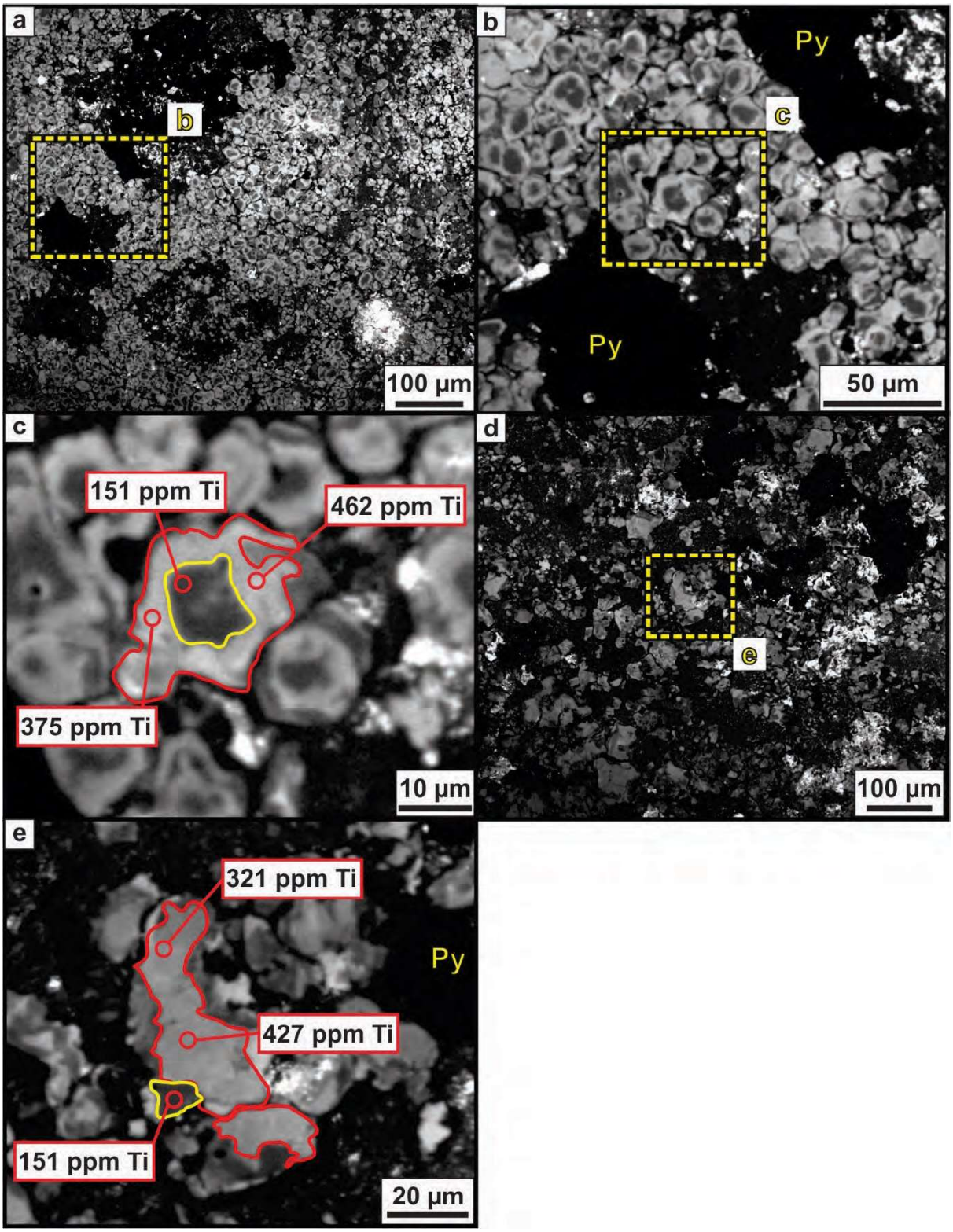

Figure 6.32. CL images and EPMA results from quartz in patchy texture groundmass. a. Pyrite and pyrophyllite on a fine-grained, zoned quartz groundmass. **b.** Detail from panel a. **c.** Detail from panel b. Zoned quartz crystal; bright CL areas are Ti-rich. **d.** Zoned quartz crystals and pyrite in a pyrophyllite groundmass. **e.** Detail from panel d. Zoned quartz crystal, bright CL areas are Ti-rich. Plagioclase-phyric andesite sample from drill hole BTG-006 at 204 m depth. Abbreviations: Py: pyrite; Ti: titanium.

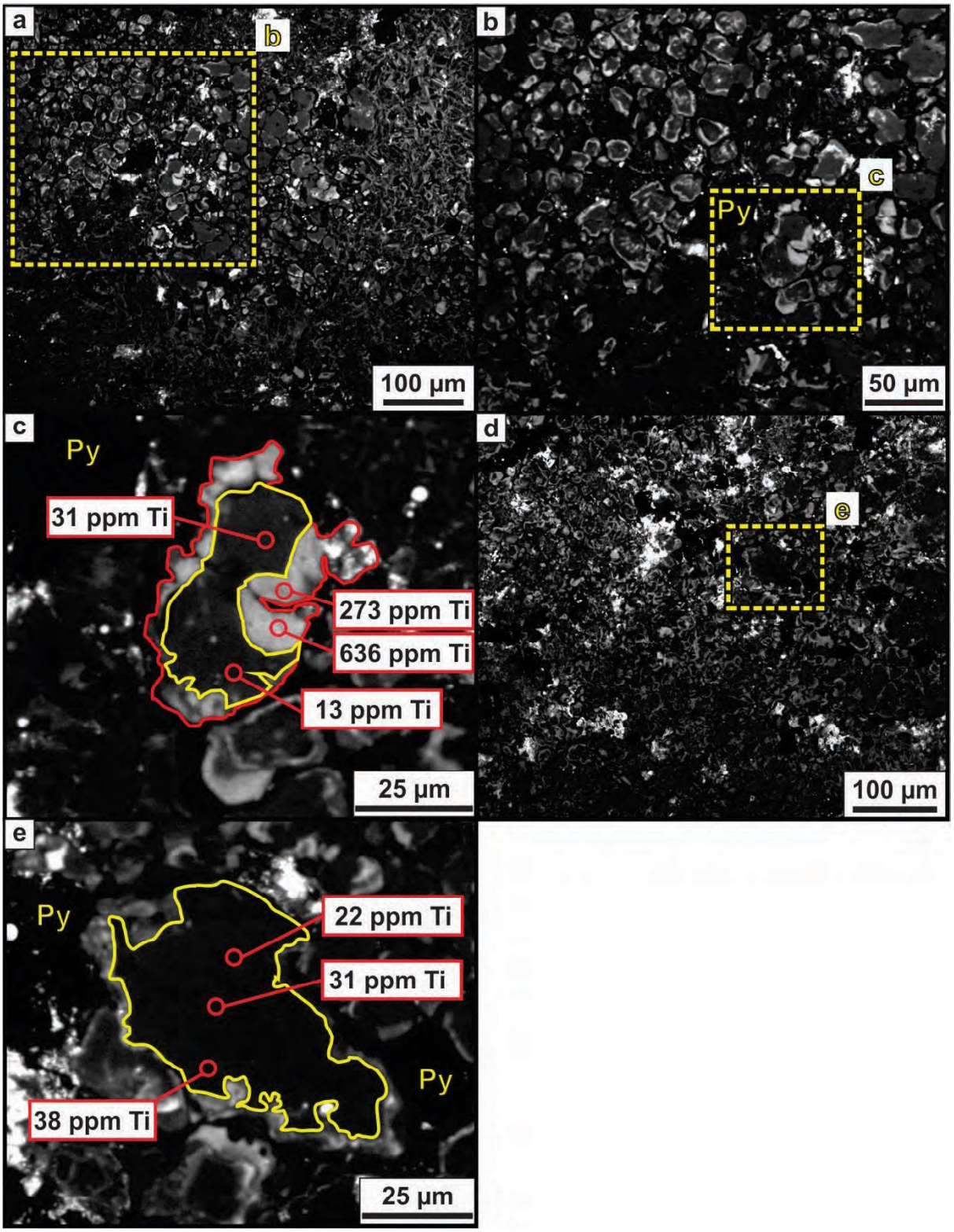

Figure 6.33. CL images and EPMA results from quartz in patchy texture groundmass. a. Fine-grained, zoned quartz crystals in alunite groundmass. **b.** Detail from panel a. **c.** Zone quartz crystal. Detail from panel b. Ti-rich quartz (bright CL response) nucleated on Ti-poor (dark Cl response) quartz. **d.** Alunite and pyrite in quartz groundmass. **e.** Detail from panel d. Zoned quartz crystal; Ti-poor quartz (dark Cl response). Plagioclase-phyric andesite sample from drill hole BTG-006 at 241 m depth. Abbreviations: Py: pyrite; Ti: titanium.

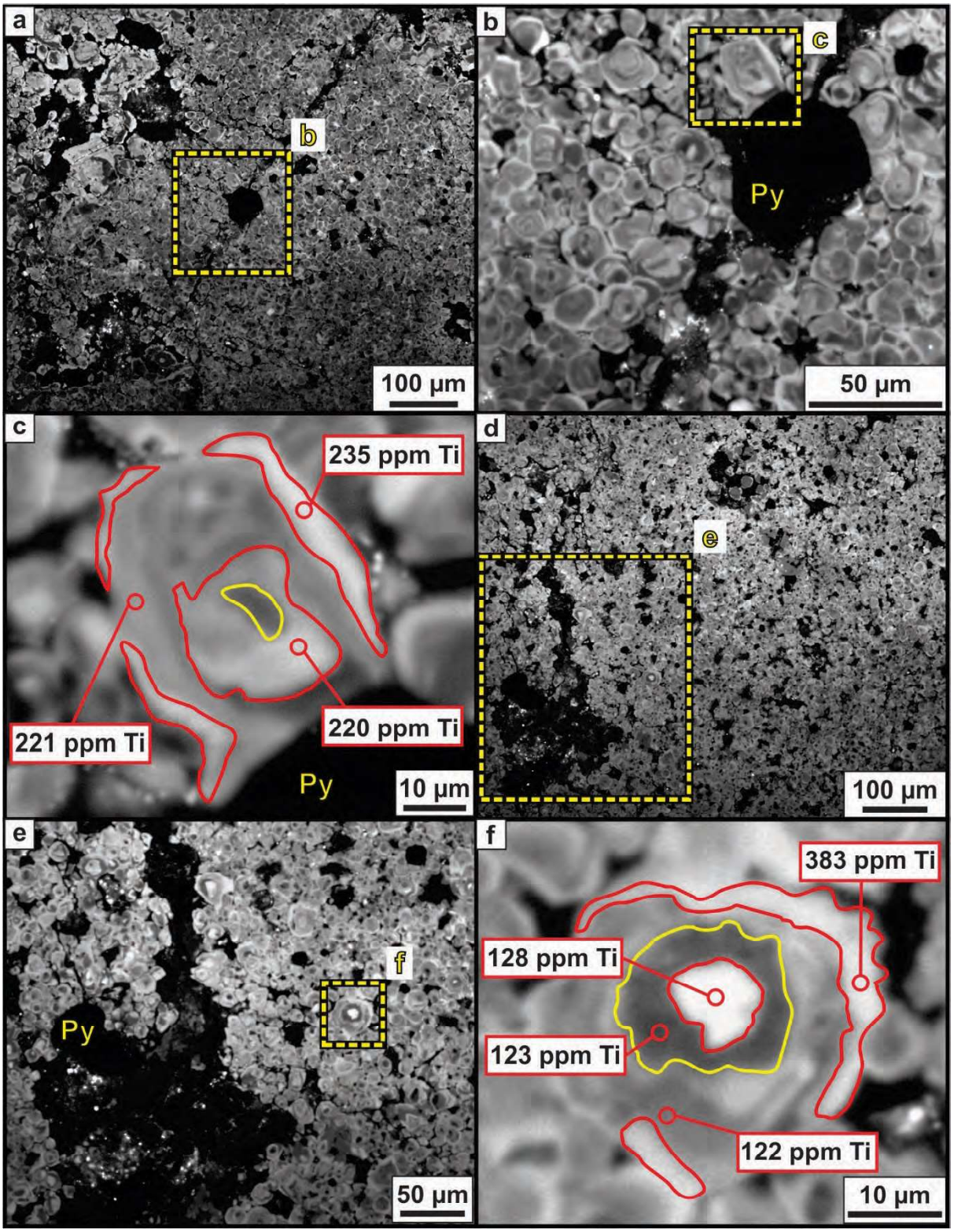

Figure 6.34. CL images and EPMA results from quartz in patchy texture groundmass. a. Fine-grained, zoned quartz groundmass. **b.** Detail from panel a. Zoned quartz groundmass. **c.** Detail from panel b. Zoned quartz crystal. Bright CL areas are Ti-rich. **d.** Fine-grained, zoned quartz groundmass. **e.** Detail from panel d. **f.** Detail from panel e. Zoned quartz crystal; bright CL zones are Ti-rich. Plagioclase-phyric andesite sample from drill hole BTG-006 at 261 m depth. Abbreviations: Py: pyrite; Ti: titanium.

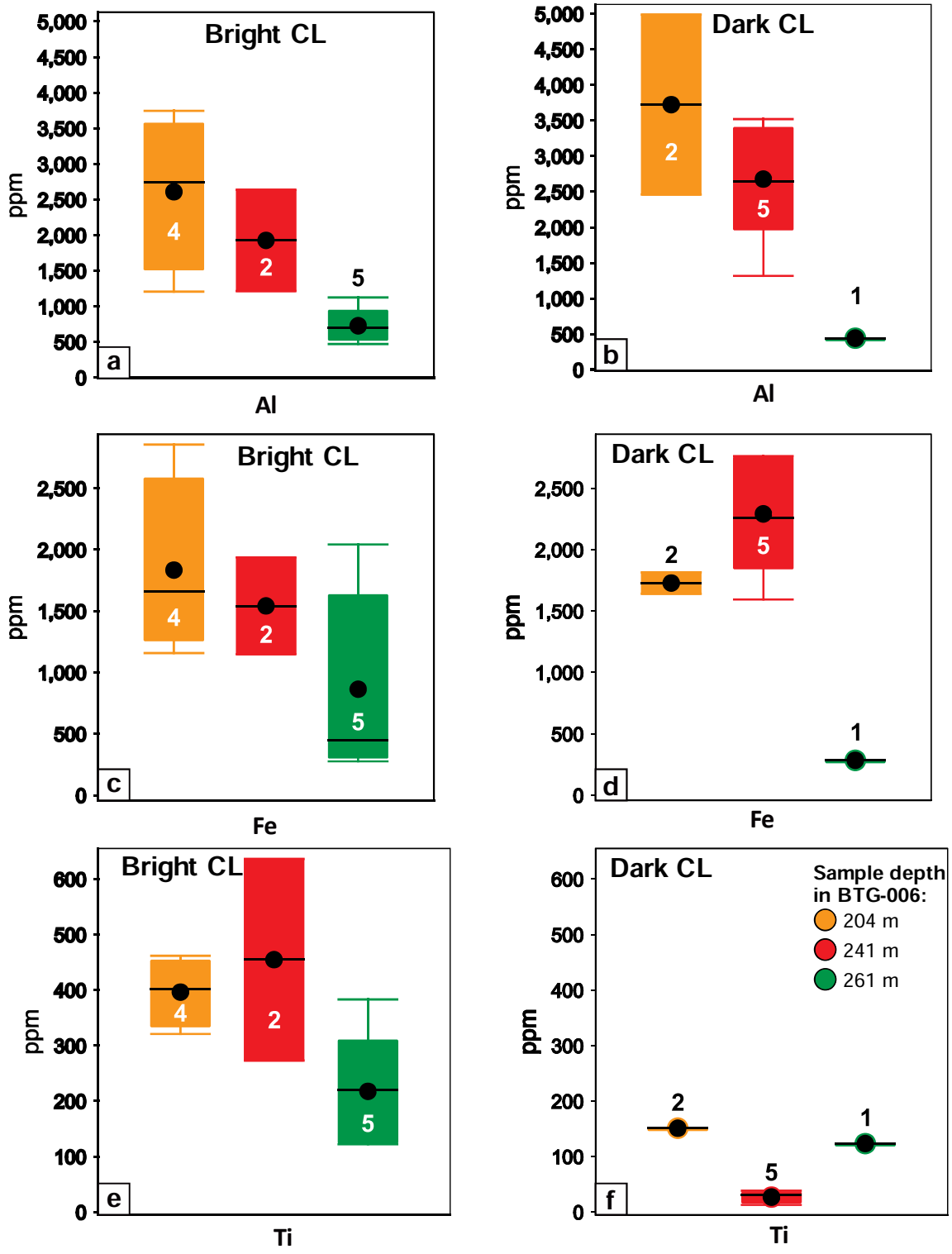

Figure 6.35. EPMA results from quartz in patchy-textured rocks from Bantug. Box plots. a. Box-Aluminium (ppm) from bright CL quartz zones. **b.** Aluminium (ppm) from dark CL quartz zones. **c.** Iron (ppm) from bright CL quartz zones. **d.** Iron (ppm) from dark CL quartz zones. **e.** Titanium (ppm) from bright CL quartz zones. **f.** Titanium (ppm) from dark CL quartz zones. All samples are from drill hole BTG-006. Numbers on boxes are number of analyses on samples. Abbreviations: Al: aluminium; CL: cathodoluminescence; Fe: iron; Ti; titanium.

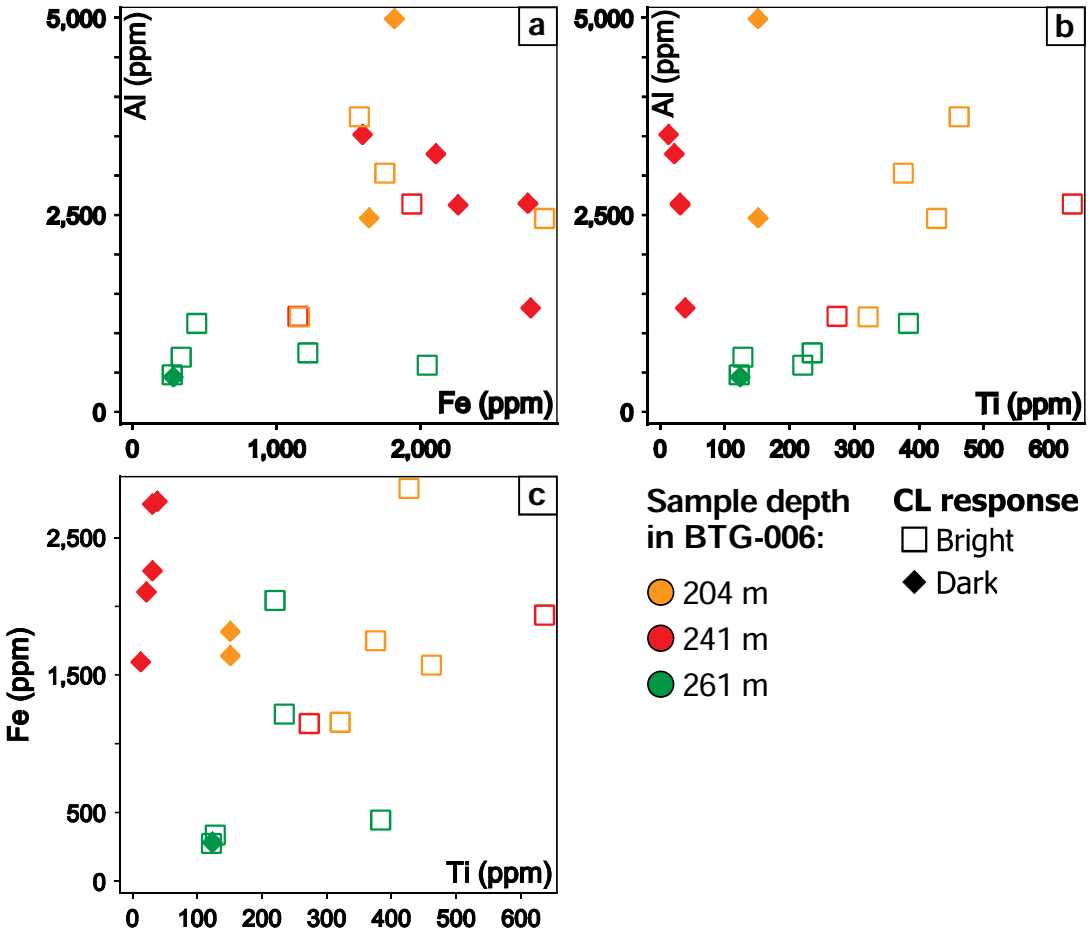

Figure 6.36. EPMA results from quartz in patchy-textured rocks from Bantug. a. Al (ppm) vs. Fe (ppm) diagram. **b.** Fe (ppm) vs. Ti (ppm) diagram. **c.** Al (ppm) vs. Ti (ppm) diagram. Red, dashed line highlights spot analyses on bright CL zones. Abbreviations: Al: aluminium; CL: cathodoluminescence; Fe: iron; Ti; titanium.

6.5. Discussion

6.5.1. Titanium in quartz geothermometer

Wark and Watson (2006) demonstrated the temperature dependence of titanium substitution for silicon in quartz. They synthesised quartz in the presence of rutile and either aqueous fluid or hydrous silicate melt at temperatures ranging from 600 to 1,000°C, at 1.0 GPa. Wark and Watson (2006) proposed a mathematical model (Equation 6.1) to describe the temperature dependence of Ti in quartz, where X_{Ti}^{qtz} is titanium concentration in quartz in ppm.

$$T(°C) = \frac{-3765}{\log\left(X_{Ti}^{qtz}\right) - 5.69} - 273 \qquad (6.1)$$

Huang and Audétat (2012) grew synthetic quartz in rutile-bearing H_2O (±NaCl) fluids between 600 and 800°C, and 1-10 kbar. Quartz crystals grew by dissolution an reprecipitation through a discrete thermal gradient. Their data was best fitted by Equation 6.2, where Ti is given in ppm, and P in kbar.

$$T\ (°C) = \frac{(-0.27943 \times 10^4 - 660.53 \times P^{0.35})}{(Log\ (Ti) - 5.6459)} - 273.15 \quad (6.2)$$

Huang and Audétat (2012) noticed that their mathematical model yielded significantly lower temperatures than that of Wark and Watson (2006). Huang and Audétat (2012) concluded that discrepancies between the two models were due to differences in quartz growth rates between experiments. They also concluded that Ti and other trace elements concentrations increase with increasing rate of quartz crystal growth. Huang and Audétat (2012) cautioned about the effects of extremely variable quartz growth rates under hydrothermal conditions on temperature and pressure calculations. They suggested that the titanium in quartz geothermometer should not be applied to quartz grown from hydrothermal fluids, and that the method is more likely to work in igneous quartz.

Given the conclusions of Huang and Audétat (2012), Thomas et al. (2015) conducted new experiments in order to review previous findings, identify potential experimental disequilibrium, and determine an accurate Ti-in-quartz calibration. They grew quartz, rutile and zircon crystals from SiO_2-, TiO_2, and $ZrSiO_4$-saturated aqueous fluids. These experiments were conducted at 925°C and 10 kbar in a piston cylinder apparatus. Thomas et al. (2015) produced a range of quartz crystal sizes which were analysed by EPMA to determine correlation between Ti concentrations and crystal size. Their cathodoluminescence and EPMA results revealed that intercrystalline and intracrystalline variations in Ti concentration are small, regardless of crystal size. Thomas et al. (2015) concluded that quartz crystals from their synthesis and recrystallization experiments have Ti concentrations that are in excellent agreement with predictions based on reported Ti-in-quartz and Zr-in-rutile solubility calibrations by Ostapenko et al. (1987, 2007), Wark and Watson (2006), and Thomas et al. (2010).

Table 6.7 and Figure 6.37 present temperature results from EPMA analyses on samples from Bantug. T^1 (Eq. 6.1; Wark and Watson, 2006) results range between 549 and 1,031°C, and T^2 (Eq. 6.2; Huang and Audétat, 2012) results between 488 and 942°C. Mean value temperatures are 807 and 731°C, respectively. T^1 results are significantly higher than those from T^2, and the difference in temperature between methods ranges from 60 to 89°C. Results from both methods yielded temperature values that are above the range estimated for hydrothermal minerals from geothermal systems (i.e., 100-340°C, Reyes, 1990) and potassic alteration (e.g., Williams et al., 1997; Seedorff et al., 2005).

T^1 and T^2 calculations, and particularly their mean values, are consistent with magmatic conditions. Temperature results from T^1 and T^2 imply that other hydrothermal minerals in patchy-textured rocks would not have been stable during crystallisation of the groundmass-altered quartz. However, textural evidence collected during this study indicates otherwise (e.g., Figs. 6.29, 6.30, 6.32 to 6.34).

Differences between the temperatures calculated using the models of Wark and Watson (2006) and Huang and Audétat (2012) can be attributed to differences in the experimental methods and subsequent Ti-activity results. At 1 ppm Ti concentration, T^1 and T^2 are 388.6 and 338.7°C, respectively. For 270 ppm Ti T^1 and T^2 are calculated to be 882.4 and 801.6°C, respectively. The temperature differences between methods at Ti concentrations of 1 and 270 ppm are 49.9 and 80.8°C, respectively. These results imply that: 1) both methods would yield temperature results well above hydrothermal and potassic alteration conditions if Ti concentrations range from 1 to 270 ppm; and 2) the temperature difference between methods increases with increasing Ti concentrations up to 80.8°C at 270 ppm.

Rusk et al. (2008) and Müller et al. (2010) presented EPMA Ti results from hydrothermal quartz in potassic-altered rocks from several Cu-porphyry deposits. Table 6.8 presents a summary of the EPMA results and their respective Ti-in-quartz calculations. Figure 6.38 compares EPMA Ti results from hydrothermal-vein quartz in potassic-altered rocks from the porphyry deposits with results from groundmass-altered quartz from patchy altered rocks from Bantug.

EPMA Ti results from Rusk et al. (2008) and Müller et al. (2010) range between 10 and 467 ppm, with a mean value of 85 ppm (Table 6.8; Fig. 6.38a). Temperature results from both methods range between 470 and 973°C, and mean values are 698 and 628°C, for T^1 and T^2 respectively (Table 6.8; Fig. 6.38b). Titanium concentrations and temperature results from most Cu-porphyry deposits are significantly lower than results from Bantug (Table 6.8; Fig. 6.38). However, analyses and calculations from Grasberg yielded similar results to those from Bantug (Table 6.8; Fig. 6.38).

These results imply that: 1) quartz precipitation processes in patchy-altered rocks at Bantug involve temperatures in excess of ~700°C, commonly reported for potassic alteration in porphyry Cu deposits (e.g., Seedorff et al., 2005; Cooke et al., 2014); or that 2) quartz precipitation processes in patchy-altered rocks at Bantug concentrate greater quantities of Ti, and geothermometry models need to be re-calibrated for lithocaps.

Textural and mineralogical features of the patchy-textured rocks at Bantug are considered to be inconsistent with extreme temperatures of formation (e.g., higher temperature than potassic alteration; Figs. 6.29, 6.30, 6.32 to 6.34). Instrumental errors may be a factor in the higher than expected temperatures; however, calibrations and analyses of internationally approved standards were performed during the experiments in this study, and errors are therefore considered acceptable. The author recommends to conduct analyses on hydrothermal quartz from diverse patchy-textured areas and lithocaps in order to determine Ti variations in hydrothermal quartz in these environments.

Table 6.7. Titanium-in-quartz crystallisation temperatures from groundmass-altered quartz in patchy-textured rocks from Bantug

Spot ID	CL response	Quartz type	Ti (ppm)	T^1(°C)	T^2(°C)	ΔT
67026g-3-1a	Dark	Groundmass	13	549	489	61
67026g-3-1b	Bright	Groundmass	636	1,031	942	89
67026g-3-1c	Bright	Groundmass	273	884	803	81
67026g-3-1d	Dark	Groundmass	31	623	558	65
67026g-3-2a	Dark	Groundmass	38	644	577	67
67026g-3-2b	Dark	Groundmass	31	623	557	65
67026g-3-2c	Dark	Groundmass	22	591	528	63
67028g-3-1a	Bright	Groundmass	221	853	773	79
67028g-3-1b	Bright	Groundmass	220	852	773	79
67028g-3-1c	Bright	Groundmass	235	861	782	80
67028g-3-2a	Bright	Groundmass	122	772	697	74
67028g-3-2b	Dark	Groundmass	123	773	699	74
67028g-3-2c	Bright	Groundmass	128	778	703	75
67028g-3-2d	Bright	Groundmass	383	939	855	84
67818g-3-1a	Dark	Groundmass	151	799	723	76
67818g-3-1b	Bright	Groundmass	375	935	852	84
67818g-3-1c	Bright	Groundmass	462	971	886	86
/67818g-4-1b	Dark	Groundmass	151	799	723	76
67818g-4-1c	Bright	Groundmass	427	958	873	85
67818g-4-1d	Bright	Groundmass	321	910	827	82

Results were calculated at 1 kbar; T^1 (°C) was calculated from Wark and Watson (2006); T^2 (°C) was calculated from Huang and Audétat (2012); ΔT is the difference between T^1 and T^2.

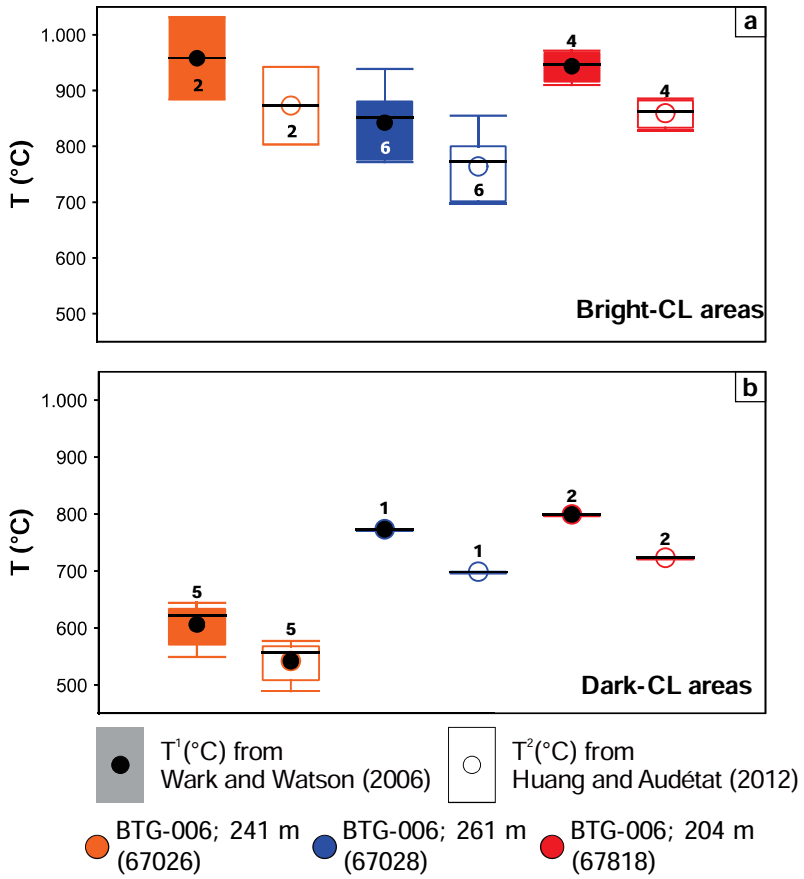

Figure 6.37. Titanium in quartz temperature results from quartz-altered groundmass in patchy-textured plagioclase-phyric andesites from Bantug. a. Results from bright-response CL areas. **b.** Results from dark-response CL areas. Colour-filled bins represent temperatures calculated with Eq. 6.1 (T^1; Wark and Watson, 2006), and hollow bins represent temperatures calculated from Eq. 6.2 (T^2; Huang and Audétat, 2012).

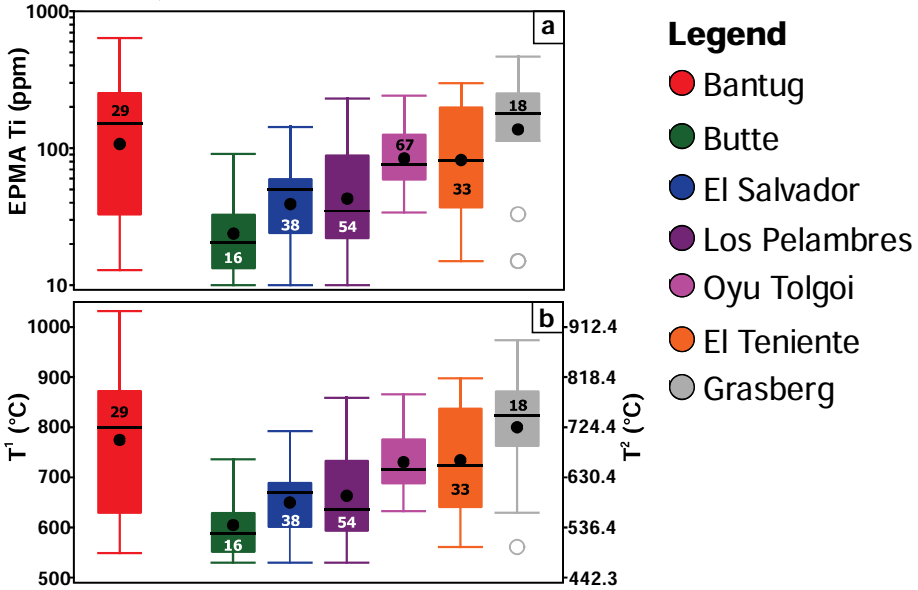

Figure 6.38. Titanium concentrations and Ti-in-quartz temperature calculations from hydrothermal quartz from Bantug and Cu-porphyry deposits. a. EPMA Ti concentrations in parts per million (ppm). **b.** Ti-in-quartz temperature calculations; Results were calculated at 1 kbar; T^1 (°C) was calculated from Eq 6.1 (Wark and Watson, 2006); T^2 (°C) was calculated from Eq. 6.2 (Huang and Audétat, 2012). Analyses from Butte, El Salvador, Los Pelambres, El Teniente, and Grasberg are from Rusk et al. (2008); analyses from Oyu Tolgoi are from Müller et al. (2010); and analyses from Bantug are from this study.

Table 6.8. Ti and Ti-in-quartz results from hydrothermal quartz

Summary	Ti (ppm)	Ti^1 (°C)	Ti^2 (°C)
All results			
n	158	158	158
Minimum	10	530	470
Maximum	636	1031	942
Mean	96	707	636
Bantug			
n	29	29	29
Minimum	13	549	489
Maximum	636	1031	942
Mean	180	775	700
Butte			
n	16	16	16
Minimum	10	530	470
Maximum	91	736	664
Mean	32	605	541
El Salvador			
n	38	38	38
Minimum	10	530	470
Maximum	143	792	717
Mean	46	650	583
Los Pelambres			
n	54	54	54
Minimum	10	530	470
Maximum	231	859	779
Mean	63	663	596
Oyu Tolgoi			
n	67	67	67
Minimum	34	632	567
Maximum	242	866	786
Mean	95	730	659
El Teniente			
n	33	33	33
Minimum	15	561	500
Maximum	298	898	816
Mean	115	734	662
Grasberg			
n	18	18	18
Minimum	15	561	500
Maximum	467	973	888
Mean	189	800	724

Results were calculated at 1 kbar; T^1 (°C) was calculated from Wark and Watson (2006); T^2 (°C) was calculated from Huang and Audétat (2012).

6.5.2. Paragenesis of patchy texture mineralogy

Petrographic and microanalyses (i.e., FE-SEM, CL, EPMA) of patchy-textured plagioclase-phyric andesites from Bantug have facilitated detailed identification of alteration minerals, their textures, and relative temporal relationships. Figure 6.38 presents a schematic representation of the paragenesis of minerals that make up patchy-textured rocks at Bantug.

The earliest-formed minerals probably occurred at the core of patchy features. The first phase to form was typically euhedral to subhedral pyrite ~300 μm (Figs. 6.17 to 6.19, 6.39). Pyrite was followed by alunite, APS, diaspore, and quartz grains (Figs. 6.17 to 6.19, 6.39) which nucleated on pyrite. Alunite was commonly observed to be intergrown with APS minerals, and nucleated on diaspore (Figs. 6.18f). APS minerals in the core of patchy features also nucleated on rutile (Figs. 6.20f), and are characterised by rhythmic zonation varying from svanbergite-weilerite to woodhouseite (Figs. 6.20 to 6.22). Zunyite and fine-grained rutile crystals also occur in the core of patchy features (Figs. 6.24 and 6.25). All these occur in a groundmass predominantly altered to pyrophyllite with lesser muscovite crystals (Figs. 6.19 and 6.22e).

The halos of fine-grained quartz that surrounds the patchy features are the products of alteration, and formed after the minerals in the core (Figs. 6.17a, and 6.18a). Quartz halos also contain pyrite, diaspore and APS minerals in lesser quantities. Pyrophyllite occurs between quartz crystals in the altered groundmass (Fig 6.19), and muscovite crystals occur with pyrophyllite (Fig 6.19). The contact between patchy features and the fine-grained halo contains abundant diaspore (Fig 6.15b and 6.15c). The contact between the fine-grained halo and the granular quartz-groundmass of patchy textures is gradual.

The granular altered groundmass in which patchy features occur is predominantly made of quartz. It is considered to have been altered during patch formation. Subrounded, subhedral, granular quartz crystals (<20 μm) nucleated on subrounded-subhedral pyrite crystals (<5 μm; Fig. 6.30). Alunite and diaspore are minor components in the altered groundmass. Small amounts of fine-grained pyrophyllite occur between granular quartz in the groundmass.

Sinuous veins made of fine-grained pyrophyllite, coarse alunite and diaspore, were observed to radiate from patchy features through the fine-grained halo and into the fine-grained granular quartz-altered groundmass (Figs. 6.15 and 6.29). Late pyrite veins were also observed to cross-cut the granular quartz-altered groundmass (Figs. 6.15 and 6.29).

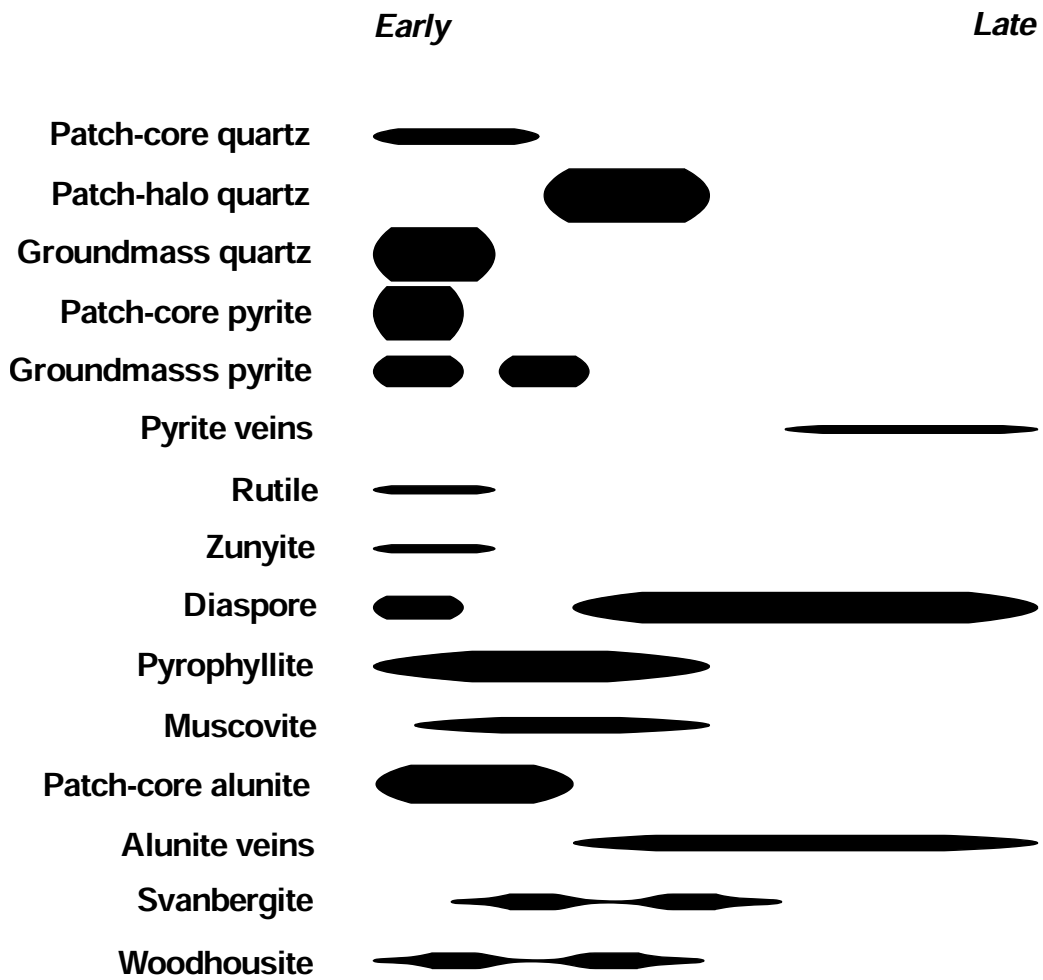

Figure 6.39. Paragenesis of patchy texture mineralogy. Line thickness represents abundance; early stages are located to the left and late stages are located to the right.

6.5.3. Whole rock geochemistry of patchy-textured rocks

The chemical composition of patchy-textured plagioclase-phyric andesites from Bantug was compared with andesites from the Canlaon Volcanic Complex (CVC) and andesites from similar subduction-related tectonic settings around the globe. A total of 2,742 least altered samples were identified (Fig. 6.40a) using the alteration box plots of Large et al. (2001) and Williams and Davidson (2004). Sixty-nine least-altered samples were identified from the CVC, and 2,673 from around the globe. Table 6.9 presents details on the number of least altered samples. Appendix B presents whole rock analyses results from other studies in Negros.

Table 6.9. Number of least altered andesites from previous studies in Negros and around the world

Study	Least altered samples
Von Bidersee et al. (1995)	34
Rae (2000)	5
Sajona et al. (2000)	11
Solidum et al. (2003)	19
GEOROC (2016)	2,672

Table 6.10 and Figures 6.40 and 6.41 summarise and compare the results. Some patchy-textured rocks have SiO_2 contents greater than 86 wt % and can be classified as silicic-altered (Fig. 6.40b). Most patchy-textured rocks are enriched in SiO_2 compared to other andesites from the CVC and elsewhere (Fig. 6.40b).

Patchy-textured andesites from Bantug are depleted in MgO, CaO, Na_2O, K_2O, MnO, and Cr_2O_3 compared to andesites from the CVC and elsewhere (Table 6.10; Fig. 6.40c). LOI values from the patchy-textured andesites are 10 times greater than those of andesites from the CVC and other locations (Table 6.10; Fig. 6.40c). Patchy-textured andesites from BTG-006 are the most depleted compared to andesites from the CVC and elsewhere (Table 6.10; Fig. 6.40c).

Yttrium and Ta are the most depleted HFSE (Table 6.10; Fig. 6.40d). Zirconium, Nb, and Hf values present little variations in comparison to other samples (Table 6.10; Fig. 6.40d). Patchy-textured andesites from BTG-006 are significantly depleted in Rb and Cs, and samples from BTG-005 and BTG-003 present similar LILE contents than andesites from the CVC and other locations (Table 6.10; Fig. 6.41a).

Light REE contents of patchy-textured andesites and least altered andesites present little variations (Table 6.10; Fig. 6.41b). However, patchy-textured andesites are depleted in heavy REE compared to the global andesites (Table 6.10; Fig. 6.41b). Patchy-textured andesites from BTG-006 are the most depleted in heavy REE (Table 6.10; Fig. 6.41b).

Patchy-textured andesites from Bantug are enriched in Cu, Mo, Pb, and As compared with andesites from other locations (Table 6.10; Fig. 6.41c). Samples from BTG-006 are the most enriched in Cu, and samples from BTG-003 are the most enriched in Pb and As (Table 6.10; Fig. 6.41c). Patchy-textured andesites from Bantug are depleted in Au, Ag, Te, Bi, W, and Sn compared with andesites from other locations. Samples from BTG-006 are the most depleted in Au and Zn (Table 6.10; Fig. 6.41c).

Table 6.10. Whole rock geochemistry summary from patchy textured plagioclase andesites from Bantug

	BTG-005	BTG-003	BTG-006	CVC	Global
Major elements	*(n=36)*	*(n=36)*	*(n=41)*	*(n=69)*	*(n=2,673)*
SiO_2	64.0	66.0	66.6	57.8	59.2
Al_2O_3	16.8	14.4	15.0	17.5	16.8
Fe_2O_3	6.7	5.9	6.5	6.7	3.1
MgO	0.9	0.6	0.0	3.1	3.7
CaO	0.3	0.4	0.2	7.1	6.5
Na_2O	0.3	0.4	0.2	3.5	3.6
K_2O	1.8	1.9	1.1	2.1	1.6
TiO_2	0.6	0.9	0.6	0.6	0.7
P_2O_5	0.2	0.2	0.2	0.2	0.2
MnO	0.0	0.0	0.0	0.1	0.1
Cr_2O_3	0.0	0.0	0.0		0.0
LOI	8.6	10.5	9.3	1.2	1.2
Alteration indexes	*(n=29)*	*(n=22)*	*(n=40)*	*(n=69)*	*(n=2,671)*
AI	82	75	73	31	34
AAAI	86	76	94	30	30
HFSE (ppm)	*(n=36)*	*(n=36)*	*(n=41)*	*(n=69)*	*(n=1,916)*
Y	14.3	18.5	8.2	22.7	21.9
Zr	116.2	184.8	122.0	112.2	133.2
Nb	4.1	6.7	4.2	3.0	7.1
Hf	3.2	4.8	3.2		3.5
Ta	0.3	0.5	0.3		0.6
LILE (ppm)	*(n=36)*	*(n=36)*	*(n=41)*	*(n=69)*	*(n=2,022)*
Rb	38.2	42.1	9.1	49.7	46.8
Sr	344.6	383.5	538.7	613.2	435.3
Cs	1.1	2.0	0.2		2.6
Ba	443.9	642.5	497.0	353.8	471.1
Th	6.2	7.5	5.0	4.6	5.2
U	2.6	3.3	2.0		2.0
REE (ppm)	*(n=36)*	*(n=36)*	*(n=41)*	*(n=34)*	*(n=1,250)*
La	15.1	16.4	14.5	15.1	18.4
Ce	30.9	34.2	29.3	32.0	37.7
Pr	3.4	4.1	3.4	3.8	4.7
Nd	12.9	16.5	13.8	16.7	18.9
Sm	2.6	3.3	2.7	3.5	4.0
Eu	0.7	0.9	0.7	1.1	1.3
Gd	2.2	3.2	2.1	3.6	3.8
Tb	0.3	0.5	0.3	0.5	0.6
Dy	2.3	3.1	1.4	3.1	3.5
Ho	0.5	0.6	0.3		0.7
Er	1.5	1.9	0.9	1.9	14.4
Tm	0.2	0.3	0.2		0.3
Yb	1.6	2.2	1.1	1.8	2.0
Lu	0.3	0.3	0.2	0.3	0.3
Pathfinder elements (ppm)	*(n=29)*	*(n=22)*	*(n=40)*	*(n=35)*	*(n=587)*
Cu	94.5	92.2	356.2		40.2
Mo	9.8	6.8	10.8		1.4
Au	0.02	0.01	0.00		0.30
Ag	0.04	0.12	0.05		13.99
Pb	21.4	59.5	17.5		10.7
Zn	47.0	76.3	9.9	62.9	72.6
As	14.0	30.7	25.2		4.0
Sb	0.3	0.7	0.3		0.4
Te	0.3	1.1	0.5		
Bi	1.3	1.2	0.8		3.7
W	1.5	1.6	1.8		112.6
Sn	6.2	3.4	3.3		2.6

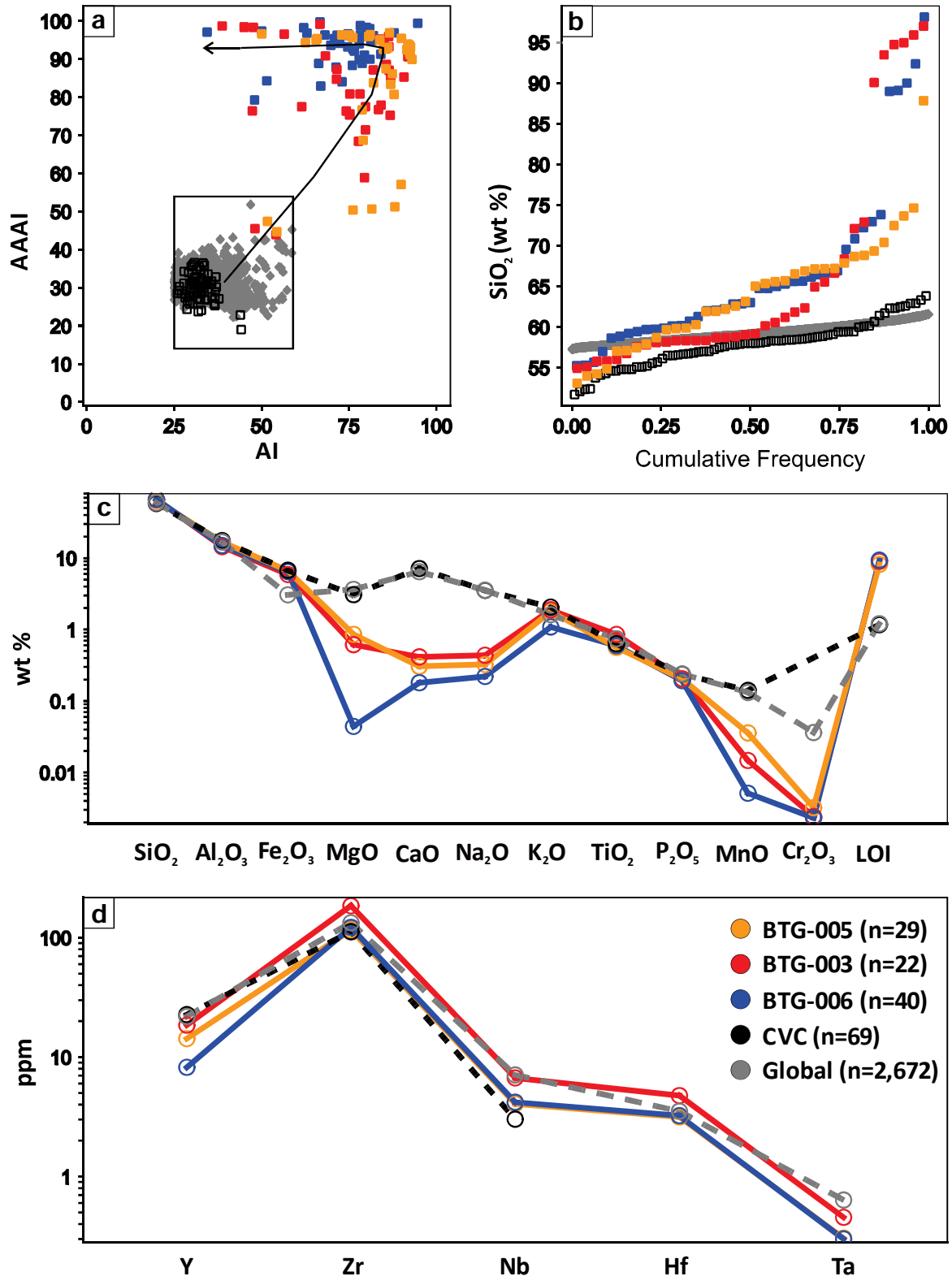

Figure 6.40. Whole rock geochemistry highlights of patchy-textured plagioclase phyric andesites from Bantug. a. Advanced argillic alteration index (AAAI) vs alteration index (AI) diagram from Williams and Davidson (2004). **b.** SiO_2 probability plot emphasizing on the intensely silicic-altered patchy-textured plagioclase-phyric andesites from Bantug. **c.** Parallel plot from major elements mean values. **d.** Parallel plot from high field strength elements mean values (HFSE). Abbreviations: CVC: Canlaon Volcanic Complex; Global: andesites from around the globe.

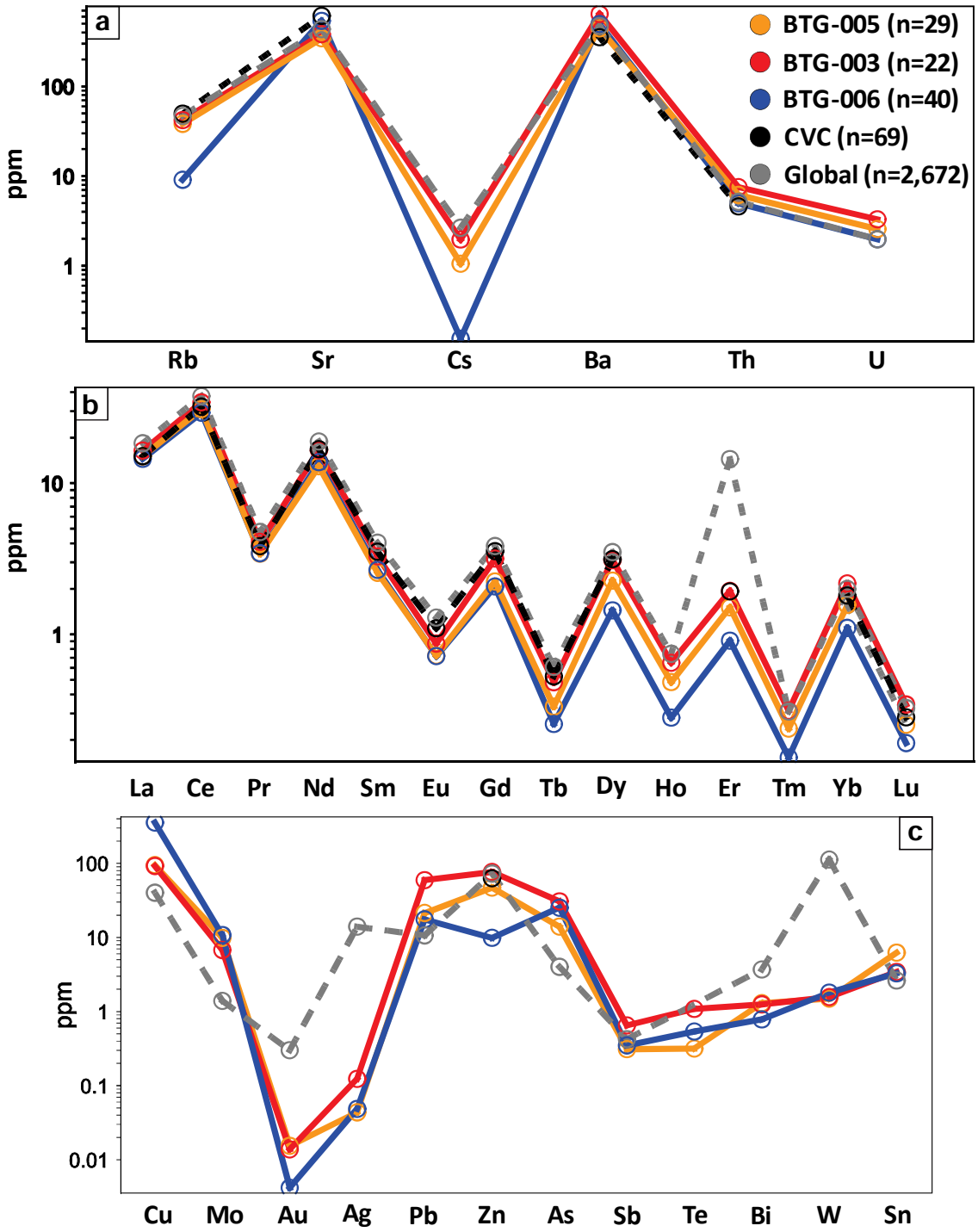

Figure 6.41. Whole rock geochemistry highlights of patchy-textured plagioclase phyric andesites from Bantug. a. Parallel plot from large ion lithophile elements mean values (LILE). **b.** Parallel plot from rare-earth elements mean values (REE). **c.** Parallel plot from mean values of the pathfinder elements to magmatic-hydrothermal mineral deposits. Abbreviations: CVC: Canlaon Volcanic Complex; Global: andesites from around the globe.

6.5.4. Origin of aluminium-phosphate-sulphate (APS) minerals

APS minerals have been found in advanced argillic altered rocks (Stoffregen and Alpers, 1987; Aoki et al., 1993; Hedenquist et al., 1994; Arribas et al., 1995; Hedenquist et al., 1998; Bajnóczi et al., 2004) and unconformity-related uranium deposits (Gaboreau et al., 2005; Gall and Donaldson, 2006; Gaboreau et al., 2007; Riegler et al., 2016). APS minerals from advanced argillic altered rocks are considered to be the product of apatite dissolution or replacement by acid hydrothermal fluids (Stoffregen and Alpers, 1987). APS minerals from unconformity-related uranium deposits are considered to be the product of diagenetic processes (Riegler et al., 2016).

The apatite dissolution hypothesis presented by Stoffregen and Alpers (1987) was supported by Valsami-Jones et al. (1998), who found synthetic hydroxylapatite to have a higher solubility than natural fluorapatite at pH values between 2 and 7. However, dissolution rates of hydroxylapatite and fluorapatite increased with decreasing pH. Valsami-Jones et al. (1998) suggested that the interaction between apatite and metals in solution (i.e., Pb^{2+} and Cd^{2+}) is controlled by apatite dissolution and resulted in the precipitation of new metal phosphates.

Tropper et al. (2013) studied apatite solubility in high-temperature, high-pressure, halogen-bearing fluids (i.e., NaF, NaCl). They found that synthetic $CePO_4$ and YPO_4 crystals are highly soluble in H_2O-NaF fluids at 800°C and 1 GPa. They found that apatite solubility increased significantly with increasing NaF concentration.

Several apatite solubility studies (e.g., Guidry and Mackenzie, 2003; Chaïrat et al., 2007; Harouiya et al., 2007) reached similar conclusions: apatite is highly soluble at lower pH values (i.e., pH < 3), and HF, NaF, and NaCl increase its solubility. APS minerals at Bantug are associated with minerals of hypogene hydrothermal origin (i.e., alunite, diaspore, pyrophyllite, zunyite) in patchy textured rocks. Thus, APS minerals at Bantug clearly have a hypogene, hydrothermal origin. However, apatite crystals or evidence for apatite replacement were not found during this study.

Strontium concentrations in patchy-textured plagioclase-phyric andesites from Bantug do not differ significantly from least altered andesites elsewhere (Fig. 6.41a). Strontium content of patchy-textured plagioclase-phyric andesites at Bantug (n=73) ranges between 4.7 and 3,322 ppm, with a mean value of 478.3 ppm. Strontium content of andesites from around the globe (GEOROC, 2016; n=2,234) ranges between 11.9 and 2,446 ppm, with a mean value of 430.1 ppm. Also, whole rock geochemistry mass balance revealed that P_2O_5 gains and losses on

patchy-textured plagioclase-phyric andesites were insignificant (Table 4.3; Figs.4.22b and 4.23).

This leads to conclude that strontium and P_2O_5 addition to patchy-textured rocks during hydrothermal alteration was unlikely. Remobilization and concentration of Sr and P_2O_5 via hydrothermal alteration are more likely. APS mineral occurrences at Bantug were controlled by the effect of high-temperature, acid, halogen-bearing fluids on primary apatite in the precursor rocks.

6.5.5. Genetic model for patchy-wormy textures at Bantug

The distribution, mineralogy, and geochemistry of patchy textures at Bantug highlight their intimate relationship with hydrothermal fluids and igneous activity. This section proposes a genetic model for patchy textures at Bantug which may help to explain their occurrence elsewhere.

For the development of a genetic model for patchy textures, four topics are considered: quartz solubility, rutile solubility, acid halogen-bearing hydrothermal fluids, and primary volcanic textures in precursor rocks.

The topic of quartz solubility has been addressed in great detail previously (e.g., Fournier, 1983; Dove and Rimstidt, 1994; Rimstidt, 1997; Fournier; 1999; Mitra, 2008; Mitra and Rimstidt, 2009; Gorrepati, 2009; Gorrepati et al., 2010). Outcomes of these studies highlighted that: i) quartz solubility increases with temperature and pressure, except for a small region near the critical point of water; ii) amorphous silica solubility increases with pH between 150 and 250°C; iii) quartz solubility increases with NaCl concentration in solution, and with temperature.

Quartz and silicate solubilities have been a major topic of discussion in the oil industry, as occurrence of these minerals can reduce oil-well productivity (Mitra, 2008; Mitra and Rimstidt, 2009; Gorrepati, 2009). Therefore, understanding and controlling quartz and silicates solubility can enhance oil production from quartz-rich formations or quartz-saturated wells. Hydrogen fluoride–hydrogen chloride (HF–HCl) mixtures have been used since 1940 in the petroleum industry for matrix acidization of sandstone oil field reservoirs to increase oil production rates by increasing permeability (Mitra, 2008; Mitra and Rimstidt, 2009; Gorrepati, 2009).

Mitra (2008) and Mitra and Rimstidt (2009) focused on quartz solubility and dissolution rates in acid fluoride solutions between 24.8 and 99.8°C. Their experiments and calculations

suggested that below a pH value of 3.16, HF is the predominant fluoride species. Above a pH of 3.16, F^- is predominant. Mitra and Rimstidt (2009) noted that both solubility and dissolution rates are strongly controlled by fluoride speciation (i.e., HF, HF_2^-). However, for higher total fluoride concentration ($>10^{-1}$ m) and higher pH (>3.5), even though quartz solubility is high, the rate of dissolution decreases with increasing pH. That is because at high pH there are insufficient H^+ ions available to maintain a fast dissolution rate. They also noted that the quartz dissolution rate achieves a maximum near pH 3.

Previous studies of quartz solubility on fluoride species proposed similar mechanisms and produced similar results (Judges,1971; Liang and Readey, 1987; Spierings and van Dijk, 1987; Prokopowicz-Prigogine, 1989; Kikuyama et al., 1992; Proksche et al., 1992; Spierings, 1993; Wolff-Boenisch et al., 2004) It is worth noting that Spierings (1993) also suggested that the dissolution model for silicate glasses can be applied to the dissolution of multicomponent glasses and compositionally related crystalline silicates such as feldspars.

Rapp et al. (2010) conducted rutile solubility experiments at high pressure and temperature in order to understand high field strength element mobility at high grade metamorphic conditions. Rutile crystals were placed in a gas apparatus for 9.5 to 103.7 hours, at 0.5 GPa, and between 800 and 1,000°C. Pressure and temperature conditions were intended to emulate conditions at ~20 km depth in the crust, where metamorphic conditions prevail. Rapp et al. (2010) determined that rutile solubility in chlorine brines (10% NaCl) was 2 to 4 times higher than in H_2O; also, that rutile solubility in fluoride brines (10% NaF) was 20 to 100 times higher than in H_2O. Rapp et al. (2010) examined the capsules used during the experiment using SEM imaging. The capsules contained partially dissolved rutile crystals as well as many small acicular rutile crystals distributed throughout the capsule. They also noted that crystals from experiments containing NaF presented evidence of more intense etching compared with crystals etched with other fluids. Tanis et al. (2016) conducted rutile solubility experiments in aqueous fluids from 0.5 to 2.79 GPa and 250 to 650°C. They concluded that fluid composition exerts the greatest control on rutile solubilities, and that increasing temperature has a positive, albeit less pronounced effect.

Tanis et al. (2016) and references therein, contributed to the growing body of evidence that favours high rutile solubility in halogen-bearing (e.g., F, Cl) aqueous fluids that evolved during metamorphism in subduction zones. High-temperature aqueous fluids in natural environments are known to be complex in composition (Philippot and Selverstone, 1991; Keppler, 1996; Scambelluri and Philippot, 2001; Manning, 2004; Rae et al., 2011).

These fluids are characterized by high concentrations of elements such as Na, K, Si, Al, Cl, and F. Figure 6.42 presents a summary from 12 studies carried in several geothermal fields around the world. These studies contain information about temperature and chemical composition of geothermal gases. The most abundant component is water which ranges between 80.6 and 9,450 mmol/mol, with a mean value of 880.4 mmol/mol (Fig. 6.42a). Other major components include CO_2, S_T (total sulphur), SO_2, HCl, H_2S, and N_2 (Fig. 6.42a). Minor components include H_2, HF, O_2, and CO. Trace components are CH_4, Ar, He, Ne (Fig. 6.42a). HCl (n=195) concentration ranges between 0.0003 and 754 mmol/mol, with a mean value of 14.9 mmol/mol. HF (n=112) concentration ranges between 0.00015 and 69 mmol/mol, with a mean value of 1.4 mmol/mol. Components that correlate well with each other are SO_2, H_2S, HCl, and HF. Temperature in 269 analyses ranged between 21 and 1,100°C, with a mean value of 323.3°C (Fig. 6.42b). HF concentrations were observed to increase with temperature in most studies (Fig. 6.42c). It is worth noting that by the time these geothermal gases were captured and chemical composition was measured, these fluids have already circulated, and consequently diluted, through host rocks in the geothermal fields.

There are several publications dealing with alteration textures and their formation processes (McPhie et al., 1993; Thompson et al., 1996; Gifkins et al., 2005; Taylor, 2009). Gifkins et al. (2005) suggested five common types of alteration textures in volcanic rocks: replacement, infill, dissolution, recrystallization, and deformation. They also suggested that incomplete destruction of primary volcanic textures, and the combined effect of a number of different overprinting alteration styles can result in false or pseudo textures (de Rosen-Spence et al., 1980; Allen, 1988; McPhie et al., 1993; Gifkins et al., 2005).

Despite the published work, accurate classification of patchy-textured rocks remains challenging. Given the significant amount of primary volcanic features that can occur in volcanic rocks, as well as the dynamic hydrothermal activity in volcanic terranes (e.g., lithocaps), the amount of final alteration products can be overwhelmingly difficult to classify.

The information presented in this chapter, and early in this section, is considered in combination to propose a genetic model for patchy textures at Bantug. In this model patches are formed by the interaction of hydrothermal fluids with primary volcanic texture features (e.g., phenocrysts, volcanic clasts). The genetic model involves high temperature, acid, halogen-bearing fluids circulating through volcanic rocks, partially dissolving pre-existing rock features (including quartz), creating secondary porosity, and precipitating new minerals, specifically pyrophyllite and alunite as patches are leached of quartz.

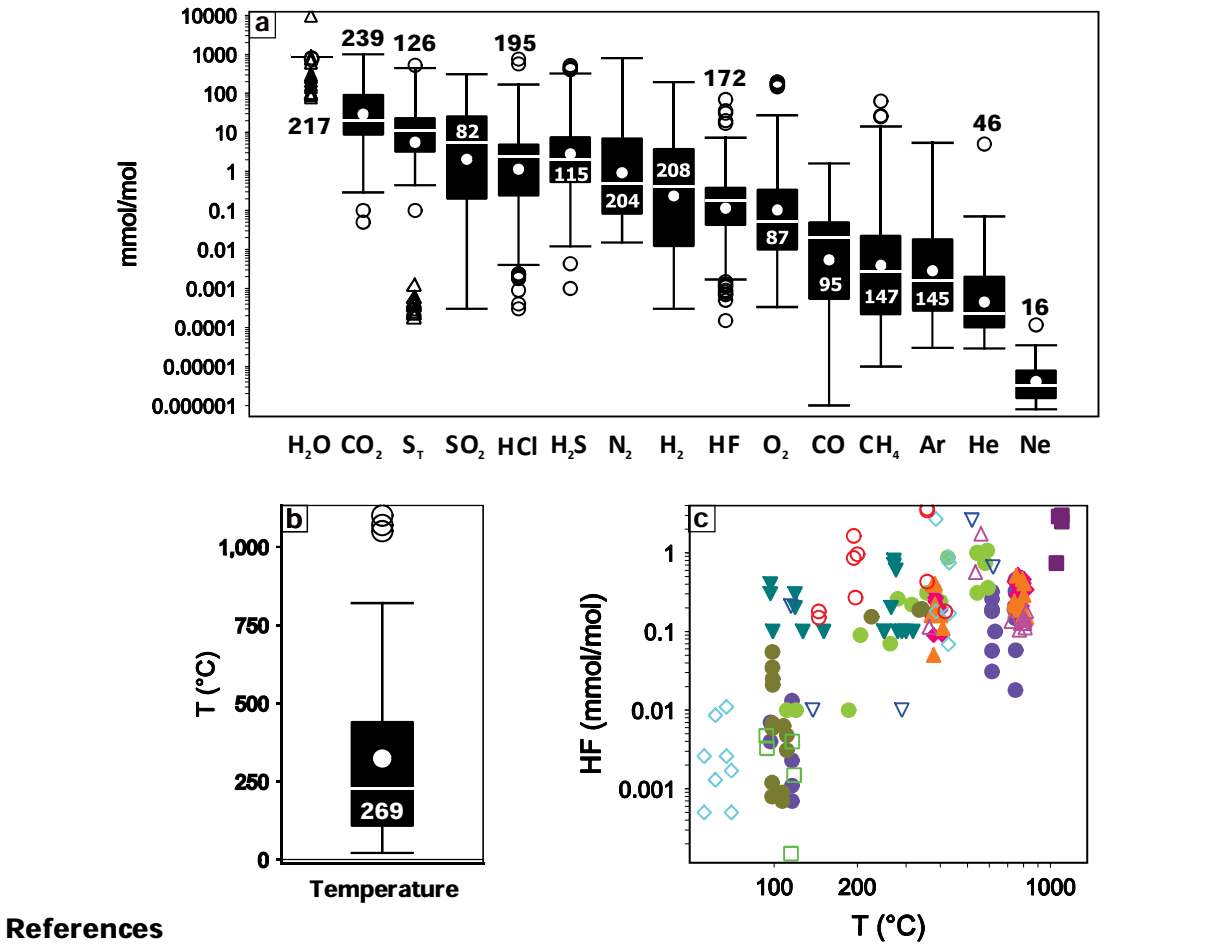

Figure 6.42. Geothermal gases composition. a. Box-plot for major components of geothermal gases. Numbers in boxes are number of analyses. **b.** Box plot for temperature of analysed gases from all geothermal study sites. **c.** HF vs Temperature diagram.

The genetic model can be described in four stages (Fig. 6.). During the initial stage, high-temperature, low-pressure, acid, halogen-bearing hydrothermal fluids (i.e., F, Cl) start to circulate through primary volcanic texture features (e.g., plagioclase-phenocrysts) creating porosity and enhancing permeability (; Fig. 6.42b). Evidence for the presence of F are zunyite crystals (Figs. 6.24 and 6.25). During this stage, hydrothermal fluids start to circulate through grain boundaries and pre-existing fractures (Fig. 6.43a to 6.43c).

During the second stage, the halogen-bearing hydrothermal fluids alter the composition of primary features, dissolving SiO_2 and other soluble components. This process enhances

secondary porosity and permeability, leaves significant amounts of aluminium behind to form pyrophyllite and titanium to form rutile. A fine-grained halo, product of dissolution and recrystallization of quartz and aluminium-rich minerals (i.e., pyrophyllite, diaspore), forms around the primary texture features as the higher-temperature hydrothermal fluid circulates through the secondary porosity (Fig. 6.43c). Micron-size fractures start to form due to dissolution and pressure, irradiating from the edges of early-stage patches.

During this stage, a small part of the fluids circulates through the groundmass, which was most likely composed of a mixture of fine-grained silicates, oxides, and/or glass. The fluid partially dissolves and recrystallises the mixture to precipitate fine-grained granular quartz, pyrophyllite, and rutile on pyrite crystals (Fig. 6.43c).

During the third stage, the primary volcanic texture features are completely replaced by hydrothermal mineral assemblages including pyrophyllite, muscovite, diaspore, alunite, zunyite, APS minerals, and pyrite. (Fig. 6.43d). Increasing pore pressure, provided by the hydrothermal fluids circulating through the patches in a plastic groundmass, could produce the subrounded geometry (Fig. 6.43d). Alternatively, dissolution and reprecipitation may lead to a subrounded geometry of altered patches. The fractures stemming from the patches become sinuous, longer, wider, and are filled with pyrophyllite, diaspore, and alunite.

During the fourth stage, patches are completely rounded. Some have connected through sinuous veins, forming complex arrangements of rounded amoeboid patches (Fig. 6.43e). New thin sinuous veins have formed. These radiate from patchy features, and connect with other patches (Fig. 6.43e). Late pyrite-alunite veins cross-cut the groundmass (Fig. 6.43e).

Each stage is suspected to be long-lived and passive rather than catastrophic, although the speed and duration of patch formation was not constrained. This inference is made because synchronous fragmentation, brecciation, or stockwork did not occur during patch formation. Processes leading to patch formation may have been repeated due to the dynamic nature of magmatic-hydrothermal systems.

At Bantug the plagioclase-phyric andesite is the preferential host rocks for patchy texture, and the phenocrysts appear to have been precursor features to the patches. High temperature, acid, halogen-bearing hydrothermal fluids in the lithocap environment migrate through diverse host rocks with a great number of texture features. Patchy textures are the result of the interaction between these fluids and host rocks. Future studies on patchy-wormy textures should also include detailed studies of least altered areas of the volcanic stratigraphy or precursor rocks.

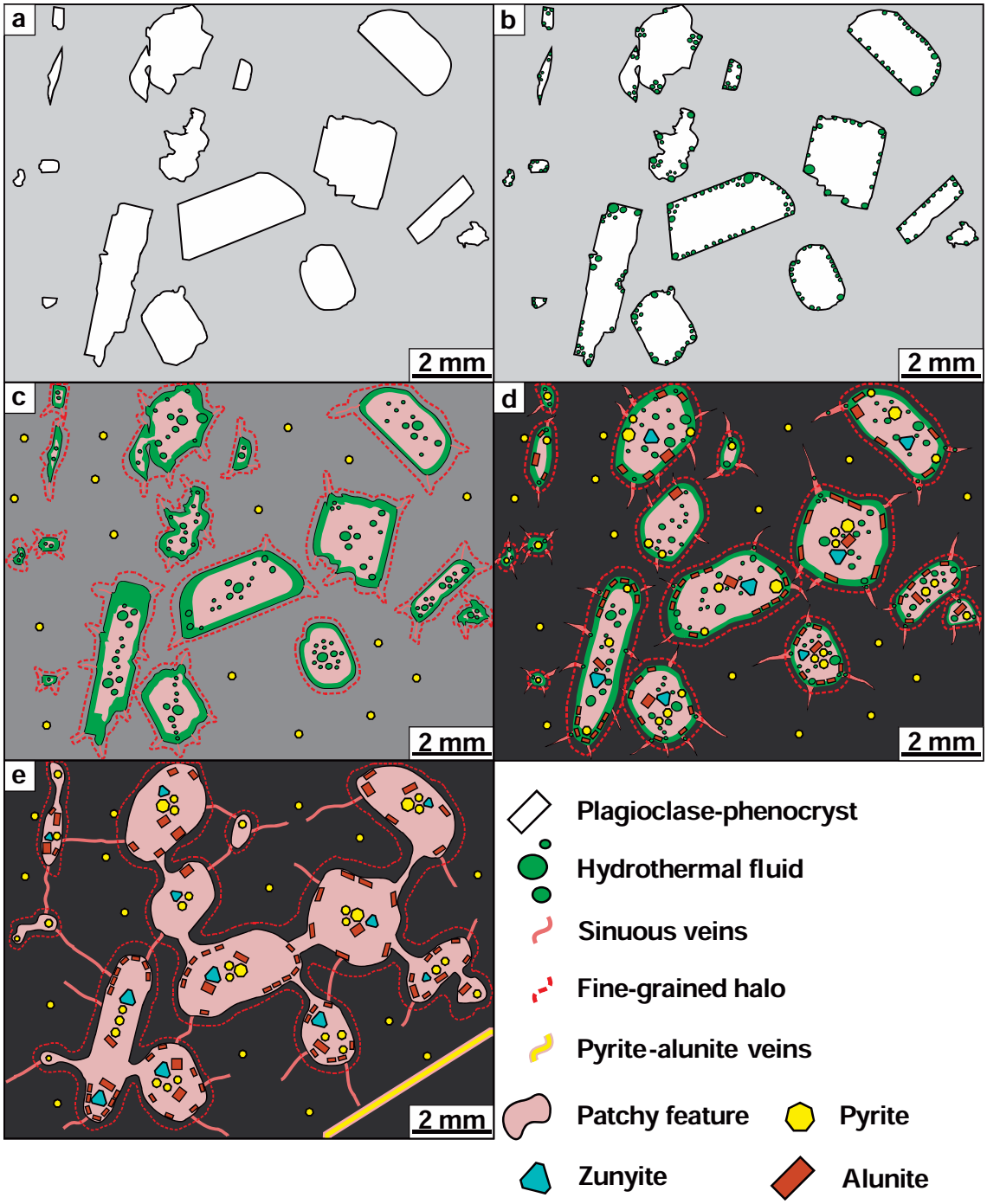

Figure 6.43. Genetic model for patchy-textures at Bantug. a. Plagioclase-phyric andesite precursor; grey colour indicates groundmass. **b.** Initial stage. High temperature, acid, halogen-bearing hydrothermal fluids begin to circulate through primary volcanic texture features. **c.** Second stage. Hydrothermal fluids partially dissolve primary volcanic texture features. **d.** Third stage. Hydrothermal fluids have created subrounded clay-rich features with zunyite, pyrite, and alunite crystals. Sinuous fractures stem from features; hydrothermal fluids circulate through the fractures. **e.** Fourth stage. Degree of roundness increases on patchy features due to fluid pressure on the patchy feature and plastic state of the groundmass. Patches have connected through sinuous fractures. Late pyrite-alunite veins cross-cut the groundmass. Differences in colour (i.e., grey scale) denotes degree of groundmass recrystallization.

6.6. Conclusions

Patchy-wormy textures occur at the base of several lithocaps. In some cases, have been observed to transition at depth into quartz stockwork and porphyry-style mineralisation (e.g., Kupfertal; Pinto, 2002; Gustafson et al., 2004). Patchy textures are characterised by subrounded to rounded amoeboid-like clusters of sulphates, clays, and sulfides in a fine-grained quartz-altered groundmass. Wormy textures are characterised by sinuous quartz veins in patchy texture. Rounded-subrounded patchy features are predominantly made of pyrophyllite, diaspore, alunite, APS minerals (i.e., svanbergite, woodhouseite), muscovite, pyrite, and bornite.

Patchy textures at Bantug occur at surface and in drill holes BTG-003, BTG-005, and BTG-006 (Figs.6.9 to 6.14). Patchy textures occur at surface in narrow discrete elongated sections; a noteworthy area of occurrence is located <200 m to the northeast of drill hole BTG-006 (Fig. 6.9). Petrography, SWIR, XRD, and SEM analyses on samples from Bantug revealed the presence of pyrophyllite, muscovite, alunite, diaspore, APS minerals, rutile, zunyite, quartz and pyrite (Figs. 6.15 to 6.19).

Zunyite, a halogen-bearing (i.e., F, Cl) aluminium-silicate, occurs in patchy-textured plagioclase-phyric andesites in drill hole BTG-006 from Bantug. The fluorine content of zunyite was observed to increase with depth in drill hole BTG-006 (Table 6.4; Figure 6.26). Rutile was also observed in patchy textures at Bantug. Rutile occurs as fine-grained acicular crystals, often associated with pyrite and APS minerals in patchy features (Figs. 6.27 and 6.28).

Patchy textures are the product of interaction between high temperature, acid, halogen-bearing fluids with volcanic rocks characterised by primary volcanic texture features. Hydrothermal fluids partially dissolved primary volcanic features, enhanced phyric textures, and precipitated alunite, pyrophyllite, and associated advanced argillic alteration minerals.

CHAPTER 7:

SUMMARY AND EXPLORATION IMPLICATIONS

7.1. Introduction

Bantug is one of several underexplored lithocaps in eastern-central Negros. This section summarises the findings of this study, the exploration implications, and recommendations for future explorations efforts in the Bantug district.

7.2. Major findings

7.2.1. Regional geology

Negros is located over a complex subduction setting where the Negros trench bends, subducting under the Central Visayas region (Figs. 2.1 and 2.2). Subduction, magmatism, and hydrothermal activity have taken place in Negros since at least 38 Ma. This magmatism has produced at least 26 porphyry prospects of Late Eocene-Early Oligocene age in southwest Negros (i.e., obtained via K-Ar dating; Burton, 1983), one porphyry prospect in northern Negros (i.e., Sagay; Celiz, in prep.), and several active and extinct geothermal fields (Rae, 2002; this study). Major Cu porphyry deposits in the southwest Negros district include the closed Sipalay and Basay mines (i.e., 807 Mt, 262 Mt, respectively; Fig. 2.18; Sinclair, 2007; Singer et al., 2008). The complex tectonic setting at which Negros is located is favourable for MASH magmatic processes (Hildreth and Moorbat, 1988; Richards, 2003; Richards and Kerrich, 2008). Furthermore, porphyry deposit endowment is indicative of fertile magmatism in this subduction-related setting. Such magmatism has produced major porphyry deposits, and it is likely that discoveries are yet to be made in this metallogenic belt.

7.2.2. Deposit-scale geology and geochemistry

The geology of the Bantug area comprises sedimentary rocks from the Pliocene-Pleistocene Caliling Formation, which are overlain by volcanic rocks from the Pleistocene Canlaon Volcanic Complex (CVC), and cut by intrusive rocks from the Late Pleistocene Bantug Intrusive Complex (BIC). Trace element composition of least altered CVC samples indicates that these are calc-alkaline volcanic arc andesites (Fig. 3.31). U-Pb LA-ICP-MS dating of zircons from the CVC returned ages between 1.82 ± 0.11 and 1.71 ± 0.16 Ma (Table 3.2; Figs. 3.34 and 3.35). Aphyric, plagioclase-phyric, and volcaniclastic breccia textures were recognised during core logging (Figs. 3.11 and 3.12). The BIC can be divided into at least three intrusive phases and two hydrothermal breccias:

- Diorite porphyry: characterised by plagioclase phenocryst, quartz in miarolitic cavities, incipient quartz-pyrite stockwork, and intense phyllic alteration (Figs. 3.13 to 3.16). U-Pb LA-ICP-MS dating of zircons returned ages between 1.37 ± 0.10 and 1.35 ± 0.30 Ma (Table 3.2; Figs. 3.34 and 3.35)
- Diorite porphyry dike I: Pyroxene-plagioclase phyric, miarolitic diorite porphyry. Characterised by weak propylitic alteration, evidenced by epidote in miarolitic cavities and chlorite replacing pyroxenes (Figs. 3.17 to 3.20). U-Pb dating of zircons from this intrusion returned ages between 1.25 ± 0.31 and 1.19 ± 0.63 Ma (Table 3.2; Figs. 3.34 and 3.35)
- Diorite porphyry dike II: Plagioclase-pyroxene phyric, crystal crowded diorite porphyry characterised by moderate argillic alteration (Figs. 3.21 to 3.24). U-Pb dating of zircons returned an age of 1.46 ± 0.15 Ma (Table 3.2; Figs. 3.34 and 3.35)
- Diorite porphyry dike III: Plagioclase-phyric, miarolitic diorite porphyry. Characterised by miarolitic cavities filled with quartz-pyrite or pyrite-anhydrite, and intense phyllic alteration (Figs. 3.25 to 3.28). U-Pb dating of zircons returned ages between 1.23 ± 0.39 and 1.24 ± 0.05 Ma (Table 3.2; Figs. 3.34 and 3.35)
- Natroalunite-pyrite cemented, polymictic, hydrothermal breccia: characterised by <4 cm long tabular silicic and advanced argillic-altered clasts. Patchy and vuggy textures were observed in clasts (Fig. 4.18)
- Quartz-pyrite cemented, polymictic hydrothermal breccia: characterised by silicic and advanced argillic-altered clasts. Clast textures vary from phyric, aphyric, vuggy, and patchy. Truncated pyrite veins were observed in clasts, as well as juvenile clasts (Fig. 4.19)

7.2.3. Deposit-scale hydrothermal alteration

The lithocap at Bantug is characterised by northeast-trending elongated silicic-altered areas, surrounded by advanced argillic-altered domains (Fig. 4.1). Hydrothermal alteration domains vary from silicic-argillic-advanced argillic on surface to advanced argillic-phyllic at depth to the northeast, where a drill hole intercepted diorite porphyry intrusions (Figs. 4.8 to 4.11). A drill hole collared in the southwest part of the studied area, intercepted at depth sedimentary rocks from the Pliocene-Pleistocene Caliling Formation altered to hornfels at depths below 550 m.a.s.l. (Fig. 4.8).

Shortwave infrared spectroscopy aided to the identification of alteration minerals and facilitated mapping of alteration domains on surface and in drill holes (Figs. 4.4 to 4.11). SWIR results indicate a transition from argillic and advanced argillic alteration in the southwest part of the studied area to advanced argillic and phyllic to the northeast (Fig. 4.3). SWIR analyses of surface samples determined the presence of muscovite, pyrophyllite, and dickite in the northeastern part of the studied area, highlighting the presence of the diorite porphyry intrusions at depth (Fig. 4.3).

Patchy-wormy textures occur at the base of several lithocaps (e.g., Escondida, Padilla-Garza, 2001; Tampakan, Rohrlach, 2002; Kupfertal, Pinto, 2002; La Zanja, Gustafson et al., 2004; Yanacocha; Oyu Tolgoi, Khashgerel et al., 2008; Caspiche, Sillitoe et al., 2013; Bantug, this study). Patchy textures are characterised by subrounded to rounded amoeboid-like clusters of sulphates, clays, and sulfides in a fine-grained quartz-altered groundmass (Figs. 6.2 to 6.3). Wormy textures are characterised by sinuous quartz veins in patchy texture (Figs. 6.3a and 6.3c). Patchy-wormy textured rocks were observed on surface and drill hole samples from Bantug. Patchy-textured rocks on surface occur in narrow discrete elongated sections in the northeastern part of the studied area (Fig. 6.8). Patchy-textured rocks were observed in the three drill holes studied but are best developed in drill hole BTG-006 (i.e., northeastern part of the lithocap; Figs. 6.13 and 6.14). SEM and XRD analyses of patchy features from Bantug revealed the presence of pyrophyllite, muscovite, alunite, diaspore, APS minerals, rutile, zunyite, quartz, and pyrite (Figs. 6.15 to 6.19; Table 6.5; Fig. 6.31). Zunyite was found on surface samples close to drill hole BTG-006, and in drill core samples from the same drill hole (Figs. 6.24 and 6.25). FE-SEM fluorine results from zunyite increased with depth in drill hole BTG-006 (Table 6.4; Fig. 6.26). Patchy textures are interpreted to be the product of interaction between high temperature, acid, halogen-bearing fluids with volcanic rocks characterised by primary volcanic texture features. Hydrothermal fluids partially dissolved primary volcanic features, enhanced porphyritic textures, and precipitated alunite, pyrophyllite, and associated advanced argillic alteration minerals.

7.2.4. Alteration geochemistry and mineral chemistry

Base and precious metals results from surface and drill core samples returned values below ore-grade (Tables 4.10 and 4.11; Figs. 4.42 to 4.47). A few samples returned encouraging Au and Ag results (i.e., 0.5 ppm and 0.8 ppm, respectively; Table 4.11; Figs. 4.45 to 4.47). However, the majority of samples returned low value results. Surface and drill core whole rock geochemistry results were used to determine alteration and advanced argillic alteration

indices (Table 4.5; Figs. 4.27 to 4.29). High AI and AAAI values (i.e. values >93.6) resulted from samples in the northeastern part of the studied area, and these are likely to reflect the presence of the diorite porphyry at depth in BTG-006 (Fig. 4.28). Advanced argillic-altered rocks from BTG-006 yielded the highest AI results (Table 4.5; Fig. 4.29), this is likely to be due to intense hydrothermal alteration caused by the diorite porphyry intrusion at depth (Fig. 4.29c). Mass balance calculations from surface samples indicated SiO_2 and TiO_2 gains in the northeastern part of the studied area (i.e., northeast of BTG-006; Table 4.4; Figs. 4.24a and 4.25d). Surface and drill hole geochemistry results revealed HFSE, REE, transition metals, and base metals anomalism in the same area (Figs. 4.31, 4.37, 4.40, and 4.43).

LA-ICP-MS results from alunite, pyrite, epidote, chlorite and magnetite samples from Bantug (Figs. 5.3 to 5.35) are comparable with results from Mankayan, Baguio, and Batu Hijau (Figs. Figs. 5.10 to 5.12, 5.17 to 5.28, 5.24, 5.30, 5.36). Alunite trace element results vary systematically with respect to the location of the diorite porphyry intrusion at depth in the northeastern part of the study area (i.e., BTG-006; Fig. 5.10). Epidote, chlorite and magnetite results from diorite porphyry samples suggest a potential heat source at distances greater than 1.5 km from the sample locations (Fig. 5.24; Table 5.18, Fig. 5.30; Fig. 5.36). Given the level of preservation of the lithocap at Bantug it is likely that the potential heat source may be located at depths greater than 1 km below the present-day surface.

Figure 7.1 presents a conceptual model, elaborated based on the information acquired during this study, for the evolution of the Bantug lithocap. It begins depicting the sedimentation of the Late Pliocene-Pleistocene Caliling Formation (MGB, 2004; Fig. 7.1a). Sedimentation is interpreted to have occurred in a marine environment after 3.6 and no later than 1.93 Ma based on the presence of pelecypods, gastropods, coral heads and coral fingers, foraminifera and nanoplankton (MGB, 2004). This is followed by deposition of volcaniclastic andesite breccias, aphyric andesites, and aphyric andesites of the Canlaon Volcanic Complex at ~1.93 Ma (Table 3.2; Fig. 7.2b). Volcanism is considered to have taken place above sea level based on textural evidence (Figs. 3.11 and 7.2b). This is followed by emplacement of the Bantug Intrusive Complex and formation of the lithocap between ~1.93 and ~1.65 Ma (Table 3.2; Fig. 7.2c). Emplacement of phyllic-altered diorite porphyry stocks is considered to have driven the hydrothermal fluids responsible for the formation of the lithocap at Bantug. The lithocap consists of an extensive domain of advanced argillic-altered volcanic rocks. Advanced argillic-altered volcanic rocks at the base of the lithocap display patchy texture. Hornfels and skarn are considered to have formed at this stage due to interaction between heat

and hydrothermal fluids from the BIC with sedimentary rocks from the Late Pliocene-Pleistocene Caliling Formation (Fig. 7.1c). This is followed by intrusion of hydrothermal breccias characterised by natroalunite cement and advanced argillic-altered clasts after 1.21 Ma (Fig. 7.1d). Erosion is considered to have taken place after hydrothermal breccia emplacement (Fig. 7.1d).

7.3. Exploration implications

The following items, which were addressed during this study, are considered to be of major relevance for future exploration in the Bantug lithocap and other lithocaps:

- **Patchy-wormy textures:** systematic and detailed description of patchy-wormy textures can help to identifying high-temperature paleo fluid flow zones at the base of lithocaps. Identification of zunyite in patchy textures is paramount as it marks zones of acid-halogen fluid flow and may be proximal to potential heat sources
- **Shortwave infrared spectroscopy:** SWIR provided great advantages in resolving with great detail hydrothermal alteration domains. Coupling of SWIR analyses with XRD and FE-SEM analyses could help to recognise key minerals that can indicate paleo hydrothermal fluid-flow channels (i.e., APS minerals, zunyite)
- **Mineral geochemistry for vectoring:** LA-ICP-MS analyses of multiple minerals at the different levels of magmatic-hydrothermal systems can assist target generation and vectoring

7.4. Recommendations for further research

- U-Pb dating of the southwest Negros porphyry-epithermal district: The age of the ore-productive magmatism in southwest Negros was determined using the K-Ar method during the 1980s. U-Pb LA-ICP-MS dating could bring new understanding or confirm with greater precision previously reported ages
- Canlaon Volcanic Complex stratigraphy: information about the thickness, facies, distribution, and textures of the volcanic units of the CVC at Bantug will contribute to the location of potential high-sulfidation deposits
- SWIR analyses of surface samples: additional surface sampling and SWIR analyses of the area north and northeast of drill hole collar BTG-006 needs to be undertaken in order to determine the extent of the phyllic alteration in that area

- Exploratory SWIR experiments: A combination of SWIR, XRF, XRD, and FE-SEM analyses in order to determine SWIR spectral features of zunyite and APS minerals in patchy-textured rocks, so as to aid in their interpretation in future exploration campaigns
- Zunyite geochemistry: FE-SEM EDS and LA-ICP-MS analyses of zunyite need to be undertaken to determine whether zunyite compositional variations in space could provide vectors towards potential heat sources and/or mineralised centres at Bantug and other lithocaps
- LA-IPC-MS analyses of magnetite from the hornfels and epidote-chlorite from propylitic alteration: Mineral chemistry studies have been heavily focused on minerals from the lithocap environment (i.e., pyrite and alunite). Analyses of epidote-chlorite from intensely propylitic-altered samples and magnetite from hornfels could provide new vectors towards potential porphyry deposits concealed by the Bantug lithocap
- ^{40}Ar-^{39}Ar dating of alunite from the Bantug lithocap: age determination of hypogene alunite will contribute to constrain the timeline of volcanism, magmatism, and hydrothermal alteration

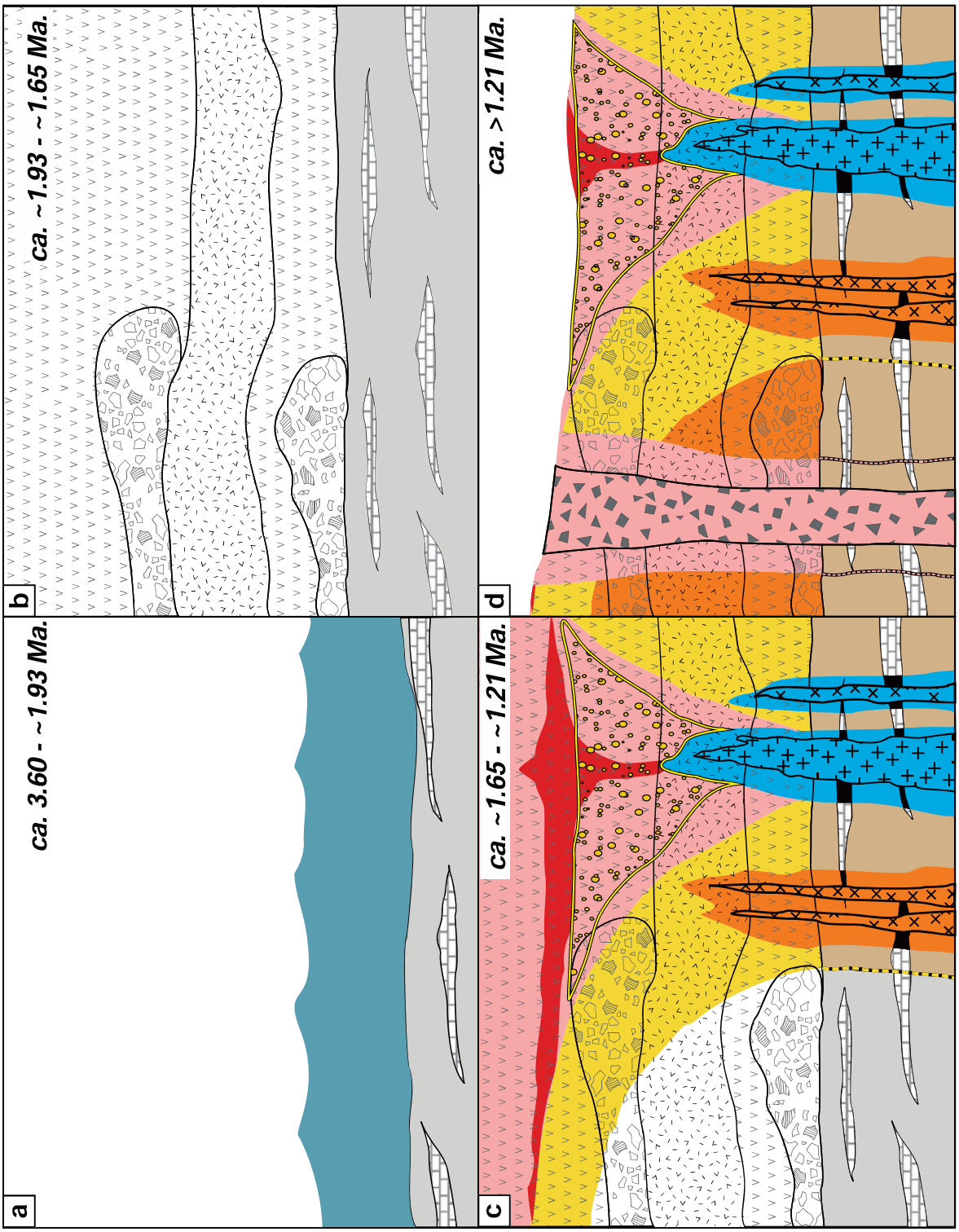

Figure 7.1. Schematic representation of the geologic evolution of the Bantug lithocap. a. Sedimentation of the Late Pliocene-Pleistocene Caliling Formation between 3.6 and <1.9 Ma. **b.** Deposition of volcaniclastic andesitic breccias, aphyric andesites, and plagioclase-phyric andesites of the Canlaon Volcanic Complex between 1.93 and 1.65 Ma. **c.** Emplacement of the Bantug Intrusive Complex and formation of the Bantug lithocap after 1.65 and no later than 1.21 Ma. **d.** Emplacement of hydrothermal breccias characterised by natroalunite cement and erosion after 1.21 Ma.

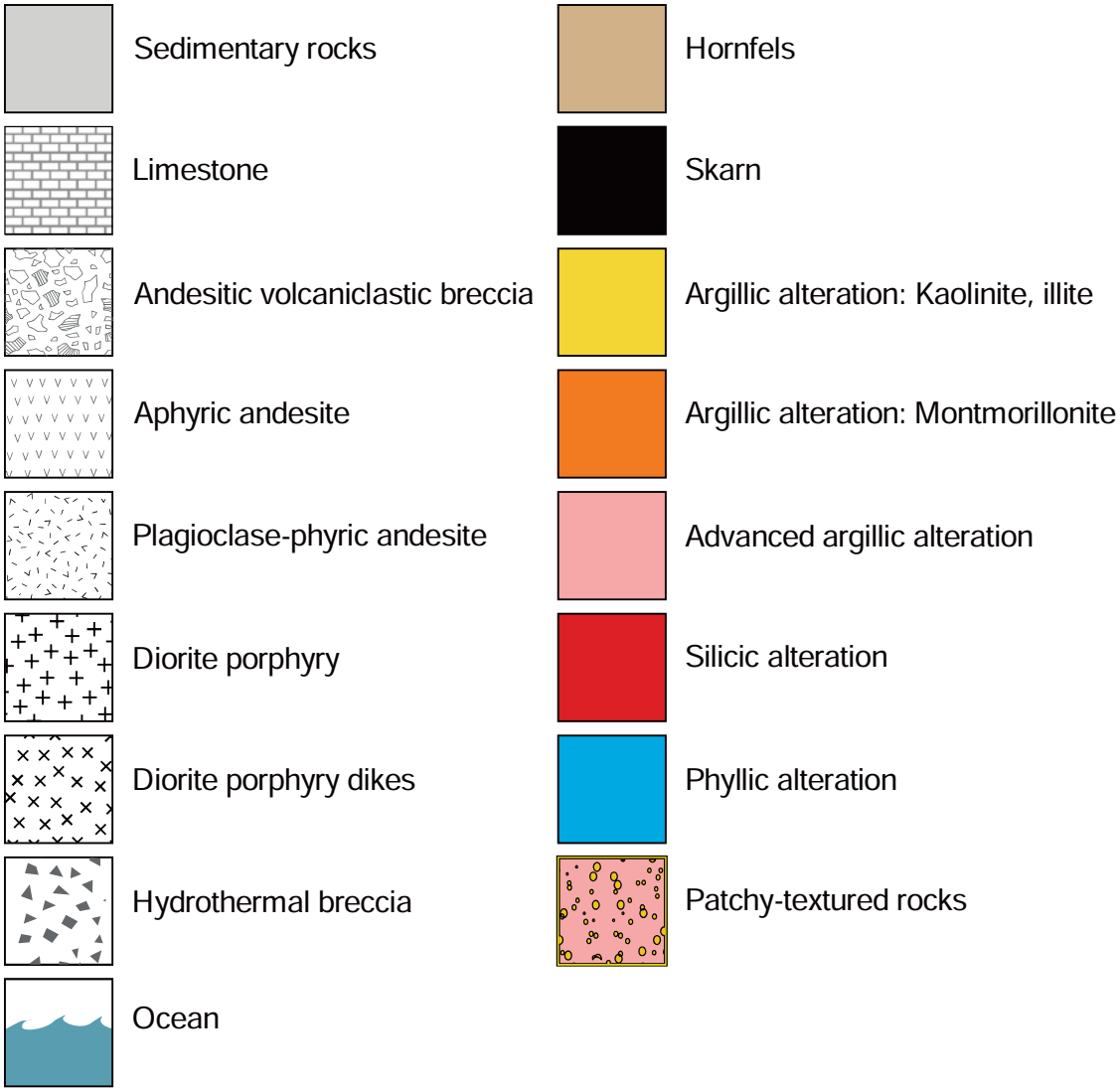

Figure 7.2. Schematic represantion of the geologic evolution of the Bantug lithocap. Legend.

References

Allen, R. L., 1988, False pyroclastic textures in altered silicic lavas, with implications for volcanic-associated mineralisation: ECONOMIC GEOLOGY, v. 83, p. 1424-1446.

Amiscaray, E. A., and Quiel, C. M., 1987, Palaeontology and stratigraphy of Abinay and nearby areas, Negros Oriental: Bureau of Mines and Geosciences, Unpublished report.

Andal, E. S., Arai, S., and Yumul, G. P. J., 2005, Complete mantle section of a slow-spreading ridge-derived ophiolite: An example from the Isabela ophiolite in the Philippines: Island Arc, v. 14, p. 272–294.

Andal, E. S., Yumul, G. P. J., Listanco, E. L., Tamayo, R. A. J., Dimalanta, C. B., and Ishii, T., 2005, Characterization of the Pleistocene volcanic chain of the Bicol arc, Philippines: Implications for geohazard assessment: Terrestrial, Atmosphere and Ocean, v. 16, p. 865-883.

Aoki, M., Comsti, E. C., Lazo, F. B., and Matsuhisa, Y., 1993, Advanced argillic alteration and geochemistry of alunite in an evolving hydrothermal system at Baguio, Northern Luzon, Philippines: Resource Geology, v. 43, p. 155-164.

Aquino, J. S., 1993, Spatio-temporal relationships and evolution of advanced argillic alteration system at Dizon porphyry copper-gold deposit, Philippines: Unpublished PhD thesis, James Cook University, 258 p.

Armstrong, J. T., 1988, Quantitative analysis of silicates and oxide minerals: Comparison of Monte-Carlo, ZAF and Phi-Rho-Z procedures: Microbeam Analysis, p. 239-246.

Arribas, A., Arribas, I., Draper, G., Hall, C., Kesler, S., McEwan, C., and Muntean, J., 2011, 40Ar/39Ar dating of alunite from the Pueblo Viejo gold-silver district, Dominican Republic: ECONOMIC GEOLOGY, v. 106, p. 1059-1070.

Arribas, A., Hedenquist, J. W., Itaya, T., Okada, T., Concepcion, R. A., and Garcia, J. S., Jr, 1995, Contemporaneous formation of adjacent porphyry and epithermal Cu–Au deposits over 300 ka in northern Luzon, Philippines: Geology, v. 23, p. 337-340.

Aurelio, M. A., 2000a, Tectonics of the Philippines revisited: Journal of the Geological Society of the Philippines, v. 55, p. 119-183.

Aurelio, M. A., 2000b, Shear partitioning in the Philippines: Constraints from Philippine Fault and global positioning data: Island Arc, v. 9, p. 584-597.

Aurelio, M. A., Pagado, E. S., and Tebar, H. J., 1993, Kinematics of the Philippine Fault System at the Tongonan Geothermal Field, N. Leyte: Implications for geothermal exploration and development: Journal of the Geological Society of the Philippines, v. 48, p. 1–20.

Ayson, J. N. R., 1987, Results of semi-detailed geological and geochemical survey of Pamplona sulphur area, SE Negros: UNDTCD PHI/85/001 Internal Technical Report GCR/86/11.

Bajnóczi, B., Seres-Hartai, E., and Nagy, G., 2004, Phosphate-bearing minerals in the advanced argillic alteration zones of high-sulphidation type ore deposits in the Carpatho-Pannonian region: Acta Mineralogica-Petrographica, v. 45, p. 81-92.

Baker, J., Peate, D., Waight, T., and Meyzen, C., 2004, Pb isotopic analysis of standards and samples using a Pb-207-Pb-204 double spike and thallium to correct for mass bias with a double-focusing MC-ICP-MS: Chemical Geology, v. 211, p. 275-303.

Baker, M. J., Crawford, A. J., and Withnall, I. W., 2010, Geochemical, Sm-Nd isotopic characteristics and petrogenesis of Paleoproterozoic mafic rocks from the Georgetown Inlier, North Queensland: Implications for relationship with the Broken Hill and Mount Isa eastern succession: Precambrian Research, v. 177, p. 39-54.

Balce, G. R., 1964, Geology and coal resources of the Biga Area, Toledo City, Cebu Island: Bureau of Mines and Geosciences, Ministry of Natural Resources, Philippines.

Balce, G. R., Alcantara, P. H., Morante, E. M., and Almogela, D. H., 1976, Tectonic framework of the Philippine archipelago: A review: Philippine Bureau of Mines Report, Manila, 59 p.

Baldwin, J. A., and Pearce, J. A., 1982, Discrimination of productive and nonproductive porphyritic intrusions in the Chilean Andes: ECONOMIC GEOLOGY, v. 77, p. 664-674.

Barnes, H. L., 1967, Geochemistry of hydrothermal ore deposits: New York, Holt, Rinehart, and Winston, p. 670.

Barrett, T. J., Jarvis, I., and Jarvis, K. E., 1990, Rare earth element geochemistry of massive sulfides-sulfates and gossans on the Southern Explorer Ridge: Geology, v. 18, p. 583-586.

Barrett, T. J., and MacLean, W. H., 1991, Chemical, mass, and oxygen isotope changes during extreme hydrothermal alteration of an Archaean rhyolite, Noranda, Quebec: ECONOMIC GEOLOGY, v. 86, p. 406-414.

Barrett, T. J., Cattalani, S., and MacLean, W. H., 1993, Volcanic lithogeochemistry and alteration at the Delbridge massive sulfide deposit, Noranda, Quebec: Journal of Geochemical Exploration, v. 48, p. 135-173.

Barrett, T. J., and MacLean, W. H., 1994a, Mass changes in hydrothermal alteration zones associated with VMS deposits of the Noranda area: Exploration Mining Geology, v. 3, p. 131-160.

Barrett, T. J., and MacLean, W. H., 1994b, Chemostratigraphy and hydrothermal alteration in exploration for VHMS deposits in greenstones and younger volcanic rocks, in Lentz , D.R., ed., Alteration and alteration processes associated with ore forming systems, 11, Geological Society of Canada Short Course Notes, p. 433-467.

Barrett, T. J., and MacLean, W. H., 1999, Volcanic sequences, lithogeochemistry and hydrothermal alteration in some bimodal volcanic-associated massive sulfide systems: Reviews in Economic Geology, v. 8, p. 101-131.

Barrett, T. J., MacLean, W. H., and Tennant, S. C., 2001, Volcanic sequence and alteration at Parys Mountain volcanic-hosted massive sulfide deposit, Wales, United Kingdom - applications of immobile element lithogeochemistry: ECONOMIC GEOLOGY, v. 96, p. 1279-1305.

Barrier, E., Aurelio, M., Muller, C., Pubellier, M., Rangin, C., Quebral, R., and Rangin, C., 1988, The Philippines fault: An active strike-slip fault behind an oblique subduction zone: Académie des Sciences Comptes Rendus, v. 311, p. 181-188.

Barrier, E., Huchon, P., and Aurelio, M. A., 1991, Philippine fault: a key for Philippine kinematics: Geology, v. 19, p. 32-35.

Batkhishig, B., Noriyoshi, T., and Greg, B., 2010, Magmatism of the Shuteen Complex and Carboniferous subduction of the Gurvansaikhan terrane, South Mongolia: Journal of Asian Earth Sciences, v. 37, p. 399-411.

Bautista, B. C., Bautista, M. L. P., Oike, K., Wu, F. T., and Punongbayan, R. S., 2001, A new insight on the geometry of subducting slabs in northern Luzon, Philippines: Tectonophysics, v. 339, p. 279-310.

Bellon, H., and Yumul, G. P., 2000, Miocene to Quaternary adakites and related rocks in Western Philippine arc sequences: Comptes Rendus de l'Académie des Sciences, v. 333, p. 343-350.

Bergman, S. C., Hutchinson, C. S., Swauger, D. A., and Graves, J. E., 2011, K-Ar ages of the Sabah Cenozoic volcanic rocks: Bulletin of the Geological Society of Malaysia.

Bethke, P. M., Rye, R. O., Stoffregen, R. E., and Vikre, P., 2005, Evolution of the magmatic-hydrothermal acid-sulfate system at Summitville, Colorado: integration of geological, stable-isotope, and fluid-inclusion evidence: Chemical Geology, v. 215, p. 281-315.

Black, L. P., and Gulson, B. L., 1978, The age of the Mud tank Carbonatite, Strangways Range, Northern Territory: Journal of Australian Geology and Geophysics, v. 3, p. 227-232.

Black, L. P., Kamo, S. L., Allen, C. M., Davis, D. W., Aleninikoff, J. N., Valley, J. W., Mundil, R., Campbell, I. H., Korsch, R. J., Williams, I. S., and Foudoulis, C., 2004, Improved 206Pb/238U microprobe geochronology by the monitoring of a trace-element related matrix effect; SHRIMP, ID-TIMS, ELA-ICP-MS, and oxygen isotope documentation for a series of zircon standards: Chemical Geology, v. 205, p. 115-140.

Black, L. P., Kamos, L., Allen, C. M., Aleinikoff, J. N., Davis, D. W., Korsch, R. J., and Foudoulis, C., 2003, TEMORA 1: A new zircon standard for Phanerozoic U-Pb geochronology: Chemical Geology, v. 200, p. 155-170.

Blackwell, J. L., 2010, Characteristics and origins of breccias in a volcanic-hosted alkalic epithermal gold deposit, Ladolam, Lihir Island, Papua New Guinea: Unpublished thesis, University of Tasmania, Hobart, Australia, 203 p.

Blackwell, J. L., Cooke, D. R., McPhie, J., and Simpson, K. A., 2014, Lithofacies associations and evolution of the volcanic host succession to the Minifie ore zone: Ladolam gold deposit, Lihir island, Papua New Guinea: ECONOMIC GEOLOGY, v. 109, p. 1137-1160.

BMG, 1977, Geology and mineral resources of Agusan Province, Geological Survey Division.

BMG, 1986, Geology and mineral resources of the Philippines: Metro Manila, Philippines, Bureau of Mines and Geosciences, Ministry of Natural Resources, 446 p.

Bobis, R., and Comia, G., 1987, Geologic setting and alteration-mineralization characteristics of the Vista Alegre gold zone, Hinobaan, Negros, Philippines, Gold ’87 in the Philippine Setting, vol. I: Manila, PIMMGE, p. 326.

Booden, M. A., Mauk, J. L., and Simpson, K. A., 2011, Quantifying metasomatism in epithermal Au-Ag deposits: A case study from the Waitekauri area, New Zealand: ECONOMIC GEOLOGY, v. 106, p. 999-1030.

Border, A. M., 2005, Hinoba-an Project, Negros, Philippines: Copper Resources Corporation Internal Report, 75 p.

Braxton, D. P., 2007, Boyongan and Bayugo porphyry copper-gold deposits NE Mindanao, Philippines: Geology, geochemistry, and tectonic evolution: Unpublished thesis, University of Tasmania, 307 p.

Braxton, D. P., Cooke, D. R., Ignacio, A. M., Rye, R. O., and Waters, P. J., 2009, Ultra-deep oxidation and exotic copper formation at the late Pliocene Boyongan and Bayugo porphyry copper-gold deposits, Surigao, Philippines: Geology, Mineralogy, paleoaltimetry, and their implications for geologic, physiographic, and tectonic controls: ECONOMIC GEOLOGY, v. 104, p. 333-349.

Braxton, D. P., and Mathur, R., 2011, Exploration applications of copper isotopes in the supergene environment: A case study of the Bayugo porphyry copper-gold deposit, southern Philippines: ECONOMIC GEOLOGY, v. 106, p. 1447–1463.

Brooks, W. E., 2011, Silver: United States Geological Survey: 2009 Minerals Yearbook, v. I Metals and Minerals, p. 68.1-68.14.

Bryner, L., 1969, Ore deposits of the Philippines - An introduction to their geology: ECONOMIC GEOLOGY, v. 64, p. 644-666.

Burnham, C. W., 1985, Energy release in subvolcanic environments: Implications for breccia formation: ECONOMIC GEOLOGY, v. 80, p. 1515-1522.

Burton, C. K., 1983, Observations on the geology of the porphyry copper sub-province of southwest Negros, Philippines: Bulletin of the Geological Society of Malaysia, v. 16, p. 215-239.

Cabanis, B., and Lecolle, M., 1989, The La/10-Y/15-Nb/8 diagram: a tool for distinguishing volcanic series and discovering crustal mixing and/or contamination: Compte Rendus de I'Académie des Sciences Series II, v. 309, p. 2023-2029.

Caguiat, A. O., 1967, Geology and oil possibilities of PECs 107, 177 and 214, northeast Negros: Anglo-Philippines Oil Corp. Unpublished report.

Cardwell, R. K., Isacks, B. L., and Karig, D. E., 1980, The spatial distribution of earthquakes, focal mechanism solutions and subducted lithosphere in the Philippine and northeastern Indonesia islands, in Hayes, D. E., ed., The tectonic and geologic evolution of South-east Asian Seas and Islands. American Geophysical Union Monograph, 23, p. 1-53.

Castillo, P. R., and Escalada, P. P., 1979, Geology of Southwestern Negros Island: Philippine Bureau of Mines Technical Information Series v. 4, p. 22.

Castillo, P. R., Janney, P. E., and Solidum, R., 1999, Petrology and geochemistry of Camiguin Island, southern Philippines: Insights to the source for adakite and other lavas in a complex arc tectonic setting: Contributions to Mineralogy and Petrology, v. 134, p. 33-51.

Castillo, P. R., and Newhall, C. G., 2004, Geochemical constraints on possible subduction components in lavas of Mayon and Taal Volcanoes, Southern Luzon, Philippines: Journal of Petrology, v. 43, p. 1089-1108.

CCVG, 2004, International association of volcanology and chemistry of the Earth's interior: Newsletter, v. 18, p. 17.

Celiz, D., In prep., The geology, alteration, and mineralisation of the Sagay deposit in northern Negros, Philippines: Unpublished MSc thesis, University of Tasmania.

Cerpa, L., Bissig, T., Kyser, K., McEwan, C., Macassi, A., and Rios, H., 2013, Lithologic controls on mineralization at the Lagunas Norte high-sulfidation epithermal gold deposit, northern Peru: Mineralium Deposita, v. 48, p. 653-673.

Chaïrat, C., Schott, J., Oelkers, E. H., Lartigue, J. E., and Harouiya, N., 2007, Kinetics and mechanism of natural fluorapatite dissolution at 25°C and pH from 3 to 12: Geochimica et Cosmochimica Acta, v. 71, p. 5901-5912.

Chamberlin, R. M., and Anderson, O. J., 1989, The Laramide–Zuni uplift, southeastern Colorado Plateau: A microcosm of Eurasian-style indentation–extrusion tectonics?: New Mexico Geological Society, v. Guidebook 40, p. 81–90.

Chang, Z., 2009, Freeport-McMoRan blind test, Negros-Philippines, AMIRA P765A: Hobart, Tasmania, CODES, p. 30.

Chang, Z., Hedenquist, J. W., White, N. C., Cooke, D. R., Roach, M., Deyell, C. L., Garcia, J., Jr., Gemmell, J. B., McKnight, S., and Cuison, A. L., 2011, Exploration tools for linked porphyry and epithermal deposits: Example from the Mankayan intrusion-centered Cu–Au district, Luzon, Philippines: ECONOMIC GEOLOGY, v. 106, p. 1365-1398.

Chouinard, A., Williams-Jones, W., Leonardson, R., Hodgson, J., Silva, P., Tellez, C., Vega, J., and Rojas, F., 2005, Geology and genesis of the multistage high-sulfidation epithermal Pascua Au-Ag-Cu deposit, Chile and Argentina: ECONOMIC GEOLOGY, v. 100, p. 463-490.

Clancy, M., 2005, The rebirth of the Philippine mining industry, Philippine Business Leaders Forum Inc.: Makati, Philippines, p. 9.

Cohen, D. R., and Bowell, R. J., 2014, Exploration geochemistry, in Holland, H., and Turekian, K., eds., Treatise on Geochemistry, 2: Radarweg 29, PO Box 211, 1000 AE Amsterdam, Netherlands, Elsevier Ltd.

Cooke, D. R., Baker, M. J., Hollings, P., Sweet, G., Chang, Z., Danyushevsky, L., Gilbert, S., Zhou, T., White, N., Gemmell, J. B., and Inglis, S., 2014, New advances in detecting the distal geochemical footprints of porphyry systems—epidote mineral chemistry as a tool for vectoring and fertility assessments, in Kelley, K., and Golden, H. C., eds., Building exploration capability for the 21st century, 18: Littleton, Colorado, USA, Society of Economic Geologists, p. 127-152.

Cooke, D. R., and Bloom, M. S., 1990, Epithermal and subjacent porphyry mineralization, Acupan, Baguio district, Philippines: A fluid inclusion and paragenetic study: Journal of Geochemical Exploration, v. 35, p. 43.

Cooke, D. R., Hollings, P., and Chang, Z., 2011, Philippine porphyry and epithermal deposits: An introduction: ECONOMIC GEOLOGY, v. 106, p. 4.

Cooke, D. R., Hollings, P., and Walshe, J. L., 2005, Giant porphyry deposits: Characteristics, distribution, and tectonic controls: ECONOMIC GEOLOGY, v. 100, p. 801-818.

Cooke, D. R., Hollings, P., Wilkinson, J. J., and Tosdal, R., 2014, Geochemistry of porphyry deposits, in Holland, H., and Turekian, K., eds., Treatise on Geochemistry, 2: Radarweg 29, Netherlands, Elsevier Ltd, p. 357-381.

Cooke, D. R., and Simmons, S., 2000, Characteristics and genesis of epithermal gold deposits: Society of Economic Geologists Reviews, v. 13, p. 221-244.

Coope, J. A., 1973, Geochemical prospecting for porphyry copper-type mineralization - A review: Journal of Geochemical Exploration, v. 2, p. 81-102.

Cox, K. G., Bell, J. D., and Pankhurst, R. J., 1979, The interpretation of igneous rocks: London, George Allen and Unwin, 450 p.

Crane, D., and Kavalieris, I., 2012, Geologic overview of the Oyu Tolgoi porphyry Cu-Au-Mo deposits, Mongolia: Society of Economic Geologists Special Publication, v. 19, p. 187-213.

David, P. P., 1982, Some larger foraminifera of Negros Occidental, Bureau of Mines and Geosciences Journal: Unpublished report.

Davies, A. G. S., Cooke, D. R., Gemmell, J. B., and Simpson, K. A., 2008, Diatreme breccias at the Kelian gold mine, Kalimantan, Indonesia: Precursors to epithermal gold mineralization: ECONOMIC GEOLOGY, v. 103, p. 28.

Danyushevsky, L., Robinson, P., Gilbert, S., Norman, M., Large, R., McGoldrick, P., and Shelley, M., 2011, Routine quantitative multi-element analysis of sulphide minerals by laser ablation ICP-MS: Standard development and consideration of matrix effects: Geochemistry: Exploration, Environment, Analysis, v. 11, p. 51–60.

De Jesus, J. V., Yumul, G. P., and Faustino, D. V., 2000, The Cansiwang melange of southeast Bohol (central Philippines): Origin and tectonic implications: Island Arc, v. 9, p. 566-575.

de Rosen-Spence, A. F., Provost, G., Dimroth, E., Gochnauer, K., and Owen, V., 1980, Archaean subaqueous felsic flows, Rouyn-Noranda, Quebec, Canada, and their Quaternary equivalents: Precambrian Research, v. 12, p. 43-77.

Debon, F., and Le Fort, P., 1983, A chemical-mineralogical classification of common plutonic rocks and associations: Transactions of Royal Society of Edinburgh, Earth Sciences v. 73, p. 135–149.

Deen, J., Rye, R., Muñoz, J., and Drexler, J., 1994, The magmatic hydrothermal system at Julcani, Peru: Evidence from fluid inclusions and hydrogen and oxygen isotopes: ECONOMIC GEOLOGY, v. 89, p. 1924-1938.

Defant, M. J., and Drummond, M. S., 1990, Derivation of some modern arc magmas by melting of young subducted lithosphere: Nature, v. 347, p. 662–665.

Defant, M. J., and Drummond, M. S., 1993, Mount St. Helens: Potential example of the partial melting of the subducted lithosphere in a volcanic arc: Geology, v. 21, p. 547-550.

Defant, M. J., Jacques, D., Maury, R. C., de Boer, J., and Joron, J., 1989, Geochemistry and tectonic setting of the Luzon arc, Philippines: Geological Society of America Bulletin, v. 101, p. 663-672.

DePaolo, D. J., 1981, Trace element and isotopic effects of combined wallrock assimilation and fractional crystallization: Earth and Planetary Science Letters, v. 53, p. 189-202.

Deyell, C. L., and Hedenquist, J. W., 2011, Trace element geochemistry of enargite in the Mankayan district, Philippines: ECONOMIC GEOLOGY, v. 106, p. 1465–1478.

Deyell, C. L., Leonardson, R., Rye, R., Thompson, J. F. H., Bissig, T., and Cooke, D. R., 2005, Alunite in the Pascua-Lama high-sulfidation deposit: Constraints on alteration and ore deposition using stable isotope geochemistry: ECONOMIC GEOLOGY, v. 100, p. 131-148.

Dilek, Y., and Furnes, H., 2011, Ophiolite genesis and global tectonics: Geochemical and tectonic fingerprinting of ancient oceanic lithosphere: Geological Society of America Bulletin, v. 123, p. 387-411.

Dimalanta, C. B., and Yumul, G. P., 2006, Magmatic and amagmatic contributions to crustal growth of the Philippine island-arc system: Comparison of the Cretaceous and post-Cretaceous periods: Geosciences Journal, v. 10, p. 321-329.

Domasig, W., 1999, Summary report on Ayungon and Bantug east-central Negros gold prospects: Normandy Asia (Philippines) Inc, 41 p.

Donovan, J. J., Lowers, H. A., and Rusk, B. G., 2011, Improved electron probe microanalysis of trace elements in quartz: American Mineralogist, v. 96, p. 274-282.

Dove, P. M., and Rimstidt, J. D., 1994, Silica-water interactions, in Heaney, P. J., Prewitt, C. T., and Gibbs, G. V., eds., Silica: Physical behavior, geochemistry, and materials applications, 29, Mineralogical Society of America, p. 1-40.

Drummond, M. S., and Defant, M. J., 1990, A model for trondhjemite-tonalite-dacite genesis and crustal growth via slab melting: Archaean to modern comparisons: Journal of Geophysical Research, v. 95, p. 21503-21521.

Encarnacion, J. P., 2004, Multiple ophiolite generation preserved in the northern Philippines and the growth of an island arc complex: Tectonophysics, v. 392, p. 103-130.

Faustino, D. V., Yumul, G. P., Dimalanta, C. B., De Jesus, J. V., Zhou, M.-F., Aitchison, J. C., and Tamayo, R. A., 2006, Volcanic hypabyssal rock geochemistry of a subduction-related marginal basin ophiolite: Southeast Bohol Ophiolite-Cansiwang Mélange Complex, Central Philippines: Geosciences Journal, v. 10, p. 91-303.

Fernandez, J. C., 1981, Geology and mineral resources of the Philippines: Bureau of Mines and Geosciences, Ministry of Natural Resources, v. 1, p. 406.

Fischer, T., Sturchio, N. C., Stix, J., Arehart, G. B., Counce, D., and Williams, S. N., 1997, The chemical and isotopic composition of fumarolic gases and spring discharges from Galeras Volcano, Colombia: Journal of Volcanology and Geothermal Research, v. 77, p. 229-253.

Fleet, M. E., 2003, Sheet silicates: micas, Rock-Forming Minerals, 2nd edition 3A: London, The Geological Society, p. 41-297.

Fournier, R. O., 1983, A method of calculating quartz solubilities in aqueous sodium chloride solutions: Geochimica et Cosmochimica Acta, v. 47, p. 579-586.

Fournier, R. O., 1999, Hydrothermal processes related to movement of fluid from plastic into brittle rock in the magmatic-epithermal environment: ECONOMIC GEOLOGY, v. 94, p. 1193-1211.

Gaboreau, S., Beaufort, D., Viellard, P., Patrier, P., and Bruneton, P., 2005, Aluminium phosphate-sulphate minerals associated with Proterozoic unconformity-type uranium deposits in the East Alligator River Uranium Field, Northern Territories, Australia: The Canadian Mineralogist, v. 43, p. 813-827.

Gaboreau, S., Cuney, M., Quirt, D., Beaufort, D., Patrier, P., and Mathieu, R., 2007, Significance of aluminium phosphate-sulfate minerals associated with U unconformity-type deposits: The Athabasca basin, Canada: American Mineralogist, v. 92, p. 267-280.

Gaetani, G. A., and Grove, T. L., 2003, Experimental constraints on melt generation in the mantle wedge: American Geophysical Union Geophysical Monograph 138, p. 107-134.

Gall, Q., and Donaldson, J. A., 2006, Diagenetic fluorapatite and aluminium phosphate-sulphate in the Paleoproterozoic Thelon Formation and Hornby Bay Group, northwestern Canadian Shield: Canadian Journal of Earth Sciences, v. 43, p. 617-629.

Garcia, W. V., 2009, Geology of the Milagros project, Alto Chicama district, La Libertad, Peru.: Unpublished thesis, Colorado School of Mines, 162 p.

Garofalo, K., Tassi, F., Vaselli, O., Delgado-Huertas, A., Tedesco, D., Frische, M., Hansteen, T. H., Poreda, R. J., and Strauch, W., 2007, Fumarolic gases at Mombacho volcano (Nicaragua): presence of magmatic gas species and implications for volcanic surveillance: Bulletin of Volcanology, v. 69, p. 785-795.

Garwin, S. L., 2000, The setting, geometry and timing of intrusion-related hydrothermal systems in the vicinity of the Batu Hijau porphyry copper-gold deposit, Sumbawa, Indonesia: Unpublished Ph. D. thesis, University of Western Australia, 320 p.

Garwin, S. L., 2002, The geologic setting of intrusion-related hydrothermal systems near the Batu Hijau porphyry copper-gold deposit, Sumbawa, Indonesia, in Goldfarb, R. J., and Nielsen, R. L., eds., Integrated methods for discovery: Global exploration in the twenty-first century, Society of Economic Geologists Special Publication 9, p. 333-366.

Gemmell, J. B., Cooke, D. R., Wilkinson, J. J., Hollings, P., Baker, M. J., Zhang, L., Fox, N., White, N., Chen, H., Piquer, J., Jimenez, C., Testa, F. J., Thompson, J. A., Lounejeva, E., and Wilkinson, C. C., 2014, Enhanced geochemical targeting in magmatic-hydrothermal systems, in AMIRA, ed., P1060: Hobart, Tasmania, University of Tasmania, CODES.

George, M. W., 2004, Gold: United States Geological Survey, 2004 minerals yearbook: Minerals Yearbook, v. I Metals and Minerals, p. 32.1-32.22.

GEOROC, 2016, GEOROC: Geochemistry of rocks of the oceans and continents, http://georoc.mpch-mainz.gwdg.de/georoc/Start.asp, 2016.

Gervasio, F. C., 1967, Age and nature of the orogenesis of the Philippines: Tectonophysics, v. 4, p. 379-402.

Gifkins, K., Herrmann, W., and Large, R., 2005, Altered volcanic rocks: a guide to description and interpretation: Centre for Ore Deposit Research, CODES, University of Tasmania, 288 p.

Giggenbach, W., 1982, The chemical and isotopic composition of gas discharges from New Zealand andesitic volcanoes: Bulletin of Volcanology, v. 45, p. 253-255.

Gill, J. B., 1981, Orogenic andesites and plate tectonics: New York, Springer Verlag, 390 p.

Gorrepati, E. A., 2009, Silica precipitation from analcime dissolution: Unpublished PhD thesis, University of Michigan, 143 p.

Gorrepati, E. A., Pattanapong, W., Raha, S., and Fogler, H. S., 2010, Silica precipitation in acidic solutions: Mechanism, pH effect, and salt effect: Langmuir, v. 26, p. 10467-10474.

Govet, G. J. S., 1983, Handbook of Exploration Geochemistry: Rock Geochemistry in Mineral Exploration, Vol. 3, 461 p.

Grant, J. A., 1986, The isocon diagram-A simple solution to Gresens' equation for metasomatic alteration: ECONOMIC GEOLOGY, v. 81, p. 1976-1982.

Gresens, R., 1967, Composition-volume relationships of metasomatism: Chemical Geology, v. 2, p. 47-65.

Guidry, M. W., and Mackenzie, F. T., 2003, Experimental study of igneous and sedimentary apatite dissolution: Control of pH, distance from equilibrium, and temperature on dissolution rates: Geochimica et Cosmochimica Acta, v. 67, p. 2949-2963.

Gustafson, L., Vidal, C., Pinto, R., and Noble, D., 2004, Porphyry-epithermal transition, Cajamarca region, northern Peru: Society of Economic Geologists Special Publication 11, p. 279-300.

Hall, R., 2002, Cenozoic geological and plate tectonic evolution of SE Asia and the SW Pacific: computer-based reconstructions, models and animations: Journal of Asian Earth Sciences, v. 20, p. 353-431.

Hamburger, M. W., Cardwell, R. K., and Isacks, B. L., 1983, Seismotectonics of the northern Philippine island arc: American Geophysical Union Monograph, v. 27, p. 22.

Harouiya, N., Chaïrat, C., Köhler, S., Gout, R., and Oelkers, E. H., 2007, The dissolution kinetics and apparent solubility of natural apatite in closed reactors at temperatures from 5 to 50°C and pH from 1 to 6: Chemical Geology, v. 244, p. 553-568.

Harris, N. B. W., Pearce, J. A., and Tindle, A. G., 1986, Geochemical characteristics of collision zone magmatism: Geological Society London Special Publications, v. 19, p. 67-81.

Hastie, A. R., Kerr, A. C., Pearce, J. A., and Mitchell, S. F., 2007, Classification of altered volcanic island arc rocks using immobile trace elements: development of the Th–Co discrimination diagram: Journal of Petrology, v. 48, p. 2341-2357.

Hawkesworth, C. J., Gallagher, K., Hergt, J. M., and McDermott, F., 1993, Mantle and slab contributions in arc magmas: Annual Review of Earth and Planetary Sciences, v. 21, p. 175-204.

Hedenquist, J. W., 1995, The ascent of magmatic fluid: Discharge versus mineralization: Magmas, Fluids and Ore Deposits Mineral Association of Canada, v. 23, p. 26.

Hedenquist, J. W., Arribas, A., and Gonzalez-Urien, E., 2000, Exploration for epithermal gold deposits: Society of Economic Geologists Reviews, v. 13, p. 245-277.

Hedenquist, J. W., Arribas, A., and Reynolds, T. J., 1998, Evolution of an intrusion-centered hydrothermal system: Far Southeast–Lepanto porphyry and epithermal Cu–Au deposits, Philippines: ECONOMIC GEOLOGY, v. 93, p. 373–404.

Hedenquist, J. W., Matsuhisa, Y., Izawa, E., White, N. C., Giggenbach, W., and Aoki, M., 1994, Geology, geochemistry, and origin of high sulfidation Cu-Au mineralization in the Nansatsu district, Japan: ECONOMIC GEOLOGY, v. 89, p. 1-30.

Hedenquist, J. W., and Taran, Y. A., 2013, Modelling the formation of advanced argillic lithocaps: Volcanic vapor condensation above porphyry intrusions: ECONOMIC GEOLOGY, v. 108, p. 18.

Hehnke, C., Ballantyne, G., Martin, H., Hart, W., Schwarz, A., and Stein, H., 2012, Geology and exploration progress at the Resolution porphyry Cu-Mo deposit, Arizona, in Hedenquist, J. W., Harris, M., and Camus, F., eds., Geology and Genesis of Major Copper Deposits and Districts of the World: A Tribute to Richard H. Sillitoe, 16. Special Publications of the Society of Economic Geologists: Lancaster, PA, USA, Special Publications of the Society of Economic Geologists, p. 147-166.

Hervé, M., Sillitoe, R. H., Wong, C., Fernández, P., Crignola, F., Ipinza, M., and Urzúa, F., 2012, Geologic overview of the Escondida porphyry copper district, Northern Chile, in Hedenquist, J. W., Harris, M., and Camus, F., eds., Geology and Genesis of Major Copper Deposits and Districts of the World: A Tribute to Richard H. Sillitoe, 16. Special Publications of the Society of Economic Geologists: Lancaster, PA, USA, Special Publications of the Society of Economic Geologists, p. 55-78.

Herrmann, W., Green, G. R., Barton, M. D., and Davidson, G. J., 2009, Lithogeochemical and Stable Isotopic Insights into Submarine Genesis of Pyrophyllite-Altered Facies at the Boco Prospect, Western Tasmania: ECONOMIC GEOLOGY, v. 104, p. 775-792.

Hildreth, W., and Moorbath, S., 1988, Crustal contributions to arc magmatism in the Andes of central Chile: Contributions to Mineralogy and Petrology, v. 98, p. 455-489.

Hollings, P., Cooke, D. R., Waters, P. J., and Cousens, B., 2011a, Igneous geochemistry of mineralized rocks of the Baguio district, Philippines: Implications for tectonic evolution and the genesis of porphyry-style mineralization: ECONOMIC GEOLOGY, v. 106, p. 1317–1333.

Hollings, P., Wolfe, R., Cooke, D. R., and Waters, P. J., 2011b, Geochemistry of Tertiary igneous rocks of northern Luzon, Philippines: Evidence for a back-arc setting for alkalic porphyry copper-gold deposits and a case for slab roll-back?: ECONOMIC GEOLOGY, v. 106, p. 1257–1277.

Hsu, L. C., 1986, The stability relationships of zunyite under hydrothermal conditions: Mining Geology, v. 36, p. 219-230.

Huang, R., and Audétat, A., 2012, The titanium-in-quartz (TitaniQ) thermobarometer: A critical examination and re-calibration: Geochimica et Cosmochimica Acta, v. 84, p. 75-89.

Ishikawa, Y., Sawaguchi, T., Iwaya, S., and Horiuchi, M., 1976, Delineation of prospecting targets for Kuroko deposits based on modes of volcanism of underlying dacite and alteration haloes: Mining Geology, v. 26, p. 12.

Jackson, S. E., Pearson, N. J., Griffin, W. L., and Belousova, E. A., 2004, The application of laser ablation-inductively coupled plasma-mass spectrometry to in situ U–Pb zircon geochronology: Chemical Geology, v. 211, p. 47-69.

Japan, J. I. C. A.-M. M. A. o., 1977, Report on geological survey of Northeastern Luzon, Phase 3: Japan International Cooperation Agency, 106 p.

Jego, S., Maury, R. C., Polve, M., Yumul, G. P., Bellon, H., Tamayo, R. A., and Cotten, J., 2005, Geochemistry of adakites from the Philippines: Constraints on their origins: Resource Geology, v. 55, p. 163-187.

Jimenez, F. A., Yumul, G. P., Maglambayan, V. B., and Tamayo, R. A., 2002, Shallow to near-surface, vein-type epithermal gold mineralization at Lalab in the Sibutad gold deposit, Zamboanga del Norte, Mindanao, Philippines.: Journal of Asian Earth Sciences, v. 21, p. 119-133.

Judges, J. S., 1971, A study of the dissolution of SiO2 in acidic fluoride solutions: Journal of the Electrochemical Society, v. 118.

Jumawan, F. T., Yumul, G. P., and Tamayo, R. A., 1998, Using geochemistry as a tool in determining the tectonic setting and mineralization potential of an exposed upper mantle-crust sequence: Example from the Amnay ophiolitic complex in occidental Mindoro, Philippines: Journal of the Geological Society of the Philippines, v. 53, p. 24-48.

Karig, D. E., 1983, Accreted terrenes in the northern part of the Philippine archipelago: Tectonics, v. 2, p. 211-236.

Karig, D. E., Sarewitz, D. R., and Haeck, G. D., 1986, Role of strike-slip faulting in the evolution of allochthonous terranes in the Philippines: Geology, v. 14, p. 852-855.

Kay, R. W., 1978, Aleutian magnesian andesites: Melts from subducted Pacific Ocean crust: Journal of Volcanology and Geothermal Research, v. 4, p. 117-132.

Keary, P., 2001, Dictionary of geology: UK, Penguin, 336 p.

Keppler, H., 1996, Constraints from partitioning experiments on the composition of subduction-zone fluids: Nature, v. 380, p. 237-240.

Khashgerel, B. E., Kavalieris, I., and Hayashi, K., 2008, Mineralogy, textures, and whole-rock geochemistry of advanced argillic alteration: Hugo Dummett porphyry Cu–Au deposit, Oyu Tolgoi mineral district, Mongolia: Mineralium Deposita, v. 43, p. 913-932.

Khashgerel, B. E., Rye, R., Kavalieris, I., and Hayashi, K., 2009, The sericitic to advanced argillic transition: Stable isotope and mineralogical characteristics from the Hugo Dummett porphyry Cu-Au deposit, Oyu Tolgoi district, Mongolia: ECONOMIC GEOLOGY, v. 104.

Kikuyama, H., Waki, M., Kawanabe, I., Miyashita, M., Yabune, T., Miki, N., Takano, J., and Ohmi, T., 1992, Etching rate and mechanism of doped oxide in buffered hydrogen fluoride solution: Journal of the Electrochemical Society, v. 139, p. 2239-2243.

Kirkham, R. V., and Dunne, K. P. E., 2000, World distribution of porphyry, porphyry-associated skarn, and bulk-tonnage epithermal deposits and occurrences: Geological Survey of Canada Open File 3792a, p. 26.

Knittel, U., and Defant, M. J., 1988, Sr-isotopic and trace element variation in Oligocene to recent igneous rocks from the Philippine island arc: Evidence for Recent enrichment in the sub-Philippine mantle: Earth Planetary Science Letters, v. 87, p. 87-99.

Kosler, J., 2001, Laser-ablation ICPMS study of metamorphic minerals and processes, in Sylvester, P. J., ed., Laser-ablation-ICPMS in the earth sciences: Principles and applications Mineralogical Association of Canada Short Course Handbook 29, p. 182-202.

Kouzmanov, K., Pettke, T., and Heinrich, C., 2010, Direct analysis of ore-precipitating fluids: Combined IR microscopy and LA-ICP-MS study of fluid inclusions in opaque ore minerals: ECONOMIC GEOLOGY, v. 105, p. 351-373.

La Roche, H. d., Leterrier, J., Grandclaude, P., and Marchal, M., 1980, A classification of volcanic and plutonic rocks using R1-R2 diagram and major element analyses; its relationships with current nomenclature.: Chemical Geology, v. 29, p. 183–210.

Large, R., Danyushevsky, L., Hollit, C., Maslennikov, V., Meffre, S., Gilbert, S., Bull, S., Scott, R., Emsbo, P., Thomas, H., Singh, B., and Foster, J., 2009, Gold and trace element zonation in pyrite using a laser imaging technique: Implications for the timing of gold in orogenic and Carlin-style sediment-hosted deposits: ECONOMIC GEOLOGY, v. 104, p. 34.

Large, R., Gemmell, J. B., Paulick, H., and Huston, D., 2001, The alteration box plot: A simple approach to understanding the relationship between alteration mineralogy and lithogeochemistry associated with volcanic-hosted massive sulfide deposits: ECONOMIC GEOLOGY, v. 96, p. 957-971.

Le Maitre, R. W., Bateman, P., Dudek, A., and Keller, J., 1989, A classification of igneous rocks and glossary of term: Recommendations of the International Union of Geological Sciences subcommission on the systematics of igneous rocks: Blackwell Scientific Publications, Oxford, 193 p.

Leys, C., Cloos, M., New, B. T., and Macdonald, G., 2012, Copper-gold±molybdenum deposits of the Ertsberg-Grasberg district, Papua, Indonesia, in Hedenquist, J. W., Harris, M., and Camus, F., eds., Geology and Genesis of Major Copper Deposits and Districts of the World: A Tribute to Richard H. Sillitoe, 16. Special Publications of the Society of Economic Geologists: Lancaster, PA, USA, Special Publications of the Society of Economic Geologists, p. 215-235.

Li, X., Long, W. G., Li, Q. L., Liu, Y., Zheng, Y. F., Yang, Y. H., Chamberlain, K. R., Wan, D. F., Guo, C. H., Wang, X. C., and Tao, H., 2010, Penglai zircon megacrysts: A potential new working reference material for microbeam determination of Hf-O isotopes and U-Pb age: Geostandards and Geoanalytical Research, v. 34, p. 117-134.

Liang, D. T., and Readey, D. W., 1987, Dissolution kinetics of crystalline and amorphous silica in hydrofluoric–hydrochloric acid mixtures: Journal of the American Ceramic Society, v. 70, p. 570–577.

Lickfold, V., 2002, Intrusive history and volatile evolution of the Endeavour porphyry Cu-Au deposits, Goonumbla district, NSW, Australia: Unpub. PhD thesis, University of Tasmania, 368 p.

Lickfold, V., Cooke, D. R., Crawford, A. J., and Fanning, C. M., 2007, Shoshonitic magmatism and the formation of the Northparkes porphyry Cu–Au deposits, New South Wales: Australian Journal of Earth Sciences, v. 54, p. 417-444.

Lickfold, V., Cooke, D. R., Smith, S. G., and Ullrich, T. D., 2003, Endeavour Copper-Gold Porphyry Deposits, Northparkes, New South Wales: Intrusive History and Fluid Evolution: ECONOMIC GEOLOGY, v. 98, p. 1607-1636.

López, L., 1982, Características geoquímicas de rocas ígneas asociadas con pórfidos cupríferos chilenos: Revista Geológica de Chile, v. 17, p. 3-19.

MacLean, W. H., and Kranidiotis, P., 1987, Immobile elements as monitors of mass transfer in hydrothermal alteration - Phelps Dodge massive sulfide deposit, Matagami, Quebec: ECONOMIC GEOLOGY, v. 82, no. 951-962.

MacLean, W. H., and Hoy, L. D., 1991, Geochemistry of hydrothermally altered rocks at the Horne Mine, Noranda, Quebec: ECONOMIC GEOLOGY, v. 86, p. 506-528.

MacLean, W. H., and Barrett, T. J., 1993, Lithogeochemical techniques using immobile elements: Journal of Geochemical Exploration, v. 48, p. 109-133.

Maglambayan, V. B., Ishiyama, D., Mizuta, T., Imai, A., and Ishikawa, Y., 1998, Geology, mineralogy, and formation environment of the disseminated gold-silver telluride Bulawan deposit, Negros Occidental, Philippines: Resource Geology, v. 48, p. 87-104.

Malterre, P., 1989, Histoire sédimentaire, magmatique, tectonique et métallogénique d'un arc océanique déformé en régime de transpression Unpublished PhD thesis, Université Bretagne Occidentale, 304 p.

Manning, C. E., 2004, The chemistry of subduction-zone fluids: Earth and Planetary Science Letters, v. 223, p. 1-16.

Marchadier, Y., and Rangin, C., 1990, Polyphased tectonics at the southern tip of the Manila Trench, Mindoro-Tablas islands Philippines: Tectonophysics v. 183, p. 273-287.

Marini, J. C., Chauvel, C., and Maury, R. C., 2005, Hf isotope compositions of northern Luzon arc lavas suggest involvement of pelagic sediments in their source: Contributions to Mineralogy and Petrology, v. 149, p. 216-232.

Mauk, J. L., and Simpson, M. P., 2007, Geochemistry and stable isotope composition of altered rocks at the Golden Cross epithermal Au-Ag deposit, New Zealand: ECONOMIC GEOLOGY, v. 102, p. 841-871.

Maury, R. C., Defant, M. J., Bellon, H., Jacques, D., Joron, F., McDermott, F., and Vidal, P., 1998, Temporal geochemical trends in Northern Luzon arc lavas (Philippines): implications on metasomatic processes in the island arc mantle: Bulletin de la Société Géologique de France, v. 1, p. 69-80.

McDermott, F., Delfin, F. G., Defant, M. J., Turner, S., and Maury, R., 2005, The petrogenesis of volcanics from Mt. Bulusan and Mt. Mayon in the Bicol arc, the Philippines: Contribution to Mineralogy and Petrology, v. 150, p. 652-670.

McQueen KG, Cross AJ, 1998, Magnetite as a geochemical sampling medium: application to skarn deposits. In: Eggleton RA (ed) The State of the Regolith. Geological Society of Australia, Brisbane, pp 194–199

McPhie, J., Doyle, M., and Allen, R. L., 1993, Volcanic textures: A guide to the interpretation of textures in volcanic rocks: Hobart, Tasmania, Centre for Ore Deposit and Exploration Studies, University of Tasmania, 196 p.

Meffre, S., Large, R., Scott, R., Woodhead, J., Chang, Z., Gilbert, S. E., Danyushevsky, L. V., Maslennikov, V., and Hergt, J. M., 2008, Age and pyrite Pb-isotopic composition of the giant Sukhoi Log sediment-hosted gold deposit, Russia: Geochimica et Cosmochimica Acta, v. 72, p. 2377-2391.

Meyer, C., and Hemley, J. J., 1967, Wall rock alteration, in Barnes, H. L., ed., Geochemistry of Hydrothermal Ore Deposits: New York, Holt, Reinhart and Winston, p. 166-235.

Middlemost, E. A. K., 1994, Naming materials in the magma/igneous rock system: Earth Science Reviews, v. 37, p. 215-224.

Mines and Geosciences Bureau, 2004, Geology and mineral resources of the Philippines: Metro Manila, Philippines, 389 p.

Mitchell, A. H. G., Hernandez, F., and de la Cruz, A. P., 1986, Cenozoic evolution of the Philippine archipelago: Journal of Southeast Asian Earth Sciences, v. 1, p. 3-22.

Mitchell, A. H. G., and Leach, T. M., 1991, Epithermal gold in the Philippines: Island arc metallogenesis, geothermal systems and geology: London, 457 p.

Mitra, A., 2008, Silica dissolution at low pH in the presence and absence of fluoride: Unpublished PhD thesis, Virginia Polytechnic Institute and State University, 84 p.

Mitra, A., and Rimstidt, J. D., 2009, Solubility and dissolution rate of silica in acid fluoride solutions: Geochimica et Cosmochimica Acta, v. 73, p. 7045-7059.

MMAJ-JICA, 1988, Mineral deposits and tectonics of two contrasting geologic environments in the Republic of the Philippines – Palawan V-VI, area, West Negros area and Samar I-IIII area: Report on the Mineral Exploration, 347 p.

Moores, E. M., 1982, Origin and emplacement of ophiolites: Reviews of Geophysics and Space Physics, v. 20, p. 735-760.

Morante, E. M., and Allen, C. R., 1973, Displacement on the Philippine fault during the Ragay Gulf earthquake of 17 March 1973: Geological Society of America Abstracts with Programs, v. 5, p. 744-745.

Müller, A., Herrington, R., Armstrong, R., Seltmann, R., Kirwin, D. J., Stenina, N. G., and Kronz, A., 2010, Trace elements and cathodoluminescence of quartz in stockwork veins of Mongolian porphyry-style deposits: Mineralium Deposita, v. 45, p. 707-727.

Müller, C., and von Daniels, C. H., 1981, Stratigraphical and paleoenvironmental studies (Oligocene - Quaternary) in the Visayan Basin, Philippines: Newsletters on Stratigraphy, v. 10, p. 52-64.

Muntean, J. L., and Einaudi, M. T., 2001, Porphyry-epithermal transition: Maricunga belt, Northern Chile: ECONOMIC GEOLOGY, v. 96, p. 743-772.

Nadoll, P., Mauk, J. L., Leveille, R. A., and Koenig, A. E., 2015, Geochemistry of magnetite from porphyry Cu and skarn deposits in the southwestern United States: Mineralium Deposita, v. 50, p. 493–515.

Nakagawa, M., and Franco, H., 1996, PGE abundance in ophiolitic rocks and soil from Samar and Dinagat islands, Philippines: Journal of the Geological Society of the Philippines, v. 51, p. 73-84.

Nakata, T., Sangawa, A., and Hirano, S. C., 1977, A report on tectonic landforms along the Philippine fault in northern Luzon, Philippines: Tohoku University Science Reports, 27: Sendai, Japan, p. 69-93.

NOAA, 2014, Global digital elevation data, in NOAA, ed.: Silver Spring, Maryland, United States.

Noble, D., Vidal, C., Miranda, M., Amaya, W., and McCormack, J., 2011, Ovoidal-and mottled-textured rock and associated silica veinlets and their formation by high-temperature outgassing of subjacent magma, Great Basin Evolution and Metallogeny, II.

Ohba, T., Hirabayashi, J.-i., Nogami, K., Kusakabe, M., and Yoshida, M., 2008, Magma degassing process during the eruption of Mt. Unzen, Japan in 1991 to 1995: Modelling with the chemical composition of volcanic gas: Journal of Volcanology and Geothermal Research, v. 175, p. 120-132.

Oliver, M., and Webster, R., 2015, Basic steps in geostatistics: The variogram and kriging, Springer International Publishing, 100 p.

Ostapenko, G. T., Gamarnik, M. Y., Gorogotskaya, L. I., Kuznetsov, G. V., Tarashchan, A. N., and Timoshkova, L. P., 1987, Isomorphism of titanium substitution for silicon in quartz: experimental data: Mineral Zh, v. 9, p. 30-40.

Ostapenko, G. T., Tarashchan, A. N., and Mitsyuk, B. M., 2007, Rutile-quartz geothermobarometer: Geochemistry International, v. 45, p. 506-508.

Oyarzun, R., Márquez, A., Lillo, J., López, I., and Rivera, S., 2001, Giant versus small porphyry copper deposits of Cenozoic age in northern Chile: Adakitic versus normal calc-alkaline magmatism: Mineralium Deposita, v. 36, p. 794-798.

Ozawa, A., Tagami, T., Listanco, E. L., Arpa, C. B., and Sudo, M., 2004, Initiation and propagation of subduction along the Philippine Trench: evidence for the temporal and spatial distribution: Journal of Asian Earth Sciences, v. 23, p. 105-111.

Padilla-Garza, R. A., Titley, S. R., and Pimentel B., F., 2001, Geology of the Escondida porphyry copper deposit, Antofagasta region, Chile: ECONOMIC GEOLOGY, v. 96, p. 307-324.

Paton, C., Woodhead, J. D., Hellstrom, J. C., Hergt, J. M., Greig, A., and Maas, R., 2010, Improved laser ablation U-Pb zircon geochronology through robust down-hole fractionation correction: Geochemistry, Geophysics, Geosystems, v. 11, p. 1525-2027.

Pearce, J. A., 1996, A users guide to basalt discrimination diagrams. Trace element geochemistry of volcanic rocks: Applications for massive sulphide exploration: Geological Association of Canada, Short Course Notes, v. 12, p. 79-113.

Pearce, J. A., 2008, Geochemical fingerprinting of oceanic basalts with applications to ophiolite classification and the search for Archean oceanic crust: Lithos, v. 100, p. 14-48.

Pearce, J. A., and Cann, J. R., 1973, Tectonic setting of basic volcanic rocks determined using trace element analyses: Earth and Planetary Science Letters, v. 19, p. 290-300.

Pearce, J. A., and Peate, D. W., 1995, Tectonic implications of the composition of volcanic arc magmas: Annual Review of Earth and Planetary Sciences, v. 23, p. 251-285.

Peña, R., 1996, On recent interpretations on the ophiolites of Central Luzon and ophiolite associations in northern Luzon: Journal of the Geological Society of the Philippines, v. 51, p. 37-47.

Perelló, J. A., Cox, D. P., Garamjav, D., Sanjdorj, S., Diakov, S. A., Schissel, D. J., Munkhbat, T.-O., and Uyun, G., 2001, Oyu Tolgoi, Mongolia: Siluro-Devonian porphyry Cu-Au-(Mo) and high-sulfidation Cu mineralization with a Cretaceous chalcocite blanket: Economic Geology, v. 96, p. 1407-1428.

Philex, M. C., 2011, Annual Report, Annual Report: Metro Manila, Philippines, 140 p.

Philippot, P., and Selverstone, J., 1991, Trace-element-rich brines in eclogitic veins: implications for fluid composition and transport during subduction: Contributions to Mineralogy and Petrology, v. 106, p. 417-430.

PHIVOLCS, 2014, Volcanic arcs in the Philippines, 2014.

Pinet, N., and Stephan, J. F., 1988, Polyphased tectonic history in a wrench faulting region: in Abstracts International, Symposium on Geodynamic Evolution of the Eastern Eurasian Margin: Paris, Université Pierre et Marie Curie, p. 89.

Pinto, R. M., 2002, Transición de un sistema de alta sulfuración a un sistema porfirico de alto nivel en Kupfertal, distrito minero de Yanacocha, Cajamarca, Perú: Unpublished thesis, Universidad Nacional Mayor de San Marcos, 89 p.

Pisiak, L. K., Canil, D., Lacourse, T., Plouffe, A., and Ferbey, T., 2017, Magnetite as an Indicator Mineral in the Exploration of Porphyry Deposits: A Case Study in Till near the Mount Polley Cu-Au Deposit, British Columbia, Canada: ECONOMIC GEOLOGY, v. 112, p. 919-940.

Plank, T., and Langmuir, C. H., 1988, An evaluation of the global variations in the major element chemistry of arc basalts: Earth and Planetary Science Letters, v. 90, p. 349-370.

Poli, S., and Schmidt, M. W., 2002, Petrology of subducted slabs: Annual Review of Earth and Planetary Sciences, v. 30, p. 207-235.

Polve, M., Maury, R. C., Jego, S., Bellon, H., Margoum, A., Yumul, G. P., Payot, B. D., Tamayo, R. A., and Cotten, J., 2007, Temporal geochemical evolution of Neogene magmatism in the Baguio gold-copper mining district (northern Luzon, Philippines): Resource Geology, v. 57, p. 197-218.

Porter, J., Schroeder, K., and Austin, G., 2012, Geology of the Bingham Canyon porphyry Cu-Mo-Au deposit, Utah: Society of Economic Geologists Special Publication, v. 16, p. 127-146.

Porth, H., Muller, C., and von Daniels, C., 1989, The Sedimentary Formations of the Visayan Basin, Philippines: Geologisches Jahrbuch, v. 70, p. 29-88.

Prokopowicz-Prigogine, M., 1989, Reactivity of a silica network of glass: Molecular mechanism of the dissolution of a silica network in aqueous HF–HCl solutions: Glastechnische Berichte, v. 62, p. 249-255.

Proksche, H., Nagorsen, G., and Ross, D., 1992, The influence of NH_4F on the etch rates of undoped SiO_2 in buffered oxide etch: Journal of the Electrochemical Society, v. 139, p. 521-524.

Pubellier, M., Ego, F., Chamot-Rooke, N., and Rangin, C., 2003, The building of pericratonic mountain ranges: Structural and kinematic constraints applied to GIS-based reconstructions of SE Asia: Bulletin of the Geological Society of France, v. 174, p. 561-584.

Pubellier, M., Quebral, R., Rangin, C., Deffontaines, B., Muller, C., and Butterlin, J., 1991, The Mindanao collision zone: A soft collision event within a continuous Neogene strike-slip setting: Journal of South East Asian Earth Sciences, v. 6, p. 239-248.

Quebral, R., Pubellier, M., and Rangin, C., 1996, The onset of movement on the Philippine fault in eastern Mindanao: A transition from a collision to strike slip environment: Tectonics, v. 15, p. 713-726.

Querubin, C. L., and Yumul, G. P., 2001, Stratigraphic correlation of the Malusok volcanogenic massive sulfide deposits, Southern Mindanao, Philippines: Resource Geology v. 51, p. 135-143.

R.E., S., and C.N., A., 1987, Woodhouseite and svanbergite in hydrothermal ore deposits: products of apatite destruction during advanced argillic alteration: Canadian Mineralogist, v. 25, p. 201-211.

Rae, A., 2002, Alteration systematics and mineralising potential of the Palinpinon geothermal field, Negros Island, Philippines: Unpublished PhD thesis, University of Tasmania, 243 p.

Rae, A., Cooke, D. R., and Brown, K. L., 2011, The trace metal chemistry of deep geothermal water, Palinpinon geothermal field, Negros island, Philippines: Implications for precious metal deposition in epithermal gold deposits: ECONOMIC GEOLOGY, v. 106, p. 1425–1446.

Rae, A., Cooke, D. R., Phillips, D., Yeats, C., Ryan, C., and Hermoso, D., 2003, Spatial and temporal relationships between hydrothermal alteration assemblages at the Palinpinon geothermal field, Philippines—implications for porphyry and epithermal ore deposits: Society of Economic Geologists Special Publication v. 10, p. 223–246.

Rae, A., Cooke, D. R., Phillips, D., and Zaide-Delfin, M., 2004, The nature of magmatism at Palinpinon geothermal field, Negros Island, Philippines: Implications for geothermal activity and regional tectonics: Journal of Volcanology and Geothermal Research, v. 129, p. 321–342.

Rainbow, A., Clark, A., Kyser, K., Gaboury, F., and Hodgson, J., 2005, The Pierina epithermal Au–Ag deposit, Ancash, Peru: paragenetic relationships, alunite textures, and stable-isotope geochemistry: Chemical Geology, v. 215, p. 235-252.

Ramos, N. T., Dimalanta, C. B., Besana, G. M., Tamayo, R. A., Yumul, G. P., and Maglambayan, V. B., 2005, Seismotectonic relations to the arc-continent convergence in central Philippines: Resource Geology, v. 55, p. 199-206.

Rangin, C., 1989, The Sulu Sea, a back-arc basin setting within a Neogene collision zone: Tectonophysics, v. 161, p. 119-141.

Rangin, C., 1991, The Philippine mobile belt: Journal of South East Asian Earth Sciences, v. 6, p. 209-220.

Rangin, C., Jolivet, L., and Pubellier, M., 1990, A simple model for the tectonic evolution of southeast Asia and Indonesian region for the past 43 My: Bulletin of the Geological Society of France, v. 8, p. 889-905.

Rangin, C., and Silver, E., 1990, Geological setting of the Celebes and Sulu seas, Ocean Drilling Program, 124: College Station, TX, p. 35-42.

Rapp, J. F., Klemme, S., Butler, I. B., and Harley, S. L., 2010, Extremely high solubility of rutile in chloride and fluoride-bearing metamorphic fluids: An experimental investigation: Geology, v. 38, p. 323-326.

Reyes, A. G., 1990, Petrology of active Philippine geothermal systems and the application of alteration mineralogy in geothermal exploration and development: Journal of Volcanology and Geothermal Research, v. 43, p. 279-309.

Richards, J. P., 2003, Tectono-magmatic precursors for porphyry Cu-(Mo-Au) deposit formation: Economic Geology, v. 98, p. 1515-1533.

Richards, J. P., 2011, Magmatic to hydrothermal metal fluxes in convergent and collided margins: Ore Geology Reviews, v. 40, p. 1-26.

Richards, J. P., and Kerrich, R., 2007, Adakite-like rocks: Their diverse origins and questionable role in metallogenesis: ECONOMIC GEOLOGY, v. 102, p. 537-576.

Richards, J. P., Spell, T., Rameh, E., Razique, A., and Fletcher, T., 2012, High Sr/Y magmas reflect arc maturity, high magmatic water content, and porphyry Cu±Mo±Au potential: Examples from the Tethyan arcs of Central and Eastern Iran and Western Pakistan: ECONOMIC GEOLOGY, v. 107, p. 295-323.

Riegler, T., Quirt, D., and Beaufort, D., 2016, Spatial distribution and compositional variation of APS minerals related to uranium deposits in the Kiggavik-Andrew Lake structural trend, Nunavut, Canada: Mineralium Deposita, v. 51, p. 219-236.

Rimstidt, J. D., 1997, Quartz solubility at low temperatures: Geochimica et Cosmochimica Acta, v. 61, p. 2553-2558.

Ringwood, A. E., 1977, Petrogenesis in island arc systems, in Talwani, M., and Pitman, W. C., eds., Island arcs, deep sea trenches, and back arc basins, American Geophysical Union [Maurice Ewing Series I], p. 311-324.

Rivera, S. L., Alcota, H., Proffett, J. M., Díaz, J., Leiva, G., and Vergara, M., 2012, Update of the geologic setting and porphyry Cu-Mo deposits of the Chuquicamata district, Northern Chile: Society of Economic Geologists Special Publication, v. 19, p. 19-54.

Rohrlach, B. D., 2002, Tectonic evolution, petrochemistry, geochronology and palaeohydrology of the Tampakan porphyry and high sulphidation epithermal Cu-Au deposit Mindanao, Philippines: Unpublished Manuscript thesis, Australian National University, 807 p.

Rohrlach, B. D., and Loucks, R. R., 2005, Multi-million-year cyclic ramp-up of volatiles in a lower crustal magma reservoir trapped below the Tampakan copper-gold deposit by Mio-Pliocene crustal compression in the Southern Philippines, in Porter, T. M., ed., Super Porphyry Copper and Gold Deposits: A Global Perspective 2, PGC Publishing, p. 369-407.

Rollinson, H., 1993, Using geochemical data: Evaluation, presentation, interpretation: Harlow, UK, Longman, 352 p.

Rusk, B. G., Lowers, H. A., and Reed, M. H., 2008, Trace elements in hydrothermal quartz: Relationships to cathodoluminescent textures and insights into vein formation: Geology, v. 36, p. 547-550.

Rutland, R. W. R., 1968, A tectonic study of part of the Philippine fault zone: Geological Society of London Quarterly Journal, v. 123, p. 295-325.

Rye, R., Bethke, P., and Wasserman, M., 1991, The stable isotope geochemistry of acid sulfate alteration: ECONOMIC GEOLOGY, v. 87, p. 225-262.

Sack, P. J., Berry, R. F., Meffre, S., Falloon, T. J., Gemmell, J. B., and Friedman, R. M., 2011, In situ location and U-Pb dating of small zircon grains in igneous rocks using laser ablation-inductively coupled plasma-quadrupole mass spectrometry: Geochemistry, Geophysics, Geosystems, v. 12, p. 1-23.

Sajona, F. G., Bellon, H., Maury, R. C., Pubellier, M., Cotten, J., and Rangin, C., 1994, Magmatic response to abrupt changes in geodynamic settings: Pliocene-Quaternary calc-alkaline and Nb-enriched lavas from Mindanao (Philippines): Tectonophysics, v. 237, p. 47-72.

Sajona, F. G., Izawa, E., Motomura, Y., Imai, A., Sakakibara, H., and Watanabe, K., 2002, Victoria carbonate-base metal gold deposit and its significance in the Mankayan mineral district, Luzon, Philippines: Resource Geology, v. 52.

Sajona, F. G., Maury, R., Pubellier, M., Leterier, J., Bellon, H., and Cotten, J., 2000a, Magmatic source enrichment by slab-derived melts in a young post-collision setting, central Mindanao (Philippines): Lithos, v. 54, p. 173-206.

Sajona, F. G., and Maury, R. C., 1998, Association of adakites with gold and copper mineralization in the Philippines: Comptes Rendus de l'Académie des Sciences, Sciences de la Terre et Des Planètes, v. 326, p. 27–34.

Sajona, F. G., Maury, R. C., Bellon, H., Cotten, J., Defant, M. J., and Pubellier, M., 1993, Initiation of subduction and the generation of slab melts in Western and Eastern Mindanao, Philippines: Geology, v. 21, p. 1007-1010.

Sajona, F. G., Maury, R. C., Prouteau, G., Cotten, J., Schiano, P., Bellon, H., and Fontaine, L., 2000b, Slab melt as metasomatic agent in island arc magma mantle sources, Negros and Batan (Philippines): Island Arc, v. 9, p. 472-486.

Sandwell, D. T., and Smith, W. H. F., 1997, Marine gravity anomaly from Geosat and ERS satellite altimetry: Journal of Geophysical Research, v. 102, p. 10039-10054.

Santos, E. A., and Velasquez, J., 1987, Geology and tectonic evolution of Southwest Negros: RP-Japan Mineral Exploration. Project report, 80 p.

Saunders, J., 1994, Silica and gold textures in bonanza ores of the sleeper deposit, Humboldt County, Nevada: evidence for colloids and implications for epithermal ore-forming processes: ECONOMIC GEOLOGY, v. 89, p. 628-638.

Scambelluri, M., and Philippot, P., 2001, Deep fluids in subduction zones: Lithos, v. 55, p. 213-227.

Schmidt, M. W., and Poli, S., 1998, Experimentally based water budgets for dehydrating slabs and consequences for arc magma generation: Earth and Planetary Science Letters, v. 163, p. 361-379.

Seedorff, E., Dilles, J. H., Proffett, J. M., Jr., and Einaudi, M. T., 2005, Porphyry deposits: Characteristics and origin of hypogene features, in Hedenquist, J. W., Thompson, J. F. H., Goldfarb, R. J., and Richards, J. P., eds., Economic Geology One Hundredth Anniversary Volume1905-2005: Littleton, CO, Society of Economic Geologists, p. 251-298.

Sherlock, R. L., and Barrett, T. J., 2004, Geology and volcanic stratigraphy of the Canatuan and Malusok volcanogenic massive sulfide deposits, southwestern Mindanao, Philippines: Mineralium Deposita, v. 39, p. 1-20.

Shinohara, H., Hirabayashi, J., Nogami, K., and Iguchi, M., 2011, Evolution of volcanic gas composition during repeated culmination of volcanic activity at Kuchinoerabujima volcano, Japan: Journal of Volcanology and Geothermal Research, v. 202, p. 107-116.

Shinohara, H., Ohba, T., Kazahaya, K., and Takahashi, H., 2008, Origin of volcanic gases discharging from a cooling lava dome of Unzen volcano, Japan: Journal of Volcanology and Geothermal Research, v. 175, p. 133-140.

Sillitoe, R. H., 1985, Ore-related breccias in volcanoplutonic arcs: Economic Geology, v. 80, p. 1467-1514.

Sillitoe, R. H., 1999, Styles of high-sulphidation gold, silver and copper mineralization in the porphyry and epithermal environments, in Weber, G., ed., Pacrim '99 Congress: Bali, Indonesia, Weber, G, p. 29-44.

Sillitoe, R. H., 2010, Porphyry copper systems: ECONOMIC GEOLOGY, v. 105, p. 3-41.

Sillitoe, R. H., and Gappe, I. M., 1984, Philippine porphyry copper deposits: geologic setting and characteristics: Committee for Co-ordination of Joint Prospecting for Mineral Resources in Asian Offshore Areas (CCOP), v. 14, p. 89.

Sillitoe, R. H., Tolman, J., and Kerkvoort, G., 2013, Geology of the Caspiche porphyry gold-copper deposit, Maricunga belt, northern Chile: ECONOMIC GEOLOGY, v. 108, p. 585-604.

Simmons, S., White, N. C., and John, D., 2005, Geological characteristics of epithermal precious and base metal deposits: ECONOMIC GEOLOGY 100th Anniversary Volume, p. 485–522.

Sinclair, W. D., 2007, Porphyry deposits, in Goodfellow, W. D., ed., Mineral Deposits of Canada: A Synthesis of Major Deposit-Types, District Metallogeny, the Evolution of Geological Provinces, and Exploration Methods, 5. Geological Association of Canada, Mineral Deposits Division, Special Publication, p. 223-243.

Singer, D.A., Berger, V.I., and Moring, B.C., 2008, Porphyry copper deposits of the world: Database and grade and tonnage models: U.S. Geological Survey Open-File Report 2008−1155 (http://pubs.usgs.gov/of/2008/1155).

Slama, J., Kosler, J., Condon, D. J., Crowley, J. L., Gerdes, A., Hanchar, J. M., Horstwood, M. S. A., Morris, G. A., Nasdala, L., Norberg, N., Schaltegger, U., Schoene, B., Tubrett, M. N., and Whitehouse, M. J., 2008, Plesovice zircon - A new natural reference material for U-Pb and Hf isotopic microanalysis: Chemical Geology, v. 249, p. 1-35.

Solidum, R. U., 2002, Geochemistry of volcanic arc lava in Central and Southern Philippines: Contribution from the subducted slab: Unpublished PhD thesis, University of California, San Diego, 250 p.

Solidum, R. U., Castillo, P. R., and Hawkins, J. W., 2003, Geochemistry of lavas from Negros Arc, west central Philippines: Insights into the contribution from the subducting slab: Geochemistry, geophysics, geosystems, v. 4, p. 1-26.

Spierings, G. A. C. M., 1993, Wet chemical etching of silicate glasses in hydrofluoric acid based solutions: Journal of Materials Science, v. 28, p. 6261-6273.

Spierings, G. A. C. M., and van Dijk, J., 1987, The dissolution of Na_2O–MgO–CaO–SiO_2 glass in aqueous HF solutions: Journal of Materials Science, v. 22, p. 1869-1874.

Steven, T. A., and Ratte, J. C., 1960, Geology and ore deposits of the Summitville district San Juan Mountains, Colorado, in Nolan, T. B., ed.: Washington, United States Geological Survey, p. 79.

Stoffregen, R. E., and Alpers, C. N., 1987, Woodhouseite and svanbergite in hydrothermal ore deposits: Products of apatite destruction during advanced argillic alteration: Canadian Mineralogist, v. 25, p. 201-211.

Subang, L. L., 2011, IP-Resistivity and soil geochem survey completion report: Makati City, Philippines, Freeport-McMoRan Exploration Corporation, 21 p.

Subang, L. L., Taningco, R., Briola, O. A., Arellano, I. L., Arcilla, J. G., Domingo, H. G., Tagura, F. C., Celiz, M. A., and Estrada, N. A., 2009, Geology of the Bantug lithocap Negros Island, Philippines: Makati City, Philippines, Freeport-McMoRan Exploration Corporation, p. 23.

Tamayo, R. A., 2001, Caractérisations pétrologique et géochimique, origines et évolutions géodynamiques des ophiolites des Philippines: Unpublished PhD thesis, Universite Bretagne Occidentale, 318 p.

Tamayo, R. A., Maury, R. C., Yumul, G. P., Polve, M., Cotten, J., Dimalanta, C. B., and Olaguera, F. O., 2004, Subduction-related magmatic imprint of most Philippine ophiolites: implications on the early geodynamic evolution of the Philippine archipelago: Bulletin de la Société Géologique de France, v. 175, p. 443-460.

Tamayo, R. A., Yumul, G. P., Maury, R. C., Bellon, H., Cotten, J., Polve, M., Juteau, T., and Querubin, C., 2000, Complex origin for the southwestern Zamboanga metamorphic basement complex, western Mindanao, Philippines: Island Arc, v. 9, p. 638-652.

Taningco, R., 2002, Potential for high-sulfidation mineralisation in the Bantug area, Negros, Philippines: Metro Manila, Philippines, Freeport-McMoRan, p. 20.

Tanis, E. A., Simon, A., Zhang, Y., Chow, P., Xiao, Y., Hanchar, J. M., Tschauner, O., and Shen, G., 2016, Rutile solubility in NaF–NaCl–KCl-bearing aqueous fluids at 0.5–2.79 GPa and 250–650°C: Geochimica et Cosmochimica Acta, v. 177, p. 170-181.

Taran, Y., Bernard, A., Gavilanes, J. C., Lunezheva, E., Cortés, A., and Armienta, M. A., 2001, Chemistry and mineralogy of high-temperature gas discharges from Colima volcano, Mexico. Implications for magmatic gas-atmosphere interaction: Journal of Volcanology and Geothermal Research, v. 108, p. 245-264.

Taran, Y., Gavilanes, J. C., and Cortés, A., 2002, Chemical and isotopic composition of fumarolic gases and the SO2 flux from Volcán de Colima, México, between the 1994 and 1998 eruptions: Journal of Volcanology and Geothermal Research, v. 117, p. 105-119.

Taran, Y., Pilipenko, V. P., Rozhkov, A. M., and Vakin, E. A., 1992, A geochemical model for fumaroles of the Mutnovsky volcano, Kamchatka, USSR: Journal of Volcanology and Geothermal Research, v. 49, p. 2690-283.

Taran, Y., Rozhkov, A. M., Serafimova, E. K., and Esikov, A. D., 1991, Chemical and isotopic composition of magmatic gases from the 1988 eruption of Klyuchevskoy volcano, Kamchatka: Journal of Volcanology and Geothermal Research, v. 46, p. 255-263.

Taylor, R., 2009, Ore Textures: recognition and interpretation, Springer-Verlag Berlin Heidelberg, 288 p.

Teal, L., and Benavides, A., 2010, History and geologic overview of the Yanacocha mining district, Cajamarca, Peru: ECONOMIC GEOLOGY, v. 105, p. 1173-1190.

Tebar, H. J., Hermoso, D. Z., and Ramos, R. C., 1984, Geology of north Okoy geothermal prospect, Southern Negros geothermal field, Negros Oriental: PNOC-EDC Internal Report.

Teng, L. S., 1990, Geotectonic evolution of late Cenozoic arc-continent collision in Taiwan: Tectonophysics, v. 183, p. 57-76.

The World Bank, 2014, Philippines, http://www.worldbank.org/en/country/philippines.

Thiéblemont, D., Stein, G., and Lescuyer, J.-L., 1997, Gisements épithermaux et porphyriques: la connexion adakite: C.R. Acad. Sci. Paris, Sciences de la terre et des planètes/Earth and Planetary Sciences, v. 325, p. 103-109.

Thomas, J. B., Watson, E. B., Spear, F. S., Shemella, P. T., Nayak, S. K., and Lanzirotti, A., 2010, TitaniQ under pressure: the effect of pressure and temperature on the solubility of Ti in quartz: Contributions to Mineralogy and Petrology, v. 160, p. 743-759.

Thomas, J. B., Watson, E. B., Spear, F. S., and Wark, D. A., 2015, TitaniQ recrystallized: experimental confirmation of the original Ti-in-quartz calibrations: Contributions to Mineralogy and Petrology, v. 169, p. 26-42.

Thompson, A. J. B., and Thompson, J. F. H., 1996, Atlas of alteration: A field and petrographic guide to hydrothermal alteration minerals: St. John's, Newfoundland, Canada, Mineral Deposits Division, Geological Association of Canada, 128 p.

Titley, S. R., and Beane, R. E., 1981, Porphyry copper deposits. Part I. Geologic settings, petrology, and tectogenesis; Part II. Hydrothermal alteration and mineralization, in Skinner, B. J., ed., Economic Geology 75th Anniversary Volume, p. 214-269.

Toro, J. C., Ortúzar, J., Zamorano, J., Cuadra, P., Hermosilla, J., and Spröhnle, C., 2012, Protracted magmatic-hydrothermal history of the Río Blanco-Los Bronces district, Central Chile: Development of world's greatest known concentration of copper, in Hedenquist, J. W., Harris, M., and Camus, F., eds., Geology and Genesis of Major Copper Deposits and Districts of the World: A Tribute to Richard H. Sillitoe, 16. Special Publications of the Society of Economic Geologists: Lancaster, PA, USA, Special Publications of the Society of Economic Geologists, p. 105-126.

Tosdal, R. M., 1996, Geological and structural setting of the Tantahuatay volcanic field and associated high-sulfidation Cu-Au mineralization, northern Peru: Lima, Peru, Compañía Minera Coimolache S.A., p. 25.

Tropper, P., Manning, C. E., and Harlov, D. E., 2013, Experimental determination of CePO4 and YPO4 solubilities in H2O–NaF at 800°C and 1 GPa: implications for rare earth element transport in high-grade metamorphic fluids: Geofluids, v. 13, p. 372-380.

United Nations Development Programme, 1987, Geology and hydrothermal alteration of the Amlan-Okoy River, Pamplona and Ayungon areas, Eastern Negros, Strengthening The Government Capability In Gold Exploration: Manila, Philippines, p. 60.

United States Geological Survey, 2015, Earthquake hazard program, https://earthquake.usgs.gov/earthquakes/search/.

Valsami-Jones, E., Ragnarsdottir, K. V., Putnis, A., and Cresser, G., 1998, The dissolution of apatite in the presence of aqueous cations at pH 2–7: Chemical Geology, v. 151, p. 215-233.

Vasquez, J. C., 1982, Supergene mineralization at the Basay porphyry copper deposits, Negros Island, Philippines: Seminar on developing new open pit mines in the Philippines, University of the Philippines, p. 17-26.

Vidal, C. E., Noble, D.C., Harvey, B., and Quiroz, A., 1997, Geology and mineral deposits of the Cajamarca area, northern Peru; Guidebook Series 1: IX Congreso Peruano de Geología: Lima, Peru, Sociedad Geológica del Perú, 52 p.

von Bidersee, H., and Pichler, H., 1995, The Canlaon and its neighbouring volcanoes in the Negros belt, Philippines: Journal of Southeast Asian Earth Sciences, v. 11, p. 111-123.

Walther, H. W., Forster, H., Harre, W., Kreuzer, H., Lenz, H., Muller, P., and Raschka, H., 1981, Early Cretaceous porphyry copper mineralization on Cebu Island, Philippines, dated with K-Ar and Rb-Sr methods: Geol. Jb., v. 48, p. 21-35.

Wark, D. A., and Watson, E. B., 2006, TitaniQ: a titanium-in-quartz geothermometer: Contributions to Mineralogy and Petrology, v. 152, p. 743-754.

Waters, P. J., Cooke, D. R., Gonzales, R. I., and Phillips, D., 2011, Porphyry and epithermal deposits and 40Ar/39Ar geochronology of the Baguio district, Philippines: ECONOMIC GEOLOGY, v. 106, p. 1335–1363.

Weber, C., and Knittel, U., 1990, Petrology and petrogenesis of the volcanic rocks on the eastern flank of Mt. Malinao, Bicol arc (Southern Luzon, Philippines): Journal of Southeast Asian Earth Sciences, v. 4, p. 267-280.

White, N. C., 1991, High sulfidation epithermal gold deposits: Characteristics and a model for their origin: Geological Survey of Japan Report, v. 277, p. 9-20.

Wiedenbeck, M., Alle, P., Corfu, F., Griffin, W. L., Meier, M., Oberli, F., Vonquadt, A., Roddick, J. C., and Speigel, W., 1995, Three natural zircon standards for U-Th-Pb, Lu-Hf, trace-element and REE analyses: Geostandards Newsletter, v. 19, p. 1-23.

Wilkinson, J. J., Chang, Z., Cooke, D. R., Baker, M. J., Wilkinson, C. C., Inglis, S., Chen, H., and Gemmell, J. B., 2015, The chlorite proximitor: A new tool for detecting porphyry ore deposits: Journal of Geochemical Exploration, v. 152, p. 10-26.

Williams, N. C., and Davidson, G. J., 2004, Possible submarine advanced argillic alteration at the Basin Lake prospect, western Tasmania, Australia: ECONOMIC GEOLOGY, v. 99, p. 16.

Williams, T. J., Candela, P. A., and Piccoli, P. M., 1997, Hydrogen-alkali exchange between silicate melts and two-phase aqueous mixtures: An experimental investigation: Contributions to Mineralogy and Petrology, v. 128, p. 114-126.

Wilson, M., 1989, Igneous petrogenesis: A global tectonic approach: Unwin Hyman, London, p. 466.

Winchester, J. A., and Floyd, P. A., 1977, Geochemical discrimination of different magma series and their differentiation products using immobile elements: Chemical Geology, v. 20, p. 325-343.

Wolfe, J. A., 1981, Philippine geochronology: Journal of the Geological Society of the Philippines, v. 35, p. 1-30.

Wolfe, R. C., and Cooke, D. R., 2011, Geology of the Didipio region and genesis of the Dinkidi alkalic porphyry Cu-Au deposit and related pegmatites, northern Luzon, Philippines: ECONOMIC GEOLOGY, v. 106, p. 1279–1315.

Wolff-Boenisch, D., Gislason, S. R., and Oelkers, E. H., 2004, The effect of fluoride on the dissolution rates of natural glasses at pH 4 and 25°C: Geochimica et Cosmochimica Acta, v. 68, p. 4571-4582.

Yang, T. F., Lee, T., Chen, C.-H., Cheng, S.-N., Knittel, U., Punongbayan, R. S., and Rasdas, A. R., 1996, A double island arc between Taiwan and Luzon: consequence of ridge subduction.: Tectonophysics, v. 258, p. 85-101.

Yumul, G. P., Balce, G. R., Dimalanta, C. B., and Datuin, R. T., 1997, Distribution, geochemistry and mineralization potentials of Philippine ophiolite and ophiolitic sequences: Ofioliti, v. 22, p. 47-56.

Yumul, G. P., Dimalanta, C. B., Maglambayan, V. B., and Marquez, E. J., 2008, Tectonic setting of a composite terrane: A review of the Philippine island arc system: Geosciences Journal, v. 12, p. 7-17.

Yumul, G. P., Dimalanta, C. B., Marquez, E. J., and Queaño, K. L., 2007, Cretaceous geology of the Philippines: A tectonic perspective, in Y-I., L., I-S., P., D-K., C., M., H., and Y-U., L., eds., Paleoclimates in Asia during the Cretaceous: Their variations, causes, and biotic and environmental responses. IGCP Project 507 Contribution No. 1, International Geoscience Programme Project 507: Seoul, p. 143-154.

Yumul, G. P., Dimalanta, C. B., and Tamayo, R. A., 2005, Indenter-tectonics in the Philippines: Example from the Palawan microcontinental block – Philippine mobile belt collision: Resource Geology, v. 55, p. 189-198.

Yumul, G. P., Dimalanta, C. B., Tamayo, R. A., and Barretto, J. L., 2000, Contrasting morphological trends of islands in Central Philippines: Speculation on their origin: Island Arc, v. 9, p. 627-637.

Yumul, G. P., Dimalanta, C. B., Tamayo, R. A., and Bellon, H., 2003, Silicic arc volcanism in Central Luzon, Philippines: Characterization of its space, time and geochemical relationship: Island Arc, v. 12, p. 207-218.

Yumul, G. P., Dimalanta, C. B., Tamayo, R. A., and Maury, R. C., 2003, Collision, subduction and accretion events in the Philippines: A synthesis: Island Arc, v. 12, p. 77-91.

Yumul, G. P., Dimalanta, C. B., Tamayo, R. A., Maury, R. C., Bellon, H., Polve, M., Maglambayan, V. B., Querubin, C. L., and Cotten, J., 2004, Geology of the Zamboanga Peninsula, Mindanao, Philippines: An enigmatic South China continental fragment?: Geological Society London Special Publications p. 289-312.

Zelenski, M., and Taran, Y., 2011, Geochemistry of volcanic and hydrothermal gases of Mutnovsky volcano, Kamchatka: evidence for mantle, slab and atmosphere contributions to fluids of a typical arc volcano: Bulletin of Volcanology, v. 73, p. 373-394.